Proceedings of
Geotechnical Earthquake Engineering Satellite Conference
Osaka, Japan, 10 September 2005

PERFORMANCE BASED DESIGN IN EARTHQUAKE GEOTECHNICAL ENGINEERING: CONCEPTS AND RESEARCH

Prepared by TC4 Committee, ISSMGE

Proceedings of
Geotechnical Earthquake Engineering Satellite Conference
Osaka, Japan, 10 September 2005

PERFORMANCE BASED DESIGN IN EARTHQUAKE GEOTECHNICAL ENGINEERING: CONCEPTS AND RESEARCH

Prepared by TC4 Committee, ISSMGE

PERFORMANCE BASED DESIGN IN EARTHQUAKE GEOTECHNICAL ENGINEERING: CONCEPTS AND SUPPORTING RESEARCH

Proceedings of Earthquake Geotechnical Engineering Satellite Conference,
Osaka, Japan, 10 September 2005

Sponsored by
TC4, Earthquake Geotechnical Engineering, International Society for Soil Mechanics and Geotechnical Engineering

Co-Sponsored by
ATC3, Geotechnology for Natural Hazard, Asian Society for Soil Mechanics and Geotechnical Engineering
MEXT 21st Century COE Program for Disaster Prevention Research Institute (DPRI), Kyoto University
Graduate School of Engineering, Osaka University

Published by
The Japanese Geotechnical Society
Sengoku 4-28-2, Bunkyo-ku, Tokyo 112-0011, Japan

ISBN 4-88644-813-5

Printed by WACO Co., Ltd.

CONTENTS

CONFERENCE PAPERS

Performance Based Design

Recent Earthquakes

Liquefaction, Liquefaction-induced Flow and Remediation

Response of Ground and Soil-structure Interaction

Pile and Underground Structures

Seismic Slope Instability

Seismic Risk Reduction

Preface

This satellite conference, held in conjunction with the 16th International Conference of the Society for Soil Mechanics and Geotechnical Engineering (ISSMGE) is one of the approaches used by TC-4, the Committee on Earthquake Geotechnical Engineering of ISSMGE, to transfer the results of research to engineering practice and to promote the development of earthquake geotechnical engineering.

The themes of these conferences reflect the current concerns and interests of TC-4. On this occasion the conference theme is performance based design which has been the focus of TC-4 efforts over the last 4 years.

The papers submitted to the conference reflect current thinking on performance based design and also present the research, and the analytical, laboratory and field studies needed to advance the development of performance based design in earthquake geotechnical engineering.

The TC-4 Committee hopes that this conference and the workshop on performance based design held as part of the 16th international Conference on Soil Mechanics and Geotechnical Engineering will stimulate the further development of performance based design and its application in geotechnical earthquake engineering practice.

On behalf of the Organizing Committee and TC-4, I wish to express my appreciation to the hard working members of TC-4, especially to the Secretary, Professor Nozomu Yoshida of Tohoku-Gakuin University. The tremendous help received from members of the Asian Technical Committee on Geotechnical Natural Hazards (ATC3), chaired by Professor T. Kokusho of Chuo University, is gratefully acknowledged. Special thanks are due to Professor S. Iai of Kyoto University for facilitating financial assistance in staging this conference and to Professor Kenji Ishihara of then Chuo University for his advice and encouragement during the development of the conference.

W. D. Liam Finn
Chairman TC-4
University of British Columbia
Canada
finn@civil.ubc.ca

INTERNATIONAL ADVISORY COMMITTEE

W. D. Liam Finn (Conference Chairman, Canada)

J. Alpanes, Spain
J. P. Bardet, USA
R. Blasquez, Spain
J. Bray, USA
J. J. Bommer, UK
T. Crespellani, Italy
R. Dobry, USA
A. Elgamal, USA
E. Faccioli, Italy
S. Frydman, Israel
J. A. Hurtoda, Peru
V. A. Ilyichev, Russia
A. Kaynia, Norway
S. Kramer, USA
S. Mora, Costa Rica
F. Nadim, Norway
K. Ozaydin, Turkey
A. Pecker, France
K. Pitilakis, Greece
P. Robertson, Canada
S. K. Sarma,UK
R. Seed, USA
K. Stokoe II, USA
K. Talaganov, Macedonia
I. Towhata, Japan
K. Tokimatsu, Japan
W. Van Impe, Belgium
F. Vinale, Italy
S. Yasuda, Japan
T. L. Youd, USA
S. Zlatovic, Croatia

A. Ansal, Turkey
P. Y. Bard, France
J. Berrill, New Zealand
A. Bodare, Sweden
G. Bouckovalas, Greece
C. H. Chen, Taiwan
V. Cuellar, Spain
T. Durgunoglu, Turkey
A. Erken, Turkey
N. Foged, Denmark
G. Gazetas, Greece
I. M. Idriss, USA
K. Ishihara, Japan
T. Kokusho, Japan
M. Maugeri, Italy
J. Muria, Venezuela
M. H. Naggar, Canada
Y. Ozkan, Turkey
M. Pender, New Zealand
S. Prakash, USA
M. Romo, Mexico
S. Savidis, Germany
R. S. Steedman, UK
J. A. Studer, Switzerland
J. Tohda, Japan
J. Troncoso, Chile
R. Verdugo, Chile
M. Vucetic, USA
N. Yoshida, Japan
Y. Zaczek, Belgium

LOCAL ORGANIZING COMMITTEE

Chairman: K. Tokida, Osaka

Y. Aoshima, Osaka
S. Iai, Kyoto
Y. Iwasaki, Osaka
M. Kanatani, Kashiwa
Y. Nabeshima, Osaka
K. Oda, Osaka
Y. Tanaka, Osaka
N. Yoshida, Tagajo

CONFERENCE PAPERS

Theoretical and experimental studies in EUROSEISTEST

K. Pitilakis[1], G. Manos[1], D. Raptakis[1], K. Makra[2], M. Manakou[1], P. Apostolidis[1], V. Terzi[1]
[1]*Department of Civil Engineering, Aristotle University of Thessaloniki, Greece*
[2] *Institute of Engineering Seismology and Earthquake Engineering, Thessaloniki, Greece*

Abstract

The European experimental site EUROSEISTEST (http://euroseis.civil.auth.gr) has been established in the epicentral area of the Thessaloniki 1978 Ms=6.5 earthquake in Greece, 10 years ago. The project has been funded by the European Commission - Directorate General for Research and Development and is a cooperation of many European Institutes under the responsibility of the Laboratory of Soil Mechanics, Foundation Engineering and Geotechnical Earthquake Engineering of the Aristotle University of Thessaloniki. It is dedicated to experimental and theoretical studies on site effects, soil and site characterization and soil-structure interaction phenomena. The aim is two fold; (a) to perform specific tests and studies in different and state of the art subjects and (b) to create a rigorous high quality data base.

In this paper the most important results of the experimental and theoretical studies performed are presented together with a briefly presentation of data and results used for the construction of the 3D model of the Mygdonian basin. Also presented the soil-structure interaction analysis conducted so far in the five infrastructure exist in the area.

Keywords— *Experimental site EUROSEISTEST, 3D structure, site effects, site characterization, soil-structure interaction*

INTRODUCTION

It has been found that local geology significantly modifies strong ground motion and controls the distribution of the earthquake damage pattern of an area during large earthquakes. Under this statement, the definition of the subsoil geometry and dynamic soil properties of a complex geological structure is of main importance for site effect analyses.

In EUROSEISTEST much insight has been gained from its operation concerning site effects. The detailed 2D geological structure across north – south direction of Mygdonian basin (Raptakis et al., 2000) has been used for 2D ground response analysis (Chavez-Garcia et al., 2000; Makra et al., 2005). The necessity to investigate site effects caused by its 3D geometry and the variations of its soil properties in three dimensions, lead to extending the 2D geometry into 3D. For the determination of the 3D structure of the basin, many geological, geotechnical, seismological and geophysical data have been used from previous made and new one survey that occurs in the region. The preliminary 3D geological structure proposed (Raptakis et al., 2005) describes the shape of the sedimentary basin. The 3D stratighrphy of the geological formations together in terms of its Vp and Vs velocities have been used in 2D theoretical site response analyses as well as in the interpretation of many earthquake recordings. Among the specific features of EUROSEISTEST research infrastructure are the two R/C model structures built and instrumented at the center of the valley where a deep down hole array is installed.

GEOLOGIC AND TECTONIC SETTING OF THE MYGDONIAN BASIN

Mygdonian basin belongs to the Serbomacedonian massif, one of the most seismotectonically active zones in Europe, which underlies the two major tectonic phenomena, observed in Northern Greece: the N-S extension of the Aegean Sea and the western termination of the north Anatolian strike-slip fault (Papazachos et al., 1979). The fault related to 1978 earthquake is the main structure that divides the western part of the basin and oriented approximately NW-SE.

In terms of geology (Figure 1), the basement of the basin consists mainly of gneiss, amphibolites and schists. The sediments which fill the basin can be classified into two main systems: the lower, the Promygdonian and the upper, the Mygdonian.

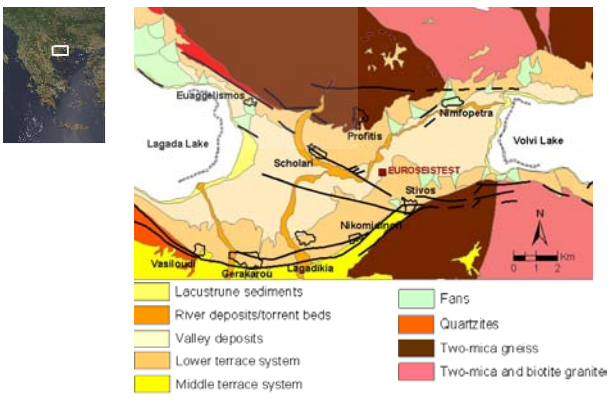

Figure. 1: Geological map of Mygdonian basin.

They consist of different fluviolacustrine, deltaic, lacustrine, lagoonal and estuarine deposits. Their thickness is changing spatially within the basin; at about 400m at the western of the basin, 200m at its central part, less than 200m at its eastern part.More details can be found on Raptakis et al., 2005.

CONSTRUCTION OF THE 3D STRUCTURE

As initial model for the 3D basin determination, has been used the 3D bedrock model of BRMG's, 1971 survey, which provided from refraction and electrical prospecting as well as deep boreholes (Figure 2). The scope of the survey which was conducted for water supply purposes was to map the aquifer sealing interface of the basin. This initial model has been updated using data from different surveys (mentioned below) and the preliminary 3D structure of the Mygdonian basin present here, was derived.

- Earthquake recordings, obtained from temporary and permanent arrays of seismographs and accelerographs, contributed to the 3D model providing spatial distribution of the resonant frequency and amplification factor of the basin geological formations.
- Microtremor recorded at single station. These measurements together with the dataset of earthquake recordings have been used for the spatial distribution of the resonant frequency of the basin geological formations.
- A dataset of electrical tomographies and soundings conducted at the edges of the basin, as the role of the basin's borders is important in wave propagation due to the generation of laterally propagated surface waves. These data used for the determination of the slope of the interface between sediments – bedrock. The results have been constrained with several boreholes and older electrical surveys (IGME, 2001).
- Two experiments have been performed along the east – west direction using underground big explosions. In these instruments have been deployed in a linear array of 8Km length approximately. The preliminary processing of these dataset which have been used in the preliminary 3D model, gave information on the Vp and Vs velocities of the basin's.
- Array microtremor measurements using SPAC method conducted at places where no information was available for the shear wave velocity of the geological formations. These measurements are in progress at the moment.
- An extensive geotechnical survey has been conducted comprising many sampling boreholes (20-200m), water table measurements, N-SPT, CPT tests, CH, DH, SASW, SWI, refraction tests and numerous laboratory conventional and dynamic soil testing (resonant column and cyclic triaxial).

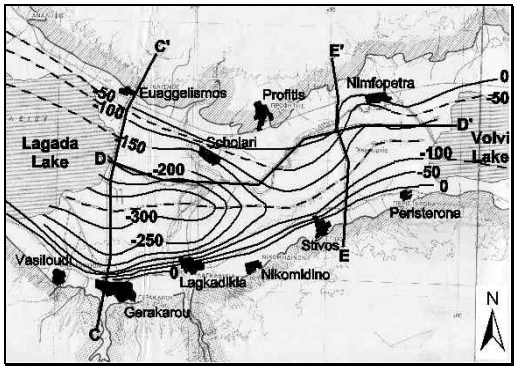

Figure 2: Contour map of the interface between bedrock - sediments in the region of Mygdonian basin obtained by BRGM during 1971. Contours countered relative to the sea level. The contour interval is 50 m. Lines CC', DD', and EE' indicate the long seismic refraction surveys performed (BRGM, 1971).

The distribution of the above measurements is depicted in Figure 3. More details about them and their processing can be found on Raptakis et al. (2005).

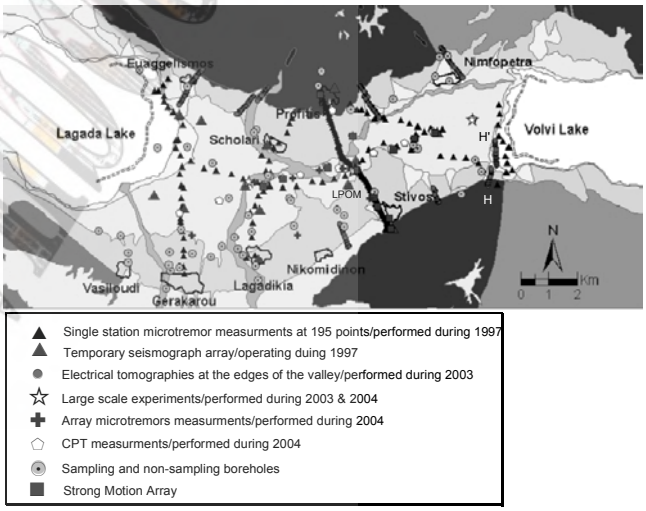

Figure 3. Location and type of different surveys, tests and measurements performed in the Mydgonian basin.

SYNTHESIS OF THE 3D STRUCTURE AND ITS 2D SITE RESPONSE

The construction of the 3D geological structure of the Mygdonian basin compiled and integrates different kinds of datasets, often heterogeneous to each other and despite the serious difficulties it was finally achieved. At this stage we present the two main interfaces describing the 3D image of the valley, i.e. between bedrock and sediments and between the two main sediment systems of the basin ProMygdonian and Mygdonian (Figure 4). The definition of a more detailed 3D structure with all soil formations together with their dynamic properties is under elaboration.

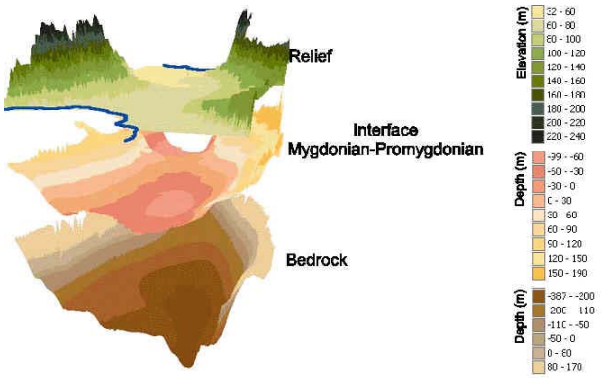

Figure 4. Preliminary 3D structure of the Mygdonian basin.

The construction of the 3D structure of the Euroseistest valley was based on the prior construction of several 2D cross sections as the one given in Figure 5 which is crossing NS the centre of the valley and coincides with one of the 2 main instrumented lines (the second being in EW direction). Dynamic soil properties of layers defined as A-G in Figure 5 are very well known.

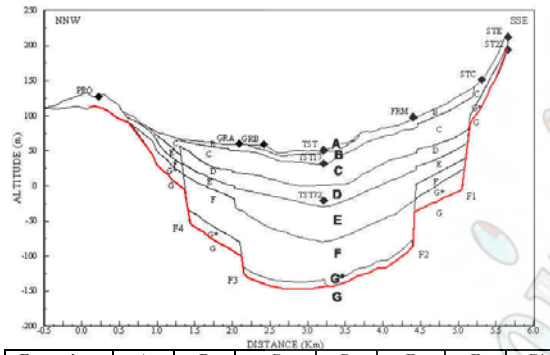

Formations	A	B	C	D	E	F	G*	G
Vp (m/s)	330	450	550	-	-	-	-	-
Vpw (m/s)	-	1500	1600	2000	2500	2600	3500	4500
Vs (m/s)	130	200	300	450	650	800	1250	2600
Qs	15	20	30	40	-	-	-	200
D (t/m^3)	2.05	2.15	2.0,2.15	2.10	2.15	2.20	2.50	2.60

Figure 5. EUROSEISTEST valley N-S cross-section (Raptakis et al., 2000).

PERMANENT ACCELEROMETRIC ARRAY

Figures 6 and 7 describe the layout of the surface and down-hole arrays deployed in Euroseistest.

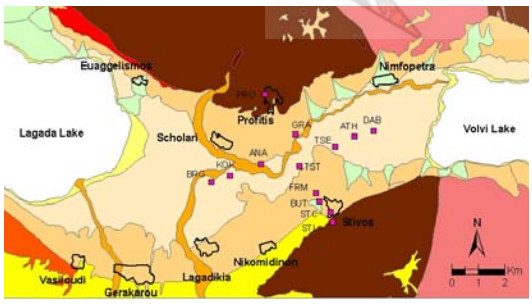

Figure 6. Surface accelerometer array.

All instruments are digital with common time and GPS. The data are retrieved remotely through modems to a central storage system. A number of about 60 seismic events have been recorded in the array.

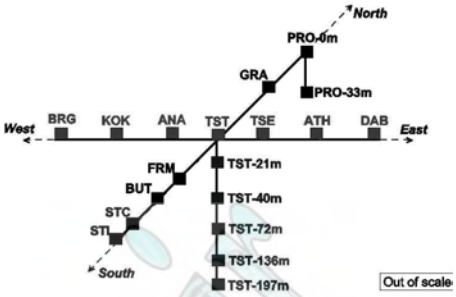

Figure 7. Vertical accelerometer arrays.

OVERVIEW OF EXPERIMENTAL AND THEORETICAL STUDIES

From the analysis of the experimental and theoretical 2D numerical analysis it is indicated that the largest amplitudes of motion are not related to the vertically propagating SH waves. It is clear from the synthetic seismograms (Figure 8) the wave-field in the valley is dominated by locally generated Love waves that converge to the center of the valley and thus, result to large amplitudes and a consequent increase of the duration (Chavez-Garcia et al., 2000); phenomena which are not seen outside the central part of valley.

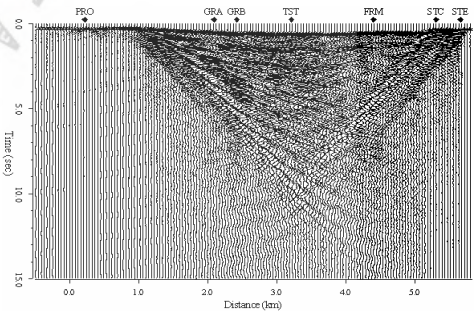

Figure 8. 2D numerical model: synthetics for f < 10 Hz (Makra, 2000).

Both 2D synthetic and recorded ground motions prove the existence and the importance of surface waves, which are locally generated at the edges of the valley and propagate to the center. 2D model is reproducing successfully the recorded time histories, while 1D modeling significantly fails to reproduce the observed (recorded) long period surface waves (Figure 9).

The 2D response spectra are larger in most bands, of frequencies and almost along the whole valley. This effect may have serious implications on design seismic motions, since the vast majority of codes are based on 1D

SH-wave. The case of Euroseistest is certainly a good and representative example of complex site effects; however to quantify the 2D and possibly 3D effects for design input motion additional cases should be examined An interesting issue for further research is also to understand the role of the complex 3D geology in site response. Few analyses have been performed so far in this direction and it is expected that Euroseistest experimental site will provide valuable data.

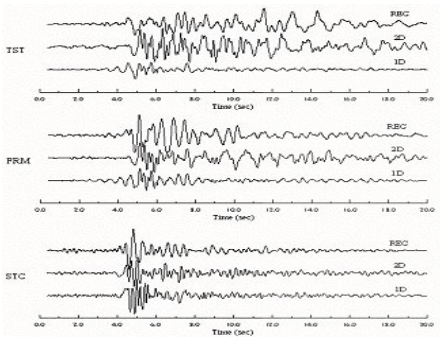

Figure 9. Variation of the 2D/1D aggravation factor (ratio of acceleration response spectra) along the Euroseistest cross-section for different periods (Makra et al., 2001).

Further examination of the importance of the 2D phenomena described above is done by introducing the notion of "aggravation factor" (Figure 10), which is the ratio of the acceleration response spectra between 2D and 1D ground response analyses, (Makra 2000, Makra et al, 2001).

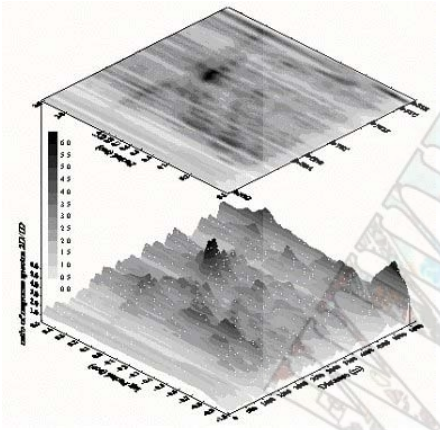

Figure 10. Comparison between recordings (REC) of the transversal component and 1D, 2D synthetics at TST (centre), FRM and STC (south) stations all filtered at fc=3.5Hz (Makra et al., 2001).

SOIL STRUCTURE INTERACTION

Description of model structures:
6-storey structure. The first model structure constructed instrumented and tested in Euroseistest concerns a 6-storey masonry infilled reinforced concrete building, with overall height 6m and overall dimensions in plan for each of the six slabs 3.5m x 3.4m. In the pre-design stage useful guidance was provided by a similar project being studied at the Chiba Experimental Station for a number of years by Professor T. Okada and his research group at the Institute of Industrial Science of the University of Tokyo. The structural model represents a 1:3 scale structure of a similar prototype building with frames spanning just over 5m and a storey height of 3m, which are typical dimensions of R.C. multi-storey structures used for residential purposes (Figure 11). Moreover, the masonry infill that where intended to be used in the pre-design stage were assumed to represent prototype masonry panels with a thickness of approximately 200mm.

Pier structure. The second model structure concerns a reinforced concrete single bridge pier model. The exact geometrical dimensions of the model are depicted in the following figures. On the top of the pier, which has a rectangular cross-section, is placed a rectangular deck (Figure 12). The surface foundation of the bridge pier model rests on the soil surface. During the experiments in the elastic range response, in order to avoid premature damage of the model structure, diagonal cables are added to connect the corners of the deck with the corners of the foundation block. The scaffolding satisfies safety purposes only and it is removed during the tests, therefore it does not participate in the structural response. The bridge pier model is similar to corresponding bridge piers that were tested at ELSA laboratories of the European Joint Research Center (Pinto 1996).

Figure 11. Model structures at the Euroseistest site.

Experiments:
6-storey structure experiments. The 6-storey building was designed to behave linearly under low intensity ground motions. However, for low to medium intensity ground motions both masonry infill and reinforced concrete members are expected to behave non-linearly. In order to achieve a low intensity excitation the procedure of the pull out test was followed.

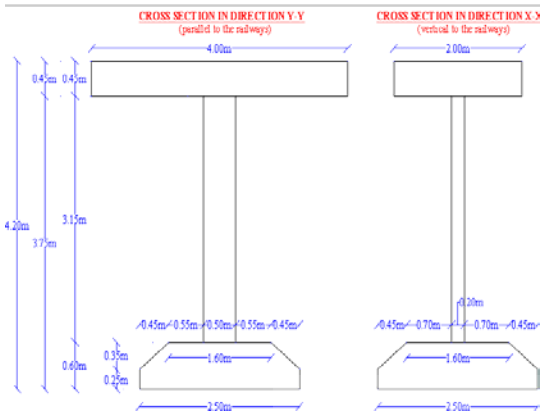

Figure 12. Geometry of the pier bridge model.

Two concrete reactions blocks (6tons each) were constructed to provide reaction mass. Moreover, pull-out points were selected at the perimeter of the slab for each storey either at the x-x or y-y axes of symmetry, or in one of the four corners of each slab. Using the appropriate anchor points at the reaction concrete blocks and the corresponding hooks at the slabs, a cable force could be applied on the structural model with a horizontal component in direction parallel to either the x-x- or y-y axis. The sudden release of the prestressed cable introduced in the body of the structure free vibration conditions.

During the aforementioned procedure a dual channel real time analyzer and two accelerometers of high gain were employed keeping the location of one of the sensors constant and changing selectively in each pull out test the location of the other. The decay of the time history of the acceleration response measured was used to estimate the damping ratio. Moreover, by comparing the two response measurements in the frequency domain, in magnitude and phase angle, and from the combination of all these comparisons for selected frequencies, that could be distinguished as the most important, the modal identification was performed.

Furthermore, relatively strong explosion teats took place at a safe distance from the model in order to record the motion of the soil surrounding the structure. On the 4th April and the 4th May 1995. two earthquakes occurred having epicentral distance from the Volvi test site approximately 40Km. despite the fact that these earthquakes generated relatively low-intensity ground motion at the test-site, the structural model was excited and the response was recorded and stored by the permanent instrumentation configuration.

Bridge pier experiments.

The cyclic post-elastic behavior of the bridge pier model was recorded at the laboratory during an initial study under cyclic horizontal loads that were applied simultaneously with the action of vertical forces. Moreover, the bridge pier model was tested at the real soil conditions transported at the EUROSEISTEST site. During the past two years various series of low intensity excitations were performed. The main type of excitation was achieved by the use of a system of cables attached to the deck in the two main directions of structural geometrical symmetry. Therefore, the deck was displaced in a controlled way and was suddenly released, introducing free-vibration conditions to the model. The second type of excitation was achieved by the use of explosives placed in a certain depth and at a certain distance from the bridge pier model in the required safety limits. The provided instrumentation could measure the acceleration and displacement response of the deck, the pier and the foundation block such as the displacements of the surrounding soil in various directions around the structure (Figure 12).

One special feature of the complex system instrumentation was the installation of pressure cells underneath the foundation in order to measure the stresses developing at the soil-foundation interface. The crucial outcome of the aforementioned low intensity experiments was the definition of the dynamic characteristics of the model in the frequency domain, such as eigen-frequencies, eigen-modes and damping. Moreover, the waves generated from the excitation of the structure and the wave propagation mode in the surrounding soil was studied (Figure 13).

The third type of excitation was achieved by the use of hydraulic pistons placed at the deck of the bridge pier model in order to provide high intensity in the body of the structure leading to inelastic behavior.

Figure 13. Instrumentation of the surrounding free-field soil.

One of the common targets between the experiments conducted at both of the model structures was the study of foundation-soil-structure interaction problems in the elastic and inelastic range, under real and quite favorable site conditions (soft-loose soils at the surface with Vs<160m/s).

A further step was the numerical prediction not only of the model behavior but of the behavior of the surrounding soil as well in order to evaluate the existing methods and tools used in the frame of soil-structure interaction analyses.

- Results:

The main targets in the process of the elaboration of the experimental results are the estimation of the frequency content, the estimation of structural or soil damping, the spatial attenuation of the soil motion amplitude, the study of the orbits of soil particles motion and different aspects regarding soil-structure interaction.

The study of the recordings in the frequency domain by the use of the Fourier transform reveals the fundamental frequency of the motion which is the frequency of the structural eigenmode activated during the experiment.

The amplitude time decay in the time domain as well as the half-power bandwidth method in the frequency domain are used for the estimation of damping. Furthermore the study of spatial attenuation of the soil motion amplitude as well as of the orbits of soil particles motion reveals the presence of Rayleigh types of waves. (Figure 14). The differences between the motion of soil particles close to the foundation of the structure and the motion of the foundation itself reveal the degree of soil-structure interaction especially in the case which the excitation of the model comes from outside such as in the explosive experiments.

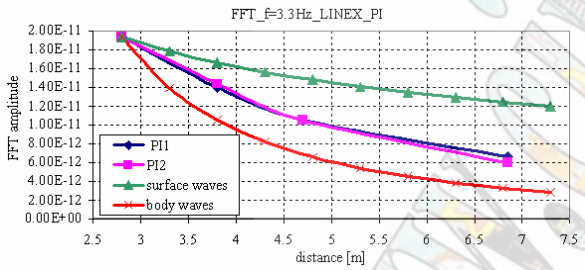

Figure 14. Spatial attenuation of amplitude of motion.

The FEM model which is prepared for the pier bridge is given in Figure 15. The analyses were performed with the code ADINA.

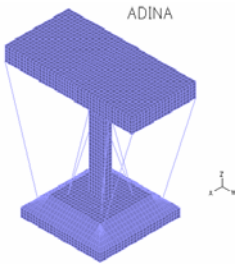

Figure 15. Numerical 3D model of the pier bridge.

The following procedure regards the validation analysis of used numerical code, which is focused in frequency as well as in time domain. If the modeling produces the same frequencies such as those that are excited by the structural motion then the degree accuracy of modeling is considered satisfying (Figure 16).

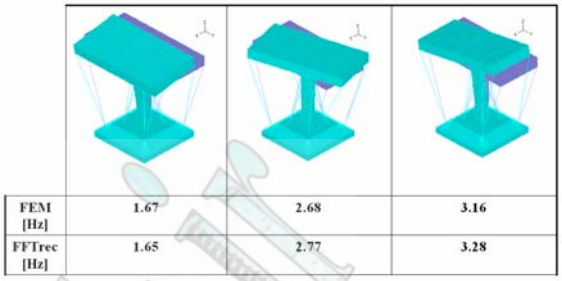

FEM [Hz]	1.67	2.68	3.16
FFTrec [Hz]	1.65	2.77	3.28

Figure 16. Comparison recorded and computed eigen-frequencies.

Furthermore, if the time histories at certain positions produced by the analysis are in accordance with the recordings at the same positions (Figure 17) then once again the modeling of the complex structural soil system is satisfying. Once the validation phase is fulfilled, various special analyses are organized such as the estimation of foundation impedances or the soil mass, which is activated since the termination of the motion.

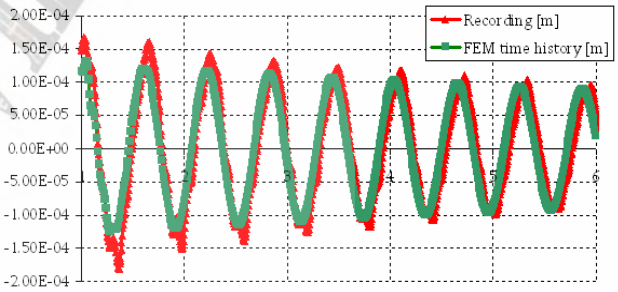

Figure 17. Validation analysis. Comparison in time domain.

CONCLUSIONS

Euroseistest experimental site provides a valuable set of experimental facilities to study both experimentally and theoretically complex site effects and soil-foundation – structure problems. Numerous publications have been already released and it is foreseen to strengthen in the near future the possibility to provide wide access to the experimental data which are already available and those that will be acquired in the future.

ACKNOWLEDGMENTS

Euroseistest has been funded by EU-DGXII. The support of EU is greatly appreciated.

REFERENCES

[1] B.R.G.M., "Etude Hydrogeologique du Basin de Mygdonia (Report style)," *O.A.E.S* (in French), 1971.

[2] Chávez-García, F.J., Raptakis, D., Makra, K., Pitilakis, K., "Site effects at Euroseistest — II. Results from 2D numerical modeling and comparison with observations (Periodical style)," *Soil Dyn. Earthq. Engrg.* Vol. 19, pp. 23-39, 2000.

[3] IGME, "Inventory – recording of water boreholes in the graben of Koronia, Thessaloniki (Report style)," 2001.

[4] IGME, "Geophysical surface survey in the graben of Koronia, Thessaloniki, in Greek (Report style)," 2001.

[5] Makra K., Raptakis, D., Chavez-Garcia, F.J., Pitilakis, K., "Site effects and design provisions (Periodical style)," Pageoph, Vol. 158, pp. 2349-2367, 2001.

[6] Makra K., "Contribution to the evaluation of site response for complex soil structure (Euroseistest valley) using experimental and theoretical approaches (Thesis or Dissertation style)," Ph.D. dissertation Dept. of Civil Engineering, Aristotle University of Thessaloniki, 2000.

[7] Makra K., Chavez-Garcia, F.J., D. Raptakis, K. Pitilakis "Parametric analysis of the seismi response of a 2D sedimentary valley: implications for code implementations of complex site effects, (Periodical style)," Soil Dyn. Earthq. Engrg. Vol. 25, pp. 303-215, 2005.

[8] Manos G.C., Kourtides V., Soulis V.J., "Cyclic and Dynamic Response of a Pier Model located at the Volvi European Test Site in Greece (Presented Conference Paper style)," presented at the 18th International Conference on Structural Mechanics in Reactor Technology (SmiRT 18), Beijing, China, 2005.

[9] Manos G.C., Demosthenous M., Triamataki M., Yasin B., Skalkos P., "Construction and instrumentation of a 5-story masonry infilled R.C. building at the Volvi-Thessaloniki EUROSEISTEST site. Correlation of measured and numerically predicted dynamic properties (Report style)," Computer Methods in Structural Masonry-3, 242-251.

[10] Pinto A. V., "Pseudo-dynamic and Shaking Table Tests on R.C. Bridges (Report style)," ECOEST PREC*8 No.8, 1996.

[11] Raptakis, D., Chávez-García, F.J., Makra, K., Pitilakis, K., "Site effects at Euroseistest — I. Determination of the valley structure and confrontation of observations with 1D analysis (Periodical style)," Soil Dyn. Earthq. Engrg., Vol. 19, pp. 1-22, 2000.

[12] Raptakis, D., Manakou, M., Chávez-García, F.J., Makra, K., Pitilakis, K., 3D "configuration of Mygdonian basin and preliminary site response (Periodical style—in press)," Soil Dyn. Earthq. Engrg, in press, 2005.

Seismic Design of Seawall and Runway of Kobe Airport

T. Sato[1], M. Yoshii[2], T. Kagawa[3], Y. Takahashi[4], M. Nambu[5]
[1] *Professor, Waseda University, Japan*
[2] *Manager, Port and Urban Projects Bureau, City of Kobe, Japan*
[3] *Head Researcher, Geo-Research Institute, Japan*
[4] *Director, Kobe Branch, Fudo Construction Co., Ltd., Japan*
[5] *Director, Kobe Branch, Oyo Corporation, Japan*

Abstract

We present procedure to evaluate seismic safety of seawall and runway of the Kobe airport which constructed as a reclaimed land about 8Km off from center of Kobe city. The Kobe airport construction was planned to activate economic environment of Kobe area by improving accessibility to all major cities in Japan. This project is a part of the twenty first century urban planning of Kobe area including redevelopment and restoration of damage to urban facilities caused by the 1995 Hyogoken Nambu (Kobe) earthquake. To keep the function of the airport and transportation to surrounding area up to a specific level during a future big earthquake we conducted realistic simulation to evaluate deformation of soil and structures taking into account the liquefaction and following ground spreading.

Keywords— *seismic design, seawall, runway, liquefaction, dynamic effective stress analysis*

INTRODUCTION

Kobe Airport is expected to contribute economic growth in urbanized area in and around Kobe city, corresponding to continuously growing demand for domestic air transportation. Construction of the airport has been promoted as a highly convenient city airport closely located to downtown Kobe. Also this offshore reclamation project is expected to support Kobe recovering from the severe disaster due to the 1995 Kobe earthquake and redeveloping for the 21st century.

This paper presents predictions of strong ground motion for aseismic design of major facilities, based on detailed surveys of active faults and ground conditions. It is essential that the airport sustains operations during and after an earthquake and can be utilized as a crisis management base. The predicted ground motions are used for dynamic analyses to evaluate deformation of liquefied reclaimed ground, and seismic performance of seawalls and runway.

OVERVIEW OF OSAKA BAY FAULT

Osaka Bay Fault was investigated and found to be a large-scale, reverse fault with accumulated vertical displacement of bedrock surface is about 1000 m from seismic reflection survey [1]. Detail information of this fault activity has been collected through surveys conducted after the 1995 Kobe earthquake [2], [3].

Location of the fault is shown in Fig. 1. The surveys suggest that the Osaka Bay fault is composed of a complex distribution of underground faults beneath Osaka Bay as expressed by a shaded line in the figure. From a comprehensive point of view, we modeled this fault structure as composed of two segmented as shown by bold line, north portion has 10 km length and south is 28 km. The northern segment crosses the area earmarked for Kobe Airport.

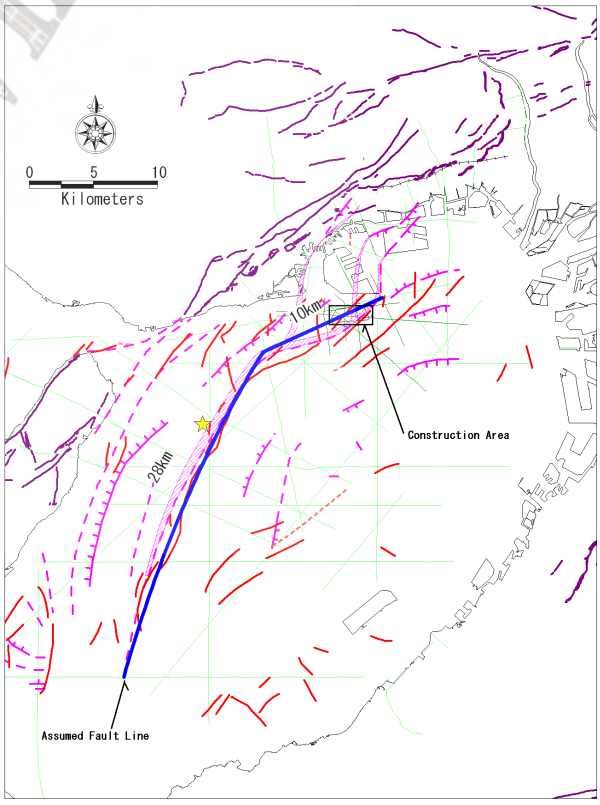

Fig. 1 Overview of Osaka Bay Fault

Drilling surveys were conducted in the airport constructing area, crossing the estimated surface trace of Osaka Bay Fault. Soil samples from the boreholes were used for geological age determination and magnetic susceptibility analysis. The results are shown in Fig. 2. Three events were confirmed: 1) between 1200 and 2700 years ago, 2) between 5700 and 6300 years ago, and 3) between 7800 and 8700 years ago. It suggests that the recurrence period of Osaka Bay Fault is 2000 - 3000 years. The mean deformation speed is estimated as 0.58 m per thousand years, from dislocation of the K-Ah volcanic ash layer and its geological age. It is also shown in Fig. 2. Assuming recurrence period as 3000 years, vertical displacement due to single event can be approximately estimated as 1.74 m.

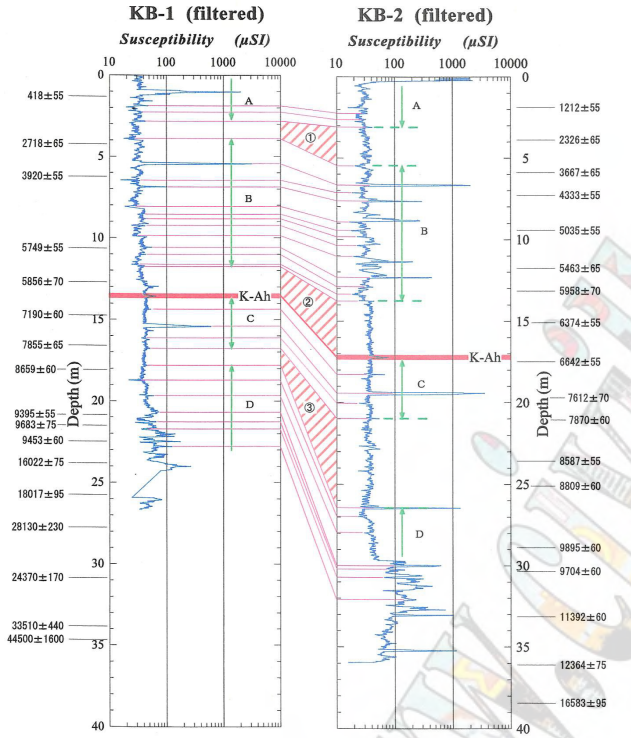

Fig. 2 Historical events detected for Osaka Bay fault

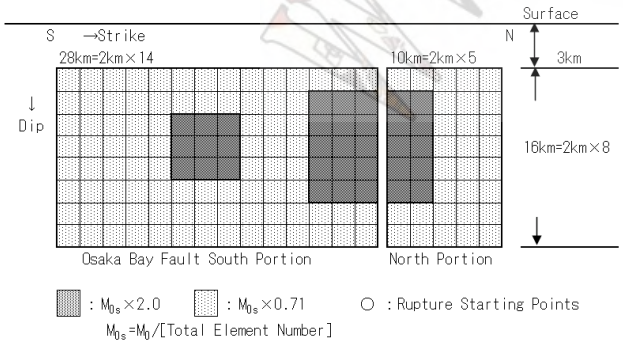

Fig. 3 Asperity model for assumed Osaka Bay Fault

Table 1 Comparison of assumed Osaka Bay Fault earthquake with the 1995 Kobe earthquake

Parameters	Assumed Osaka Bay fault earthquake	The 1995 Kobe earthquake
Number of fault segments	2	3
Fault length	38 km	57 km
Fault width	16 km	21.8 km
Hypocentral depth	16 km	17 km
Fault rupture area	608 km^2	1242.6 km^2
Magnitude (M_J)	7.0	7.2

PREDICTION OF STRONG GROUND MOTIONS

An empirical non-uniform slip model derived from previous earthquakes [4] was applied to the assumed fault shown in Fig. 1. The fault rupture model used for simulation of earthquake motion is shown in Fig. 3. Fault rupture area is 38 km x 16 km, and seismic moment is 1.42 x 10^{26} dyne·cm, it corresponds to M_W 6.7 and M_J 7.0 [5]. The assumed earthquake is slightly smaller than the 1995 Kobe earthquake (M_W 6.9, M_J 7.3) as shown in Table 1. From the field surveys, vertical deformation is dominant for the fault. We however assumed a dip angle of 80 degrees and lateral/vertical slip ratio of 2:1 which are almost same as the fault rupture model of the 1995 Kobe earthquake. Densely shaded elements in Fig. 3 represent asperities, the areas from where large seismic energy is radiated vy assuming twice large slips and about five times larger stress drops than averages. Asperities cover about 22% of the total rupture area [4]. The asperities are located where large displacements are found from field surveys. A star symbol in Fig. 4 indicates rupture starting point. In addition, parametric study was undertaken on rupture starting point as indicated by open circles. We confirmed that ground motion in Kobe Airport area is largest if rupture starts from star symbol than those from other starting points.

Currently used hybrid method [6] was employed to simulate strong ground motion. In this method, long period ground motions are simulated by using 3-D finite difference method [7] with 3-D Osaka Basin structure model [8], and stochastic Green's function method [9] is applied to generate short period motions. The ground motions in both period ranges are superimposed to simulate rational ground motion in broad period range. Therefore, the estimated strong ground motions can be used as input motions of aseismic design for various types of structures.

Calculated ground motion on engineering base layer

(bottom of Ma12 layer) at southern seawall (gently sloping rubble mound breakwater) of the airport island is shown in Fig. 4. This is NS component and equals approximately to the fault normal direction. A pulse like time history characterizes the earthquake motion which is similar to the record on the bottom of Ma12 layer observed at Port Island site during the 1995 Kobe earthquake, as shown in Fig. 5. Comparing response spectra in Figs. 4 and 5, the ground motion generated by rupturing Osaka Bay Fault has almost same level with that of the Kobe earthquake in period range shorter than 1 sec. Also even in the longer period ranger than 1 sec., level of the acceleration response is considerably high for aseismic design. Thus the predicted ground motions induce severe response effect on structures with wide rang of natural periods.

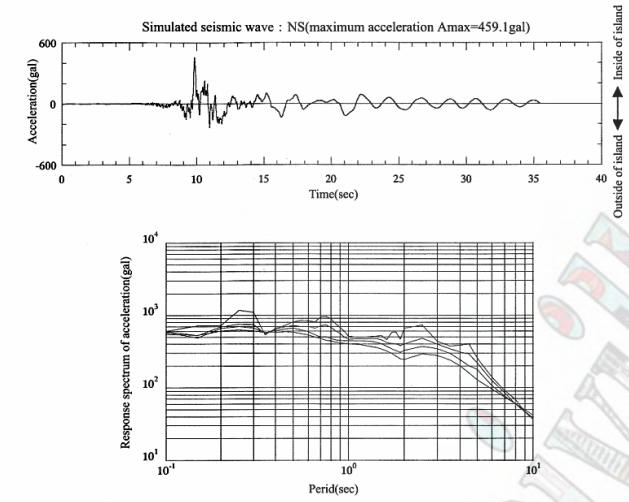

Fig. 4 Simulated ground motion and acceleration response spectra caused by Osaka Bay Fault

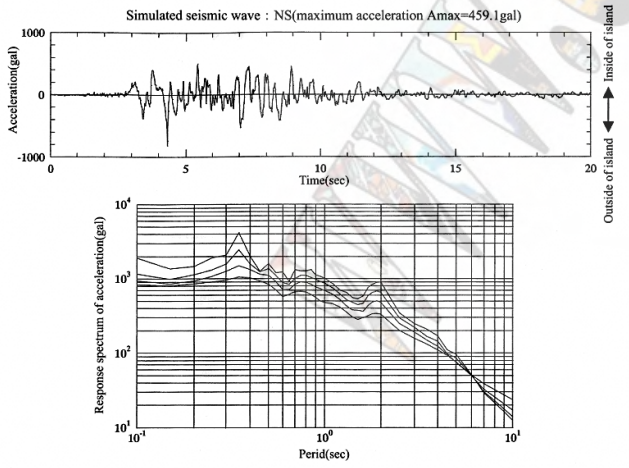

Fig. 5 Same as Fig.4 but for the Port Island wave due to the 1995 Kobe earthquake

METHOD AND CONDITION OF ASEISMIC DESIGN FOR SEAWALL AND RUNWAY

Target of study and analysis tools

Earthquake-generated deformation and excess pore water pressure at the seawalls and runway were estimated using the waveforms simulated by rupturing Osaka Bay Fault and observed record at Port Island during Kobe earthquake. Dynamic effective stress analyses were conducted by using Finite Element Analysis of Liquefaction Program (FLIP) and Coupled Analysis of Liquefaction (LIQCA).

Conditions of Analysis

Target section: Through a preliminary study on the shape of the seawalls, a gently sloping rubble mound seawall was selected because of its reasonable cost and excellent quake-resistant performance. The section used for analysis is shown in Fig. 6. This is the cross section after seabed ground being consolidated due to dead load of infilled soil. The layer of infill covers total area of 272 ha with approximately 32 m thickness on soft ground at water depth of approximately 17 m. The bottom of the Ma12 layer was taken as the engineering basement at where ground motions are input.

Input ground motions: The input ground motions used for the analysis were the simulated earthquake motion assuming the rupture of Osaka Bay Fault described above (max. acceleration: 459.1 gal) and the motion recorded at the bottom of the Ma 12 layer at Port Island during the 1995 Kobe earthquake (max. acceleration: 817.0 gal after modification). Durations of the motions are 36 and 20 sec, respectively. Total analysis times were set as 40 and 70 sec. respectively, considering effect of free oscillation of the structure.

Physical properties: The physical properties of soil composing the ground are assigned as shown in Table 2 from insitu and laboratory tests of the infill soil and previous data. Liquefaction strength of the infill material (Suma soil) was estimated from Fig. 7. Values of MIX1 and MIX2 in Fig. 7 were determined from mixture rate of infill soils at various blocks in the reclamation area.

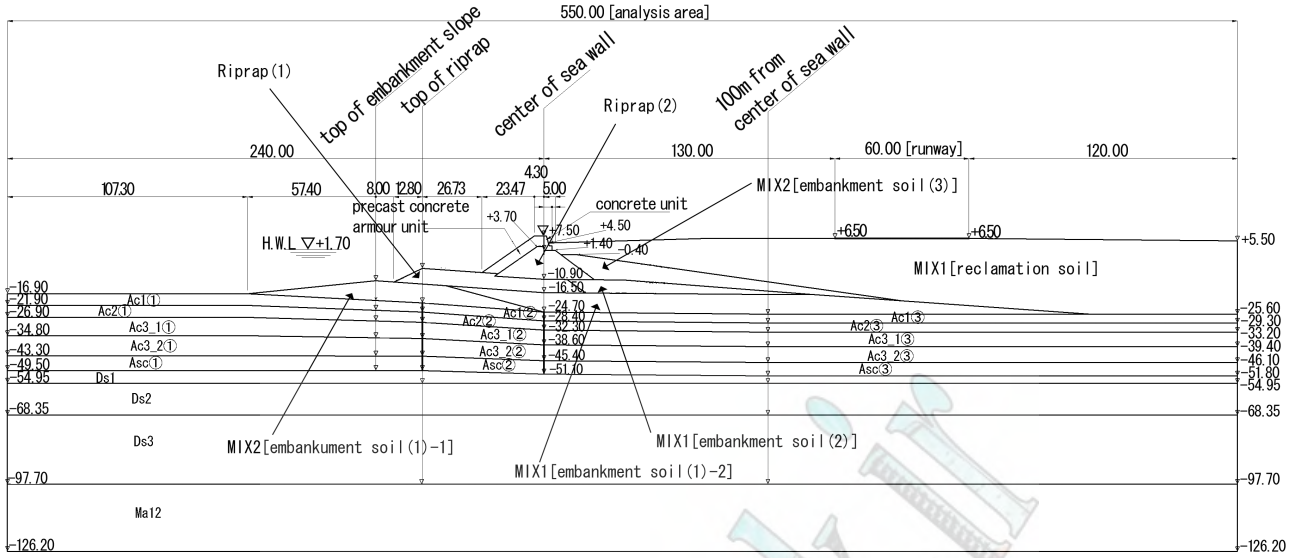

Fig. 6 Analytical cross section

Table 2 Physical properties of each stratum [FLIP]

Stratum	Element type	Vs(m/s)	Vp(m/s)	ρ (t/m^3)	n	ν	G_{m0} (kN/m^2)	K_{m0} (kN/m^2)	S_{m0} (kN/m^2)	m_G, m_K	Kw (kN/m^2)	h_{max}	C (kN/m^2)	f_f (degree)
MIX1 upper water level	Multi spring	230	1600	1.90	0.45	0.33	102950	268480	200	0.5	2.2E+6	0.108	0.0	36
MIX1 under water level	〃	230	1600	2.00	0.45	0.33	102950	268480	200	0.5	2.2E+6	0.108	0.0	36
MIX2	〃	230	1600	2.00	0.45	0.33	102950	268480	200	0.5	2.2E+6	0.108	0.0	37
Ac1①	〃	70	1500	1.50	0.45	0.33	7000	18250	30	1.0	2.2E+6	0.170	0.0	30
Ac1②&③(after consolidation)	〃	190	1500	1.65	0.45	0.33	61000	159080	267	1.0	2.2E+6	0.250	0.0	30
Ac2①	〃	70	1500	1.50	0.45	0.33	7000	18250	30	1.0	2.2E+6	0.170	0.0	30
Ac2②&③(after consolidation)	〃	190	1500	1.65	0.45	0.33	61000	159080	267	1.0	2.2E+6	0.250	0.0	30
Ac3-1①	〃	100	1500	1.60	0.45	0.33	15000	39120	80	1.0	2.2E+6	0.180	0.0	30
Ac3-1②&③(after consolidation)	〃	210	1500	1.70	0.45	0.33	77000	200800	300	1.0	2.2E+6	0.260	0.0	30
Ac3-2①	〃	100	1500	1.60	0.45	0.33	15000	39120	80	1.0	2.2E+6	0.180	0.0	30
Ac3-2②&③(after consolidation)	〃	210	1500	1.70	0.45	0.33	77000	200800	300	1.0	2.2E+6	0.260	0.0	30
Asc①	〃	160	1510	1.70	0.45	0.33	32000	83450	93	1.0	2.2E+6	0.155	0.0	30
Asc②&③(after consolidation)	〃	210	1500	1.70	0.45	0.33	77000	208000	300	1.0	2.2E+6	0.260	0.0	30
Ds1	〃	190	1700	2.00	0.45	0.33	44000	114750	160	0.5	2.2E+6	0.220	0.0	40
Ds2	〃	360	1940	2.10	0.45	0.33	140000	365100	280	0.5	2.2E+6	0.180	0.0	40
Ds3	〃	300	1730	2.00	0.45	0.33	110000	286860	490	0.5	2.2E+6	0.200	0.0	40
Ma12	〃	270	1550	1.75	0.45	0.33	140000	365100	730	1.0	2.2E+6	0.150	0.0	30
Ds4(bearing stratum)	Bottom damper	350	1660	1.93	---	---	---	---	---	---	---	---	---	---
riprap(1),(2)	Multi spring	---	---	2.01	---	0.33	180000	469410	98	0.5	0.0	0.240	19.6	35
Precast concrete armour units	〃	---	---	1.16	---	0.33	30500	79540	98	0.5	0.0	0.240	26.0	10.44
Concrete units	Linear element	---	---	2.30	---	0.167	E=2.0×10^{7}kN/m^2	---	---	---	---	---	---	---

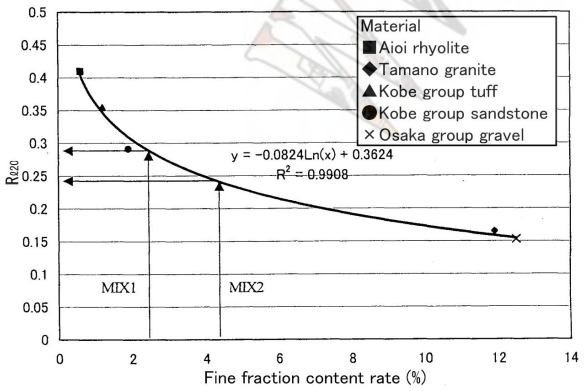

Fig. 7 Relation between fine fraction content rate and $R_{\ell 20}$ of each reclamation sample

RESULTS

Earthquake-generated displacement and liquefaction

Distributions of maximum responses obtained by FLIP analysis are shown in Fig. 8. Distribution of lateral displacement at the surface obtained by LIQCA analysis is shown in Figs. 9 and 10. Residual displacements are shown in Table 3. We can see remarkable lateral residual displacement up to about 50 m behind the seawall, due to seawall deformation. It becomes almost constant at about 150 m behind the seawall. Residual settlement is considered to be affected by seawall deformation up to about 50 m behind the seawall. However it becomes almost constant beyond 50 m. The runway section (130-190 m behind the seawall) shows quite small residual lateral displacement and settlement compared with the normal direction of the seawall. In the case of simulated earthquake motion assuming Osaka Bay Fault rupturing, residual lateral displacement and settlement at the top of the seawall are about twice larger than the case of the Port Island earthquake motion. As for liquefaction, excess pore water pressure ratios in the reclaimed layers were 80-100% for any combination of input waves analysis. This suggests high possibility of liquefaction.

Post-earthquake settlement in liquefaction layer

Program LIQCA is used to evaluate the post-earthquake settlement which occurs by the consolidation of liquefaction layer, since program FLIP can not analyze the effect of excess pore water dissipation. Calculations are continued until excess pore water pressures in infill layer are dissipated and settlements of the ground surface are terminated. Thus total durations of actual calculation time were extended to about 19 hours for the case of assumed Osaka Bay Fault wave input and about 10 hours for the Port Island wave input. Final surface displacements in the infill layer are shown in Figs. 9 and 10.

The assumed Osaka Bay Fault wave input arose about 60 cm of settlement around the central part of the runway during dissipation process of excess pore water pressure in the infill layer. Subsequently, uneven settlement of 30 cm and maximum settlement of 120 cm occurred in the runway area (130-190 m behind the seawall). However, the degree of settlement close to the seawall is quite small as 2 cm, because of porous nature of rubble mound structure. Degree of settlement increases around 130 m from normal line of reclamation. It is considered to be caused by differences of layer structures and their physical properties.

In case of the Port Island wave input, settlement of about 40 cm occurred during dissipation process of excess pore water pressure in the infill layer. This trend is same as the case of assumed Osaka Bay Fault wave input. However, degree of settlement around central section of the runway accompanying post-earthquake dissipation of pore water pressure is greater than residual settlement occurred during the earthquake motion input.

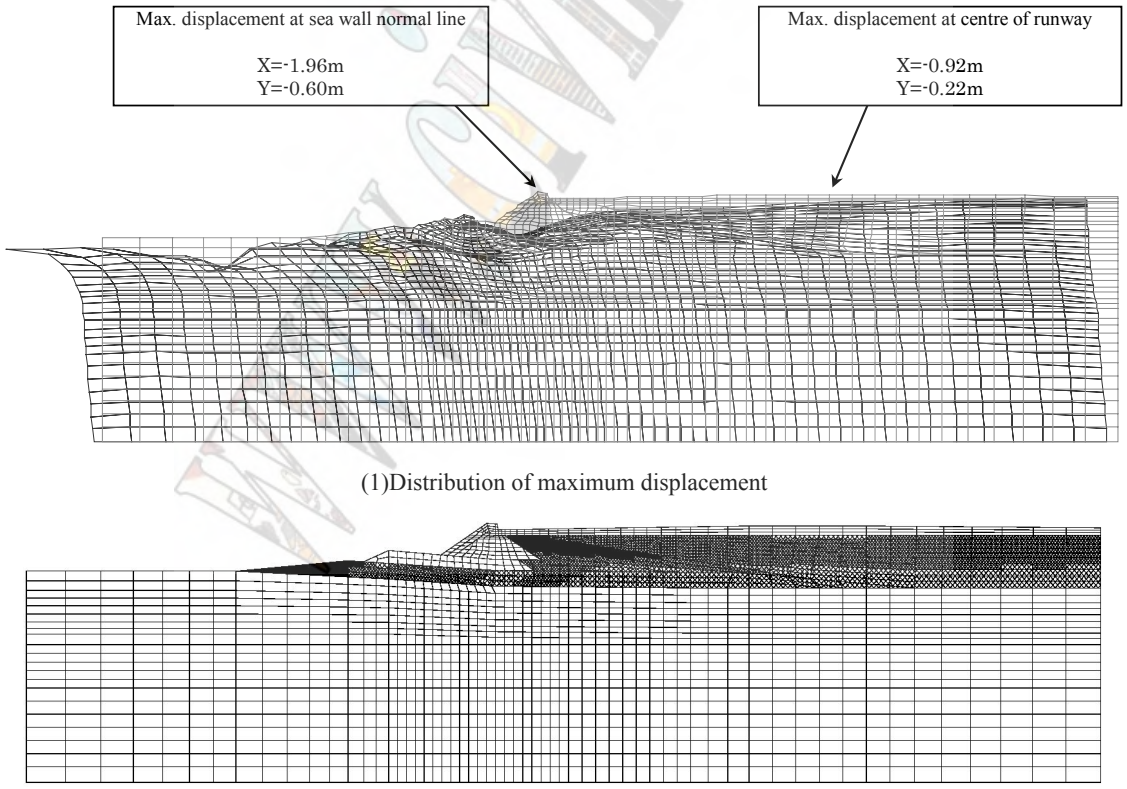

(1)Distribution of maximum displacement

(2)Distribution of maximum ratio of excess pore water pressure

Fig.8 FLIP analysis using assumed Osaka Bay Fault wave

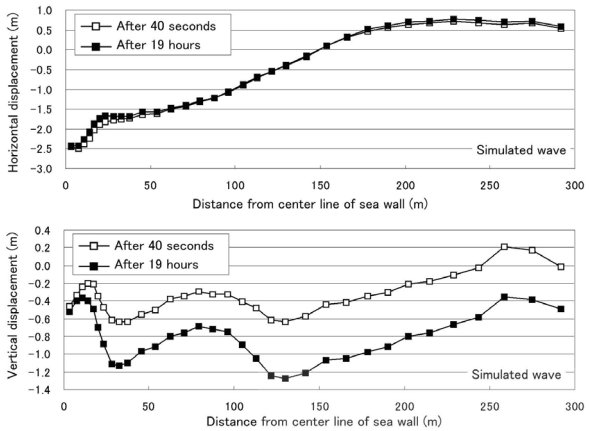

Fig. 9 Horizontal and vertical displacement at ground surface (Simulated seismic wave by Osaka Bay Fault earthquake [LIQCA])

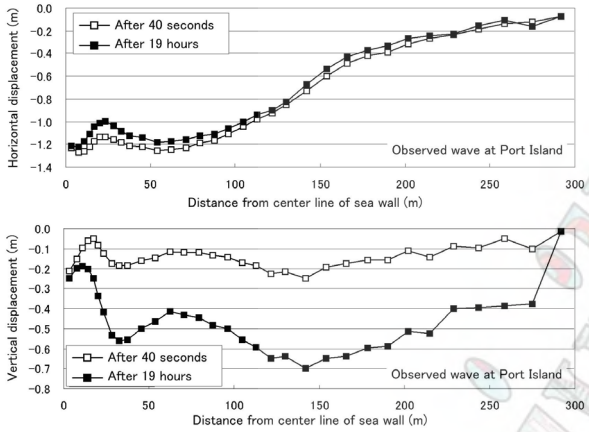

Fig. 10 Horizontal and vertical displacement at ground surface (Observed wave at Port Island due to the 1995 Kobe earthquake [LIQCA])

Table 3 Residual displacement

Input earthquake motion	Study location	Analysis program	Residual horizontal displacement	Residual settlement	Settlement after earthquake
Simulated seismic wave by Osakawan Fault Earthquake	Crest of sea wall	FLIP	1.89	0.54	---
		LIQCA	2.42	0.50	0.02
	Center of runway	FLIP	0.12	0.17	---
		LIQCA	0.26	0.44	0.59
Observed wave at Port Island by Hyogoken Nambu Earthquake	Crest of sea wall	FLIP	1.06	0.31	---
		LIQCA	1.20	0.22	0.04
	Center of runway	FLIP	0.15	0.06	---
		LIQCA	0.47	0.19	0.44

CONCLUSIONS

Dynamic effective stress analysis methods were used for aseismic design for a sloping rubble mound seawall and runway. Effect of strong ground motion due to active fault close to the site was considered. The design earthquake motion was simulated assuming non-uniform fault rupture and 3-D sedimentary structure. Gently sloping rubble mound seawall was well perform for the deformation caused by liquefaction during the level 2 earthquake input that is almost same level of the 1995 Kobe earthquake motion. Based on the analyses the minimum requirement of the seawall crest height (KP +3.7 m) was guaranteed even after the strong shaking though ground settlement occurred due to the ground shaking and dissipation of excess pore water pressure of liquefied ground layer during post-earthquake.

However, the results indicated that considerable settlement occurred to the runway, due to ground shaking and liquefaction. In order to sustain the airport operations immediately after an earthquake and ensure its function as a crisis management base, no significant settlement or uneven settlement can be tolerated. We have to employ suitable soil improvement method for liquefaction countermeasure.

REFERENCES

[1] Iwasaki, Y., Kagawa, T., Sawada, S., Matsuyama, N., Oshima K., Ikawa, T. and Onishi, M. (1994) "Basement structure by airgun reflection survey in Osaka Bay, southwest Japan" (in Japanese with English abstract), *Zisin2,* 46, pp. 395-403.

[2] Yokokura, T., Kano, N., Yamaguchi, K., Miyazaki, M., Ikawa, T., Ota, Y., Kawanaka, T. and Abe, S. (1998) "Deep structural prospecting of Osaka Bay using reflection method" (in Japanese), *Bull. Geol. Survey. Jpn.*, 49(11), pp. 571-590.

[3] Kobe City (1999) Hanshin-Awaji Earthquake and Active Faults around Kobe (in Japanese).

[4] Somerville, P. G., Irikura, K., Graves, R. W., Sawada, S., Wald, D., Abrahamson, N., Iwasaki, Y., Kagawa, T., Smith, N. and Kowada, A. (1999) "Characterizing crustal earthquake slip models for the prediction of strong ground motion", *Seism. Res. Lett.*, 70, pp. 59-80.

[5] Takemura, M. (1990) "Relation between magnitude and seismic moment of shallow earthquakes occurring in the Japanese islands and surrounding areas" (in Japanese with English abstract), *Zisin 2*, 43, pp. 257-265.

[6] Kamae, K., Irikura, K. and Pitarka, A. (1998) "A technique for simulating strong ground motion using hybrid Green's function", *Bull. Seism. Soc. Am.*, 88, pp. 357-367.

[7] Pitarka, A. (1999) "3D elastic finite-difference modeling of seismic motion using staggered-grid with non-uniform spacing", *Bull. Seism. Soc. Am.*, 89, pp. 54-68.

[8] Miyakoshi, K., Kagawa, T., Zhao B. M., Tokubayashi, M. and Sawada, S.(1999) "Modelling the deep sedimentary structure in the Osaka Basin (3)" (in Japanese), *JSCE J. Earthq. Engng.*, 25, pp. 185-188.

[9] Kamae, K., Irikura, K., and Fukuchi, Y. (1990) "Prediction of strong ground motion for M7 earthquake using regional scaling relations of source parameters" (in Japanese with English abstract), *Journal of Struct. Constr. Engng. AIJ*, 416, pp. 57-70.

[10] Iai, S., Matsunaga, Y. and Kameoka, T. (1990) "Strain space plasticity model for cyclic mobility", *Report of the Port and Harbour Research Institute*, 29(4), pp. 27-56.

[11] Oka, F., Yashima, A., Shibata, T., Kato, M. and Uzuoka, R. (1994) "FED-FDM coupled liquefaction analysis of a porous soil using an elasto-plastic model", A*pplied Scientific Research*, 52, pp. 209-245

Performance-based approach for designing remediation of liquefiable soils

S. Iai[1] and T. Tobita[1]
[1]*Disaster Prevention Research Institute, Kyoto University, Japan*

Abstract

The paper gives an overview of performance-based approach for designing remediation of liquefiable soils. Case histories of implementation and performance of remediation measures during past earthquakes are reviewed. The paper discusses the applicability and limitations of the conventional simplified approach for designing remediation of liquefiable soils and how these limitations can be overcome in the performance-based approach that explicitly considers residual displacements and structural strains beyond elastic limit as primary performance criteria parameters.

Keywords—*Deformation, earthquake, effective stress analysis, liquefaction, performance-based design*

INTRODUCTION

Seismic damage to geotechnical structures is often associated with significant deformation of a soft or liquefiable soil deposit. Designing appropriate remediation of liquefiable soils is essential to improve the seismic performance of geotechnical structures. The conventional simplified approach based on pseudo-static force equilibrium provides reasonable guidelines for designing remediation of liquefiable soils against moderate earthquake motions. However, there are cases where the conventional simplified approach is not readily applicable. For example, for intense earthquake motions, acceptable residual displacements and structural strains beyond elastic limit become the primary design criteria parameters, which are not evaluated by the conventional simplified approach. There are a number of cases where site specific constraints pose difficulties in implementing the liquefaction remediation measures as suggested by the conventional simplified approach. Objective of this paper is to discuss the applicability and limitations of the conventional simplified approach for designing remediation of liquefiable soils and how these limitations can be overcome in the performance-based approach.

STANDARD PROCEDURE

Remedial measures against liquefaction can be classified into two broad categories [1-2]:

a) soil improvement to reduce the potential of liquefaction;

b) structural solutions to minimize damage in the event of liquefaction.

In practice, a combination of these two measures is often adopted.

A flowchart illustrating a standard design procedure for liquefaction remediation is shown in Fig. 1. Once the strategy has been determined, it is common practice to select a method first, and then to compare the advantages and disadvantages of different solutions for the particular project. Typically, a number of different solutions will need to be assessed before a final decision can be reached. Sometimes, solutions will be combined to achieve the optimum design. The procedure illustrated in Fig. 1 is intended to be used as a guide only; it may often be more efficient to screen out remediation methods that are clearly unsuitable at an early stage based on a rough assessment of the likely area to be treated and any project specific constraints.

A combination of two or more remediation methods is often very effective. A typical example might be the combination of a low noise/low vibration method, such as the use of drain, combined with compaction around the improved area, to constrain or confine the overall site. At present, however, formal procedures for selecting the most efficient combination of methods for a specific site have not been developed and the engineer must use judgment and experience to reach the optimum solution.

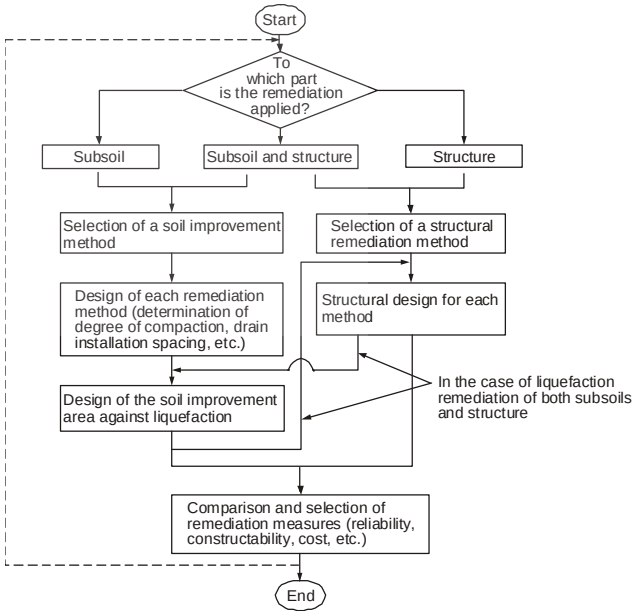

Fig. 1 Standard procedure for liquefaction remediation [1]

CONVENTIONAL APPROACH

The design requirements for a specific soil improvement area will be based on an assessment of the mechanism of damage likely to be induced in the natural soils by liquefaction. In particular, it is critical to determine whether the damage will be caused primarily by reduction in the shear resistance of the liquefied soil, or by additional external forces due to excessively large displacements. Large displacements of the liquefied subsoil may affect the foundations of existing and new structures, or cause serious damage to lifeline facilities (such as gas, water and telecommunication pipelines and conduits), and special consideration will be necessary in respect of these cases. There are many other cases, however, in which remediation measures against loss of shear resistance will provide benefits against the risk of large displacements; ground compaction being one example.

Generally, even if the soil is predicted to undergo liquefaction over a wide area, it may be possible to limit the area requiring soil improvement to the area that controls the stability of the structure. For example, the zone within the subsoil that contributes predominantly to the stability of spread foundation structures is the part directly below and immediately around the structure; ground far away from the structure does not contribute to the same extent. A key issue is therefore to establish how far the soil improvement needs to extend laterally from the structure. This can be determined by following the procedure summarized below [3-4].

The design procedure for a soil improvement area presented below is based around use of the compaction method. The procedure may, however, be adapted for other methods with appropriate modification by considering the appropriate characteristics of the improved soil (such as permeability and cyclic strength/deformation).

(1) Propagation of excess pore water pressure into the improved zone

Outside the zone of improved soil, excess pore water pressures will exceed those inside, resulting in a hydraulic gradient driving fluid into the zone of improved soil. This is a complex issue, as the deformation characteristics of dense saturated sand are highly non-linear. As a simplified design procedure, this phenomenon may be addressed as follows:

For excess pore water pressure ratios $u/\sigma_v' < 0.5$, the effect of the excess pore water pressure increase may be ignored because laboratory test data indicate a very small strain generation below this level. For $u/\sigma_v' > 0.5$, however, it is necessary to take into account the effect of excess pore water pressure increase. Shaking table tests and seepage flow analyses suggests that the pore water pressure ratio $u/\sigma_v' > 0.5$ within an area defined by the square ABCD in Fig. 2. In this area, the soil shear resistance must be reduced for the purposes of the design. The tests also indicate that an area defined by the triangle ACD exhibited unstable characteristics. This area should therefore be assumed in the design to be liquefiable and treated accordingly.

The exception to this recommendation is when a drain or impermeable sheet or zone has been installed at the perimeter of the improved area in order to shut out the inflow of pore water into the improved area. Under these conditions, the area corresponding to the square ABCD need not be included as part of the improvement plan.

(2) Pressure applied by the liquefied sand layer

At the boundary between liquefied and non-liquefied ground there is a dynamic force as indicated in Fig. 2 and a static pressure corresponding to an earth pressure coefficient K = 1.0 which acts on the improved ground due to the liquefaction of the surrounding soils. These forces may greatly exceed the forces acting in the opposite direction from the non-liquefied ground. For a retaining structure backfilled with soil and subject to active static and dynamic lateral earth pressures at EF as shown in Fig. 2, the area of soil improvement must be large enough that there is no influence of liquefaction in the active failure zone. To accommodate the net outward force, it is essential to check that sufficient shear resistance can be mobilized along the passive failure surface GC.

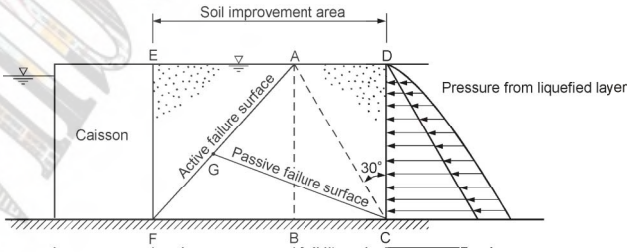

Fig. 2 Schematic diagram for investigation of stability with respect to pressures applied from the liquefied sand layer [3]

(3) Loss of shear strength in liquefied sand layer

In the simplified design procedure, unimproved soil of loose or medium relative density should be considered to have negligible shear strength after liquefaction (i.e. the soil is treated as a heavy fluid). Since the shear strength of the improved ground in triangle ACD also cannot be relied upon (see (1) above), then the improvement area should be wide enough to obtain sufficient bearing capacity from the shear resistance along the solid lines EFG and HI in Fig. 3.

In practice, lateral pressure from surrounding liquefied sand layers may contribute to the stability of certain structures. Figure 3 shows how the dynamic earth pressure may be subtracted from the enhanced static lateral earth pressure (based on an earth pressure coefficient K = 1.0) in certain stability calculations. The section on which the pressure from the liquefied sand layer is applied can be assumed to be along the lines GG' or II'.

Although this figure shows only four examples of

foundation types, the same principles can be applied to other design arrangements.

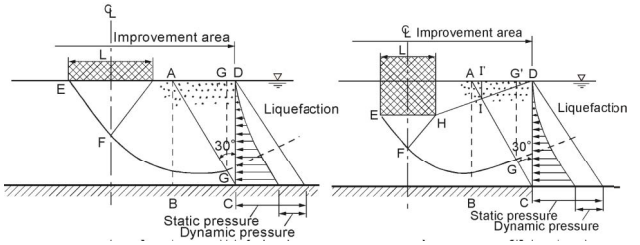

(a) Shallow foundation (b) Foundation with shallow embedment

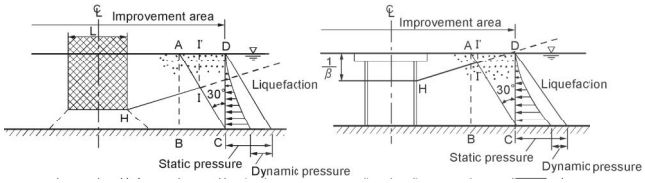

(c) Foundation with deep embedment (d) Pile foundation

Fig. 3 Schematic diagrams for investigation of stability for determining the soil improvement area [1, 3]

(4) Design of soil improvement area

Key parameters for any assessment of the area of soil improvement include the angle of internal friction for sands and the anticipated intensity of earthquake shaking. A stability analysis method will also need to be specified. Standard design procedures adopt a simplified, pseudo-static approach to the prediction of earthquake loads and response. Despite this, experience suggests that with appropriate care and selection of parameters, these methods generally provide satisfactory design solutions.

The soil improvement area required for a typical gravity quay wall based on this approach is shown in Fig. 2. For anchored sheet pile walls, the zone of improvement in the vicinity of the anchor wall must be carefully considered. For flexible anchor walls, soil improvement must extend to sufficient depth below the tie rod level to ensure that the adequate capacity is maintained to resist the tie rod force.

PERFORMANCE AT MODERATE EARTHQUAKE MOTIONS

The design procedure based on the conventional simplified approach described in the previous chapter provided a basis for implementing the liquefaction remediation in conventional practice. A number of case histories of implementing liquefaction remediation were gradually increasing. The first opportunity to test the effectiveness and adequateness of the remedial measures against liquefaction was provided during 1993 Kushiro-Oki earthquake of magnitude 7.8 [5]. Kushiro Port located at 15 km from the epicenter was shaken with a peak horizontal acceleration of 0.47g. If the spiky wave due to cyclic mobility is filtered out, the effective peak ground acceleration was in the order of 0.3g.

Many of the quay walls at Kushiro port suffered damage due to liquefaction of backfill sand. The most serious damage to the sheet pile quay walls is shown in Fig. 4. This quay wall was of a steel sheet pile type anchored by battered steel piles. The ground consists of loosely deposited backfill sand with a thickness of about ten meters, underlain by medium to dense sand deposit that forms the original ground. Liquefaction at the backfill caused serious deformation in the sheet pile wall as shown by the solid line in this figure. Detailed investigation of the sheet pile wall by diving in the sea revealed that cracks opened in the steel sheet pile wall at an elevation of four meters below the water level.

In contrast to the damaged sheet pile quay wall, quay walls with compacted backfill sand survived the earthquake without damage. An example, shown in Fig. 5, is of a steel pipe pile wall anchored by a steel sheet pile wall with a water depth of 12 meters. The ground at this wall originally consisted of fill sand with a thickness of about ten meters, underlain by the original ground of medium to dense sand. The backfill sand was later treated by a sand compaction pile method as shown in this figure. In order to avoid the affecting the existing steel pipe pile wall during the installation of ground compaction work, gravel drains were installed near the wall as shown in Fig. 5.

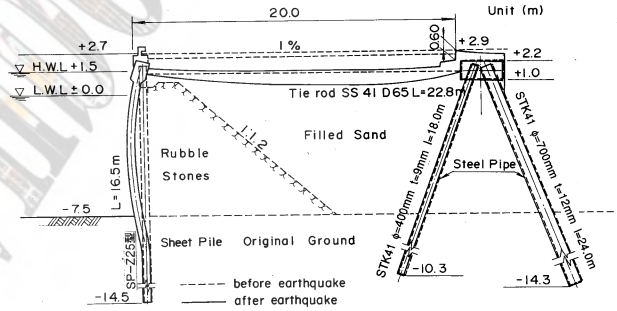

Fig. 4 Damaged sheet pile quay wall at South Fishery Wharf, Kushiro Port, during 1993 Kushiro-oki earthquake [5]

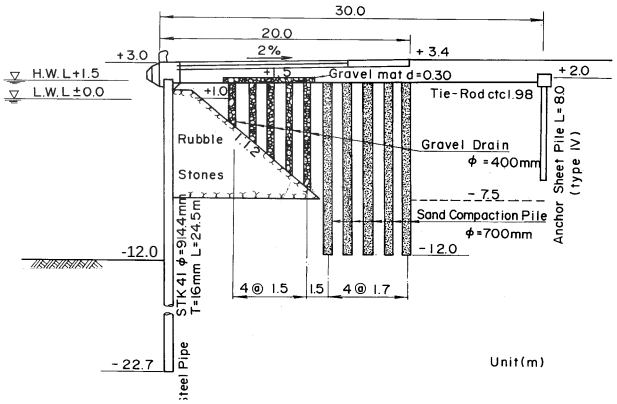

Fig. 5 Undamaged sheet pile quay wall at South West Port No.1 Wharf, Kushiro Port, during 1993 Kushiro-oki earthquake [5]

Despite the earthquake motions with a peak acceleration of 0.3g level, there was no damage to this quay wall. This case history demonstrated that the measures against liquefaction and design of quay walls according to the procedure based on the conventional simplified approach are sufficient to provide adequate resistance to this level of earthquake motions.

PERFORMANCE AT INTENSE EARTHQUAKE MOTIONS

1995 Hyogoken-Nambu earthquake with magnitude 7.2 provided a good opportunity to re-evaluate the limitations of the conventional simplified approach of seismic design. Shaken with a peak ground acceleration of 0.5g, many quay walls in Kobe Port, Japan, suffered serious damage. The damage involves large seaward displacement, settlement and tilt as shown in Fig. 6. The damage was cause mainly by deformation in the loosely deposited foundation soil beneath the caisson wall [6].

In order to evaluate the effects of liquefaction, a series of effective stress analyses were performed. A strain space multiple mechanism model for sand was used for the analysis [7]. Case-1 is the analysis that simulates the conditions in-situ during the earthquake. In this case, both the foundation soils beneath the caisson wall and the backfill soils were liquefiable decomposed granite. Cases-2 through 4 are defined by the extent of the non-liquefiable soil relative to the caisson wall as shown in Fig. 7.

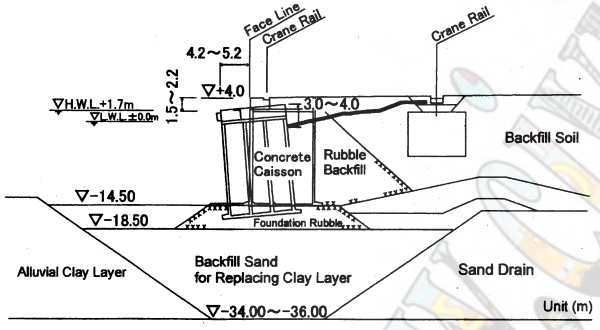

Fig. 6 Damage to a caisson quay wall at Kobe Port during 1995 Hyogoken-Nambu earthquake [6]

Case-1 analysis was successful in simulating the damage to a caisson type quay wall as shown in Fig. 8. The major results of the parameter study are summarized in Table 1. These results indicate that the deformation of the gravity wall may be reduced up to about one half of that at the earthquake if the excess pore water pressure increase was prevented in the subsoil as in Case-2. In particular, horizontal displacements of Cases-3 and 4 are 0.5(=2.1-1.6) and 0.9(=2.5-1.6)m larger than that of Case-2, suggesting that the effect of the pore water pressure increase in the foundation soil beneath the caisson wall (Case-4) is about twice as that of the backfill (Case-3).

These results were compared with the performance of the quay walls at Port Island (phase II). One (PC-13) was constructed on a loose deposited foundation similar to that shown in Fig. 6, whereas others (PC-14 and -15) were constructed on a foundation improved by the sand

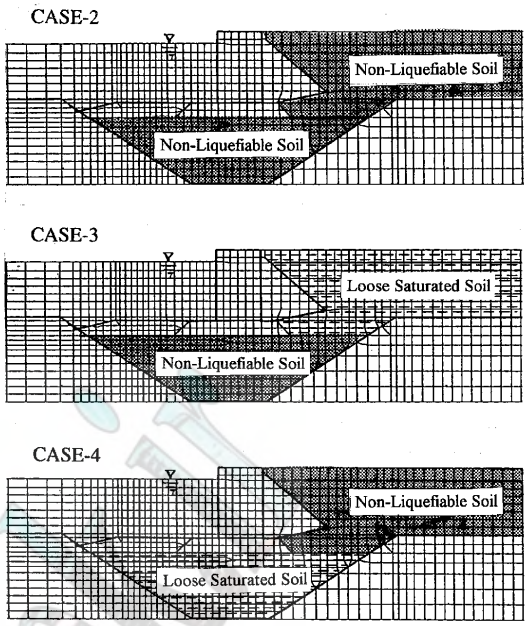

Fig. 7 Conditions assumed for parametric study, Cases 2 through 4 [7]

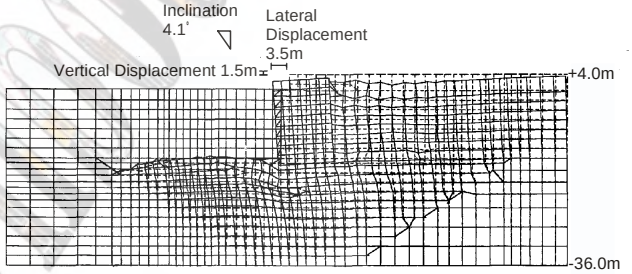

Fig. 8 Computed deformation of a gravity quay wall, Case-1 [8]

Table 1 Major results of parametric study for gravity quay wall [8]

Case	Residual Displacements of Caisson Horizontal (m)	Vertical (m)	Tilt (degrees)
Case 1	3.5	1.5	4.1
Case 2	1.6	0.6	2.4
Case 3	2.1	0.7	3.1
Case 4	2.5	1.1	2.2

compaction pile (SCP) method as shown in Fig. 9. Although these quay walls were constructed along a straight face line, displacements of the quay walls PC-14 and -15 were about 2.5 m and 0.3 m in horizontal and vertical directions whereas those at PC-13 were about 3.5 m and 1.5 m in horizontal and vertical directions. The analysis conditions of Case-3, having non-liquefiable foundation, approximate the performance of the quay walls PC-14 and 15. The analysis condition of Case-1, having loose deposited foundation, approximates the performance of the quay wall PC-13. The results for the parameter study of Cases-1 and 3 discussed above can

explain the difference between the quay walls constructed on SCP and a loose deposited foundation [8].

For variations in the peak acceleration of the earthquake motion input at the base, the horizontal residual displacement at the top of the caisson wall was computed as shown in Fig. 10. These response curves constitute the basis for performance-based design described in the next section.

The case history of seismic performance of quay walls during 1995 Hyogoken-Nambu earthquake provided a number of valuable lessons. In particular, the case history and analysis described above suggest that (1) liquefaction remediation is effective for improving performance of quay walls even for intense earthquake motions, (2) some

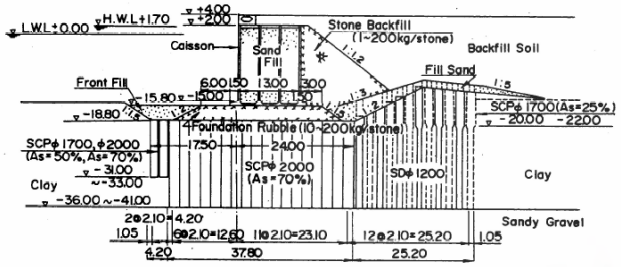

Fig. 9 Cross section of a quay wall in Kobe Port improved with sand compaction piles (SCP) [6, 8]

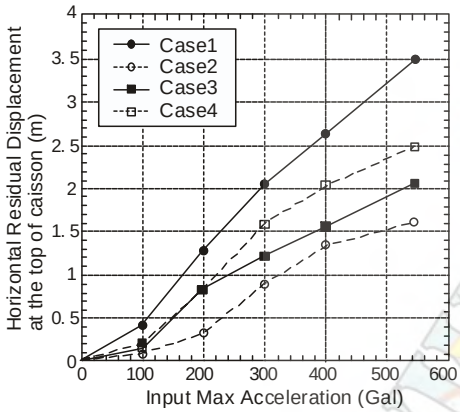

Fig. 10 Effects of input acceleration levels on horizontal residual displacement [2]

residual deformation may be acceptable, (3) deformations in ground and foundation soils and the corresponding structural deformation and stress states are key design parameters, and (4) conventional simplified limit equilibrium-based methods are not well suited to evaluating these parameters. All of these issues indicate that there is a strong need to develop performance-based approach for liquefaction remediation [2].

TOWARD PERFORMANCE-BASED DESIGN

The goal of the performance-based design is to overcome the limitations present in conventional simplified seismic design. The conventional seismic design is based on providing capacity to resist a design seismic force, but it does not provide information on the performance of a structure when the limit of the force-balance is exceeded. If we demand that limit equilibrium not be exceeded in conventional design for the relatively high intensity ground motions associated with a very rare seismic event, the construction/retrofitting cost will most likely be too high. If force-balance design is based on a more frequent seismic event, then it is difficult to estimate the seismic performance of the structure when subjected to ground motions that are greater than those used in design.

In performance-based design, appropriate levels of design earthquake motions must be defined and corresponding acceptable levels of structural damage must be clearly identified. Two levels of earthquake motions are typically used as design reference motions, defined as follows:

Level 1 (L1): the level of earthquake motions that are likely to occur during the life-span of the structure;

Level 2 (L2): the level of earthquake motions associated with infrequent rare events, that typically involve very strong ground shaking.

The acceptable level of damage is specified according to the specific needs of the users/owners of the facilities and may be defined on the basis of the acceptable level of structural and operational damage given in Table 2. The structural damage category in this table is directly related to the amount of work needed to restore the full functional capacity of the structure and is often referred to as direct loss due to earthquakes. The operational damage category is related to the amount of work needed to restore full or partial serviceability. Economic losses associated with the loss of serviceability are often referred to as indirect losses. In addition to the fundamental functions of servicing sea transport, the functions of port structures may include protection of human life and property,

Table 2 Acceptable level of damage in performance-based design*

Acceptable level of damage	Structural	Operational
Degree I : Serviceable	Minor or no damage	Little or no loss of serviceability
Degree II : Repairable	Controlled damage**	Short-term loss of serviceability***
Degree III: Near collapse	Extensive damage in near collapse	Long-term or complete loss of serviceability
Degree IV: Collapse****	Complete loss of structure	Complete loss of serviceability

* Considerations: Protection of human life and property, functions as an emergency base for transportation, and protection from environmental threats from spilling hazardous materials such as oils, if applicable, should be considered in defining the damage criteria in addition to those shown in this table.
** With limited inelastic response and/or residual time for repairs
*** Structure out of service for short to moderate duration
**** Without significant effects on surroundings

functioning as an emergency base for transportation, and as protection from environmental threats from spilling

hazardous materials such as oils. If applicable, the effects on these issues should be considered in defining the acceptable level of damage in addition to those shown in Table 2.

Once the design earthquake levels and acceptable damage levels have been properly defined, the required performance of a structure may be specified by the appropriate performance grade S, A, B, or C defined in Table 3. In performance-based design, a structure is designed to meet these performance grades.

Table 3 Performance grades S, A, B, and C

Performance grade	Design earthquake	
	Level 1(L1)	Level 2(L2)
Grade S	Degree I : Serviceable	Degree I : Serviceable
Grade A	Degree I : Serviceable	Degree II : Repairable
Grade B	Degree I : Serviceable	Degree III : Near collapse
Grade C	Degree II : Repairable	Degree IV : Collapse

The principal steps taken in performance-based design are shown in the flowchart in Fig. 11:

1) Choose a performance grade from S, A, B, or C: This step is typically done by referring to Tables 2 and 3 and selecting the damage level consistent with the needs of the users/owners. Another procedure for choosing a performance grade is to base the grade on the importance of the structure. Degrees of importance are defined in most seismic codes and standards. If applicable, a performance grade other than those of S, A, B, or C may be introduced to meet specific needs of the users/owners.
2) Define damage criteria: Specify the level of acceptable damage in engineering parameters such as displacements, limit stress states, or ductility factors.
3) Evaluate seismic performance of a structure: Evaluation is typically done by comparing the response parameters from a seismic analysis of the structure with the damage criteria. If the results of the analysis do not meet the damage criteria, the proposed design or existing structure should be modified. Soil improvement including remediation measures against liquefaction may be necessary at this stage. Details of liquefaction remediation can be found in the publication of the Port and Harbour Research Institute [1].

More comprehensive discussions on the performance-based design of port structures can be found in a publication by a working group on seismic effects for port structures, International Navigation Association [2].

Design charts useful for determining the area of ground improvement within the context of performance-based design were obtained in early 1990s. An example for a caisson quay wall is shown in Figs. 12 and 13, where based on a series of shaking table tests and effective stress analysis (Fig. 12) by varying the extent of ground improvement area (Fig. 13(a)), the area of ground improvement is shown in normalized design chart (Fig. 13(b)) [8].

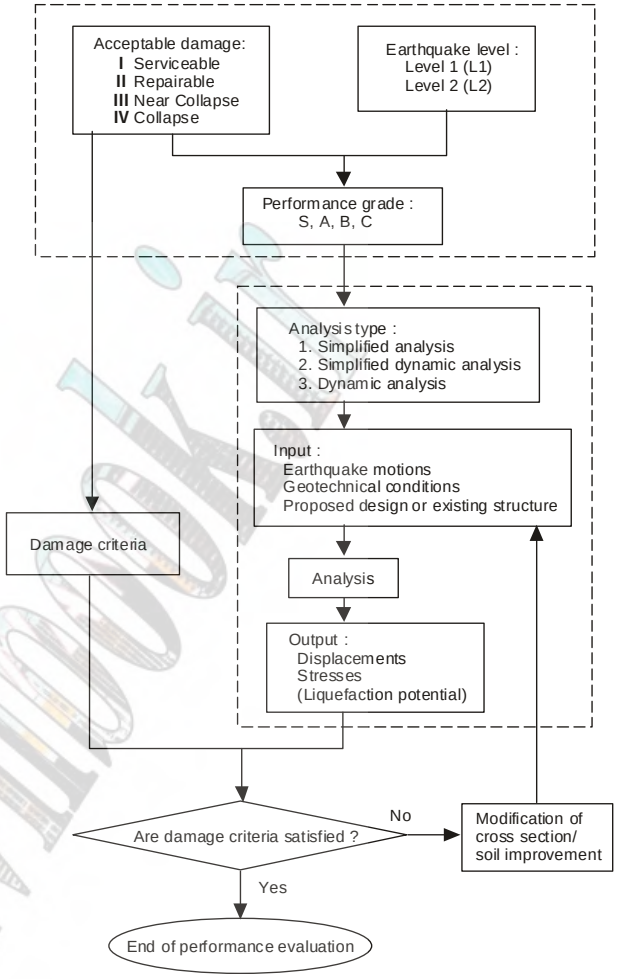

Fig. 11 Flow chart for performance evaluation [2]

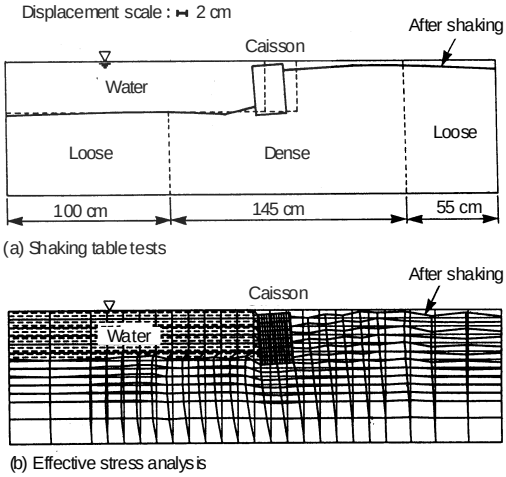

Fig. 12 Model test and computed results of residual deformation of a caisson quay wall [9]

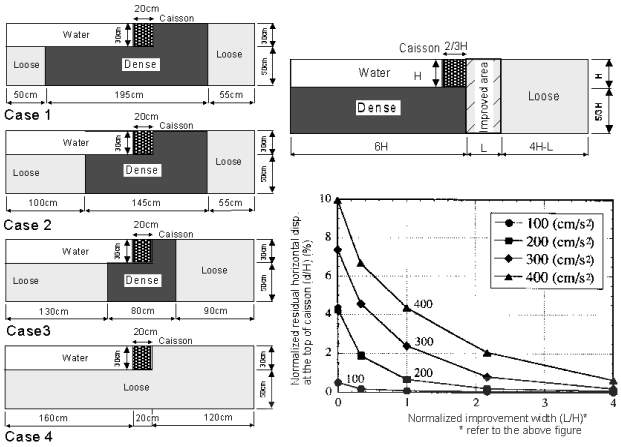

(a) Variation of cross section

(b) Width of compaction area vs. residual horizontal displacements

Fig. 13 Design chart for ground improvement area [9]

Another example is the degree of uplift of a buried structure due to liquefaction as shown in Figs. 14 and 15 [10]. Similar work was also performed on a sheet pile quay wall [1, 11, 12].

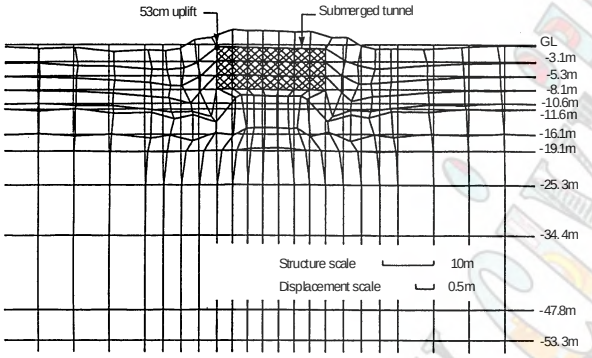

Fig. 14 Example of computed uplift of a buried structure in liquefied soil [11]

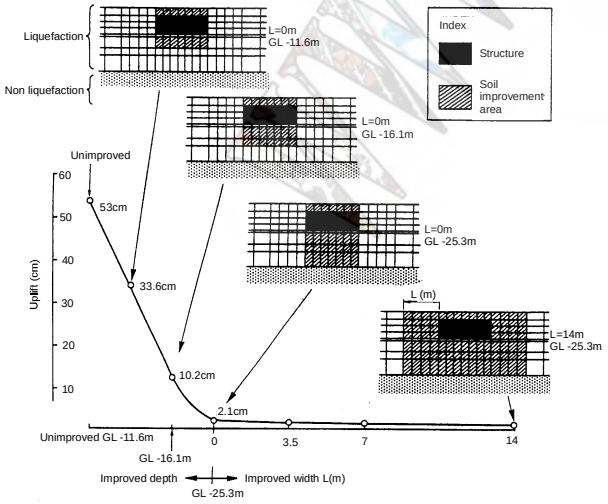

Fig. 15 Uplift and improved depth of buried structures [1]

In the framework of performance-based design, an example of the liquefaction remediation for a gravity quay wall may be given using the design chart shown in Fig. 13 as follows. In this example, let us assume that the quay wall was given the performance grade A with seismic criteria over L1 (PGA=250 cm/s^2) and L2 (PGA=400 cm/s^2) earthquake motions specified by the residual displacements (d/H) of less than 1% for maintaining full operation and 4% for allowing quick recovery of operation. By referring to Fig. 13, the L1 criterion gives the area L/H=1.7 whereas the L2 criterion gives the area of L/H=1.2. Thus, the improvement area required to meet these performance requirements is L/H=1.7. In this particular example, stronger L2 excitation does not govern the final design that was highly influenced by a high performance requirement for L1.

Performance-based approach can readily be applicable to other types of structures, including pile-supported wharves (shown in Figs. 16 and 17), that may require the structural damage criteria with respect to piles and a deck as well as displacements of dykes or retaining structures. Details can be found in the guidelines by PIANC [2].

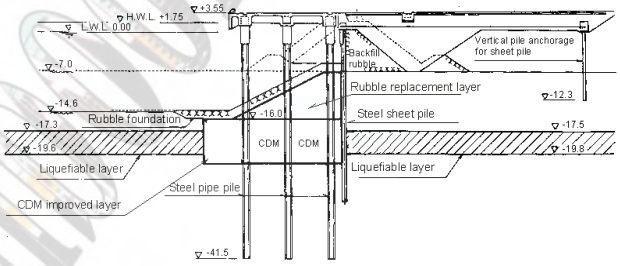

Fig. 16 Example of ground improvement for a pile-supported wharf [2]

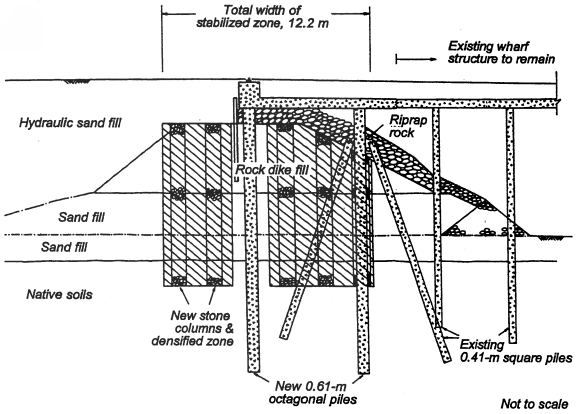

Fig. 17 Example of ground improvement for a pile-supported wharf [13]

CONCLUSIONS

Seismic damage to geotechnical structures is often associated with significant deformation of a soft or liquefiable soil deposit; hence, if the potential for

liquefaction exists, implementing appropriate remediation measures against liquefaction is an effective approach to significantly improve seismic performance. The conventional simplified approach based on pseudo-static force equilibrium provides reasonable guidelines for designing remediation of liquefiable soils against moderate earthquake motions. However, there are cases where the conventional simplified approach is not readily applicable. For example, for intense earthquake motions, acceptable displacements and structural stresses become the primary design criteria, which are not evaluated by the conventional simplified approach. There are a number of cases where site specific constraints pose difficulties in implementing the liquefaction remediation measures as suggested by the conventional simplified approach. In order to meet these situations, performance-based approach provides a reasonable framework to work on for adequate liquefaction remediation. Case histories of performance and examples of design described in the paper may be useful to apply these conclusions in practice.

REFERENCES

[1] Port and Harbour Research Institute (ed.): *Handbook on Liquefaction Remediation of Reclaimed Land*, Balkema, , 1997, 312p.

[2] PIANC, International Navigation Association: *Seismic Design Guidelines for Port Structures*, Balkema, 2001, 474p.

[3] Iai, S., Koizumi, K. and Kurata, E.: "Basic consideration for designing the area of the ground compaction as a remedial measure against liquefaction," *Technical Note of Port and Harbour Research Institute*, 1987, No. 590, pp.l-66 (in Japanese).

[4] Iai, S., Koizumi, K. and Kurata, E.: "Ground compaction area as a remedial measure against liquefaction," *Tsuchi-to-Kiso, JSSMFE*, **39**(2), 1991, pp.35-40 (in Japanese).

[5] Iai, S., Matsunaga, Y., Morita, T., Miyata, M., Sakurai, H., Oishi, H., Ogura, H., Ando, Y., Tanaka, Y. and Kato, M.: "Effects of remedial measures against liquefaction at 1993 Kushiro-Oki earthquake," *Proc. 5th U.S.-Japan Workshop on Earthquake Resistant Design of Lifeline Facilities and Countermeasures against Soil Liquefaction*, NCEER-94-0026, 1994, pp.135~152.

[6] Inagaki, H., Iai, S., Sugano, T., Yamazaki, H. and Inatomi, T.: "Performance of caisson type quay walls at Kobe Port," *Soils and Foundations, Special Issue*, 1996, pp.119-136.

[7] Iai, S., Matsunaga, Y. and Kameoka, T. [1992] "Strain space plasticity model for cyclic mobility," *Soils and Foundations*, **32**(2), 1-15.

[8] Iai, S., Ichii, K., Liu, H., and Morita, T.: "Effective stress analyses of port structures," *Special Issue on Geotechnical Aspects of the January 17 1995 Hyogoken-Nambu Earthquake, No.2, Soils and Foundations*, 1998, pp.97-114.

[9] Iai, S.: "Area of ground compaction against soil liquefaction," *Proc. 13th International Conference on Soil Mechanics and Foundation Engineering*, New Delhi, 1994 pp.1075~1078.

[10] Iai, S. and Matsunaga, Y.: "Mechanism of uplift of underground structures due to liquefaction," *Proc. International Symposium on Natural Disaster Reduction and Civil Engineering, Osaka*, JSCE, 1991, pp.297~306.

[11] Iai, S. and Matsunaga, Y.: "Soil improvement area against liquefaction," *Proc. 8th Japan Earthquake Engineering Symposium*, 1990, pp.867-872

[12] McCullough, N.J. and Dickenson, S.E.: "Estimation of seismicaaly induced lateral deformations for anchored sheetpile bulkheads," *Geotechnical Earthquake Engineering and Soil Dynamics III, Geotechnical Special Publication* No.75, ASCE, 1998, pp.1095-1106.

[13] Egan, J.A., Hayden, R.F., Scheibel, L.L., Otus, M., and Serventi, G.M.: "Seismic repair at Seventh Street Marine Terminal," *Special Geotechnical Publication* **30**, ASCE, 1992, pp.867-878

Pseudo static vs. performance based seismic bearing capacity of footings on liquefiable soil

G. D. Bouckovalas, A. I. Valsamis, K. I. Andrianopoulos
School of Civil Engineering, National Technical University of Athens, Greece

Abstract

The effect of liquefaction on the post-shaking bearing capacity and settlement of strip footings is explored, focusing on the case where a thin clay layer is overlying the liquefiable sand. Starting with a simple analytical model of bearing capacity degradation developed earlier, both the use of a more realistic failure surface and a more accurate simulation of the strength degradation in the liquefiable sand are explored and consequently verified against pseudo-static numerical analysis. Furthermore, a parametric dynamic numerical analysis is performed in order to study the coupled excess pore pressure-settlement response of the foundation and evaluate the overall accuracy of the simplified analytical approach. Comparison of the analytical (pseudo-static) with the numerical predictions shows that: (a) the former may provide reasonable estimates of the degraded bearing capacity, however (b) the use of a reduced friction angle to model liquefaction-induced shear strength degradation may prove overlay conservative, and (c) for common static factors of safety, settlements at the end of shaking are an order of magnitude higher than initial static settlements and consequently they should form the basis of design.

Keywords--*Liquefaction, foundation, bearing capacity, settlements*

INTRODUCTION

Since the first liquefaction-induced extensive damage to engineered structures was recorded, during Niigata 1964 earthquake, this form of soil strength degradation is considered as one of the most ominous earthquake hazards. In fact, many seismic codes rate liquefiable soils in the prohibited (X-) soil category where ground improvement and re-inforcement are mandatory prerequisites. Nevertheless, this approach is gradually giving ground to quantitative evaluations of the bearing capacity and the deformations of the liquefied ground, as a more rational means for deciding upon the necessity, the type and the extend of the required remedial measures. The empirical evaluation of the residual shear strength of liquefied soils ([4], [12], [19]), the computation of lateral spread displacements ([15], [21]), as well as the evaluation of liquefaction-induced lateral loads on piles ([5], [7], [10]) are typical advancements in this direction.

This article deals with the bearing capacity degradation of strip foundations resting upon a liquefiable soil layer with a relatively thin non-liquefiable soil cap. The photographs in Fig. 1 are typical of this type of foundation failure. They show buildings with relatively low height over width ratio, less than about 1.5, which settle almost vertically, with little deviation from verticality. A punch-through failure mode is observed, with minor heave of the ground surface around the building.

A simple analytical solution for this practical problem was presented earlier by Cascone and Bouckovalas [3], assuming the failure mechanism of Fig. 2. Namely, based on the analytical solutions for strip and square footings on two layered soils proposed by Meyerhof and Hanna [9], it was possible to derive correction coefficients for the static bearing capacity, in terms of the initial soil properties, the geometry of the footing and the soil profile, as well as the average excess pore pressure ratio that is expected to develop under the footing at the end of shaking. Furthermore, the minimum required thickness of the clay cap was estimated so that liquefaction of the underlain sand layer does not affect the bearing capacity.

The research that is summarized herein, focuses upon three tasks of immediate practical interest for the accuracy of the analytical predictions:

(a) Numerical verification and improvement of the failure mechanism assumed by the Meyerhof and Hanna bearing capacity solutions (Fig. 2).

(b) Exploration of alternative ways that may be used to model the shear strength degradation of the liquefiable sand, as well as introduction of the residual strength concept.

(c) Numerical simulation of earthquake-induced settlements and post-shaking bearing capacity of vertically loaded footings, where excess pore pressure build up in the sand layer, bearing capacity and foundation settlements are consistently coupled with seismic ground shaking.

REFINEMENT OF BEARING CAPACITY MECHANISM

As of [3], the pseudo-static evaluation of bearing capacity degradation due to liquefaction follows the following basic steps:

- The nominal bearing capacity of the footing $q_{ULT,O}$ is first evaluated, as if the sand layer did not exist and failure occurred totally within the clay cap.

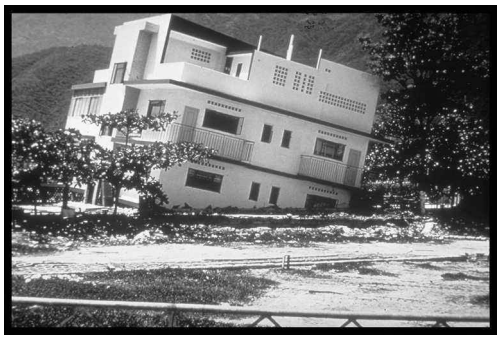

(a)

(b)

Fig. 1: Typical examples of bearing capacity failure of foundations on liquefiable soil, from (a) Caracas 1967 earthquake and (b) Kocaeli 1999 earthquake.

- An average excess pore pressure ratio $U=\Delta u/\sigma'_{vo}$ (σ'_{vo} is the initial effective vertical stress) is computed for the liquefiable sand.
- An equivalent reduced friction angle φ^* is consequently evaluated in terms of U and the actual friction angle φ:

$$\tan\varphi^* = (1-U)\tan\phi \qquad (1)$$

- The degraded bearing capacity of the footing $q_{ULT,D}$ is then evaluated, assuming a combined failure mechanism that affects both the liquefiable sand layer and the clay cap (Fig. 2).
- The bearing capacity degradation factor is consequently defined as $\zeta = q_{ULT,D}/q_{ULT,O}$.

From the above brief presentation, it becomes evident that the assumed failure mechanism is a key element of the analysis. To meet the requirements of [9], the aforementioned solution assumed that, during seismic shaking, the sand layer will eventually become weaker than its clay cap leading to a punch-through failure mechanism with vertical slip surfaces developing within the clay cap. To verify this assumption, a number of elastoplastic pseudo-static numerical analyses were performed with the Finite Difference method [11], for varying footing width B, clay thickness H and soil strength

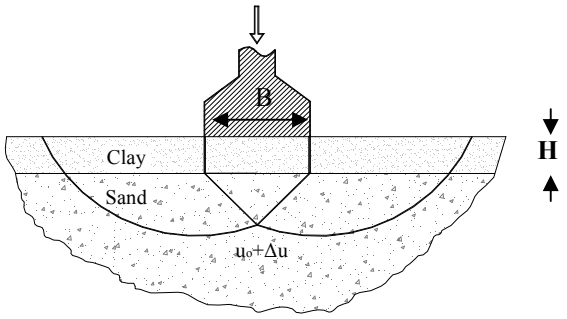

Fig. 2: Footing resting on liquefiable sand with a clay cap: failure surface assumed by [3]

properties. The numerical simulation assumed a total stress, Tresca failure criterion for the clay cap and an effective stress, Mohr-Coulomb failure criterion for the sand.

Results from this parametric study are shown in Fig. 3, for a typical case with $H/B=0.5$, initial friction angle of sand $\varphi=30^o$, and undrained shear strength of the clay cap $c^*=c/\gamma B=1.0$. In the above definitions γ is the buoyant unit weight of the clay cap, H is the thickness of the clay cap and B is the width of the footing. It is observed that, the slip surface in the clay is indeed not vertical, but converges gradually with depth towards the foundation axis. Driven by the above finding, the failure mechanism of Cascone and Bouckovalas [3] was modified as shown in Fig. 4. Thus, it was possible to compute a deviation angle α of the slip surface in the clay from verticality after imposing limit equilibrium analysis and consequently minimizing the resulting ultimate load.

The resulting analytical expression is:

$$\alpha = \arctan\left(\frac{1}{4}\frac{2\gamma N_\gamma B - 4\sqrt{\gamma N_\gamma cH}}{\gamma N_\gamma H}\right) \qquad (2)$$

where γ is the liquefiable buoyant unit weight of the liquefiable sand and N_γ is the bearing capacity factor.

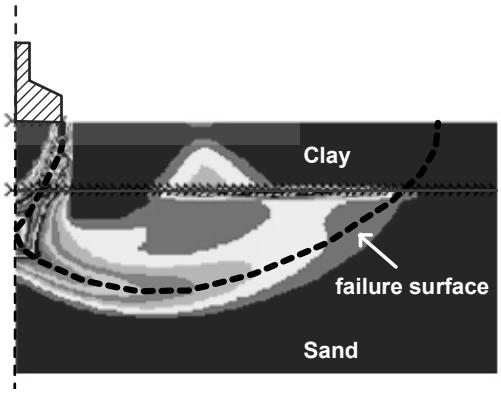

Fig. 3: Typical contours of shear strain rate at failure and trace of equivalent failure surface

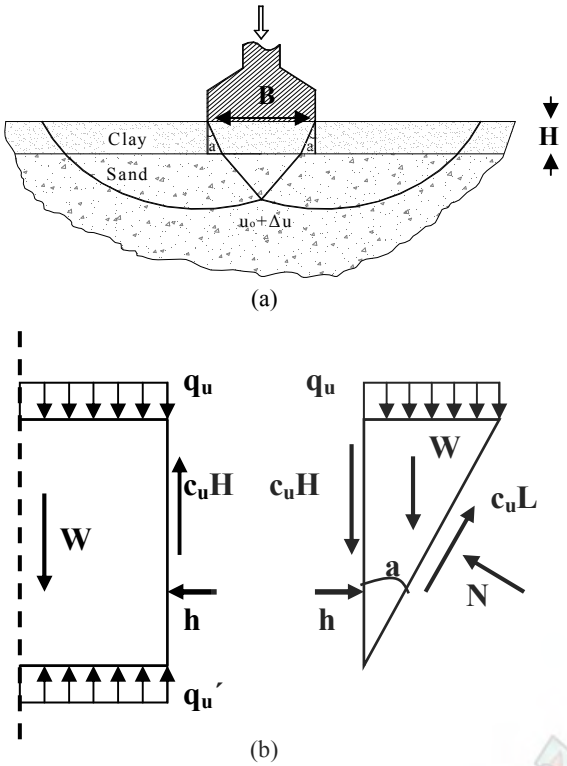

Fig. 4: Footing resting on liquefiable sand with a clay cap: (a) Refined failure mechanism and (b) Limit equilibrium model

This procedure proved adequately accurate, as it led to deviation angles α fairly similar to these obtained numerically. This is shown in Fig. 5, where the analytically computed refined failure surface in the clay cap is compared to the numerically predicted shear strain rate contours at failure. Nevertheless, the more accurate failure mechanism had a rather minor effect on the degraded bearing capacity $q_{ULT,D}$. For instance, Fig. 6 shows a typical comparison between the degradation factors $\zeta=q_{ULT,D}/\ q_{ULT,O}$ derived from the basic and the refined failure mechanisms shown in Figs. 2 and 4 respectively. The observed differences are indeed secondary and can be readily overlooked in view of other more crucial problem uncertainties (e.g. the evaluation of a representative excess pore pressure value for the whole foundation area).

EFFECT OF LIQUEFACTION-INDUCED SHEAR STRENGTH DEGRADATION

The method of Cascone and Bouckovalas [3] assumes the simplified degradation mechanism suggested by many seismic codes, namely that the friction angle of the sand degrades gradually with excess pore pressure build up, according to Eq. 1, and finally diminishes to zero. However, it is widely known that liquefiable soils attain a residual strength even when effective stresses approach to

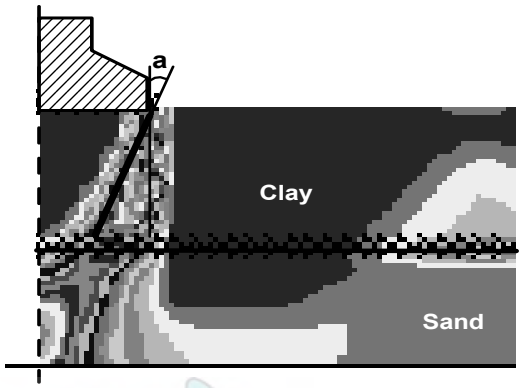

Fig. 5: Comparison of analytically predicted failure surface in the clay cap with numerically computed strain increment contours at failure.

zero. To model this, the degraded in situ shear strength of sand τ_f was simply expressed as:

$$\tau_f = (1-U)\sigma_{VO}^{'} \tan\phi + U\tau_{res} \tag{3}$$

where, τ_{res} represents the residual shear strength of the liquefied sand. Among the various empirical correlations which are available for the estimation of τ_{res} (e.g. [12], [17], [18]) the one proposed by Stark and Mesri [18] was used here. In average terms, this correlation can be approximately written as:

$$\tau_{res} = 0.011 N_{1,60} \sigma_{VO}^{'} \tag{4}$$

where $N_{1,60}$ is the corrected number of SPT blow count (e.g. [20]) and σ'_{vo} is the initial vertical consolidation stress.

There are two ways to introduce the above shear strength degradation into conventional bearing capacity computations. The first is to define a reduced friction angle φ^*, in a way similar to that followed in the initial development of the method:

$$\tan\varphi^* = \left[(1-U)\tan\varphi + U\tan\varphi_{res}\right] \tag{5}$$

where the value of the residual friction angle of the sand is given as:

$$\tan\varphi_{res} = 0.011\, N_{1,60} \tag{6}$$

The second way is to define an apparent buoyant unit weight γ^*, in terms of the nominal buoyant unit weight γ of sand and U:

$$\gamma^* = \gamma'(1-U) + U\gamma_{res} \tag{7}$$

with

$$\gamma_{res} = \frac{0.011 N_{1,60}}{\tan\phi}\gamma' \qquad (8)$$

Note that, using either Eqs. 5 & 6 or Eqs. 7 & 8 one comes to essentially the same relation for the degraded insitu shear strength of the sand (Eq. 3). Still, the different methods of simulating the degradation of shear strength lead to considerably different values for the bearing capacity degradation factor ζ. This is because bearing capacity formulas are highly non-linear with respect to the friction angle (φ or φ^*), while they are linear with respect to the buoyant unit weight of the soil (γ or γ^*).

To show the potential effect of the different assumptions regarding shear strength degradation, Fig. 7 compares the variation of ζ with U for a loose sand ($\varphi=30^o$, $N_{1,60}$ = 7), computed (a) for a degraded friction angle with a $\varphi_{res}=0$ or $\varphi_{res}=4^o$, and (b) for a reduced buoyant unit weight with $\gamma_{res}=0$ or $\gamma_{res}=2.42kN/m^3$.

Observe that degrading the friction angle of sand is by far more conservative than reducing the buoyant unit weight. The difference between the two approaches is remarkably large and cannot be simply overlooked for the benefit of increased safety. Furthermore, note that taking into account the post-liquefaction residual strength of sand leads to reasonably lower degradation of the bearing capacity (i.e. greater values for factor ζ), regardless of the basic approach that was used to simulate liquefaction effects.

COUPLED DYNAMIC ANALYSES OF BEARING CAPACITY DEGRADATION AND SETTLEMENT

In order to evaluate the validity and the accuracy of the pseudo-static approach, a series of numerical analyses was performed, where:

a) The foundation was first loaded statically, with an initial uniform vertical load less than the ultimate.

b) Consequently, seismic shaking was applied, under constant static load, and a 2-D field of excess pore pressures was computed in the liquefiable sand layer.

c) Following the end of shaking, the foundation load was further increased until failure.

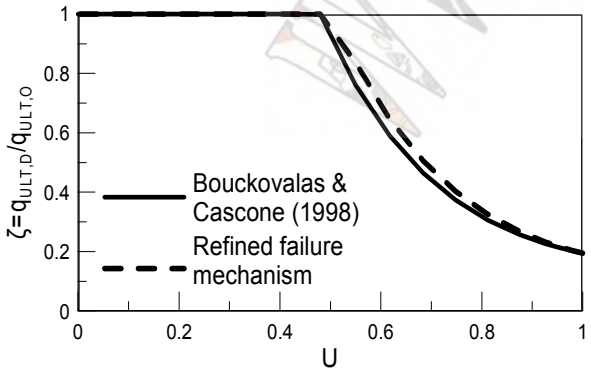

Fig.6: Effect of bearing capacity mechanism on analytically computed correction factor ζ ($c^*=1.0$, $\varphi=30^o$, $H/B=0.5$)

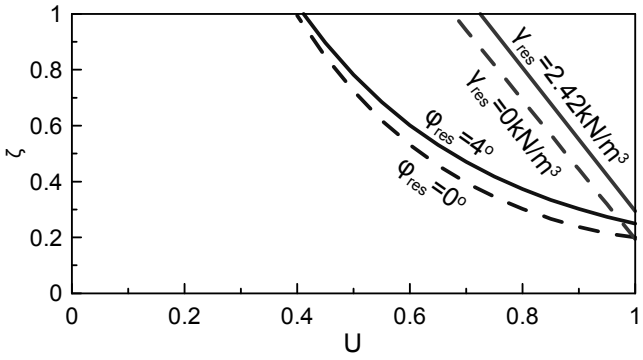

Fig. 7: Effect of sand degradation model on analytically computed correction factor ζ ($c^*=1.0$, $\varphi=30^o$, $H/B=0.5$).

A total of ten (10) cases were examined, for various initial loading conditions corresponding to average contact pressure between 0 and 130 kPa. In all analyses, seismic shaking was applied under undrained conditions. On the other hand, static loading was applied under undrained conditions for the clay cap and under drained conditions for the underlying sand. The analyses were performed with the Finite Difference computer code FLAC [11] appropriately extended to account for excess pore pressure build up during cyclic loading. A uniform grid of 1000 square 1mx1m elements was used. The first 2 m of depth consisted of clay with $c=40KPa$ and $\varphi=0^o$, while the rest 18m consisted of sand with $c=0KPa$ and $\varphi=30^o$. The width of the foundation was $B=4m$, giving an H/B ratio of 0.5. The base of the sand layer was excited with the acceleration time history shown in Fig. 8.

The soil element response was taken as elastic-perfectly plastic with failure described by the Mohr-Coulomb criterion. Pore pressure build-up during seismic shaking was simulated via a coupled effective stress – plastic volumetric strain analysis. Namely, the rate of plastic volumetric strain due to cyclic loading was defined by the following empirical relation (based on [6]):

$$\Delta\varepsilon_{vol} = bA\gamma_{cyc}^{a}\left(\frac{\varepsilon_{vol}}{A\gamma_{cyc}^{a}}\right)^{b} \qquad (8)$$

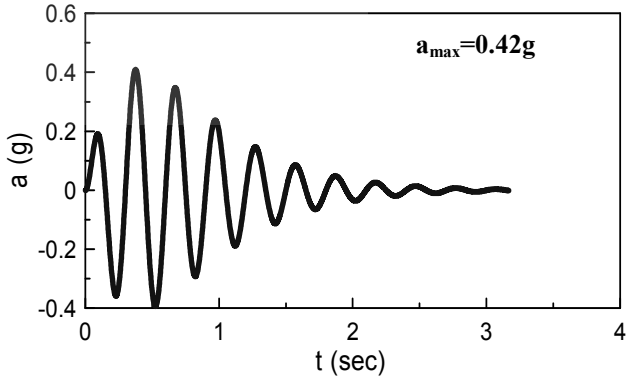

Fig. 8: Acceleration time history for coupled dynamic analyses

where ε_{vol} is the permanent volumetric strain that would have developed after N cycles of drained cyclic loading with strain amplitude $\gamma_{cyc,}$ while $A=5.0$, $\alpha=1.26$ and $b=-1.50$ are average model parameters determined for cyclic simple shear tests on a number of relatively uniform graded sands. The plastic volumetric strain was then converted to an effective stress change Δσ' by reducing according to the following relation:

$$\Delta\sigma'_{ij} = C^{e}_{ijkl}(\Delta\varepsilon_{kl} - \frac{\Delta\varepsilon_{vol}}{3}\delta_{kl}) \qquad (9)$$

where C^{e}_{ijkl} is the elastic stiffness matrix of the soil skeleton. Under constant volume (i.e. undrained conditions) this effective stress change gives the increase of pore pressure Δu due to cyclic loading. The same procedure has been successfully used Byrne [2] for the implementation of the empirical model of Martin et al. [8] in the finite difference code FLAC [11].

Typical results for the vertical load-deformation response of the footing, obtained from this numerical experiment, are shown in Figs. 9 and 10. Namely, Fig. 9 shows typical pore pressure contours in the foundation soil, at the end of shaking, while Fig. 10 shows the load (average contact pressure)-displacement curves for:

a) One case of static loading with initial (pre-shaking) soil conditions and a continuous soil profile consisting of clay. This condition is used as reference for the definition of the degradation factor ζ.

b) One case of static loading with initial (pre-shaking) soil conditions and the actual soil profile consisting of liquefiable sand with a clay cap. This condition is used as reference for the definition of the initial static factor of safety (*F.S.*), before the onset of shaking.

c) Three typical cases of coupled static and seismic loading, for uniform initial contact pressures q_{ST}=0, 50 and 90 kPa.

There are two main observations in this figure. First, note that the degraded bearing capacity of the footing depends on the magnitude of the initial static load, i.e. the design load of the foundation and the corresponding factor of safety against conventional static failure. At first glance

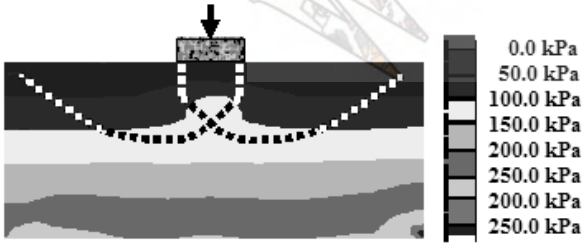

Fig. 9: Pore pressure contours at the end of shaking for q_{ST}=50kPa

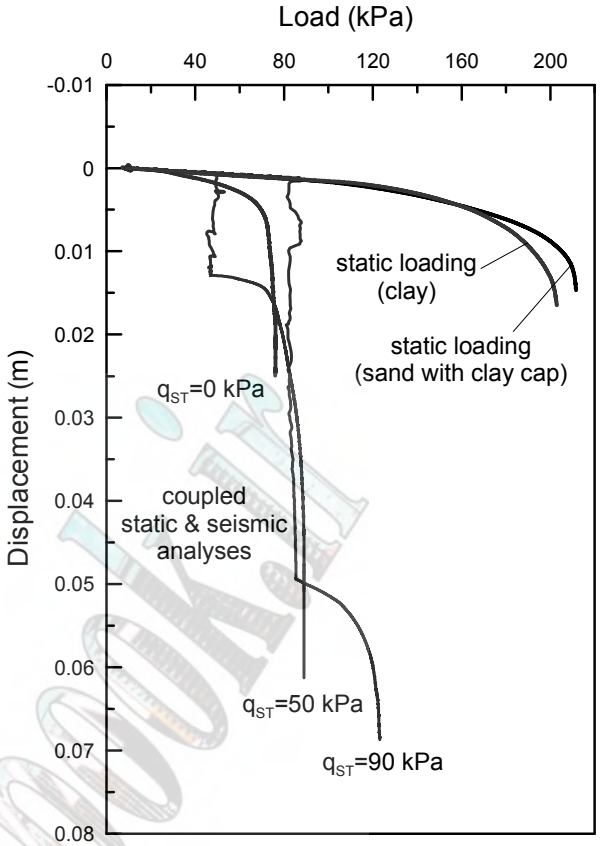

Fig. 10. Results from static and coupled static-seismic numerical analyses: typical load-displacement curves (*for c*=1.0, φ=30°, H/B=0.5*)

this observation is disturbing as it suggests that there is no unique degradation factor ζ that can be defined in terms of the initial soil conditions, the foundation geometry and the intensity of shaking. However, such an interpretation would prove premature, as the observed differences can be adequately explained by the different values of the excess pore pressure ratio U corresponding to each curve in Fig. 10.

To show this, Fig. 11 correlates the degradation factors ζ obtained from all numerical analyses to the corresponding average values of the excess pore pressure

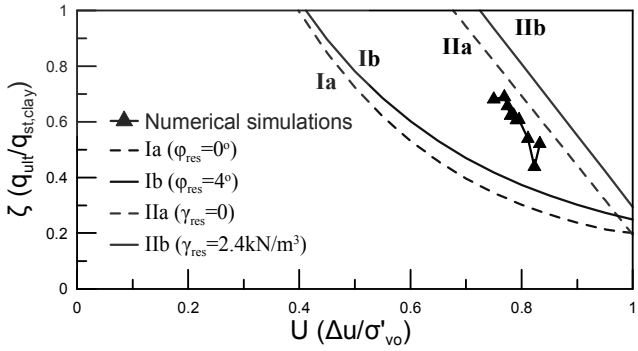

Fig. 11: Comparison between analytical and numerical predictions of bearing capacity degradation factors ζ

ratios U at the end of shaking. The numerical predictions are compared to the ζ-U curves predicted analytically for the same soil and foundation conditions, assuming either degradation of the friction angle or reduction of the buoyant unit weight of the sand. In all cases, the average value of U was calculated on the basis of the numerically computed values along the respective failure surface (e.g. see Fig. 9). Observe that the data points from the dynamic analyses define a more or less unique ζ-U relation which lays between the analytical predictions for degraded friction angle and those for decreased buoyant unit weight of the sand.

The second observation of practical interest is that the displacements at failure are considerably larger for the degraded soil conditions than for the reference static analyses for non-degraded soil. This difference is mostly due to the permanent settlements accumulated during shaking (vertical branch of the load-displacement curves) and increases rapidly with the magnitude of the initial static load. Taking into account that seismic loading takes place under undrained conditions, as well as that the constitutive model used for the analyses allows for permanent shear and deviatoric strain accumulation upon failure only, it is concluded that this branch of the load-displacement curves is attributed to instantaneous foundation failure, each time ground accelerations exceed a critical level. This phenomenon, under drained soil conditions, has been given detailed attention by Richard et al. [16].

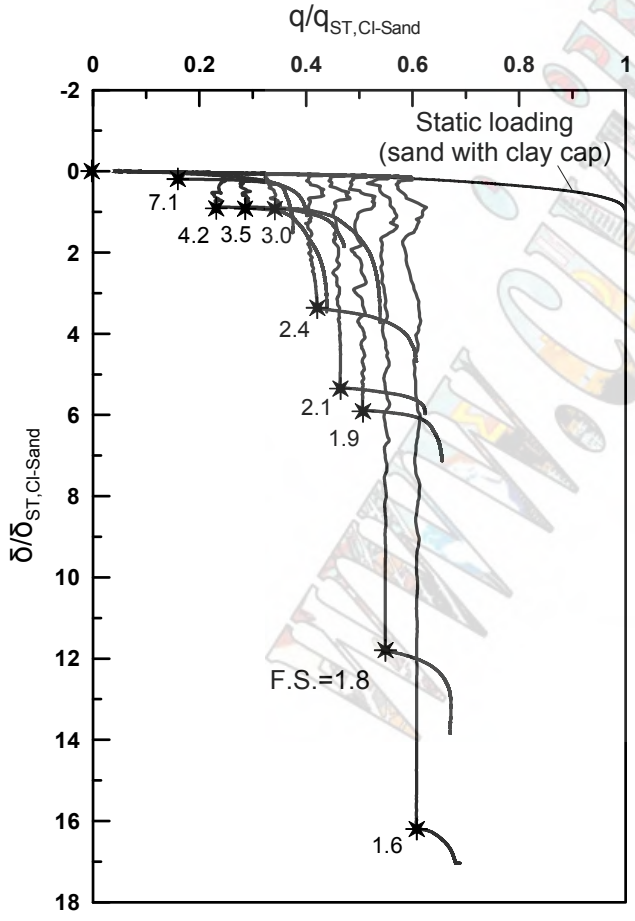

Fig.12. Results from static and coupled static-seismic numerical analyses: Normalized load – displacement curves. (*for c^*=1.0, φ=30°, H/B=0.5*).

For the benefit of further insight, Fig. 12 shows the load displacements curves from the reference static analysis (b), for uniform clay soil over sand, as well as from all coupled static and seismic analyses. To highlight the relative magnitude and the potential importance of the accumulated settlements, applied loads have been normalized against the ultimate load for non-degraded sand properties ($q'_{ULT,O}$), while displacements have been normalized against the corresponding diplacements at the onset of failure $\delta'_{ULT,O}$. Focusing upon the end of shaking, denoted with a black star on the normalized load-displacement curves, it is realised that the corresponding displacements may become one order of magnitude higher than those at conventional static failure while applied static loads are still less than the degraded ultimate loads.

This is shown more clearly in Fig. 13, where the static factor of safety $F.S.=q'_{ULT,O}/q_{ST}$ is correlated to the normalized displacements at three loading history instants: the onset of shaking, the end of shaking and at post-shaking failure. Observe that the normalised vertical load that will provide the same settlements at the end of shaking as the the reference ultimate static loading ranges between 0.20 and 0.35, corresponding roughly to factors of safety between 3.0 and 5.0. When the factor of safety is reduced to about 2.0, liquefaction-induced settlements increase by an order of magnitude.

In other words, there is a clear need to define a performance based failure criterion of the foundation that will depend upon settlements rather than on the bearing capacity it self.

CONCLUSION

In summary, the preceding study has shown that:

(a) Analytical predictions of liquefaction effects on the bearing capacity of surface foundations are not sensitive to the exact shape of the assumed failure surface in the top clay layer, that lays between the foundation and the liquefiable soil.

(b) On the contrary, they depend strongly on the method used to model the post-shaking degraded strength of the sand. Based on the results of static and dynamic numerical analyses, it appears that gradual degradation of the friction angle leads to lower bound estimates of the degradation factor ζ while gradual decrease of the effective buoyant weight provides upper bound estimates.

(c) Implementation of the residual shear strength of sand to the degraded bearing capacity computations reduces bearing capacity degradation (increases ζ) while limits somewhat the gap between the two different

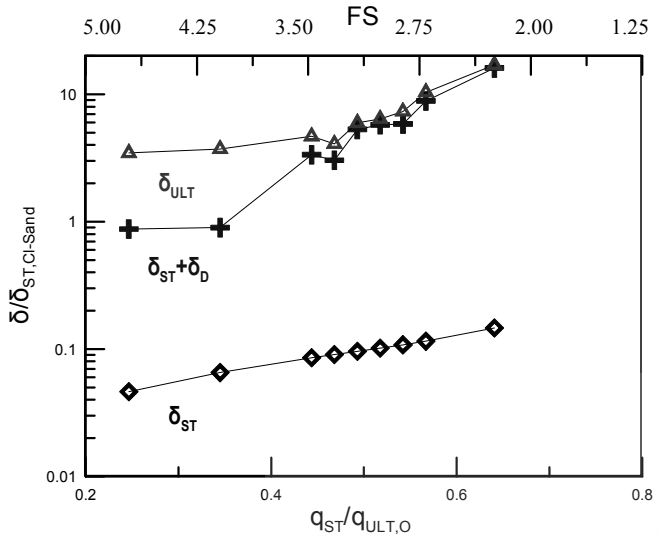

Fig.13. Results from static and coupled static-seismic numerical analyses: Effect of initial static load on foundation settlements. (*for c*=1.0, φ=30°, H/B=0.5*)

models of strength degradation in the liquefiable sand.

(d) Pseudo-static simulation of the effects of liquefaction fails to predict the very large foundation settlements at the end of shaking. Based on the present results, the level of settlement at conventional static failure is obtained at the end of shaking even though the static load applied to the foundation corresponds to a factor of safety between 3 and 5. When this factor of safety is reduced to about 2, post shaking settlements increase by an order of magnitude.

(e) The bearing capacity of surface foundations on liquefiable subsoil, is better defined on the basis of performance rather than on soil failure criteria.

It is acknowledged that the constitutive models that were used in the present study, do not provide the quantitative accuracy that is necessary for detailed bearing capacity and seismic ground response analyses. In view of this shortcoming, this stage of the study focused upon a qualitative rather than quantitative exploration, on the basis of a mostly non-dimensional parametric analysis. Nevertheless, it is our present aim to improve the numerical accuracy of the analyses so that quantitatively sound design guidelines can be established. This will be achieved with the aid of a critical state plasticity constitutive model [13], [14], that has been extensively validated against monotonic and cyclic test data and implemented to FLAC [1], as well as an extensive analysis of published case histories and model experiments. This activities are currently under progress.

ACKNOWLEDGMENTS

The work presented herein has been financially supported by the General Secretariat for Research and Technology (Γ.Γ.Ε.Τ.) of Greece, through research project ΕΠΑΝ-ΔΠ23 ("X-SOILS"). Dr. Ach. Papadimitriou was instrumental for the implementation of the excess pore pressure build up model to FLAC. These contributions are gratefully acknowledged.

REFERENCES

[1] Andrianopoulos K. I. 2005, Numerical simulation of static and dynamic loading on elastoplastic soils, *Ph.D. Dissertation, National Technical University of Athens, Greece* (in Greek)

[2] Byrne P. 1991. A Cyclic Shear-Volume Coupling and Pore-Pressure Model for Sand. *Proc Second International Conference on Recent Advances in Geotechnical Earthquake Engineering and Soil Dynamics (St. Louis, Missouri, March, 1991),* Paper No. 1.24, 47-55.

[3] Cascone E. & Bouckovalas G. 1998. Seismic bearing capacity of soils. *Proc. 11th European Conference in Earthquake Engineering,* Paris, September 1998

[4] De Alba Pedro, 2004. Residual strength after liquefaction: A rheological approach, *11th International conference on Soil dynamics & earthquake engineering, 3rd International conference on earthquake geotechnical engineering*, 7-9 January 2004, Berkeley

[5] Dobry Ricardo, Abdoun Tarek, O'Rourke Thomas & Goh S. H., 2003. Single piles in lateral spreads: Field bending moment evaluation, *Journal of Geotechnical and Geoenviromental engineerin*g, Vol. 129,No.10, October 1, 2003.

[6] Egglezos D.N., Bouckovalas G., 1998. Analytical relationships for earthquake-induced pore pressure in sand, clay and silt, Proc. 11th European Conference on Earthquake Engineering, Paris, September.

[7] Finn W.D.L., Fujita N. 2002. Piles in liquefiable soils: seismic analysis and design issues, *Soil Dynamics and Earthquake Engineerin,g* 22 (2002) pp. 731-742.

[8] Martin, G. R., W. D. L. Finn and H. B. Seed. 1975. Fundamentals of Liquefaction Under Cyclic Loading, *Journal of Geotechnical Engineering, ASCE,* Vol 101(GT5), 423-438.

[9] Meyerhof G.G. & Hanna A.M. 1978. Ultimate bearing capacity of foundations on layered soils under inclined load.*SCanadian Geotechnical Journal,* vol 15 (4): 565-572.

[10] Ishihara K. & Cubrinovski M., 1998, Soil-pile interaction in liquefied deposits undergoing lateral spreading, *XI Danube-European Conference,* Croatia, May 1998.

[11] Itasca 1998. Flac version 3.4: Fast Langrangian Analysis of Continua. *RItasca Consulting Group,* Minneapolis, Minnesota.

[12] Olson S. M. and Stark T. D. 2002, Liquefied strength ratio from liquefaction flow failure case histories, *Canadian Geotechnical Journal,* Vol. 39, pp. 629-647

[13] Papadimitriou Ach., Bouckovalas G., Dafalias Y. 2001, A plasticity model for sand under small and large cyclic strains, *Journal of Geotechnical and Geoenvironmental Engineering, ASCE*, 127(11),

[14] Papadimitriou Ach., Bouckovalas G. 2002, Plasticity model for sand under small and large cyclic strains: a multiaxial formulation*, Soil Dynamics and Earthquake Engineering*, 22

[15] Rauch A. F. & Martin J. R. II 2000, EPOLLS Model for Predicting average displacements on lateral spreads, *Journal of Geotechnical and Geoenviromental*

engineering, Vol 126, No. 4, pp. 360-371

[16] Richard R., Elms D. G. & Budhu M., 1990. Dynamic fluidization of soils, *Journal of Geotechnical Engineering, ASCE,* Vol. 119 (4), pp 662-674.

[17] Seed R. B. and Harder L. F. 1990, SPT-based analysis of cyclic pore pressure generation and undrained residual strength, *in J. M. Duncan ed., Proceedings H. Bolton Seed Memorial Symposium, University of California, Berkeley,* Vol. 2, pp. 351-376

[18] Stark T.D. & Mesri G. 1992. Undrained Shear Strength of Liquefied Sands for Stability Analysis. *Journal of Geotechnical Engineering, ASCE,* Vol 118 (11), November 1992

[19] Yoshimine M. and Ishihara K., 1998. Flow potential of sand during liquefaction, *Soils and Foundations,* Vol. 38 (3), pp. 189-198

[20] Youd T. L. and Idriss I. M. 2001, Liquefaction resistance of soils: Summary report from the 1996 NCEER and 1998 NCEER/NSF workshops on evaluation of liquefaction resistance of soils, *Journal of Geotechnical and Geoenvironmental Engineering, ASCE,* Vol. 127 (4), pp. 297-313)

[21] Youd T. L., Hansen C. M. & Barlett S. F. 2002, Revised multilinear regression equations for prediction of lateral spread displacement, *Journal of Geotechnical and Geoenviromental engineerin*g, Vol. 128,No.12, December

Cyclic Soil-Structure Interaction Model for Performance-Based Design

N. Allotey[1], M. H. El Naggar[1]
[1]*Department of Civil & Environmental Engineering, University of Western Ontario, Canada*

Abstract

Work is currently underway at the University of Western Ontario to develop a generic beam-on-a-nonlinear-Winkler foundation (BNWF) model for performance-based seismic design of structures founded on shallow and deep foundations. The model is developed as a stand-alone module to be included in commercial nonlinear structural analysis programs. This paper highlights various important aspects of the model including: backbone curves; various unloading and reloading rules; modeling gap formation with the option of accounting for soil fall-in; and modeling cyclic hardening/degradation and radiation damping. The capability of the model to represent different response features observed in experimental *p-y* curves is demonstrated, and this highlights the usefulness of the model as a performance-based design tool.

Keywords — *Cyclic response, performance-based design, soil-structure interaction, Winkler model*

INTRODUCTION

Performance based design involves designing structures to achieve a target performance under expected loading events. To provide this specified performance at reasonable cost, reliable analysis of the entire structure-foundation system is important. The design approach relies heavily on nonlinear forms of analysis, and in particular, nonlinear dynamic analysis. There is therefore a need for robust and efficient analysis tools that are acceptable to both structural and geotechnical engineers [4]. The procedures used for performing nonlinear dynamic analysis of soil-structure systems include approaches where the soil is considered as a continuum and is discretized and others where the soil is modeled using discrete springs. Although increases in computational power have reduced the time required for the former, it still remains unattractive to many structural design engineers. It is thus common-practice for design engineers to model structural elements with advanced cyclic macro-models, but to account for the soil flexibility using effective linear springs.

The beam-on-a-nonlinear Winkler foundation (BNWF) approach is an improvement on the effective linear spring approach. The main drawback of the approach is that it idealizes the soil continuum with soil reactions at different points (and degrees of freedom) that are decoupled from each other. Nevertheless, it is widely used by design engineers for predicting the nonlinear static response of soil-structure systems. Dynamic BNWF models on the other hand are less popular, and SPASM8 [23] was the first to be developed. Since then, other specific stand-alone programs [8, 10, 14, 30, 21, 27, 28, 33] and spring-dashpot-gap element combination models in commercial finite element programs [16, 25] have been developed. Most of these, however, account for only certain aspects of nonlinear soil-structure interaction (SSI) response, and can therefore not be used for modeling a wide range of problems. Most of the stand-alone programs have also been developed mainly for foundation analysis and are not available to structural engineers.

To account for some of the drawbacks of the BNWF approach, coupled BNWF models have recently been developed. The accuracy of these models has however been noted to depend largely on the accurate modeling of the cyclic normal force-displacement response [3, 20]. The objective of a current study is therefore to develop a generic dynamic normal force-displacement BNWF model, which can be used for modeling different foundation and soil types under different loading conditions. The model is developed as a stand-alone module to be included in nonlinear structural analysis programs. This paper will concentrate on presenting the various features of the model as implemented in the nonlinear structural analysis program SeismoStruct® [32] that is available online. Only a summary of the model development is given here, and more detailed information can be found in [2]. The model presented is an improvement of an earlier one developed by the authors for another nonlinear structural analysis program [15].

CYCLIC SSI EXPERIMENTAL RESULTS

Early experimental studies on soil-pile behaviour were driven mainly by the needs of the offshore industry. This resulted in the development of static and cyclic pseudo-static *p-y* and *t-z* curves that are widely used in determining nonlinear soil-pile response [1]. Recent research driven by the needs of the earthquake

[1] References to pile also apply to retaining walls and footings.

engineering community has resulted in some studies focused on identifying the factors that influence the soil-pile cycle-by-cycle response [12, 13, 24, 37, 38]. These have been conducted for different soil types and loading conditions and show that the response is affected by a complex interaction of various factors. Fig. 1 shows some examples of cyclic *p-y* loops obtained from these studies. The main factors that were observed from the different studies can be summarized as following:

i) the cyclic response for the upper portions of piles is generally unconfined, and are characterized by inverted S-shaped hysteresis loops. At lower depths, a confined response is observed, and an oval shape characterizes the hysteresis loops. For the case of loose sand undergoing significant degradation, the upper unconfined response is more oval-shaped than S-shaped [13, 38];

ii) the middle region of low stiffness (i.e., the slack zone) in the case of S-shaped loops is due to soil nonlinear behaviour, and in particular the soil's memory of past maximum displacement [12, 37]. For soils such as stiff clays, this region can be characterized by the formation of a pure gap;

iii) the slack zone is characterized by a strain-hardening response, which is mainly a result of the recompression of caved-in soil. However, for medium dense to dense saturated sands, the strain-hardening response can result in a marked increase in the strength of the *p-y* curve. This is due to dilatancy effects, which result in the soil response passing through the phase transformation point [31, 37];

iv) the *p-y* curves are observed to harden or degrade with increasing number of loading cycles. This is attributed to volumetric and pore pressure changes in the near field. For loading through ground-motion, this is directly linked to hardening/degrading mechanisms occurring in the free-field [12, 19, 37];

v) a strain-softening behaviour (i.e., a peak-post-peak behaviour) is observed to occur for some soils (e.g., stiff clays);

vi) under one-way cyclic loading, an increase in permanent displacement is observed to occur with increasing number of loading cycles. This increase in displacement is observed to either stabilize (shakedown) or increase in an unbounded fashion; and

vii) the cyclic *p-y* curve is a combination of side-shear and normal-frontal components. The contributions of these different components to the total response are observed to change based on the position of the pile [36].

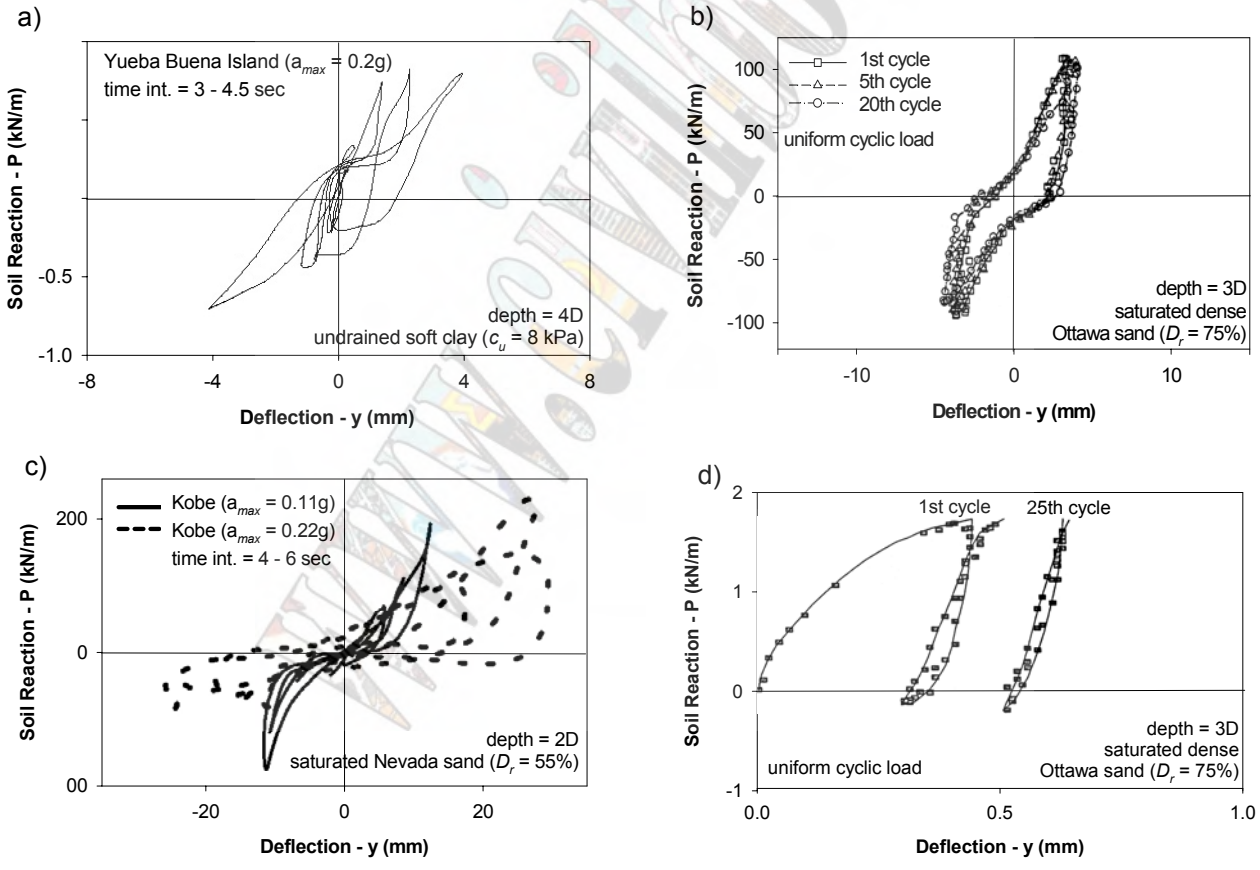

Fig. 1: Typical *p-y* hysteresis loops for different cyclic/seismic pile load tests: a) from [24]; b) from [12]; from [37]; and from [38].

Considering the above, the goal of the study is to develop a generic model that can be easily adapted to model different kinds of cyclic *p-y* responses. Other parameters in addition to those currently used to develop static *p-y* curves will need to be introduced; attention is however given to introduce standard physical parameters, that can be readily obtained from experiments.

MODEL DESCRIPTION

Backbone Curve

The soil reaction at any point is modeled using compression-only spring elements. For a pile foundation, two elements are placed on the opposite sides of the pile, whereas for the case of a retaining wall or footing, one element is used. The static normal force-displacement curve (i.e., static *p-y* curve in the case of a pile) defines the backbone curve and is modeled using an Iwan-like formulation with four multi-linear segments. A schematic of the curve is shown in Fig. 2 (segments 1, 2, 3 and 4). The backbone curve can be either monotonically-increasing (represented by solid lines in Fig. 2), or can exhibit a peak-post-peak (residual) behaviour (segments 3 and 4 represented by dotted lines in Fig. 2). For monotonic backbone curves, the peak strength $p_f = p_3$, whereas for the peak-post-peak case, $p_f = p_2$. The parameters needed to establish the backbone curve (p_1-p_3, y_1-y_3, α_2, α_3) can be evaluated using graphical methods, or by curve-fitting [18]. The multi-linear formulation renders the model more general and useful in modeling different types of backbone curves.

Fig. 2 shows that the backbone curve can be shifted horizontally to the left to allow for an initial force (p_i) at zero displacement. This represents a pre-straining effect (i.e., an initial displacement of y_0), which occurs for the case of driven piles or footings. The curve can also be shifted vertically (i.e., $p = p_0 > 0$) to allow for the modeling of soil reactions in the case of retaining walls, where a minimum force exists (active pressure) [9, 11, 17].

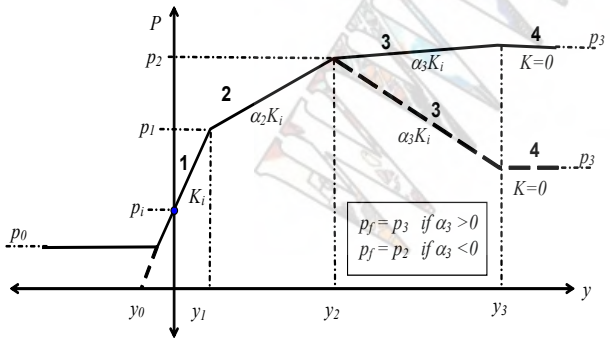

Fig. 2: Possible forms of backbone curve.

Standard Reload and General Unload Curves

Fig. 3 shows a schematic of the standard reload curve (SRC) — segments 7-8-9-10, and general unload curve (GUC) — segments 5-6. The SRC follows the shape of the backbone curve (similar to Iwan formulations) but is scaled based on the force at the reloading starting point (p_{r0}, y_{r0}). This is done by using a modified form of Pyke's equation [29] given in Eq. (1b). Pyke's original model did not account for cyclic strength degradation/hardening, and this is accounted for by calculating the scaling factor based on the current strength, $\delta_t p_f$ (δ_t is the strength degradation/hardening factor). For peak-post-peak curves, the SRC comprises segments 7-8-9 (i.e., segments 9 and 10 merge together). The stiffness and strength degradation/hardening factors, δ_k and δ_t,, which are calculated based on the current number of loading cycles, are used to degrade or harden the scaled backbone response. Fig. 3 also shows the expressions for computing the turning points of the SRC (p_{r1}, y_{r1}; p_{r2}, y_{r2}; p_{r3}, y_{r3}). In the event where the SRC crosses the initial backbone curve, subsequent movement follows: i) the original backbone curve similar to extended Masing rules [34]; or ii) continues along the SRC which is the case for some hardening types of responses [31, 38].

$$\kappa = 1 + \frac{p_{u0}}{\delta_t p_f} \text{ - unloading; } \kappa = 1 - \frac{p_{r0}}{\delta_t p_f} \text{ - reloading} \quad (1)$$

The general unloading curve (GUC) is similar to the SRC, however, the modified Pyke scaling parameter is calculated using Eq. (1a), which is based on the unloading starting point (p_{u0}, y_{u0}). Since unloading occurs only in the first quadrant, mainly stiffness degradation/hardening affects the response and $\delta_t = 1$. The option exists for δ_k to change with the number of cycles, or be set to a specific constant value. The expression for computing the turning point (p_{u1}, y_{u1}) of the GUC is also shown in Fig. 3.

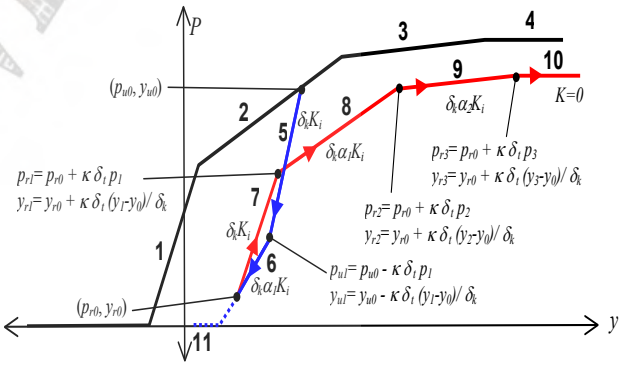

Fig. 3: Standard reload and general unload curves.

Movement at Minimum Force Level

When the soil resistance during the unloading phase reaches the minimum force level, movement continues in the negative direction with the soil reaction (p) remaining equal to the minimum force (i.e., with zero stiffness). Two types of responses are possible along this segment: the $p = 0$ case; and the $p > 0$ case. The $p = 0$ case models the condition where the foundation separates from the soil; and the $p > 0$ case models the case where the foundation experiences a constant minimum soil reaction (active force) as it moves in the negative direction (shown in Fig. 2). For the $p = 0$ case, the option exists to account for side-shear forces that could develop on the sides of a

pile as it moves through the slack zone.

Direct Reload Curve

The direct reload curve (DRC) models the resistance of the soil as the foundation moves in the slack zone. This is represented by a single line segment (segment 12) shown in Fig. 4. For the $p = 0$ case, it starts from the side-shear contribution force level, and for the $p > 0$ case, it starts from the minimum force level. The DRC ends at the point where it intersects the current base-SRC (explained below), and subsequent movement follows this curve.

It was noted earlier that recompression of caved-in soil and dilatancy effects are the causes of the strain-hardening response observed in experimental cyclic *p-y* curves (Fig. 1). It was observed in [12] and [37] that dilatancy effects mainly affected strength increase, whereas, the memory of past maximum displacement and soil cave-in affected displacement. The average stiffness of the soil in the slack zone is represented by the stiffness of the DRC. Loose soils are more S-shaped, whereas, denser soils are more oval-shaped. Extended Masing rules have been shown to satisfactorily model oval-shaped *p-y* loops [13], and this is due to the ability of soil to memorize the past maximum force (stress) experienced [34]. Based on this, a force parameter, λ_f, that is referenced to the past maximum force is used to estimate the target reloading point of the DRC. Depending on the value of this parameter, either oval or S-shaped loops can be formed. For a pure gap condition $\lambda_f = 0$, and for a fully confined response with significant cave-in $\lambda_f = 1$. As an example, $\lambda_f = 0.5$ for the loops in Fig. 1b.

Fig. 4 shows two standard reload curves. Curve *A* represents the SRC corresponding to the case where a stable pure gap is formed. For this case, the foundation moves all the way back to meet the soil at the point where it separated; the DRC for this case is therefore a horizontal line along the minimum force level. This is the approach used in many BNWF programs to account for gap formation (e.g., [10] and [14]). Curve *B* shows the same curve shifted to the left by an amount Δy_s. This distance is linked to the volume of soil that caves-in and is explained below.

The strain-hardening behaviour is associated with a decrease in the voids ratio and an increase in the mean

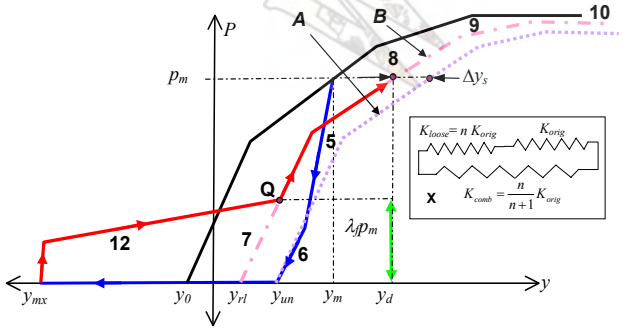

Fig. 4: Direct reload curve with inset X showing two-spring analogy.

effective confining pressure, which can be represented by a two-spring analogy: an inner spring representing the loose soil, and an outer spring representing the original soil (inset X in Fig. 4). Initially, the combined stiffness of the two springs is controlled by the loose soil, and this experiences most of the deformation and densifies. As the stiffness of the loose soil increases, it becomes comparable to the original soil, and should in theory follow curve *A*. This is, however, not the case and it rather follows curve *B*. This is due to the compressed loose soil under a similar confining pressure to that of the original soil occupying a finite volume of the gap formed. More soil cave-in, therefore, results in a larger shift of the curve, and this has been noted in experiments [7, 13]. Curve *B* is termed the current base-SRC, and is SRC along which the movement occurs after the DRC ends.

To estimate the end-point of the DRC, the origin of the current base-SRC has to be estimated. Using the results of a large dataset of one-way, intermediate and two-way constant cyclic field load tests on piles in sand [22], a hyperbolic function was developed for estimating this point. This is shown in Fig. 5, which shows the effect the type of loading has on the cyclic response. In the figure, ϕ_h (varies from -1 to 0) is the ratio of the maximum distance moved at the minimum force level, to that for the case of a constant force two-way cyclic load. The case of $\phi_h = -1$ represents two-way cyclic loading, whereas, $\phi_h = 0$ represents the one-way cyclic loading case (soil cave-in not possible for this case and $\beta_h = 1$). It is assumed that the maximum amount of soil cave-in occurs under two-way cyclic loading, and $\beta_h = \beta_h|_{\phi_h = -1}$. Between these extremes, a hyperbolic curve is used to estimate the effect of soil cave-in. A value of $\Lambda = 5$ was observed to fit the proposed values given in [22], however, the values were only mean estimates.

Using this approach, the origin of the current base-SRC can be estimated as:

$$y_{rl} = y_0 + \beta_h \left(y_{un} - y_0 \right), \tag{2a}$$

where $$\beta_h = \frac{1}{1 - \Lambda \phi_h} \quad \text{and} \quad \phi_h = \frac{y_{mx} - y_{un}}{y_m + y_{un} - y_0}. \tag{2b,c}$$

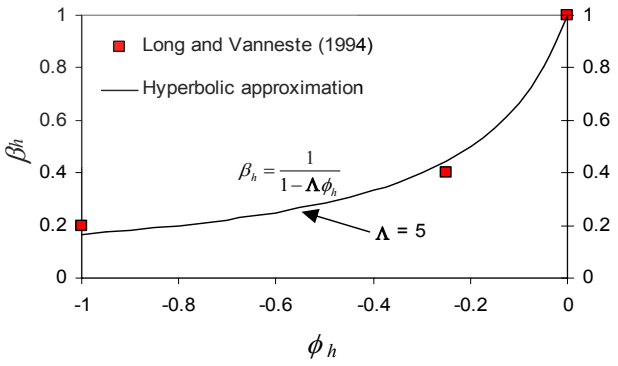

Fig. 5: Empirical curve for estimation of origin of current base-SRC.

In Eq. (2), y_{mx} is the minimum displacement at the minimum force level, y_m is the displacement corresponding to two-way cyclic action, and y_{un} is the current "most-right" unload displacement at the minimum force level.

Modeling Cyclic Degradation/Hardening

The degradation/hardening factors are used to scale the backbone curve to form the SRC and GUC. These factors are estimated using a stress-independent elliptical degradation/hardening function [1] in combination with a chosen S-N response curve. The S-N curve defines a particular fatigue failure condition. For example, this could be the attainment of initial liquefaction, a specified percentage reduction in stiffness/strength, etc. The curve can generally be obtained from cyclic triaxial or simple shear tests. It is defined by the $N = 1$ intercept, S_1, and the slope, η_{SN} (Fig. 6). The two S-N curve types that are implemented in the model are a log-log model and a semi-log model.

Rainflow cycle counting is known in fatigue studies to be the most accurate variable-amplitude cycle counting procedure. In its standard form, the time-history of the force (stress) must be known apriori. Anthes [5] however, developed a modified rainflow counting algorithm that circumvented this problem. For estimating cumulative damage, a modified version of Anthes' rainflow counting algorithm is therefore used. Fig. 7 shows a flow chart of the modified algorithm. After estimating the current cumulative damage, D, the stiffness and strength degradation/hardening factors δ_k and δ_t are computed using the elliptical degradation/hardening functions given in Eq. (3) (subscripts k and t refer to stiffness and strength, respectively).

$$\delta_{k,t} = 1 + \left(\delta_{km,tm} - 1\right)\left[1 - \left(1 - D\right)^{\theta_{k,t}}\right]^{1/\theta_{k,t}}, \qquad (3a)$$

where D is given by:

$$D = \sum_{i=1}^{m} \frac{1}{2N_{fi}}. \qquad (3b)$$

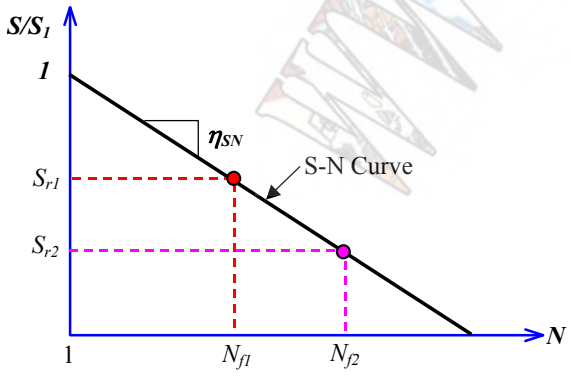

Fig. 6: Schematic of S-N curve.

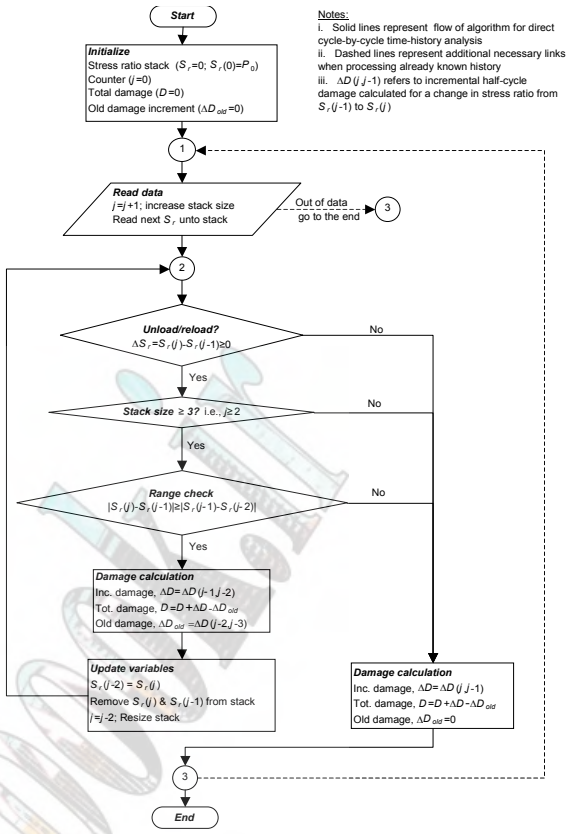

Fig. 7: Flow chart of modified Anthes rainflow counting algorithm.

In Eq. (3), $\delta_{km,tm}$ is the minimum or maximum amounts of degradation or hardening, and $\theta_{k,t}$ is the curve shape parameter. From Fig. 6, N_{fi} is the number of cycles resulting in fatigue failure at a relative cyclic stress (force) ratio of $S_{ri} = S_i/S_1$, where S_i is the current stress ratio, and S_1 is the stress ratio corresponding to $N = 1$. m also represents the total number of loading half-cycles.

Modeling of Radiation Damping

Radiation damping is modeled using a damper placed in parallel with each spring element. Recent work by [2] has shown that placing a linear damper in parallel with a nonlinear spring as implemented in SPASM8, PAR, etc., can result in unrealistically large damping forces. This results from forces bypassing the hysteretic system by way of the linear parallel dashpot. This occurs mostly in soft soils undergoing strong shaking, due to considerable soil nonlinear behaviour. For predominantly linear response, linear parallel radiation damping has been shown to give reliable results. To account for this problem, a parallel nonlinear damping model in which the limiting damping force was related to the yield displacement was developed in [6]. The use of such a parallel nonlinear damping model was confirmed in [14] and is the approach used in the model.

The radiation damping model is given in Eq. (4) and is based on a stiffness-proportional formulation similar to

that used in [6]. The damping factor is related to the current soil stiffness, and its initial value is estimated using impedance functions for a cylinder in a viscoelastic halfspace [26].

$$P_d = \left[c(a_o)\psi\right]\dot{u} \tag{4a}$$

$$c(a_o) = G_{\max} a_o S_u(a_o, \nu) \tag{4b}$$

In Eq. (4), a_o is the dimensionless frequency; G_{max} and ν, the small-strain shear modulus and Poisson ratio; c, the damping constant; ψ, the current soil stiffness ratio; and P_d and $\dot{u}$, the damping force and relative velocity. With this approach, the computed radiation damping is small when movement occurs in the slack zone, and as expected, becomes entirely zero for the case of a pure gap. Also, a reduction in radiation damping occurs for degrading systems, and an increase occurs for hardening systems, which is also expected.

EXAMPLES OF TYPICAL MODEL RESPONSES

Typical example hysteretic loops for different soil types and loading conditions are presented in this section to highlight the different capabilities of the model. Representative values of the various parameters for various soil types are obtained from the literature. The S-N curve parameters used in the following cases are S_1 = 0.8, η_{SN} = 0.1.

One-way Loading Examples

Fig. 8 shows a typical response of a foundation under uniform one-way load-controlled cyclic load. Fig. 8a represents a degrading response, which is characteristic of undrained soft clays that generally undergo more stiffness degradation than strength degradation. Fig. 8b on the other hand, shows a hardening response that is typical of dry sandy soils. It can be observed from the figure that the curve-shape parameters (θ_k, θ_t) have a significant effect on the response. It takes 7, 8 and 9 cycles to achieve a displacement ratio of 16 for θ_k = 0.5, 1.0 and 2.0. It can also be observed from the latter two loops in the figure that after reaching the minimum level of degradation, δ_{km}, further increase in the number of cycles results in a similar increase in displacement ratio, for the different cases. For the hardening example, a maximum displacement ratio of 15, 12 and 9 can be observed under 8 cycles of loading for $\theta_{k,t}$ = 0.5, 1.0 and 2.0. Both results show the importance the degradation curve-shape factor has on the prediction of permanent displacements, which is the variable of interest for such loading cases. It is noteworthy to mention that none of the existing BNWF models take this into account.

Fig. 8c shows the combined response for the case of a pile. The initial stiffness can be seen to be twice that of the single spring, but reduces to that of the single spring after the initial confining pressure has been exceeded. It is also interesting to note the model is able to capture the feature where unloading crosses into the negative region, under one-way cyclic loading (Fig. 1d).

Two-way Loading Examples

Fig. 9 shows typical two-way displacement-controlled cyclic *p-y* loops for a degrading unconfined response, and a hardening confined response. The degradation/hardening parameters are the same as those for the one-way loading example. In addition, Λ = 5, and λ_f = 0.5 and 1.0, for the unconfined and confined cases. The characteristic oval and S-shapes of confined and unconfined responses are evident from both figures. As expected, in Fig. 9a the degrading response results in an increase in displacement, whereas, a reduction in displacement is observed for the hardening response.

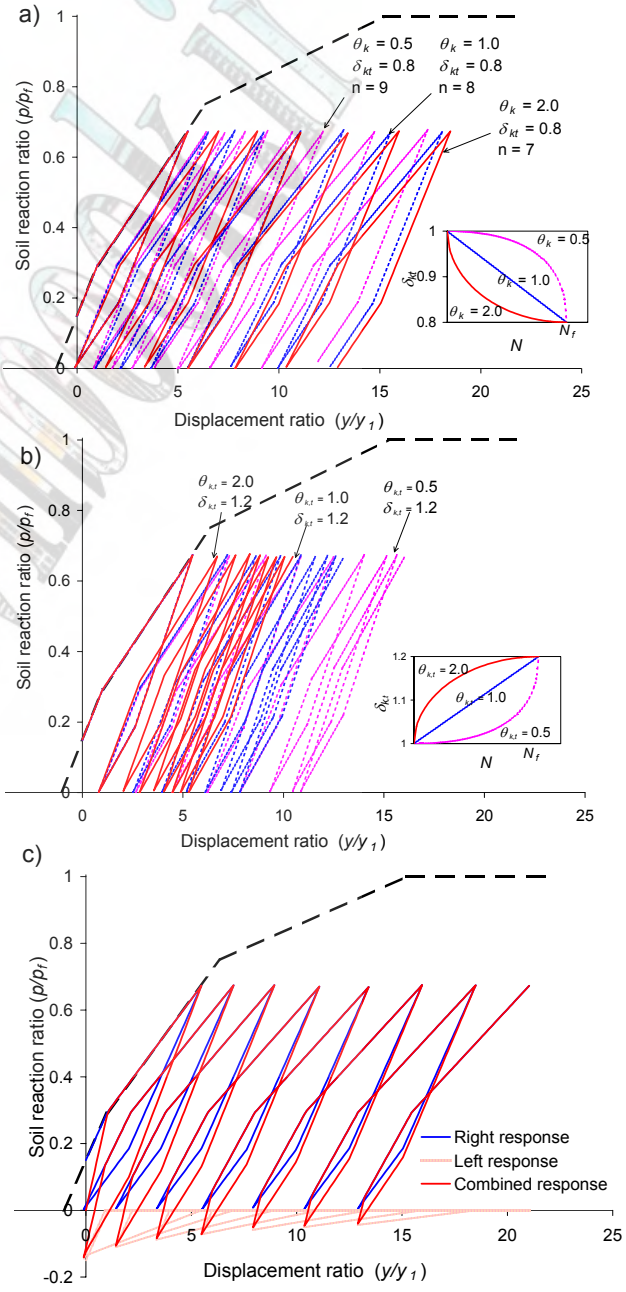

Fig. 8: Typical one-way loading response: a) degradation response; b) hardening response, c) combined left and right responses.

Fig. 9c also shows a two-way cyclic variable-loading amplitude example, exhibiting a peak-post-peak behaviour that is typical of stiff clays. A pure gapping feature is modeled ($\mathbf{\Lambda} = 1$, $\lambda_f = 0$), and reload of a given side occurs only after the pile traverses the full gap distance.

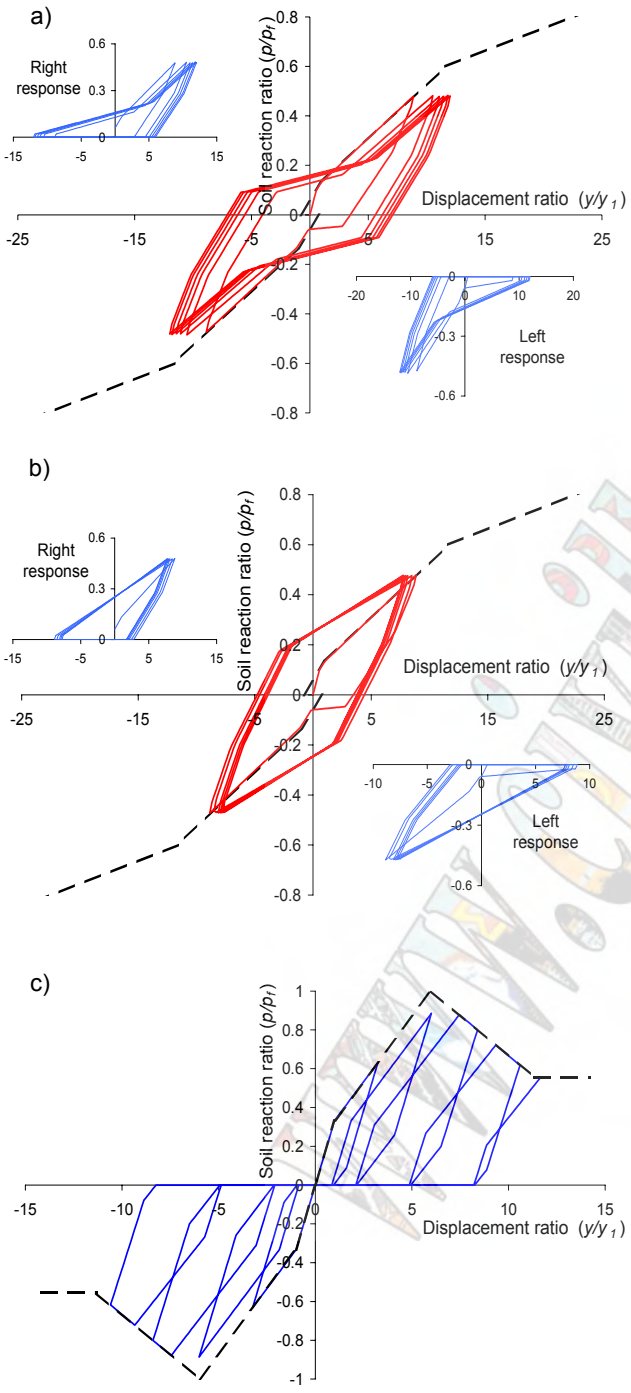

Fig. 9: Typical two-way loading response: a) degrading unconfined response; b) hardening confined response; and c) peak-post-peak response with pure gap.

CONCLUSIONS

A summary of the various features of a dynamic normal force-displacement BNWF model was presented. It was shown that the model is capable of accounting for several important aspects of nonlinear SSI response. The various aspects of the model that were discussed are: the types of backbone curves, the different unloading and reloading curves, the method used to account for soil cave-in, and the way in which cyclic degradation/hardening and radiation damping are modeled. The capabilities of the model were also demonstrated for typical soil and loading conditions. Comparison of the predictions of the model with various field and laboratory experiments is currently underway.

REFERENCES

[1] Allotey, N. K. and El Naggar, M. H., "New class of degradation models for geotechnical applications," submitted to Geotechnique.

[2] Allotey, N. K. and El Naggar, M. H., "Cyclic normal-force displacement model for nonlinear soil-structure interaction analysis: SeismoStruct® implementation," Geotechnical Research Center Report No. GEOT-02-05, Univ. of Western Ontario, London, Ontario.

[3] Allotey, N. K. and Foschi, R. O., "Coupled p-y t-z analysis of single piles in cohesionless soil under vertical and/or horizontal ground motion," *J. Earthquake Engng.*, in press.

[4] Allotey, N. K. and El Naggar, M. H., "Soil-structure interaction in performance-based design — a review," *Proc. 11th Int. Conf. Numer. Methods Geomech.*, Torino, Italy, Pap. No. 351, 2005.

[5] Anthes, R. J., "Modified rainflow counting keeping the load sequence," *Int. J. Fatigue*, Vol. 19, No. 7, pp. 529-535, 1997.

[6] Badoni, D. and Makris, N., "Nonlinear response of single piles under lateral inertial and seismic loads," *Soil Dyn. Earthquake Engng.*, Vol. 15, pp. 29-43, 1996.

[7] Barton, Y. O., "Laterally loaded model piles in sand: centrifuge tests and finite element analysis," Ph.D. dissertation, Cambridge University, UK, 1982.

[8] Boulanger, R. W., Curras, J. C., Kutter, B. L., Wilson, D. W. and Abghari, A., "Seismic soil-pile-structure interaction experiments and analysis," *J. Geotech. Geoenv. Engng.*, ASCE, Vol. 125, No. 9, pp. 750-759, 1999.

[9] Briaud, J. L. and Kim, N. K., "Beam-column method for tieback walls," *J. Geotech. Geoenv. Engng.*, ASCE, Vol. 124, No. 1, pp. 67-79, 1998.

[10] Brown, D. A., O'Neill, M. W., Hoit, M., McVay, M., El Naggar, M. H. and Chakrabotry, S., "Static and dynamic lateral loading of pile groups," Transportation Research Board, Washington, DC, NCHRP Rep. No. 461, 2001.

[11] Carubba, P. and Colonna, P., "A comparison of numerical methods for tied walls," *Comp. Geotech.*, Vol. 27, pp. 117-140, 2000.

[12] Dou, H., Byrne, P. M., "Dynamic response of single piles and soil-pile interaction," *Can. Geotech. J.*, Vol. 33, pp. 80-96, 1996.

[13] Gohl, W. B., "Response of pile foundation to simulated earthquake loading: experimental and analytical results,"

Ph.D. dissertation, Univ. of British Colombia, Vancouver, BC, 1990.

[14] El Naggar, M. H. and Bentley, K. J., "Dynamic analysis for laterally loaded piles and dynamic p-y curves," *Can. Geotech. J.*, Vol. 37, pp. 1166-1183, 2000.

[15] El Naggar, M. H. and Allotey, N. K., "Versatile cyclic p-y curve for lateral pile response analysis," *Proc. 57th Can. Geotech. Conf.*, Quebec, Pap. No. G15-108, 2004.

[16] El Naggar, M. H., Shayanfar, M. A., Kimiaei, M. and Aghakouchak, A. A., "Simplified BNWF model for nonlinear seismic response analysis of offshore piles with nonlinear input ground motion analysis," *Can. Geotech. J.*, Vol. 42, pp. 365-380, 2005.

[17] Jeong, S. and Seo, D., "Analysis of tieback walls using proposed p-y curves for coupled soil springs," *Comp. Geotech.*, Vol. 31, pp. 443-456, 2004.

[18] Joyner, W. B. and Chen, A. T. F., "Calculation of nonlinear ground response in earthquakes," *Bull. Seismological Soc. Am.*, Vol. 65, No. 5, pp. 1315-1336, 1975.

[19] Klar, A., Baker, R. and Frydman, S., "Seismic soil-pile interaction in liquefied soil," *Soil Dyn. Earthquake Engng.*, Vol. 24, pp. 551-564, 2004.

[20] Kucukarslan, S. and Banarjee, P. K., "Behaviour of axially loaded pile group under lateral cyclic loading," *Engng. Struct.*, Vol. 25, pp. 303-311, 2003.

[21] Lermitte, S., Janoyan, K. D., Stewart, J. P., and Wallace, J. W., "Experimental and analytical studies of full-scale drilled shaft bridge columns," *Proc. 7th U.S. Nat. Conf. Earthquake Engng.*, Boston, MA, Pap. No. 00149, 2002.

[22] Long, J. H. and Vanneste, G., "Effects of cyclic lateral loads on piles in sands," *J. Geotech. Engng.*, ASCE, Vol. 120, No. 1, pp. 225-243, 1994.

[23] Matlock, H., Foo, S. and Bryant, L. M., "Simulation of lateral pile behaviour under earthquake motion," *Proc. ASCE Specialty Conf. Earthquake Engng. Soil Dyn.*, Pasadena, CA., Vol. II, pp. 600-619, 1978.

[24] Meymand, P. J., "Shaking table scale model tests of nonlinear soil-pile-superstructure interaction in soft clay," Ph.D. dissertation, Univ. of California, Berkeley, CA, 1998.

[25] Mostafa, Y. and El Naggar, H. M., "Response of fixed offshore platforms to wave and current loading including soil-structure interaction," *Soil Dyn. Earthquake Engng.*, Vol. 24, pp. 357-368, 2004.

[26] Novak, M., Nogami, T. and Aboul-Ella, F., "Dynamic soil reactions for plane strain case," *J. Engng. Mech. Div.*, ASCE, Vol. 104, No. 4, pp. 953-959, 1978.

[27] *NONSPS: User's Manual*, McClleland Engineers Inc., Houston, TX, 1983.

[28] PMB Systems Engineering, SPSS Phase 2, Final Report to Shell Oil Company, 1979.

[29] Pyke, R. "Nonlinear soil models for irregular cyclic loading," *J. Geotech. Engng.*, ASCE, Vol. 105, No. GT6, pp. 715-726, 1979.

[30] Rha, C., Wallace, J. W., Taciroglu, E., "Analytical modeling of soil-structure interaction for bridge columns," *Proc. 13th World Conf. Earthquake Engng.*, Vancouver, BC, Pap. No. 2388, 2004.

[31] Rollins, K. M., Gerber, T. M., Lane, J. D. and Ashford, S. A., "Lateral resistance of a full-scale pile group in liquefied sand," *J. Geotech. Geoenv. Engng.*, ASCE, Vol. 131, No. 1, 115-125, 2005.

[32] SeismoSoft (2003). *SeismoStruct — A computer program for static and dynamic nonlinear analysis of framed structures* [Online]. Available: http://www.seismosoft.com.

[33] Vazinkhoo, S., Byrne, P. M., Lee, M. K., and Foschi, R. O., "CYCPILE — A computer program for analysis of cyclic and monotonic lateral loads on single piles," *Proc. 49th Can. Geotech. Conf.*, St. John's, Newfoundland, pp. 393-400, 1996.

[34] Vucetic, M., "Normalized behavior of clay under irregular loading," *Can. Geotech. J.*, Vol. 27, pp. 29-46, 1990.

[35] Wang, S., Kutter, B. L., Chacko, J. M., Wilson, D. W., Boulanger, R. W., and Abghari, A., "Nonlinear seismic soil-pile-structure interaction," *Earthquake Spectra*, Vol. 14, No. 2, pp. 377-396, 1998.

[36] Whelan, M. J. and Janoyan, K. D., "Mobilization of component interface stresses between soil and pile under lateral loading," *Advances in Deep Foundations — Geo-Frontiers 2005*, ASCE Geotechnical Special Publication, No. 132, pp. 905-914, 2005.

[37] Wilson, D. W., "Soil–pile–superstructure interaction at soft and liquefying soil sites," Ph.D. dissertation, Univ. of California, Davis, Davis, CA, 1998.

[38] Yan, L., "Hydraulic gradient similitude method for geotechnical modelling tests with emphasis on laterally loaded piles," Ph.D. dissertation, Univ. of British Columbia, Vancouver, BC, 1990.

Influential factors affecting pile stress in liquefiable soils

K. Tokimatsu[1], H. Suzuki[1], M. Sato[2]
[1]*Department of Architecture and Building Engineering, Tokyo Institute of Technology, Tokyo, Japan*
[2]*Hyogo Earthquake Engineering Research Center, National Research Institute for Earth Science and Disaster Prevention, Hyogo, Japan*

Abstract

Effects of inertial and kinematic forces on pile stresses are studied based on large shaking table tests on pile-structure models in dry and liquefiable saturated sand deposits. The test results show that the combination of inertial and kinematic effects on bending moment, shear force and axial force varies depending on such factors as the relation of natural periods of a superstructure and ground, the presence of foundation embedment, and pile stiffness. A pseudo-static analysis is presented into which these findings are incorporated and its effectiveness is examined by estimating pile stresses in large shaking table tests. The estimated pile stresses are in good agreement with the observed ones, regardless of the occurrence of soil liquefaction. Sensitively analysis using the same pseudo-static method is then conducted to estimate the errors in pile stress induced by errors in the inertial force from the superstructure, the ground displacement, and p-y relation of both liquefied and non-liquefied crust. It is shown that: (1) The pile stress in liquefied soil with low stiffness is governed by inertial force from the superstructure, while that with high stiffness is governed by the ground displacement; (2) The effects of inertial force on pile stress become less significant with a non-liquefiable crust overlying a liquefiable/soft layer than without it; and (3) The bending moment at the pile head without embedment is sensitive to scaling factor for p-y spring but becomes insensitive when the foundation is embedded in a non-liquefied crust.

Keywords- *Large shaking table tests, liquefaction, piles, pseudo-static analysis*

INTRODUCTION

Field investigation and subsequent analyses after resent catastrophic earthquakes confirmed that kinematic effects arising from the ground movement as well as inertial effects from superstructure had significant impact on damage to pile foundations particularly where liquefaction and/or laterally spreading occurred [1]. Many studies have, therefore, been made based on physical model tests as well as theoretical and numerical analyses [2]-[6], in order to examine contribution of both inertial and kinematic effects on pile foundations during earthquakes and to take such effects into account in seismic design of pile foundations. Several design procedures reflecting the results of those studies have been already proposed for liquefied and laterally spreading ground [6]. Little is known, however, concerning not only the degree of contribution of the inertial and kinematic effects on pile stress but also the sensitivity of the pile stress with respect to possible influential factors such as the inertial force from superstructure, ground displacement, and scaling factor for horizontal subgrade reaction of pile (p-y relation).

The objective of this study is to examine how inertial and kinematic effects during earthquakes are taken into account in the pseudo-static analysis and to examine the sensitivity of pile stress with respect to various influential factors, based on large shaking table test results and parametric studies.

LARGE SHAKING TABLE TESTS

Outline of large shaking table tests

Several series of shaking table tests were conducted on nearly full-scale soil-pile-structure systems using the shaking table facility at the National Research Institute for Earth Science and Disaster Prevention [7]-[12]. Fig. 1 illustrates fifteen soil-pile-structure models, the results of which are used in this study. A 2x2 pile group was used in all the tests. Their heads were fixed to a foundation with or without a superstructure. A model ID consisting of three or four alphabets specifies the test conditions. The first one indicates soil condition (D: dry sand; and S: saturated sand), the second one the presence of foundation embedment (A: no; and B: yes), and the third one the presence of a superstructure and its natural period (T_b) relative to those of non-liquefied soil (T_g) (N: no; S: $T_b<T_g$; and L: $T_b>T_g$). The forth one, if exists (R), indicates that the piles are stiff; otherwise, they are flexible.

The dry sand deposit prepared in the laminar box consisted of a homogeneous layer of 4.0 or 4.5 m. The liquefiable saturated sand deposit consisted of three layers including a top non-liquefiable sand layer 0.5 m thick (if a foundation was embedded), a liquefiable saturated sand layer 3 to 4 m thick and an underlying dense sand or gravel layer about 1.5 m thick. Prior to each shaking table test, cone penetration tests were conducted to estimate density distribution of the deposit with depth.

Either artificial accelerogram called Rinkai or the one

recorded during the 1940 El Centro Earthquake was used as an input motion to the shaking table. In total, thirty-one tests listed in table 1 were conducted on the soil-pile-structure models with Rinkai and El Centro with a maximum acceleration adjusted to 1.2-2.4 m/s^2.

Test results

Fig. 2 [12] shows the maximum pile stresses including shear forces, bending moments and axial forces at pile heads with respect to the maximum inertial forces in all the thirty-one tests. There is a definite trend in which the pile stresses increases with increasing inertial force. The increase in pile stresses with respect to the inertial force in non-liquefied ground is more significant in tests without foundation embedment (tests models DAS and DAL) than in tests with foundation embedment (tests models DBS and DBL).

It is interesting to note that the shear force in the test models DBS and DBL is smaller than the inertial force from the superstructure and the foundation, while that in the test models DAS and DAL is as large as the inertial force (Fig. 2(a)). This suggests that the presence of foundation embedment does have a significant effect on reducing shear force transmitted from the superstructure to the piles. In addition, the pile stresses become larger in tests with a short-period superstructure (test models DAS and DBS) than in tests with a long-period superstructure (test models DAL and DBL). This is because the inertial force and ground displacement are in phase in tests with a short-period superstructure but out of phase in tests with a long-period superstructure [12]. These findings confirm that factors other than the magnitude of inertial force, i.e., the presence of foundation embedment and relative natural periods between superstructure and ground, affect the pile stress.

The increase in pile stresses with respect to the

Table 1: Conduced tests on soil-pile-structure models

Model ID	Input motion (m/s^2)	Observed values: Inertial force (kN)	Observed values: Ground disp. (mm)	Model ID	Input motion (m/s^2)	Observed values: Inertial force (kN)	Observed values: Ground disp. (mm)
DAN	Rinkai 1.2	4.6	2	DBL	Rinkai 1.2	25.0	2
	Rinkai 2.4	8.6	7		Rinkai 2.4	60.3	9
	El Centro 2.4	7.3	4		El Centro 2.4	55.2	6
DAS	Rinkai 1.2	69.9	2	SAN	Rinkai 1.2	3.1	48
	Rinkai 2.4	124.8	7	SAS	Rinkai 1.2	16.6	35
	El Centro 2.4	118.6	6		Rinkai 2.4	20.1	72
DAL	Rinkai 1.2	24.1	2	SAL	Rinkai 1.2	11.4	26
	Rinkai 2.4	54.6	7	SBN	Rinkai 1.2	4.8	33
	El Centro 2.4	51.0	5		Rinkai 2.4	14.8	108
DBN	Rinkai 1.2	4.4	2	SBS	Rinkai 1.2	15.9	30
	Rinkai 2.4	7.9	10		Rinkai 2.4	24.2	73
	El Centro 2.4	7.2	7	SBL	Rinkai 1.2	21.1	28
DBS	Rinkai 1.2	42.3	3		Rinkai 2.4	27.8	68
	Rinkai 2.4	78.8	10	SBNR	Rinkai 1.5	6.1	48
	El Centro 2.4	75.8	8	SBSR	Rinkai 2.0	78.9	61
				SBLR	Rinkai 2.0	51.3	63

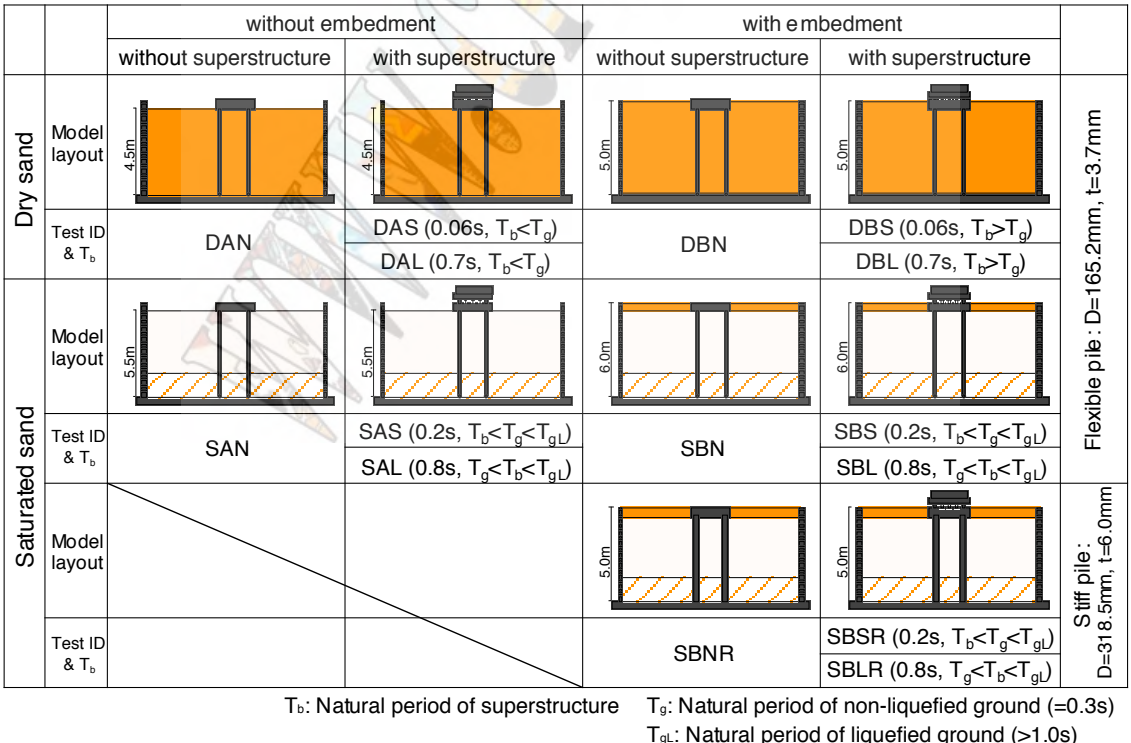

Fig. 1: Soil-pile-structure models

inertial force in liquefied ground is more significant in the tests with foundation embedment (model IDs starting with SB) than in tests without foundation embedment (model IDs starting with SA). The shear force in the test models starting with SB is larger than the inertial force from the superstructure and the foundation (Fig. 2(d)). This suggests that the presence of foundation embedment does have an opposite effect on pile stresses before and after liquefaction in such a way that it reduces the shear force transmitted to piles before liquefaction but increases it after liquefaction. It is interesting to note that, if the foundation is embedded, stresses in piles without a superstructure becomes as large as those with a superstructure after liquefaction, despite their different inertial forces (Fig. 2(d)(e)).

A comparison between the trends in pile stresses in dry sand and liquefied saturated sand indicates that increases in pile stresses with respect to inertial force are larger in liquefied sand (Fig. 2(d)(e)(f)) than in dry sand (Fig. 2(a)(b)(c)). This is probably caused by drastic change in soil resistance due to liquefaction. In non-liquefied sand, the soil near the ground surface can resist most of the inertial force from the superstructure, reducing shear force transmitted to the piles. In liquefied sand, by contrast, the non-liquefied crust overlying liquefied layer and liquefied upper soil layer becomes unable to resist most of the inertial force or even push the foundation to increase the shear force in piles.

PSEUDO-STATIC ANALYSIS

Beam-on-Winkler-springs method

A pseudo-static design method based on Beam-on-Winkler-springs method has been presented, in which significant findings from the large shaking table tests are incorporated [12]. Described below is a brief outline of the procedure.

The pseudo-static design method using p-y curves for pile foundations is based on the following equation [13][14]:

$$EI\frac{d^4y}{dz^4} = -p = -k_h B_p\left(y - y_g\right) \tag{1}$$

in which z is the depth, y and y_g are the pile and ground displacements, EI is the flexural rigidity, p is the subgrade reaction, k_h is the coefficient of horizontal subgrade reaction, and B_p is the pile diameter.

In the estimation of pile stress from Eq. (1), the combination between inertial force and ground displacement, p-y behavior of a pile and earth pressure acting on an embedded foundation must be considered as shown in Figs. 3-6. The combination of inertial force and ground displacement may be determined based on the natural period of the superstructure (T_b) relative to that of the ground (T_g), according to the following.

Case I ($T_b<T_g$): The pile stress may be estimated, provided that the maximum (design) inertial force and ground displacement are applied to the pile at the same time (Fig .4(a)).

Case II ($T_b>T_g$): The pile stress may be given by the square root of the sum of the squares of the two values estimated, provided that the maximum (design) inertial force and ground displacement are applied to the pile separately (Fig. 4(b)).

The earth pressure, P_E, acting on the embedded foundation is given by the difference in passive-side and active-side earth pressures and may be defined by the following equation [8][10] (Fig. 5):

$$P_E = P_{Ep} - P_{Ea} = \frac{1}{2}\gamma H^2 B\left(K_{Ep} - K_{Ea}\right) \tag{2}$$

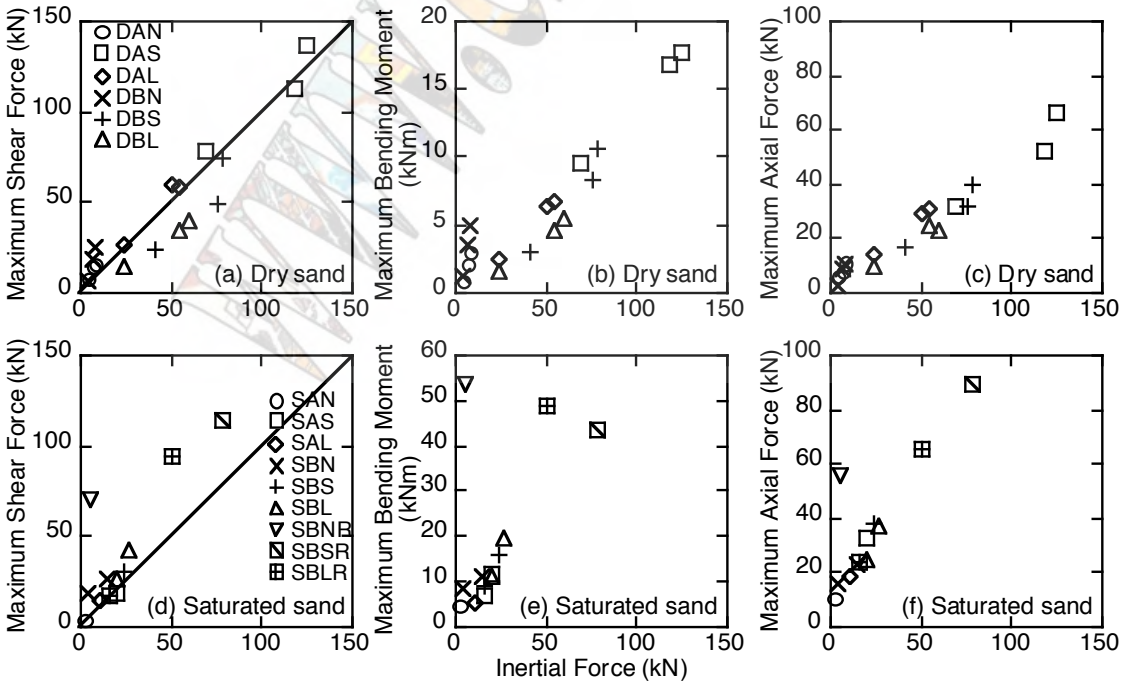

Fig. 2: Relation of maximum pile stresses with maximum inertial force in large shaking table tests

in which γ is the unit weight of soil, H and B are the height and width of foundation and K_{Ea} and K_{Ep} are the coefficients of earth pressures on the active and passive sides. Zhang et al. [15] introduced the earth pressure coefficients in Eq. (2), K_{Ea} and K_{Ep}, which can be expressed by a function of relative displacement between the foundation and the ground, as shown in Fig. 5. Thus, the total earth pressure for any relative displacement can be determined from Eq. (2).

The coefficient of subgrade reaction, k_h, in Eq. (1) is given by [9][13] (Fig. 6):

$$k_h = k_{h1}\frac{2\beta}{1+|y_r/y_1|} \tag{3}$$

$$k_{h1} = 80E_0B_0^{-0.75} \tag{4}$$

$$E_0 = 0.7N \tag{5}$$

in which k_{h1} is the reference value of k_h defined as Eqs. (4) and (5), β is the scaling factor for liquefied soil, y_r is the relative displacement between pile and soil, y_r (= y-y_g), y_1 is the reference value of y_r, E_0 (MN/m^2) is the Young's modulus of soil, N is the SPT N-value, and B_0 is the pile diameter in cm. Further details of the procedures have been described elsewhere [9].

Estimation of pile stresses in shaking table tests

To demonstrate the effectiveness of the pseudo-static analysis, the maximum bending moment, shear force and axial force in all the thirty-one tests are computed. It is assumed that the inertial force is equal to the observed maximum and the ground displacement above the base of the foundation is equal to the observed maximum at the ground surface and decreases linearly to zero at the base of the laminar box for dry sand or at the bottom of the liquefied layer for saturated sand. The N-value to be used in Eq. (5) is estimated from the CPT-value measured prior to each shaking table test [16]. It is also assumed that β is 0.1 for liquefied sand and 1.0 for the non-liquefied sand and gravel and y_1 in Eq. (3) is 1.0 % of the pile diameter.

Fig. 7 compares the estimated maximum bending moments, shear forces, and axial forces at pile heads with observed ones. The computed pile stresses agree reasonably well with the observed values irrespective of such factors as input acceleration, ground displacement, pile stiffness, natural periods of structure and ground, and presence of embedment. The good agreement indicates that the proposed pseudo-static analysis considering such factors as the combination of inertial and kinematic effects, earth pressure acting on embedded foundation, and scaling factor for p-y spring is promising for estimating pile stress during earthquakes.

SENSITIVITY ANALYSIS

To investigate crucial and less crucial factors for reasonably estimating pile stress, sensitivities of the moment at the pile head with respect to such factors as the

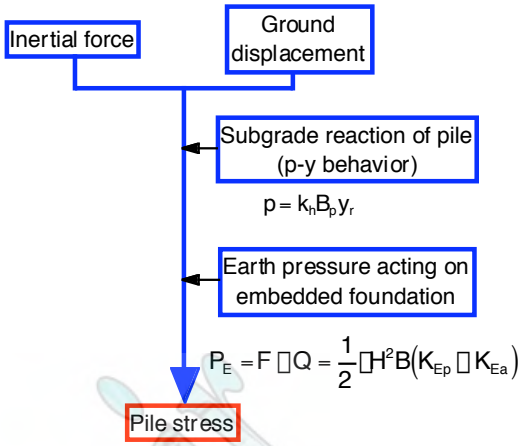

Fig. 3: Estimation of pile stresses

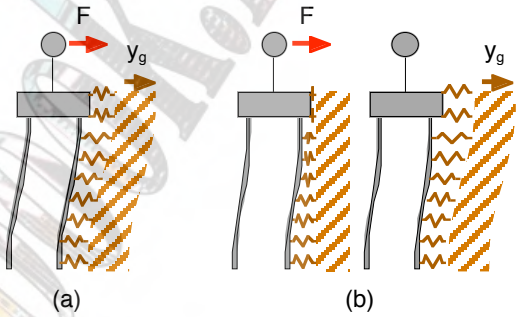

Fig. 4: Combination of inertial force and ground displacement

$$P_E = F = Q = \frac{1}{2}\gamma H^2 B(K_{Ep} - K_{Ea})$$

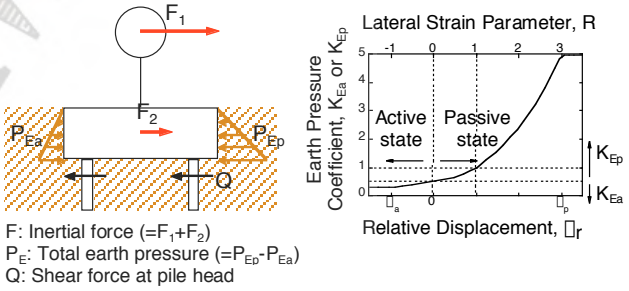

F: Inertial force (=F_1+F_2)
P_E: Total earth pressure (=P_{Ep}-P_{Ea})
Q: Shear force at pile head

Fig. 5: Earth pressure acting on embedded foundation

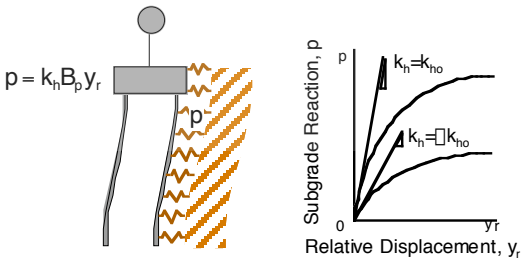

Fig. 6: p-y behavior

inertial force from the superstructure, the ground displacement, the scaling factor for p-y spring, and the presence of foundation embedment (a non-liquefiable crust layer overlying a liquefiable layer) are examined

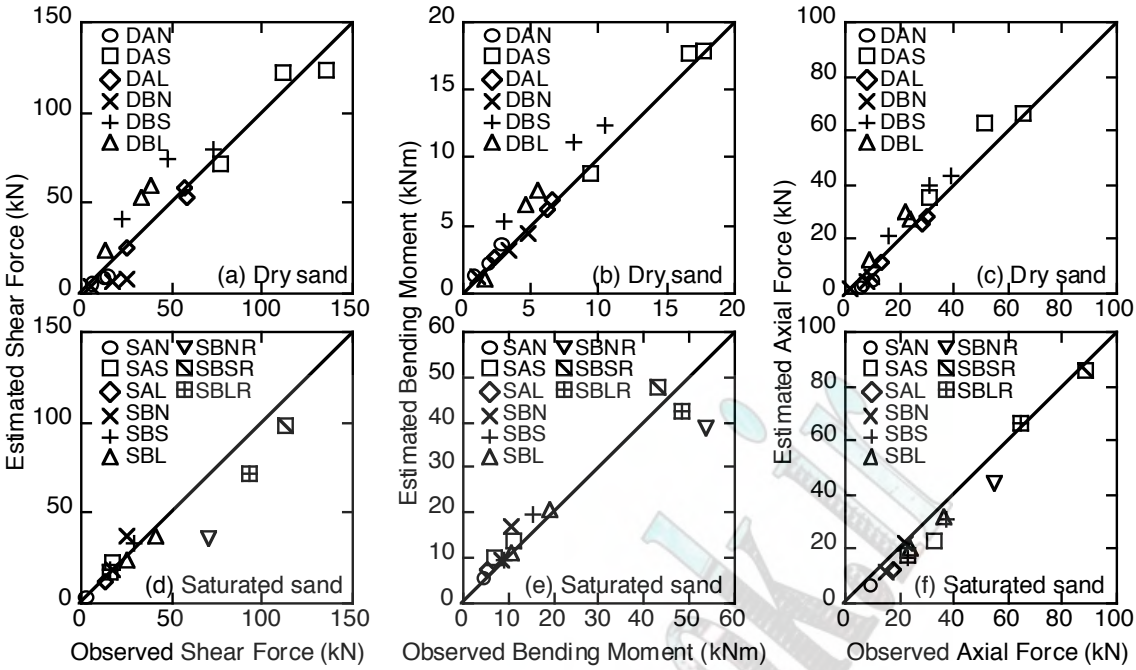

Fig. 7: Comparison of estimated pile stresses with observed pile stresses

using the same pseudo-static analysis on soil-pile-structure models shown in Fig. 8.

The sensitivity of the moment at the pile head may be estimated through the following ratio of two computed moments:

$$D = \frac{M_c}{M_0} \tag{6}$$

in which D is hereby called the moment ratio, M_0 is the reference moment computed for a test with the maximum inertial force, F_{max}, and ground displacement, y_{gmax}, observed in the test as well as with the scaling factor of 0.1 for p-y spring and the earth pressure model described in the previous chapter, and M_c is the one computed for the same test but with different values of the parameters. In the computation of M_c, the magnitudes of inertial force and ground surface displacement are varied from 0.5 to 2.0 times the observed maximum ones, with a scaling factor for p-y spring from 0.01 to 0.5. The ratios of the assumed inertial force, F_c, and ground displacement, y_{gc}, with respect to the observed maxima, F_{max} and y_{gmax}, are hereby called inertial force ratio (= F_c/F_{max}) and ground displacement ratio (= y_{gc}/y_{gmax}). It is assumed that the ground displacement is constant above the bottom of the foundation and decreases linearly to zero at the bottom of the liquefied layer, and that the pile is always elastic. Two test models SAS (without foundation embedment) and SBS (with foundation embedment in a non-liquefiable crust) that were subjected to a maximum input acceleration of about 2.4 m/s^2 are considered in the analysis.

Figs. 9 and 10 show contours of the moment ratio in a two-dimensional plane, the vertical and horizontal axes of which are the inertial force ratio and ground displacement ratio.

Fig. 9 shows that the contour lines with scaling factor less than 0.1 tend to be horizontal but that those with a larger scaling factor incline from the upper left to the lower right and becomes more vertical than horizontal when □ = 0.5. This is because the liquefied soil with a small scaling factor (with low stiffness) can neither resist inertial force from superstructure nor push piles while that with a large scaling factor (with high stiffness) can do both. This suggests that the inertial force effects dominate over the ground displacement in controlling stress in pile without foundation embedment when □ <0.1 but that both inertial and kinematic effects have strong effects when □ > 0.2 and may dominate when □ > 0.5.

Fig. 10 shows that the contour lines with any scaling factor incline from the upper left to the lower right and are more vertical than horizontal irrespective of □. The larger the value of □, the more vertical the contour line. This suggests that the effect of ground displacement becomes dominant when the foundation is embedded in a non-

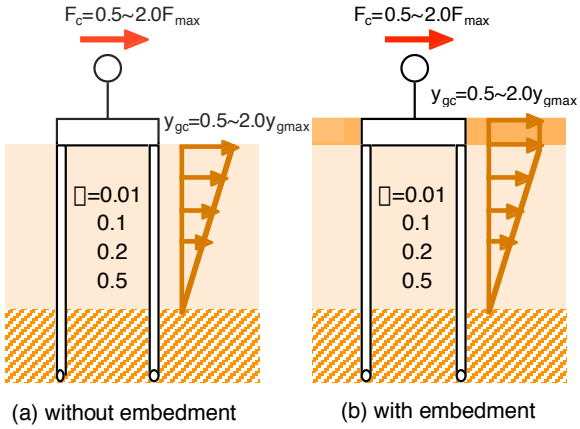

Fig. 8: Soil-pile-structure models in sensitive analysis

liquefiable crust. This is because the earth pressure acting on the embedded foundation, which does not exist in the case shown in Fig. 9, could play an important role in controlling pile stresses.

Figs. 11 and 12 show the variation of the moment ratio against either inertial force or ground displacement ratio with the other fixed to unity for □ = 0.01, 0.1, 0.2 and 0.5 for the two test models. For the piles without foundation embedment (Fig. 11), the moment ratio for □ = 0.01 is linearly proportional to the inertial force ratio (Fig. 11(b)) but almost constant against the ground displacement ratio (Fig. 11(a)). The moment ratio for □ = 0.5, in contrast, is insensitive to the inertial force ratio (Fig. 11(b)) but sensitive to the ground displacement ratio (Fig. 11(a)). This suggests that the error in inertial force is crucial but the error in ground displacement may not be crucial in the liquefied soil with low stiffness, but that the error in ground displacement may become critical in the liquefied soil with high stiffness.

Unlike the case in Fig. 11 without foundation embedment, the pile moment ratio with foundation embedment in a non-liquefiable crust in Fig. 12 is more sensitive to ground displacement ratio than inertial force ratio. This suggests that the ground displacement may be significant and, in same cases, more crucial than the inertial force. It is interesting to note that the computed moment ratios at the pile head with foundation embedment in a non-liquefiable crust layer are almost the same regardless of □ in Fig. 12. This is probably because the earth pressure acting on the embedded foundation becomes to have dominant effects, masking the effects of difference in scaling factor for p-y spring. This suggests that the scaling factor for liquefied sand seems less important in estimating stress at the pile head with

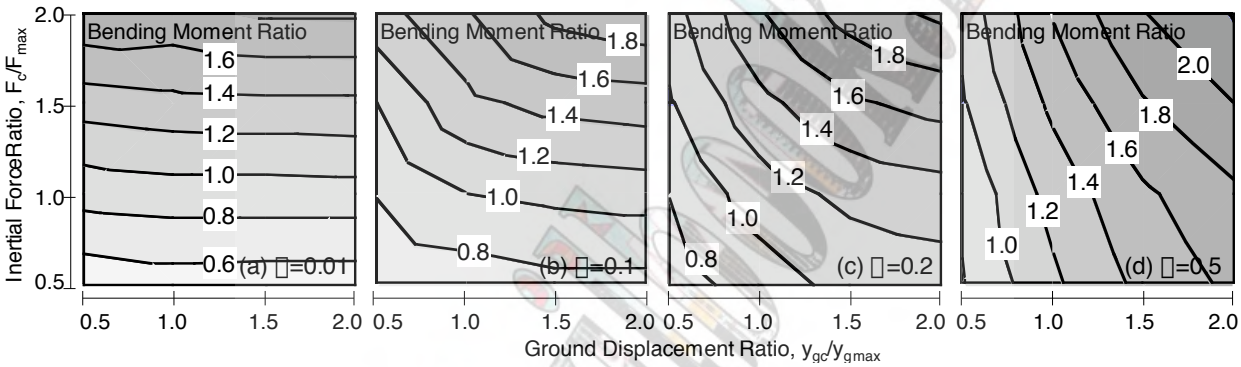

Fig. 9: Contour of bending moment ratios of pile without foundation embedment

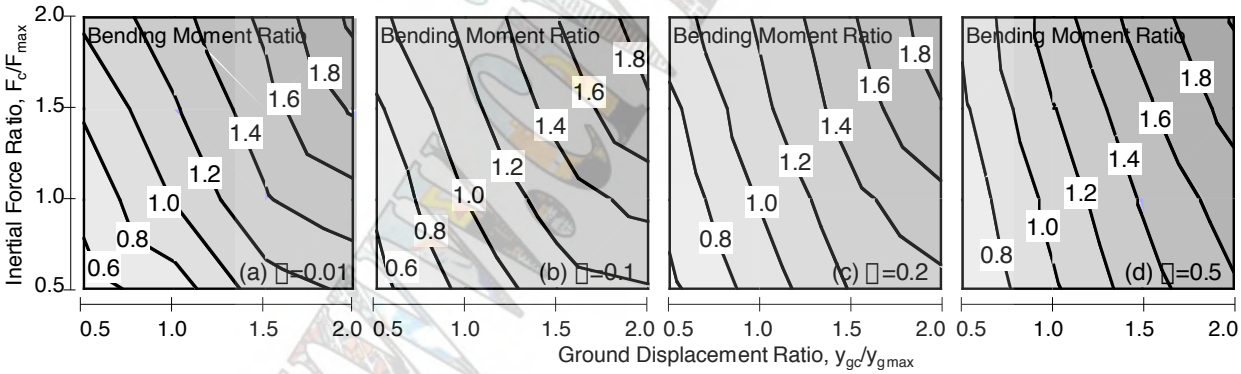

Fig. 10: Contour of bending moment ratio of pile with foundation embedment in non-liquefiable crust

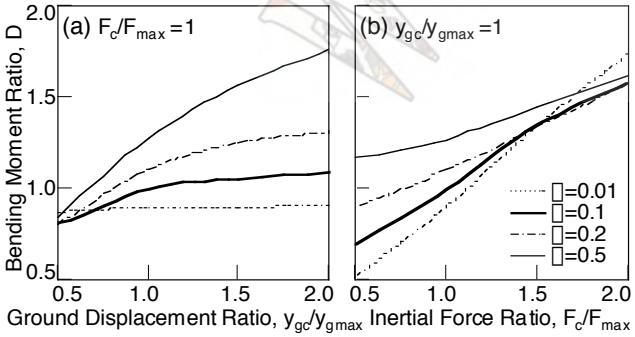

Fig. 11: Relation of bending moment ratios with inertial force or displacement for pile without foundation embedment

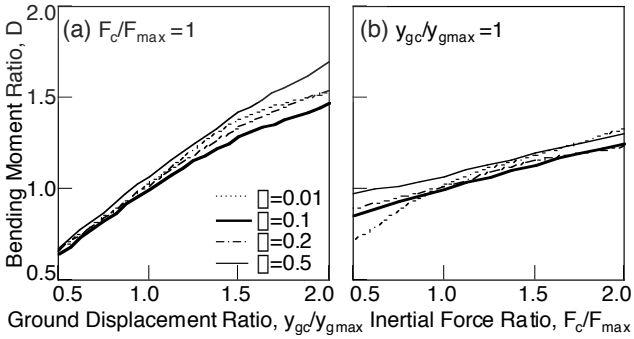

Fig. 12: Relation of bending moment ratios with inertial force or displacement for pile with foundation embedment in non-liquefiable crust

foundation embedment in a non-liquefiable crust layer. It is noted that this may not be the case for pile stress at the bottom of the liquefied soil.

CONCLUSIONS

Pseudo-static analysis for estimating pile stress in liquefiable and non-liquefiable sand has been presented in which inertial and kinematic effects observed in large shaking table tests are incorporated, and its effectiveness has been demonstrated through the comparison of observed and computed pile stresses in the shaking table tests. Sensitivity analysis has been made to differentiate from crucial and less crucial factors affecting pile stress in liquefied soil. The following conclusions may be tentatively made based on the test results, analytical results, and their discussions:

1) Pile stresses during earthquakes are affected not only by the inertial force from the superstructure and kinematic force due to ground displacement but also by their relative phase controlled by the natural periods of both superstructure and ground.

2) The pseudo-static analysis, in which effects of the combination between inertial force and ground displacement, p-y behavior and earth pressure acting on an embedded foundation are considered, can estimate the pile stresses in large shaking table tests with a reasonably degree of accuracy, regardless of pile stiffness, the presence of foundation embedment and the occurrence of soil liquefaction.

3) The pile stress in liquefied soil with low stiffness is governed by inertial force from the superstructure, while that with high stiffness is governed by the ground displacement. The effects of inertial force on pile stress become less significant when the foundation is embedded in a non-liquefiable crust overlying a liquefiable/soft layer.

4) The bending moment at the pile head without embedment is sensitive to scaling factor for p-y spring but becomes insensitive when the foundation is embedded in a non-liquefiable crust.

Since the cases tested and analyzed are limited, the above conclusions may not be applicable in general and thus further studies are required.

ACKNOWLEDGMENTS

The study described herein was made possible through two research projects related to soil-pile-structure interaction using the large shaking table at the NIED, including Special Project for Earthquake Disaster Mitigation in Urban Areas, supported by the Ministry of Education, Culture, Sports, Science and Technology (MEXT). The authors express their sincere thanks to the above organization.

REFERENCES

[1] BTL Committee, *Research Report on liquefaction and lateral spreading in the Hyogoken-Nambu earthquake* (in Japanese), 1998.

[2] Mitsuji, K., Yokoi, Y. and Sugimoto, Y., "Evaluation of horizontal load of piles based on results of dynamic analysis (Part 2 Proposal of horizontal load)" (in Japanese), *Proc. of Twenty-eighth Japan National Conference on Geotechnical Engineering*, Vol. 2, pp. 1847-1848, 1993.

[3] Nishimura, A., "Design of structures considering ground displacement" (in Japanese), *Kisoko*, Vol. 6, No. 7, pp. 48-56, 1978.

[4] Nishimura, A., Murono, Y., and Nagatsuma, S., "Experimental studies on the seismic design method for pile foundations in the soft ground (Part 1)-(Part 3)" (in Japanese), *Proc. of Thirty-second Japan National Conference on Geotechnical Engineering*, Vol. 1, pp. 961-966, 1997.

[5] Boulanger, R. W., Curras, J. C, Kuter, B. L., Wilson, D. W. and Abghari, A., "Seismic soil-pile-structure interaction experiments and analyses", *Journal of Geotechnical and Geoenvironmental Engineering*, Vol. 125, No. 9, pp. 750-759, 1999.

[6] Boulanger, R. W., Kutter, B. L., Brandenberg, S. J., Singh, P. and Chang, D., "Pile foundations in liquefied and laterally spreading ground during earthquakes: Centrifuge experiments & analyses", Center for Geotechnical modeling, University of California, Davis, Report No. UCD/CGM-03/01, 2003.

[7] Tamura, S., Tsuchiya, T., Suzuki, Y., Fujii, S., Saeki, E. and Tokimatsu, K., "Shaking table tests of pile foundation on liquefied soil using large-scale laminar box (Part 1 Outline of test)" (in Japanese), *Proc. of Thirty-fifth Japan National Conference on Geotechnical Engineering*, Vol. 2, pp. 1907-1908, 2000.

[8] Tamura, S., Tokimatsu, K., Miyazaki, M., Yahata, K. and Tsuchiya, T., "Seismic earth pressure action on embedded footing based on liquefaction test using large scale shear box" (in Japanese), *Journal of Structural and Construction Engineering*, No. 554, pp. 95-100, 2002.

[9] Tokimatsu, K., Suzuki, H. and Saeki, E., "Modeling of horizontal subgrade reaction of pile during liquefaction based on large shaking table" (in Japanese), *Journal of Structural and Construction Engineering*, No. 559, pp. 135-141, 2002.

[10] Tokimatsu, K., Tamura, S., Miyazaki, M. and Yoshizawa, M., "Evaluation of seismic earth pressure acting on embedded footing based on liquefaction test using large scale shear box" (in Japanese), *Journal of Structural and Construction Engineering*, No. 570, pp. 101-106, 2003.

[11] Tokimatsu, K. and Suzuki, H., "Pore water pressure response around pile and its effects on p-y behavior during soil liquefaction", *Soils & Foundations*, Vol. 44, No. 6, pp. 101-110, 2004.

[12] Tokimatsu, K. and Suzuki, H., "Effects of inertial and kinematic interaction on seismic behavior of pile foundations based on large shaking table tests", *Proc. of Second International Conference on Urban Earthquake Engineering*, pp. 207-214, 2005.

[13] Architectural Institute of Japan, Recommendations for design of building foundations (in Japanese), 1988, 2001.

[14] Nishimura, A., Murono, Y., and Nagatsuma, S., "Seismic response characteristics of pile foundation in soft ground

and its application to seismic design" (in Japanese), *Proc. of Thirty-third Japan National Conference on Geotechnical Engineering*, Vol. 1, pp. 1079-1080, 1998.

[15] Zhang, J. -M. Shamoto, Y. and Tokimatsu, K., "Evaluation of earth pressure under any lateral displacement", *Soils and Foundations*, Vol. 38, No. 2, pp. 143-163, 1998.

[16] Yamada, K., Kamao, S., Yoshino, H. and Masuda, Y., "Correlation between N-value and cone index" (in Japanese), *Tsuchi-to-Kiso*, Vol. 40, No. 8, pp. 5-10, 1992.

Recent Several Studies and Codes on Performance-based Design for Liquefaction in Japan

S. Yasuda
Department of Civil and Environmental Engineering, Tokyo Denki University, Saitama, Japan

Abstract

In Japan, several studies on performance-based design procedure for liquefaction have been carried out recently. Several results have been introduced in seismic design codes. In the performance-based design, two items must be developed: methods to estimate the deformation of structures, and the allowable values of deformation of the structures. In the estimation of deformation of structures and grounds, three grades of methods have been developed: empirical methods, static and dynamic analyses. In parallel to the development of the estimation methods, allowable values of deformation of structures have been studied. For river dikes and railway embankments, allowable deformations have already introduced in design manuals. For timber houses and buried sewage pipes, allowable settlement and floatation have been proposed, respectively.

Keywords— *Performance-based design, liquefaction, earthquake*

INTRODUCTION

In Japan, studies on liquefaction started after the 1948 Fukui earthquake and accelerated after the 1964 Niigata earthquake. In 1971, liquefaction was first taken into consideration in the design code for harbor facilities. Immediately after, the effect of liquefaction was also introduced in the design codes for road bridges, railways and buildings. After 1978, the codes for oil tanks, LNG tanks, water facilities, tailing dams and sewage facilities included provisions to reduce damage due to liquefaction. Estimation methods had been revised two or three times in some codes before the 1995 Kobe earthquake.

The Kobe earthquake caused severe liquefaction in and around City of Kobe and raised several problems. Of them, the method to predict the occurrence of liquefaction under very strong shaking was very important. Many studies on these problems have been carried out since the Kobe earthquake. The code for highway bridges was revised in November 1996 based on the studies. In the code, evaluation method for very strong shaking, so called Level 2 earthquake motion, was introduced. Then evaluation methods for Level 2 earthquake motion were introduced in the design codes for high-pressure gas facilities, water works facilities and sewage works facilities. The design acceleration for Level 2 earthquake motion is about twice to three times the acceleration for Level 1 earthquake motion.

In the current design for liquefaction, assessment of liquefaction potential is done first. Then the acceptability of the likely degree of damage is roughly judged and, if necessary, appropriate countermeasures are selected. However, in general, the degree of damage expected from liquefaction is not evaluated because it is difficult to evaluate. In the design under around 200 gals or less of the maximum surface acceleration, it is not always necessary to judge the degree of damage because it is easy to improve the ground not to liquefy under this level of shaking. On the contrary, liquefaction cannot be prevented by current countermeasures under the Level 2 earthquake motion, because the critical soil density at which liquefaction occurs, increases with the increase of earthquake motion. Therefore, it is necessary to introduce a new design concept based not on the occurrence of liquefaction but on the likely degree of damage to structures. This new design concept, so called performance-based design, is rational and will be used for not only for Level 2 earthquake motion but also normal ground shaking.

NEW DESIGN CONCEPT BASED ON PERFORMANCE OF STRUCTURES

New methods for the prediction of the occurrence of liquefaction under Level 2 earthquake motion, developed after the 1995 Kobe earthquake

Very strong shaking caused severe damage to structures in Kobe. Many buildings, bridges, and houses collapsed. Therefore, it was necessary to investigate new design concepts that could withstand very strong shaking.

The Japan Society of Civil Engineering organized a technical committee to deal with these problems after the Kobe earthquake. This committee submitted its first proposals in 1996 [1]. It suggested basing earthquake-resistant design on two types of ground motion: Level 1 earthquake motion, which is likely to strike a structure once or twice while it is in service, and Level 2 earthquake motion, which is very unlikely to strike a structure during the structure life time, but when it does, it is extremely strong.

According to this concept, design accelerations for Level 1 and Level 2 earthquake motion have been introduced in several design codes. For example, in the design code for high-pressure gas facilities, the following

design seismic coefficients were introduced to estimate the occurrence of liquefaction:

i) Level 1 earthquake motion: 0.12g to 0.3g

ii) Level 2 earthquake motion: 0.24g to 0.6g

Some studies have been conducted to develop a new method for the estimation of liquefaction potential under violent shaking. In the new specification for highway bridges [2], the formula for evaluating undrained cyclic strength was revised because the previous formula could not be applied to "Level 2 shaking". Several cyclic triaxial tests were carried on frozen samples and case studies, and a new formula was proposed. Figure 1 shows the relationship between N_a and R_L for clean sand. For sandy soil, N_a is calculated by the following formulae, where N_1 is normalized SPT N-value for the effective overburden pressure of 98kPa:

$$N_a=c_1N_1+c_2 \quad (1)$$

c_1=1 (0%≦F_c<10%), $c_1=F_c/20$ (60%≦F_c)

$c_1=(F_c+40)/50$ (10%≦F_c<60%)

c_2=0 (0%≦F_c<10%), $c_2=(F_c-10)/18$ (10%≦F_c)

Two types of ground motion: ① generated by interplate fault in the ocean (named Type 1), and ② generated by inland fault (named Type 2) are introduced in the specification. The maximum surface acceleration for the two types of ground motions are 0.3 G to 0.4 G and 0.6 G to 0.8 G in high seismic zones, respectively.

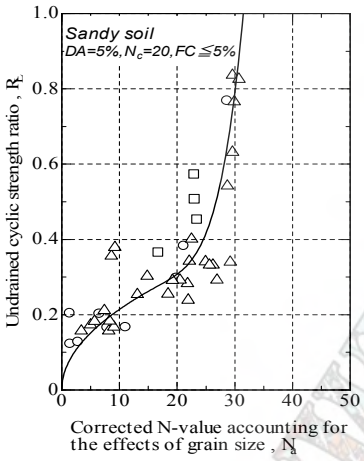

Fig.1: Relationship between N_a and R_L [2]

Behavior of structures in liquefied grounds

As the maximum surface acceleration in the "Level 2 shaking" is very high, even dense sand ground is judged to induce liquefaction. If a clean sand ground is assumed, the maximum SPT N-value which causes liquefaction under different maximum surface accelerations can be calculated based on Eq.(1). Figure 2 shows the relationship between the maximum surface acceleration and the calculated critical SPT N_1-value at the depth of GL-8.1m, where effective overburden pressure σ'_v=98 kPa. As shown in the figure, the critical SPT N-value increases with the maximum surface acceleration. If the maximum surface acceleration is 0.15 g to 0.20 g ("Level 1 shaking"), the critical SPT N-value is about 10 to 15. On the contrary, under the violent shaking of 0.35 g to 0.60 g ("Level 2 shaking"), the critical SPT N-value becomes about 20 to 25 [3]. Therefore, it can be said that medium-dense and dense sand with relative density of about 50 % to 90 % liquefies under Level 2 earthquake motion but does not liquefy under Level 1 earthquake motion. However, dense ground compacted by sand compaction piles and rod compaction methods did not liquefy during the Kobe earthquake though their SPT N-values were 18 to 31 [4].

One more interesting phenomena observed during the Kobe earthquake was that medium-dense ground treated

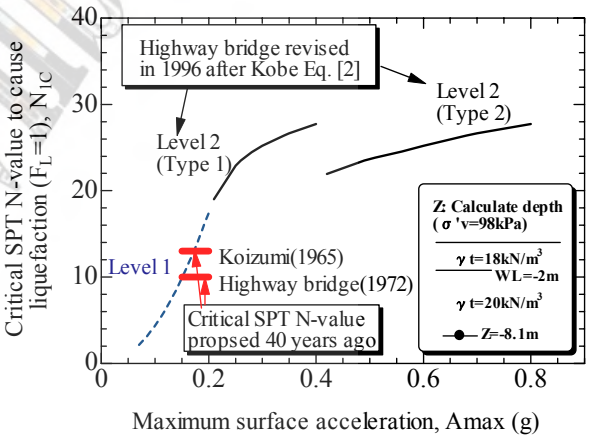

Fig.2: Critical SPT N-value to cause liquefaction under different maximum surface accelerations estimated by JRA method

Table 1: Relationship between the density of the ground, the level of shaking and damage to structures and ground

		SPT N value		
		Less than about 10 (Loose)	About 10 to 25 (Medium dense)	More than about 25 (Dense)
Level 1 earthquake motion (As_{max} is about 150 to 200 Gals)	Liquefaction	Occurs	No occurrence	No occurrence
	Damage to structures	Severe	No occurrence	No occurrence
Level 2 earthquake motion (As_{max} is about 350 to 600 Gal)	Liquefaction	Occurs	Occurs	No occurrence
	Damage to structures	Severe	Occurs but not severe	No occurrence

by sand drains subsided less than untreated ground [4]. According to model tests, not only the subsidence of ground but also the settlement of structures or floatation of buried structures is influenced by the density of the ground [3]. These examples imply that the damage to structures in medium dense ground is not so severe, as summarized in Table 1. Therefore, it is necessary to evaluate not only the occurrence of liquefaction but also the deformation of structures. And the serviceability of the structure should be considered in the design procedure, based on the evaluated deformation. This kind of design method can be called as "Performance-based design."

Two items necessary for the development of the performance-based design

In the performance-based design two items must be developed: methods to estimate the deformation of structures, and the allowable values of deformation of the structures. Critical condition of structures due to liquefaction must be considered to determine the allowable values. Recent studies on these items are introduced below.

PERFORMANCE-BASED DESIGN FOR EMBANKMENTS

Critical condition

Many road, river and railway embankments slid or settled during past earthquakes. If an embankment slides, destructive failure such as large settlement and lateral spread occurs. Therefore, the slid of an embankment has been considered as critical condition. In general, safety factor of slope, F_s is evaluated by slip surface analyses, such as Fellenius's method. After the 1978 Miyagiken-oki earthquake, in Japan, this approach has been applied to the analyses of liquefaction-induced failure of embankments by considering excess pore water pressure and seismic force as follows:

$$F_s = \frac{\sum\left[cl + \{(W - ub)\cos\alpha - k_h W \sin\alpha\}\tan\phi\right]}{\sum\left(W\sin\alpha + \frac{h}{r}k_h W\right)} \cdots (2)$$

where, u: pore water pressure including excess pressure due to liquefaction, and
k_h: horizontal seismic coefficient

Then, this approach was introduced in the design codes for road embankments [5] and river dikes [6]. Appropriate countermeasures were designed and applied also based on this approach. For example, the embankment for super express train, named Shinkansen, was strengthened by installing sheet piles and connected their heads with tie rods [7].

However, it becomes necessary to evaluate not only the safety against sliding but also deformation of embankments after the 1995 Kobe earthquake. In river dikes, aim of the dikes is to protect from flood. Therefore, critical condition of the dikes is not to cause overflow of river water, as schematically shown in Fig. 3(a). In road embankments, emergency vehicles mus run just after earthquakes. For example differential settlement of approaches to bridges from embankments must be within the appropriate value for the vehicles, as shown in Fig. 3(b). Thus, differential settlement must be one of the critical conditions in road embankment.

One more reason why the evaluation of deformation of embankments must be introduced in the seismic design, is that the calculated safety factor against sliding, Fs, is apt to lower than 1.0 under the Level 2 earthquake motion, even the ground is medium dense. Therefore F_s cannot be used in the design under Level 2 shaking.

Studies on the allowable settlement

Recently allowable settlements for super levees, railway embankments and river levees were introduced in their design manual or guideline in Japan, as shown in Table 2. In the manual for super levee, allowable settlements are 50 cm for the top of levee and face of backside slope, and 20 cm for the ground on the super levee. As the super levees are used for residential areas as shown in Fig.4(b), similar safety as urban area is necessary. Then these allowable values were introduced in the design manual.

In the guideline for railway, damage levels of deformation of embankments are classified into four grades as shown in Table 3 and Table 4 for embankments and approach to bridges, respectively [9]. If the settlement is greater than 50 cm it can be judged that long term restore work is necessary. On the contrary, It can be judged that the damage is slight if the settlement is less

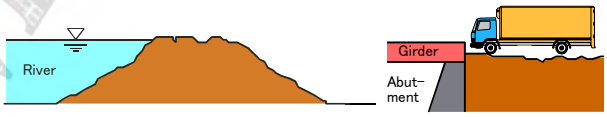

Fig.3: Critical conditions for river and road embankments

Table 2: Proposed allowable deformation for super levee and railway embankment

Structure	Allowable deformation
Super levee [8]	Level 1: Allowable settlement is 50 cm at crest and face of back slope, and 20 cm on the ground of super levee
Railway embank-ment [9]	Level 1: Allowable settlement is 0 to 20 cm Level 2: Allowable settlement is 20 to 50.

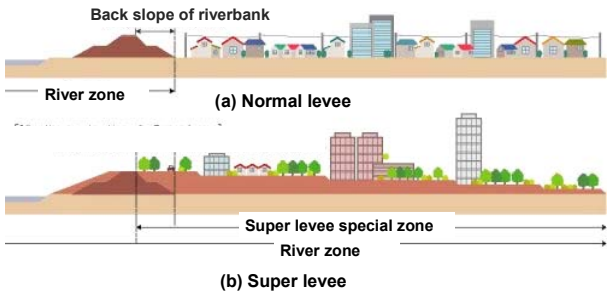

Fig.4 Difference of normal and super levees

than 20 cm. Therefore allowable settlements under Level 1 and 2 earthquake motions were decided as 20 cm and 50 cm, respectively as shown in Table 2.

Recently, seismic diagnosis of existing river dikes has been conducted in Japan [10]. In the diagnosis, allowable settlement is defined as Fig. 5. It is recommended that the level of river crest after the earthquake must be more than 2 m higher than mean monthly highest water level, by considering the height of waves etc.

Estimation methods for liquefaction-induced settlement

In the estimation of liquefaction-induced deformation of structures, three grades of methods; empirical method, static analyses and dynamic analyses, are available.

One empirical method is introduced in the design manual for river dikes, as shown in Table 5 [6]. In this method, settlement of a dike is estimated by safety factor of slope F_s. Two kinds of F_s must be calculated: F_s (k_h) which considers seismic coefficient, and F_s(⊿u) which considers excess pore water pressure due to liquefaction. Then the settlement is estimated by lower F_S. Relationship shown in Table 5 was derived form the correlation between settlement of damaged dikes and F_s during past several earthquakes [10] [11].

Table 3: Damage level for railway embankment [9]

Deformation level	Damage level	Settlement, S (roughly speaking)
1	No damage	None
2	Slight damage	S<20cm
3	Medium damage (restoration is available with emergency repairs)	20cm≦S <50cm
4	Severe damage (long term restoration is necessary)	S≧50cm

Table 4: Damage level for differential settlement between abutment and embankment [9]

Deformation level	Damage level	Differential settlement between abutment and embankment, S_d (roughly speaking)
1	No damage	None
2	Slight damage	S_d<10cm
3	Medium damage (restoration is available with emergency repairs)	10cm≦S_d<20cm
4	Severe damage (long term restoration is necessary)	S_d≧20cm

Table 5: Relationship between F_s and settlement [6]

Safety factor of slope, F_s		Settlement (maximum)
$F_{sd}(k_h)$	F_{sd}(⊿u)	
1.0<F_{sd}		0
0.8<F_{sd}≦1.0		0.25H
F_{sd}≦0.8	0.6<F_{sd}≦0.8	0.5H
	F_{sd}≦0.6	0.75H

Figure 6 shows another empirical relationship between settlement of dikes of Kiso, Nagara and Ibi Rivers during the 1944 Tohnankai earthquake, and liquefaction potential, P_L at the damaged sites [12]. As show in this figure, the settlement increased with the P_L.

For railway embankments, a relationship among settlement, height of embankments, density, number of cycles and liquefaction potential, P_L is prepared to estimate the settlement of embankments as shown in Fig. 7. This relationship was derived form shaking table tests.

In dynamic and static analyses, several methods have been proposed and applied to estimate the deformation of embankments. A technical committee organized by the Japanese Institute of Construction examined the efficiency of these analytical approaches. [11] [13]. In the examination, two kinds of dynamic analytical methods:

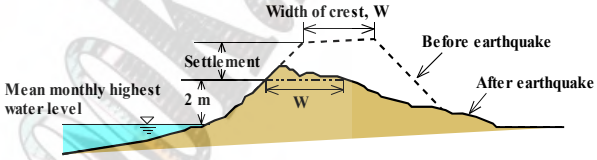

Fig.5: Definition of allowable settlement for river dike [10]

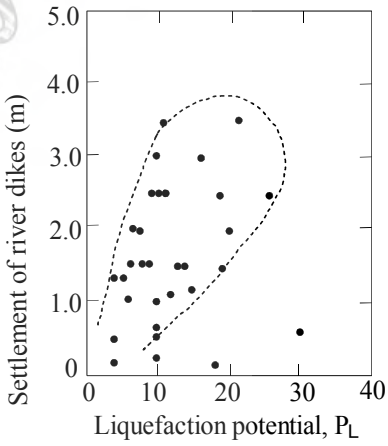

Fig.6: Relationship between P_L and settlement of river dikes[12]

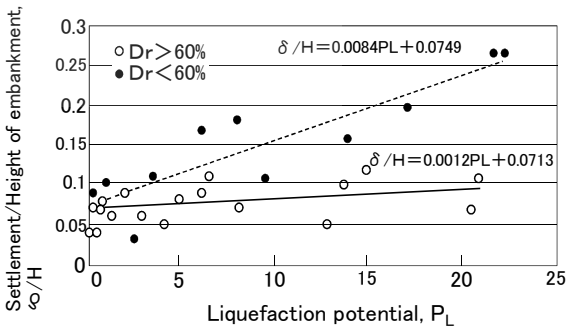

Fig.7: Relationship between P_L and settlement ratio for railway embankments

LIQCA and FLIP, and two static methods: ALID and Towhata's method, were applied to seven actual river dikes which were damaged and non-damaged during the 1993 Hokkaidonansei-oki earthquake and 1995 Hyogoken-nambu earthquake. LIQCA and FLIP are two dimensional effective stress analysis computer codes developed by Oka et al. [14] and Iai et al. [15], respectively. ALID is a simplified method using static FEM developed by Yasuda et al. [16] by assuming that residual deformation would occur in liquefied ground due to the reduction of shear modulus. Towhata's method was developed based on minimum energy principle [17]. Figure 8 shows the comparison between the calculate dike settlements and the observed settlements [11]. Estimated settlement by the empirical approach shown in Table 5 is compared in the figure. The predicted settlements by the analytical approach agree fairly well. Figure 9 shows the analyzed deformation by ALID at the severely settled dike [18]. These methods were also applied to the models with countermeasures tested by shaking table apparatus, to demonstrate the applicability of the analytical methods to the dikes with countermeasures.

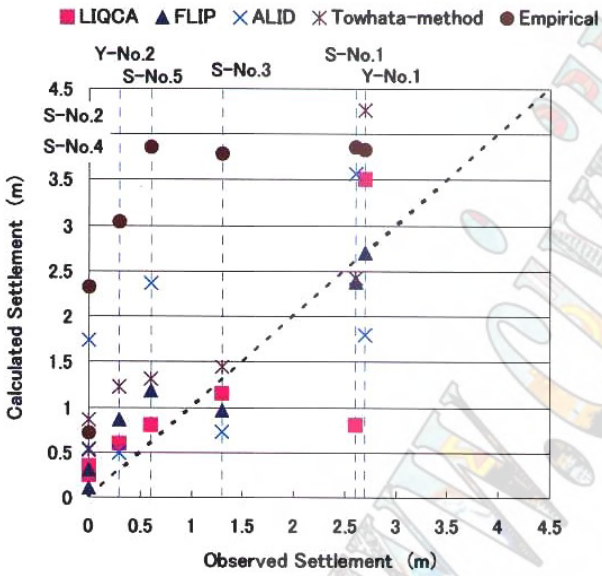

Fig.8: Comparison between calculated and observed settlements [11]

PERFORMANCE-BASED DESIGN FOR SPREAD FOUNDATIONS

Critical condition

During the construction of a structure with spread foundation, settlement of the structure increases gradually with the increase of load. When the load reaches to ultimate bearing capacity, the settlement rapidly increases as shown in Fig.10. Allowable bearing capacity is decided by dividing a safety factor. This ultimate bearing capacity is the critical condition by focusing the load as external load.

In case of liquefaction, external load is earthquake shaking. Therefore, critical condition must be related with the shaking intensity. Figure 11 shows schematic diagram of relationship between the shaking intensity and the settlement of a structure. If the ground is loose and clean sand, settlement of the structure is small when the shaking intensity is lower a critical intensity to cause liquefaction. Once the shaking intensity exceeds the critical intensity, large settlement occurs. On the contrary, in medium dense sand ground or silty sand ground, large settlement does not occur even the shaking intensity exceeds the critical intensity to cause liquefaction. The settlement increases gradually with the shaking intensity. Therefore, amount of the settlement of a structure must be considered in the design for liquefaction.

Studies on the allowable settlement

Liquefaction causes not only uniform settlement but also differential settlement of structures. Therefore, two items: average settlement and tilting angle of the structures, must be considered. In buildings, the average settlement relates to the damage of underground pipes which are buried in the ground through buildings. Large settlement of piers or abutments of bridges causes traffic accident or falling down of bridge girders. On the contrary, tilting of buildings or houses compels uncomfortable life for residents, as mentioned later.

In Japan, performance-based design has been introduced in the design of buildings. In Recommendations for Design of Building Foundations [19], three levels of critical conditions are stipulated: ultimate limit state, repair limit state and service limit state. For spread foundations, relationship among the three limits and a load-settlement curve is schematically

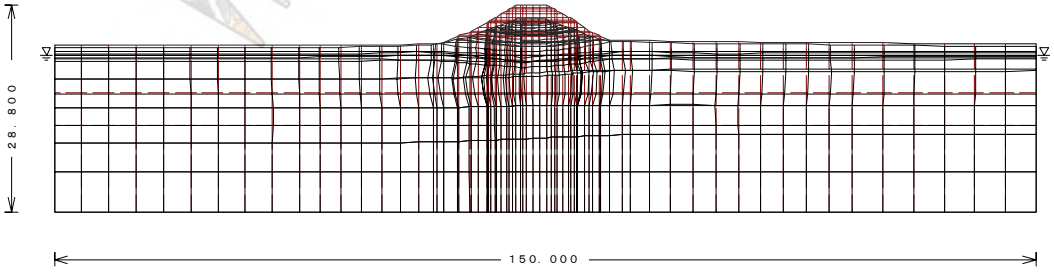

Fig. 9: Analyzed deformation by ALID (Shiribeshi-toshibetsu River, No.1) [18]

shown in Fig.10. In the evaluation of liquefaction potential, about 150 to 200 Gals and 350 Gals of design accelerations are recommended for repair limit level and ultimate limit level, respectively.

In case of differential settlement, allowable angle of inclination has been stipulated in several structures, such as buildings and oil tanks, for consolidation settlement and immediate settlement during construction of structures. However, in the case of the differential settlement in liquefied ground, only few studies have been conducted. The author and his colleagues studied the allowable angle of inclination for timber houses during the 2000 Tottoriken-seibu earthquake in Japan [20]. More than 100 timber houses settled and tilted due to liquefaction at a housing development during the earthquake. Among the damaged houses, 47 houses tilted more than 15/1000. In the heavily tilted houses, inhabitants felt giddy and nausea, and could not live in the houses after the earthquake, though walls, pillars and windows of the houses had no damage. Then heavily tilted houses were restored to a horizontal position. Their superstructures were lifted by jacks, their footings were repaired or reconstructed to become horizontal, then, the superstructures were replaced on the footings. The cost of the restoration work for one house was about three to four million Yen (about US$ 25000 to 35000). On the contrary, slightly tilted houses were not restored. Yasuda et al. studied the boundary of the angle of the restored and non-restored houses [20]. According to the study, the critical angle for restoration was about 1/100, as show in Fig. 12.

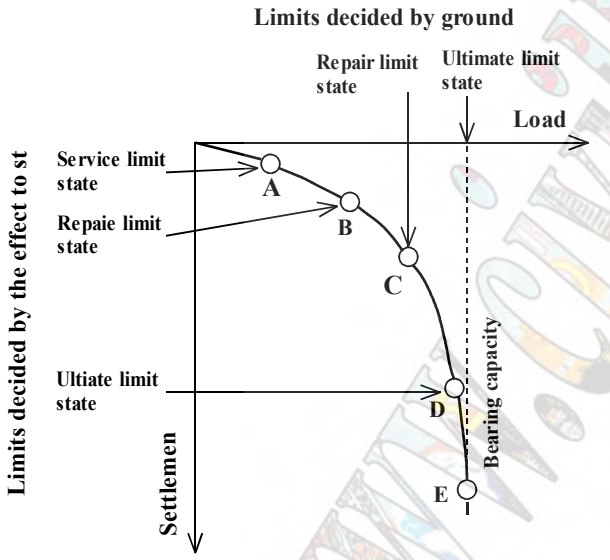

Fig.10: Three levels of critical condition [19]

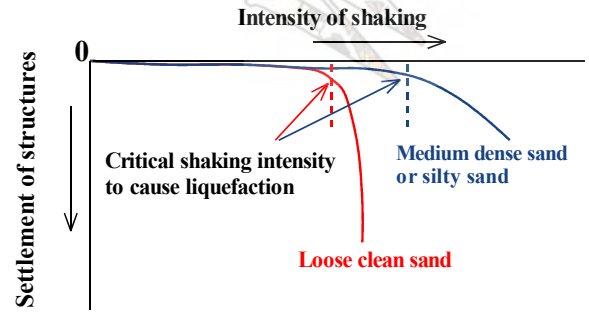

Fig.11: Schematic diagram of relationship between shaking intensity and settlement of spread foundation

Estimation methods for liquefaction-induced settlement

Yoshimi and Tokimatsu collected data on the settlement of buildings during the 1964 Niigata earthquake, and found the relationship between the width ratio and settlement ratio [21]. This relationship can be used for the estimation of the settlement of buildings in clean and loose sand ground. Kawasaki et al. conducted many dynamic centrifuge tests on the footing for a power transmission tower [22]. Based on the test results and case studies during the 1964 Niigata earthquake, an equation to estimate the settlement of footings was proposed. In the equation, nine factors: thickness of liquefiable layer, thickness of non-liquefiable layer, density of ground, grain size, amplitude of acceleration number of cycles of loading, width of footing, load intensity, and penetration depth, were considered. These are empirical methods to estimate the settlement.

The settlement of spread foundations can be evaluated by a dynamic or static analysis in which liquefaction is considered. Joint analyses for the settlement of raft foundation were carried out in 2003 in Japan [23]. A hypothetical model of ground beneath a storage tank was used for the analyses. Six different cases with varying configurations in cross section were analyzed, to evaluate the improvement due to compaction. Storage tank is 10 m in width and 12 m in height. Seven different liquefaction analysis codes were used for the analyses. Among them, four effective stress analysis codes, STADAS2, LIQCA, DIANA and STADAS, were developed based on elasto-plasticity theory. Two other effective stress analysis codes, FLIP and NUW2, were developed based on multi-mechanism theory and undrained stress path model, respectively. In addition, ALID, a residual deformation method mentioned before,

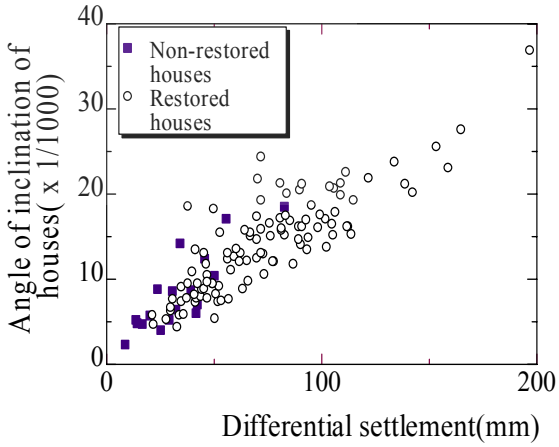

Fig. 12 Angle of inclination of restored and non-restored houses at Abehikona housing lot in Yonago City [20]

was applied. The NS direction wave component recorded at a depth of GL-16.4 m in Kobe Port Island during the 1995 Kobe earthquake was used as the input wave for the simulation. The maximum amplitude of the wave was 410 gals. Figure 13 shows relationships between vertical displacement of the tank and maximum acceleration of input wave. As shown in these figures, large settlements of the order of several ten centimeters could be evaluated by these codes. However, the results analyzed by the different analytical methods vary significantly, even though the same liquefaction strength is expected. The main reason for this variation is, even though liquefaction strength curves for a particular strain level are fitted, analyses do not always give acceptable results under wide range of strain.

Estimation of angle of inclination due to differential settlement is not easy, because many buildings tilted even though distribution of their loads is uniform. Empirical correlation between average settlement, S_{av} (cm) and angle of inclination, θ (deg.) may be useful. The author and his colleagues summarized this relationship during three earthquakes and derived the following relationship [24]:

$$\theta = 0.05 S_{av} \qquad (2)$$

PERFORMANCE-BASED DESIGN FOR UNDERGROUND STRUCTURES

Critical condition

Many types of damage of underground structures occur due to liquefaction, such as floatation, bending and buckling of buried pipes. Among them, this paper focuses floatation of buried pipes and manholes only.

Many sewage manholes and buried pipes floated due to liquefaction during the 1993 Kushiro-oki, 1993 Hokkaido-nansei-oki, 1994 Hokkaido-toho-oki, 2003 Tokachi-oki and 2004 Niigataken-chuetsu earthquakes in Japan. Maximum floatation of manholes was about 1.5 m in each earthquake. The floatation of manholes prevents not only the flow of sewage water but also road traffic. Especially high floatation of manholes from the surface of roads blocks the traffic of emergency vehicles just after an earthquake. About 1400 manholes floated due to the liquefaction of backfill soils during the 2004 Niigataken-chuetsu earthquake as shown in Photo 1. A car collided with a floated manhole and crushed in Nagaoka City. Therefore, not only the judge of floatation but also the amount of floatation must be considered in the design of underground structures.

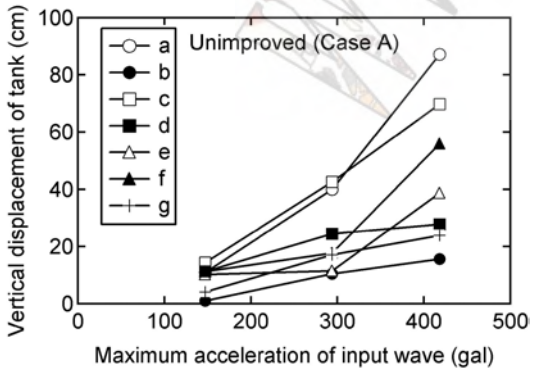

Fig.13: Relationship between maximum acceleration and calculated vertical displacement by 7 methods [23]

Studies on the allowable floatation

Honda et al. researched the allowable floatation for the passage of fire engine trucks by hearings from about 900 fire stations in Japan. Results showed that the allowable floatation is about 13 cm and 23 cm for narrow and wide roads, respectively [25].

Honda et al. studied critical floatation of sewage pipes also. They collected damaged pipes which had to be reconstructed after the Kushiro-oki earthquake, because sewage did not flow due to the floatation of pipes. Then, it was clarified that if the floated pipes inclined more than 3 %, it was necessary to reconstruct the pipes.

Estimation methods for liquefaction-induced floataion

Design methods for the liquefaction-induced floatation have been proposed based on the balance of floating force, friction and weight. For example, such a design method was introduced in the design code for common utility ducts in 1986 in Japan. In the methods, safety factor for floatation, *Fs* is evaluated. And possibility of floatation is judged. However, the amount of floatation cannot be estimated.

In empirical approach, Taniguchi et al. studied the relationship between the safety factor for floatation, F_S

Photo 1 Floated manholes during the 2004 Niigataken-chuetsu earthquake

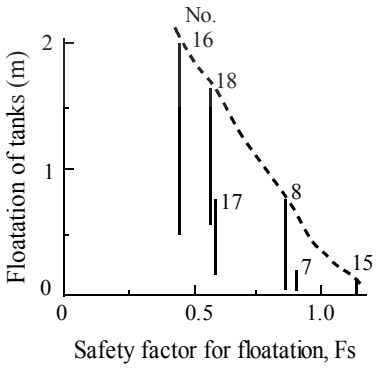

Fig.14: Relationship between F_S and floatation of tanks [26]

and amount of floatation of underground oil tanks during the 1983 Nihonkai-chubu earthquake [26] as shown in Fig.14. Though the data are scattered, floatation increased with the decrease of F_S.

Joint analyses for the floatation of buried pipes were carried out in 2003 in Japan [27]. In the analyses, several dynamic and static analytical methods were applied and possibility of evaluation of floatation was demonstrated.

CONCLUDING REMARKS

Several studied and codes on performance-based design for liquefaction in Japan are introduced in this paper. It is necessary to study the allowable deformations for many structures from now. In the determination of the allowable deformation, the following several items must be considered:

i) Stability of the structure,
ii) Importance of the structure
iii) Ease of restoration work
iv) Serviceability of the facilities
v) Damage to human life
vi) Ability of transportation of emergency vehicles

REFERENCES

[1] Japan Society of Civil Engineers, "Proposal on earthquake resistance for civil engineering structures,"1996.

[2] The Japan Road Association (1996): Specification for Highway Bridges. (in Japanese)

[3] Yasuda, S., "Evaluation of liquefaction-induced deformation of structures," *Recent Advances in Earthquake Geotechnical Engineering and Microzonation (Edited by A. Ansal)*, *Kluwer Academic Publishes*, Ch.6, pp.199-230, 2004.

[4] Yasuda, S., Ishihara, K., Harada, K. and Shinkawa, N., "Effects of soil improvement on ground subsidence due to liquefaction," *Soils and Foundations*, *Special Issue on Geotechnical Aspects of the January 17, 1995 Hyogoken-Nambu Earthquake*, pp.99-107, 1996.

[5] Japanese Road Association, "Highway Earthwork Series, Manual for slope protection" 1999. (in Japanese)

[6] Public Works Research Institute, "Design and construction manual for remediation of river dikes against liquefaction," *Research report of PWRI,* Vol.3513, 1997. (in Japanese)

[7] Civil Division of Japan Railway, "Design guide on improvement of embankment against earthquake (Draft)," 1979. (in Japanese)

[8] Japanese River Association, "Manual criteria for river works," 1997. (in Japanese)

[9] Railway Technical Institute, "Seismic design code for Japanese railway facilities," 1999. (in Japanese)

[10] River Bureau, "Technical manual for seismic diagnosis of existing river dikes," River Bureau, MLIT, 1995. (in Japanese)

[11] Sasaki, Y, Kano, S. and Matsuo, O., "Research and prectices on remedaial measures for river dikes gainst soil liquefaction" *Jornal of Japan Association for Earthquake Engineering*, Vol.4, No.3 (Special Issue), pp.312-335, 2004.

[12] Nakamura, Y. and Murakami, Y., "A study on the seismic stability of embankments of three big rivers in Nobi Plain," *34th Technical Conference of Ministry of Construction*, pp.96-104, 1980. (in Japanese)

[13] Japan Institute of Construction Engineering, "Methods to predict seismically induced dike deformation," *JICE Report* No.102001, 2002. (in Japanese)

[14] Oka, F., Yashima, A., Tateishi, A. Taguchi, Y. and Yamashita, S., "A cyclic elasto-plastic constitutive model for sand considering a plastic-strain dependence of the shear modulus." *Geotechnique* Vol.49, No. 5, pp.661-680, 1999.

[15] Iai, S., Matsunaga, Y. and Kameoka, T., "Strain space plasticity model for cyclic mobility," *Soils and Foundations*, Vol.32, No.2, pp.1-15, 1992.

[16] Yasuda, S., Yoshida, N., Adachi, K., Kiku, H., Gose, S. and Masuda, T., "Simplified practical method for evaluating liquefaction-induced flow." *Journal of geotechnical engineering, Japanese Society of Civil Engineer*, No.638/III-49, 71-89, 1999. (in Japanese)

[17] Towhata, I., Sasaki, Y., Tokida, K. Matsumoto, H., Tamari, Y. and Yamada, K., "Prediction of permanent displacement of liquefied ground by means of minimum energy principle." *Soils and Foundations*, Vol. 32, No. 3. pp. 97-116, 1992.

[18] Yasuda, S., Ideno,T., Sakurai, Y., Yoshida, N. and Kiku, H., "Analyses for liquefaction-induced settlement of river levees by ALID," *Proc. of the 12th Asian Regional Conference on Soil Mechanics and Geotechnical Engineering*, pp.347-350, 2003.

[19] Architectural Institute of Japan, "Recommendation for the design of building foundations," 2001. (in Japanese).

[20] Yasuda, S., Hitomi, T. and Hashimoto, T., "A detailed study on the liquefaction-induced settlement of timber houses during the 2000 Tottoriken-seibu earthquake, *Proc. of the 5th International Conference on Case Histories in Geotechnical Engineering*, Paper No.3.33, 2004.

[21] Yoshimi, Y. and Tokimatsu, K., " Settlement of buildings on saturated sand during earthquakes," *Soils and Foundations,* Vol.17, No.1, pp.23-38, 1977.

[22] Kawasaki, K., Sakai, T., Yasuda, S. and Satoh, M., "Earthquake-induced settlement of an isolated footing for power transmission tower," *Centrifuge 98,* pp.271-276, 1998.

[23] Harada, K., Yasuda, S., Yoshida, N., Sato, M and Sento, N., "Comparative study on the effectiveness of compaction as a countermeasure against liquefaction during a strong earthquake," *Proceedings of the 3rd International Conference on Earthquake Geotechnical Engineering and 11th International Conference on Soil Dynamics & Earthquake Engineering*, Vol.1, pp.56-566, 2004.

[24] Yasuda, S., Irisawa, T. and Kazami, K., "Liquefaction-induced settlements of buildings and damages in coastal areas during the Kocaeli and other earthquakes," *Proc. of the Satellite Conference on Lessons Learned from Recent Strong Earthquakes, 15th ICSMGE*, pp.33-42, 2001.

[25] Honda. N., Nakase, H., Suehiro, T. and Yasuda, S., "Study on the allowable floatation of buried structures," *Proc. of the 57th Annual Conference of the Japanese Society of Civil Engineering*, 1-720, 2002. (in Japanese)

[26] Public Works Research Institute, "Report on the disaster caused by the Nihon-kai-chubu earthquake of 1983," *Report of PWRI Repot*, *Vol.*165, 1985. (in Japanese)

[27] The Japanese Geotechnical Society, "Report on the study of the liquefaction-induced floatation of underground structures," 2003. (in Japanese)

Ground Deformations and Lateral Spreading Around the Shore of Sapanca Lake induced by the 1999 Kocaeli earthquake

Ö. Aydan[1], V.O. Atak[2], R. Ulusay[3], H. Hamada[4], J.P. Bardet[5]
[1]*Department of Marine Civil Engineering, Tokai University, Shizuoka, Japan*
[2]*Department of Geodesy, General Command of Mapping, Ankara, Turkey*
[3]*Department of Geological Engineering, Hacettepe University, Ankara, Turkey*
[4]*Department of Civil Engineering, Waseda University, Tokyo, Japan*
[5]*Department of Civil Engineering, South California University, Los Angeles, USA*

Abstract

The 1999 Kocaeli earthquake with a magnitude of 7.4 induced permanent deformation of ground due to both liquefaction and faulting. The permanent ground deformation along the Shore of Sapanca Lake was measured through the aerial photogrammetry technique. In this study, the areas around the Sapanca Vakıf Hotel and Eşme were chosen and investigated. Furthermore, 14 new boreholes were drilled nearby the hotel in addition to the existing boreholes by Iller Bank of Turkey. A series of analyses on the liquefaction susceptibility of the area was carried out by using a method of Japan Roadway and Bridges Society [1] and Youd et al. [2]. The permanent ground displacements were estimated according to methods proposed by Hamada and Wakamatsu [3] and Youd et al. [2]. Then the estimations are compared with theoretical predictions and the measured data in the vicinity of the Sapanca Vakıf Hotel area. The permanent ground displacements were also estimated by using the sliding block method and residual visco-elastic finite element methods and compared with observations and empirical methods.

Keywords—*Sapanca Lake, ground deformation, liquefaction, faulting, lateral spreading, Kocaeli earthquake*

INTRODUCTION

Turkey is one of the most seismically active countries in the World and most of her damaging earthquakes are of in-land type. These earthquakes mostly result in permanent ground deformation as a result of both faulting and liquefaction. The effect of liquefaction on permanent ground deformation, which is called *lateral spreading,* became to be known after the 1964 Niigata earthquake. Hamada et al. (1986) carried out the first quantitative measurements of permanent ground deformation due to liquefaction. This work was extended to other earthquakes in Japan, Philippine and USA. The Kocaeli earthquake of August 17, 1999 with a magnitude of 7.4 induced permanent deformation of ground due to both liquefaction and faulting and resulted heavy damage to both superstructures and infrastructures (Figure 1). Liquefaction phenomenon was widespread for a length of 120 km almost along the earthquake fault break. The ground fissures and sand boils were evidently observed in Adapazari City, along the Sakarya River up to the Black Sea coast, Akyazi, the southern shores of the Sapanca Lake and Izmit Gulf as far as Yalova whenever saturated Quaternary loose deposits exist

A collaborative research study among institutes from Turkey, Japan and USA was undertaken as the first quantitative measurement of permanent ground deformation and associated strain fields induced by ground liquefaction in Turkey [4,5]. In this collaborative research project, the permanent ground deformation was measured through the aerial photogrammetry technique at several sites within the earthquake stricken region. Among them, the areas around the Sapanca Vakıf Hotel and Eşme along the Shore of Sapanca Lake were chosen and investigated in this article. In the vicinity of the hotel, 14 new boreholes were drilled in addition to the existing boreholes drilled by Iller Bank of Turkey [6]. A series of analyses on the liquefaction susceptibility of the area was carried out empirical methods proposed by Japan Roadway and Bridges Society [1] and Youd et al. [2], and the permanent ground displacements were estimated by empirical methods proposed Hamada and Wakamatsu [3] and Youd et al. [2] and a new empirical equation. In addition, the sliding block method and residual visco-elastic finite element methods proposed by Aydan & Ulusay [7] and Aydan [8,9,10] were used to estimate permanent ground deformations of the liquefied ground. These estimations are compared with measurements and discussed.

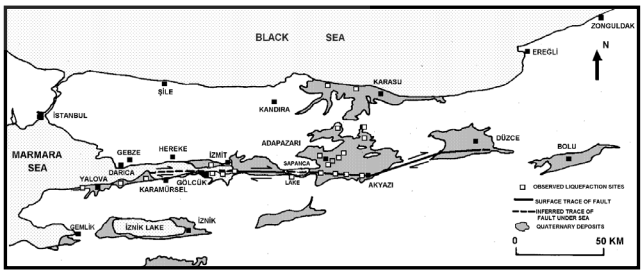

Figure 1. Liquefaction locations observed in the 1999 Kocaeli earthquake and distribution of alluvial deposits [11]

GEOLOGY AND SEISMO-TECTONICS

The survey area is located in a tectonic pull-apart basin, which extends from Sakarya River to the Gulf of Izmit. Elevation of the survey area ranges between 30 and 45 m. Inclination of natural slopes is very low and ranges between 0.1 and 0.3 %, and 2 and 4 % at the western and southern parts of Lake Sapanca, respectively. Sapanca and its vicinity are comprised of Paleozoic aged metamorphic rocks and Quaternary deposits. Many alluvial fans and recent alluvium have deposited along the southern shore of the lake. They are composed of gravel, sand, silt and clay sized material, and their thickness reaches up to 100 m. These deposits are carried by several creeks around Sapanca Lake. Their deltas cover areas from 3 to 6 km^2.

Sapanca Lake is structurally controlled by the segments of the North Anadolu Fault Zone (NAFZ) and it is one of the products of pull-apart mechanism associated with the strike-slip motion of the NAFZ. The focal plane solutions of the earthquakes occurred in the region indicated that the largest events took place by right lateral strike-slip faulting [11]. The largest seismic event before the 1999 Kocaeli earthquake was the 1967 Mudurnusuyu earthquake (Ms=6.8). This event also induced heavy damage and severe liquefaction along Sapanca Lake as well as in Adapazarı city.

OBSERVATIONS ON GROUND DEFORMATIONS AROUND SAPANCA LAKE

Ground deformations associated with lateral spreading induced by ground liquefaction and faulting were observed around Sapanca Lake and they caused severe damage to structures. Liquefaction phenomenon was widespread particularly along the southern shore of Sapanca Lake. The liquefaction observed in the vicinity of Hotel Sapanca was spectacular and the hotel building sank and moved towards the lake (Figure 2). The general trends of the eruption fissures were systematically parallel to the shore with an orientation of N75W (Figure 2). This area was also liquefied in the 1967 earthquake.

Liquefaction and lateral spreading of ground also took place in Eşme town in the northern shore of Sapanca Lake (Figure 3). The ground moved towards the Lake and settled. The settlement was more than 50cm However, it was not extensive as observed nearby the Hotel Sapanca. This area was also liquefied in the 1967 earthquake.

In addition, the earthquake caused some ground ruptures and deformations associated with the primary strike-slip faulting and the secondary normal faulting (Figure 4). The strike-slip faulting caused some structural damages to railways and pipelines at the east and west ends of Sapanca Lake while the secondary normal faulting caused some damage to roadways, railways and slopes nearby Eşme and Sapanca towns on the northern and southern side of the lake.

Figure 2: Damaged hotel and sand fissures and boils

Figure 3: Lateral spreading at Eşme

(a) East end (b) West end (Seka)

Figure 4: Damages by faulting around Sapanca Lake

GEOTECHNICAL CONDITIONS

Iller Bankası of Turkey [6] drilled boreholes for the sewage network of Sapanca town municipality (Figure 5). These boreholes are denoted with capital "S" in the respective figure. 14 new boreholes up to a depth of 10 m below the ground surface were drilled in the area of interest [5]. In these boreholes, SPT was carried out at every 1 m interval and groundwater levels were measured. Depth of the groundwater level was generally shallow and it was less than 2 m below the ground level. Figure 6 illustrates the ground conditions based on the new borehole data. Figure 7 shows a geological cross-section nearby the hotel area. The ground was broadly classified into five subgroups, namely, artificial fill, organic soil, sandy soil, silty soil, gravelly soil. The soil conditions differ from east to west. While the ground mainly consists of sandy and gravelly soils in the east (Sub-Areas 1 and 2), the silty and clayey soil became dominant in west (Sub-Areas 3 and 4). Furthermore, the gravelly soil becomes thicker as the distance from the shore increases. Thickness of the silty sand layers range between 1 and 6.5 m, however, it decreases away from the shoreline. Energy and overburden corrected SPT-N values, $(N_1)_{60}$, of these layers are generally between 3 and 30.

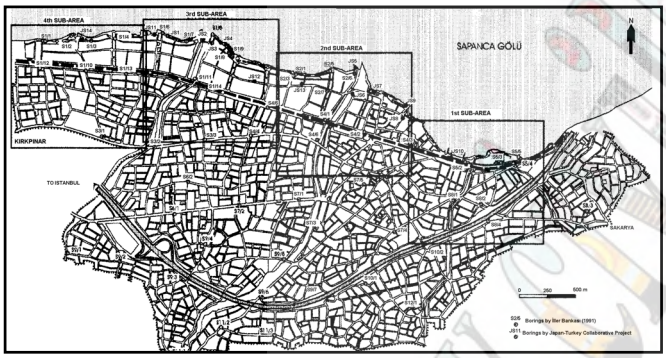

Figure 5: Locations of borings and sub-areas

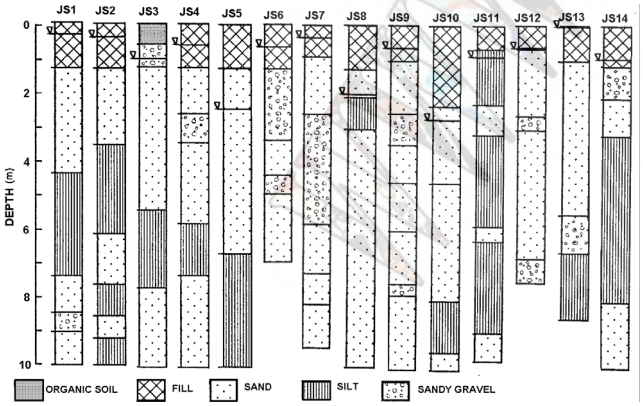

Figure 6: Geological conditions of new borings

Laboratory grain size distribution analyses performed on SPT samples indicated that mean grain size of the soils (D_{50}) vary between 0.12 and 0.35 mm, and an important portion of the samples fall into SM and SW-SP soil groups representing silty sands and poorly graded sands. The majority of the curves fall within the well-known bounds for liquefaction and these layers seem to be susceptible to liquefaction in terms of their grain sizes (Figure 8).

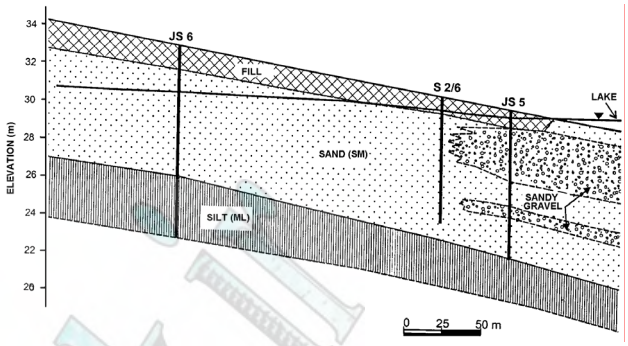

Figure 7: A geological cross-section along the hotel area

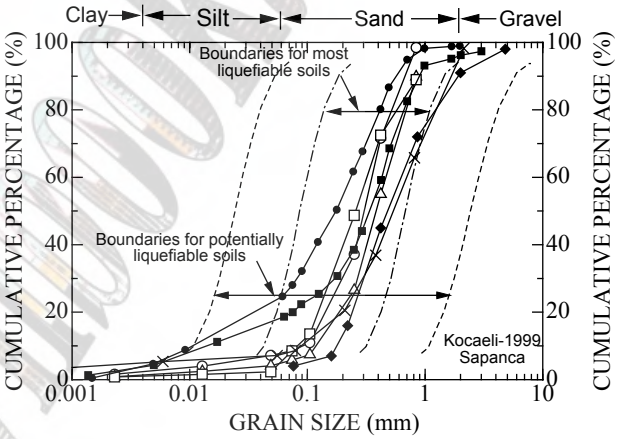

Figure 8: Grain size distributions of samples

AERIAL PHOTOGRAMMETRY MEASUREMENTS

The liquefaction-induced ground displacements in the study area were measured using both pre- and post-earthquake photographs by General Command of Mapping of Turkey [4]. The method based on aerial photogrammetry technique proposed by Hamada et al. [12] was employed. Aerial photographs used in the photographic interpretation were taken in 1994 and 1999 before and after the Kocaeli earthquake, respectively. In the pre-earthquake case, the scale was 1/35.000, while scale of the post-earthquake photographs was 1/16.000. As for measurements points, the manholes and tree roots were taken as points on the ground while the roof, bridges and poles were used as points off the ground. The three-dimensional coordinates of the common points on pre-post earthquake photographs were determined and their differences are interpreted as the earthquake induced permanent displacements. The error in aerial photogrammetry measurements was estimated to be about 50-60 cm. After the preliminary aerial photogrammetry measurements, the region shown in Figure 5 was

investigated in detail and this area was also subdivided into 4 sub-regions as shown in Figure 5. Figure 9 shows the ground displacements in Area 2, which are described in detail in the next section.

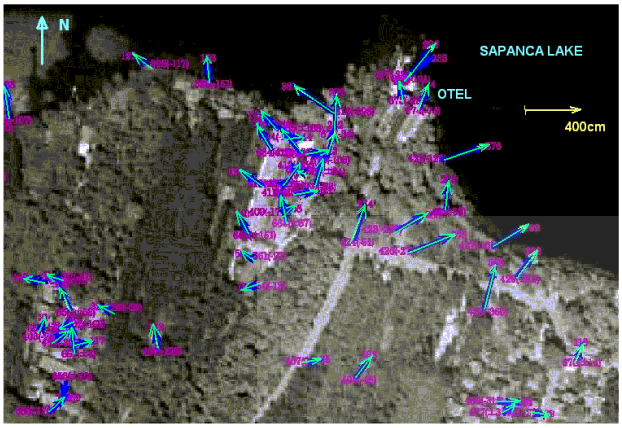

Figure 9: Ground deformation nearby the hotel (Area 2)

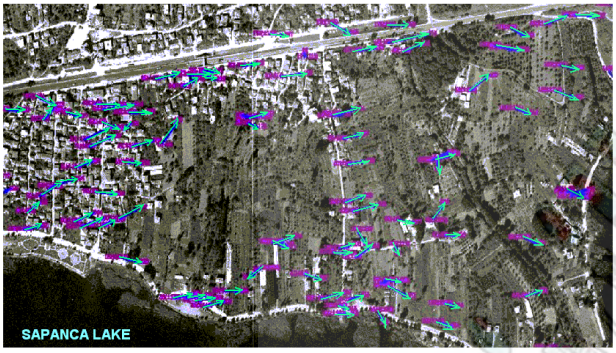

Figure 10: Ground deformation at Eşme

Figure 10 shows the ground displacement at Eşme town along the northern shore of Sapanca Lake. The ground displacements are generally associated with the crustal deformations associated with faulting event rather than lateral spreading induced by ground liquefaction. Nevertheless, some ground displacements in the SW direction towards the lake also occurred.

LIQUEFACTION SUSCEPTIBILITY ANALYSES

Liquefaction analyses were carried our according to methods proposed by Japan Roadway and Bridges Society [1] and Youd et al. [2]. Liquefaction analyses were performed at boreholes and the liquefaction resistance factors and liquefiable layer thickness were computed at each borehole. The maximum horizontal ground acceleration imposed from the bedrock into the liquefiable ground was estimated from the empirical relation proposed by Aydan [13] for the firm ground and bedrock and also from the nearby Sakarya strong motion station of TURK-NET. The maximum ground acceleration on bedrock was estimated as 294 gals from Aydan's relation for the parameters of the 1999 Kocaeli earthquake. The maximum ground acceleration was 407 gal at Sakarya station of the TURK-NET. In this article, the results of liquefaction analyses computed for the base acceleration of 400 Gals using the empirical methods proposed by Japan Roadway and Bridges Society (JRABS) [1] and Youd et al. [2] are only presented. Figure 11 compares the liquefiable layer thickness obtained from two different techniques. As seen from the figure, the liquefiable layer thickness obtained by the method of Youd et al. [2] is less than that by the method of Japan Roadway and Bridges Society [1].

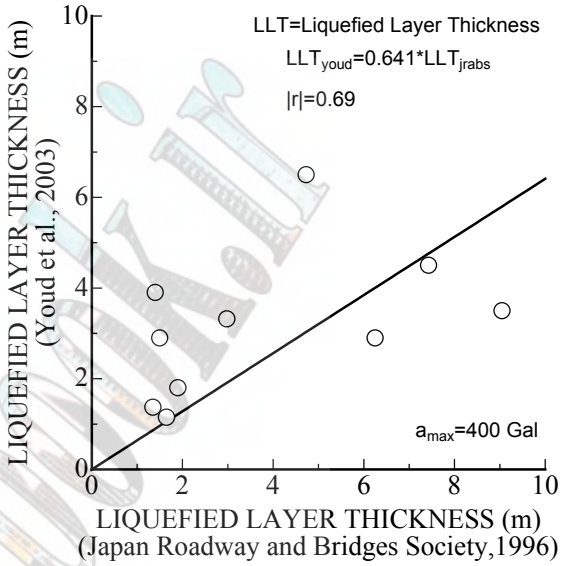

Figure 11: Comparison of thickness of liquefiable layers

LATERAL SPREADING EVALUATIONS

There are basically three different techniques to estimate ground deformations induced by ground liquefaction, namely, 1) Empirical methods, 2) Sliding block analysis and 3) Finite Element Method. These three techniques were used and compared with each other.

Empirical Methods

Empirical methods utilize the ground inclination and liquefiable ground layer thickness as the fundamental parameters and empirical relations are obtained through regression analyses [14,2,15]. Recently Hamada [15] also introduced time history parameter for the consideration of shaking duration.

The boreholes JS10, JS6, JS2 and JS4 were omitted in the lateral spreading analyses, as their topography was complex. The maximum distance from the lakeshore was taken as 100 m for lateral spreading analyses. The ground displacement at each borehole was estimated by using a method proposed by Hamada et al. [12] Hamada and Wakamatsu [3], MLR of Youd et al. [2] and Bardet et al. [15]. The details of the analyses can be found in the theses by Inuzuka [16] and Kanıbir [17]. In addition to these empirical equations, the following empirical equation is proposed for estimating the displacement of the liquefied ground:

$$\delta = \frac{\gamma_s H_l^2}{G} \sin\theta \; v_{\max} \qquad (1)$$

Where γ_w is the unit weight of liquefied ground. H_l is liquefied layer thickness. G, θ and v_{max} are residual shear modulus of liquefied ground, ground inclination and maximum ground velocity, respectively. Figure 12 compares the estimations with observations of ground displacement at a given borehole as a function of liquefiable layer thickness obtained from the method of JRABS [1]. The maximum ground velocity was computed from the EW component of Sakarya record. Although the general trend is quite similar to the empirical relation, there is some discrepancy when the liquefiable layer thickness is small. This may be due to the difference between the estimated thickness and actual thickness of liquefiable layer at the given boreholes and the value of the residual shear modulus of ground.

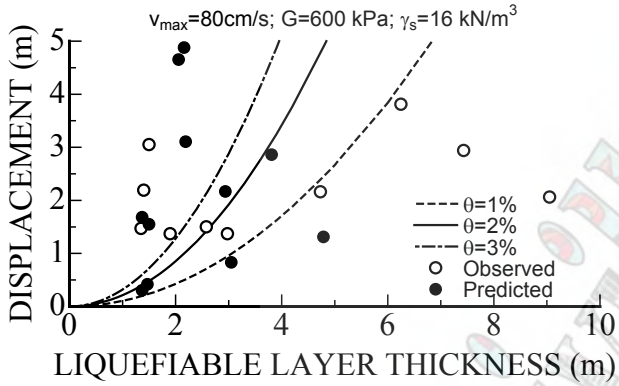

Figure 12: Comparison of estimations with observations

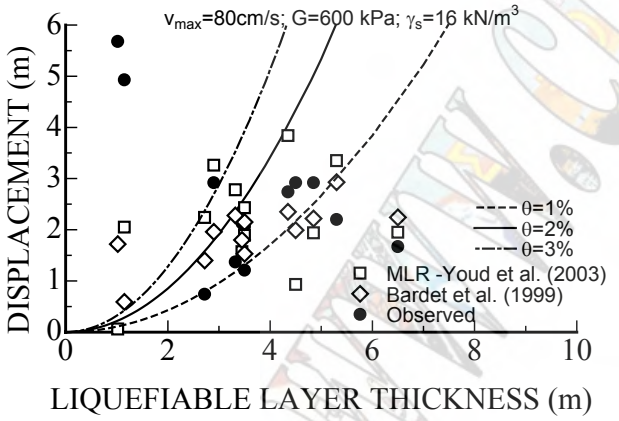

Figure 13: Comparison of estimations with observations

Figure 13 compares the estimations from the empirical equation with those from the methods of Youd et al. [2] and Bardet et al. [15] together with observed ground displacement at the vicinity of the boreholes. The general trend is quite similar. Nevertheless, there is a huge discrepancy between the observations and estimations. This is once again should be due to the difference between the estimated thickness and actual thickness of liquefiable layer and the value of the residual shear modulus of ground at a given borehole.

Evaluation by Sliding Body Method

The methods based on the sliding block analysis originally proposed by Newmark [18] and they are used to estimate the rigid body motion of liquefied layer through the consideration of input-waves and shear strength mobilized along the sliding plane [19]. The most difficult aspects in this method are how to select the residual shear strength properties and pore pressure variation during shaking and motion of the ground. In-spite of numerous laboratory tests on the liquefaction of soils, the properties of liquefied soils are scarce. The shear strength of liquefied ground under dynamic shaking, which is relevant to actual conditions in-situ, are those for undrained state. Some of these data was recently compiled by Ishihara [20]. The normalized shear strength (may be viewed as the residual friction angle coefficient) may range between 0.1 (5.7^o) and 0.2 (11.3^o) for pure sand. This value decreases as the plasticity index increases (silty or clayey sandy soil). In this study, the sliding resistance of ground is modeled as brittle frictional soil (once the peak strength is achieved, the residual friction angle is mobilized). The friction angle was varied between 5 and 15^o while the peak friction angle was set to 30^o.

The second important issue is how to assign the pore pressure during shaking in this type of approaches. The static pore pressure coefficient for a gently inclined soil layer may be easily set as follows

$$\beta_s = \frac{\gamma_w}{\gamma_s}\frac{h_w}{H} \qquad (2)$$

Where γ_w and γ_s are unit weight of water and liquefied ground. h_w and H are water table height above the sliding surface and layer thickness. The following pore pressure coefficient for dynamic conditions is assigned

$$\beta_d = \left(\frac{\gamma_s}{\gamma_w}\frac{H}{h_w} - 1\right)\frac{|a|}{g} \qquad (3)$$

Where $|a|$ is absolute value of ground acceleration at a given time and g is gravitational acceleration.

The theoretical formulation for this problem has already been presented elsewhere [7]. The only difference in this study from the previous formulation is associated with the assumption of the dynamic component of the pore pressure during ground shaking. The applications of this approach to the ground deformation at the Shore of Sapanca Lake are now presented herein. The nearest strong motion station to the site is Sakarya station of Turkish National Strong Motion Network. Unfortunately, the NS component of this station was mal-functioning at the time of earthquake and the records of EW and UD components are only available. In computations these two components are utilized. The ground surface inclination ranged between 0.86 to 4% while it was about 1.5-2% for the greater part of the ground profiles (80%).

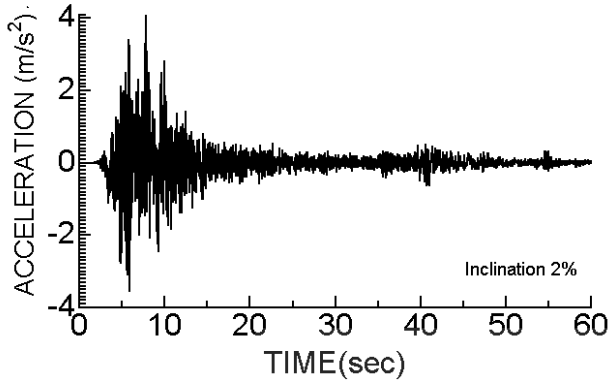

Figure 14: Effective ground acceleration

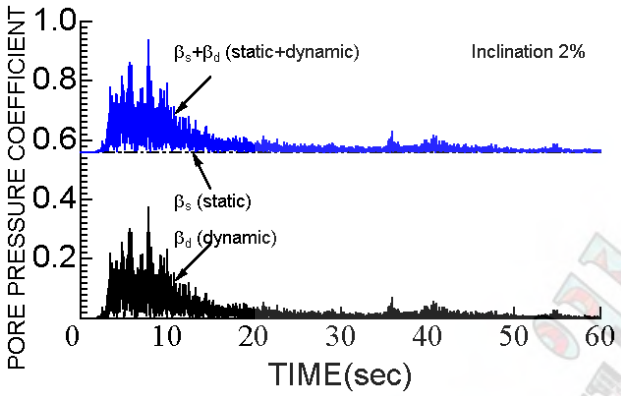

Figure 15: Assumed pore pressure variation

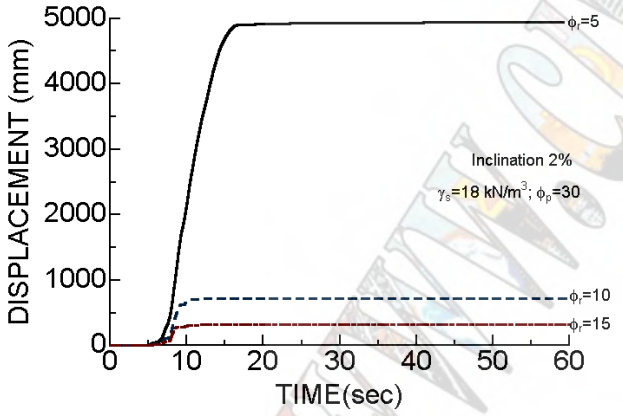

Figure 16: Computed displacement of liquefied ground

Figures 14, 15 and 16 show the equivalent ground acceleration acting on the sliding direction, pore pressure variations and computed displacement responses for three different residual friction angles, namely, 5, 10 and 15°. The maximum ground displacement is about 5000mm for the residual friction angle of 5° while it becomes 340mm for the residual friction angle of 15°. The ground was silty sand where the maximum ground deformation was measured. In view of the residual strength values compiled by Ishihara [20], it was likely that the residual friction angle of the soil should have been less than 10°. The estimations of deformation for these values of residual friction angle are very close to the measured values. However, it is difficult to assess the effect of layer thickness on ground deformations if this approach is used.

Evaluation by Visco-elastic Finite Element Approach

Liquefaction and lateral spreading of ground are modeled by the finite element methods. The most appropriate model is a two-phase modelling based on the Biot-type formulation. Nevertheless, it becomes quite difficult to assign appropriate constitutive models for solid and liquid phases once the ground becomes liquefied. Therefore, a single-phase approach is commonly used in such analyses. The lateral spreading of the liquefied ground is modeled by assuming that the liquefied ground is either elastic solid with highly reduced deformability coefficient or viscous Bingham fluid [21,22,23]. Aydan [8,9] combined these two approaches by proposing a finite element method in which a visco-elastic model for the liquefied ground is used. In this analysis the properties relevant to liquefied ground (residual properties) are used. Aydan [10] also developed a simplified finite element procedure for two-dimensional problems by taking into account the both experimental and numerical facts, that is, the ground deformation is parabolic at a given section.

Hamada et al. [12] suggested that the lateral spreading of the liquefied ground takes place following the main shock purely under gravitational forces. They validated their reasoning through experiments. The methods by Aydan were initially developed for numerical analyses of those experiments. Hamada and his co-workers [3,12,14] determined visco-elastic characteristics of the liquefied ground, which may also be visualized as the residual mechanical properties of the ground. The constants determined by Hamada and his co-workers are based on infinitely long visco-elastic modeling of the motion of liquefied ground. The simplified 2D finite element analyses are concerned with ground motions of a finite region.

First dynamic 1D modeling of liquefied ground is presented. In the 1D analyses, the effects of visco-elastic properties and layer thickness were investigated. The finite element method is purely based on the shear response of the ground, which implies that there is no volumetric variation [10]. The previous studies by Aydan [8,9] showed that the fluctuations of displacement and velocity as a function of time depend upon the viscous properties of the ground while the final deformation depends upon the residual shear modulus. With these in mind, several parametric studies were carried out to infer material properties of liquefied soil along the southern shore of Sapanca lake. In the computations, the elastic shear modulus and viscous shear modulus were varied and the values used were quite similar to those determined by Hamada [14]. From parametric studies, it was inferred that the elastic shear modulus of 600 Pa would be appropriate value for the liquefied ground along the shores of Sapanca Lake.

First the effect of layer thickness on the amplitude of the ground deformation is investigated. The empirical estimations for the liquefiable layer thickness indicated that the liquefiable layer thickness might range between 3m to 5m. The properties used in the analysis are shown in Figure 17 and the ground surface inclination was set to 2%. The amplitude of ground deformation is about 10m, 6m and 3m for the layer thickness of 5, 4 and 3m, respectively. These results indicate that the liquefied ground thickness should be less than 5m at the site.

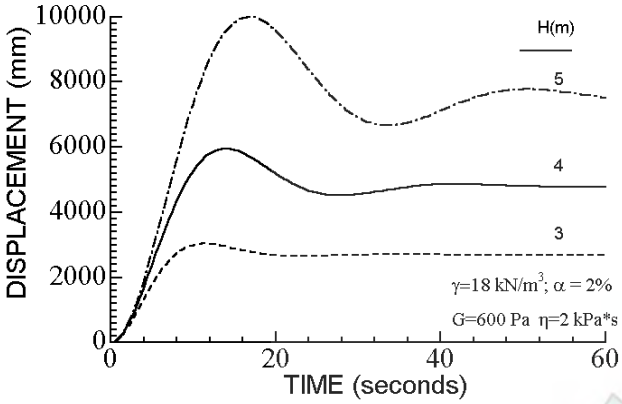

Figure 17: Effect of layer thickness on displacements

The simplified 2D visco-elastic finite element approach fundamentally models the ground as a finite region undergoing purely shear deformation [10]. Since the inertia term is neglected in the formulation, the displacement and velocity responses becomes parabolic in time domain. The region was 100m long and the ground surface inclination was 2%. The mechanical properties used were the same and are given in the respective figures.

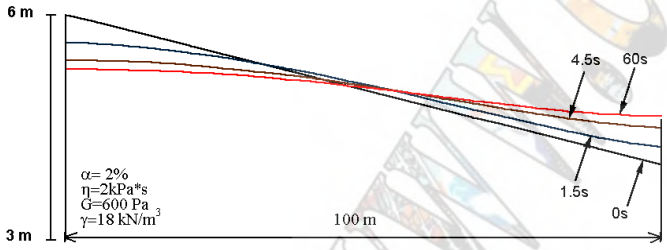

Figure 18: Ground surface profiles at selected times

Figure 18 shows the ground surface profile at selected time steps while Figures 19 and 20 show the horizontal and vertical displacement responses of the ground surface at selected locations. As expected, the ground subsides in the upper part and heaves in the lower part. The ground surface deformation becomes the largest at the middle part of the region and it is about 4m, which is different from that for infinitely long layer model. This is a natural consequence of the boundary conditions of the models as they are different from each other.

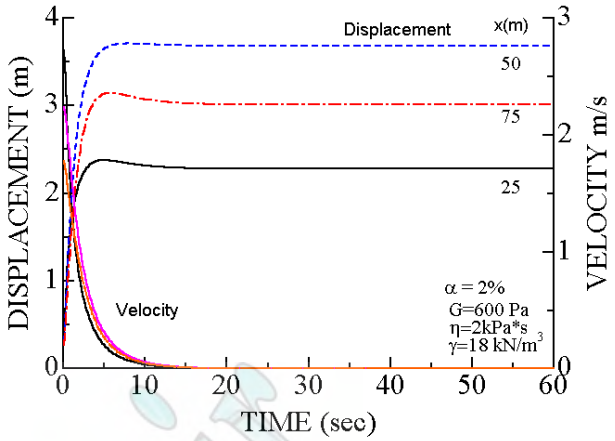

Figure 19: Time variations of displacement and velocity

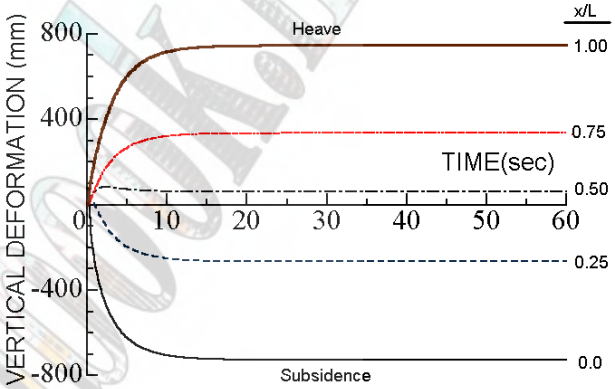

Figure 20: Time variations of displacement at some points

CONCLUSIONS

The authors described a part of the research project with the collaboration of General Command of Mapping of Turkey on the liquefaction induced lateral spreading and related damage in the region from Adapazarı to Yalova, caused by 1999 Kocaeli earthquake. The findings and conclusions can be drawn as follows based on this study.

Liquefaction at Sapanca during the 1999 Kocaeli earthquake occurred primarily within Quaternary alluvial deposits. The major areas of liquefaction and liquefaction-induced lateral spreading are located along the shore and the creeks.

Among four empirical methods employed in this study, the ground displacements estimated from the empirical model proposed in this article showed a better agreement with the observed displacements.

Some lateral displacements, which extend southward beyond a distance of 100 m from the lakeshore and were detected from aerial photogrammetry technique. However, they are not considered in this article.

The ground deformations induced by the lateral spreading of liquefied ground along the shore of Sapanca Lake by the 1999 Kocaeli earthquake were estimated using the block sliding model and visco-elastic finite

element models, in which, residual properties are utilized. If the residual friction angle of the surface between liquefied and non-liquefied ground is between 5-10 degrees, it is possible to estimate the ground deformations through the use of ground acceleration measured at Sakarya station and the block sliding approach, provided that the dynamic pore pressure coefficient is chosen as described in this article. The estimated ground deformations are quite close to those measured by the aerial photogrammetry technique.

The 1D and 2D visco-elastic finite element approaches with the use of residual state properties of liquefied ground reported by Hamada [14] also estimate the ground deformations. If the chosen properties are appropriate, these type estimations may be superior to those of empirical approaches.

ACKNOWLEDGEMENTS

This study is dedicated to the late Professor Dr. Rifat YARAR of Istanbul Technical University, Turkey. The authors sincerely acknowledge S. Inuzuka and A. Kanibir, former graduate students of Waseda University and Hacettepe University, respectively for their help in some of computations reported in this article.

REFERENCES

[1] Japan Roadway and Bridges Society (1996). *Roadway and Bridges Design Standard*, Chapter V: Earthquake Resistance Design.

[2] Youd, T. L., Idriss, I. M., Andrus, R. D., Arango, I., Castro, G., Christian, J. T., Dorby, R., Finn, W. D. L., Harder, L. F., Hynes, M. E., Ishihara, K., Koester, J. P., Liao, S. S. C., Marcuson, W. F., Martin, G. R., Mitchell, J. K., Moriwaki, Y., Power, M. S., Robertson, P. K., Seed, R. B. and Stokoe, K. H. (2001). Liquefaction resistance of soils: summary report from the 1996 NCEER and 1998 NCEER/NSF workshops on evaluations of liquefaction resistance of soils. Journal of Geotechnical and Geoenvironmental Engineering, ASCE, 127 (10), 817-833.

[3] Hamada M. Wakamatsu K. (1998): A study on ground displacement caused by soil liquefaction. *Geotechnical Journal JSCE*, 596/III-43: 189-208.

[4] Atak, O., Aksu, O., Aydan, Ö., Önder, M., Toz, G. (2004): Measurement of Ground Deformation Induced By Liquefaction and Faulting In The 1999 Kocaeli Earthquake Area**.** XXth ISPRS Congress, 12-23 July 2004 Istanbul, Turkey**,** Paper 648.

[5] Aydan, Ö., Hamada, M., Bardet, J. P. , Ulusay, R. and Kanibir, A. (2004): Liquefaction induced lateral spreading in the Kocaeli earthquake. Turkey: Case study around the Hotel Sapanca. 13th World Conference on Earthquake Engineering. Vancouver, B.C., Canada, Paper No. 2921.

[6] İller Bank of Turkey (1991). Reports on boreholes of Sapanca municipality. (*Unpublished Turkish report*).

[7] Aydan, Ö., Ulusay, R. (2002): A back analysis of the failure of a highway embankment at Bakacak during the 1999 Düzce-Bolu earthquake. Environmental Geology, 42, 621-631.

[8] Aydan, Ö. (1994). The dynamic shear response of an infinitely long visco-elastic layer under gravitational loading. *Soil Dynamics and Earthquake Engineering,* **13**, 181-186.

[9] Aydan, Ö. (1995). Mechanical and numerical modelling of lateral spreading of liquefied soil. *Int. Conf. on Earthquake Geotechnical Engineering, IS-TOKYO,* 881-886.

[10] Aydan, Ö. (1997). A simplified finite element approach for modeling the lateral spreading of ground. The 2nd Japan-Turkey Workshop on Earthquake Disaster Prevention Research in Turkey, Istanbul, JICA-ITU, 1-10.

[11] Aydan Ö. Ulusay R. Hasgür Z. Taşkın B. "A site investigation of Kocaeli Earthquake of August 17, 1999". Turkish Earthquake Foundation, 1999; TDV/DR 08-49, 180 pp.

[12] Hamada M, Yasuda S, Isoyama R, Emoto K. (1986): Study on liquefaction-induced permanent ground displacements and earthquake damage. Geotechnical Journal, JSCE, III-6(376):221-229 (in Japanese).

[13] Aydan Ö. "Comparison of suitability of submerged tunnel and shield tunnel for Subsea passage of Bosphorus" *Geological Engineering Journal of Turkey* 2001; 25 (1): 1-17 (in Turkish).

[14] Hamada, M. (1999). Similitude law for liquefied-ground flow. Proceedings of the 7th U.S-Japan Workshop on Earthquake Resistant Design of Lifeline Facilities and Countermeasures Against Soil Liquefaction, 191-205.

[15] Bardet, J.P., Mace, N., Tobita, T., and Hu, J., 1999. Large-scale modeling of liquefaction-induced ground deformation Part I: A four-parameter MLR model. Proceedings of the 7th U.S.-Japan Workshop on Earthquake Resistant Design of Lifeline Facilities and Countermeasures Against Soil Liquefaction, 155-173.

[16] Inuzuka S. (2002): Lateral spreading in Kocaeli earthquake, Turkey in 1999; *Case study around the Hotel Sapanca*. Master Thesis, Civil Engineering Department of Waseda University (unpublished, in Japanese).

[17] Kanıbir A. (2003): Investigation of the lateral spreading at Sapanca and suggestion of empirical relationships for predicting lateral spreading. Master Thesis, Geological Engineering Department of Hacettepe University (unpublished, in Turkish).

[18] Newmark, N.M. (1965): Effects of earthquakes on dams and embankments. Geotechnique, 15(2), 139-160.

[19] Dobry, R. and Baziar, M.H. (1992): Modelling of lateral spreads in silty sands by sliding soil blocks, A Specialty Conference on Stability and Performance of Slopes and Embankments, University of California, Berkeley, 1-28.

[20] Ishihara, K. (1993): Liquefaction and flow failure during earthquakes. Geotechnique, 43(3), 351-415.

[21] Towhata, I., Matsumoto, H. (1992). Analysis of development of permanent displacement with time in liquefied ground. *The 4th US-Japan Workshop on Earthquake Resistant Design of Lifeline Facilities and Countermeasures for Soil Liquefaction,* Honolulu, **2,** 335-349.

[22] Yasuda, S., Nagase, H., Kiku, H., Uchida, Y. (1990). A simplified procedure for the analysis of a permanent displacement. The 3rd US-Japan Workshop on Earthquake Resistant Design of Lifeline Facilities and Countermeasures for Soil Liquefaction, San Francisco, 225-236.

[23] Hadush, S., Yashima, A., Uzuoka, R. (2000): Importance of viscous fluid characteristics in liquefaction induced lateral spreading analysis. Computers and Geotechnics, 27, 199-224.

Failure of Harbor Quaywall in the Lefkada 2003 Earthquake

G. Gazetas[1], I. Anastasopoulos[1], and P. Dakoulas[2]
[1] *School of Civil Engineering, National Technical University, Athens, Greece*
[2] *Department of Civil Engineering, University of Thessaly, Volos, Greece*

Abstract

Among the numerous failures of harbor quaywalls in the M_w 6.4 Lefkada earthquake, the paper concentrates on the excessive deformation patterns observed in the Lefkada Marina, a small harbor that had just been completed at the time of the earthquake. Despite its state-of- practice code design for an effective peak acceleration of 0.36 g, one of the 5 x 5 m^2 block quaywall at 3.5 m depth of water experienced an outward top displacement of 0.22 m –– about four to five times larger than a Newmark–type Richards & Elms procedure would have predicted. The likely causes of such under-prediction are explored with the help of 2–D elastoplastic finite–element analyses.

Keywords : ––*Lefkada earthquake ; case history ; quaywall ; sliding ;*

INTRODUCTION : SEISMOLOGICAL AND GEOTECHNICAL OVERVIEW

The strike–slip M_w 6.4 event of 14 August 2003 was no surprise : Lefkada along with the islands of Cefalonia and Ithaca have the highest seismicity in Europe and one of the highest on Earth. Located next to the major Cefalonia Transform Fault, which usually produces about a dozen $M_s > 6$ events per century (Fig. 1). Lefkada had already suffered three $M_s \approx 6.5$ earthquakes in the 20th century (two in 1948 and one in 1914), in addition to several $M_s \approx 6$ events (including one in 1973). They all occurred on the same fault within a length of about 50 km (Fig. 1). Seismological details on the earthquake and the seismicity of the region can be found in Benetatos et al [1] and Louvari et al [2].

As a result of this high and frequent seismic activity, the structural systems prevailing on the island are well designed to resist strong ground shaking. Design, effective peak acceleration (EPA) is presently at 0.36 g (up from about 0.22 g before 1995). This high level of design requirements may explain at least partly the minor structural damage and the lack of fatalities in the 2003 event––despite the close proximity to the seismogenic source (8 km of the main town from the fault) and the high intensity of shaking.

The single accelerogram on the island, plotted in Fig. 2 along with its 5%–damped response spectra, implies a *destructive* motion : effective peak acceleration A ≈ 0.58 g, dominant period range $T_p \approx 0.30–0.60$ *sec*, and several substantial cycles (8 cycles of about 0.30 g) . In fact, the fault–normal component is even stronger with max $S_A \approx$ 2.20 g at T ≈ 1 seconds (Mylonakis [3], personal communication).

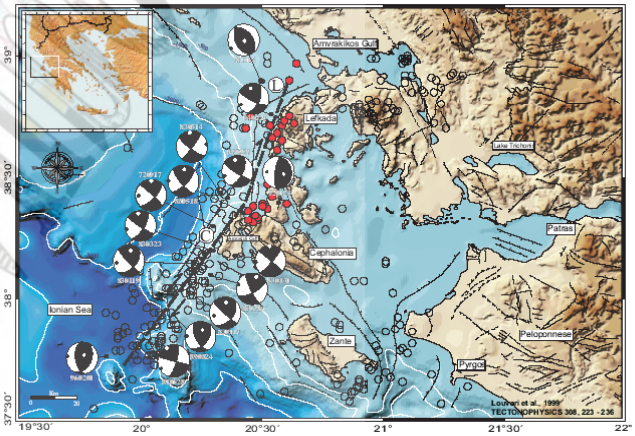

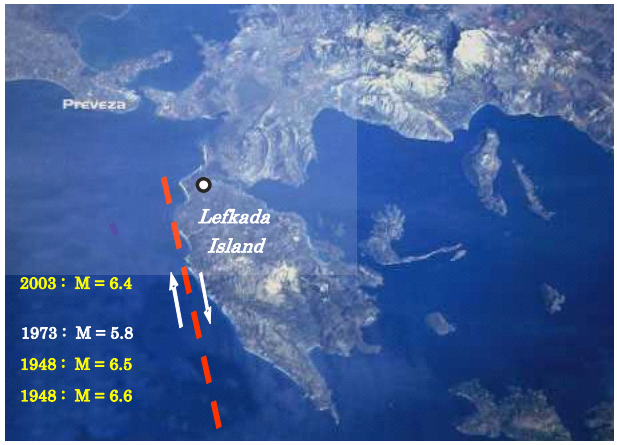

Fig. 1 : Top : The Cefalonia Transform Fault with the fault mechanism of a number of pre-1999 events [2]. Bottom : Satellite view of the Lefkada island and the approximate location of the 2003 rupture of the Transform Fault [1].

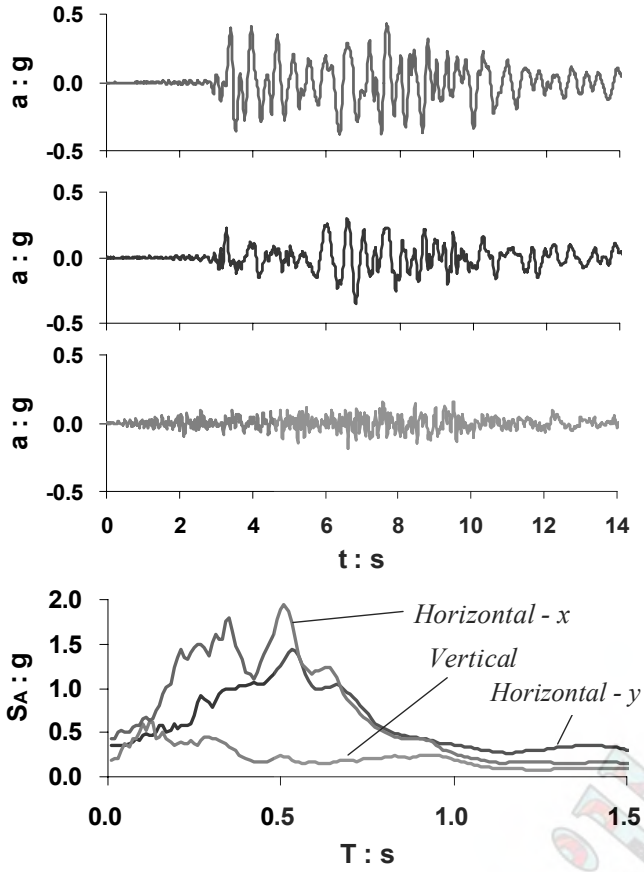

Fig. 2 The recorded accelerogram and its response spectra

Geotechnical failures were abundant : large–scale landslides, liquefaction and lateral spreading, and (most significantly) numerous harbor quaywall failures.

Massive landslides occurred on the west coast of the island, which is located only 1–2 km away from, and almost parallel to, the seismogenic fault. Numerous were the instances of liquefaction in the main town as well as in the villages along the east coast. However, the extent of liquefaction was in general small, and only in a few cases were the consequences of significance. Ejection of liquefied material above ground was observed in many cases, as for example near the harbor of the main town, indicative of liquefaction at relatively shallow depths; subsequent settlement of the ground surface just exceeded 30 cm in the harbor. Ground was lost to the sea at least in two locations as a result of such liquefaction–related settlement, but most significant were the resulting differential settlements of near–coast buildings.

Lateral spreading was clearly observed only in one location, in a section of the Lefkada Marina, which had just been completed at the time of the earthquake. This is discussed later herein.

SOIL AMPLIFICATION

A rather limited geotechnical and geophysical exploration program in the town of Lefkada (areal extent : 1 x 0.5 km^2) has revealed that the typical profile consists of about 15 meters of alluvium underlain by marl. Sandy clay and silty clay layers prevail in the alluvium, with occasional presence of thin layers of more sandy material. Shear wave velocities in the marl are about 550 m/s, while in the alluvial layers shear wave velocity ranges from as low as 120 m/s to as much as 300 m/s.

Extensive 1–D soil amplification analyses show a fairly wide range of possible surface motions, similar in general appearance with the recorded motion (on the basis of which they were computed). For the Marina region the resulting values of PGA, T_p, and $maxS_a$, range from 0.3 g – 0.5 g , 0.30–0.60 seconds, and 1.2 g – 2.0 g, respectively. Clearly the filtering role of soil was undoubtedly significant for the town of Lefkada. Its further exploration however is beyond the scope of this paper.

DEFORMATION AND FAILURE OF HARBOR QUAYWALLS — THE "MARINA" (LEISURE HARBOR)

The east and south coast of the island have numerous small harbors serving the fishing and tourist industry. The water depth in these harbors ranges between 2.5 and 4.5 meters, only. Yet, all harbors (with no exception) suffered some form of "damage": excessive displacement or rotation of the quaywall; settlement and cracking of the retained backfill ; lateral spreading, extending over distances of about 30–50 meters, several times larger than the height of the quaywall ; and complete overturning. Typical photographic examples are given in Gazetas [4].

Most of these "failures" involved rather old small harbors, designed and, especially, constructed with methods that do not conform with current state of the art or even conventional practice. The one interesting exception was the Lefkada Marina, located about 100 meters across the harbor of the island. It was part of a major development that had just been completed (only half the stores had just opened) at the time of the earthquake.

A plan of the Marina with its main facilities is depicted in Fig 3. The seismic design of the quaywalls was based on modern displacement concepts ("Newmark" sliding block analysis), using 0.36 g as the basic peak ground acceleration, in accordance with the Greek seismic code EAK–2000 [5]. Six boreholes with SPT measurements and undisturbed–sample testing provided soil information.

More significantly, the very small original depth of the sea water (less than 1 m) allowed the construction of the whole project under dry conditions, thus avoiding some of the difficulties of underwater construction. This must, in principle at least, have resulted in improved quality of the facility, above what is usually the case with underwater constructed quaywalls and backfills.

The design was quite conservative : all buildings (one or two–story tall) were founded on 0.8 meter diameter and 15 meter long cast-in-place reinforced concrete piles ;

the quaywall comprised rigid concrete blocks 5 x 5 meters, founded on 3 m of a rockfill base which had replaced the original soil.

(a)

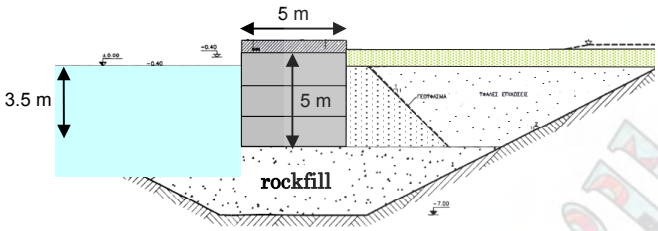

(b)

Fig. 3 : (a) Aerial view of the Lefkada Marina, (b) the cross-section of the quaywall and backfill in the Lefkada Marina.

One might not have expected that this facility will have experienced problems in an earthquake that produced no human injuries ! Yet, almost all types of deformation that a harbor facility may undergo were actually observed (but of course in a small scale, commensurate with the scale of the facility):

(1) **Lateral Spreading** in the corner "a" (see plan of Fig 4**),** extending from the two perpendicularly–intersecting walls to the back of the small hotel, including the in-between (still unused at the time) swimming pool. Ground fissures, lateral displacement and rotation of the quaywalls, and severe cracking of the small retaining walls at the edges of the apparently displaced mass, are the main manifestation features of the spreading.

(2) **Settlement** of the backfilled ground in the regions "c" and "d" (see Fig 5) with respect to :
- the pile–supported buildings, which apparently stayed in place having experienced only elastic (recoverable) deformation.
- the quaywalls, which displaced and rotated, but without much settlement

(3) **Differential horizontal displacement** between neighboring quaywall blocks of different geometry and foundation. An example : the 15 cm differential movement between the "pier" of a small pedestrian bridge and the two neighboring quaywalls –– reminiscent of the numerous such cases in the Kobe harbor in 1995.

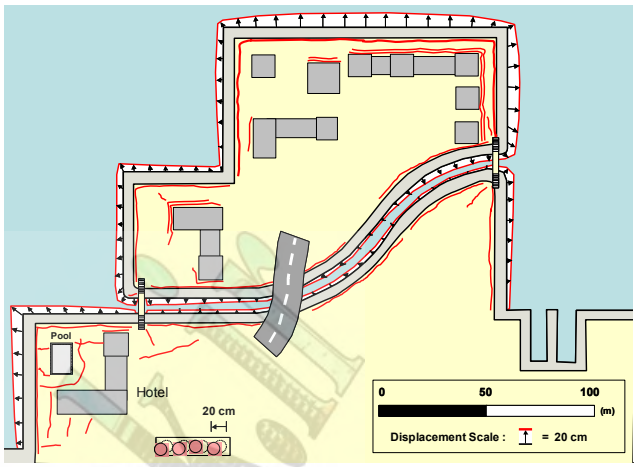

(a)

Fig. 4 : (a) Plan of the Marina with a sketch of the observed deformations, and (b) manifestation of lateral spreading around the swimming pool of area "a".

ANALYSIS OF THE MARINA QUAYWALL DISPLACEMENT

A. The Design

The Marina quaywalls were designed for an effective peak acceleration A = 0.36 g, as specified by the greek seismic code EAK–2000 [5]. To allow for a limited sliding permanent displacement of the order of 10 cm or less, the code permits pseudo–static design for an acceleration level equal to A/2 = 0.18 g. In the design stability calculations, a factor of (minimum) safety of 1.2 was achieved against rotation on a circular sliding surface starting in the backfill and passing through the base rockfill, under the wall block. This implies a critical ("yield") acceleration $A_c \approx 0.22\ g$. Equivalently, for the code earthquake of $A = 0.36\ g$, this would lead to a permanent displacement of the order of 6 cm or less (e.g using the Makdisi–Seed [6] diagram).

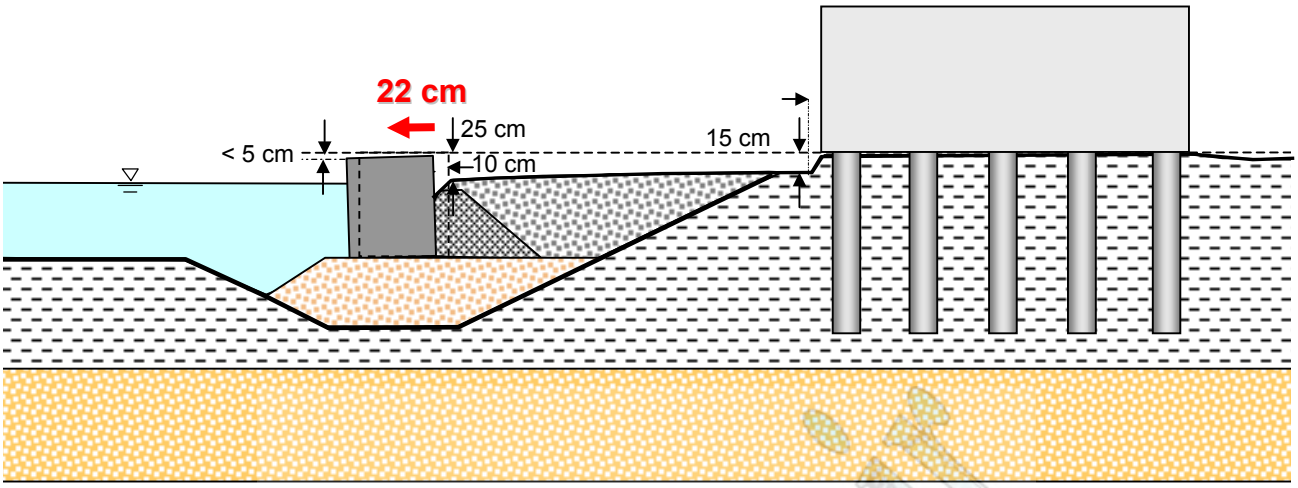

Fig. 5 : Settlement and displacement of quaywall and backfill soil in the areas “b” and “c”

For such a “rational” design and the probable good quality of construction, one would have expected a better performance in the earthquake.

B. Conventional State–of–Practice Analysis

Current seismic codes require : a pseudo–static computation of the dynamic active force on the walls for a particular level of design peak acceleration $A_d = a_d\, g$; determination of the (critical) acceleration level $A_c = a_c\, g$ that would induce “failure” (i.e., factor of safety = 1) in either sliding, or overturning, or bearing capacity exceedance ; and then estimation of the permanent inelastic deformation in each of the above modes of failure if $A_d > A_c$. Sliding is often the critical condition for a wall having a large width to height ratio (B/H), as is the case here (B/H = 1).

Seismic active earth pressures are determined conventionally with the Mononobe–Okabe method, for an effective horizontal acceleration $A_d = ag$. Numerous parametric dynamic studies have unequivocally shown that vertical acceleration has no appreciable effect on the response of the quay wall system –– a fact that would be especially true with the very high–frequency vertical acceleration of the Lefkada record. This is in accord with several other studies on the subject (e.g. Seed & Whitman [7], Gazetas et al [8]), as well as with the recommendations of Japanese (JSCE–1992 [9] OCDI–2002 [10]) and international (PIANC–2002 [11]) codes.

The M–O expression for the total (static plus dynamic) active earth–pressure force is

$$P_{AE} = \tfrac{1}{2}\, \gamma\, H^2\, K_{AE} \qquad (1a)$$

where :

$$K_{AE} = \frac{\cos^2(\varphi-\psi)}{\cos\psi\ \cos(\psi+\delta)\,[1+\{\sin(\varphi+\delta)\sin(\varphi-\psi)\,/\,\cos(\delta+\psi)\}^{1/2}\,]^2} \qquad (1b)$$

in which φ = the angle of shearing resistance of the retained soil, and δ = the angle of adhesion along the vertical wall–soil interface. The angle ψ is a function of the apparent seismic coefficient α':

$$\psi = \arctan\ (\alpha') \qquad (2)$$

The value of α' reflects not only the level of the basic seismic coefficient α, but also the effect of submergence in water (Ebeling & Morison [12], Matsuzawa et al [13]).

For a partially submerged backfill as in this case here (the water table in the Marina is at sea level, *i.e.* 1.5 m below the top of the retained soil), by weighing thrusts based on the volume of soil in the failure wedge below and above the water surface results in the following expressions for the *apparent seismic coefficient* (of an equivalent "homogeneous" soil) :

$$\alpha' = \alpha' \frac{\gamma_{sat}\ H_w^2 + \gamma\ H_{sur}^2 + 2\gamma\ H_w\ H_{sur}}{\gamma_b\ H_w^2 + \gamma\ H_{sur}^2 + 2\gamma\ H_w\ H_{sur}} \qquad (3)$$

and the effective unit weight of soil :

$$\gamma' = \gamma_b \left(\frac{H_w}{H}\right)^2 + \gamma\left[1 - \left(\frac{H_w}{H}\right)^2\right] \qquad (4)$$

in which $H = H_w + H_{sur}$ is the total height of the wall ; $H_w = 3.5\ m$ is the height below the water surface where the buoyant unit weight γ_b controls ; and $H_{sur} = 1.5\ m$ is the height above the water surface where the soil is not in buoyancy and has a unit weight γ . Eqns (3) and (4) are used in Eqns (1) and (2) to determine the effective static–plus–dynamic earth thrust. Static water pressures from the two sides balance out.

The underlying assumptions for the above treatment of a submerged backfill are : *(i)* that pore-water pressures do not change as a result of horizontal motion, and *(ii)* that backfill permeability is low enough for the water to move as a unit with the mineral skeleton. According to the PIANK [11] manual the threshold permeability for the latter condition is of the order of $k \approx 10^{-2}$ cm/s.

The yield acceleration in sliding is obtained from the horizontal equilibrium of the block under the action of :

- M–O effective total (static+dynamic) force : $P_{AE}\ cos\delta$
- wall inertia : $W\ a_c$
- hydrodynamic "tension" in front of the wall (á la Westergaard)

Since P_{AE} is a function of a_c an iterative trial-and-error solution is implemented giving :

$$A_c \approx 0.22\ g \qquad (5)$$

that is, a value very similar to the value obtained by the designers for a circular sliding surface.

Applying the greek (EAK) [5] and european (EC8) [14], seismic codes : $A_d = A = 0.40\ g$. Then the sliding displacements are obtained using the following methods :

- The Richards & Elms [15] expression

$$\Delta \approx 0.087\ \frac{V_{max}^2 A_{max}^3}{A_C^4} \qquad (6)$$

which for $A_{max} = A = 0.40\ g$, $V_{max} = 0.35\ m/s$ (from the aforementioned results of 1–D wave propagation analysis) gives

$$\Delta \approx 3\ cm \qquad (7)$$

- The Makdisi & Seed [6] diagram. For M = 6.5 and $A_c/A = 0.21/0.40 \approx 0.53$ gives an upper bound

$$\Delta \leq 7\ cm \qquad (8)$$

In view of the many cycles in the Lefkada ground motion, this upper bound is the most appropriate prediction of the method.

- The Yegian et al [16] method relates the dimensioless residual displacement $\Delta' = \Delta / (An_{eq}T^2)$ to the A_c / A ratio, where :
  - n_{eq} = the number of significant cycles, taken here as 8
  - T = the dominant period of motion, taken here as 0.50 seconds

  The resulting displacement is

$$\Delta \approx 5\ cm \qquad (9)$$

- Finally, direct numerical integration for the sliding block displacement results is value in the range :

$$4\ cm \leq \Delta \leq 6\ cm \qquad (10)$$

Evidently, the Newmark–type sliding block analysis methods do not explain the large permanent displacement (22 cm) of the Lefkada quaywall. Therefore, a 2–D inelastic dynamic analysis is used to explore the nature of the quaywall response.

C. Two–Dimensional Dynamic Analysis of Wall Displacements

Several limitations of the conventional code analysis are worthy of note :

- horizontal displacement of the wall is due not only to its sliding on the base but also to the elastic deformation of the underlying soil.
- rotation of the wall at its base also contributes to displacement at the top, especially in view of the relatively soft soils that are present at shallow depths.
- development of excess pore water pressures in the foundation soil may further amplify the above two displacements, as was unquestionably the

case with the quaywalls of Port and Rokko islands in the Kobe 1995 earthquake [17,18, 19, 20].

The results of finite–element analysis using two different records as excitation are shown in Figs 6 and 7. The soil is modeled as a Mohr–Coulomb elastoplastic material, the stiffness of which has been obtained on the basis of the last iteration of an equivalent linear dynamic analysis.

Two motions are used as excitation. They correspond to the Lefkada (2003) record and the Aegion (1995) record. One-dimensional deconvolution was used in both cases to derive the base "rock" motion. The two records are of roughly similar effective peak acceleration (≈ 0.58 g and 0.50 g, respectively) and dominant period. (Tp ≈ 0.40–0.60 seconds). They differ mainly in the number of cycles (8 for Lefkada versus 2 for Aegion) and the peak ground velocity (35 cm/s for Lefkada versus 64 cm/s for Aegion).

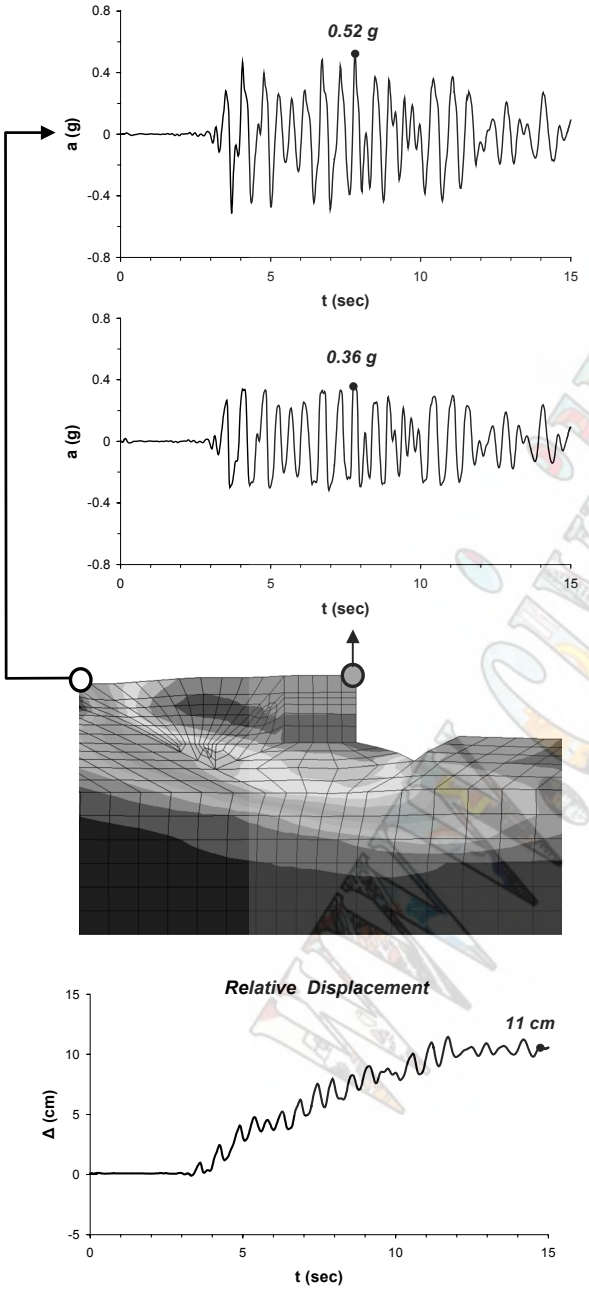

Fig. 6 : Dynamic transient analysis of the marina quaywall subjected to the Lefkada 2004 seismic record : acceleration and relative displacement time histories. Excess porewater pressures ignored

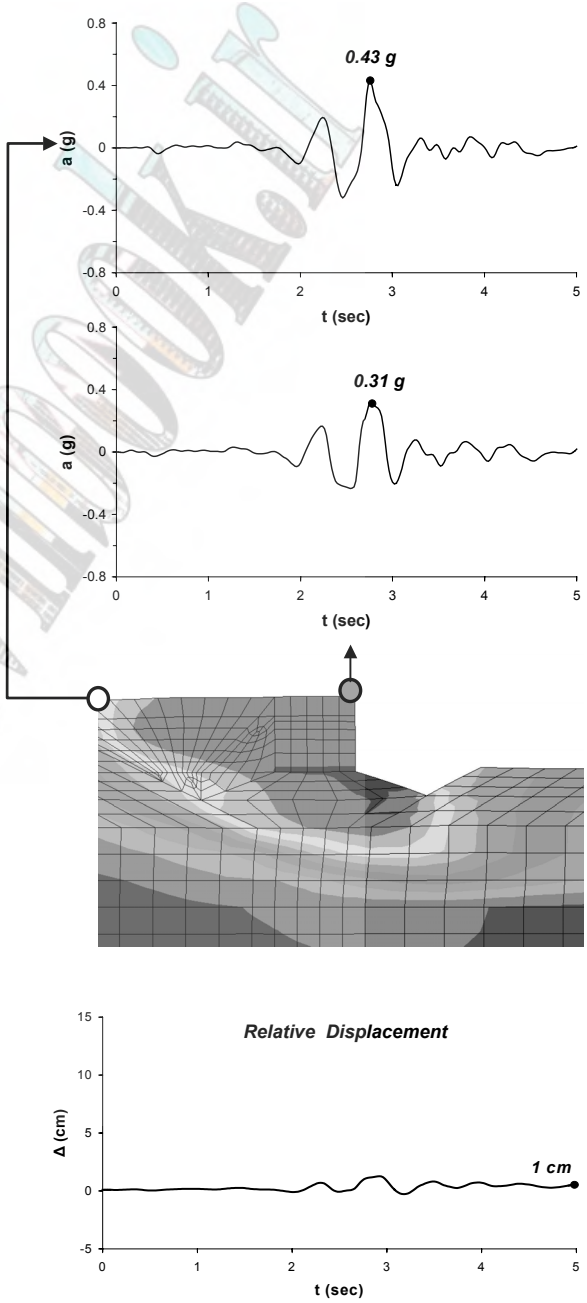

Fig. 7 : Dynamic transient analysis of the marina quaywall subjected to the Aegion 1995 seismic record : acceleration and relative displacement time histories. Excess porewater pressures ignored

The first set of analysis ignores the development of pore water pressures in the foundation soil. Yet, the trends are clear : the computed displacement (for the Lefkada record), about 11 cm, is two to three times as large as that predicted with the conventional methods. Moreover, it is seen that the nature of ground motion is of utmost significance : despite its equal intensity, the Aegion record leads to rather insignificant permanent displacement. The accumulation of outward permanent displacement during the Lefkada multi–cycle motion is therefore one of the causes of the observed large deformation.

Finally in Fig 8, to account in an admittedly very crude way for the unavoidable development of excess pore–water pressures, we assume that a silty soil layer 1.5–3 meters below the ground surface at the bottom of the sea experiences large excess pore-water pressures, so that its strength is described by an "effective" angle $\varphi r = 9.5^o$ (for its $N_{SPT} \approx 15$). The resulting acceleration time history of the seaward corner of the quaywall shows an amplification over the free–field acceleration. But most significantly, the accumulation of permanent outward displacements is now faster, with an end result of 20 cm, which is very close to the actually observed 22 cm.

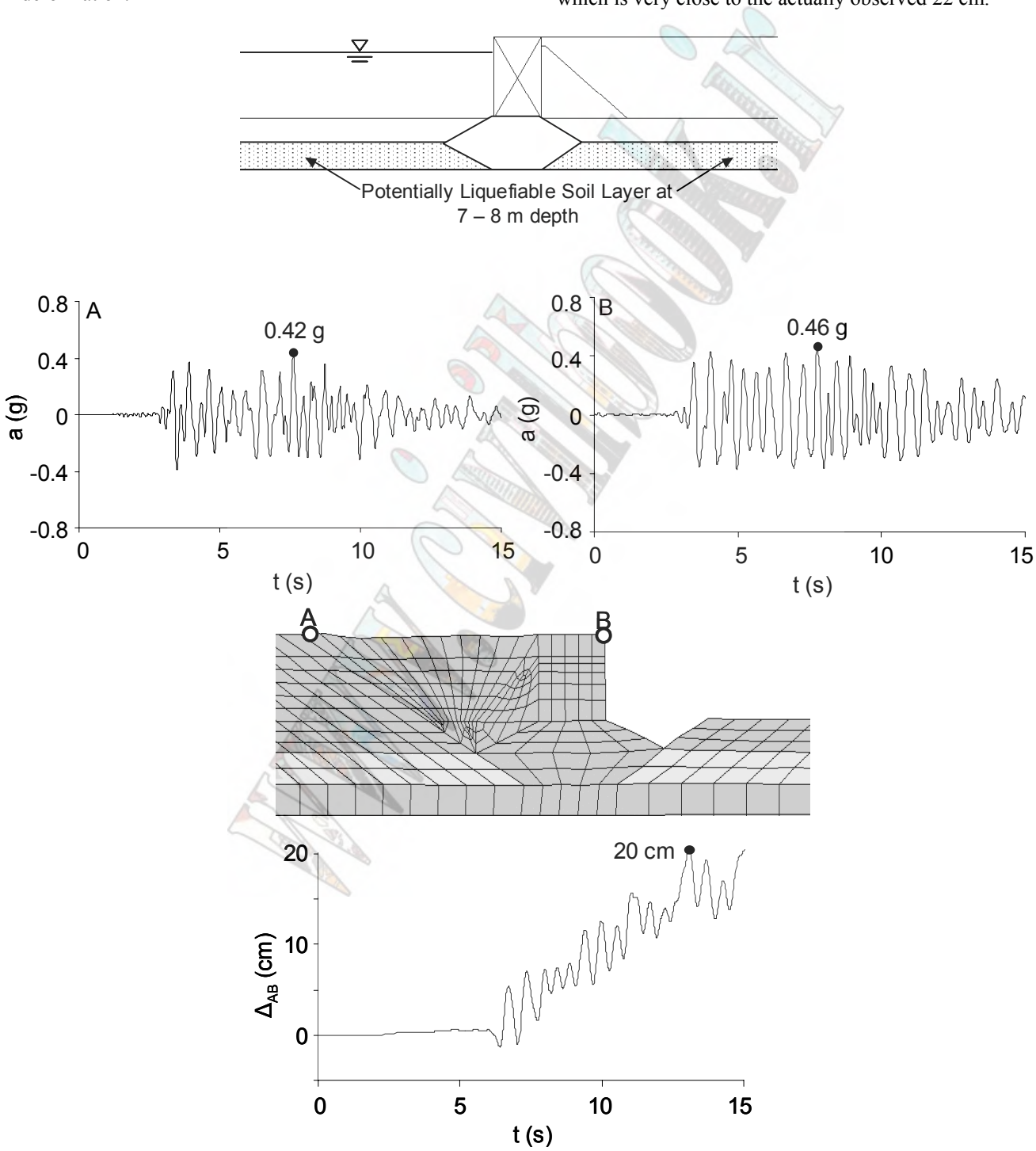

Fig. 8 : Dynamic transient analysis of the marina quaywall subjected to the Lefkada 2003 seismic record, but with a potentially liquefiable soil layer at 7 to 8 m depth : acceleration and relative displacement time histories

Without paying too much attention to this near−coincidence of analysis and measurements, we can safely conclude that *sliding at the base is not the main mechanism of quaywal displacement* −− as was abundantly demonstrated in the analyses for the Kobe 1995 earthquake [17−20].

ACKNOWLEDGEMENT

The financial support of the Organization of Antiseismic Protection (OASP) of Greece, though a grant to the National Technical University, is kindly acknowledged.

REFERENCES

[1] Benetatos C., Kiratzi A., Roumelioti Z. Stavrakakis G., Drakatos G. & Latousakis I. (2004) : "The 14 August 2003 Lefkada island (Greece) earthquake : Focal mechanisms of the mainshock and of the aftershock sequence". *Journal of Seismology, xxx, 1−20.*

[2] Louvari E., Kiratzi A., Papazachos B. (1999). "The Cephalonia transform fault and its extension to western Lefkada Island (Greece)". *Tectonophysics 308*, 223−236.

[3] Mylonakis G. (2004) : Personal Communication

[4] Gazetas G., (2004) : "Geotechnical aspects of the M_s 6.4 Lefkada island, Greece 2003 earthquake : preliminary assessment". *Proceedings of the Fifth International Conference on Case Histories in Geotechnical Engineering, New York.*

[5] EAK (2000): *Greek Antiseismic Code",* OASP/SPME

[6] Makdisi F.I. & Seed H.B, (1978) : "Simplified procedure for estimating dam and embankment earthquake−induced deformations". *Journal of the Geotechnical Engineering Division, ASCE, 104 (GT7), 849−867.*

[7] Seed R. B. & Whitman R. (1970) : " Design of earth retaining structures for dynamic loads", *Specialty Conference on Lateral Stresses in the Ground and Design of Earth Retaining Structures*, ASCE, 103-147.

[8] Gazetas G., Psarropoulos P., Anastasopoulos I., Gerolymos N. (2004) : "Seismic behaviour of flexible retaining systems subjected to short−duration moderately strong excitation". *Soil Dynamics and Earthquake Engineering,* 24, 537−550

[9] JSCE (1992) : *Earthquake Resistant Design for Civil Engineering Structures in Japan.* Earthquake Engineering Committee, Japan Society of Civil Engineers.

[10] OCDI (2002) : *Technical Standards and Commentaries for Part and Harbor Facilities in Japan.* Oversea Coastal Area Development Institute, Japan.

[11] PIANC (2001): *Seismic Design Guidelines for Port Structures.* International Navigation Association, A.A. Balkema Publishers, Tokyo, 324.

[12] Ebeling R.M. & Morison EE. (1992) : *"The seismic design of waterfront retaining structures",* US Army Corps of Engineers, Technical Report ITL-92-11, Washington DC.

[13] Matsuzawa H., Ishibashi I., & Kawamura M (1985) : "Dynamic soil and water pressures of submerged soils". *Journal of Geotechnical Engineering,* ASCE, 111(10), 1161−1176.

[14] Eurocode EC8 (1996) : "Structures in seismic regions, Part 5 : Foundations, retaining structures, & geotechnical aspects". *Commission of the European Communities*.

[15] Richards R.J. and Elms D. (1979) : "Seismic behavior of gravity retaining walls". *Journal of the Geotechnical Engineering Division*, ASCE, 105 (GT4), 449−464

[16] Yegian M.K., Marciano E., and Gharaman V.G (1991) : "Earthquake-induced permanent deformations : probabilistic approach." *Journal of Geotechnical Engineering, ASCE, 117(1), 35−50.*

[17] Inagaki H., Iai S., Sugano T., Yamazaki H., & Inatomi, T. (1996): "Performance of caisson type quay walls at Kobe port", *Soils and Foundations, Special Issue of Geotechnical Aspects of the January 17, 1995 Hyogoken-Nambu Earthquake*, pp. 119-136.

[18] Ghalandarzadeh A., Orita T., Towahata I., & Yun F. (1998) : "Shaking table tests on seismic deformation of gravity quay-walls", *Soils and Foundations, Special Issue on Geotechnical Aspects of the January 17, 1995 Hyogoken-Nambu Earthquake*, pp. 115−132.

[19] Iai S. (1998): "Seismic analysis and performance of retaining structures", *Geotechnical Earthquake Engineering and Soil Dynamics III,* P. Dakoulas, M. K. Yegian, R. Holtz (editors), Geotechnical Special Publication, ASCE, Vol. II(75), pp. 1020-1044.

[20] Dakoulas P. & Gazetas G. (2004): "Effective Stress Analysis of Gravity Quay Walls", *11th International Conference on Soil Dynamics & Earthquake Engineering,* San Francisco, 1, 326−333.

Liquefaction reconnaissance of the Niigata-ken Chuetsu, Japan, earthquake of October 23, 2004

Kazue Wakamatsu[1], Nozomu Yoshida[2] and Hiroyoshi Kiku[3]
[1]*Kawasaki Laboratory, Earthquake Disaster Mitigation Research Center, NIED, Kawasaki, Japan*
[2]*Department of Civil and Environmental Engineering, Tohoku-Gakuin University, Tagajyo, Japan*
[3]*Department of Civil and Environmental Engineering, Kanto-Gakuin University, Yokohama, Japan*

Abstract

The Niigata-ken-Chuetsu earthquake of October 23, 2004 caused widespread liquefaction in the alluvial plain of the Shinano River and southwestern coastal lowlands facing the Sea of Japan in Niigata Prefecture. We conducted reconnaissance investigations immediately following the earthquake, focusing on soil liquefaction and associated damage to structures. In addition to the field reconnaissance, we interpreted aerial photographs taken after the earthquake to determine the spatial extent of liquefaction. Severe liquefaction effects were observed in alluvial lowlands and artificial fills within an area approximately 30 km from the epicenter. Sand boiling was identified in several of the same areas where liquefaction occurred during the 1964 Niigata earthquake along the Shinano and Kariyata Rivers north of the epicenter and coastal plain north west of the epicenter. Liquefaction resulted in sand boiling in farmland, road cracks and subsidence, uplift of manholes, breakage of utility lines, and differential settlement of residential houses. The liquefied soils classified into four types: fluvial sands of the Shinano River and its tributaries, backfill on gravelly deposits, fill and/or backfill on soft cohesive deposits and Aeolian sand lies on coastal dune.

Keywords—*Liquefaction, 2004 Niigata-ken Chuetsu Earthquake, backfill, fill, fluvial sand, Aeolian sand*

INTRODUCTION

On October 23, 2004 at 5:56:00 PM (local time in Japan), a JMA Magnitude (M_J) 6.8 earthquake struck 80 km to the south-southwest of Niigata, on the west coast of the Honshu Island, Japan, as shown in Figure 1. The epicenter of the earthquake was located at 37.29-N, 138.87-E at a depth of 13 km [1]. The earthquake killed 48 people and seriously injured 634. 3,181 buildings were destroyed and 13,531 buildings were heavily damaged in Niigata Prefecture. 1055 buildings in Gunma Prefecture and 1 building in Fukushima Prefecture were also damaged [2]. In Niigata Prefecture, many roads, bridges, and rail lines were damaged, sewage facilities were damaged significantly, and several gas, water, and power lines were damaged. 11 fires and 3791 landslides occurred [3], and about 103,000 people had to live in emergency shelters [2]. The main earthquake was followed by a series of strong aftershocks on the same day: M_J 5.3 (17:59 PM), M_J 6.3 (18:03 PM), M_J 5.7 (18:07 PM), M_J 6.0 (18:11 PM), M_J 6.5 (18:34 PM), M_J 5.1 (18:36 PM), M_J 5.3 (18:57 PM), M_J 5.3 (19:36 PM), M_J 5.7 (19:45 PM), and M_J 4.4 (19:48 PM) [1]. The earthquake damage was concentrated within a 40 km radius of the epicenter, and caused no damage to Niigata city, 80 km to the north-northeast.

We conducted reconnaissance investigations immediately following the earthquake to assess geotechnical aspects of the event; we particularly focused on soil liquefaction and associated damage to structures. During field reconnaissance from 26 to 28 October, we quantified the severity and abundance of liquefaction from Niigata to Ojiya by car. In addition, we interpreted 205 sets of aerial photographs taken on October 24 and 28 to determine the spatial extent of liquefaction. The aerial photo interpretation allowed us to target the locations for several additional field investigations in November.

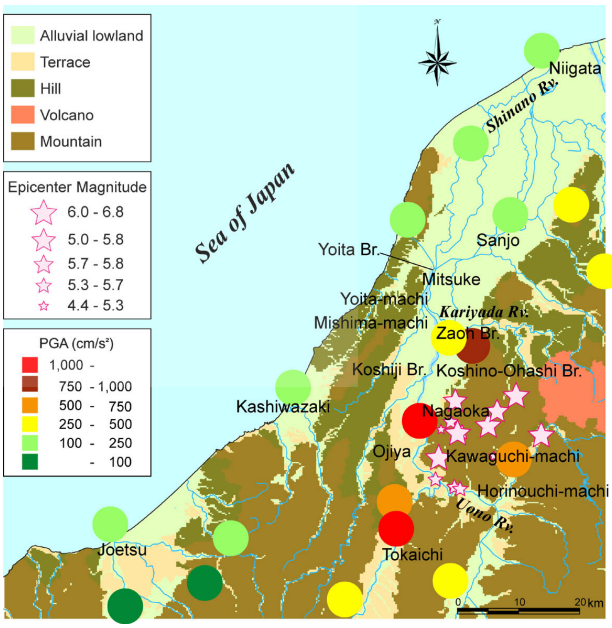

Figure 1: Geomorphologic map showing the epicenters and observed peak ground accelerations (PGA) for 2004 Niigata-ken Chuetsu earthquake

LIQUEFACTION AND ASSOCIATED DAMAGE TO STURCUTURES

The central area of Niigata Prefecture is located in the flat and low–lying alluvial plain of the Shinano River and its tributaries, including the Kariyata and Uono Rivers; these areas are commonly used as paddy fields. The Shinano River flows northward longitudinally through the center of the plain and drains into the Sea of Japan at Niigata City. Figure 2 shows locations where sand boiling and lifting of manholes were observed. Sand boiling was more frequent and severe in the northern region bordering the Shinano River than in the southern region surrounding the epicenter. Liquefaction features in these areas are discussed below.

The most distant site of the liquefaction damage is Todoroki, Tsubame City, which is located at 43 km north from the epicenter, where two residential houses were damaged by settling due to liquefaction.

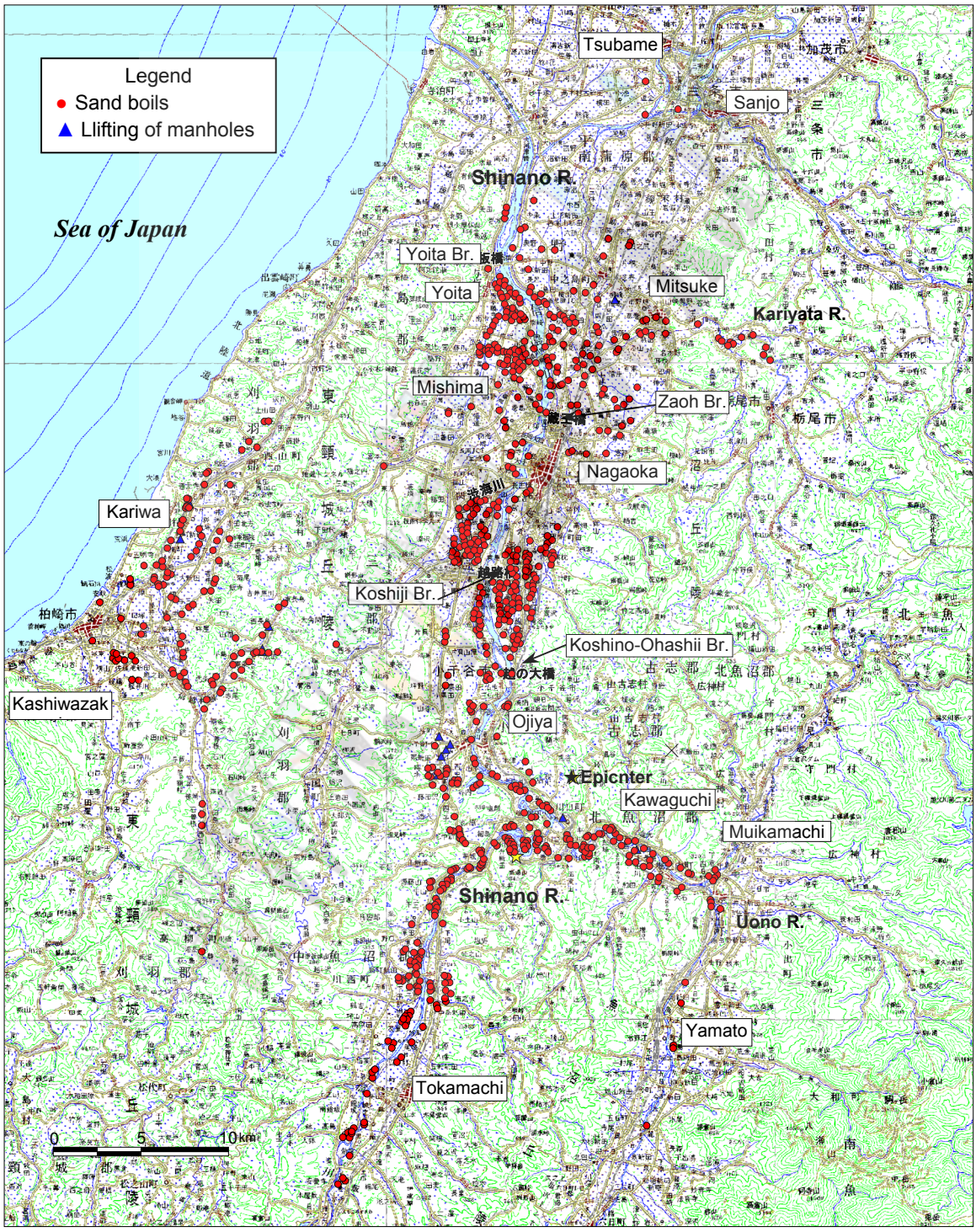

Figure 2: Distribution of sand boilings and lifting of manholes caused by the 2004 Niigata-ken-Chuetsu earthquake

Mitsuke City and its vicinity

Liquefied sites in Mitsuke and its vicinity are shown in Figure 3. In general, sand boiling was observed sporadically in this area; however, a large amount of ejecta was observed at several places as shown in Photo 1. The ejecta at the site in Photo 1 was gray and clean, indicating that native soil sand liquefied during the earthquake. At Point E in Figure 3, liquefaction was also identified during the 1964 Niigata earthquake [4].

Although most of the sand boiling points are located behind levees of the Kariyada River, some were found in downtown Mitsuke away from the river, such as at Points A and B in Figure 3. A number of residential houses were damaged due to liquefaction in the downtown. At (Point A, sand boils and ground deformation were found in the parking area of a supermarket (Photo 2). These effects were not limited to the parking area, but spread to roads and housing lots nearby. When we visited after the five months after the earthquake, the supermarket came down completely, which indicates that the building suffered structural damage.

Figure 4 shows a topographic map of the area in 1931. The map reveals that all the points of liquefaction in Mitsuke City, including Points A to C, are located on the path of the Kariyata River or at the adjoining natural levee at that time. Figure 5 shows the soil profile at Point A shown in Figure 3. The ground surface at the time of drilling (before filling) was nearly at sea level and the ground water level is as shallow as GL.-0.85 m. Beneath 0.6 m of thick cultivated soil, there is an approximately 5 m thick layer of loose silty fine sand and medium sand. This layer is presumed to be the old river channel deposits overlying a gravel layer, and seemed to easily liquefy during the earthquake.

Area between Yoita Bridge and Zaoh Bridge

Extensive evidence of liquefaction was observed in the agricultural land along the Shinano River from the Yoita Bridge to the Zaoh Bridge, which are located 30 km and 14 km from the epicenter of the main shock, respectively, as shown in Figure 2. Numerous sand boils littered the paddy fields as shown in Photos 3, but few structures were damaged because the majority of the affected areas are used for agriculture. Typical damage in this area included tilted or subsided electric poles and deformed roads as shown Photo 4.

Figure 6 shows the detailed distribution of sand boils to the south of the Yoita Bridge. The sand boils were highly concentrated on the meander belts of the old path of Shinano River, indicated by blue allows, and were sparse farther from the belts. Liquefaction effects were also observed during the 1964 Niigata earthquake [4] in most of these locations. Figure 7 shows the soil profile at Point A (Yoita High School) in Figure 6, where sand boiling was observed in the schoolyard. Loose saturated sands accumulate as thick as approximately 5 m beneath

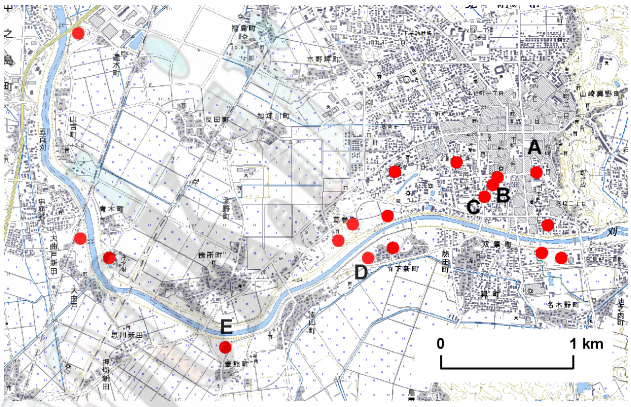

Figure 3: Locations of sand boiling observation in Mitsuke City and its vicinity

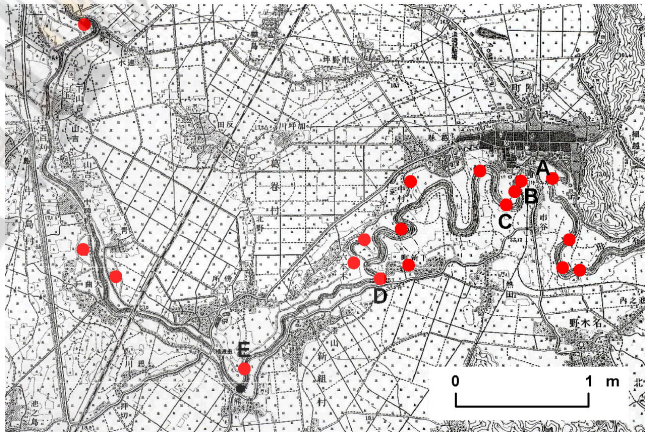

Figure 4: Topographical map of the Kariyada River in 1931

Photo 1: Sand boiling at Point D in Figure 3

Photo 2: Sand boiling at Point A in Figure 3

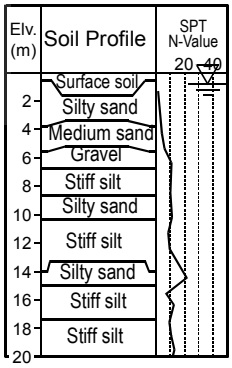

Figure 5: Soil profile and SPT *N*-value at Point A in Figure 3

Photo 3: Aerial view of paddy field after the earthquake. Many sand boils, white threads in the photo, were observed on the field.

Photo 4: Tilt of electric poles and deformation of the road were found in many places where sand boiling was observed in the nearby paddy field.

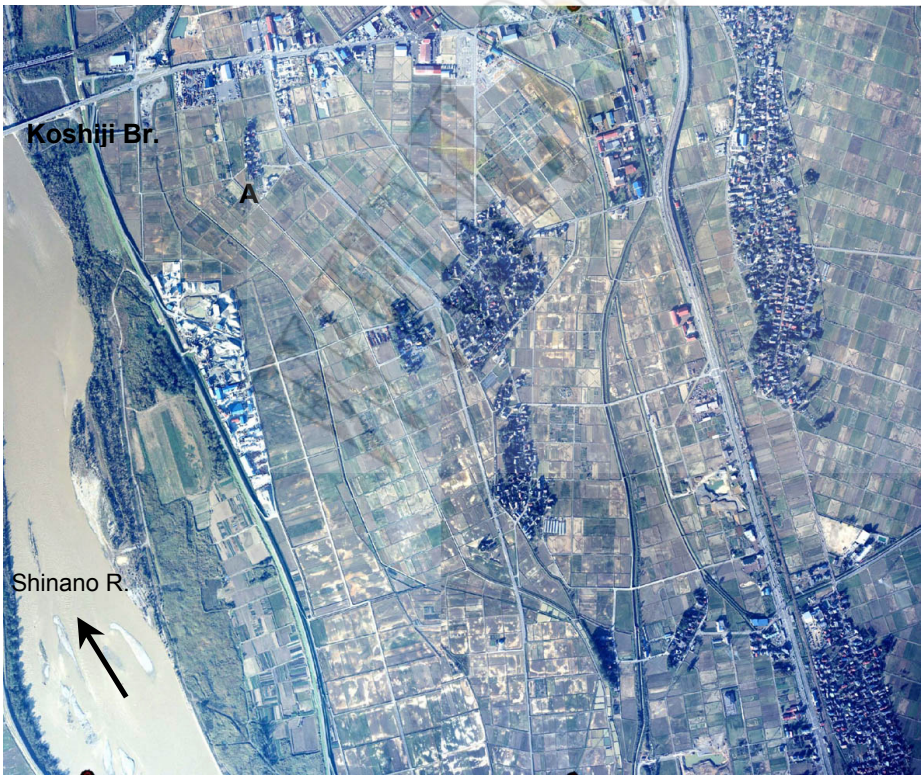

Photo 5: Sand boils in paddy fields on the right bank along the Shinano River in Nagaoka

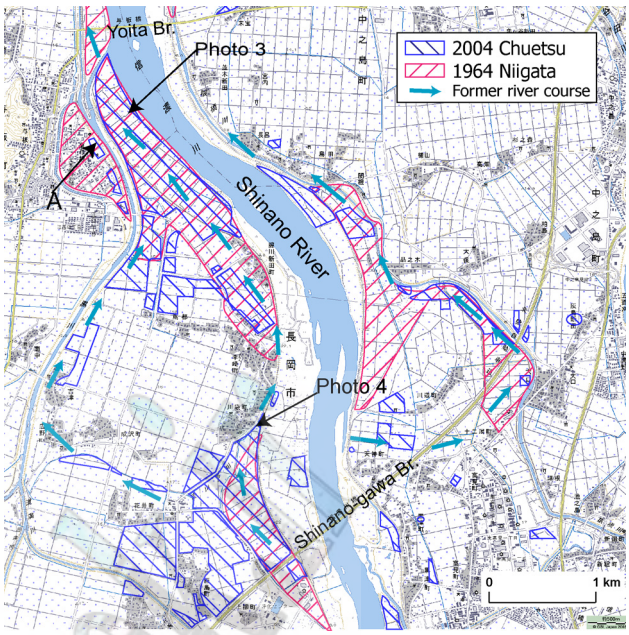

Figure 6: Areas where sand boiling was observed during the 2004 and 1964 earthquakes

the ground water level. This site also had a record of liquefaction at the time of the Niigata earthquake. The spatial distribution of liquefaction shown in Figure 6 and the soil profile of borehole data imply that the river sands liquefied in this area. This depositional condition seems to have resulted in dense and extensive sand boiling in this area even though it is located approximately 30 km away from the epicenter.

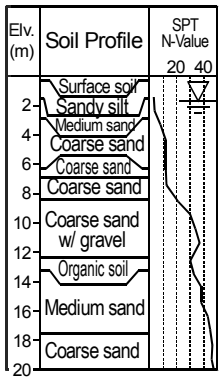

Figure 7: Soil profile and SPT *N*-value at Point A in Figure 6

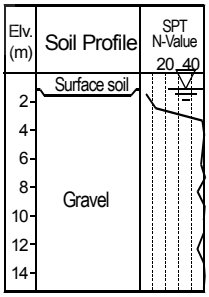

Figure 8: Soil profile and SPT *N*-value for gravelly ground in the alluvial fan

Photo 6: Gravel extraction at a paddy field

Photo7: Back-filling at the scraped site

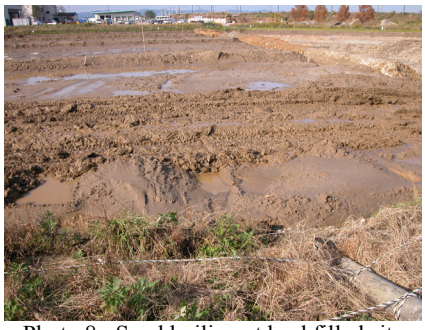

Photo 8: Sand boiling at backfilled site

Photo 9: Raised manhole and settlement of a backfill trench at west of Ojiya

Photo 10: FRP manhole that was raised out of the ground at south of Ojiya

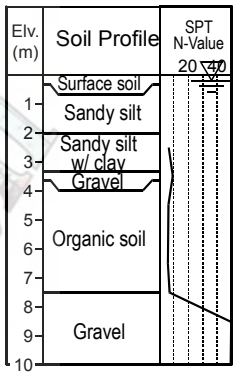

Figure 9: Soil Profile of the native ground adjacent to the raised manhole

Area between Zaoh Bridge and Koshino-Ohashi Bridge

South of the Zaoh Bridge, we expected no severe liquefaction effects because of gravelly subsurface soil conditions as shown in Figure 8. The ground water level is as high as GL-1.1 m, but the soil under the capping consists of a thick gravel layer. However, numerous sand boils were observed in the paddy fields behind the levees of the Shinano River between the Zaoh Bridge and the Koshino-Ohashi Bridge as shown in Photo 5.

We interviewed a resident at Point A of Photo 5 to determine why liquefaction occurred under these soil conditions. The resident stated that paddy fields where sand boiled severely were used to gather gravel for aggregate, whereas fields where gravel was not scraped suffered no damage or slight damage. A huge amount of water spouted from the recently scraped sites during the earthquake and these areas were still submerged a month after the quake

According to gravel extraction companies, the extraction business requires approval from the local government. Gravel shall be scraped from paddy fields for a maximum period of one and a half years. Scraping shall be done by open cut, as shown in Photo 7, to the depth ranged between 5 to 15 m. The soil extracted from the ground shall be directly loaded onto a dump truck and brought to an aggregate plant. The coarse aggregate and fine aggregate shall be selected from the soil at the plant, and the remaining soil shall be loaded onto a dump truck and returned to the original location of scraping (Photo 7). The scraped site shall be backfilled up to 1 m below the ground surface with the returned surplus soil, and pit sand shall be scattered to approximately 70 cm thickness.

Photo 11: Sand boils on point bars along the Shinano River in Kawaguchi. Circles indicate areas of sand boiling.

Finally, arable soil shall fill the remaining thickness of 30 cm, and the land shall be returned to the owner as farmland. As shown in Photo 8, sand boiling was observed in the backfilled area adjacent to the site in Photo 7 when we visited after the earthquake. The brown color of the sand ejecta was similar to the backfill of pit sand, which indicates that the backfill soil liquefied.

South of the Koshino-Ohashi Bridge

The area south of the Koshino-Ohashi Bridge is mostly hilly and mountainous. In this area, Holocene deposits that are susceptible to liquefaction are limited within the valleys of the Shinano River and its tributaries. Actually, this hilly and mountainous region suffered fewer liquefaction effects compared with areas downstream. Liquefaction effects in this area can be classified into two types: lifting of manholes in the valley floodplain, and sand boiling on paddy fields in the point bar along the meander channel.

Many uplift of manholes and settlement of backfill trenches were reported in the suburbs of Ojiya, Kawaguchi-machi and Horinouchi-machi. Significant liftings of more than 1 meter were observed at several places as shown in Photo 9. The most spectacular effect was a manhole completely raised out of the ground surface as shown in Photo 10. According to the borehole data in Figure 9, the subsurface ground consists of soft cohesive soils and organic soil, and there are no soils susceptible to liquefaction. Actually, there were no apparent signs of liquefaction in the surrounding native soils in these areas, which indicates that liquefaction of backfill material is responsible for the lifting of manholes.

The Shinano River meanders markedly upstream from Ojiya City and forms point bars along the channel. A number of sand boils were observed in paddy fields along the river as shown in Photo 11. They were located on the point bars of the current flood plain and river terraces, which are a little higher than the flood plain. River terraces are generally less susceptible to liquefaction because of the low water table. However, when we investigated the area, we often found that large amounts of ground water flow out from the hillside behind the terraces. This implies that the water level rises due to the water supply from the hills, resulting in liquefaction of sandy and/or gravelly deposits of point bar.

Coastal plain in Kashiwazaki City and Kariwa Village

We observed a number of liquefaction effects to residential houses in the coastal plain approximately 30 km from the epicenter of the earthquake. Figure 9 shows a topographic map on which the locations of liquefaction effects were plotted. Sand boils were observed, more than

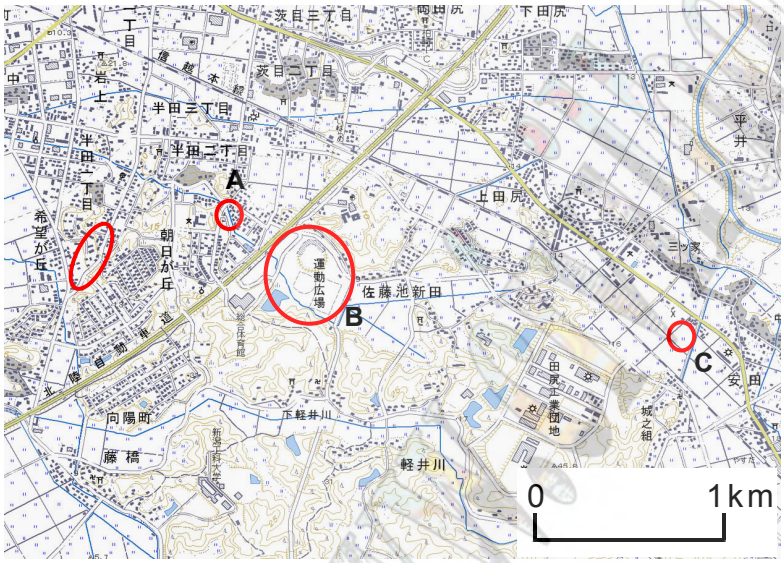

Figure 9: Locations where liquefaction effects were observed in Kashiwazaki City

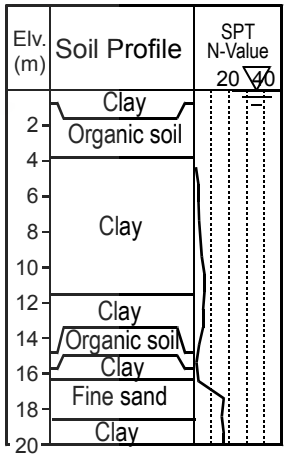

Figure 10: Soil Profile before the filling at a point between Points A and B in Figure 9

Photo 12: Residential houses suffered differential settlement at Point C in Figure 9

Photo 13: Settlement of backfill at Point B in Figure 9

twenty residential houses were damaged by settling, and water and gas pipes were damaged due to liquefaction at these points in Figure 9. Topographic maps of the area prior to 1980 showed that the damaged area used to be swampy paddy fields, including a pond, surrounded by hills. In the past quarter century, the residential area was developed by cutting the hills and filling the paddy fields with soil from the hills. When we visited the area, no large hills were found because of ground leveling.

Figure 10 shows the soil profile at a point between Points A and B in Figure 9 prior to filling. The subsurface ground consists of very soft clay and organic soils. The ground water level is close to the ground surface. According to Swedish Sounding at the damaged houses after the earthquake at Point A in Figure 9, the thickness of the fill was approximately 4 m. Although the surrounding hills had been excavated to provide fill material, the damaged areas were low spots in the neighborhood, which implies that the ground water is liable to collect from the surrounding areas into the damaged area. In other words, the water table might rise up to the fill. Indeed, the surface ground at the sites of damaged houses was damp when we visited even though it was not after rainfall. Consequently, the fill materials seemed to be liquefied during the earthquake. In the case of this area, the extremely soft cohesive soil deposits beneath the fill material amplified the ground motion, resulting in the occurrence of liquefaction.

In Kariwa village located northeast of Kashiwazaki, a number of residential houses were damaged due to liquefaction. Figure 11 shows a topographic map on which the locations of severe liquefaction effects were plotted. More than a hundred residential houses supported by spread footing were settled as shown in Photo. 14. These houses are located on gently sloping ground along base of coastal dune. The subsurface ground in the upper 6 m consists of very loose aeolian sands and the ground water level is close to the ground surface. At Kariwa railway station in Figure 11 liquefaction was also identified during the 1964 Niigata earthquake [4].

In the eastern area of coastal sand dune, liquefaction effects were also observed; settlement of houses and uplift of sewage manhole as shown in Photos 15 and 16. The damaged areas used to be swampy paddy fields. In the past fifty years, the residential lots have been developed by filling the paddy fields with dune sand. The owner of the house in Photo 15 stated that a large amount of sand and water blow out during the earthquake and the house settled and deformed severely. Similar liquefaction effects were observed in the area during the 1964 Niigata earthquake. For an example, a house next to the damaged house were damaged by settling due to liquefaction and built a new house supported by pile foundation after the 1964 earthquake. The house survived the 2004 earthquake.

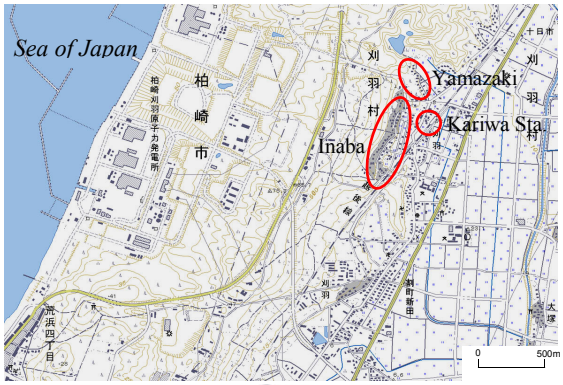

Figure 11: Locations where liquefaction effects were observed in Kariwa (Circles show Liquefied area)


Photo 14: A waiting house of Kariwa Station suffered differential settlement


Photo 15: Residential houses suffered differential settlement in Shinyashiki. Kariwa Village


Photo 16: Raised manhole and settlement of a backfill trench at Tohkaichi, Kariwa Village

CONCLUSIONS

In the Niigata-ken Chuetsu Earthquake of October 23, 2004, numerous and severe liquefaction occurred in alluvial lowlands and artificial fills within an area approximately 30 km from the epicenter, and many sand boiling events were observed, especially along the Shinano River. Sand boiling was identified in several of the same areas where liquefaction occurred during the 1964 Niigata earthquake along the Shinano and Kariyata Rivers in Yoita, Mitsuke, northern Nagaoka and Kariwa. Liquefaction resulted in sand boiling in farmland, road cracks and subsidence, raising of manholes, breakage of utility lines, and differential settlement of residential houses; however, the impact on structures was rather small considering the occurrence of liquefaction over such a wide area.

The liquefied deposits can be classified roughly as follows based on their geomorphologic and geotechnical conditions:

1) Fluvial sands of the former meander channel, natural levees, and point bars of the Shinano River and its tributaries.
2) Backfill materials at gravel scraped sites in the alluvial fan.
3) Fill and/or backfill materials lies on soft cohesive soils and organic soil in the lower swampy flood plain.
4) Aeolian sand lies on coastal dune.

ACKNOWLEDGMENTS

The authors wish to thank Mr. Toshio Ozaki, Mr Kazuhiro Okajima and Ms Yoko Miyayama who provided information about damage in Kashiwazaki and Kariwa.

REFERENCES

[1] Japan Meteorological Agency (October 24, 2005) Preliminary report on the 2004 Niigata-ken Chuetsu Earthquake. Available: http://www.seisvol.kishou.go.jp/eq/2004_10_23_niigata/index.html.(URL)

[2] Cabinet Office (July 1, 2005). On the 2004 Niigata-ken Chuetsu Earthquake, (55 ed.). Available: http://www.bousai.go.jp/saigaikinkyu/index.html

[3] Ministry of Land, Infrastructure and Transport (January 13, 2005). Follow-up report on occurrence of slope failure caused by the 2004 Niigata-ken Chuetsu Earthquake. Available: http://www.mlit.go.jp/kisha/kishi05/05/050113_.html. (URL)

[4] K. Wakamatsu, *Maps for Historic Liquefaction Sites in Japan* (Book style). Tokai University Press (in Japanese with English abstract). 1991.

Evaluating Cyclic Failure in Silts and Clays

R. W. Boulanger and I. M. Idriss
Department of Civil & Environmental Engineering, University of California, Davis, USA
e-mail: rwboulanger@ucdavis.edu & imidriss@aol.com

Abstract

New procedures are described for evaluating the potential for significant strains or strength loss in saturated silts and clays during earthquake loading. First, recently developed liquefaction susceptibility criteria are used to determine whether the cyclic loading behavior of a fine-grained soil is best evaluated using procedures modified from those for sands versus procedures appropriate for clays. The term liquefaction is used to describe the onset of significant strains or strength loss in fine-grained soils that behave more fundamentally like sands, while the term cyclic failure is used to describe similar phenomena in fine-grained soils that behave more fundamentally like clays. Analysis procedures are presented for evaluating cyclic failure potential, using a framework that is similar to that used for most semi-empirical liquefaction procedures. The new procedures are illustrated by their application to a recent case history involving areas of non-failure and failure in fine-grained soils.

Keywords—*Liquefaction, cyclic failure, silt, clay, seismic*

INTRODUCTION

Evaluating the seismic behavior of a saturated soil, from sand to clay, requires addressing the potential for significant strains or strength loss that can contribute to ground deformations or instability during or following the occurrence of an earthquake. The procedures that are best used to estimate potential strains and strength loss during earthquake loading are different for sand from those for clay, in the same way that the procedures for estimating their static shear strength and stiffness properties are different. The situation is, however, more complicated for low-plasticity silts and clays that are near the transition between "sand-like" and "clay-like" behavior. Recent experiences with ground failure in low-plasticity silts and clays during strong earthquakes have highlighted the need for an improved fundamental understanding of their seismic behavior and for related guidance on the engineering procedures that are most appropriate for evaluating their seismic behavior.

This paper provides a brief overview of the recommended liquefaction susceptibility criteria, the analysis procedures for evaluating cyclic failure potential in clay-like fine-grained soils, and an application of these criteria and procedures for a case history from the 1999 Chi-Chi earthquake in Taiwan. More detailed descriptions of these criteria, analysis procedures, and case histories are given in Boulanger and Idriss (2004).

LIQUEFACTION SUSCEPTIBILITY CRITERIA

Liquefaction susceptibility criteria for fine-grained soils started with the Chinese Criteria (Wang 1979, Seed and Idriss 1982), which used the Liquid Limit (LL), natural water content (w_c), and minus 5 μm fraction as indices of susceptibility. Andrews and Martin (2000) suggested revised criteria based on LL and minus 2 μm fraction, while Seed et al. (2003) and Bray et al. (2004a,b) suggested criteria based on Plasticity Index (PI), LL, and w_c. The criteria by Bray et al. (2004b), for example, are that fine-grained soils with PI≤12 and w_c>0.85LL are susceptible to liquefaction, while soils with 12<PI<20 and w_c>0.8LL are "systematically more resistant to liquefaction but still susceptible to cyclic mobility." The criteria by Seed et al. (2003) are similar to Bray et al.'s, but with slightly different w_c/LL limits and additional constraints on the LL.

Existing liquefaction susceptibility criteria for fine-grained soils have been developed, at least implicitly, by trying to answer the question, "what types of silts and clays are susceptible to liquefaction?" The approach taken to answering this question has been primarily empirical, whereby sites where "liquefaction" has occurred are characterized, samples are obtained from critical strata, and index test-based criteria are developed to envelope the types of soils observed to have "liquefied" in past earthquakes. The resulting guidelines are dependent on the theoretical framework that is used to interpret and organize the case history experiences, with an adequate theoretical framework being important for minimizing the uncertainty in the conditions for which the empirical guidelines are applicable. Development of liquefaction susceptibility guidelines for silts and clays are, however, complicated by difficulties in defining the meaning of liquefaction and by the fact that observations from the ground surface at damaged sites provide little insight into the soil mechanics behavior of the problem soils, other than the fact that they have developed significant strains and excess pore water pressures. Some investigators have used the results of cyclic laboratory tests to guide the

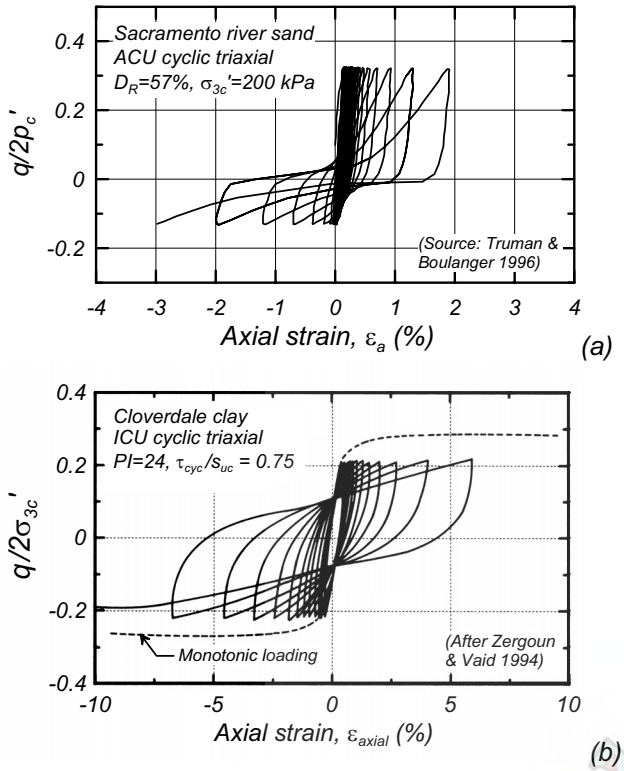

Fig. 1: Undrained cyclic loading response of (a) Sacramento river sand and (b) Cloverdale clay

development of liquefaction susceptibility criteria (e.g., Bray et al. 2004b), but the difficulty remains in defining what types of cyclic loading responses should be called "liquefaction." This quandary is illustrated by the cyclic test results for a clean sand specimen in Fig. 1(a) and a clay sample in Fig. 1(b), wherein both soils develop high excess pore pressures and significant shear strains during cyclic loading. The clay sample reached an excess pore pressure ratio (r_u) of only about 80% and dissipated more hysteretic energy than the sand, but it still developed large shear strains, which could certainly be manifested as ground deformations in a field situation.

An alternative approach to developing liquefaction susceptibility criteria is to ask the question: "what is the best way to estimate the potential for strength loss and large strains in different types of fine-grained soils?" In answering this question, Boulanger and Idriss (2004, 2005) reviewed experimental findings in the literature, and concluded that fine-grained soils can be grouped into soils that behave more fundamentally like sands in monotonic and cyclic undrained loading, and soils that behave more fundamentally like clays. Consequently, the question can be restated as: "what types of fine-grained soils are best evaluated using procedures modified from those for sands, versus procedures that are appropriate for clays?" In this regard, a key aspect is that monotonic and cyclic shear strengths of clay exhibit a relatively unique dependence on consolidation stress and consolidation stress history, while the strengths of sands do not. These differences are widely recognized and accounted for in the ways that the static shear strengths of sands and clays

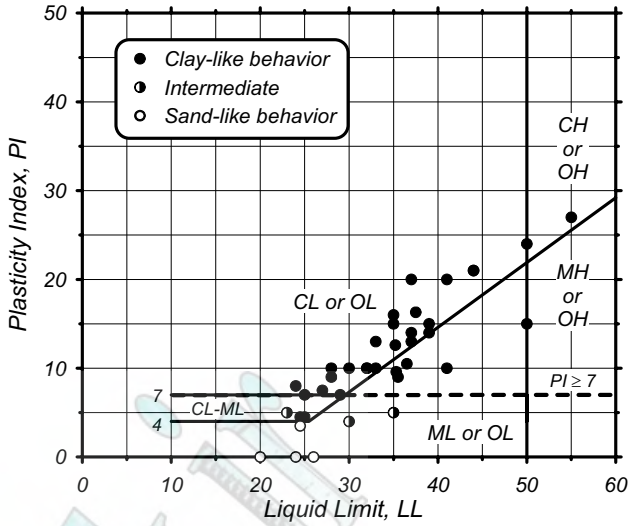

Fig. 2: Atterberg limits chart showing representative values for soils exhibiting clay-like, sand-like, and intermediate stress-strain behaviors

are estimated. Consequently, experimental results for silts and clays from the literature were compiled onto the plasticity chart in Fig. 2, with each soil categorized as either exhibiting sand-like, clay-like, or intermediate behavior in monotonic and cyclic undrained loading.

Fine-grained soils that exhibited clay-like behavior included ML soils with PI values as low as 9 and CL-ML soils with PI values as low as 4. Intermediate behavior was observed for samples classifying as CL-ML and ML with PI values of 4 to 5. Sand-like behavior was observed only for ML soils (below the A-line).

The actual soil behavior would undoubtedly show a smooth transition between sand-like and clay-like soil behavior across a range of Atterberg Limits. This transition appears to occur between PI values of 3 to 8, with the transition being at lower PI values for CL-ML soils and at higher PI values for ML soils. In the absence of detailed in situ or laboratory testing that shows otherwise, it is recommended that fine-grained soils be considered to have clay-like behavior if they have PI≥7, and sand-like behavior if they have PI<7. This criterion provides a slightly conservative interpretation of the likely transition interval. If a soil plots as CL-ML, the PI criterion may be reduced by 1 or 2 points and still be consistent with the data. For soils whose Atterberg Limits plot significantly away from the data points in Fig. 2 (e.g., an unusual combination of high LL and low PI), it would be prudent to perform an appropriate program of in situ and laboratory testing to evaluate the soil's behavior.

The recommended criteria do not use any gradational or water content indices, as used in many other liquefaction susceptibility criteria. The percentage of clay-sized minerals does not correlate very well with engineering properties, which is consistent with the observations by Bray et al. (2004a,b). The water content (w_c) relative to the Atterberg Limit values, whether expressed as w_c/LL or as a liquidity index (LI = (w_c-PL)/(LL-PL), provides useful information for

evaluating the potential consequences of cyclic failure in clays and in silts that exhibit clay-like behavior. High w_c/LL or high LI values are indicative of more sensitive soils, where sensitivity is the ratio of the peak undrained shear strength (s_u) to the fully remolded (residual) undrained shear strength (s_{ur}). The w_c/LL or LI values are not, however, appropriate indices for determining whether a fine-grained soil will exhibit clay-like versus sand-like behavior.

In summary, it is recommended that fine-grained soils exhibiting sand-like behavior be evaluated using SPT- and CPT-based methodologies and that the term "liquefaction" be reserved for these types of soils. Conversely, it is recommended that soils exhibiting clay-like behavior be evaluated using procedures appropriate for clays, and that the term "cyclic failure" be used to describe failure in these types of soils. Fine-grained soils contain more than 50% fines (i.e., passing the #200 sieve), but these criteria may reasonably be extended to soils with lower fines fractions whenever the fines constitute the load carrying skeleton of the soil, which generally corresponds to fines fractions exceeding about 35% to 40% (e.g., see Mitchell 1976).

PROCEDURES FOR EVALUATING CYCLIC FAILURE POTENTIAL OF CLAY-LIKE FINE-GRAINED SOILS

Procedures for evaluating the cyclic failure potential of clay-like fine-grained soils were developed using a framework similar to that used in most semi-empirical liquefaction procedures. The advantage of using a similar framework is the ability to directly compare cyclic strengths for sand-like and clay-like fine-grained soils within the same soil profiles.

The Seed-Idriss simplified procedure is used to estimate the in situ cyclic stresses that are induced by vertically propagating shear waves through level sites during earthquake shaking. The cyclic stress ratio (CSR) induced by an earthquake of magnitude M is computed as:

$$CSR_M = 0.65 \cdot a_{max} \frac{\sigma_{vc}}{\sigma'_{vc}} r_d \qquad (1)$$

Where a_{max} is the peak ground surface horizontal acceleration (in g's), σ_{vc} is the total vertical stress, σ_{vc}' is the effective vertical consolidation stress, and r_d is a stress reduction factor that accounts for flexibility of the soil column. The factor of 0.65 is used to produce a CSR that is representative of the most significant cycles over the full duration of shaking.

The undrained cyclic shear resistance of clay-like soils can be normalized by their corresponding undrained shear strengths (s_u), as illustrated by the direct simple shear test data for four natural fine-grained soils in Fig. 3. These and other results were compiled by Boulanger and Idriss (2004) and adjusted to a cyclic loading rate of 1 Hz. The compiled data set showed that the cyclic stress ratios (τ_{cyc}/s_u) to cause cyclic failure (onset of rapidly increasing strains, which initiates at about 3% shear strain) in a specified number of uniform loading cycles fell within a reasonably narrow range of values for a broad range of

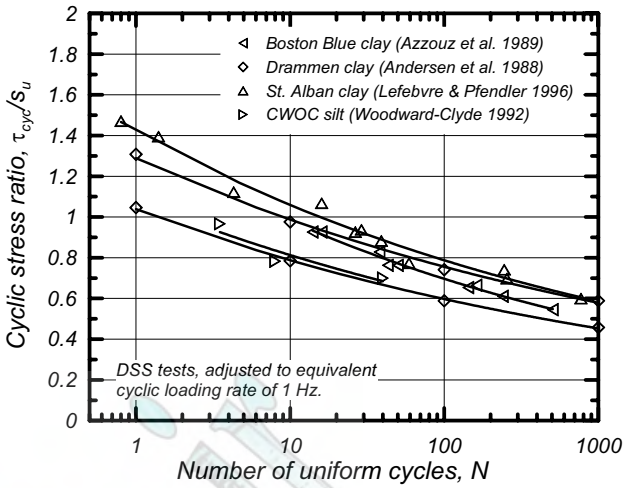

Fig. 3: Cyclic resistance ratios versus number of uniform loading cycles to failure (3% shear strain) for four clay soils in direct simple shear tests

fine-grained soils that exhibited clay-like behavior.

Specifying a cyclic resistance ratio (CRR) for clay requires determining the equivalent number of uniform loading cycles (N) that would be associated with a given earthquake magnitude (M). A correlation was developed between N and M based on a large set of recorded motions using the procedures outlined in Seed et al. (1975). The CRR-N relations for clays were approximately fit with a power relation, and the exponent on that relation (which is the slope on a log(CRR) versus log(N) plot) controls the conversion of irregular time series to equivalent uniform time series. The slope of this relation is flatter for clays than for sands, such that the same earthquake time series will convert to different numbers of uniform loading cycles for clay than for sand. The flatter slope for clay produced approximately 30 equivalent uniform cycles [at 65% of the peak stress, per equation (1)] for M=7.5 earthquakes, as opposed to about ½ that number of cycles for sands. The cyclic strength of clays was subsequently estimated, based on the above value for N and the range of experimental data compiled in Boulanger and Idriss (2004), as:

$$\left(\frac{\tau_{cyc}}{s_u}\right)_{M=7.5} = 0.83 \qquad (2)$$

A magnitude scaling factor (MSF) for clay soils was then derived that accounts for the dependence of the cyclic resistance ratio (CRR) on the number of equivalent uniform loading cycles, which is correlated to earthquake magnitude. The definition of MSF is:

$$MSF = \frac{CRR_M}{CRR_{M=7.5}} \qquad (3)$$

and its derivation only requires estimating cyclic resistance ratios for different earthquake magnitudes. Boulanger and Idriss (2004) performed this conversion for typical clay properties and a large set of ground motions, and derived the MSF relation in Fig. 4. The MSF relation for clay is flatter than for sand, which reflects the fact that the CRR-N relation is flatter for clay than for sand.

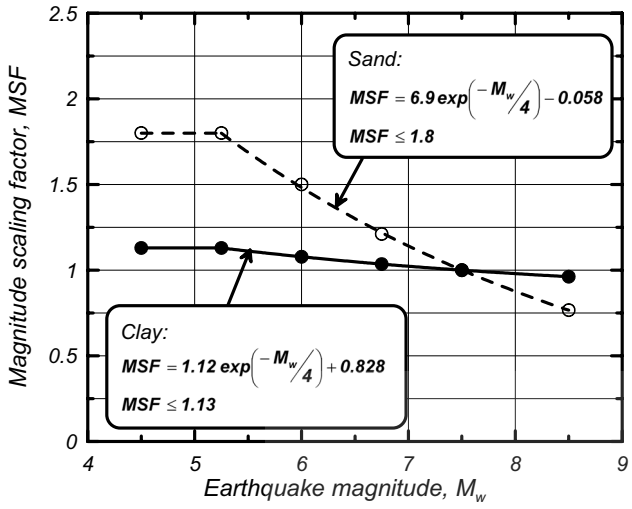

Fig. 4: Magnitude scaling factors for sand and clay

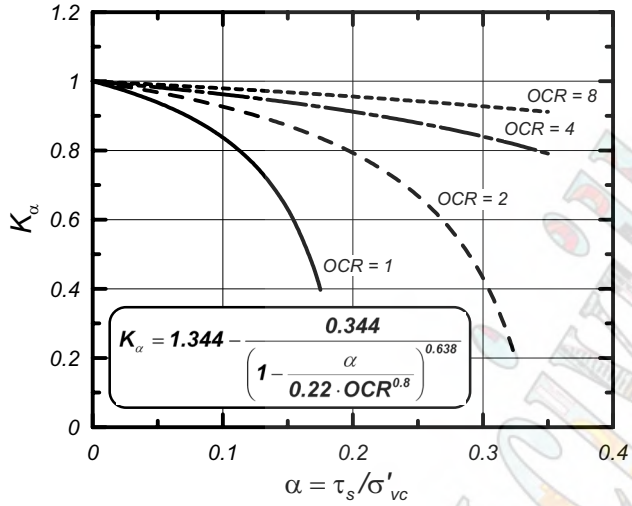

Fig. 5: K_α correction factor for effect of initial static shear stress ratio on CRR of clay

The effect of static shear stresses on clay CRR was accounted for by introducing a K_α factor, as introduced by Seed (1983) for liquefaction problems. The K_α relation for clay soils was derived based on experimental results for clays presented in Goulois et al. (1985), Andersen et al. (1988), and Lefebvre and Pfendler (1996). The resulting correlation, as shown in Fig. 5, illustrates how static shear stresses (τ_s) are particularly detrimental in normally consolidated clays and decrease in their importance with increasing overconsolidation ratio.

The cyclic shear resistance of clay can now be normalized by the vertical effective consolidation stress to arrive at a $CRR_{M=7.5}$ value:

$$CRR_{M=7.5} = C_{2D} \cdot \left(\frac{\tau_{cyc}}{s_u}\right)_{M=7.5} \cdot \frac{s_u}{\sigma'_{vc}} \cdot K_\alpha \qquad (4)$$

The parameter C_{2D} accounts for the effects of two-dimensional shaking, and was estimated to be about 0.96. Substituting the empirical value for $(\tau_{cyc}/s_u)_{M=7.5}$ gives:

$$CRR_{M=7.5} = 0.96 \cdot 0.83 \cdot \frac{s_u}{\sigma'_{vc}} \cdot K_\alpha \qquad (5)$$

$$CRR_{M=7.5} = 0.8 \cdot \frac{s_u}{\sigma'_{vc}} \cdot K_\alpha \qquad (6)$$

The MSF can now be implemented by either adjusting the cyclic resistance ratio to the design earthquake magnitude:

$$CRR_M = 0.8 \cdot \frac{s_u}{\sigma'_{vc}} \cdot K_\alpha \cdot MSF \qquad (7)$$

or adjusting the earthquake-induced cyclic stress ratio to the equivalent value for a M=7.5 earthquake:

$$CSR_{M=7.5} = 0.65 \cdot a_{max} \frac{\sigma_{vc}}{\sigma'_{vc}} r_d \cdot \frac{1}{MSF} \qquad (8)$$

The factor of safety against cyclic failure is then computed as the ratio of resistance to demand at the same reference value for the earthquake magnitude, using either:

$$F = \frac{(CRR)_M}{(CSR)_M} \qquad (9)$$

or the algebraically-equivalent expression:

$$F = \frac{(CRR)_{M=7.5}}{(CSR)_{M=7.5}} \qquad (10)$$

The derived CRR relations for clay emphasize the fact that its cyclic behavior can be directly related to its static undrained shear strength. Consequently, the CRR of clay may be evaluated using one of three approaches:

- Approach A: Measure CRR by cyclic laboratory testing.
- Approach B: Measure s_u by in situ or laboratory testing and then multiply s_u by an empirical factor to get CRR.
- Approach C: Empirically estimate CRR and/or s_u based on the consolidation stress history profile.

Guidance on each of these approaches is given in Boulanger and Idriss (2004). The direct measurement of s_u in Approach B provides increased confidence in the estimated CRR, compared to the simplest Approach C, while the direct measurement of CRR in Approach A provides the highest level of insight and confidence. These different approaches provide the opportunity to evaluate a site with progressively increasing levels of confidence, while considering the potential benefits that additional information may provide given the uncertainties in the current level of analysis.

The consequences of triggering cyclic failure, which corresponds to the onset of shear strains exceeding about 3%, then depend on the sensitivity of the clay, which can be correlated to its Liquidity Index or directly measured. The consequences can range from dramatic strength losses at high LI values (e.g., very sensitive or quick soils), to relatively minor strength losses at low LI values (e.g., compacted clays). This is analogous to recognizing that the consequences of triggering liquefaction in sands can range from large deformations for loose sands, to relatively minor deformations for dense sands.

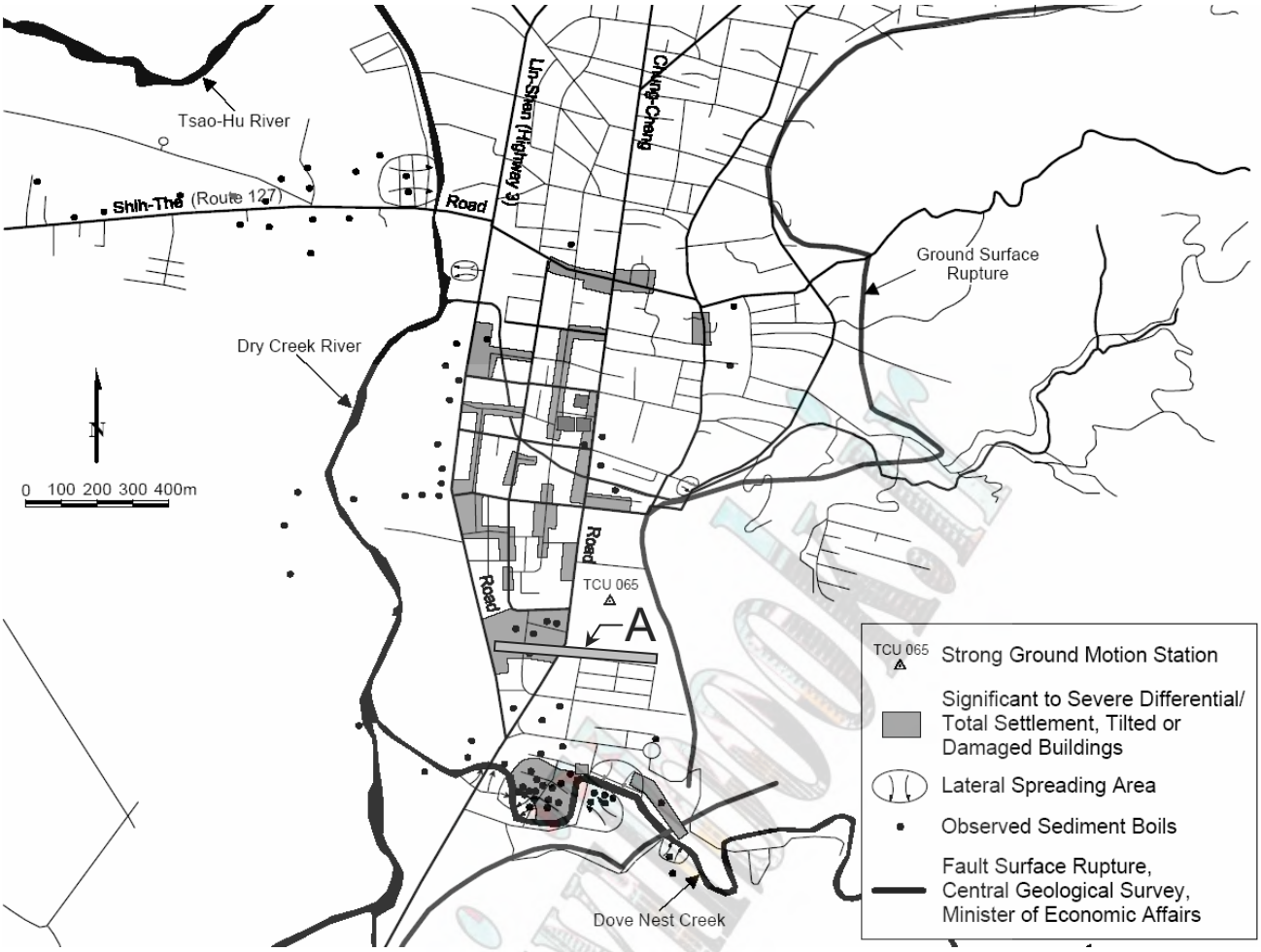

Fig. 6: Map of Wufeng showing locations of Site A, ground failure, and TCU065 station (Stewart and Chu 2002)

CASE HISTORY

Recent experiences in Wufeng, Taiwan, provide an excellent opportunity to evaluate the proposed procedure's abilities to differentiate between observations of ground failure and no ground failure around buildings founded over a deposit containing thick layers of fine-grained soils. Chu et al. (2003, 2004) and Stewart et al. (2003, 2004) characterized several sites in detail and documented their findings and data for public distribution. Boulanger and Idriss (2004) subsequently used data from four specific building locations within Site A (Fig. 6) to evaluate the proposed procedures. The pattern of observations was that the taller buildings (5- and 6-story) tended to experience significant settlements or foundation failures, while there tended to be little or no ground failure in the free field or beneath 1-story buildings. Analysis results for the tallest and shortest buildings are presented herein to illustrate the overall findings.

- Boring WAS-3 and CPT sounding WAC-8 were at the location of a 6-story building that experienced foundation failure and significant settlement, along with structural damage, as shown in Figs. 7a and 7b. Note that the ground surface away from the buildings showed relatively little evidence of ground failure.
- Boring WAS-1 and CPT sounding WAC-2 were in an area of 1-story buildings that showed no evidence of building settlements or ground failure away from the buildings, as shown in Fig. 7c.

A strong ground motion instrument located within 1 km north of Site A recorded peak ground surface accelerations of 0.814g E-W and 0.603g N-S during the 1999 Chi-Chi earthquake. The geometric mean for these two components is 0.70g, which is the value used in the subsequent analyses of potential ground failure at Site A.

The soil profiles at Site A generally consisted of 1 to 2 m of fill overlying 4 to 7 m of firm to stiff, fine-grained CL, ML, and CL-ML soils. The fine-grained soils are underlain by primarily medium-dense and dense silty sands with inter-layers of stiff to very stiff silts and clays, extending to depths of 15 m or more (approximate limit of exploration at most locations). The water table depth ranged from 0.5 to 1.1 m. Soil profiles for two of the building locations are presented in Figs. 8 and 9.

The characteristics of the 4- to 7-m thick layer of firm to stiff clay-like soils (CL, ML, and CL-ML) that is present at the four exploration locations are of primary importance to the analyses of these sites. In evaluating these characteristics, the information from the four exploration locations can be considered together because

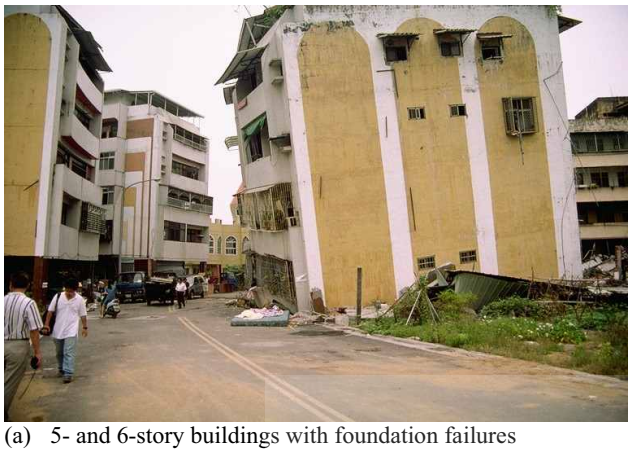

(a) 5- and 6-story buildings with foundation failures (photograph by R. B. Seed)

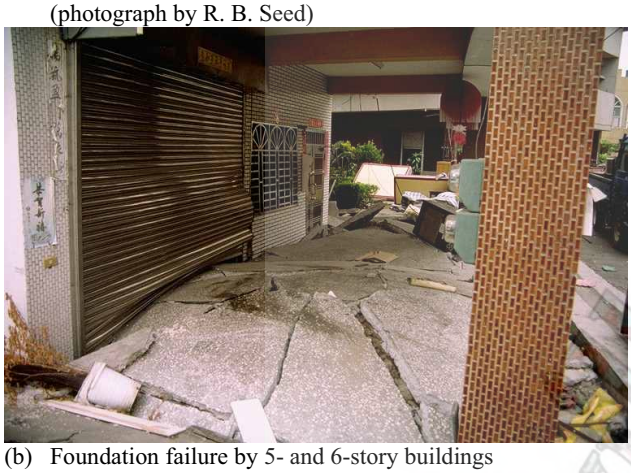

(b) Foundation failure by 5- and 6-story buildings (photograph by R. B. Seed)

(c) 1-story buildings without evident ground failure or building settlement

Fig. 7: Photographs of buildings at Site A in Wufeng (peer.berkeley.edu/lifelines/research_projects/3A02/)

it is a common geologic stratum that does not appear to vary substantially across these locations based on comparisons of the CPT and borehole data. The PI values obtained from 20 samples in this stratum are plotted in Fig. 10; slightly less than half of the samples would classify as sand-like based on a PI < 7, while slightly greater than half would classify as clay-like. However, 5 samples classified as CL-ML with PI values of 5 or 6, for which a slightly lower criterion would be equally

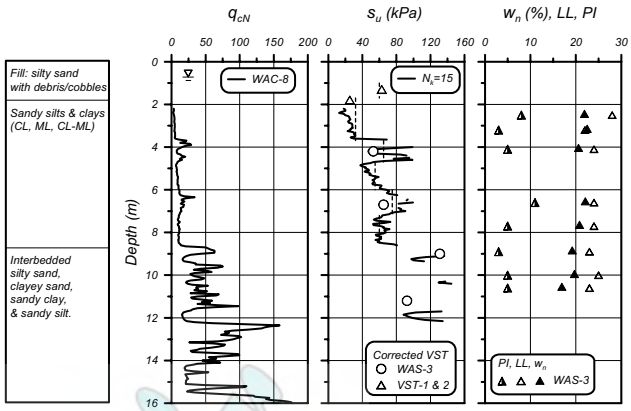

Fig. 8: Boring, CPT, and VST data at 6-story building (source peer.berkeley.edu/lifelines/research_projects/3A02/)

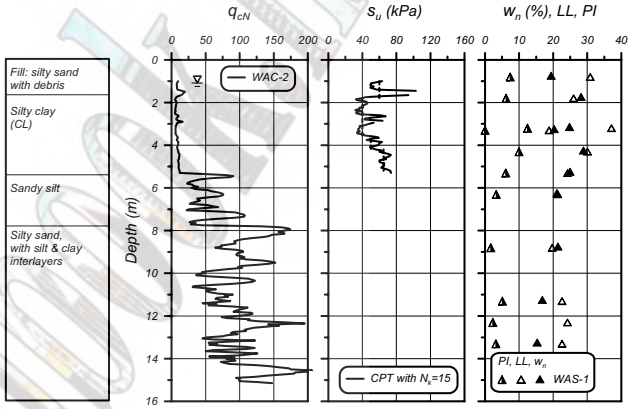

Fig. 9: Boring and CPT data near 1-story buildings (source peer.berkeley.edu/lifelines/research_projects/3A02/)

consistent with the empirical data in Fig. 2. If the CL-ML samples are considered as clay-like, then only 20% of the 20 samples would classify as sand-like while 80% would classify as clay-like. In addition, occasional thin lenses of sands appear to be present within this stratum based on the CPT soundings.

The s_u values measured by vane shear tests (VST) in the firm to stiff clay-like soil stratum ranged from 35 to 64 kPa (average of 48 kPa), and generally increased with depth. Sensitivities from the VST ranged from 1.2 to 3.1, with an average of about 2, making this a slightly sensitive to medium sensitivity soil. CPT tip resistances provided comparable s_u values throughout the majority of the stratum (excluding what appear to be sand lenses), based on a calibrated cone bearing factor of N_k=15. The dashed lines in Figs. 8 and 9 represent the s_u values chosen for subsequent analyses of cyclic failure potential.

The sand-like portions of this stratum would be expected to liquefy based on established liquefaction analyses because these soils have low penetration resistances and the levels of shaking are very high. The consequences of these sand-like portions having liquefied depend on their extent and spatial distribution within the stratum. Consider the following two possibilities.

If almost half of the stratum is considered sand-like (based on the PI < 7 criterion), then liquefaction of the

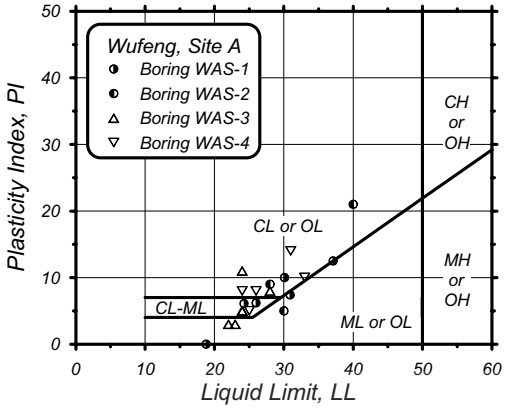

Fig. 10: Atterberg limits for upper strata of silts and clays

sand-like soils would be expected to result in ground failure throughout the area, which is not consistent with the general trend of greater damage beneath buildings while the free-field areas showed no or relatively little ground failure. Consequently, this possibility is not pursued further.

If only 20% of the stratum is considered sand-like (i.e., the CL-ML soils with PI values of 5 or 6 behave as clay-like), then liquefaction of these portions may have contributed to the observed ground failure patterns and to any observed soil boils, but it is most likely that the overall pattern of damage was controlled by the clay-like sediments within this strata. This possibility (i.e., 80% of the stratum is clay-like) is more likely based on the additional insight provided by the CPT and VST results, and provides an opportunity to evaluate the analysis procedures recommended herein. Consequently, the following analyses will focus on the potential for cyclic failure of the clay-like soil portions of the stratum and on whether the computed factors of safety are consistent with observed damage patterns throughout Site A.

Analysis results for the cyclic failure potential of the clay-like soils at these two building locations are presented in Figs. 11 and 12. Results are only presented for the clay-like soils because the underlying inter-layered dense silty sands are not expected to have been the primary cause of the observed patterns of ground failure, even if they developed high excess pore water pressures, because they are dense enough to develop only limited strains and deep enough that the overlying clay-like soils likely played a dominant role. The induced CSR was computed for a peak ground surface acceleration of 0.70 g and using the r_d relation by Idriss (1999). The CRR and factor of safety against cyclic failure are computed for both the free-field conditions and beneath the buildings. For the 6-story building, this includes analyses for the spread footings under the front columns and for the mat foundation over the rear portion of the building. The presence of the buildings was accounted for in the computation of vertical stresses, horizontal shear stresses (from the building base shear), and the presence of monotonic shear (bearing) stresses (Boulanger and Idriss 2004).

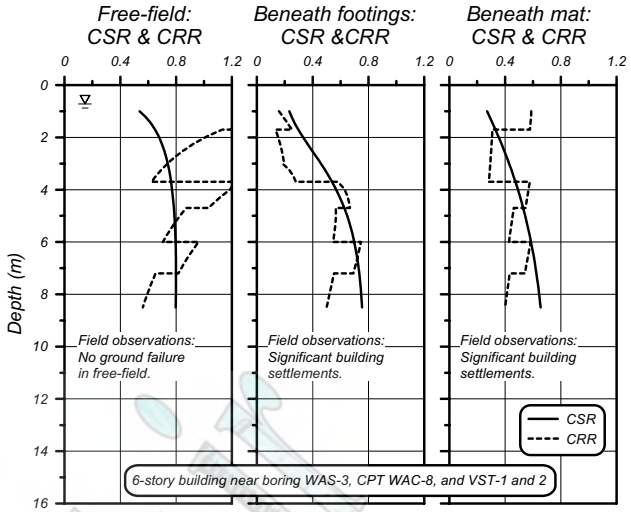

Fig. 11: Comparison of CSR and CRR for clay-like soils in the free-field and beneath the 6-story building

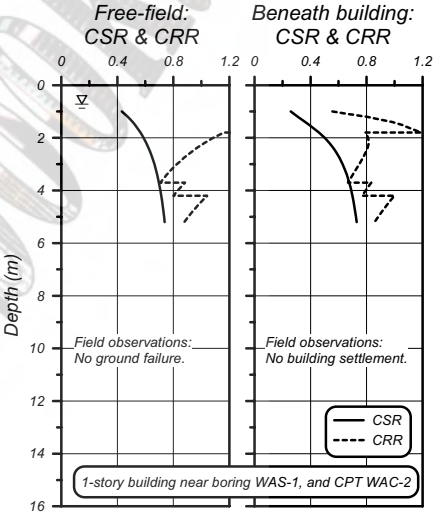

Fig. 12: Comparison of CSR and CRR for clay-like soils in the free-field and beneath the 1-story building

For the 6-story building (Fig. 11), the factors of safety against cyclic failure beneath the column spread footings were less than 1.0 throughout most of the clay-like stratum (depths of 1.0 to 8.2 m), which are consistent with the observed bearing failures (e.g., photos in Figs. 7a and 7b). The factors of safety beneath the mat portion were slightly greater but still predict cyclic failure throughout much of the clay-like stratum, which is again consistent with the observed foundation settlements. For the free-field, the factors of safety are substantially larger and cyclic failure is only predicted within thin intervals at depths of 3.5, 6, and 8 m. Cyclic failure in thin zones in the free field would not be expected to cause significant ground distress because the site is relatively flat and the soils are only slightly sensitive. Thus, the free-field analysis results are consistent with the field observations of relatively little ground distress away from the influence of the building.

For the 1-story buildings near boring WAS-1, the analysis results in Fig. 12 show that cyclic failure would

not be expected at any depth in either the free-field or beneath the buildings. These results are in good agreement with the observed absence of ground distress or building settlements in this area (e.g., photo in Fig. 7c).

Spatial heterogeneity in the undrained shear strengths of the clay-like soil layer in the depth range of about 1 to 8 m, is an important consideration when evaluating the results of the above analyses. For example, the undrained shear strengths between depths of 2 and 3 m (an important depth interval for support of the shallow foundations) were about 40, 60, 32, and 38 kPa near borings WAS-1, 2, 3, and 4, respectively, which represents a factor of about 2 between the strongest and weakest values. The undrained shear strengths at other depths within this clay-like soil layer varied, from strongest to weakest, by factors of about 1.3 to 1.9. In this regard, it is important to recognize that the soil explorations (borings, CPT soundings, and vane shear tests) were not necessarily fully representative of the conditions across the footprint of the buildings being analyzed. Thus, the actual undrained shear strengths at each of the four building locations could reasonably vary from the values estimated herein, with only small variations being necessary to increase or decrease computed factors of safety above or below unity. Recognizing this inherent limitation, it is concluded that the computed potential for cyclic failure of the clay-like soils at these four buildings are entirely consistent with the general pattern of field observations showing significant settlements for the tallest buildings and the absence of deformations in the free-field or beneath 1-story buildings.

The role of the buildings on the computed potential for cyclic failure in the clay-like soil layer has several important components.

- The static load from a building produces static shear stresses that reduce the underlying clay-like soil's CRR, as represented through the K_α value.
- The horizontal inertia of a building increases the cyclic horizontal shear stresses (or CSR) in the underlying soil.
- The horizontal inertia of a building also produces cyclic loads on its foundation elements (vertical, horizontal, and overturning loads) that further increase the potential for cyclic failure in the underlying soils.
- Each of these effects decreases with depth below the building because the stresses from the building become smaller (relative to those from the soil alone) with increasing depth.

Another important factor is that cyclic failure of soils beneath a building will be accompanied by the accumulation of biased strains and deformations under the building's static weight. Without a building or with a very light building, cyclic failure of clay-like soils over limited depths in a level-ground area may not necessarily be accompanied by the accumulation of permanent displacements and therefore the ground surface may not exhibit any signs of deformation or damage.

The observed consequences of cyclic failure in the clay-like soils also appear to be consistent with the available data on their sensitivity. The VST measurements produced S_t values of 1.2 to 3, which suggest that their fully remolded strengths would still be on the order of ½ their pre-earthquake values. This range of values would appear consistent with the observations of buildings in this level-ground area having settled various amounts, but not having developed dramatic bearing failures (such as might be expected if the soils had been highly sensitive or quick).

The analysis results for Site A show that the recommended procedures are able to distinguish between conditions leading to ground failure or building settlements and conditions where ground failure did not occur. The analyses could be better refined with more information about the building loads and configurations, and the development of improved methods for representing the effects of buildings on the cyclic failure potential of underlying soils. While such improvements are needed, the main conclusions presented herein are unlikely to be affected.

In contrast, the liquefaction susceptibility criteria of Bray et al. (2004b) and Seed et al. (2003) would have classified 56% and 64%, respectively, of the silt and clay samples between depths of 1 and 8 m as "liquefiable." The w_c/LL ratio is a key factor in applying these criteria because 92% of the samples would have classified as liquefiable based on their Atterberg Limits alone (e.g., compare Fig. 10 with Bray et al.'s PI ≤ 12 criteria). A subsequent liquefaction analysis of the susceptible silts and clays using an SPT- or CPT-based liquefaction correlation would predict widespread ground failure beneath the buildings and in the free-field, and thus could not have distinguished between the areas of good and poor performance.

CONCLUSIONS

New criteria were presented for distinguishing between fine-grained soils that will exhibit sand-like versus clay-like behavior during the undrained cyclic loading imposed by earthquakes (Boulanger and Idriss 2004, 2005). For practical purposes, clay-like behavior can be expected for fine-grained soils that have a PI ≥ 7, although a slightly lower transition point for CL-ML soils (perhaps PI ≥ 5 or 6) would be equally consistent with the available data summarized in Fig. 2. The transition between sand-like and clay-like behavior may be adjusted on a site-specific basis if justified by results of in situ and laboratory testing.

The potential for liquefaction of fine-grained soils that exhibit sand-like behavior can be evaluated using SPT- and CPT-based correlations for cohesionless soils (e.g., Idriss and Boulanger 2004).

The potential for cyclic failure of clay-like soils can be evaluated using the procedures presented in Boulanger and Idriss (2004), which relate the soil's cyclic strength to its monotonic undrained shear strength.

The recommended criteria and analysis procedures were used to analyze Wufeng Site A during the 1999 Chi-Chi earthquake, using the site investigation data by Chu et al. (2003, 2004) and Stewart et al. (2003, 2004). Analyses that focused on the potential for cyclic failure in the upper 4- to 7-m thick layer of clay-like soil (CL, CL-ML, ML) layers provided a reasonable means for explaining the occurrence of ground failure beneath the five- and six-story buildings and the general absence of ground failure in the free-field or beneath one-story buildings.

While a number of issues remain to be addressed, it is nonetheless hoped that the new liquefaction susceptibility criteria and cyclic failure analysis procedures will prove useful in engineering practice for assessing potential ground failure hazards in silts and clays during earthquakes, and provide a framework for future developments and refinements in this area.

ACKNOWLEDGMENTS

Professor Jonathon P. Stewart and Dr. Daniel Chu provided the data for Wufeng Site A. Their assistance and valuable discussions are greatly appreciated.

REFERENCES

[1] Andersen, K, Kleven, A., and Heien, D. (1988). "Cyclic soil data for design of gravity structures," *Journal of the Geotechnical Engineering Div.*, ASCE, 114(5): 517-539.

[2] Andrews, D. C. A., and Martin, G. R. (2000). "Criteria for liquefaction of silty soils." Proc. 12th World Conference on Earthquake Engineering, Auckland, New Zealand.

[3] Boulanger, R. W., and Idriss, I. M. (2005). "New criteria for distinguishing between silts and clays that are susceptible to liquefaction versus cyclic failure." Proceedings, Technologies to Enhance Dam Safety and the Environment, 25th Annual United States Society on Dams Conference, USSD, Denver, CO, 357-366.

[4] Boulanger, R. W., and Idriss, I. M. (2004). "Evaluating the potential for liquefaction or cyclic failure of silts and clays." Report No. UCD/CGM-04/01, Center for Geotechnical Modeling, Dept. of Civil & Environmental Engineering, University of California, Davis, 129 pp., http://cgm.engineering.ucdavis.edu/Publications/reports.htm.

[5] Bray, J. D., Sancio, R. B., Durgunoglu, T., Onalp, A., Youd, T. L., Stewart, J. P., Seed, R. B., Cetin, O. K., Bol, E., Baturay, M. B., Christensen, C., and Karadayilar, T. (2004a). "Subsurface characterization at ground failure sites in Adapazari, Turkey." J. Geotechnical and Geoenvironmental Engineering, ASCE, 130(7), 673-685.

[6] Bray, J. D., Sancio, R. B., Riemer, M. F., and Durgunoglu, T. (2004b). "Liquefaction susceptibility of fine-grained soils." 11th Int. Conf. on Soil Dynamics & Earthquake Engrg. & 3rd Int. Conf. on Earthquake Geotechnical Engrg., Stallion Press, pp 655-662.

[7] Chu, D. B., Stewart, J. P., Lee, S., Tsai, J. S., Lin, P. S., Chu, B. L., Seed, R. B., Hsu, S. C., Yu, M. S., Wang, M. C. H. (2004). "Documentation of soil conditions at liquefaction and non-liquefaction sites from 1999 Chi-Chi (Taiwan) earthquake." Soil Dynamics and Earthquake Engineering, 24(9-10), 647-657.

[8] Chu, D. B., Stewart, J. P., Lee, S., Tsai, J. S., Lin, P. S., Chu, B. L., Moss, R. E. S., Seed, R. B., Hsu, S. C., Yu, M. S., Wang, M. C. H. (2003). "Validation of liquefaction-related ground failure models using case histories from Chi-Chi, Taiwan earthquake." U.S.-Taiwan Workshop on Soil Liquefaction, Hsinchu, Taiwan, November 2-5, 2003.

[9] Goulois, A. M., Whitman, R. V., and Hoeg, K. (1985). "Effects of sustained shear stresses on the cyclic degradation of clay," *Strength Testing of Marine Sediments: Laboratory and In-Situ Strength Measurements*, ASTM STP 883, ASTM, Philadelphia, 336-351.

[10] Idriss, I. M. (1999). "An update to the Seed-Idriss simplified procedure for evaluating liquefaction potential." *Proc., TRB Workshop on New Approaches to Liquefaction*, Publication FHWA-RD-99-165, Federal Highway Administration.

[11] Idriss, I. M., and Boulanger, R. W. (2004). "Semi-empirical procedures for evaluating liquefaction potential during earthquakes." Proc., 11th Intl. Conf. on Soil Dynamics and Earthquake Engineering, and 3rd Intl. Conf. on Earthquake Geotechnical Engineering, D. Doolin et al., eds., Stallion Press, Vol. 1, 32-56.

[12] Lefebvre, G., and Pfendler, P. (1996). "Strain rate and preshear effects in cyclic resistance of soft clay." J. Geotechnical and Geoenvir. Engrg., ASCE, 122(1), 21-26.

[13] Mitchell, J. K. (1976). Fundamentals of Soil Behavior, 1st Edition, John Wiley and Sons, Inc.

[14] Seed, H. B. (1983). "Earthquake resistant design of earth dams." Proc., Symposium on Seismic Design of Embankments and Caverns, ASCE, N.Y., 41-64.

[15] Seed, H. B., and Idriss, I. M. (1982). Ground motions and soil liquefaction during earthquakes, Earthquake Engineering Research Institute, Berkeley, CA, 134 pp.

[16] Seed, H. B., Idriss, I. M., Makdisi, F., and Banerjee, N. (1975). "Representation of irregular stress time histories by equivalent uniform stress series in liquefaction analyses," Rpt. 75-29, Earthquake Engineering Research Center, University of California, Berkeley.

[17] Seed, R. B., Cetin, K. O., Moss, R. E. S., Kammerer, A., Wu, J., Pestana, J., Riemer, M., Sancio, R. B., Bray, J. D., Kayen, R. E., and Faris, A. (2003). "Recent advances in soil liquefaction engineering: A unified and consistent framework." 26th Annual ASCE Los Angeles Geotechnical Spring Seminar, Long Beach, CA.

[18] Stewart, J. P., Chu, D. B., Guglielmo, E., Chu, B. L, Hsu, S. C., Kayen, R., Lee, S., Lin, P. S., Seed, R. B., Tsai, J. S., Wang, M. C. H., and Yu, M. S. (2004). Documentation of soil conditions at liquefaction sites from 1999 Chi-Chi, Taiwan earthquake. PEER Lifelines website, http://peer.berkeley.edu/lifelines/research_projects/3A02/.

[19] Stewart, J. P., Chu, D. B., Lee, S., Tsai, J. S., Lin, P. S., Chu, B. L., Moss, R. E. S., Seed, R. B., Hsu, S. C., Yu, M. S., and Wang, M. C. H. (2003). "Liquefaction and non-liquefaction from 1999 Chi-Chi, Taiwan, earthquake," *Advancing Mitigation Technologies and Disaster Response for Lifeline Systems*, Tech. Council on Lifeline Earthquake Engineering, Monograph 25, 1021-1030.

[20] Stewart, J. P., and Chu, D. B. (2002). "Lessons on liquefaction from Taiwan," Proceedings, US-Japan Seminar on Seismic Disaster Mitigation in Urban Area by Geotechnical Engineering, Anchorage, AK, June 26-27, University of Tokyo, Japan, pp. 71-93.

[21] Wang, W. S. (1979). "Some findings in soil liquefaction." Water Conservancy and Hydroelectric Power Scientific Research Institute, Beijing, China.

[22] Zergoun, M., and Vaid, Y. P. (1994). "Effective stress response of clay to undrained cyclic loading," Canadian Geotechnical Journal, 31, 714-727.

Main Factors that Control Liquefaction of Tailings Sands

R. Verdugo
Department of Civil Engineering, University of Chile, Santiago, Chile

Abstract
One of the primary concerns of tailings dams located in seismically active regions is the assessment of their stability during earthquake disturbances. Additionally, tailings disposals will exist well after the mining operation is ended, and therefore, the seismic stability has to be ensured for a large period of time, for the so-called abandon condition. Seismic failures of tailings dams have been associated with the occurrence of liquefaction, and accordingly, this paper addresses the main geotechnical factors that control this phenomenon

Keywords—*Tailings dams, liquefaction, flow failure, cyclic mobility*

INTRODUCTION

The most common procedure to recover minerals from mother rock consists of crushing extracted ore to the size of fine sand and clayey silt. The minerals can then be retrieved, leaving behind a significant amount of waste material known as tailings. For example, it is possible to indicate that in the Chilean copper mines less than one percent by weight of the crushed ore corresponds to copper, while the other 99% corresponds to tailings that must be stored. In general, the tailings are fully saturated due to the mining process and therefore, it is necessary to safely dispose millions of cubic meters of saturated tailings at minimal cost.

The conventional system of tailings disposal consists of one or several dykes that confine the saturated loose tailings (slimes) in a pond. The dikes or embankments are mostly constructed with the sandy fraction of the tailings, which is accomplished by the cycloning method. According to the procedure of deposition, it is possible to distinguish between the upstream, downstream and centerline method of construction.

Projects associated with huge tailings dams are considered acceptable and attractive solutions for mine waste disposals. For example, in Chile there are in operation tailings dams with a height of 150 meters and reservoirs with more than one billion tons of slimes (Valenzuela et al, 1995). Moreover, there are projects under construction that will result in tailings dams of more than 220 meter in high.

It is important to realize that tailings dams correspond to waste disposals, and therefore, any over design does not produce any real benefit. On the other hand, an under design may be the cause of a failure as has been observed in many cases, with catastrophic results from all points of view, economic, environmental and loss of life.

Another important issue is related to the fact that tailing dams will remain as a waste deposit well after the mining activities are ended. This long period of time corresponds to the abandon of the tailing dams, and it has a tremendous impact in the estimation of the magnitude of the potential seismic disturbances that could disturb tailings dams.

On the other hand, there are several case histories indicating that seismic disturbances may cause failure of tailings dams due to the occurrence of liquefaction. In general, saturated deposits of loose cohesionless soils have shown to be susceptible to liquefaction during the occurrence of earthquakes; this phenomenon has been observed in tailing dams, hydraulic fill, as well as in natural slopes of loose sandy soils (Ishihara et al, 1980; 1984; Ishihara, 1985).

In this paper, the seismic stability of conventional tailing dams is discussed, centered on the evaluation of liquefaction.

SEISMIC FAILURES OF TAILINGS DAMS

Most of the seismic failures of tailings dams are attributed to increases in pore water pressure and to the occurrence of liquefaction (Finn, 1980). Fig. 1 shows one of the oldest documented flow failures in a tailings dam that occurred at El Teniente copper mine in Chile, following the earthquake of October 1, 1928.

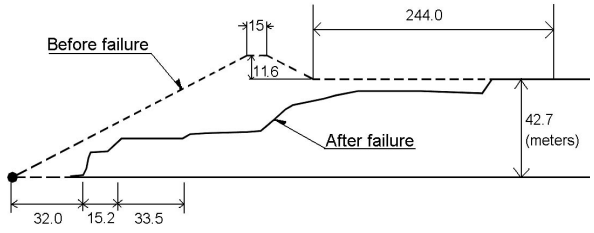

Fig. 1: Failure of Barahona tailings dam, (Agüero, 1929).

A 65 m high embankment collapsed 3 minutes after the main shock, involving 4 million tons of material that flowed along the valley, killing 54 persons. On the cross section of the remaining tailings showed in Fig. 1, it is interesting to observe the existence of several terraces with an inclination almost horizontal toward the downstream slope (Aguero, 1929).

Later, during the earthquake of March 28, 1965, El Cobre tailings dams located in Chile failed catastrophically and more than 2 million tons of material flowed approximately 12 km in a few minutes, killing more than 200 people and destroying El Cobre town. At the time of the failure, the dam was about 33 m high and it had a downstream slope as steep as 35º to 40º with respect to the horizontal (Dobry et al. 1967). A cross section of the tailings dam before and after the failure is shown in Fig. 2, where it is possible to observe the final profile of the tailings consisting of several terraces with a 1º slope towards the valley (Dobry et al. 1967).

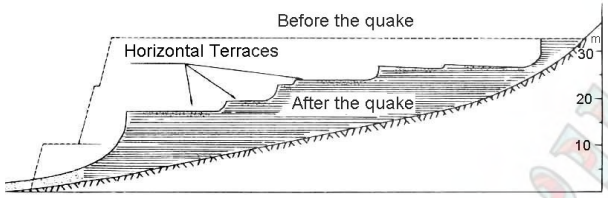

Fig. 2: Failure of El Cobre tailings dam, (Dobry el al. 1967)

Another well documented seismic failure of a tailings dam took place after the earthquake of January 14, 1978, at the dikes No. 1 and 2 of Mochikoshi gold mine in Japan. The dike No. 1 collapsed around l0 seconds after the main shock, and involving the flow of 60 thousands cubic meters of slimes. The dike No. 2 failed 24 hours after the main earthquake, at a time when there was not any shaking, and a total volume of 3 thousand cubic meters of material flowed into the valley for a distance of about 240 m. The cross sections of these two dikes showing the situation before and after the failure are presented in Fig. 3 (Ishihara 1984). In this case, the remaining tailings in the pond adopted an average slope of 8º towards the valley.

Furthermore, during the Chilean earthquake of March 3, 1985, with a Magnitude 7.8, two tailing dams failed due to the occurrence of liquefaction. The 30 m high Cerro Negro dam failed and about 130 thousand tons of tailing material flowed into the valley for a distance of about 8 Km, (Castro et al. 1989). The second failure caused by this earthquake occurred at Veta de Agua No. 1 dam, which at the time of the shaking had a maximum height of 15 m. According to a witness, the failure took place in the central part of the dam a few seconds after the shaking had stopped. The tailing material stored in the pound traveled along the El Sauce creek for about 5 km (Castro et al. 1989).

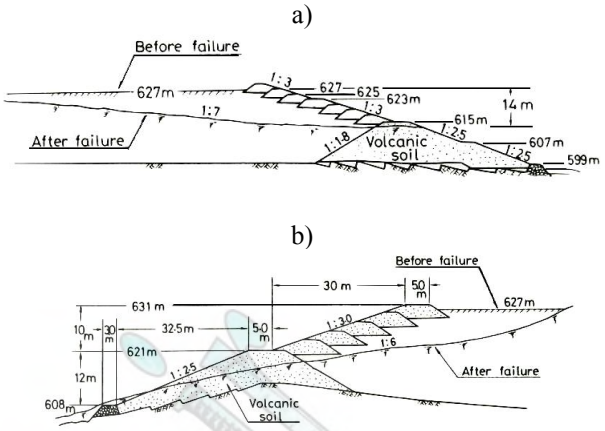

Fig. 3: Failure of Mochikoshi tailing dams. (a) Dike Nº 1 and (b) Dike Nª 2, (Ishihara, 1984).

A valuable summary of the observed seismic response of tailings dams constructed with the upstream method has been reported by Conlin (1987) and extended by Xin et al. (1992) with the overall seismic performance of Chinese tailings dams (Finn 1996). This compilation of data presented in Fig. 4 together with many other seismic failures that have occurred all around the world emphasize the importance of careful studies concerning the seismic response of tailings dams, with special focus on the liquefaction phenomena.

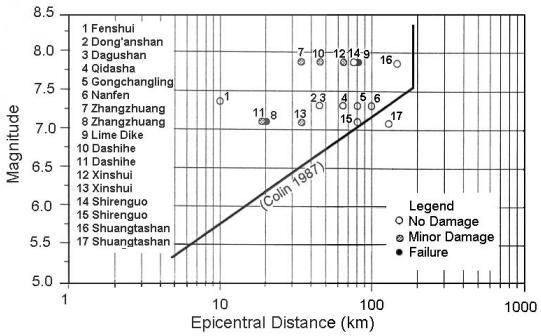

Fig. 4: Seismic response of tailings dams (Xin et al, 1992)

LIQUEFACTION PHENOMENON

It seems that Hazen (1920) was the first to use the term liquefaction to describe a soil failure. He used it in relation to the failure of the hydraulic fill of Calaveras Dam that occurred on March 24th, 1918. The upstream toe of the dam, which was under construction near San Francisco in California, suddenly flowed moving approximately 700,000 m^3 of material for a distance of around 90 m. It is interesting to mention that apparently at the time of this failure no special disturbance was noticed,

suggesting a failure under static loading conditions.

Currently, the word liquefaction is often used in a broad sense for two rather different phenomena where either a loss of strength or stiffness reduction takes place in a saturated cohesionless soil mass. However, in order to understand the real soil behavior it is of great importance to distinguish between these two different phenomena: cyclic mobility (or strain softening) and flow failure (or true liquefaction).

The term cyclic mobility or strain softening was proposed by Casagrande (1975) for the phenomenon where the cyclic loading generates a pore pressure buildup that causes a reduction in the stiffness of the soil mass. Typical experimental results for loose and dense sands showing this phenomenon are presented in Fig.5 (Ishihara, 1985). In both cases (loose and dense sandy soils) the soil mass does not undergo any loss in strength, but important deformations are developed after each cycle due to stiffness degradation.

The most common outcome of the large buildup in pore water pressure is the action of seepage forces that induce upward water flow, and eventually can transport soil particles to the ground surface, generating sand boils with their typical volcano shape. During seismic loading, the level of deformation reached by the soil mass (due to cyclic mobility) can be unacceptable for some structures and consequently, this phenomenon can generate significant damages.

The stability analysis of tailings dams against potential liquefaction, due to cyclic mobility is critical. Such liquefaction can generate significant deformations, which can easily go beyond the maximum acceptable. A very comprehensive summary of this subject has been reported by Finn (1996).

Casagrande proposed the term true liquefaction or flow failure, for the phenomenon where a sudden loss in strength is developed in a soil mass. This type of failure is characterized by the short period of time that it takes, a few minutes, and by the large deformations of the soil mass.

After failure has occurred, the soil mass involved in the collapse tends to reach very flat slopes, typically angles of 1º to 8º have been observed. This failure can be triggered not only by earthquakes, but also by disturbances that are fast enough to induce an undrained response of the soil mass.

True liquefaction or flow failure is the phenomenon that has been observed in the failures of tailings dams. It has caused catastrophic scenarios because it can compromise a significant amount of soil mass which can flow hundreds of meters in a few minutes. Consequently, seismic stability analysis of tailings dams must include a study associated with the eventual occurrence of flow failure. The condition of flow failure generates a large level of deformation where the steady state is reached, allowing the use of this concept in the evaluation of any potential flow failure.

a)

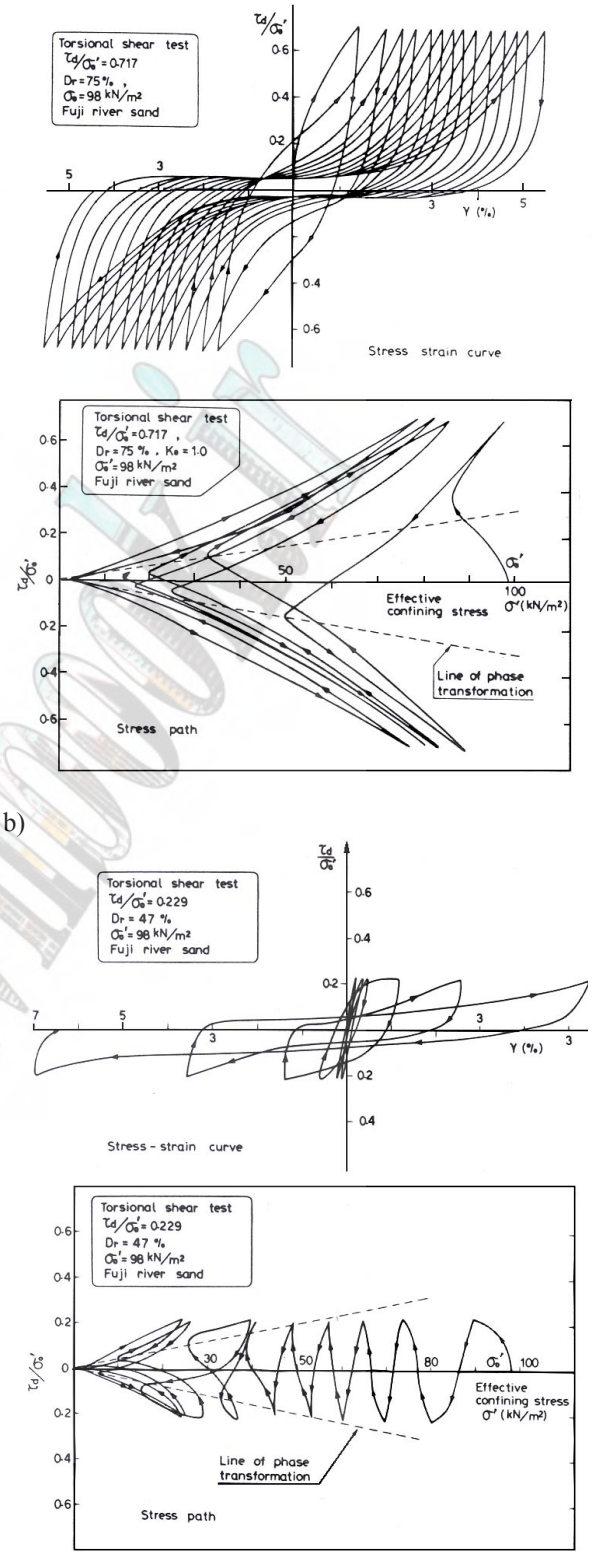

b)

Fig. 5 Cyclic response on sand, (a) dense and (b) loose

Experimental results reported by Castro (1969), using load controlled undrained triaxial tests, show the development of a sudden collapse of loose sands associated with the condition of a flow failure. A typical

result obtained in a loose specimen is presented in Fig. 6, where it can be observed that during the first 14 minutes the sample yielded a common stress strain curve with a peak strength at approximately 0.5% of axial strain. Thereafter, the next small load increment triggered the flow failure of the sample and in a fraction of a second (0.6 second) it developed a deformation of around 20%. In addition, the strength dropped to a small and constant value.

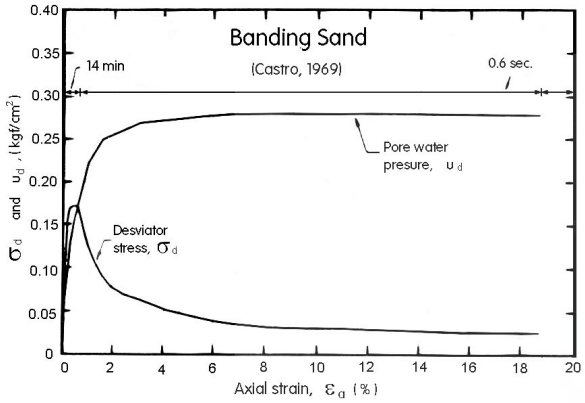

Fig. 6: Stress strain curve and pore water pressure developed on a loose sand specimen under undrained load-controlled test.

From this experimental result, it is readily apparent that true liquefaction or flow failure is associated with a great loss of strength, and it does not necessarily mean zero resistance or zero effective stress. Furthermore, the pore water pressure increases significantly during and after the application of loading reaching a constant value close to 95% of the initial effective stress. Referring to Fig. 6, it is seen that after the flow failure takes place, the shear stress that the specimen is able to withstand is essentially constant while the continuous deformation is taking place. Besides, the pore pressure, and therefore the effective stress, also remains basically constant after the flow failure has occurred. This particular state of the specimen has been referred by Poulos (1981) as the steady state of deformation. Regarding the final soil fabric, it has been postulated that the steady state of deformation is achieved only after all particle orientation has reached a statistically steady state condition, and after all particle breakage, if any, is completed, and the shear stress needed to continue deformation remains constant.

Poulos (1981) defined the steady state for a condition of constant velocity of deformation. However, this is not necessary. In fact the original experimental results reported by Castro (1969) were obtained from triaxial tests performed under load controlled condition, where after the drop in strength the applied dead weight induced an acceleration of the sample during its collapse. Thus, the steady state condition can be achieved under any rate of deformation.

Experimental results of undrained triaxial tests performed on samples at the same void ratio after consolidation are shown in Fig. 7 (Ishihara,1993; Verdugo et al., 1996). It can be seen that for samples with the same void ratio, regardless of the initial level of confining pressure, the same ultimate state or undrained steady state strength is achieved.

a)

b)

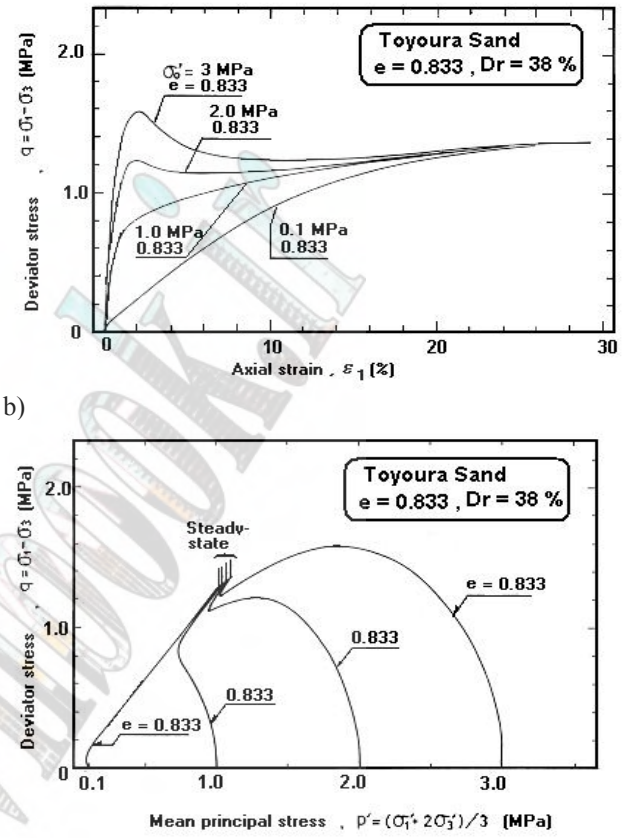

Fig. 7: Undrained steady state strength (Ishihara, 1993)

It is important to keep in mind that a contractive response of a soil mass with a drop in strength is only possible when the initial state of density and confining pressure is well above the steady state line in the e-p´ plane. Therefore, only these initial states are susceptible to develop a flow failure. However, even a soil mass in such state of potential collapse needs an additional condition for the occurrence of flow failure. The permanent driving forces, or the initial static shear stresses, have to be greater than the undrained steady state strength.

CYCLIC MOBILITY AND AGING

It has been recognized that the resistance to liquefaction tends to increase with the age of the deposit, a phenomenon that can be associated with the development of light cementation or welding at points of grain contact. This is specially important in the case of tailings due to the chemical bonds that can be rapidly created between particles. To study the effect of the time

of deposition in the cyclic strength of tailings sands, Troncoso et al, (1988) performed series of cyclic triaxial tests "undisturbed" samples retrieved from an old tailing dam at different depths, which basically means different ages of the samples. The test results are summarized in Fig. 8, indicating that the cyclic stress ratio required to produce a state of softening with 5% double amplitude strain tends to increase by a factor of 3.5, 2.4 and 2 for the samples of 30, 5 and 1 years of sustained deposition, respectively.

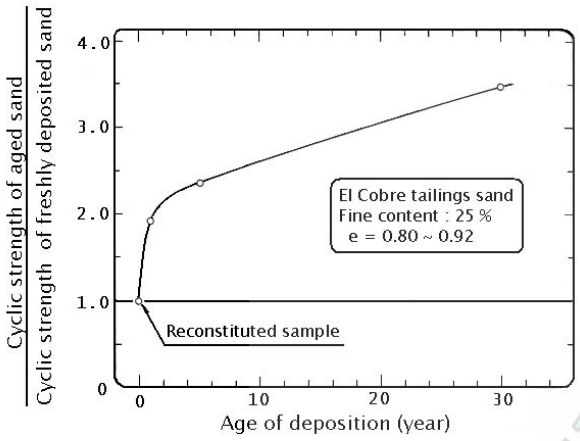

Fig. 8: Aging effect on the cyclic strength of tailing sands

It is strongly recommended to estimate the effect of aging for stability analysis considering the abandon period. This type of study can be done when the tailings dam has been in operation for several years, so it is possible to retrieve samples at different depths, which are associated with different years of deposition. By testing these "undisturbed" samples, it is possible to establish the improvement of cyclic strength with the age of deposition.

EFFECT OF INITIAL FABRIC

During the genesis of any soil deposit, the sedimentation and placement of soil particles is affected by gravity, which generates a preferential particle orientation that creates an anisotropic soil structures. Casagrande et al, (1944) named this initial anisotropy caused by the geological process of deposition Inherent Anisotropy. Depending upon the environmental conditions existing during the sedimentation process, the inherent anisotropy may significantly affect the soil response. This situation is particularly important in hydraulic fill as in the case of tailings dams, where there is not only a preferential orientation of particles, but also a segregation that may result in a heterogeneous soil structure. In this regard, Mulilis et al, (1975) have shown the tremendous effect generated by the sample preparation procedures on the cyclic strength of sandy soils, which essentially can be associated with the effect of different initial fabrics on liquefaction resistance.

In the case of tailings dams an initial fabric of potentially significant importance should be expected and therefore, the use of "undisturbed" samples in the characterization of tailings deposits is recommended. In the present study the initial fabric is investigated by means of triaxial tests on "undisturbed" samples.

CYCLIC MOBILITY AND FINES CONTENT

In copper tailings Troncoso and Verdugo (1985) have studied the effect of low plastic fines content on the cyclic strength using reconstituted samples compacted at the same initial void ratio. Test results associated with the number of cycles required to develop 100% of pore water pressure build-up are shown in Fig. 9, where a clear degradation of cyclic strength exhibited by the tailing sands with the presence of low plastic tailings fines is observed.

These results are indicative of the significant increase in liquefaction potential caused by the presence of low plastic fines in the sandy soil tailings.

In the present study the effect of fines on the undrained strength is investigated

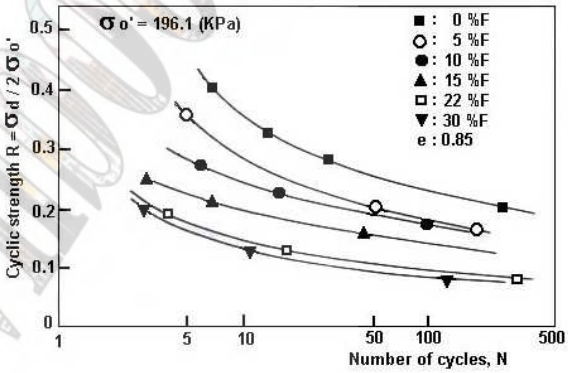

Fig. 9: Effect of low-plastic fines on the cyclic strength of tailings sandy soils (Troncoso et al, 1985).

EXPERIMENTAL PROGRAM AND MATERIAL TESTED

Among the different factors that control the liquefaction strength it has been considered important to study the effect of initial fabric and fines content. Accordingly, an experimental program was carried out in the Geotechnical Laboratory of the University of Chile using a tailings sand retrieved from the main dike of a Chilean copper mine. This tailings sand deposited in the dike presents, after passing by the cyclones, a fines content of 17%. Passing a part of this sand through mesh # 200 (0.074 mm) a batch of non-plastic fines was obtained. Another part of the tailings sand was washed and a clean sand was obtained. Then two mixtures with 9 and 23% of fines content were produced. In addition, block "undisturbed" samples were retrieved from a pit of 2 m depth.

CIU Triaxial tests were carried out in order to define the steady state condition and the undrained strength, and cyclic triaxial tests were performed to establish the cyclic strength.

The reconstituted samples were compacted inside a metallic mould of 10 cm in height and 5 cm in diameter. The wet tamping procedure of sample preparation was adopted, using a 5% water content. The samples were compacted in five layers, with each layer of identical initial height and wet weight. The saturation of the samples was performed applying first CO_2 gas, then percolation with de-aired water, and then back-pressure. The degree of saturation was considered acceptable when the B-value was equal or greater than 0.96. The void ratios were evaluated by means of the water content measured at the end of the tests (Verdugo, 1992; Verdugo et al, 1996).

ANALYSIS OF TEST RESULTS

An average specific gravity of 2.75 was obtained. The grain size distribution curves of the different batches are shown in Fig. 10. The measured maximum and minimum void ratios of the three mixtures are presented in Fig. 11. Using other tailings mixtures Verdugo et al, (1996) have shown the validity of the minimum void ratios for low-plastic fines contents greater than 50%.

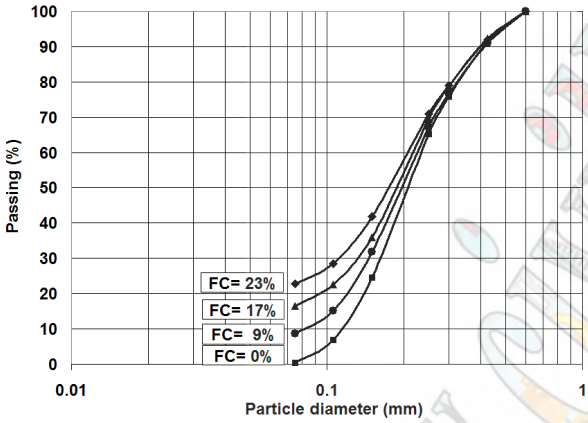

Fig. 10: Grain size distribution curves

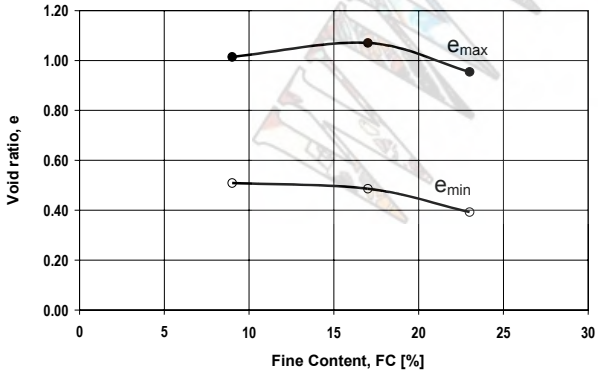

Fig. 11: Maximum and minimum void ratios of mixtures

The effect of the non-plastic fines content on the steady state line was studied by means of CIU triaxial tests on reconstituted samples of mixtures of 9, 17 and 23% fines content, and the results are presented in Fig. 12. It can be seen that the resulting steady state lines remain approximately parallel to each other, but as the non-plastic fines content increases the location of the lines goes down, suggesting that the non-plastic fines induce a more contractive behavior of the mixtures.

To confirm this effect, the parameter Relative Contractiveness, Rc, introduced by Verdugo et al, (1996) to evaluate the intrinsic potential of liquefaction, has been estimated for the three tested mixtures. The maximum and minimum void ratios at 1 kg/cm^2 associated with the loosest and densest states have been approximated to the normal maximum and minimum void ratios. The estimated values of Rc are 0.2, 0.43 and 0.45, for non-plastic fines contents of 9, 17 and 23%, respectively. These results confirm that the increase in non-plastic fines content makes the mixture more contractive with a higher intrinsic potential of liquefaction.

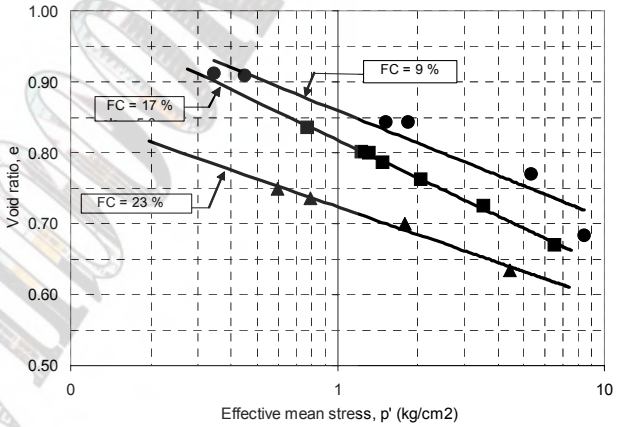

Fig. 12: Steady state lines of mixtures

The effect of the initial fabric was investigated comparing the experimental results of "undisturbed" and reconstituted samples. Fig. 13 shows the steady state line obtained by means of reconstituted samples and the data points obtained from "undisturbed" samples.

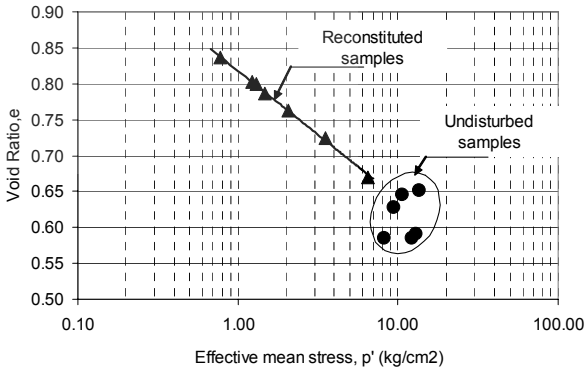

Fig. 13: Steady state condition obtained in reconstituted and "undisturbed" samples of tailings sand

It can be observed that the steady state line defined by the reconstituted samples tends to pass throughout the results of "undisturbed" samples, which suggests that the initial fabric developed by the tailings deposited in the dam is rather homogenous and it is lost with the large deformations associated with the ultimate state. This confirm previous results reported by Verdugo et al, (1995).

The results of cyclic triaxial tests are shown in Fig. 14, where a clear difference is observed between "undisturbed" and reconstituted samples.

The significant higher cyclic strength developed by the "undisturbed" samples can be explained by the sum of two factors: initial fabric and aging. Therefore, it is strongly recommended to estimate the cyclic strength by means of "undisturbed" samples.

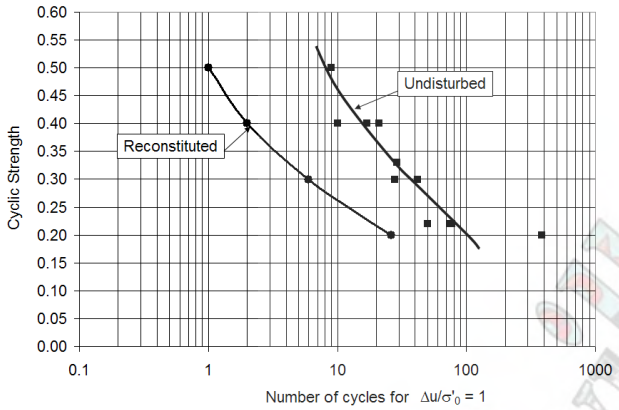

Fig. 14: Cyclic strength of reconstituted and "undisturbed" samples of tailings sand.

CONCLUSIONS

Economical, environmental and technical considerations have induced the construction of huge tailings dams in terms of high, extension and stored volume. The seismic stability analysis of these earth structures is therefore of great practical interest. There exists evidence showing that conventional tailings dams are susceptible to catastrophic failures due to the occurrence of liquefaction triggered by the action of strong earthquakes. Therefore, the study of this phenomenon on tailings materials is of great importance.

It has been shown that the initial fabric has an important effect on the cyclic strength, and although the recovery of "undisturbed" samples is rather complicated, its use is strongly recommended. Nevertheless, for the tailings that have been tested, the undrained strength developed at large strains was rather unaffected by the initial fabric, suggesting that the initial fabric could be lost after some level of deformation.

The experimental results also indicate that the non-plastic fines significantly affect the soil response making it more contractive and therefore, more susceptible to liquefaction.

ACKNOWLEDGMENTS

The author wants to acknowledge the review and many useful comments done by Mr. T. Thompson. Also, thanks are due to Mr. Wladimir Retamal, undergraduate student of U. of Chile, for running all the laboratory tests and to Miss. Karen de la Hoz, graduate student of U. of Chile, for her assistance in the preparation of the draft.

REFERENCES

[1] Agüero, G. (1929). *Formation of Tailings Deposits in El Teniente Mine*. Anales del Inst. de Ingenieros de Chile. pp.164-187.

[2] Casagrande, A. (1975): "Liquefaction and Cyclic Deformation of Sands – A Critical Review," V Panamerican Conference on Soil Mech.& Foundation Eng. Buenos Aires, Argentina.

[3] Casagrande, A, and Carrillo, N. (1944): "Shear Failure of Anisotropic Materials," Proc. Boston Soc. of Civil Eng. Vol. 31, pp. 74-87.

[4] Castro, G. (1969): "Liquefaction of Sands," Doctoral Thesis, Harvard University, Cambridge, Mass. USA.

[5] Castro, G. and Troncoso, J. (1989): "Effects of Chilean Earthquake on Three Tailing Dams," International Seminar on Dynamic Behavior of Clays, Sands & Gravel. Kitakyushu, Japan.

[6] Conlin, B. (1987): "A Review of the Performance of Mine Tailings Impoundments Under Earthquake Loading Conditions," Proceedings Vancouver Geotechnical Society Seminar on Earthquake. Geot. Canada.

[7] Dobry, R. and Alvarez, L. (1967): "Seismic Failures of Chilean Tailings Dams," Journal of Soil Mechanics and Foundation Division, ASCE, Vol. 93, SM6, pp. 237-260.

[8] Finn, W. (1980): "Seismic Response of Tailings Dams," Proceedings, Seminar on Design and Construction of Tailings Dams. Colorado School of Mines. USA.

[9] Finn, W. (1996): "Seismic Design and Evaluation of Tailings Dams: State of the Art," Int. Symposium on Seismic and Environmental Aspects of Dam Design: Earth, Concrete and Tailing Dams. Chile.

[10] Hazen, A. (1920): "Hydraulic-Fill Dams," ASCE Transactions, Vol. 83, pp. 1713-1745.

[11] Ishihara, K. (1984): "Post-Earthquake Failure of a Tailings Dam Due to Liquefaction of the Pond Deposit. International Conference on Case Histories in Geotechnical Engineering. St. Louis. USA.

[12] Ishihara, K. (1985): "Stability of Natural Deposits During Earthquakes," XI International Conference on Soil Mechanics and Foundation Engineering. Vol. 2, pp.321-376.

[13] Ishihara, K. (1993): "Liquefaction and Flow Failure During Earthquakes," 33rd Rankine Lecture. Geotechnique, Vol. 43, No. 3, pp. 351-415.

[14] Ishihara, K., Troncoso, J. and Kawase, Y. (1980): "Cyclic Strength Characteristics of Tailings Materials," Soils and Foundations, Vol.20, No.4, pp. 128-142.

[15] Mulilis, J., Chang, C. and Seed, H. (1975): "The Effect of Method of Sample Preparation on the Cyclic Stress-Strain Behavior of Sands," University of California, Berkeley. Report EERC 75-18.

[16] Poulos, S. (1981): "The Steady State of Deformation. Journal of Geotechnical Engineering Division, ASCE, Vol. 107, No. GT5, pp. 553 562.

[17] Troncoso, J. and Verdugo, R. (1985): "Silt Content and Dynamic Behavior of Tailings Sands," XI International Conference on Soil Mechanics and Foundation Engineering. Vol. 3. pp. 1311-1314.
[18] Troncoso, J., Ishihara, K. and Verdugo, R. (1988): "Aging Effects on Cyclic Shear Strength of Tailings Materials," IX World Conference on Earthquake Engineering, Vol.3, pp.121-126. Tokyo, Japan.
[19] Valenzuela, L., and Barrera, S. (1995): "Large Tailings Dams: Current Practice in Chile," X Panamerican Conference on Soil Mechanics and Foundation Engineering. Mexico. Vol. 3, pp. 1556-1569.
[20] Verdugo, R. (1992): "Characterization of Sandy Soil Behavior Under Large Deformations," Doctoral Thesis, University of Tokyo.
[21]Verdugo, R. and Ishihara, K. (1996): "The Steady State of Sandy Soils," Soils and Foundations. Vol. 36, No.2, pp. 81-91.
[22] Verdugo, R. and Bard, E. (1996): "Maximum and Minimum Densities in Cohesionless Soils," X Panamerican Conference on Soil Mechanics and Foundation Engineering, Guadalajara, Mexico. Vol. 1, pp. 582-592.
[23] Verdugo, R., Castillo, P. and Briceño, L. (1995): "Initial Soil Structure and Steady State," First International Conference on Earthquake Geotechnical Engineering. Japan. Vol. 1, pp. 209-214.
[24] Xin, H., Finn, W. and Wang, Y. (1992): "Lessons from Seismic Performances of Chinese Tailings Dams," Report of Department of Civil Engineering, University of British Columbia, Canada.

Modeling flow liquefaction, its mitigation, and comparison with centrifuge tests

E. Naesgaard[1], P. M. Byrne[1], M. Seid-Karbasi[1], and S.S. Park[1]
[1]*Department of Civil Engineering, University of British Columbia, Vancouver, Canada*

Abstract

There is a common misconception among practicing engineers that loose sand soils behave in an undrained manner during earthquake loading. Recently it has been demonstrated that pore water flow and pressure redistribution which occurs during and following earthquake shaking may result in relatively thin zones with very high void ratio, or in the extreme, water inter-layers, immediately below low permeability layers. These high void ratio/water inter-layer zones have very low to near zero shear strength, much lower than obtained from undrained laboratory element tests. Without a low permeability barrier to retard the escape of groundwater, flow liquefaction generally does not occur, even for loose sands on relatively steep slopes subjected to strong shaking. A program of simple shear and centrifuge testing was carried out to calibrate a numerical model. Flow failure with post-shaking localized shear immediately below a low permeability barrier was modeled in the centrifuge and emulated in the numerical analyses. Procedures for numerically modeling the flow liquefaction and localization under the barrier are discussed. The analyses demonstrate that the strength reduction effects of the low permeability barrier can be captured by the numerical analyses and that drainage slots are an effective means of mitigating flow deformations.

Keywords— *Centrifuge, earthquake, flow, liquefaction, numerical, pore water, redistribution*

INTRODUCTION

Numerous flow failures have occurred during or following strong earthquake shaking when liquefaction is triggered [1][2][3][4]. These flow liquefaction failures are deemed to occur when the static driving stress exceeds the soil shear strength. Shear strength of soil following triggering of liquefaction has been called residual strength, and has commonly been assumed to be an undrained strength parameter. Seed [3] back-calculated these strengths from case histories while others [5] attempted to determine them from laboratory tests. Recent work [6][7][8][1][9][10] has shown that the undrained assumption is not correct and may be unconservative. They have demonstrated that pore water flow and pressure redistribution which occurs during and following earthquake shaking may result in relatively thin zones with very high void ratio, or in the extreme, water inter-layers, below low permeability layers. These high void ratio/water inter-layer zones have very low to near zero shear strength, much lower than obtained from undrained laboratory element tests. Without a low permeability barrier to retard the escape of groundwater, and/or some form of soil mixing, flow liquefaction generally does not occur, even for loose sands on relatively steep slopes subjected to strong shaking.

A constitutive model, UBCSAND, and analysis procedure has been developed at the University of British Columbia for modeling the behavior of sandy soils during earthquake shaking; including the modeling of liquefaction triggering and related deformations [12]. A program of cyclic simple shear and dynamic centrifuge testing has recently been carried out specifically for the purpose of calibrating the numerical model.

This paper examines the flow liquefaction modeling aspects and procedures for mitigating the effects of low permeability barriers within sand soil deposits. The constitutive model, analysis procedures and comparison of numerical analyses and centrifuge test predictions are described.

SOIL LIQUEFACTION AND PORE WATER REDISTRIBUTION OVERVIEW

When typical loose sand, D_r = 40% is tested in the laboratory in drained cyclic simple shear it is initially contractive on loading and unloading. However at large strains in loading the soil becomes dilative when the stress state exceeds the constant volume friction angle, φ_{cv}. Dense sand behaves in a similar manner except the dilative response is much more pronounced. Both soils are always contractive on unloading. The net result of cyclic loading is generally a reduction in sample volume.

If the pores are filled with water that is prevented from escaping the sample (undrained condition), then pore pressures increase when the soil skeleton attempts to contract and decrease when the soil skeleton attempts to dilate. As pore pressure builds up the effective stress and shear strength decreases, however with attempted dilation the effective stress and shear strength increases. Dilative response is deemed to occur when the stress path exceeds the phase transformations or φ_{cv} line. With repeated cycles the stress path may reach the zero effective stress / zero shear strength origin and true liquefaction occurs. However upon continued monotonic shearing to large strains the soil will dilate, moving up the failure envelope gaining strength and the so-called *residual strength* will not be reached until, (i) the pore-water cavitates and thus allows the sample to increase in volume and reach the steady state, or (ii) the high mean effective stress

generated by dilation suppresses the dilation and the soil reaches its critical state strength, or (iii) the sand grains crush and the soil reaches a critical state of the crushed material. The strength of the sand reached in (i), (ii) or (iii) is generally much higher than the commonly accepted 'undrained" residual strengths back-calculated from case histories [13], and is likely much higher than the drained strength.

If, in lieu of undrained loading, a small inflow of water is allowed to occur, it will reduce or eliminate the strength gain resulting from expansion [6]. If the inflow volume exceeds the expansion due to shear induced dilation then the soil quickly reaches the state of zero effective stress and has truly liquefied.

There are numerous case histories where soil liquefaction occurred during earthquake shaking but related flow failure did not occur until some time after end of shaking. The classical examples are the Lower San Fernando Dam [3] and in Niigata eyewitnesses reported that the girders of the Showa Ohashi Bridge began to fall a few minutes after the earthquake motion had ceased [2].

Natural and many man-made soils are often layered and have variations in grain-size and related permeability throughout the deposit. Earthquake shaking and related liquefaction will induce a generally upward gradient and pore-water flow. When there is a low permeability layer or barrier, the upward migrating pore water gets trapped under or within the bottom portion of the barrier and forms an interface with low effective stress. At the limit an actual water interlayer with zero shear strength will develop.

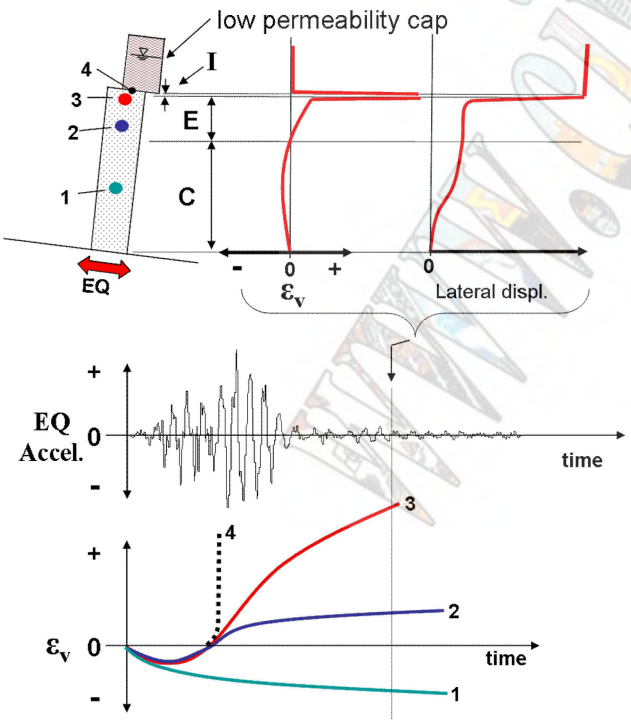

Fig. 1 Volumetric strain (ε_v) within an infinite slope column with a low permeability crust over loose sand

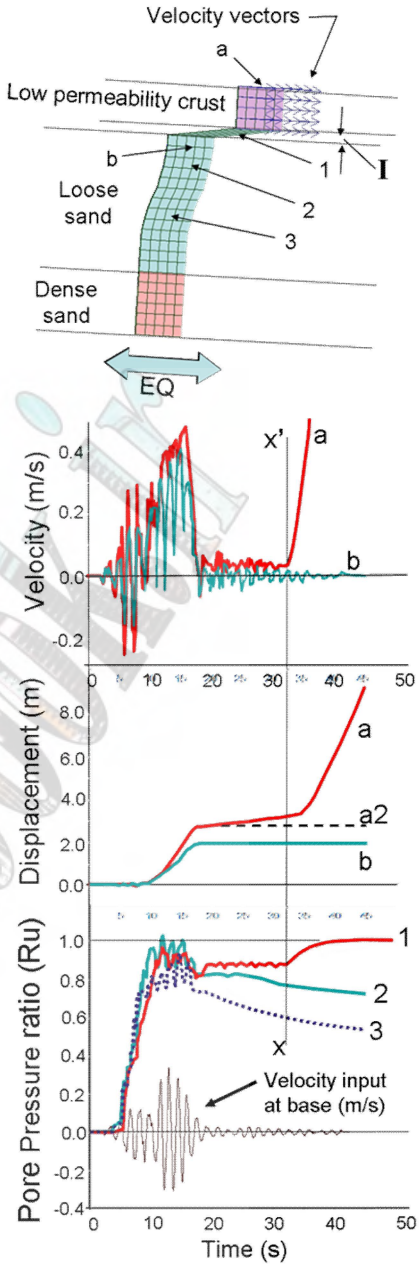

Fig. 2 Infinite slope (1D) column with low permeability barrier cap. At time x-x' zone 'I' has expanded to the critical state, dilation goes to zero, and flow failure is initiated.

ANATOMY OF A LOOSE SAND LAYER UNDERLYING A LOW PERMEABILITY BARRIER

Based on numerical analysis of a one dimensional column with a small static bias, [10] showed that the loose soil, of thickness 'L' underlying a low permeability barrier consists of three zones: a lower contractive-zone (Zone 'C'), an upper expansive zones (Zone 'E'), and a thin very expansive interface layer (Zone 'I') at the top (Fig. 1 & 2).

At the onset of earthquake shaking Zones 'E' and 'I' have not developed and the full depth of soil is

contractive. However with time, pore water flows upward from the lower layer 'C' and expansive Zones 'E' and 'I' develop. The blockage effect on flow caused by the presence of the barrier causes the highest rate of expansion to occur directly beneath the barrier. This is important as this causes localization and formation of a thin very weak layer at the interface. The dilation or expansion within zone 'E' and 'I' is due to a combination of dilation induced by the static shear bias and, more importantly, by the influx of water from Zone 'C' below.

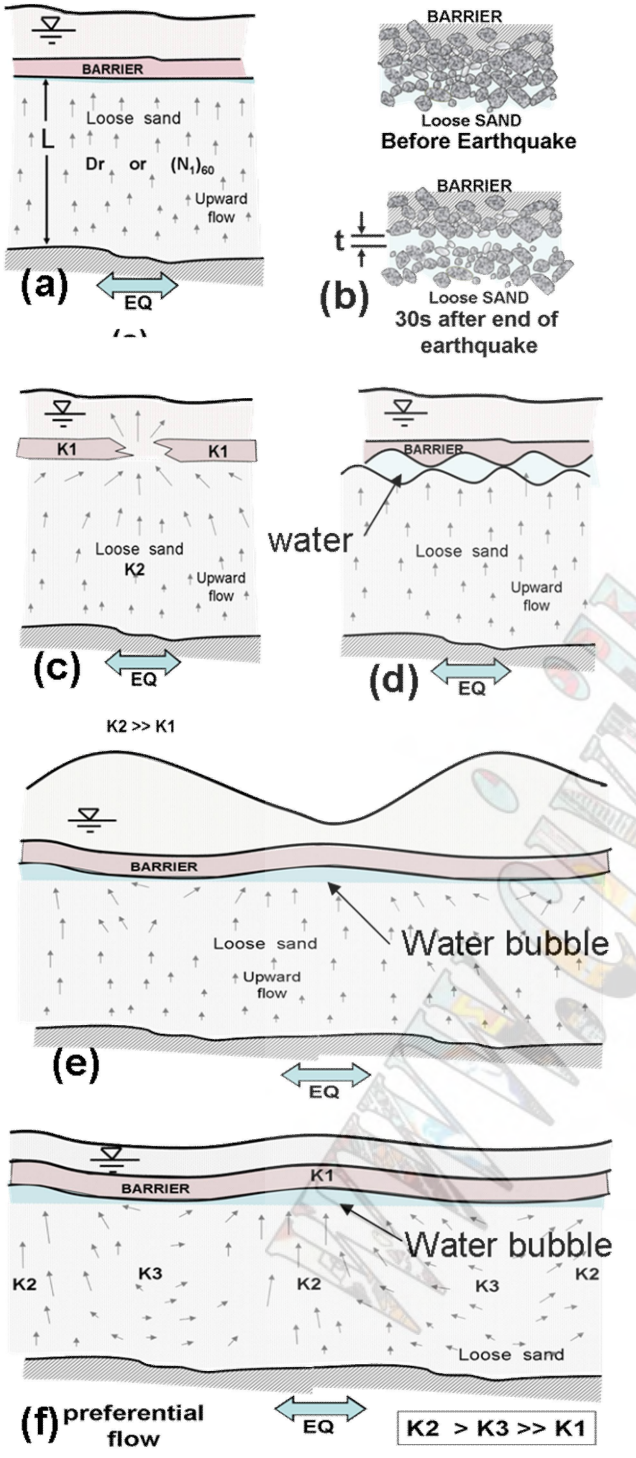

Fig. 3. Factors affecting the thickness and residual strength of the localized shear zone underlying a low permeability barrier (a) density & thickness L, (b) grainsize, (c) continuity and permeability of barrier, (d) interface roughness, (e) total stress variation, and (f) preferential flow paths.

If zone 'I' is thought of as a very thin soil element, with plane boundaries, then a small influx of pore water will cause a large volumetric strain at the barrier. This will result in the element quickly going to the critical state with zero effective stress and zero shear strength. Further inflow will cause localization and formation of a water film or interlayer. Further shearing will not induce dilation. The strength will remain zero until the excess pore water drains.

If the soil has a static shear bias the zone 'I' layer will attempt to fail prior to reaching the critical state and zero strength. This may cause dilation, which in turn may cause a temporary drop in pore pressure and related strength increase. However with continued inflow the layer quickly reaches the critical state and any further inflow leads to zero effective stress and zero shear strength.

In real soils the boundary of Zone 'I' will not be perfectly plane, infinitely thin or of infinite lateral extent but will have undulations, varying normal stresses, finite grain sizes, etc. These items will result in the 'residual' shear strength along the interface varying both in time and space with an average value that is greater than zero. Some items that influence the shear strength of the barrier interface (Zone 'I') include:

1) *Net volume of inflow*: The volume of inflow will be a function of the thickness of the loose layer, relative density of the loose layer, drainage conditions (whether essentially vertical 1D drainage conditions or combined vertical and lateral drainage), and earthquake shaking amplitude and duration (Fig. 3a). The greater the irregularities, undulations, etc. of the interface layer the greater the net inflow required to achieve zero effective stress.

2) *Grain-size*: The grain-size of zone I will have an effect on the dilation required in order to reach the critical state. The larger the grains the greater the inflow required for steady state shear to be achieved (Fig. 3b).

3) *Permeability and continuity of the barrier*: Leakage through the barrier will reduce the net inflow into the interface and therefore will reduce the effectiveness of the barrier (Fig. 3c).

4) *Boundary undulations*: Undulations in the boundary of the barrier layer will affect the volume of inflow required to achieve zero strength (Fig. 3d). These may be undulations that precede the earthquake shaking and/or may be due to deformations induced by strong earthquake shaking.

5) *Variations in vertical stress*: Variations in vertical stress along the barrier boundary will allow the higher stressed sections to maintain some strength while the lower stressed sections heave (Fig. 3e)

6) *Concentration of groundwater seepage*: The upwelling groundwater may be preferentially

concentrated (Fig. 3f) due to variations in permeability and discontinuities within the ground.

7) *Soil Frictional properties*: The frictional properties of portions of the barrier that do not have zero strength will affect the average strength.

The "residual strength" that is back-calculated from case histories [13] may approximately represent the average shear strength of the interface layer at the time of failure. This 'residual strength' is dependent on many parameters in addition to the normally assumed $(N_1)_{60}$ of the loose layer [9].

NUMERICAL MODELING OF PORE WATER REDISTRIBUTION AND FLOW LIQUEFACTION

Much of the behavior of the pore water redistribution and flow liquefaction behavior can be captured using an appropriate numerical program. Desirable features for the program include:

a) An effective stress constitutive model with coupled mechanical stress-strain – pore water flow features.
b) A mechanism to account for the localization that occurs adjacent to the low permeability barrier interface.
c) The model should capture the drained and undrained behavior of element tests with similar stress paths to that expected in the field during earthquake loading. This should include capturing shear induced contraction and dilatancy, and ability to model inflow tests.
d) The model should be relatively simple and only require a limited number of input parameters that can be determined from commonly available field and laboratory tests.
e) The model should be able to emulate the behavior of field case histories and/or centrifuge tests.

Item (b) above is problematic. Localization means that the behavior will be element size dependent. The localization of the barrier interface could be modeled by (i) using many very small elements; (ii) the use of larger elements with a dilation cut-off (iii) an interface with a dilation cut-off, or (iv) by using a total stress residual strength immediately below or within the barrier for the latter portion of the numerical analysis. Each of these is discussed in more detail below.

The alternatives for numerically modeling the barrier interface and related localization

(i) *Use very small elements in vicinity of barrier*: Very small elements with a function that sets dilation to zero when the critical state void ratio is reached would model the localization in a realistic manner. Grain size, boundary undulations, and other barrier properties could be physically modeled with the very small elements. The down side is that the very small elements make most existing programs excessively slow and impractical.

(ii) *Large element with dilation cut-off*: A large element

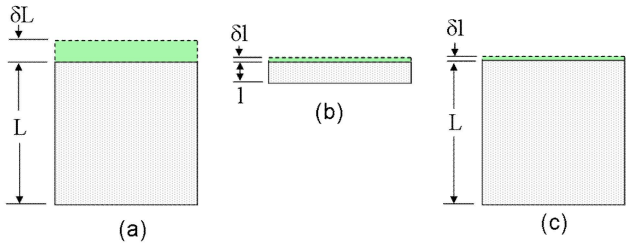

Fig 4. Large element(c) emulating the behavior of a small element (b). If (a) and (b) are at critical state with $\delta l/l = \delta L/L$ then (c) can be made to behave similar to (b) by setting dilation to 0 when the volumetric strain is equal to $\delta l/L$.

can be tricked into behaving like a small element by having a function that 'kills' dilation at a pre-specified void ratio or volumetric expansion of the element. As illustrated in Fig. 4, this pre-specified volumetric expansion is much less than that required to get the whole element to the true critical state. The volume of inflow permitted prior to 'killing' dilation would be a function of the material grain size, boundary undulations, etc. and could be approximated from the back-calculation of case-histories and centrifuge tests.

(iii) *Numerical interface with no dilation*: A numerical interface could be used to model the layer underlying a barrier. This interface could have simple Mohr Coulomb frictional properties with no dilation. The shear strength on the interface would go to zero when the effective stress was zero. The behavior of the interface would be similar to an infinitely thin element. The surface of the interface could be undulated to model irregularities in the barrier.

(iv) *Switch the element or numerical interface to a total stress 'residual strength'*: An alternative to using a dilation cut-off or an interface with no dilation would be to change the soil properties, at an appropriate time (possibly end of strong shaking), within the layer underlying the barrier layer, or the barrier layer itself, from effective stress to a total stress 'residual strength'. Volumetric strain (similar to that used to trigger dilation-cut-off in (iii) above could be used to trigger when to change to the strength within the layer to the total stress residual strength value. If the residual strength is less than the static driving stress then a flow deformations would occur. Note that this is different than the current practice of changing the properties of the whole loose sand layer to the residual strength when liquefaction is triggered. In the proposed procedure the residual strength would only be used in the barrier elements, elements immediately below the barrier, or the barrier interface. The remainder of the loose sand elements would still use the effective stress constitutive model. The residual strength selected would have to be tied to case histories and would be similar to that proposed by [13] & [14].

NUMERICAL ANALYSES

Numerical analyses of simple shear laboratory tests, 1-D soil columns, and centrifuge tests with low

permeability barrier layers, has been conducted as part of the UBC – C-Core Liquefaction Initiative. The effective stress constitutive model UBCSAND [15][12], running in commercially available finite difference program FLAC [16], was used for the analyses.

The UBCSAND constitutive Model

UBCSAND is an elastoplastic effective stress model with the mechanical behavior of the sand skeleton and pore water flow fully coupled. The model includes a yield surface related to the developed friction angle, non-associative flow rule, and definitions for loading, unloading, and hardening. A hyperbolic relationship is used between stress ratio and plastic shear strain. 2% Raleigh damping is used with the UBCSAND model to provide energy dissipation at small strain levels. Key elastic and plastic parameters used are adjusted so as to give a good match with simple shear laboratory tests as the loading path of this test, including rotation of principal stress axes, closely approximates that which occurs during earthquake loading. A series of simple shear tests, including cyclic drained and undrained tests with and without static bias, and monotonic drained and undrained tests were conducted for this purpose [17]. Fig. 5 shows a typical comparison of a simple shear test result to that predicted by the UBCSAND model. Reference [18], showed that the model could also emulate the behavior of triaxial tests with fluid inflow [6].

During the dynamic analysis the pore pressures are generated by shear induced plastic volume change. This

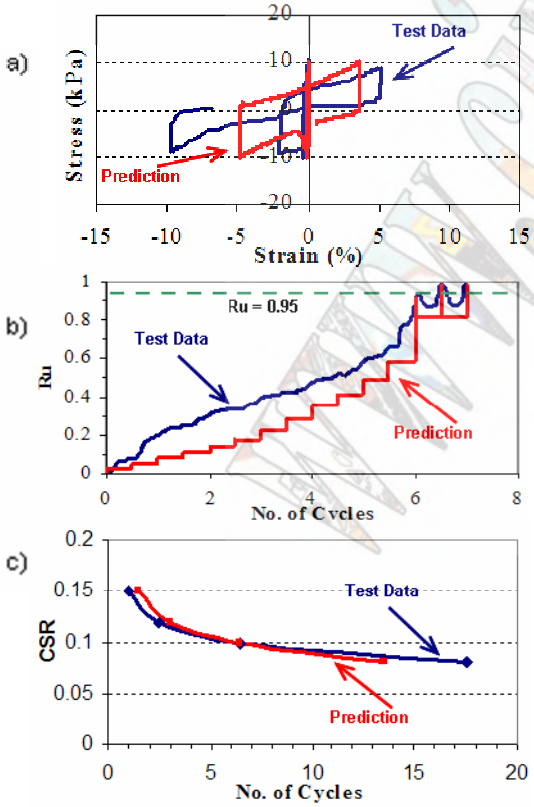

Figure 5. Comparison of undrained simple shear tests to UBCSAND predictions [10][17]

reduces mean effective stress and initiates pore water flow from zones of high head to low head. Volumetric strain is monitored in each element and when a pre-set strain is reached dilation in the element is set to zero (this threshold will typically only be reached when the element is underlying a low permeability barrier).

When the grid is submerged, water is modeled as an applied pressure to the top of the mesh. This pressure has to be updated periodically during the dynamic analyses in order for the applied pressure to be compatible with grid deformations.

The pore pressure in a FLAC element is the average of the nodal values. Therefore low permeability layers have to be at least two elements thick if high pore pressures are to be achieved within the underside of the barrier. Localization was accounted for by using a volumetric expansion dilation-cut-off. For a one meter thick element the dilation was set to zero when a volumetric expansion strain of 0.005 was reached. This seemed to give reasonable correlation with centrifuge test results. However this value is preliminary and further calibration work is required.

1D Analyses

Infinite slope 1D numerical analyses are useful for developing insights into the behavior of the low permeability barrier and flow slide mechanisms. Figs. 1 and 2 illustrate a typical 1D column analysis with typical volumetric strain time histories at various locations within the column. Fig. 2 shows a displaced grid with velocity time histories above and below the barrier. Note how a flow slide or flow failure condition is initiated (increasing velocity) at time x-x'. This is the critical state when shear induced dilation goes to zero. Shear strain is concentrated (localized) immediately below the low permeability barrier, and the flow failure is independent of the inertial forces from strong shaking.

Analyses of centrifuge tests with and without impermeable barrier

A series of eight centrifuge tests were carried out at the C-CORE facility in Newfoundland [20][21]. The centrifuge tests modeled submerged slope configurations with and without: low permeability silt barrier, soil densification dyke, and drainage trenches. Air pluviated Fraser River sand with a relative density of approximately 40% and minimum and maximum void ratio of 0.62 and 0.94 was used. Non-plastic commercial ground silica silt was used for the low permeability barrier and clear uniform coarse sand was used for the drainage layers. D_{10} and D_{50} for the loose sand was 0.16 mm and 0.26 mm, for the silt was 0.005 mm and 0.016 mm, and for the drainage sand was 2.2mm and 2.9 mm respectively. The centrifuge tests were at 70g with a water plus hydroxypropyl-methylcellulose fluid with a viscosity of 35 times that of water. Simulated earthquake motion was applied during flight using a hydraulically actuated shaker. All dimensions, time histories, etc. given in this paper are in the scaled prototype dimensions rather than the actual

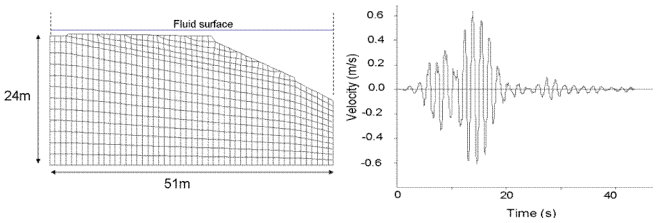

Fig. 6. Grid and time velocity time history used for centrifuge predictions

centrifuge dimensions. During centrifuge spin-up there are large changes in effective stress which result in 'stress densification' of loose sandy soils [19]. This was accounted for in the analyses. A typical grid and input earthquake record is shown in prototype scale in (Fig. 6). The side forces that would occur within the centrifuge box were accounted for during the dynamic analysis by applying internal nodal forces that were a function of the out-of-plane effective stress (σ'_z) times the sidewall friction coefficient. Normalized velocities were used to give the direction of the internal nodal forces.

Liquefaction flow failure was observed in the tests which included the low permeability silt barrier and higher levels of shaking. Flow failure generally did not occur when the barrier was absent or if drainage trenches were placed through the barrier. Similar behavior has been observed by others [8][1][9].

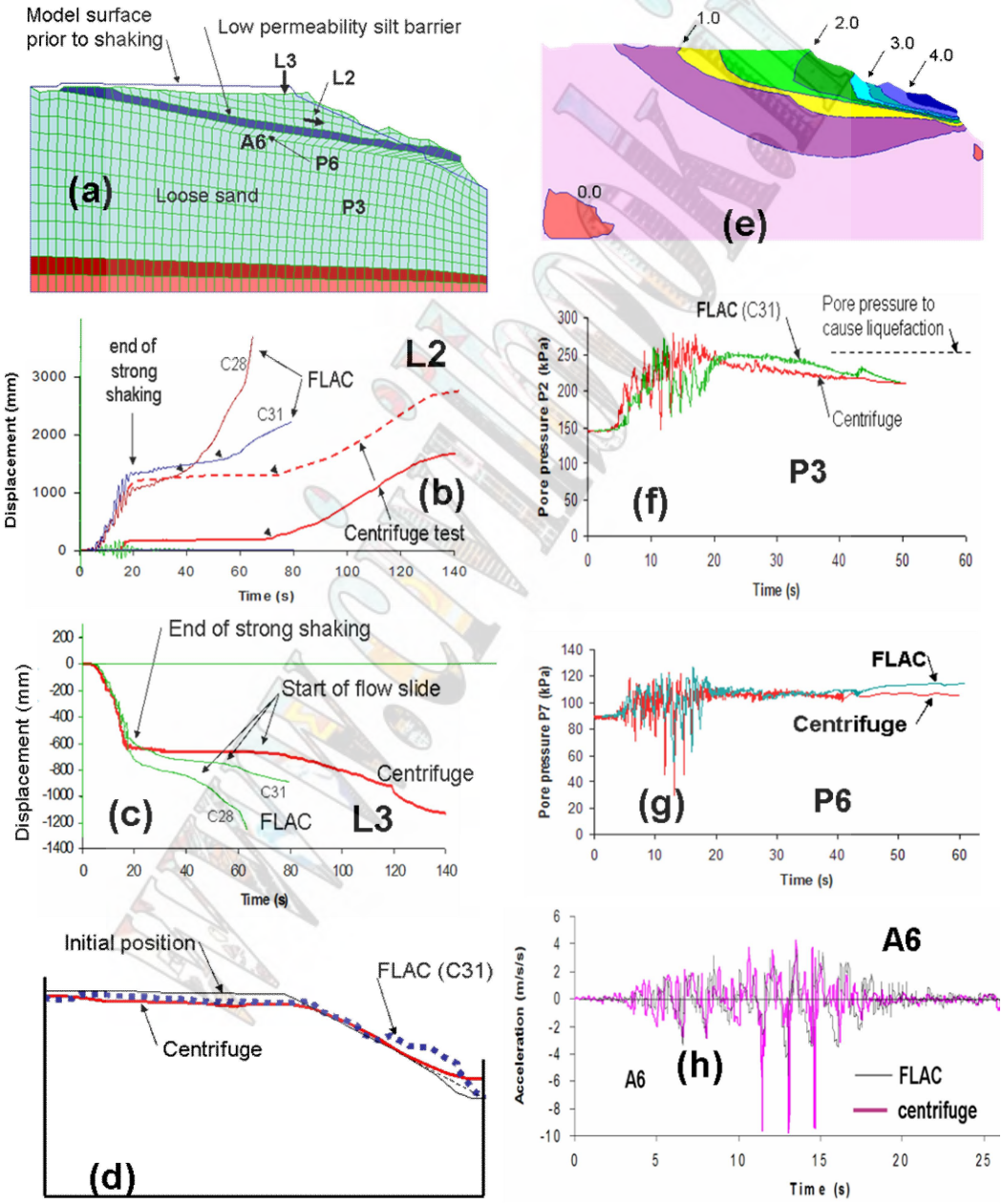

Fig. 7. Comparison of Centrifuge tests and numerical results for profile with low permeability silt barrier (COSTA-C). (a) displaced grid, (b) Horizontal displacement of sliding block over barrier (for the centrifuge data the solid line is measured & the dashed line is corrected to better match final displacements), (c) vertical displacement at crest, (d) centrifuge & numerical surface profiles, (e) calculated lateral displacement contours in meters, (f) & (g) pore pressure time histories at P3 & P6, (h) acceleration time history at A6.

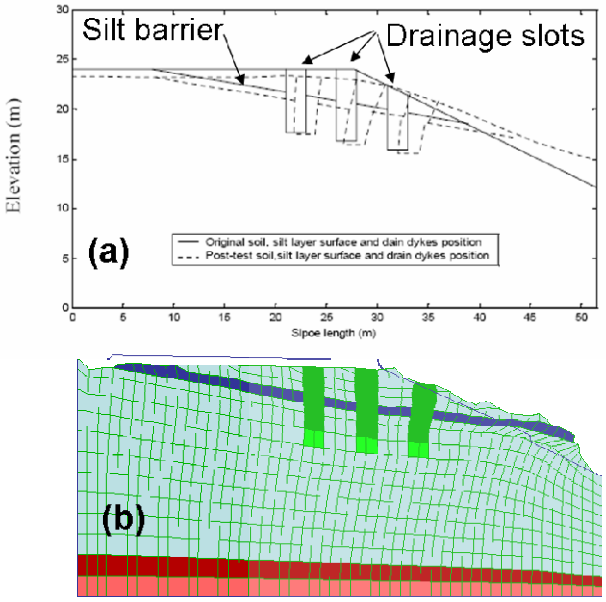

Fig. 8. (a) Initial and displaced profile of centrifuge test CT5 with three drainage slots (b) numerical analysis of same.

Fig. 7 compares centrifuge and numerical results for the COSTA-C test [20] that included a low permeability barrier. In the COSTA-C test a flow slide occurred at the barrier interface at approximately 50s after end of strong shaking. Figs. 8 shows displaced profiles for a similar model, CT5 [21] that had permeable drainage slots through the silt barrier. With drainage slots (Figs. 8 & 9) all deformation occurred during strong shaking (t<20s) and flow deformation is prevented.

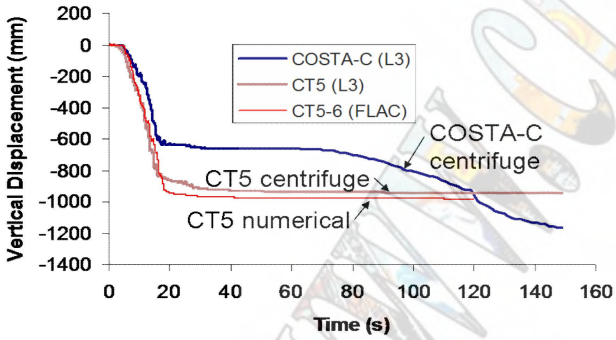

Fig. 9. Comparison of vertical displacement near crest with (CT5) and without (COSTA-C) drainage slots. Post-shaking flow initiated in the COSTA-C test at approximately 70s.

MITIGATION OF FLOW LIQUEFACTION

As illustrated in Fig. 9, drainage is an effective means of mitigating low permeability barrier induced flow sliding. However, even with drains significant deformations may still occur during strong shaking, but post-shaking flow movements do not occur. If the movements induced during heavy shaking are of concern then ground densification, possibly combined with drainage measures, or use of dowels combined with drains could be considered. These suggested ground improvement measures are schematically illustrated on Fig. 10. Mitigation with relief wells (drains) only (Fig. 10(b)) will prevent the occurrence of flow slides but large movements may still occur during strong shaking. Ground densification alone will reduce movements during strong shaking however post-shaking migration of pore water may lead to weak zones. Combining ground densification with some relief wells (Fig. 10(c)) is an optimum solution as it reduces movements during strong shaking and prevents pore pressure build-up within the densified block. Piles may be used as dowels and for compaction. This is useful in interlayered silt and sand soils that do not respond well to normal densification methods. Inclusion of relief wells between the piles (Fig. 10(d)) improves the performance by mitigating pore pressure build-up.

One of the strengths of numerical analyses is the ability to assess the effectiveness of various mitigative measures and the ability to optimize the designs by conducting parametric analyses. Numerical analyses also bring considerable insight on behavior mechanisms. This procedure was used for the seismic upgrade design of George Massey tunnel in Greater Vancouver, British Columbia [22][23]. The 1.5 km long submerged-tube tunnel underlies the Fraser River and is buried in loose liquefiable sand. Effective stress numerical analyses were used to demonstrate that drains and densification placed adjacent to the tunnel could mitigate excessive upward and lateral tunnel displacements. Good correlation was obtained between the numerical analyses and those from centrifuge tests made to calibrate the model. Construction of the seismic upgrade measures is currently in progress.

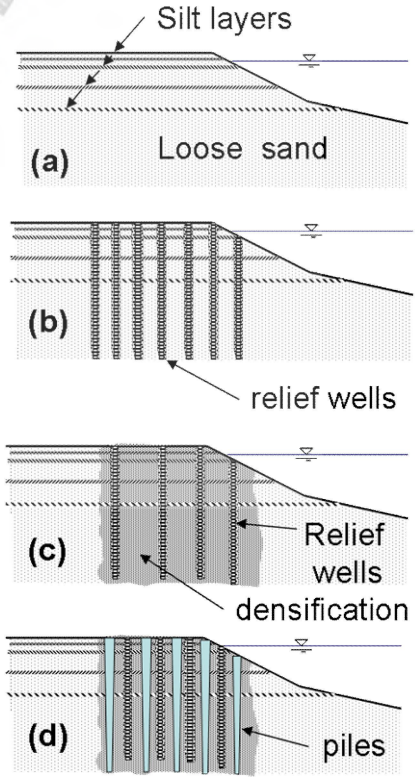

Fig. 10. Mitigation schemes for hypothetical water edge with low permeability silt layers

CONCLUSIONS

The Liquefaction induced displacements and flow failures observed in the centrifuge tests have been successfully simulated numerically using the UBCSAND model within the commercially available program FLAC. UBCSAND is an effective stress model with full coupling between mechanical behavior and groundwater flow.

Special features in the numerical model for the back-analyses of the centrifuge tests include: allowance for stress densification during spin-up, allowance for variation in fluid modulus with saturation and confining pressure, inclusion of internal force vectors to account for side friction within the centrifuge container, and a volumetric-strain-triggered-dilation-cut-off to account for the localization or element size effects that occur immediately below the low permeability barrier.

This paper examines the flow liquefaction modeling aspects and procedures for mitigating the effects of low permeability barriers within sand soil deposits. The constitutive model, analysis procedures and comparison of numerical analyses predictions to those of the centrifuge tests are described. One of the strengths of numerical analyses is the ability to assess the effectiveness of various mitigative measures and the ability to optimize the designs by conducting parametric analyses. Numerical analyses also bring considerable insight on behavior mechanisms.

The inclusion of drains through the low permeability layers is shown to be an effective measure for mitigation of post-earthquake flow failure.

ACKNOWLEDGMENTS

The authors acknowledge the support from the Ministry of Transportation UBC Professional Partnership program, the Canadian Council of Professional Engineers, Trow Associates Inc., and the National Scientific and Engineering Research Council through Strategic Liquefaction Grant No. NSERC 246394, and NSERC COSTA No. 03608-CG068625. Centrifuge tests were conducted by Ryan Phillips, Minqiang Tu, and Stephen Coulter at C-CORE, and their expertise and assistance is appreciated. Laboratory testing by D. Wijewickereme & S. Sriskandakumar was an integral part of the work.

REFERENCES

[1] Kokusho, T., "Current state of research on flow failure considering void redistribution in Liquefied deposits," *Soil Dynamics and Earthquake Engineering* 23, 585-603, 2003.

[2] Hamada, M., "Large ground deformations and their effects on lifelines: 1964 Niigata Earthquake" *Proc., Lifeline Performance during Past Earthquakes, V. 1: Japanese Case Studies Tech. Rep NCEER-92-0001,* Buffalo, N.Y., 3/1-3/123, 1992.

[3] Seed, H.B., "Design problems in soil liquefaction," *J. Geotechnical Eng. Div., ASCE*, Vol. 113, No.8, 827-845, 1987.

[4] Ishihara, K., "Post-earthquake failure of a tailings dam due to liquefaction of the pond deposit," *Proc. Inter. Conf., Case Histories in Geotechnical Engineering*, Rolla, Missouri, V. 3, pp. 1129-1143, 1984..

[5] Poulos, S.J., Castro, G., and France, W., "Liquefaction evaluation procedure," *J. Geotechnical Engineering Div., ASCE*, Vol. 111, No.6, pp. 772-792, 1985.

[6] Vaid, Y.P., and Eliadorani, A., "Instability and liquefaction of granular soils under undrained and partially drained states," C*anadian Geotech. J.* Vol. 35, pp. 1053–1062, 1998.

[7] Yoshida, N., and Finn, W.D.L., "Simulation of liquefaction beneath an impermeable surface layer," Soil Dyn. Earthquake Eng. 19, pp. 333-338, 2000.

[8] Kokusho, T., "Water film in liquefied sand and its effect on lateral spread," *J. Geotech. Geoenviron. Eng.* 125(10), pp. 817–826, 1999.

[9] Kulasingam, R., Malvick, E.J., Boulanger, R.W., and Kutter, B.L., "Strength loss and localization of silt interlayers in slopes of liquefied sand," *J. of Geotech. Geoenviron. Eng., ASCE*, Vol. 130, No. 11, November 1, pp. 1192-1202, 2004..

[10] Seid-Karbasi, M., and Byrne, P.M., "Liquefaction, lateral spreading and flow slides," Proc. 57th Canadian Geotechnical Conf., Session 2c, pp. 23-30, 2004.

[12] Byrne, P.M., Park, S.S., Beaty, M., Sharp, M., Gonzalex, L., Abdoun, T., "Numerical modeling of dynamic centrifuge tests," *13th World Conference on Earthquake Engineering, Vancouver, B.C.*, paper 3387, 2004.

[13] Seed, R.B., and Harder, L.F., Jr., "SPT-based analysis of cyclic pore pressure generation and undrained residual strength.," *In* Proc. of the H.B. Seed Memorial Symposium, Bi-Tech Publishing Ltd., Vol. 2, pp. 351–376, 1990.

[14] Olson, S. M. and Stark, T. D., "Liquefied strength ratio from liquefaction flow failure case histories," Canadian Geot. J., Vol 39, pp. 629–647, 2002.

[15] Beaty, M., and Byrne, P.M., "An effective stress model for predicting liquefaction behaviour of sand," Geotechnical Earthquake Engineering and Soil Dynamics III. P. Dakoulas, M. Yegian, and R Holtz (eds.), ASCE, Geotechnical Special Publication 75 (1), pp. 766-777, 1998.

[16] ITASCA "FLAC - Fast langrangian analysis of continua, Version 4.0 ITASCA Consulting Group Inc., Minneapolis, Minnesota, 2002.

[17] Sriskandakumar, S., "Cyclic loading response of Fraser River sand for numerical models simulating centrifuge tests," M.A.SC. Thesis, Civil Eng. Dept., University of British Columbia, Vancouver, B.C., 2004.

[18] Atigh, E. and Byrne, P.M., "Liquefaction flow of submarine slopes under partially undrained conditions: an effective stress approach," *Canadian Geotech. J.*, V. 41, pp. 154-165, 2004.

[19] Park and Byrne, "Stress densification and its evaluation," 2004, Canadian Geotech.l J., *Vol.41(1), pp. 181-186,* 2004.

[20] Phillips, R., and Coulter, S., "COSTA-C Centrifuge Test Data Report", C-CORE Report R-04-082-075, January, 2005.

[21] Phillips, R.,, Tu, M., and Coulter, S., "C-CORE. Earthquake Induced Damage Mitigation from Soil Liquefaction. Data report – Centrifuge Test CT5". Contract Report Prepared for University of British Columbia. C-CORE Report R-04-068-145, December, 2004.

[22] Naesgaard, E., Yang, D., Byrne, P.M. and Gohl, B., "Numerical analyses for the seismic safety retrofit design of the immersed-tube George Massey Tunnel," *Proc. 13th World Conf. on Earthquake Engineering*, Vancouver, paper 112, August, 2004.

[23] Yang, D., Naesgaard, E., and Gohl, B. "Geotechnical seismic retrofit design of George Massey Tunnel." *Proc. 12th Pan-American Conf. on Soil Mechanics and Geotech.l Eng., Cambridge*, USA, June 22-26, pp. 2567 – 2574, 2003,

Flow liquefaction due to mixing of layered deposits

Ernest Naesgaard[1], Peter M. Byrne[1]
[1]*Department of Civil Engineering, University of British Columbia, Vancouver, Canada*

Abstract

Many natural and man-made soils are layered with fine and coarse seams. The inclusion of low permeability barriers and pore water redistribution can produce weak zones of high void ratio or even water interlayers. Another mechanism that can also give very weak zones is soil mixing. When fine and coarse layers mix the resulting "residual" undrained shear strength is much lower than that of the individual layers at the same void ratio. At the Mufulira Mine medium dense layered sandy silt and silty sand tailings mixed and flowed as a liquefied mass long distances through cracks in the underlying rock. A similar mechanism may account for the low "residual" strength back-calculated for end-of-failure of the Lower San Fernando dam. Under specific grain size conditions cyclic shear can readily induce soil mixing. Rudimentary cycle shear tests were conducted within a 12mm internal diameter vinyl tube. These tests showed that layered cohesionless soils will readily mix under cyclic loading when the filter-like criterion ($(D_{15})_{coarse\ layer}$ / $(D_{85})_{fine\ layer}$) is greater than three to four, but will be difficult to mix when the ratio is less.

Keywords—*Cyclic shear, flow, layered, liquefaction, mixing*

INTRODUCTION

For some time there has been discrepancy between the residual shear strength of liquefied sands as measured from undrained strengths in the laboratory and that determined from back-analysis of field case histories [1], [2]. A similar discrepancy occurs between liquefaction behaviors in the centrifuge as compared to field conditions. Very loose homogeneous sand samples can not be made to flow within centrifuge tests, whereas there are numerous examples of flow failure in the field, some with very large run-out distances. The reason for the difference between laboratory and field performance is postulated to be due to the field deposits not being homogeneous and not necessarily behaving in an undrained manner. In undrained element tests in the laboratory, sand tends to dilate when sheared monotonically at large strains. This dilation results in a strength gain and therefore little or no flow slide movement. Recent work [3], [4] & [5] has shown that the inclusion of low permeability barriers within a sand deposit results in the trapping of pore water and the formation of thin layers with very high void ratio and low to zero shear strength. These low strength inter-layers have helped to explain the low residual strengths back-analyzed from some field case histories. The mechanism also helps explain the phenomenon of failures occurring after the end of earthquake shaking. In this paper we are promoting another mechanism for flow liquefaction that may occur independently and/or together with that discussed above. This mechanism is soil mixing.

Natural soils and hydraulic fills are often layered due to variations in the depositional environment. It is postulated that when a fine layer overlies a coarse layer and the fine layer does not meet suitable filter criteria with regard to the coarse layer, that upon being disturbed (by landslide or earthquake shaking) the fine particles will migrate into the voids of the coarse particles as illustrated in Fig. 1. This gives net volumetric strains much larger than that which would occur due to shaking of the individual homogeneous layers and can result either in the formation of a water film (Fig. 1b) or in a mixed soil with near zero residual shear strength (Fig. 1c).

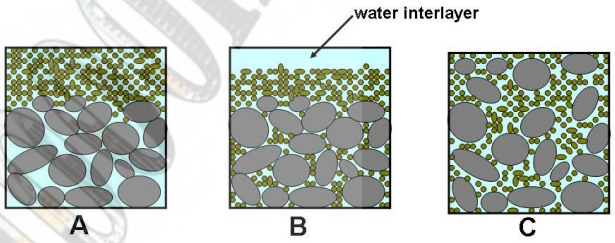

Fig. 1: Cartoon illustrating the effects of soil mixing. Elements 'A', 'B' and 'C' have the same (number and volume) of large and small particles. 'A' is the element with a fine layer over a coarse layer prior to disturbance. 'B' represents the case where the fine particles fall into the voids between the large particles and leave a water filled void or interlayer at the top of the element. 'C' represents the case where the particles mix evenly and the larger particles move into a looser arrangement. Both 'B' and 'C' will have significantly lower shear strength then 'A' if mixing is not allowed.

This phenomenon has been observed in the field and has been recreated by simplistic shear tests in the laboratory.

MUFULIRA MINE CASE HISTORY

Byrne [6], [7] & [8] postulated soil mixing as the reason for the flow of tailings into the Mufulira mine in Zambia. At this site a tailings pond overlay underground mine workings as shown schematically in Fig. 2. In 1968 the underground hanging walls collapsed and sink holes with steep side slopes formed in the tailings pond with two cases of minor inflow of tailings into the underground workings. Then in 1970 a large sink hole formed and

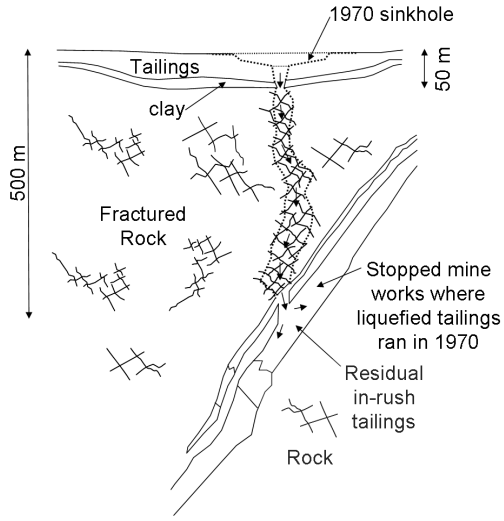

Fig. 2: Profile through 1970's Mufulira tailings liquefaction failure

Fig. 3: Photograph of 1970 Mufulira sink hole (from [9])

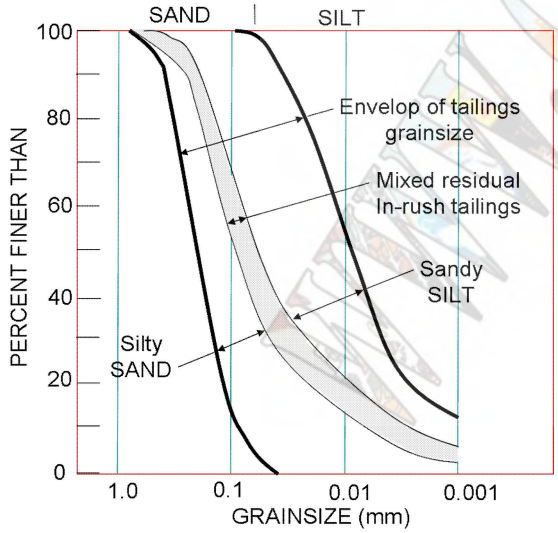

Fig. 4: Grain-size of Mufulira tailings [7], [11].

failed back along a very shallow angle of 10 degrees (Fig. 2 & 3) to develop a diameter of over 250 m. One million tons of tailings flowed into the underground mine

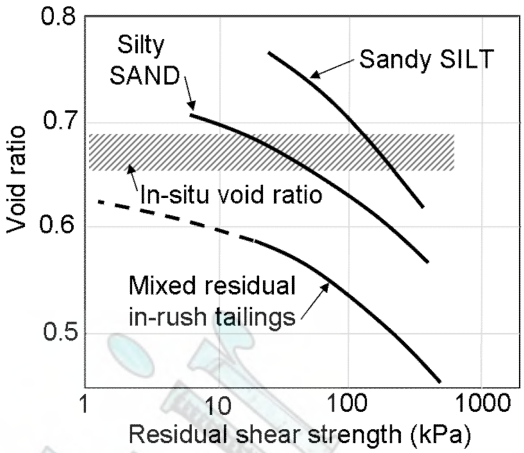

Fig. 5: Void ratio versus residual shear strength (τ_{res} = $(\sigma_1-\sigma_3)/2$) relationship for sandy silt, silty sand, and mixed residual in-rush tailings. Note how the mixed tailings have essentially zero shear strength at the in-situ void ratio.

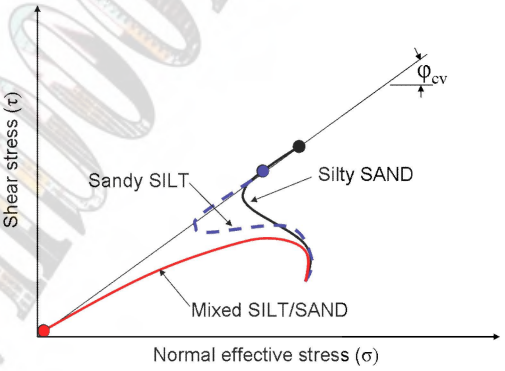

Fig. 6: Cartoon showing undrained triaxial compression stress path for silty *sand*, sandy *silt* and *mixed silt-sand* at same void ratio and initial stress state.

workings killing 89 people [9]. From a study in 1988/89 [7], [10] & [11] it was noted that the tailings within the overlying pond comprised of alternating layers of sandy silt and coarser silty sand, whereas in the tailings within the core of the sink holes and those that had flowed into the underground mine workings (residual in-rush or mixed tailings), were the same materials but highly mixed and homogeneous (Fig. 4). The silty sand made up about 65% of the total deposit, and sandy silt the remaining 35%. The layers were clearly visible with thickness averaging 100 to 150 mm but varying from less than 50mm to 250mm. Water contents were in the range of 21 to 34% with an average of 25% and average in-situ void ratio was around 0.65 to 0.7. An extensive series of undrained triaxial compression and extension tests on the soil of the individual layers gave high residual undrained strengths and could not account for the liquefaction observed at the site. However, when the fine and coarse

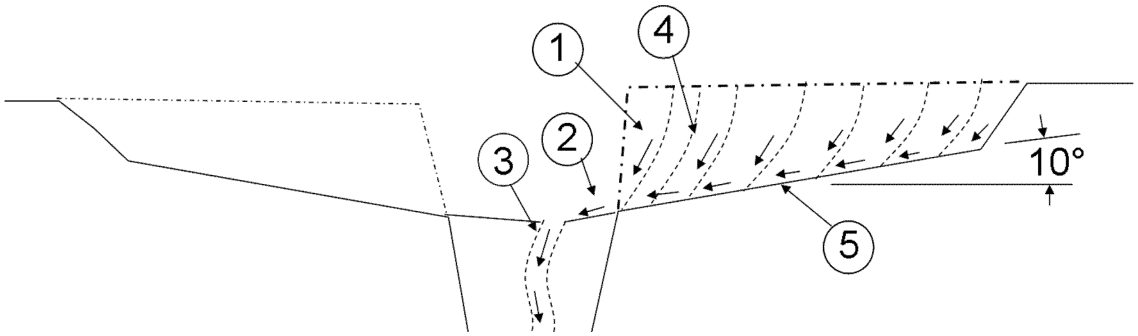

Fig. 7: Postulated progressive failure mechanism of 1970 sinkhole. (1) Sides of initially step sided sinkhole failes, (2) as soil slides to bottom of slope the layers mix and due to the mixing loose nearly all strength (liquefy), (3) the liquefied soil flows away into mine workings, (4) mechanism is repeated giving a progressive failure mechanism, and (5) the final stable slope at shallow 10° angle.

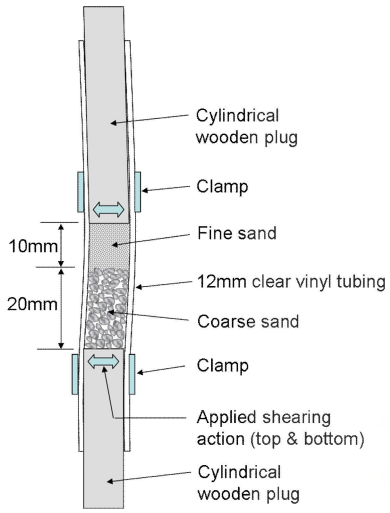

Fig. 8: Rudimentary simple shear test with saturated layered sample

materials were mixed at the same average in-situ void ratio corresponding to an "average" undrained state, the resulting soil had essentially zero strength (Fig. 5 & 6). It is postulated that the sides of the 1970 sinkhole were initially steep and then failed progressively as illustrated in Fig.7. As the soil on the initially steep sided sinkhole failed the silt and sand layers mixed, leading to near complete loss of strength that allowed it to flow as liquefied slurry into the underground mine workings.

RUDIMENTARY LABORATORY CYCLIC SHEAR TESTS

Rudimentary cyclic shear tests have been conducted in order to demonstrate that earthquake or other cyclic shear may also induce mixing in susceptible layered soils. A clear vinyl tube of 12mm inside diameter with plugged ends, as illustrated in Fig. 8, was used for the tests. The samples were prepared by removing the plug from one end, filling the tube with water, and then pluviating the sand through the water. Once a layer of sufficient thickness was in place the surface of the sand was tapped very lightly with a rod to get the surface level, then another layer was placed in a similar manner if required, or the plug was placed and clamped. The sample is then manually sheared by grabbing the top and bottom and pushing it back and forth while keeping the top and bottom of the sample parallel. Sample heights ranged from 27 to 40mm. Strain on typical cycles is estimated to be in the range of 10% to 20%. Table 1 summarizes the configurations and results of six typical tests. The grain size distributions of the sands and glass beads used are shown in Fig. 9. Migration of the fine sand particles into the voids of the underlying coarser material was readily evident during test "A". The thickness of the water layer that formed at the top of the sample stabilized with approximately 20 shear cycles (Fig. 10). When the same test as "A" was carried out with homogeneous fine sand only or coarse sand only (tests "B" and "C") then the induced volumetric strain was appreciably smaller (Fig. 11). Tests "D" (Fig. 12) and "E" shows that the ease of mixing becomes substantially more difficult as the size difference between the coarse and fine layer decreases. Test "F" illustrates that cyclic mixing does not readily occur without gravity or some other mechanism to move the fines into the coarser layer.

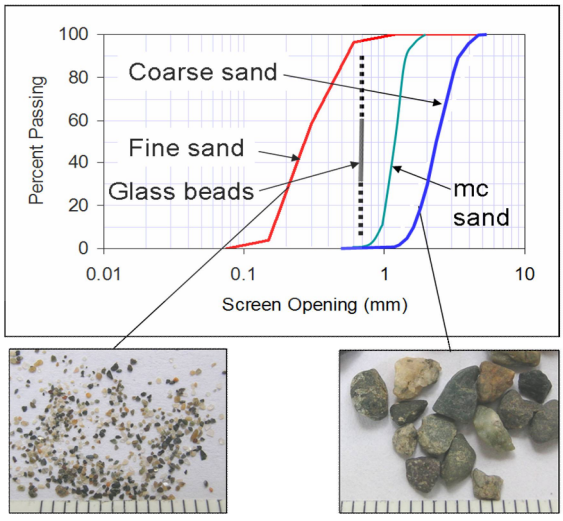

Fig. 9: Grain size of fine and coarse sand used in rudimentary simple shear tests.

Table 1 Summary of Rudimentary Cyclic Shear Tests

Test	Sample Description (prior to shearing)[a]	Post-shearing		$\frac{(D_{15})_{coarse\ layer}}{(D_{85})_{fine\ layer}}$ [c]	Remarks
		water film thickness (mm)	Volumetric strain [b] (%)		
A	13mm fine sand over 20mm coarse sand	5.5	17	1.7/0.5= 3.4	Fine and coarse sand mixed in approximately 20 shear cycles (Fig. 10);
B	36 mm fine sand	0.5	1.4	NA	Sample given 50 shear cycles (Fig. 11)
C	36mm coarse sand	0.5	1.4	NA	Sample given 50 shear cycles (Fig. 11)
D	15mm glass beads over 25mm coarse sand	0 to 3.5	0 to 9	0.8/0.5= 1.3	No water layer or mixing with 20 cycles, but sample mixed when given over 100 shear cycles and light tapping of specimen (Fig. 12)
E	10mm fine sand over 20mm medium coarse (mc) sand	1 to 4	3 to 13	1.0/0.5= 2	Minimal mixing with 20 cycles, but sample mixed when given over 100 shear cycles & light tapping of specimen.
F	24mm coarse sand over 12mm fine sand[d]	1.0	2.8	1.7/0.5= 3.4	Minimal mixing with over to 100 shear cycles

[a] Dimensions given are thickness of layers. Sand gradations are shown on Fig. 9.
[b] Volumetric strain = water film thickness/total thickness x 100
[c] D_{15} = particle diameter with 15% of particles smaller; D_{85} = particle diameter with 85% of particles smaller
[d] Note in this case the coarse sand is above rather than below the fine sand.

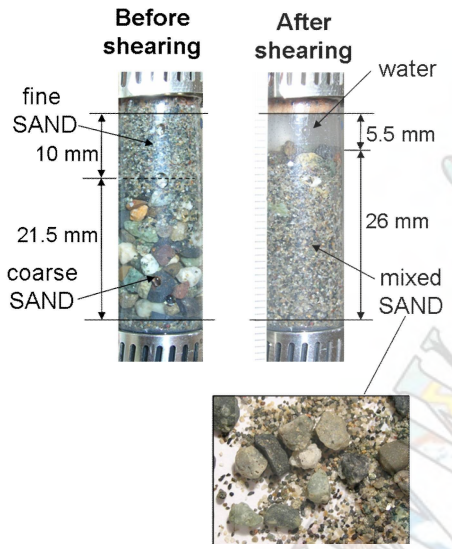

Fig. 10: Test "A" before and after cyclic shearing

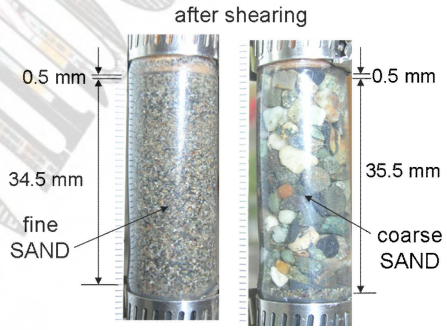

Fig. 11 Post-shearing for non-layered tests "B" & "C"

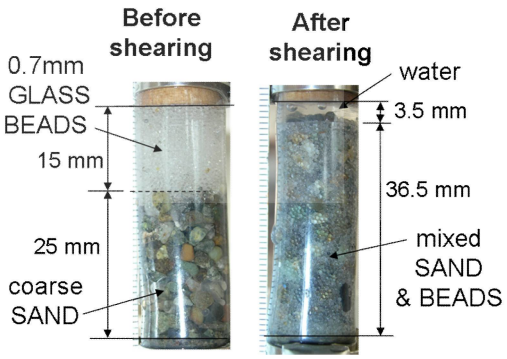

Fig. 12: Before and after cyclic shearing for test "D" with glass beads and coarse sand.

DISCUSSION

The susceptibility to mixing induced strength loss is deemed to be dependent on particle and layer properties (particle shape, grain size gradation of individual layers, layer thickness), in-situ effective stresses, the disturbing forces (hydraulic gradient, gravity, number & magnitude of strain cycles), orientation of layers relative to the disturbing forces, saturation, and drainage constraints (permeability, presence of low permeability barrier and rate of disturbance). Several conditions must be met

before mixing and the resulting dramatic reduction in shear strength will occur.

1) There has to be alternating layers of coarse and fine grained soil. Ideally the layer thicknesses should be such the available volume of fine grain soils will fit within voids of the coarse grained layers.

2) There has to be a disturbing force that will initiate the mixing. This could be a high hydraulic gradient, gravity induced shear (slope failure), cyclic loading (from an earthquake, wind, waves or machine vibrations), or a combination of these.

3) There has to be a substantial volume of water present in the voids and this water should not be able to escape quickly so that mixing results in low effective stresses (liquefaction) rather than drainage and consolidation.

4) There has to be freedom for the fine particles to migrate into the voids of the coarser layer. Ideally the fine particles should fit between the voids of the coarse layer. The ease with which mixing occurs will be related to a criterion similar to the $((D_{15})_{filter} / (D_{85})_{soil}) < 4$ to 5 criteria used to prevent internal erosion when designing granular filters. From the rudimentary cyclic shear tests it is concluded that if the ratio $((D_{15})_{coarse\ layer} / (D_{85})_{fine\ layer}) > 3$ to 4 then cyclic mixing will readily occur whereas if the ratio is less than this , the soils will not mix easily. Cohesion and/or cementation will also hinder mixing.

In the rudimentary cyclic shear tests mixing progresses with each loading cycle until the sample was totally mixed. The cyclic shearing action dislodges the fine particles from the soil skeleton in the vicinity of the contact with the coarse layer and then gravity carries the fine particles into the voids of the coarse layer. When the coarse layer is above the fine layer (test "F") the shearing action still dislodges the fine particles from the soil skeleton near the interface with the coarse layer, however in this case there is no mechanism to move the loosened fine particles up into the coarse layer and therefore mixing does not occur or is minimal. In other situations the fine particles may be moved by a hydraulic gradient rather than gravity. With sufficient hydraulic gradient mixing could occur between vertical boundaries (such as the core of a dam) or with fine particles moving into an overlying coarse layer.

Mixing can occur independently of, or together with, the low permeability barrier/pore water migration mechanism [3], [4][5] that also gives water interlayers and/or very low soil strengths zones. If mixing and pore water redistribution occur together then the strength loss would be even more pronounced.

Mixing may result in a water interlayer as observed in the rudimentary cyclic shear tests and illustrated in Fig. 1b, or just in an extremely loose liquefied soil as illustrated in Fig. 1c and the Mufulira case history.

Others [12], [13], have conducted cyclic triaxial tests on layered silt–sand samples without observing any significant mixing effects during the tests. In both cases the layered samples behaved similar to that of homogeneous samples of the individual layers. The reason for mixing not occurring in these cases may be due to the grain size criteria $(((D_{15})_{coarse\ layer} / (D_{85})_{fine\ layer}) > 3$ to 4) not being met, possibly to the presence of some minor cohesion, and possibly to the triaxial loading not being as conducive to mixing as simple shear. Remolding (mixing) was postulated by [12], [6] as a possible reason for the low "residual strength" observed at the end of flow failure of the Lower San Fernando Dam. Triaxial tests by [12] (Fig. 13) showed that the residual strength of the mixed soil was 4 times less than the residual strength of the layered soil with the same void ratio.

CONCLUSIONS

Many natural and man-made hydraulically placed soils are layered. When the fine and coarse layers mix the resulting "residual" shear strength is much lower than that of the individual layers at the same void ratio. This mixing is an explanation for the flow liquefaction observed at the Mufulira Mine site and possibly for the low end-of-failure residual shear strength back-calculated for the Lower San Fernando Dam failure.

Rudimentary cyclic shear tests carried out in a 12mm internal diameter vinyl tube demonstrate that cyclic shear similar to that which would occur in an earthquake can induce soil mixing. The ratio of the grain size of the coarse and fine layers is shown to be a key factor in a layered soils susceptibility to mixing. A preliminary postulation is that cohesionless soils will readily mix when $((D_{15})_{coarse\ layer} / (D_{85})_{fine\ layer}) > 3$ to 4.

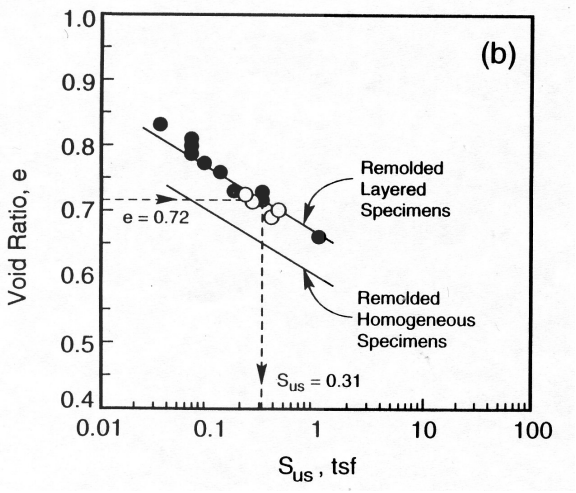

Fig. 13: Steady state void ratio vs residual strength (S_{us}) for reconstituted (remolded) Lower San Fernando Dam soil. Note that the residual strength for the combined (mixed) homogeneous specimens is much lower (by factor of 4) than that of the layered not-mixed specimens. From [12].

ACKNOWLEDGMENTS

The authors wish to acknowledge the support from the Ministry of Transportation/UBC Professional Partnership program, the Canadian Council of Professional Engineers, Trow Associates Inc., and the National Scientific and Engineering Research Council through Strategic Liquefaction Grant No. NSERC 246394. We also wish to acknowledge the insight from the work on gap-graded filters by R.J. Fannin and R. Moffat, and thank M. Seid-Karbasi for providing references on laboratory tests with layered soils.

REFERENCES

[1] Poulos, S.J., Castro, G., and France, W., "Liquefaction evaluation procedure," *J. Geotechnical Engineering Div., ASCE*, Vol. 111, No.6, 772-792, 1985.

[2] Seed, H.B., "Design problems in soil Liquefaction," *J. Geotechnical Engineering Div., ASCE*, Vol. 113, No.8, 827-845, 1986.

[3] Kokusho, T., "Water film in liquefied sand and its effect on lateral spread," *J. Geotech. Geoenviron. Eng.* Vol. 125 No. 10, 817–826, 1999.

[4] Kokusho, T., "Current state of research on flow failure considering void redistribution in Liquefied deposits," *Soil Dynamics and Earthquake Engineering* 23, 585-603, 2003.

[5] Kulasingam, R., Malvick, E.J., Boulanger, R.W., and Kutter, B.L., "Strength loss and localization of silt interlayers in slopes of liquefied sand," *J. of Geotech. Geoenviron. Eng., ASCE,* Vol. 130, No. 11, Nov., 1192-1202, 2004.

[6] Byrne, P.M., and Beaty, M., "Postliquefaction shear strength of granular soils: Theoretical/conceptual Issues [Keynote Paper],' In *Proceedings of the Workshop on Shear Strength of Liquefied Soils*, Urbana, NSF Grant CMS-95-31678, pp 9-39, 1997.

[7] Barrett, J.R., Byrne, P.M, "Review of mining below TD#3, Mufulira Mine, 1988,". Report to Mines Safety Department, Republic of Zambia and Zambia Consolidated Copper Mines Ltd. 1988.

[8] Byrne, P.M., "Evaluation and Use of Residual Strength in Seismic Safety Analysis of Embankments," Earthquake Spectra, Vol. 7, No. 1, Feb., pp. 145-148. 1991.

[9] tailings.info, "Mufulira Mine tailings breach, Zambia," On-line at http://www.tailings.info/mufulira.htm, 2005.

[10] Byrne, P.M., "Liquefaction review report, Mufulira mine, Zambia," Report to Mines Safety Department, Republic of Zambia and Zambia Consolidated Copper Mines Ltd., 1989.

[11] Horsfield, D.W., and Been, K., "Field and Laboratory Testing of Tailings Dump #3, Residual Inrush and Sandfill Tailings, Mufulira Copper Mine," Golder Associates report to Zambia Consolidated Copper Mines Ltd., 1989.

[12] Baziar, M.H., and Dobry, R., "Residual strength and large deformation potential of loose silty sands," *J. Geotech. Engineering Div.*, ASCE, Vol. 121 (12), pp. 896-906, 1995.

[13] Amini, F., and Qi, G.Z., "Liquefaction testing of stratified silty sands," *J. of Geotech. Geoenviron. Eng.*, ASCE, Vol. 126, No. 3, March, pp. 208-217, 2000.

Two Criteria for Liquefaction-induced Flow

N. Yoshida[1], S. Yasuda[2], Y. Ohya[3]
[1]*Department of Civil and Environmental Engineering, Tohoku Gakuin University, Miyagi, Japan*
[2] *Department of Civil and Environmental Engineering, Tokyo Denki University, Saitama, Japan*
[3]*Structural Engineering Department, JIP Techno-Science Corp., Tokyo, Japan*

Abstract

Two criteria are defined for explaining liquefaction-induced flow based on past researches. The fact that liquefaction-induced flow has occurred even in nearly level ground or under very small existing stress in Japan is emphasized at first. Then conventional concept of the liquefaction-induced flow, in which a stability criterion is defined by comparing existing stress and residual stress, is introduced, and is shown not to be able to explain liquefaction-induced flow at nearly level ground because residual stress is much larger than existing stress. A new criterion, named a deformation criterion, is developed in order to explain them, and is shown to be consistent with past researches such as behaviors during liquefaction and stress-strain curve after liquefaction. The difference between two criteria is that displacement cannot be predicted in the former case whereas it can be evaluated in the latter case, although we can call both of them as failure because large deformation is expected.

Keywords—*Liquefaction, post liquefaction, liquefaction-induced flow, stability, deformation*

INTRODUCTION

Soil liquefaction has been one of the predominant factors to cause damage to various structures under earthquakes. Typical damages caused by the soil liquefaction are settlement of heavy super structures and uplift of light underground structures. They were caused because soil looses bearing capacity or intergranular force by the excess porewater pressure generation under cyclic loading such as an earthquake. It is well known that these types of damage were firstly recognized at the 1964 Niigata earthquake, which triggered research of soil liquefaction.

Another important feature associated with soil liquefaction was found after the 1983 Nihonkai-chubu earthquake. Large horizontal displacement of the order of several meters was identified to occur in the widespread liquefied area by comparing the aerial photos taken before and after the earthquake [1]. Case histories to the past and subsequent earthquakes have shown that same phenomena had occurred in the many earthquakes [2], and it was named liquefaction-induced flow [3][4]. Subsequent researches clarified that two types of geotechnical conditions, shown in Figure 1, were responsible for the liquefaction-induced flow. When the ground surface or top of the liquefied layer tilted as shown in Figure 1(a), surface ground moves downward along the slope. On the other hand, when quay wall fails or moves toward the sea or river in the case Figure 1(b), the back ground move toward the quay wall. Among two geotechnical conditions, it is easy to recognize the mechanism of the liquefaction-induced flow in the latter case because it is clear that failure or movement of the quay wall triggered displacement of the back ground. The mechanism of the former case, however, was not clear because horizontal displacement of order of several meters occurred in almost level ground, as explained in the subsequent section, in Japan.

Therefore, researches on the liquefaction-induced flow started in order to investigate why such large displacement is possible in almost level ground by researchers mainly in Japan. Many mechanisms were considered and their applicability was investigated. Finally very low or zero stiffness region which appears when soil liquefies is found to be responsible. Discussion is still undergoing whether liquefied soil behaves as solid or liquid. History of the research is compiled in Ref. [3], for example.

Recently, ISO on earthquake design code is going to be compiled [5]. Here, liquefaction-induced flow was originally defined as "If residual strength of a liquefied soil (i.e. shear strength of the soil after failure due to liquefaction) can be evaluated for the liquefiable zones within the earth structure, the possibility of a flow slide

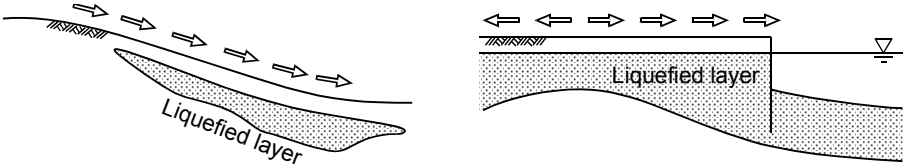

(a) Tilted surface (b) Lateral open space

Figure 1. Geotechnical condition of liquefaction-induced flow

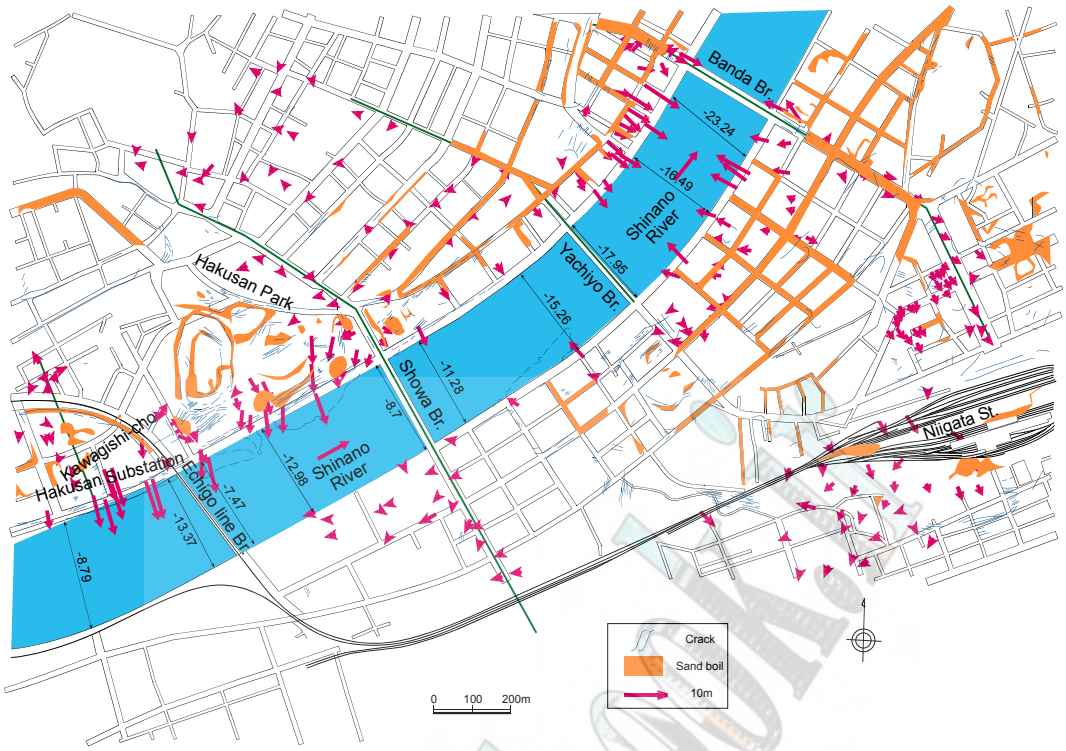

Figure 2. Permanent ground displacement in Niigata city during the 1964 Niigata earthquake [6]

can be estimated from a static limit equilibrium analysis as follows." This description treats the liquefaction-induced flow as stability criteria. In other words, Infinite deformation or very large deformation is possible if existing stress is greater than the residual stress. Although fairly long time has passed when the original draft was first published, it did not change. It indicates that the concept based on a stability criterion is commonly accepted feature.

We intend to make another aspect of the liquefaction-induced flow, which is named deformation criteria, in this paper based on our and other researcher's experiences and researches.

LIQUEFACTION-INDUCED FLOW IN JAPAN

Liquefaction-induced flow was first found after the 1983 Nihonkai-chubu earthquake [1]. A technique to measure horizontal displacement after the earthquake by comparing the aerial photos taken before and after the earthquake brought this fruit. After that, attempts to measure horizontal displacement due to liquefaction were made at various sites and in various earthquakes, and it was found that liquefaction-induced flow is not an extraordinary phenomenon, but it have occurred in many past earthquakes as well as earthquakes after the 1983 Nihonkai-chubu earthquake. Among many case studies, typical ones that are important in the following discussion are introduced briefly.

Figure 2 shows horizontal displacement in the Niigata city during the 1964 Niigata earthquake. Horizontal displacements of order of 10 meters were observed near the Shinano River, and the river width became narrow for more than 10 meters at some places [2]. Increase of lateral pressure due to onset of liquefaction exceeded bearing capacity of quay wall, which resulted in movement of quay wall towards the river and horizontal displacement in the back ground. Since this is same with the case of Figure 1(b), mechanism of this damage is easy to recognize. On the other hand, although displacement is not as large as this case, another important features can be seen in Figure 2. Horizontal displacements of order of a few meters are observed near the Niigata station. The ground surface here is almost level; a simple mechanism such as above is difficult to explain the horizontal displacement at this site.

There are cases where more horizontal displacement than the case in Figure 2 was observed in the nearly level ground. Figure 3 is an example of these sites. The site is located in the Ebigase district, Niigata city, and more than 5 meters horizontal displacement occurred during the 1964 Niigata earthquake [2]. There is a river, named Tsusen River, in the downstream direction of the flow, but this river is much smaller river than the Shinano River and horizontal displacement of the quay wall was not reported. Therefore, existence of the river is not the reason of this large displacement. Moreover, as shown in the soil profiles in Figure 4, this site is also nearly level.

During the 1995 Hyogoken-nambu (Kobe) earthquake, many quay walls in the fill areas in the Hyogo Prefecture moved toward the sea, as typically shown in Figure 5. Loss of bearing capacity of the foundation ground by soil liquefaction or shear failure was responsible in this damage [3]. Liquefaction-induced flow towards the quay wall was also observed in many locations. This type of damage is the case with open space

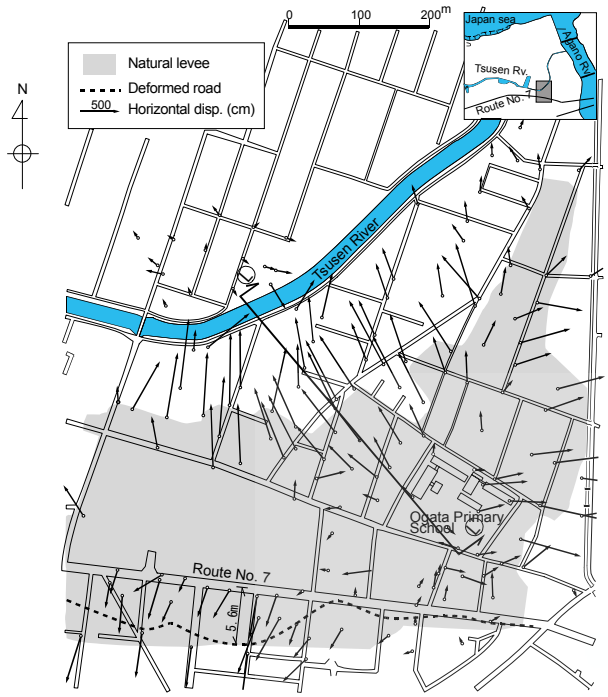

Figure 3. Horizontal displacement at Ebigase District during the 1964 Niigata earthquake [2]

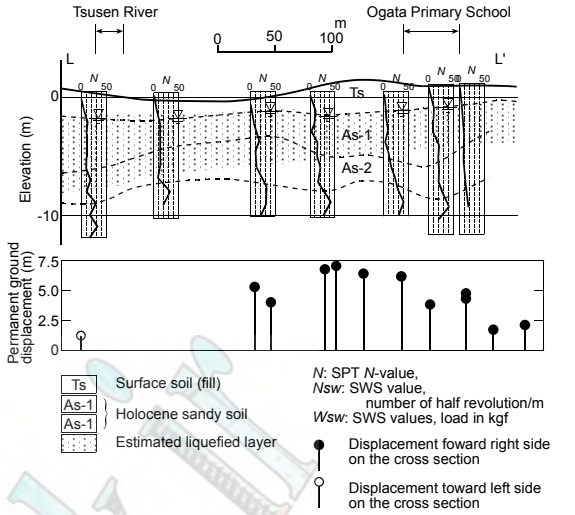

Figure 4: Soil profiles and horizontal displacement in Ebigase district, Niigata city

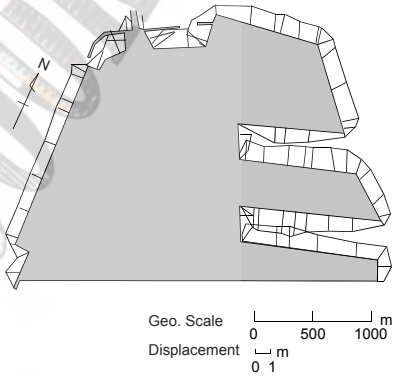

Figure 5: Horizontal displacement of Port Island during the 1995 Hyogoken-nambu (Kobe) earthquake (modified from ref. [8])

in Figure 1(b). Therefore, as described in the preceding, it is clear that movement of the quay wall triggered displacement at the back ground. The authors made analyses of this type of flow (e.g. [7]); shear stress at the backfill ground associated with movement of the quay wall was fairly small.

As shown in the preceding, liquefaction-induced flow or large horizontal displacement at the liquefied site is found to occur at nearly level ground or back ground of the quay wall, i.e., under small existing stress.

CRITERION BASED ON STABILITY PROBLEM AND ITS SHORTAGE

Conventional definition of the liquefaction-induced flow is infinite deformation triggered by soil liquefaction, which is the same idea with ISO on earthquake design code [5] described in the preceding and is called stability criterion in this paper. This concept is explained by many references, such as ref. [9] and [10]. According to ref [9], behavior after the soil liquefaction is classified into two categories: liquefaction and limited liquefaction shown in Figure 6(a). If stress-strain relationships show steady state or have residual strength and existing stress is greater than the residual stress, unlimited deformation occurs. On the other hand, if shear stress increases at large strains, then unlimited deformation does not occur, but deformation stops after certain strain, which is defined as limited liquefaction. Similar concept is reported in ref. 2, which is shown in Figure 6(b).

These concepts seem to be based on the behavior

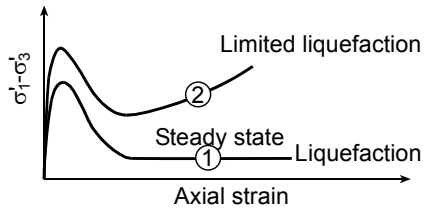

(a) Types of contractive deformations [9]

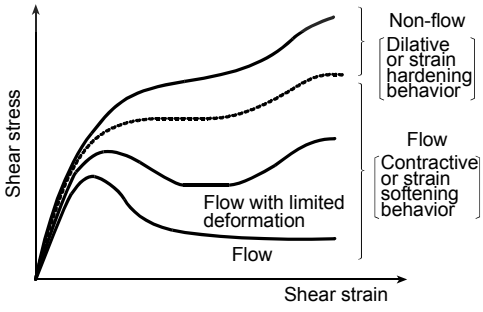

(b) Classification of undrained behavior [10]

Figure 6. Schematic figure showing liquefaction-induced flow

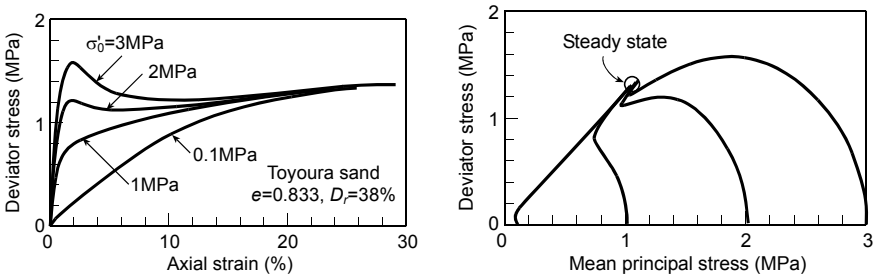

Figure 7. Undrained behavior of Toyoura sand [10]

under monotonic loading, and therefore easy to recognize. As explained in the following, however, they have shortage that they cannot explain the liquefaction-induced flow observed in Japan, i.e., the case where existing stress is small shown in the preceding section.

According to stability criterion, liquefaction-induced flow does not occur if initial shear stress or existing stress is less than steady state stress or residual stress. Then we need to know the value of residual stress and existing stress.

As explained in the preceding section, liquefaction-induced flow was observed at nearly level ground in Japan. As an example, therefore, let consider, a simple slope ground, for simplicity, whose buoyancy unit weight is 10 kN/m^3, slope of the layer is 1/100, thickness of surface liquefiable layer is 10 m, and water table is ground surface. Then the initial shear stress yields

$$10\ \text{kN/m}^3 \times 10\ \text{m} / 100 = 1\ \text{kPa}. \quad (1)$$

We will use this value to investigate the possibility whether flow occurs or not; it will be referred the typical case.

Figure 7 is an example of the stress-strain curve and stress path under monotonic loading [10]. The relative density of this sand is 38 %, which relative density is the smallest in the actual field according to the author's experience. Even in this loose sand, residual strength is a little larger than 1 MPa, which is huge value compared with the typical case (1 kPa). Liquefaction-induced flow is, therefore, never expected.

Since the confining pressure in Figure 7 is very large, another example is shown in Figure 8. The relative density is 16%, which is looser than actual sand. However, the residual stress is about 0.03 Mpa = 30kPa, which is still much larger than the existing shear stress of typical case. It is also noted that, as shown in the figure, cyclic

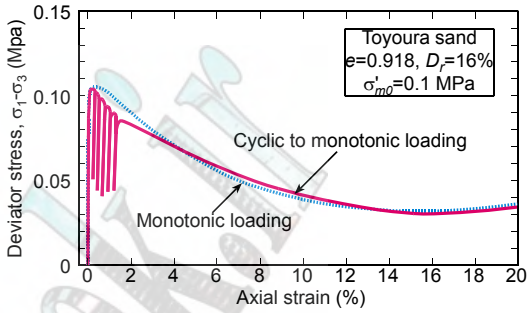

Figure 8: Undrained behavior of loose Toyoura sand [10]

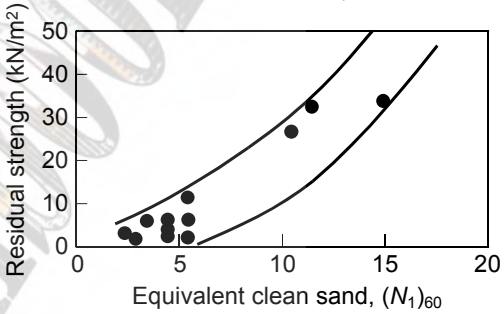

Figure 9. Estimated residual strength [11]

loading does not affect the residual strength, which indicates that mechanism based on monotonic loading, as shown in Figure 6, is difficult to explain liquefaction - induced flow in Japan.

Figure 9 shows residual strengths evaluated by back calculating the past flow failure [11]. Evaluated residual stresses become considerably smaller than that in Figure 7, but they are still large to explain the typical case. Several reasons can be considered why it cannot explain the typical case although they are back-analyzed value. Since the residual strengths in Figure 9 are evaluated from the residual deformation, they may not be the shear stress at the time of the flow [12]. Another possibility is that the

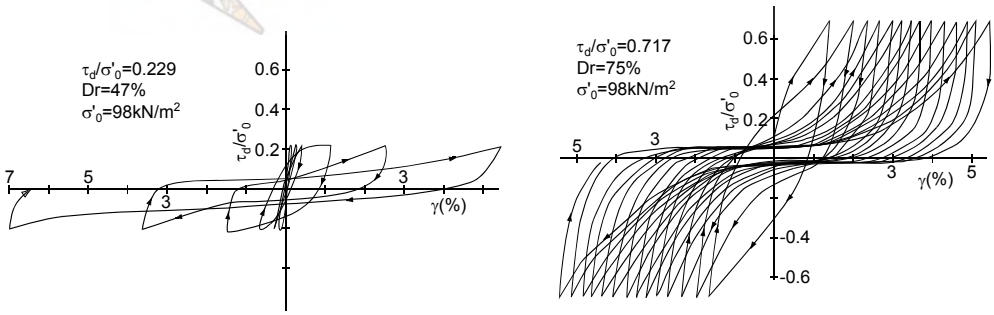

Figure 10. Example of test result by liquefaction strength test [13]

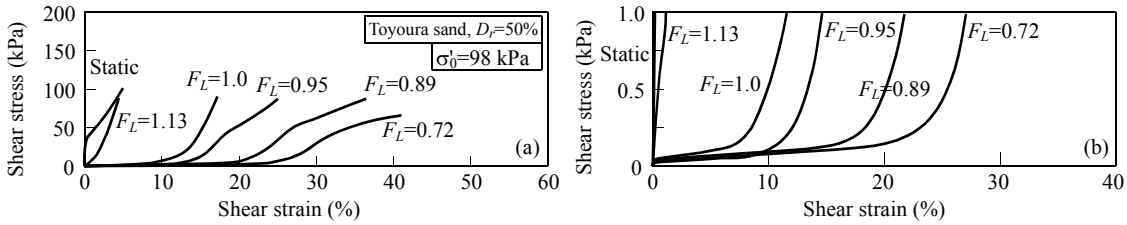

Figure 11. Stress-strain curve after liquefaction (Vertical axis is enlarge by 200 in (b))

slope angle of the cases in Figure 9 is larger than the typical case; therefore, existing stress was larger.

As shown, criterion based on monotonic loading is easy to recognize, but it cannot explain liquefaction-induced flow at small slope ground.

CRITERION BASED ON CYCLIC LOADING

Cyclic loading tests have been made frequently in order to obtain liquefaction strength and dynamic deformation characteristics. Figure 10 is an example of stress-strain relationships of loose and dense sands [13]. Both stress-strain curves are quite different from the one under monotonic loading such as Figure 7 or schematic figure in Figure 6. Firstly, strain when peak stress appears (strain at the peak stress hereafter) is about 2% in axial strain, i.e., about 3% shear strain in the monotonic loading in Figure 7, but shear strain in Figure 10 is already larger than the strain at the peak. This is not an exception. Onset of liquefaction, for example, is frequently defined to be 5% double amplitude axial strain, which corresponds to 3.75% single-amplitude shear strain. Moreover, liquefaction strength test is frequently made up to 10% double amplitude axial strain or 7.5% shear strain. These strains are larger than the strain at the peak under monotonic loading, but flow does not occur. Moreover, they do not show peak stress. This indicates that we need to use different criterion from stability criterion under dynamic loading. It is also noted that shear stress amplitude in Figure 10 is of the order of several tens percents, which is smaller than residual stress in Figure 7. This may explain why flow or unstable behavior does not occur in these and many other liquefaction strength tests.

Stress-strain relationships after the soil liquefaction is shown are Figure 11(a) [14] as an example. This curve is obtained under the monotonically increasing strain after subjected to prescribed cyclic load until onset of liquefaction or even more. The F_L value in the figure is a liquefaction resistant factor, and can be used to represent the amount of loading after the soil liquefaction; F_L=1 indicates just onset of liquefaction and smaller F_L value indicates more loading is subjected after the liquefaction before moving the monotonically increasing strain loading.

The stress-strain curve shown by "Static" in Figure 11 is a stress-strain curve under monotonic loading without cyclic loading; therefore, it can be compared with the stress-strain curve in Figure 7. Stress-strain curve with F_L=1.13 is the case when cyclic load stopped before the sample liquefy. Although the curve is somewhat different between the cases with "Static", resultant strain is small and flow behavior is not observed.

The stress strain curves after the liquefaction (FL≤1.0) is quite different with those under monotonic loading in Figure 7 or "Static" case in Figure 11(a). The shear stress is almost zero until certain strain, which will be called low rigidity region in the following. Then the shear stress increases again. Large amount of shear strain, however, is necessary before sand recovers its load carrying capacity. The shear stress in the low rigidity region is almost zero in Figure 11(a), but if we enlarge vertical axis by 200 %, which is shown in Figure 11(b), it is not zero, but have small value. The shear stress in low rigidity region is smaller than 1 kPa, therefore large strain of order of several tens percents is expected in the typical case.

Recover of shear stress corresponds to cyclic mobility behavior or dilative behavior described in ref [10]. Strain when stiffness recovers is order of several tens percent, which is the same order of the strain at the site where liquefaction-induced flow was observed during the past earthquakes.

Since shear stiffness and strength recovers at certain strain, this behavior is not failure. Strains of several tens percent is, however, sufficiently large strains to cause damage to various structures. Therefore, it may be natural engineering sense to treat this behavior as failure of the ground. Since infinite deformation will not to be expected, deformation is predictable; therefore, we can call it deformation criterion in order to distinguish from the stability criterion.

PROPERTY OF SAND AFTER LIQUEFACTION

Long discussion has been made whether liquefied material behaves as solid or liquid. Difference between two opinions is, however, very small according to the author's opinion. The phenomena that stiffness recovers at certain strains are accepted in two opinions [14][15]. Therefore, the difference is the stiffness at the low rigidity region, typically shown in Figure 11. It is small but nonzero if liquefied soil is considered as solid, whereas it is zero if liquefied soil behaves as liquid. Since soil has shown strain rate dependent property, we can count strain rate property or liquid-like property even if solid-like behavior is assumed in the post liquefaction state.

The remaining problem is what kind of mechanism distinguishes solid and liquid-like behavior. The author pointed out the following possibility [16][17] on the mechanism of deformation of liquefied soil.

Figure 12 shows schematic figure showing how liquefaction occurs. Mechanism of liquefaction is usually explained using a figure similar to this figure. Here, Figure 12(a) is a structure before the earthquake; (b) is a structure after shaking when pore material is air, in which simultaneous settlement occurs according to the negative dilatancy of the sand. However, since volume change is not allowed for saturated less permeable material such as the sand, effective stress or intergranular stress becomes zero, and soil particles uplift in the pore fluid as shown in Figure 12(c), resulting in liquid-like behavior. Zero intergranular stress, however, need not directly cause uplift of soil particles; they can stay their original position as Figure 12(a). Of course, since there is no intergranular stress, skeleton is instable. Therefore, it will be destroyed by a small external disturbance or driving force. If the structure is destroyed, soil behaves as liquid. If deformation occurs a little, however, then a new skeleton is developed again and the material behaves as solid. In the actual situation, this kind of repetition between solid and fluid associated with the development and destruction of skeleton structure, respectively, continuously occurs, and liquefied material looks as if it behaves very viscous fluid under the action of driving force in global. In other words, if there is no driving force, it behaves as solid, which situation occurs in the laboratory test as typically shown as low stiffness region in Figure 11. Small shaking after the main part of ground motion that caused liquefaction and seepage force associated with excess porewater dissipation towards the ground surface are considered as typical driving forces.

A part of this assumption is proved in ref. [18], in which a ground with tilted surface is investigated by the centrifugal test. Typical test result is shown in Figure 13.

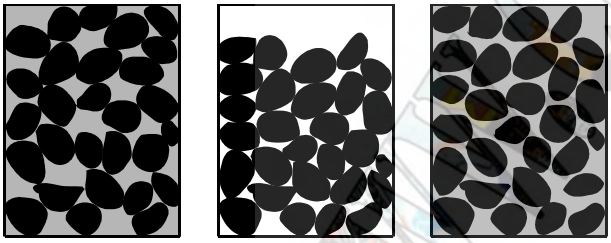

Figure 12 Schematic figure showing mechanism of liquefaction

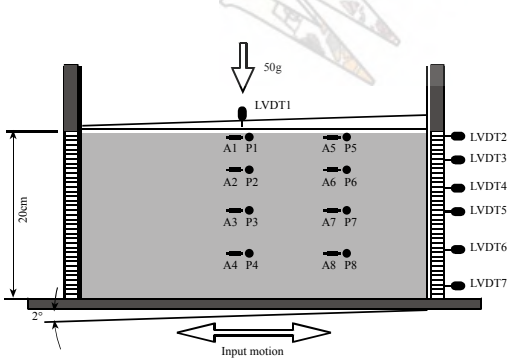

(a) Test apparatus

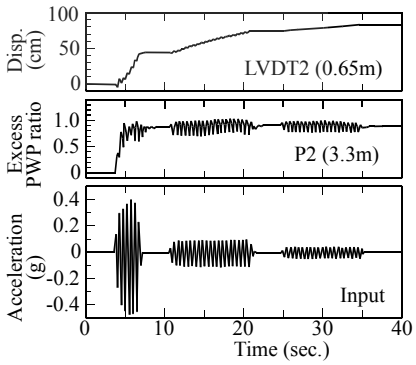

(b) Time histories

Figure 13 Relation between small shaking and horizontal displacement

Horizontal displacement occurs only when the ground vibrates, and it does not occur when there is no vibration although completely liquefied state holes in both cases.

There is no direct evidence so that seepage force works as driving force to keep soils liquid. We can easily imagine it, however, when looking at the video at the Niigata airport during the 1964 Niigata earthquake [19]. Liquid-like material erupted from the apron of the airport. Another example is an observation of the site liquefied by blasting [20]. Significant amount of water or sand-water mixture boiled up for about 10 minutes after blasting. In these cases, structure of soil particle is completely destroyed without making a new skeleton because of large seepage force.

TWO CRITERIA FOR LIQUEFACTION-INDUCED FLOW

As shown in the preceding, there are two phases in the liquefaction-induced flow. Figure 14 shows these phases schematically.

The stress-strain curve under monotonic loading (backbone curve hereafter) is shown in solid line OABCD in the figure. It is not affected by cyclic loading [10][21]. On the other hand, dashed lines such as OB and OC are stress-strain curves after the soil liquefaction. Behavior near the origin may be different from OB (or OC) because stress-strain curve under the cyclic loading due to ground shaking looks like those in Figure 10, but it does not affect the discussion here because stress-strain curve after the liquefaction is discussed.

Criteria for liquefaction-induced flow can be classified into two in the following.

1) Stability criteria: If the existing stress is larger than the residual strength, then conventional stability criterion can be used. Flow failure occurs in the three cases.
   - When liquefaction occurs under one pulse, state point moves O $\rightarrow$ A $\rightarrow$ B $\rightarrow$ C $\rightarrow$ D. This behavior is identical to those explained as an extension from the monotonic behavior in Figure 6. Liquefaction-induced flow occurs when dynamic stress or stress caused by ground shaking is larger than the peak strength.
   - When liquefaction occurs under certain amount of cycles of loading, then stress-strain behavior may be

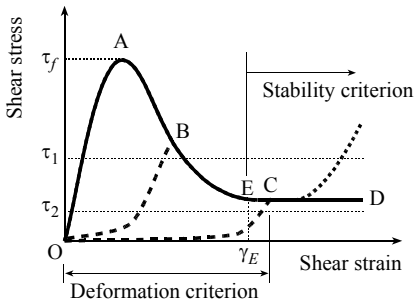

Figure 14. Two criteria on liquefaction-induced flow

O→B→C→D. Dynamic stress makes the peak stress smaller than original (point A) if sufficient excess porewater pressure is developed in the preceding cycles of loading. Therefore, liquefaction-induced flow is easier to occur than previous case.

- If sufficient loading is applied, the behavior becomes O→C→D. Stress-strain curve does not show peak stress. Even in this case, liquefaction-induced flow can occur when existing stress is larger than residual stress. Point E where stress yields residual stress distinguishes states with peak stress or not.

2) Deformation criteria: If the existing stress is smaller than the residual stress, liquefaction-induced flow does not occur based on previous criterion. In the process to O→B or O→ C, however, strain can reach several tens percent or more as shown in Figure 11 as an example. Therefore, this stage can also be considered as failure of ground in the engineering sense. Since strain does not become infinite, another technical term is better to define this state. We name this criterion "deformation criteria."

The relation between existing stress and residual stress distinguishes two criteria. If existing stress is greater than residual stress, stability criterion is applicable. If, on the other hand, existing stress is smaller than residual stress, deformation criterion is applicable.

Resulting strain or deformation may depend on various factors such as stiffness of low rigidity region, type of driving force and its duration, viscosity during liquid-like behavior, etc. Success of simplified method to predict liquefaction-induced flow [7][22], however, indicates importance of the behavior as solid in evaluating the residual deformation although liquefied material may show liquid-like behavior in the process to residual state. This can be recognized that static equilibrium should hold when driving force terminates, in which soil behaves as solid. Sand boiling may be an important index to indicate onset of liquefaction, but it is local behavior and does not a representative behavior of whole liquefied layer, which can be recognized from the observation of trench excavation that liquefied layer is not disturbed [23], and observation of sand boiling in the shake table test that sand near the top of the liquefied layer is caught by boiling porewater to form sand boiling [24].

CONCLUDING REMARKS

In this paper, we discussed the mechanism of liquefaction-induced flow. So-called liquefaction-induced flow can be classified into two criteria, i.e., stability and deformation criteria. The former was well known, but it cannot explain liquefaction-induced flow when existing stress is very small which case frequently has observed in Japan. Then a new criterion is proposed in this paper. Both flow causes sufficiently large ground deformation to damage to structures. Therefore it may be natural to treat them as failure of the ground. There are, of course, differences. Difference between two criteria is that deformation cannot be evaluated in the stability criterion, whereas it can be or may be evaluated in the deformation criteria.

REFERENCES

[1] Hamada, M., Yasuda, S., Isoyama, R. and Emoto, K., "Observation of permanent displacements induced by soil liquefaction," *Jour. of Geotechnical Engineering*, Proc., JSCE, No. 376/III-6, 1986, pp. 211-220 (in Japanese)

[2] Hamada, M. and O'Rourke, T. D., *Case studies of liquefaction and lifeline performance during past earthquakes*, Volume 1 Japanese Case Studies, Technical Report NCEER-92-0001, National Center for Earthquake Engineering Research, 1992

[3] Yoshida, N. (1998): Mechanism of liquefaction-induced flow, *Proc., Symposium on Flow and Permanent Displacement of Ground and Soil Structures during Earthquakes*, Japanese Geotechnical Society, pp. 53-70 (in Japanese)

[4] Yasuda, S. "Introduction of the course, Liquefaction-induced flow of ground and its effect to structures," *Tsuchi-to-Kiso*, Vol. 47, No. 5, 2000, pp. 53-54

[5] ISO/TC98/SC3/WG10, "Seismic actions on geotechnical works," N71Rev, July 2004

[6] Hamada, M., Yasuda, S., Isoyama, R. and Emoto, K. (1986): Study on liquefaction induced permanent ground displacements, Association for Development of Earthquake Prediction

[7] Yasuda, S., Yoshida, N., Adachi, K., Kiku, H., Gose, S. and Masuda, T., "A simplified practical method for evaluating liquefaction-induced flow," *Journal of Geotechnical Engineering*, Proc. JSCE, No. 638/III-49, 1999, pp. 71-89

[8] Editorial Committee for the Repost on the Hanshin-Awaji Earthquake Disaster, *Port and coastal facilities, Damage to civil engineering structures*, Report on the Hanshin-Awaji Earthquake Disaster, Maruzen, 1998

[9] Finn, W. D. L., "State-of-the-art of geotechnical earthquake engineering practice," *Soil Dynamics and Earthquake Engineering*, Vol. 20, Special Issue, 9ICSDEE, 2000, pp. 1-15

[10] Ishihara, K., *Soil behavior in Earthquake Geotechnics*, Oxford Engineering Science Series 46, Oxford Science Publications. 1996

[11] Seed, H.B., "Design problems in soil liquefaction," *J. of Geotechnical Engineering*, ASCE, Vol. 113, No. 8, 1987, pp.827-845

[12] *Remedial measures against soil liquefaction*, Geotechnical engineering practice series 18, Japanese Geotechnical Society, 2004, pp.75-76 (in Japanese)

[13] Yasuda, S., *From investigation to remedial measures against liquefaction*, Kajima Shupankai, 1988 (in Japanese)
[14] Yasuda, S., Yoshida, N., Adachi, K., Kiku, H., Gose, S. and Masuda, T., "A simplified practical method for evaluating liquefaction-induced flow," *Journal of Geotechnical Engineering*, Proc. JSCE, No. 638/III-49, 1999, pp. 71-89 (in Japanese)
[15] Hamada, M. and Wakamatsu, K., "A study on ground displacement cause by soil liquefaction," *Journal. of Geotechnical Engineering*, Proc. of JSCE, No. 596, III-43, 1998, pp. 189-208 (in Japanese)
[16] Yoshida, N., "Lateral spreading of ground due to liquefaction -solid or liquid ?-," *Forum of Applied Mechanics*, JSCE, 1995, pp. 12-17
[17] Yoshida, N., Nagase, H. and Miura, K., "Liquefaction-induced flow and its effect to structures," *Tsuchi-to-Kiso*, Vol. 47, No. 8, 1999 , pp. 47-52 (in Japanese)
[18] Okamura, M., Abdoun, T. H., Dobry, R., Sharp, M. K. and Toboada, V. M., "Effects of sand permeability and weak aftershocks on earthquake-induced lateral spreading," *Soils and Foundations*, Vol. 41, No. 6, 2001, pp. 63-77
[19] *Photographs and motion picture of the Niigata City immediately after the earthquake in 1964*, The Japanese Geotechnical Society, 2004
[20] *Remedial measures against soil liquefaction*, Geotechnical engineering practice series 18, Japanese Geotechnical Society, 2004, pp. 286-289 (in Japanese)
[21] Kiku, H. and Yoshida, N. "Dynamic deformation property tests at large strains," *Proc., 12th World Conference on Earthquake Engineering*, Auckland, New Zealand, 2000, Paper No. 1748
[22] Yasuda, S., Ideno, T., Sakurai, Y., Yoshida, N. and Kiku, H., "Analyses for liquefaction-induced settlement of river levees by ALID," *Proc., 12th Asian Regional Conference on Soil Mechanics and Geotechnical Engineering, Singapore*, 2003, paper No. JP43
[23] Nanjo, A., Kubota, K. and Morita, Y., "Test pit in reclaimed ground," Proc. 31st JSCE Earthquake Engineering Symposium-1996, pp. 371-372 (in Japanese)
[24] Yamaguchi, A., Tobita, Y. and Yoshida, N., "Mechanism of sand boiling and its onset condition,' in preparation

Residual strength of soils involved in earthquake-induced landslides

Y. Tsukamoto[1], K. Ishihara[1]
[1]*Department of Civil Engineering, Tokyo University of Science, Chiba, Japan*

Abstract

In an attempt to determine the residual strength of soils under rapid landslides that took place during 2004 Niigata-ken Chuetsu Earthquake in Japan, a new type of laboratory tests termed as "constant-volume triaxial tests" was performed on non-saturated specimens of silty soils prepared at varying water contents. Two samples of soils involved in the actual landslides induced during this earthquake were tested in the laboratory to assess the residual strength. The results of the tests disclosed that the water content or saturation ratio is a key parameter governing the residual strength of the non-saturated soils tested in the above manner.

Keywords—*Residual strength, rapid landslides, earthquakes*

INTRODUCTION

On October 23, 2004, the devastating earthquake measuring the magnitude of M = 6.8 struck the hilly regions in Niigata at a local time of 17:56, followed by two huge aftershocks measuring M = 6.0 and 6.5 at 18:11 and 18:34. Most probably harmed also with the heavy rainfall passing three days before the earthquake, these hilly regions suffered from numerous landslides, especially in the Yamakoshi area, where tertiary deposits mainly prevailed. Figure 1 shows the epicentres of the main shock and the subsequent two aftershocks and also the locations of landslides. The reverse faults hidden locally in the direction of NE-SW are known to be responsible for these earthquakes, and the areas devastated by numerous landslides are concentrated on the side of hanging-wall.

The Yamakoshi area forms a hilly region typically with 300 to 400 metres above sea level, surrounded by the Echigo plains on the west side, on which Shinano river flows, and also by the Echigo mountain ranges on the east side, which are as high as 2000 metres above sea level. This area had been isolated from outside for some days after the earthquakes, due to the roads ruthlessly cut off by the landslides. This area has since been evacuated for longer than half a year.

SITES OF LANDSLIDE EXPLORED

Two sites of tertiary-type landside were chosen for the reconnaissance investigation in the present study. The details of the general features of these two landslides are described in the following.

Landslide at Higashi-Takezawa

The site of landslide at Higashi-Takezawa is shown in Fig. 1, which is located along Imo river. Imo river flows from the north to south direction in the Yamakoshi area. The stream of this river had been distracted at several locations by great amounts of the debris induced by the landslides during earthquakes. The upstream riverbeds at such locations were flooded and the natural water reservoirs were formed, which were found to be in danger of collapse. The landslide at Higashi-Takezawa investigated in the present study was one of them, forming the natural reservoir behind the debris. Along Imo river were distributed tertiary deposits of weathered sandstone, which collapsed during the earthquakes, and moved downwards to form the debris on the riverbed. Numerous landslides were found in the regions covered by tertiary deposits of weathered sandstone, as shown in Fig. 1. Figure 2 shows the photographic view of this landslide. At the slip plane of about 20 ° inclination on the slope was found a clear smooth rock surface of non-weathered sandstone, along which weathered sandstone had been sliding down. Figures 3 and 4 show the plan

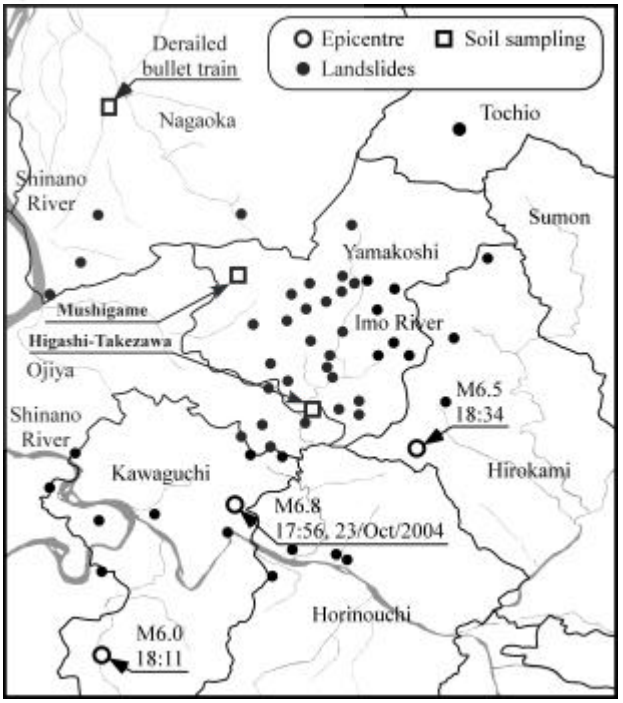

Fig. 1: Epicentres and locations of landslides

view and side view of the site of landslide. This kind of sliding can be characterized by two regimes, sliding of soil mass on the slope and spreading of debris over plain fields.

Fig. 2: View of landslide at Higashi-Takezawa.

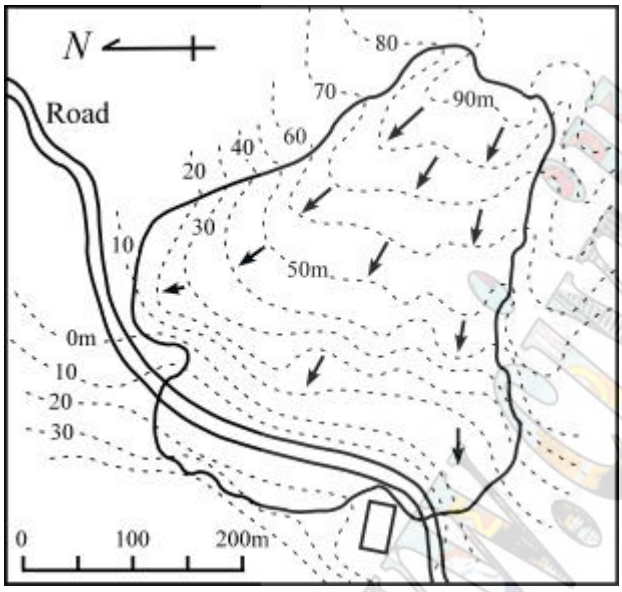

Fig. 3: Plan view of landslide at Higashi-Takezawa

Landslide at Mushigame

The site of landslide at Mushigame is also shown in Fig. 1. The tertiary deposits ofweathered mudstone are distributed around this area, on which shelved paddy fields are often found. Figure 5 shows the photographic view of this landslide from the uphill. The deep-seated slip failure was found on the top of the hill, followed by spreading of debris over the road. This was one of the rarely seen landslides that occurred in the regions of weathered mudstone deposits. Figures 6 and 7 show the plan view and side view of the site of landslide. This landslide is also characterized by the two regimes of sliding and spreading.

VOLUME-CONSTANT TRIAXIAL TEST

Test apparatus

The problems associated with landslides are twofold. The first problem is to assess whether a given slope would slide or not during rainfalls and earthquakes, and the second is to estimate how far downhill the sliding mass of soils would travel. The issue of triggering has been discussed extensively by professionals in the disciplines of geology, geomorphology and geotechnology. The issue of the post-failure travel distance has also been the subject of concern for many researchers and numerous attempts have been made to clarify mechanisms of debris flow based on case studies and analyses. Of key importance for estimating the run-out distance would be the residual strength of soils, which is mobilized at a largely deformed state prevailing in the vicinity of the sliding surface. Since the materials are not necessarily saturated, it would be desirable to know the residual strength in non-saturated state in general. When rapid landslides such as observed during recent earthquakes are concerned, there would be little time for soils to change their volume in the course of rapid movement. Therefore, it is reasonable to assume that rapid landslides would take place under such conditions of little or practically no volume change. In order for a potentially contractive soil to keep its volume unchanged during shearing, the overburden stress acting initially on the soil skeletons needs to be reduced, and instead, the portion of the initial overburden stress must

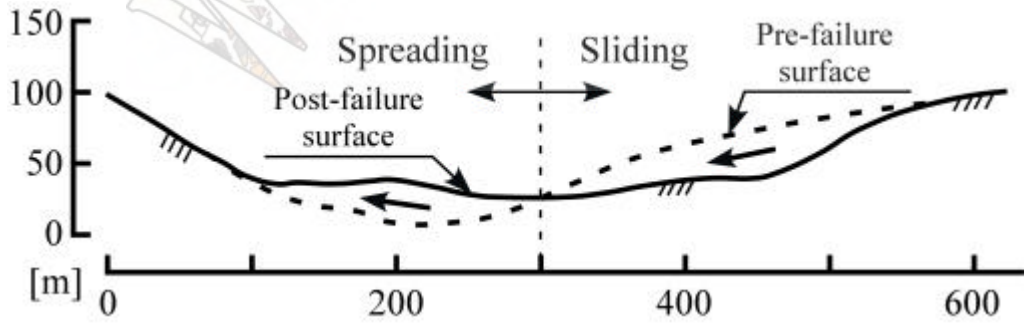

Fig. 4: Side view of landslide at Higashi-Takezawa.

be temporarily carried by other substances such as air-containing water or dust-containing air existing in the voids. Thus, it is assumed in the present study that the volume of even partly saturated soils is maintained almost unchanged during shearing and the initial overburden stress is reduced during shearing. The laboratory testing method for triaxial tests is described below.

Fig. 5: View of landslide from the uphill at Mushigame.

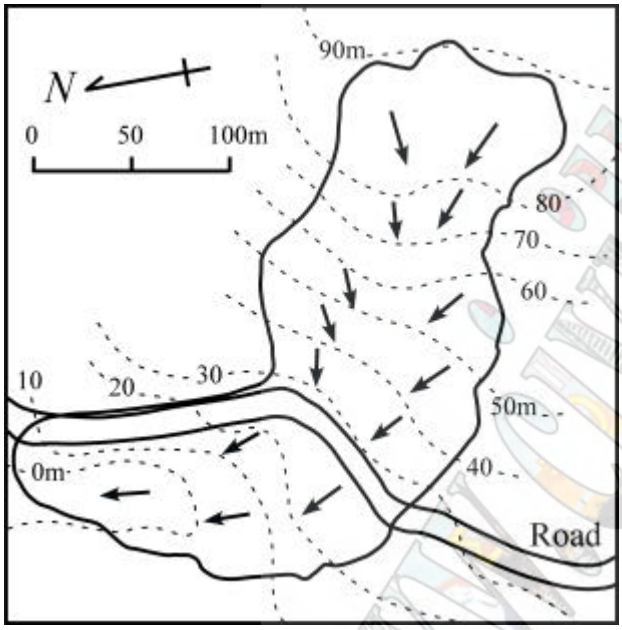

Fig. 6: Plan view of landslide at Mushigame.

The large triaxial test apparatus equipped with an inner cell was used in the present study, as shown in Fig. 8. This apparatus can accommodate cylindrical triaxial soil specimens of 12.0 cm in diameter and 24.0 cm in height, as described in [1]. The installation of the inner cell within the triaxial cell was intended to monitor the volume change of non-saturated soil specimens during axial loading. When the non-saturated soil specimen submerged in the water of the inner cell changes its volume, the water level located at the narrow mouth of the inner cell changes accordingly. This change in the water level can be monitored via a minute differential pressure transducer. Thus, the volume change of the specimen can be calculated as a change in the water level multiplied by the area of the cross section of the narrow mouth of the inner cell.

Test procedures

The volume-constant condition in non- saturated soil specimens was implemented in drained triaxial compression tests as follows. The non-saturated soil specimen was prepared with the method of wet tamping, and a confining stress is applied to produce a state of consolidation. The soil specimen was then axially loaded in a strain-controlled manner. The volume change of the specimen was monitored during this phase of axial loading. Since the soil specimen generally begins to decrease its volume during the early phase of shearing, it is necessary to reduce the cell pressure to keep the volume of the specimen unchanged. The cell pressure is reduced until it becomes equal to zero. However, the axial loading was continued until the axial strain of 10% was achieved.

TEST RESULTS

Soil samples

The two soil samples were tested as shown in the grain size distribution curves of Fig. 9. The soil sample taken

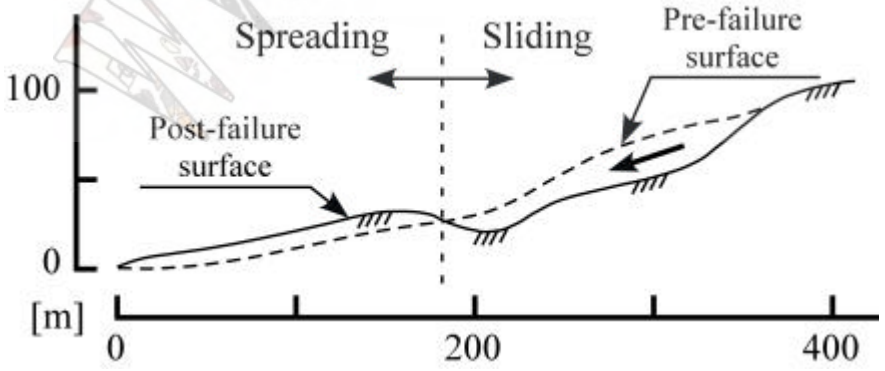

Fig. 7: Side view of landslide at Mushigame.

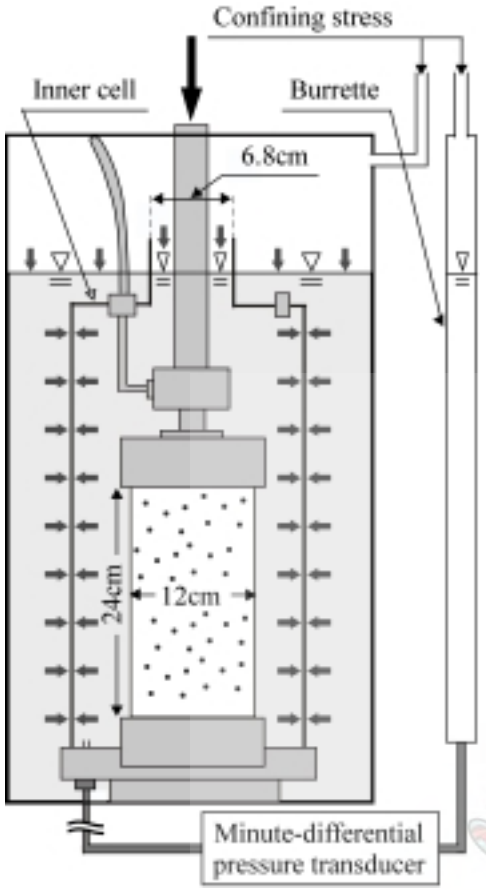

Fig. 8: Triaxial test apparatus with an inner cell.

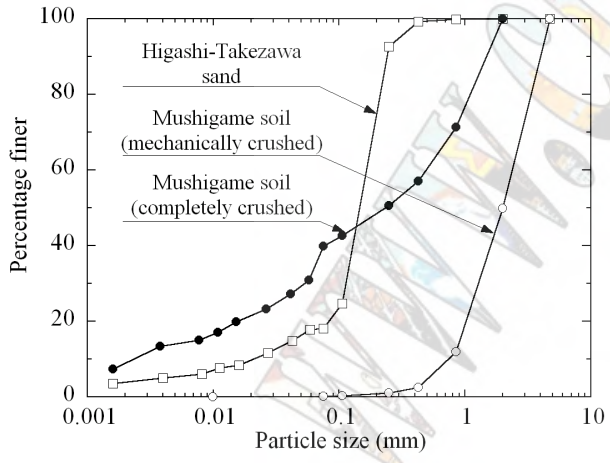

Fig. 9: Grain size distributions of soils used in the tests.

from the site at Higashi-Takezawa was of weathered sandstone, and was found to be non-plastic. On the other hand, the soil sample from the site at Mushigame was of weathered mudstone, and was found to be cohesive with the plasticity index of I_p = 26. This originally crushable soil sample was mechanically crushed and used in triaxial tests. The grain size distributions at the mechanically crushed state and the completely crushed state are

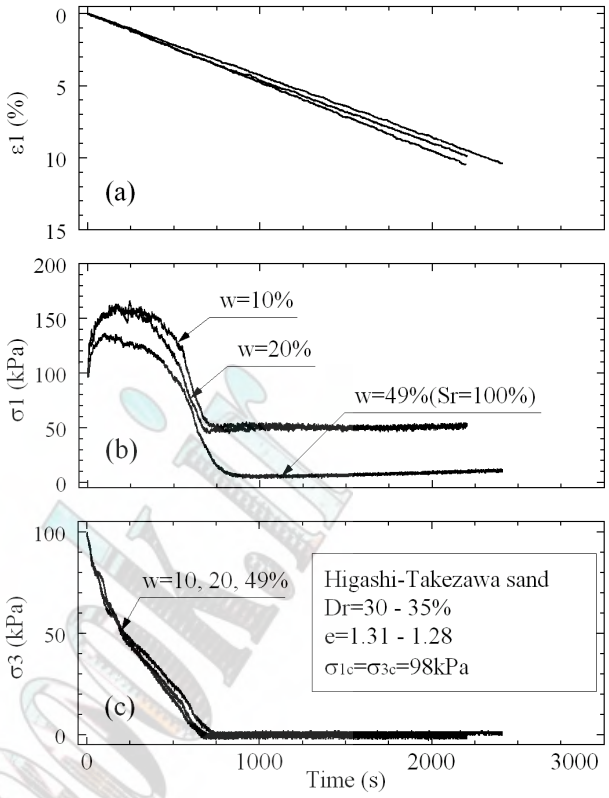

Fig. 10: Time histories of axial strain, confining stress and axial stress in the constant-volume test on Higashi-Takezawa sand.

indicated in Fig. 9.

Test results on soils from Higashi- Takezawa

It was found in the earlier study conducted by our group that amongst various factors including density and water content of soils an confining stress, the residual strength of non-saturated soils is most affected by the water content. Based on the outcome of this earlier study, a series of the tests were conducted on the soil sample taken from Higashi-Takezawa. The purpose of the tests was to examine the effects of water content on the residual strength of non-saturated soils. The tests were carried out on the soil specimens all consolidated to a confining stress of σ_{3c} = 98 kPa, with relative densities of D_r = 30 to 35% observed after consolidation. Three tests were performed on the specimens with different water contents of w = 10, 20 and 49%. The water content of w = 49% effectively corresponds to the condition of full saturation. The conduct of the tests can be seen in the test data presented in Fig. 10. The time histories of the axial strain ε_1, axial stress σ_1 and lateral confining stress σ_3 are plotted against time. The axial strain ε_1 was increased with a constant rate, and the lateral confining stress σ_3 was reduced intentionally. The axial stress σ_1 was found to increase in the early phase and then to begin to reduce later. Figure 11 shows the same data demonstrated in the form of time histories in the parameters of the void ratio e, deviatoric stress q and effective mean stress p. It was

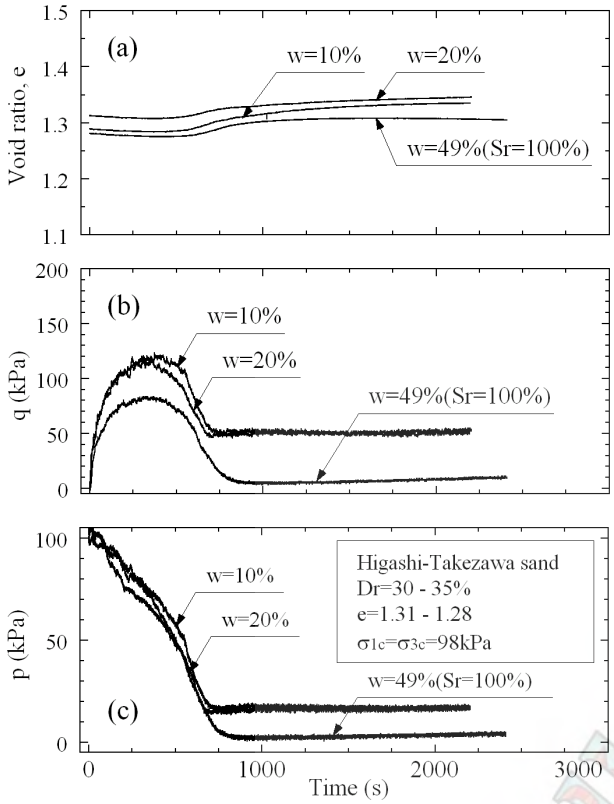

Fig. 11: Time histories of e, q and p on Higashi- Takezawa sand.

intended in the tests that the void ratio be maintained constant throughout the tests. However, there are some dilations of the soil specimens at axial strains in excess of ε_1 = 3%. The set of four diagrams is presented in Fig. 12, consisting of the plots of p against e, ε_1 against e, stress path of p against q, and stress-strain relations of ε_1 against q. It can be seen in the plots of ε_1 against q that the residual strength mobilized at a largely deformed state tends to decrease with increasing water content, particularly in the range of water content in excess of about 20%.

Test results on soils from Mushigame

The same series of the tests were conducted on the soil sample from Mushigame. The soil specimens were prepared with the initial relative density of Dr = 90%, which corresponds to the loosest density achievable. The tests were carried out on the soil specimens all consolidated to a confining stress of σ_{3c} = 98 kPa, with relative densities of D_r = 112 to 134% observed after consolidation. This cohesive soil sample was found to be very compressible during consolidation. Three tests were performed on the specimens with different water contents of w = 9, 17 and 24%. The time histories of the axial strain ε_1, axial stress σ_1 and lateral confining stress σ_3 are plotted against time in Fig. 13. The time histories of the void ratio e, deviatoric stress q and effective mean stress p

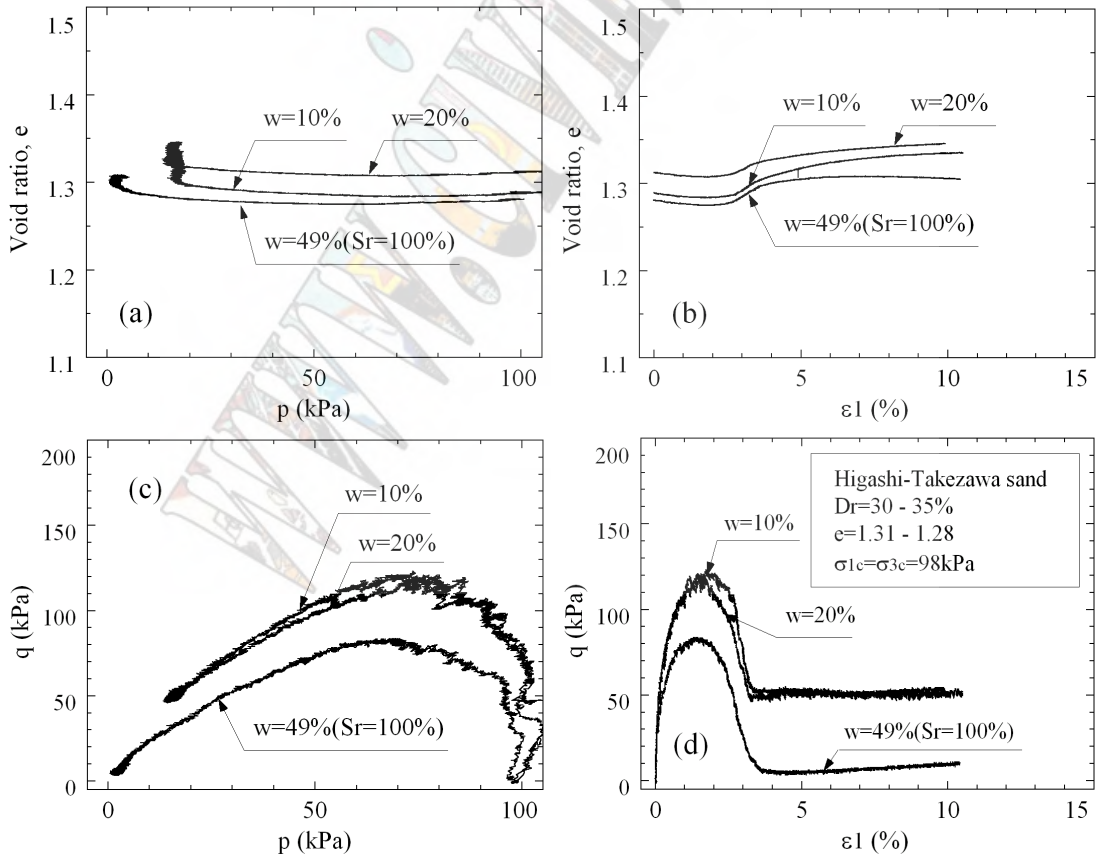

Fig. 12: Stress path, stress-strain, e – p' and e – ε_1 diagrams on Higashi-Takezawa sand.

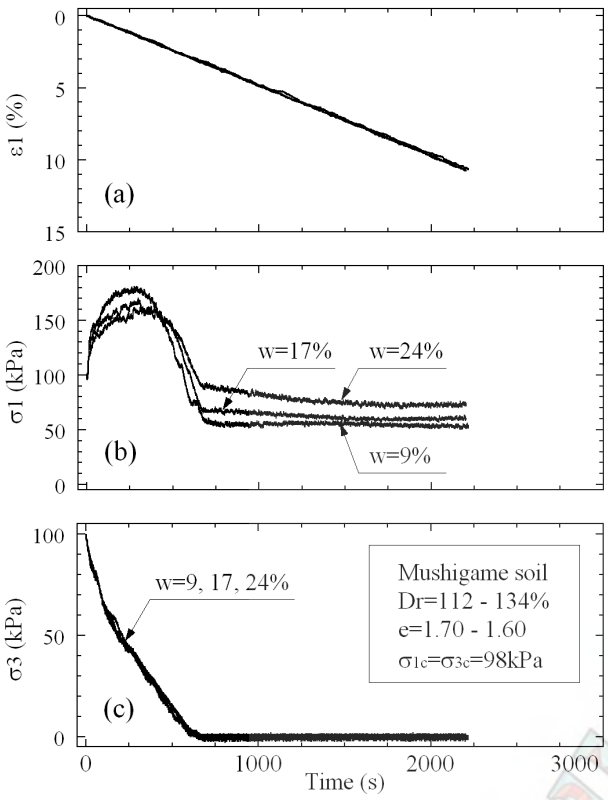

Fig. 13: Time histories of ε_1, σ_3 and σ_1 on Mushigame soil.

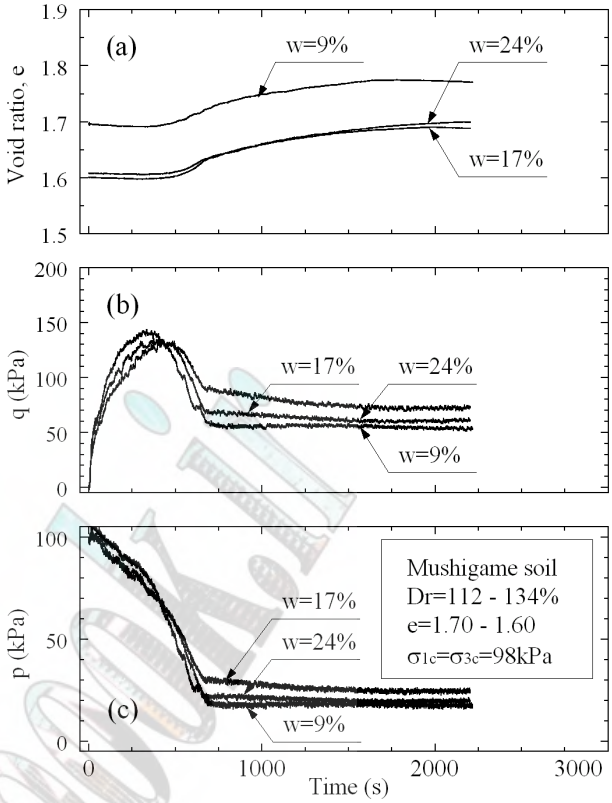

Fig. 14: Time histories of e, q and p on Mushigame soil.

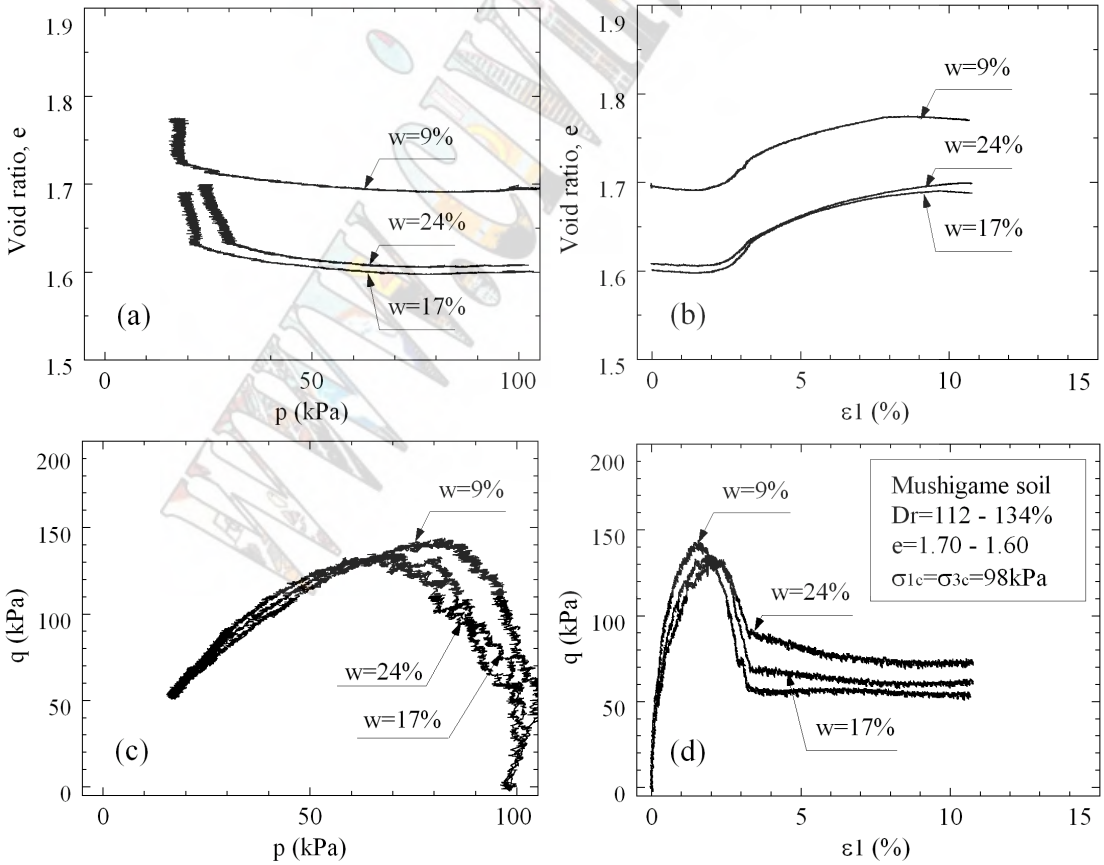

Fig. 15: Stress path, stress-strain, e – p' and e – ε_1 diagrams on Mushigame soil.

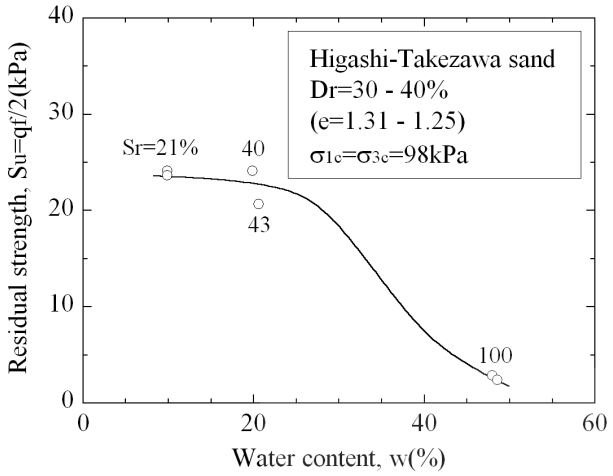

Fig. 16: Plots of residual strength against water content, (Higashi-Takezawa sand).

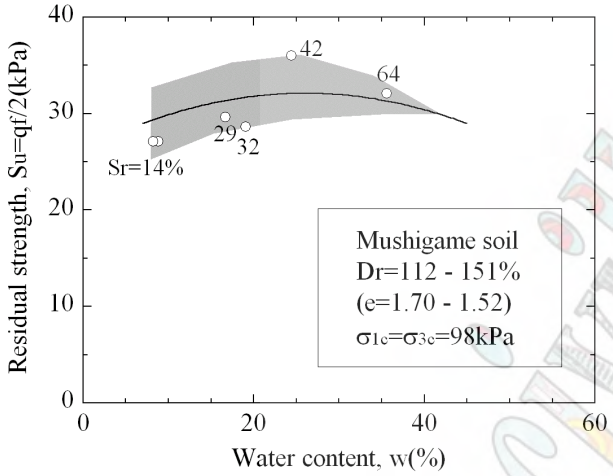

Fig. 17: Plots of residual strength against water content, (Mushigame soil).

are shown in Fig. 14. The plots of p against e, ε_1 against e, stress path of p against q, and stress-strain relations of ε_1 against q are shown in Fig. 15.

Plots of residual strength against water content

The residual strength of soils is defined as half of the deviator stress at a large strain level in the present study. The values of the residual strength thus defined can be read off from the data shown in Fig. 12(d) and Fig. 15(d), for the soil samples of Higashi-Takezawa and Mushigame, respectively. The values of the residual strength thus determined are plotted against the water content and saturation ratio, as shown in Figs. 16 and 17. In the case of the soil sample from Higashi-Takezawa, it can be seen in Fig. 16 that the residual strength defined as $S_u = q_f/2$ takes a nearly constant value of 24 kPa up to the water content of about 20%. However, it reduces sharply with increasing water content down to S_u = 3 kPa. In the case of the soil sample from Mushigame, it can be seen in Fig. 17 that the residual strength is found to take values ranging between 27 and 36 kPa at the water content of 10 to 35%. Herein, the water content of 35% does not correspond to the condition of full saturation. However, it was difficult to prepare soil specimens with the saturation ratio of more than Sr = 70%, and the data of the residual strength at the water content of over w = 40% were not obtained in the present study.

CONCLUSIONS

The residual strength of soils exerted under rapid landslides induced during earthquakes was examined based on the constant-volume triaxial tests. The two soil samples were taken from the sites of landslide that took place during 2004 Niigata-ken Chuetsu Earthquake. The non-saturated specimens of these silty sands were prepared at varying water contents, and the constant-volume triaxial tests were conducted. The results of the tests disclosed that the water content or saturation ratio is an important parameter governing the residual strength of the non-saturated soils tested in the above manner.

ACKNOWLEDGEMENTS

The authors would like to thank the past and current students of Tokyo University of Science, M. Nakamura, Y. Imaizumi, K. Ishikawa, Y. Kobari and S. Nakamura for their conduct of the laboratory tests reported in the present paper. Thanks are also extended to Dr. S. Otsuka and Dr. H. Toyota of Nagaoka Institute of Technology and Science, for their generous support in obtaining soil samples from the sites of landslide in Niigata.

REFERENCES

[1] Sawada, S., Tsukamoto, Y. and Ishihara, K., "Residual deformation characteristics of partially saturated sandy soils subjected to seismic excitation", *Soil Dynamics and Earthquake Engineering*, Special Issue, in press.

Evaluation of Liquefaction Resistance of Ground Improved by the Sand Compaction Method

K. Harada, J. Ohbayashi,T. Ideno[1], S. Yasuda, T. Tanaka[2]
[1]*Fudo Construction Co., Ltd, Tokyo, Japan*
[2]*Tokyo Denki University, Tokyo, Japan*

Abstract

The sand compaction pile method is the most common method of ground improvement used as a countermeasure against liquefaction. And its effectiveness has been confirmed in many case studies of damage caused by past earthquakes. The ground improved by sand compaction piles has been suffered a seismic force greater than conditional force and no damage was observed. This paper considered the factors causing the mean liquefaction resistance of an area of compacted ground as a whole to be higher than liquefaction resistance calculated from the ground's N-values between sand piles. Then extra factors of liquefaction resistance were determined from the results of an analysis of relative settlement in unimproved and improved sections of ground after the Hyogoken Nambu earthquake, and the liquefaction resistance of the improved ground was found to be approximately 1.5-2.0 times that of the ground between piles. From the results of laboratory tests, the extra factor due to the rise in coefficient of earth pressure was found to be 1.1-1.3, and the extra factor due to the composite ground effect was found to be 1.1-1.3.

Keywords—*sand compaction pile method; coefficient of earth pressure at rest; composite ground*

INTRODUCTION

The sand compaction pile (SCP) method is the most common method of ground improvement used as a countermeasure against liquefaction, and its effectiveness has been confirmed in many case studies of damage caused by past earthquakes. The authors have made a series of studies evaluating the factors at play and their effectiveness, in cases where ground improved by compaction has been suffered by a seismic force greater than assumed and no damage was observed.[1)]

This report considers the factors causing the mean liquefaction resistance of an area of compacted ground as a whole to be higher than the liquefaction resistance calculated from the ground's N values between sand piles, and reports the results of a quantitative study of several of these factors.

Degree of deformation in ground improved by compaction and evaluation criteria

A. Analysis of cases of damage due to the Hyogoken Nambu earthquake

Matsuo et al.[2), 3)] looked at two reclaimed lands in Kobe affected by the Hyogoken Nambu earthquake, Port Island Phase 1(PI) and Rokko Island (RI). They divided the sites into zones based on whether or not the ground had been compaction-improved, and using the relative settlement of structures and the condition of the ground in unimproved and compacted sections, they undertook a statistical analysis of safety factor for liquefaction F_L, liquefaction index P_L, etc., conforming to highway bridge codes. Figs. 1 to 3 shows the relation of relative settlement, S, (cm) with, respectively, mean F_L, mean P_L and percentage, P, of F_L<1.0, for each of the zones.

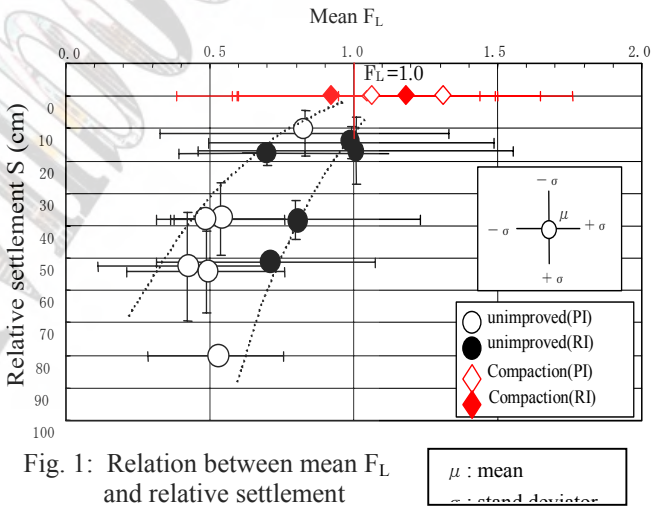

Fig. 1: Relation between mean F_L and relative settlement

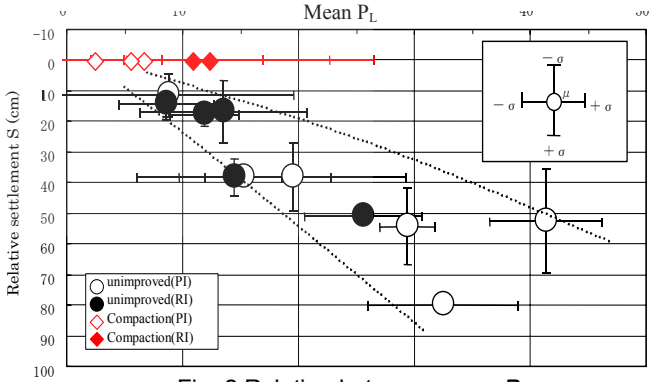

Fig. 2: Relation between mean P_L and relative settlement

Extending the plots for unimproved ground, critical values for settlement can be considered as approximately F_L>1.0, P_L<5, and P<40%.

However, determining mean F_L, mean P_L and the percentage, P, of F_L<1.0 from *N* values for improved ground by compaction between piles gives discontinuous, widely scattered plots compared with those for unimproved ground. These analytical results suggest that the current design method of evaluation using the *N* values of ground between piles after improvement may under-evaluate the mean liquefaction resistance of the ground as a whole after improvement by compaction.

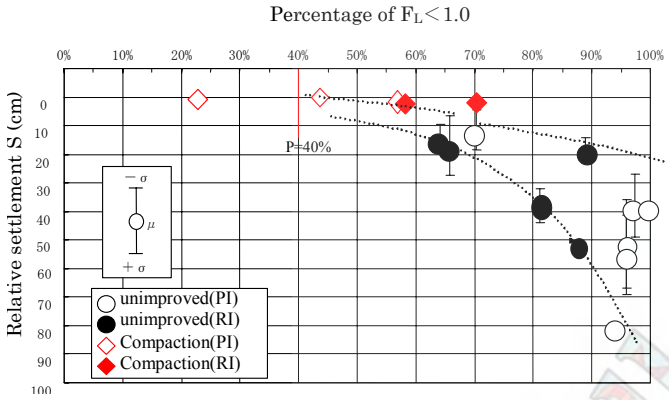

Fig. 3: Relation between mean P_L and relative settlement

B. *Evaluation of liquefaction resistance of compaction-improved ground*

Harada et al [4] have shown that liquefaction resistance of improved ground by compaction tends to be high compared with that of naturally deposited ground with the same *N* values. Thus, when considering factors such as composite ground effect in an evaluation of improved ground by compaction as a whole, the following properties may be thought to play some part in improved ground by compaction:

a) Increase in ground density (C_1)
b) Increase in horizontal effective stress (increase in coefficient of earth pressure at rest K_0) (C_2)
c) Increase in overall strength of improved ground by compaction (composite ground effect) (C_3)
d) Micro-structural variation due to cyclic shear history (C_4)
e) Drainage effect of sand piles (C_5)
f) Decrease in degree of saturation (C_6)

Thus, if a) increase in ground density (C_1) is taken as evaluated by only the increase in *N* values between piles, the liquefaction resistance of the compaction-improved ground as a whole can be evaluated from the following formula (1):

$$RL\ (\text{whole improved ground}) = C \cdot RL\ (\text{improved ground between piles}) = C_2 \cdot C_3 \cdot C_4 \cdot C_5 \cdot C_6 \cdot R_L\ (\text{improved ground between piles}) \quad (1)$$

where C, C_1~C_6 are extra factors of liquefaction resistance

C. *Extra factor of liquefaction resistance*

Taking as a parameter the liquefaction resistance extra factor, C, shown in Formula (1), adjusted values for mean F_L, mean P_L, and the percentage, P, of F_L<1.0 for improved ground by compaction are shown in Figs 4, 5, and 6 respectively.

From the figures, the extra factor of liquefaction resistance at the estimated critical values for settlement mentioned above of F_L>1.0, P_L<5, P<40% can be taken as

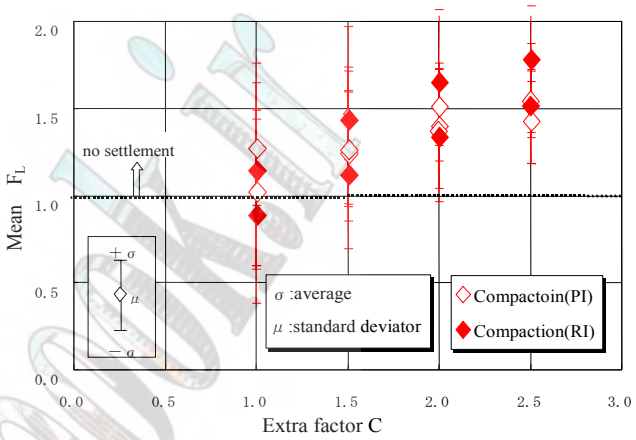

Fig. 4: Relation between extra factor and mean F_L

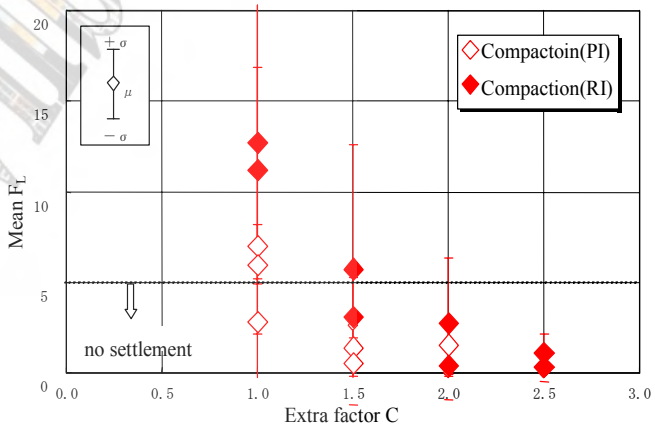

Fig. 5: Relation between extra factor and mean P_L

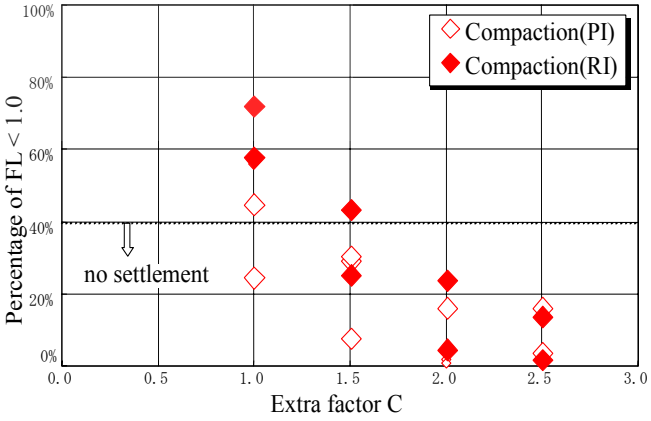

Fig. 6: Relation between extra factor mean P

about C=1.5~2.0. Thus, the mean liquefaction resistance of an improved ground by compaction as a whole is about 1.5~2.0 times the liquefaction resistance determined from *N* values of ground between the piles.

Extra factors of liquefaction resistance of improved ground by compaction

A. Extra factor due to increase in coefficient of earth pressure at rest, K_0

To determine the effect of the increase in K0 on N values and liquefaction resistance of improved ground by compaction, laboratory standard penetration container tests and cyclic torsional shear tests were undertaken taking relative density as a parameter. Three specimens with different fine content were used as shown in Fig. 7.[4] These were Toyoura sand (referred to below as TS), Takahama sand (TA) and Oku clay (OK).

As representative of the results, Fig. 8 shows the results of the laboratory standard penetration tests and Fig. 9 the results of the cyclic torsional shear tests, both for the TS specimen. Putting together the results from Figs. 8 and 9, Fig. 10 shows the relation between liquefaction resistance R_L, relative density D_r and *N* values, with K_0 as a

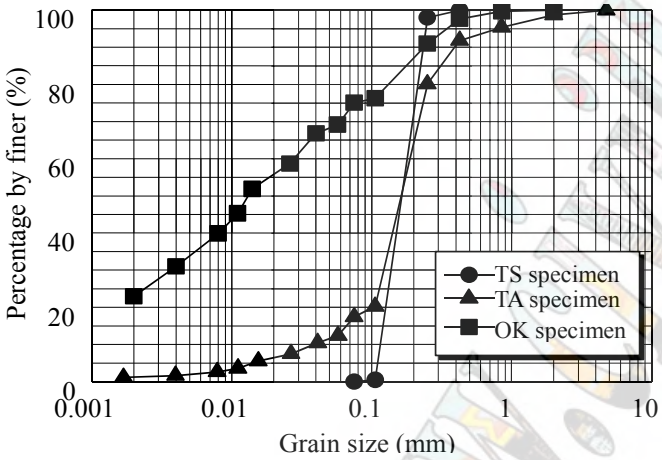

Fig. 7: Grain size distribution curves of used materials

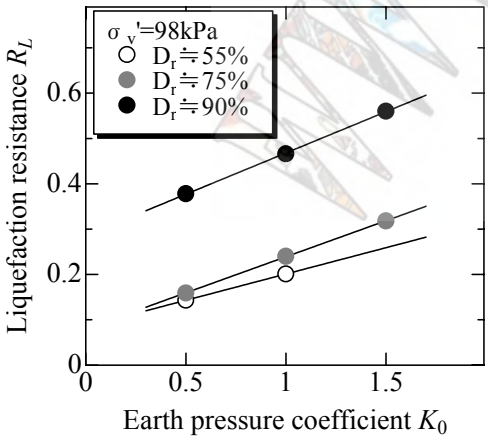

Fig. 8: Relation between *N* values and coefficient of earth pressure at rest, K_0 (TS specimen)

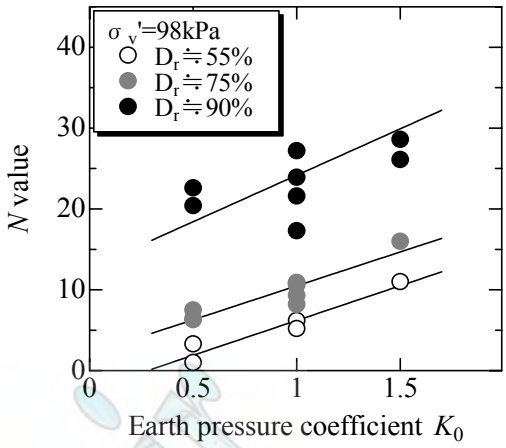

Fig. 9: Relation between liquefaction resistance R_L and coefficient of earth pressure at rest, K_0 (TS specimen)

parameter. The solid plots in Fig. 10 show the mean values from the test results, from which curves are drawn for each value of K_0. To determine the relation between *N* values and R_L under the same K_0 conditions, R_L plots for the same *N* values are shown as outlines. Comparing *N* values for the same relative density with K_0, *N* values

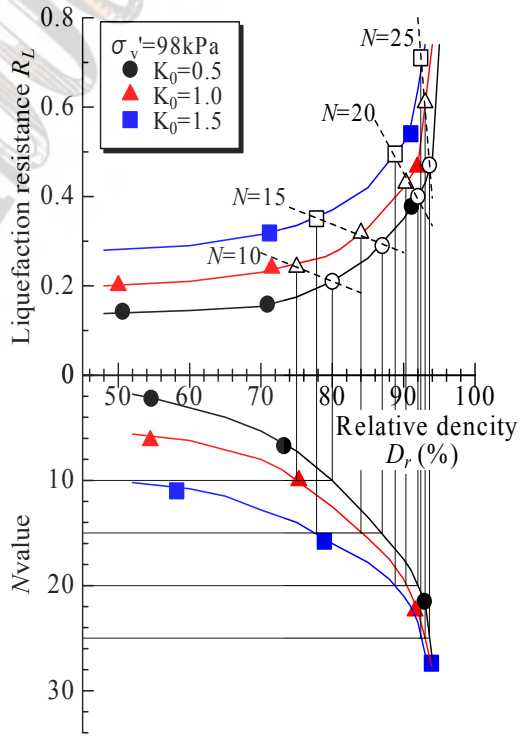

Fig. 10: Relation between D_r, R_L and *N* values (TS specimen)

increase with the rise in K_0. With regard to liquefaction resistance, liquefaction resistance increases with an increase in relative density, and the effect of K_0 for the same relative density declines after relative density exceeds 90%.

The relation between liquefaction resistance and *N* values shown in highway bridge codes (1996) is determined assuming K_0 to be 0.5, the value normally obtained from natural ground. Fig. 11 shows the relation

between liquefaction resistance and *N* values in highway bridge specifications as well as test results for the various specimens obtained on this occasion. For the liquefaction resistance curve of the highway bridge codes fine content has been adjusted to the specimens used in these tests (TS: 0%, TA: 18%, OK: 70%). From the figure, apart from the TS specimen where, for an N value around 20, the calculated liquefaction resistance is somewhat higher than the test result, we can see that the test results for all the specimens conform well with liquefaction resistance curves from highway bridge codes.

Next, the effect of fine grain content on the increase in liquefaction resistance due to a rise in K_0 was studied. For the same density conditions, liquefaction resistance at K_0=1.0 and 1.5 compared with that at K_0=0.5 was shown on the vertical axis and plotted against the different levels of fine content, as shown in Fig. 12. Although there is some scattering, we can see from the figure that liquefaction resistance due to a rise in K_0 increases by approximately 1.1~1.3 times for a increase in K_0 of 0.5 to 1.0, and by approximately 1.2~1.5 times for a 0.5 to 1.5 increase. This rate of increase is fairly consistent and not related to fine content. Thus in Formula (1), for an increase in K_0 from 0.5 to 1.0, the liquefaction resistance extra factor C_2 is 1.1 to 1.3.

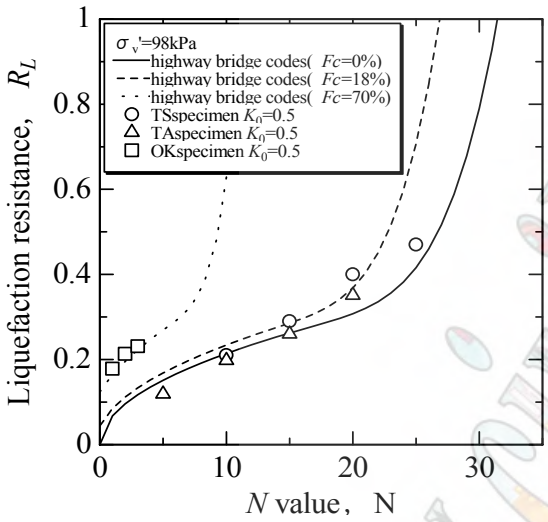

Fig. 11: Relation between liquefaction resistance R_L and *N* values. (K_0=0.5)

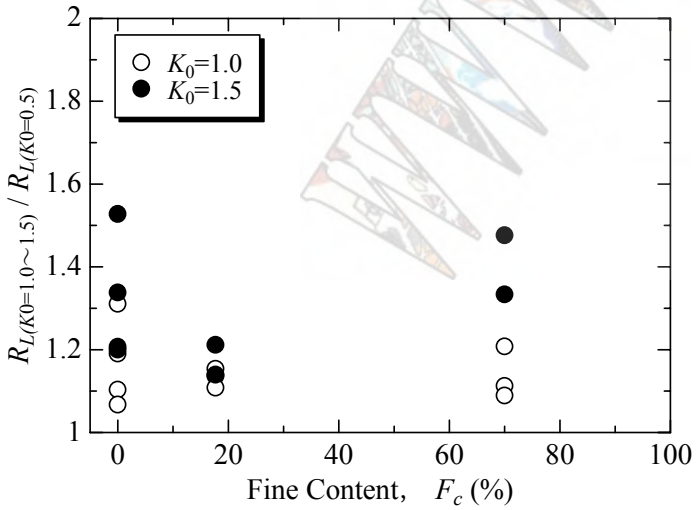

Fig. 12: Liquefaction resistance extra factors due to increase in K_0

B. Extra factor due to composite ground effect

To determine the effect of the increased rigidity of the compacted ground overall (composite ground effect), the TS specimen described above was used to make a composite ground model in a shear container as shown in Fig. 13, and shaking table tests were carried out.[5] For the tests, the strength of the unimproved ground (uniform

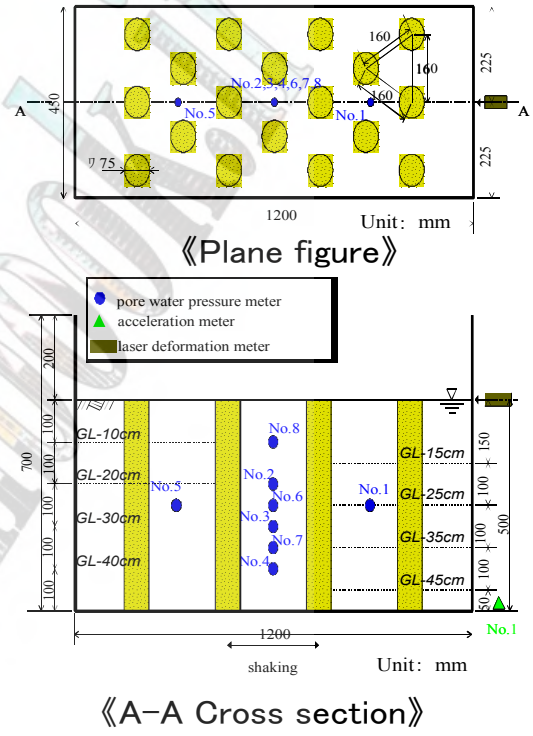

Fig. 13: Composite ground

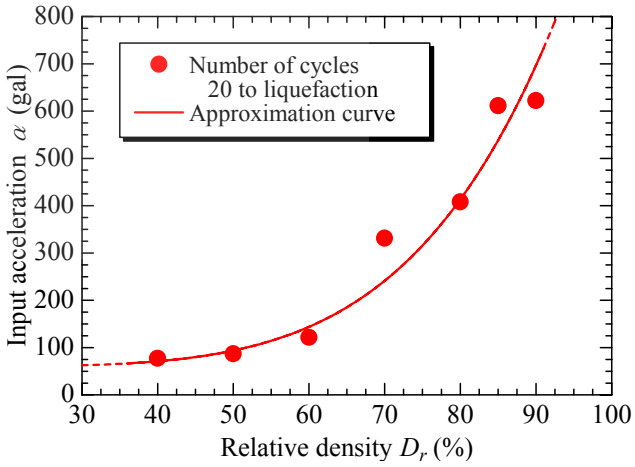

Fig. 14: Relation between acceleration at which liquefaction occurs and relative density

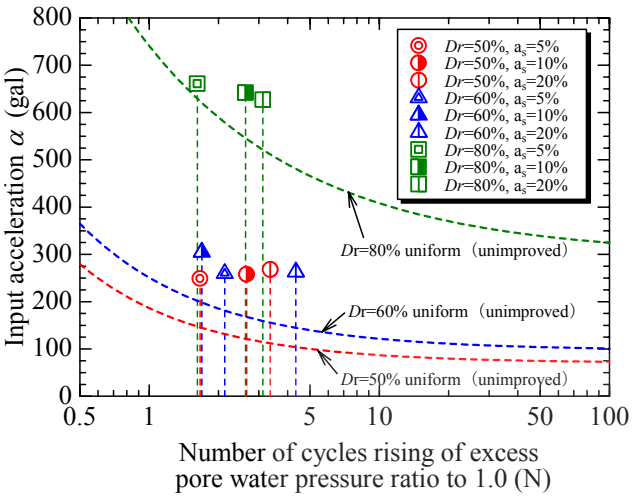

Fig. 15: Relation between input acceleration and number of cycles required for liquefaction

ground) was first determined by shaking ground for each relative density (D_r=40% to 90%) using 3 Hz sine waves for 30 secs., varying acceleration over several levels. Next, to determine the increase in strength of the improved ground (composite ground) over the unimproved ground, 30-sec. periods of shaking with 3 Hz sine waves were performed on composite ground with relative density, D_r, of 50% to 90% and improvement ratio of 5% to 15%.

Fig. 14 shows the relation between the acceleration at which liquefaction occurred in the unimproved ground and relative density. The acceleration at which liquefaction occurred means the acceleration at which liquefaction occurred after 20 cycles of shaking, and liquefaction was taken to mean the point at which excess pore water pressure in the mid section of the ground reached 1.0. The curve in the figure approximates to the results and corresponds to the safety ratio for all relative densities of F_L =1.0.

Fig. 15 shows the relation between input acceleration and number of cycles required for liquefaction to occur for the improved ground. The curves represent the critical limits beyond which liquefaction will occur, obtained from the results of tests on unimproved ground. These curves are taken to represent F_L=1.0, and a multiplier for the relation between acceleration and number of cycles required for liquefaction to occur in the improved ground over that for unimproved ground was determined. This was used to establish F_L for the improved ground.

The relation between this F_L, relative density and improvement ratio is shown in Fig. 16. Here, D_r* is the relative density of the composite ground taken to be pile centers and ground between piles, and it is defined in Formula (2).

$$D_r^* = a_s D_p + (1 - a_s) D_g \quad (2)$$

where D_r* is relative density of composite ground (%)
D_p is relative density of pile centers (%)
D_g is relative density of ground between piles (%)
a_s is the improvement ratio (%)

From the figure we can see that as increase in *N* values grow larger and of composite ground relative density before improvement increases, composite ground effect tends to decline, but if the relative density of composite ground remains the same relative density of uniform ground, the higher the improvement ratio, the greater the composite ground effect becomes.

When using the compaction method to countermeasure against liquefaction, to improve the ground to withstand a level 2 earthquake it will be necessary to improve to equivalent *N* values, *N1* values, of at least 25 (relative density about 80%).[6] As an example, in natural ground with *N* values in the range 5 to 10, for *N1* values to reach 25 improvement at a ratio of 15~20% will be needed. From Fig. 16, when Dr=80% and as=15~20%, the extra for liquefaction resistance due to composite ground effect, C_3, in Formula (1) will be in the range 1.1 to 1.3.

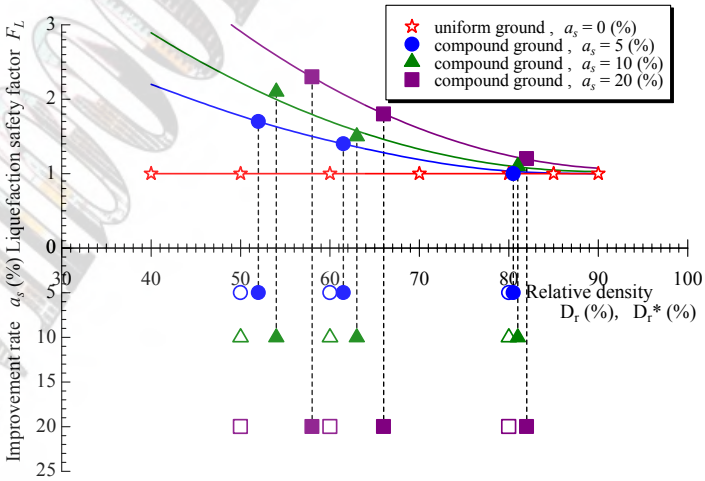

Fig. 16: Relation between relative density and liquefaction safety factor

CONCLUSIONS

This paper reports on a study of liquefaction resistance in improved ground by compaction. Extra factors were determined from the results of an analysis of relative settlement in unimproved and improved sections of ground after the Hyogoken Nambu earthquake, and overall, the liquefaction resistance of the improved ground as a whole was found to be approximately 1.5~2.0 times that of the ground between piles.

From the results of laboratory tests to study the rise in K_0 and the composite ground effect, the extra factor due to the rise in K_0, C_2, was found to be 1.1~1.3, and the extra factor due to the composite ground effect, C_3, was found to be 1.1 ~ 1.3.

REFERENCES

[1] Ohbayashi, J., Harada, K., Yamamoto, M. and Sasaki, T.: Evaluation of liquefaction resistance in compacted ground, Proceedings of 10th Japan Association for Earthquake Engineering Symposium,1998, pp.1411-1416.

[2] Matsuo, O., Yasuda, S., Harada, K., Ishiguro, T. and Uzuoka, M.: Evaluation of improved ground after level 2 earthquake, Proceedings of 32nd Japanese Conference on Geotechnical Engineering, 1997, pp. 1065-1066.

[3] Matsuo, O., Yasuda, S., Yamamoto, M., Harada, K., and Hashimoto, T.: Evaluation method of improved ground and damage sustained under level 2 earthquake, Japan Society of Civil Engineers, Proceedings of 52nd Annual Technical Lecture Series, 1997, pp 408-409.

[4] Harada, K., Ohbayashi, J., Yamamoto, M. Yasuda, S.: N values of compaction-improved ground and evaluation of liquefaction resistance, Proceedings of 11th Japan Association for Earthquake Engineering Symposium, 2002, pp. 707-710.

[5] Yasuda, S., Harada, K., Tanaka, T., Uchiyama, Z., Ozu, Y., and Nishikawa, K.: Experimental Study on Effectiveness of reducing Liquefaction Occurrence in Composit Ground by Compaction Method, Proceedings of 39th Japanese Conference on Geotechnical Engineering, 2004, pp. 1939-1940.

[6] Yasuda, S.: Lecture materials for study course on ground liquefaction and flow—Liquefaction countermeasures and design method to counter flow, Japanese Geotechnical Society, October, 1998, pp. 60-61.

Liquefaction Resistance of Ground Improved by Permeable Grouting Method

K. Kawamura[1], M. Kazama[2], R. Uzuoka[2], N. Sento[2], T. Suzuki[2], T. Oshima[1]
[1] *Penta-Ocean Construction Co.,Ltd., Tokyo, Japan*
[2] *Department of Civil Engineering, Graduate School of Engineering, Tohoku University, Sendai, Japan*

Abstract

A strain-controlled cyclic triaxial test and an on-line test were conducted in order to confirm the liquefaction resistance and residual displacement of improved sand by Permeable Grouting Method. In these tests, either a constant strain amplitude or an irregular strain loading history, such as a seismic wave was applied to soil specimens under the undrained condition. Subsequently, a re-consolidation test during the dissipation process of excess pore pressure due to cyclic shear was examined in each test. Even though the improved sand was of low unconfined strength at 30kN/m^2, the specimen did not liquefy in the tests. From the view point of ductility, the improved soil could store much larger dissipation energy than unimproved sand on the shear stress-shear strain relationship. Additionally, it was confirmed that the volume change of the improved sand was 60% less than that of the unimproved sand in the re-consolidation tests. Based on these results, the deformation characteristics of the improved sand to cyclic shear loading were evaluated quantitatively.

Keywords— *Permeable Grouting Method, Liquefaction, Strain-controlled cyclic triaxial test, Online-test*

INTRODUCTION

Permeable Grouting Method [1] [2] involves injecting a solvent-type grouting chemical with good permeability into sandy soil to make liquefaction resistance high by replacing the pore water in the sandy soil with a gel substance. From previous studies, it is understood that the improved sand with strength (q_u) by unconfined compression test which ranges from 50 to 100kN/m^2 has a liquefaction strength (R_{L20}) of between 0.3 to 0.5. It is found that the improved sand has enough liquefaction resistance against comparatively small inter-plate earthquakes. This liquefaction strength is only based on the conditions at 5.0% double amplitude of axial strain obtained from the stress-controlled cyclic triaxial test regardless of whether the effective stress became zero. On the current design method of improved ground, the R_{L20} of improved soil is determined to satisfy a condition which the safety factor of liquefaction (F_L) is unity, and the deformation characteristics of improved soil are not taking into account explicitly. To our regret, it is difficult to accurately evaluate the ductility of improved sand in this design method.

To overcome the above problems, the evaluation of the ductility of the improved sand was studied. At first, the strain-controlled cyclic triaxial test of the improved sand was conducted and the liquefaction resistance of improved sand against constant amplitude strain history was confirmed. Next, on-line tests of the improved sand were executed to confirm the liquefaction resistance of improved sand against irregular strain histories such as seismic waves. Subsequently, re-consolidation tests during the dissipation process of the excess pore water pressure due to the cyclic shear loading were conducted to study the re-consolidation characteristic of improved sand.

OUTLINE OF EXPERIMENT

A. Unconfined Compression Strength of Improved Sand

The sample sand used in the experiment were sample sand A and sample sand B, whose Fc is 0%, and sample sand C, which mixed three kinds of sand so that Fc might become 10%. The unimproved sand specimen and the improved sand specimen were made using these three kinds of samples so that Dr might become 60%. The improved sand specimen was made to become a fixed dry density using the chemical grouting with a silica concentration of 2.0%-6.0%. After being curied for 28 days under condition to make the temperature constant of 20 degrees, an unconfined compression test, a cyclic triaxial test and an on-line test were executed. Fig. 1 shows the relationship between the silica concentration of the chemical grouting and q_u of the improved sand in each sample sand.

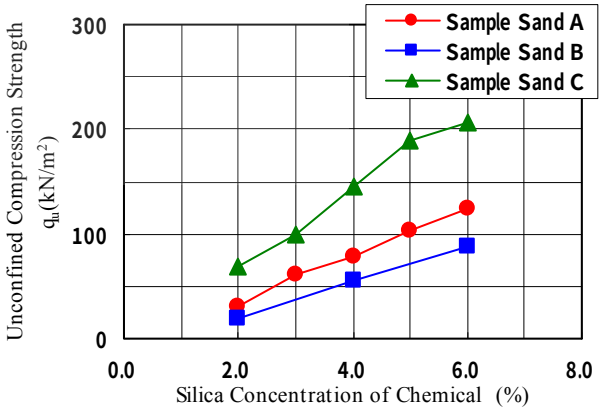

Fig. 1 : Unconfined Compression Strength of Improved Sand

B. Outline of Strain-Controlled Cyclic Triaxial Test

The stress-controlled cyclic triaxial test is conducted to evaluate liquefaction resistance of sand. However, it is difficult to evaluate the ductility of the soil appropriately because the fatigue failure strength of the soil is obtained. According to the method based on the normalized dissipation energy proposed by Kazama [3], a strain-controlled cyclic triaxial test was executed and the liquefaction resistance of the improved sand was evaluated. In this test, the relationship between the shear modulus ratio and the normalized dissipation energy during the cyclic loading was of particular interest. Dissipation energy is defined as follows: The cumulative dissipation energy is represented by an area enclosed by the hysteresis loop during the cyclic shearing process. This energy was normalized by the effective overburden pressure.

C. Outline of On-Line Test

Fig. 2 shows the outline of the on-line test [4] [5]. This figure shows a comparison between the ordinary seismic response analysis and the on-line test in the time area. The equation of motion is solved step by step in the time domain in both methods. The way to acquire the shear restoration force is fundamentally different. The constitutive model is used in the seismic response analysis, but an element test which uses an actual soil sample is used in the on-line test. In the on-line test, the earthquake motion can be input from the bed rock as well as the seismic response analysis. Therefore, this method is adopted for evaluating the liquefaction behavior to irregular waves. The on-line control of the test apparatus and acquisition of the data were achieved by a personal computer. In the on-line test, the element test was executed using a hollow cylindrical torsional shear apparatus.

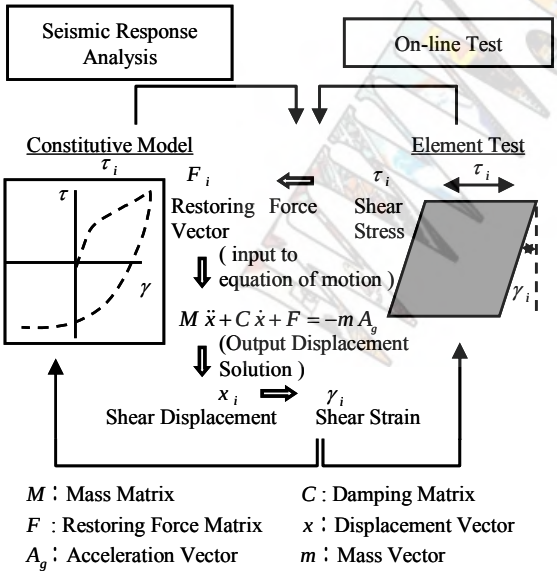

Fig. 2 : Outline of On-line Test

LIQUEFACTION CHARACTERISTIC OF IMPROVED SAND SUBJECTED TO CONSTANT CYCLIC STRAIN LOADING

A. Test Condition

Table 1 shows the test case. A strain-controlled cyclic triaxial test was conducted using specimens of unimproved sand and improved sand with five different levels of silica concentration in samples A and C. Two axial strain amplitudes (0.2% and 0.5%) were selected for the cyclic test. A sine wave with a frequency of 0.1Hz was applied to the specimen. The number of loading cycles was 100.

After the cyclic loading, the re-consolidation test was carried out under isotropic stress conditions. The volumetric strain rate was kept at a constant of 0.01%/min in the improved sand and 0.02%/min in the unimproved sand.

Table 1 : Testing Case of Strain-controlled Cyclic Triaxial Test

Case	Sample Sand	Axial Strain	Concentration of SiO_2 of Grouting Chemical
Case-A-1-0	A (Fc=0.0%)	0.20%	Unimproved
Case-A-1-2			2.0%
Case-A-1-3			3.0%
Case-A-1-4			4.0%
Case-A-1-5			5.0%
Case-A-1-6			6.0%
Case-A-2-0		0.50%	Unimproved
Case-A-2-2			2.0%
Case-A-2-3			3.0%
Case-A-2-4			4.0%
Case-A-2-5			5.0%
Case-A-2-6			6.0%
Case-C-1-0	C (Fc=10.0%)	0.20%	Unimproved
Case-C-1-2			2.0%
Case-C-1-3			3.0%
Case-C-1-4			4.0%
Case-C-1-5			5.0%
Case-C-1-6			6.0%
Case-C-2-0		0.50%	Unimproved
Case-C-2-2			2.0%
Case-C-2-3			3.0%
Case-C-2-4			4.0%
Case-C-2-5			5.0%
Case-C-2-6			6.0%

B. Cyclic Shear Characteristic of Improved Sand

Fig. 3 shows the relationship between the shear stress and the shear strain in Case-A-1-0 and Case-A-2-0 of the unimproved sand of sample A. Fig. 4 shows the relationship between the shear stress and the shear strain in Case-A-1-3 and Case-A-2-3 of the improved sand of sample A. The unimproved sand, regardless of the magnitude of the amplitude of the axial strain, the shear modulus decreased and the area enclosed by the hysteresis loop becomes almost zero with cyclic loading. In the case with 0.5% in the amplitude of the axial strain, the shear modulus decreased rapidly at an early stage of the cyclic loading. On the other hand, in the improved sand,

regardless of the magnitude of the amplitude of the axial strain, the shear modulus decreases gradually, but the area enclosed by the hysteresis loop is larger than the unimproved samples. Therefore, shear resistance remains and the effective stress does not become zero.

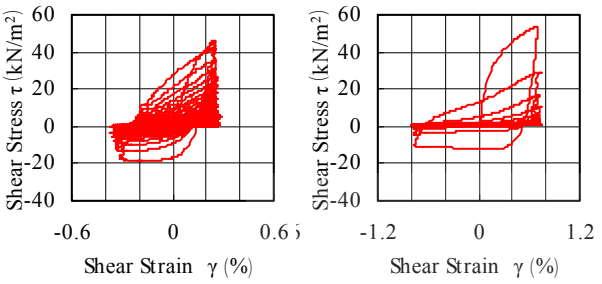

(a) Case-A-1-0 (b) Case-A-2-0

Fig. 3 : Relationship between Shear Stress and Shear Strain of Unimproved Sand

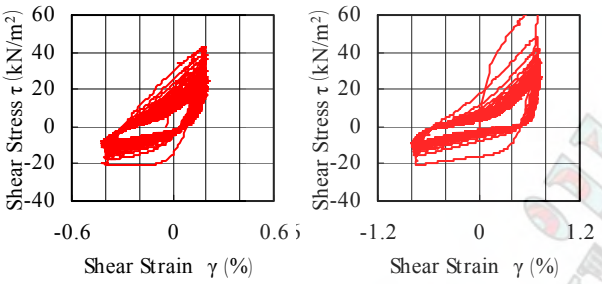

(a) Case-A-1-3 (b) Case-A-2-3

Fig. 4 : Relationship between Shear Stress and Shear Strain of Improved Sand

C. *Liquefaction Characteristic of Improved Sand*

Fig. 5 shows the relationship between the number of cycles and the shear modulus ratio. These figures show the results of the case of 0.5% axial strain amplitude loading for five silica concentration samples in sample A. The shear modulus ratio (G/G_1) is a value into which the secant shear modulus of each loading cycle (G) is divided by the initial secant shear modulus (G_1) in the relationship between the shear stress and the shear strain. The shear modulus of the unimproved sand drops sharply and becomes almost zero at 10 cycles. On the other hand, in the case of the improved sand, the shear modulus ratio decreases gradually, but the shear modulus is steady at a constant value after the 40th cyclic loading and does not become zero. The shear modulus ratio becomes small in the presence of high silica concentrations in the improved sand. And, in the improved sand with a low silica concentration of 2%, 30-40% of the initial secant shear modulus is maintained.

Fig. 6 indicates the relationship between the number of cycles and the normalized dissipation energy in the same cases shown as Fig. 5. In the case of the unimproved sand, the normalized dissipation energy becomes steady since the area of the hysteresis loop becomes almost zero as shown in Fig. 3. On the other hand, in the case of the improved sand, the normalized dissipation energy increases linearly because the constancy of the area of the hysteresis loop is maintained even if the loading is continually applied. Additionally, the higher the silica concentration of the improved sand, the larger the normalized dissipation energy. As a result, the liquefaction resistance considering the deformation characteristics of improved sand becomes larger.

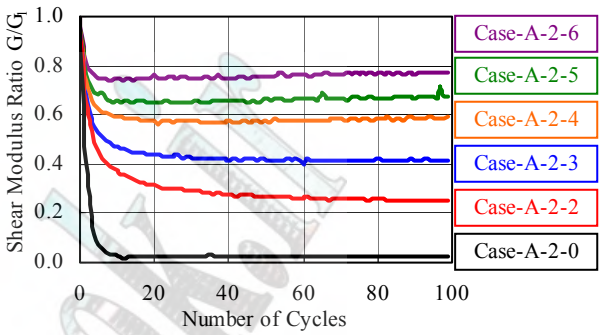

Fig. 5 : Relationship between Shear Modulus Ratio and Number of Cycles (Case-A-2-0～6)

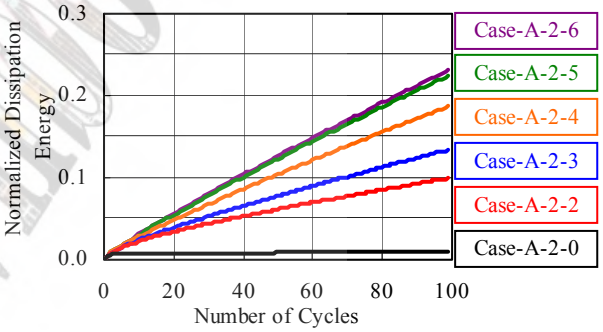

Fig. 6 : Relationship between Normalized Dissipation Energy and Number of Cycles (Case-A-2-0～6)

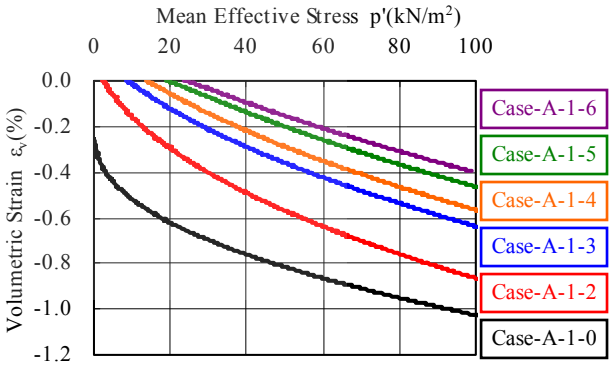

Fig. 7 : Relationship between Volumetric Strain and Mean Effective Stress (Case-A-1-0～6)

D. *Re-Consolidation Test of Improved Sand*

Fig. 7 and Fig. 8 show the results of the re-consolidation test after cyclic loading. Fig. 7 shows the results of 0.2% axial strain amplitude loading for five

different levels of silica concentration in sample A, and Fig. 8 shows the results of 0.5% axial strain amplitude loading for five different levels of silica concentration samples in sample A. In these figures, the horizontal axis shows the mean effective stress and the vertical axis shows the volumetric strain. The volumetric strain becomes smaller as the silica concentration of the improved sand increases. The results of 0.5% of the amplitude of the axial strain show the volumetric strain for the improved sand is about half, or less than half the volumetric strain for the unimproved sand. Moreover, the volumetric strain is generated slowly with the recovery of the mean effective stress in the improved sand. On the other hand, the volumetric strain is rapidly generated in the unimproved sand at the low mean effective stress.

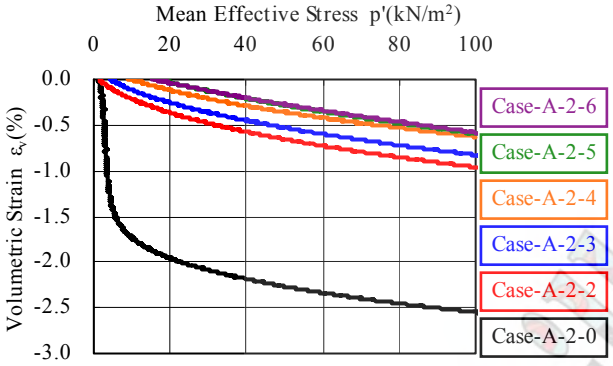

Fig. 8 : Relationship between Volumetric Strain and Mean Effective Stress (Case-A-2-0～6)

LIQUEFACTION CHARACTERISTIC OF IMPROVED SAND AGAINST ACTUAL EARTHQUAKE MOTION

A. Condition of On-Line Test

Fig. 9 shows the hypothetical subsoil profile of the on-line test. The subsoil profile was divided into ten sub-layers. The thickness of the subsoil was 20 m and the each sub-layer thickness was set to 2m. The ground-water level was set to the ground surface. The 8th layer adopted the element test layer carried out the hollow cylindrical torsional shear test since the mean effective stress at the center position of the 8th layer is 100kN/m^2 assuming K_0 is 0.5. The other layers adopted a hyperbolic model with the parameters shown in the figure. The reference strain was set to 0.1% to prevent strong nonlinear behavior in the model layer. Time integration was achieved by the central differential method with a finite time step of 0.005 seconds. Rayleigh damping, which was proportional to the stiffness matrix, was used and the value of β was determined by the damping factor of 0.01 and the frequency ω of the system. Further information about the testing procedure is described in Sento et al. [5].

Table 2 shows the test case. The on-line test was carried out for both the specimen of unimproved sand and improved sand with three different levels of silica concentration (2, 4, 6%) in sample B. Two types of input earthquake motion were used as shown in Fig. 10. The Hachinohe NS component with a maximum acceleration of 209.89Gal was used as the inter-plate earthquake motion, and the Kobe Port Island GL-32.4m NS component with a maximum acceleration of 543.59Gal was used as the strong shallow crustal earthquake.

After cyclic loading, the re-consolidation test was conducted as well as the cyclic triaxial tests.

Fig. 9 : Model Ground of On-line Test

Layer	Thick-ness (m)	Density (t/m^3)	Vs (m/sec)	γ_γ (%)	σ_m' (kN/m^2)	Type
1	2.0	2.0	200	0.1	-	Hyperbolic
2						
3						
4						
5						
6						
7						
8				**-**	**100**	**Test**
9			240	0.1	-	Hyperbolic
10						
Base			400			Elastic

Table 2 : Testing Case of On-line Test

Case	Sample Sand	Input Motion	Concentration of SiO_2 of Grouting Chemical
Case-B-1-0	B (Fc=0.0%)	Hachinohe wave	Unimproved
Case-B-1-2			2.0%
Case-B-1-4			4.0%
Case-B-1-6			6.0%
Case-B-2-0		Kobe PI wave	Unimproved
Case-B-2-2			2.0%
Case-B-2-4			4.0%
Case-B-2-6			6.0%

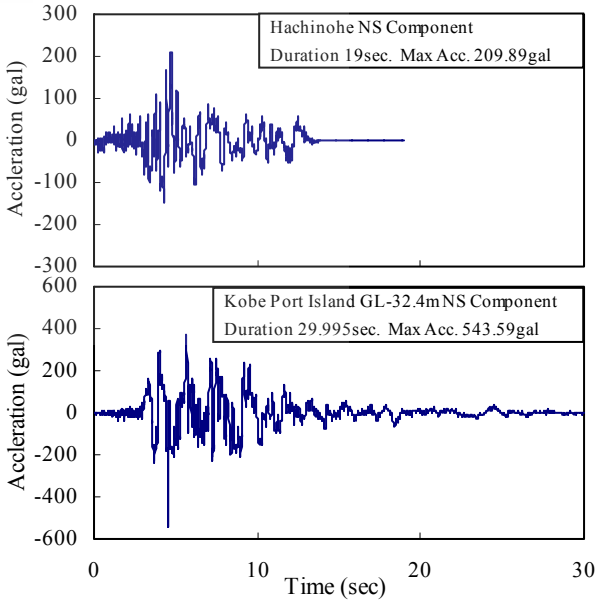

Fig. 10 : Earthquake Input Motion

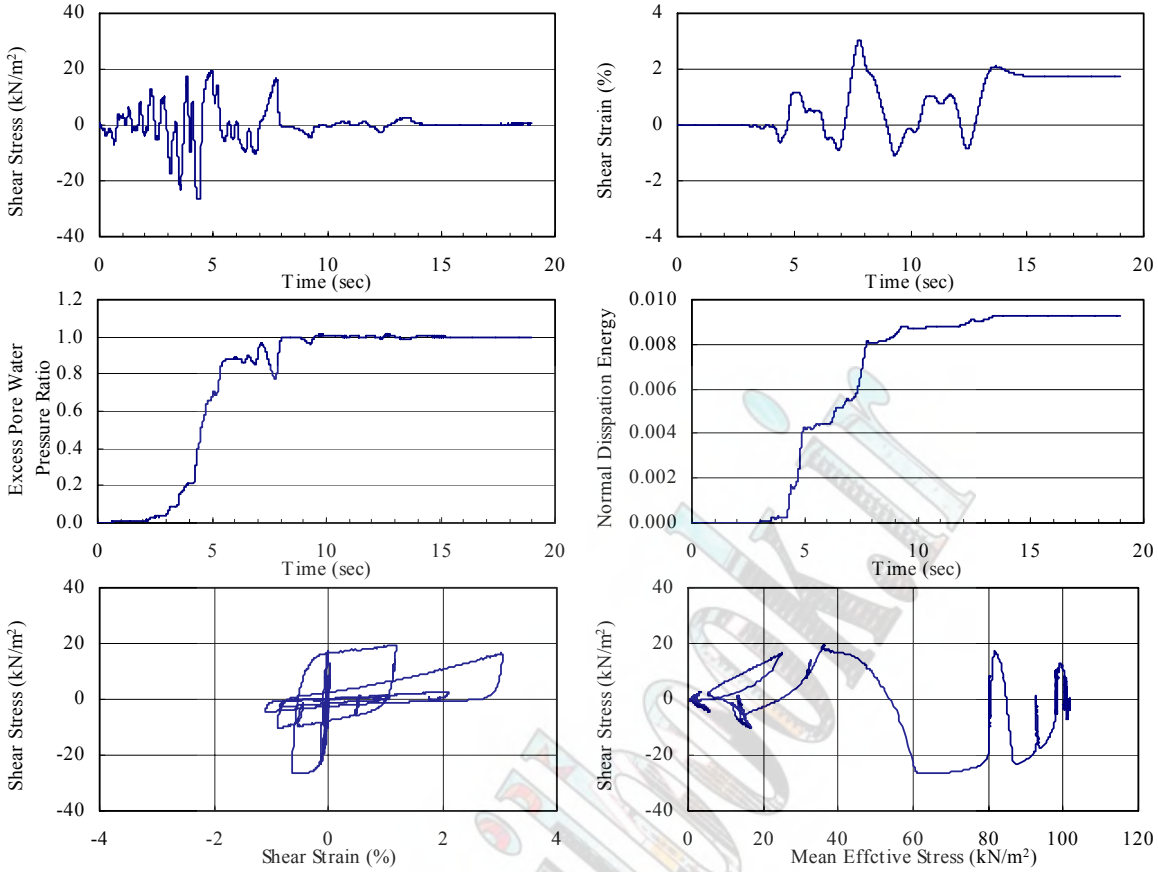

Fig. 11 : Results of Unimproved Sand (Case-B-1-0)

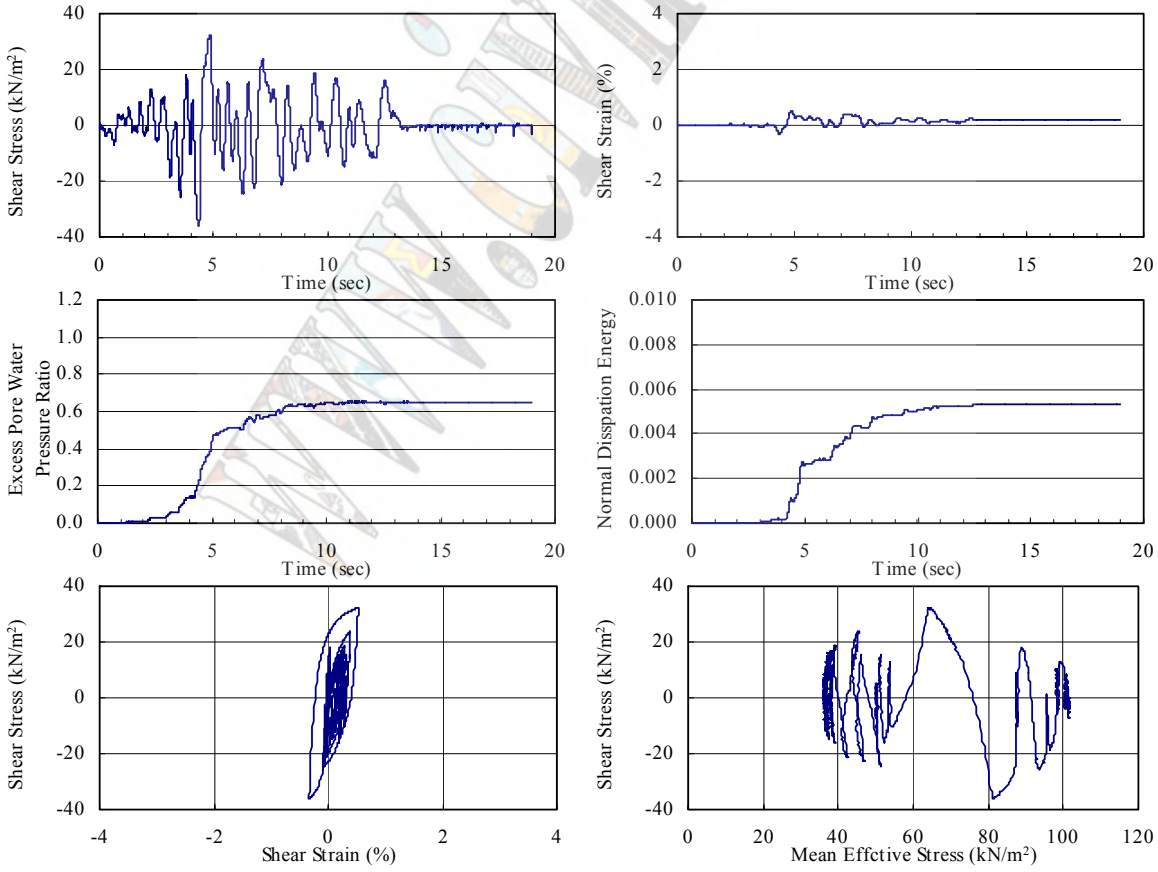

Fig. 12 : Results of Improved Sand (Case-B-1-2)

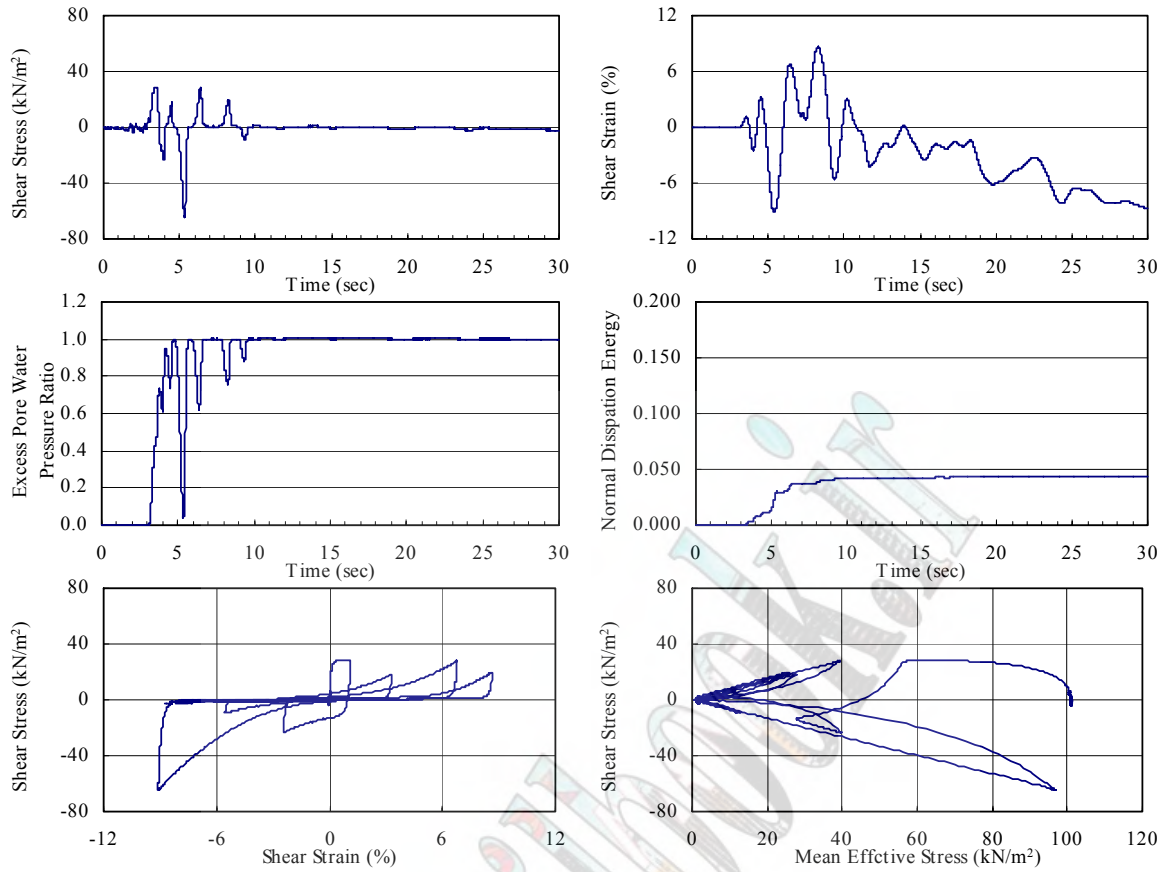

Fig. 14 : Results of Unimproved Sand (Case-B-2-0)

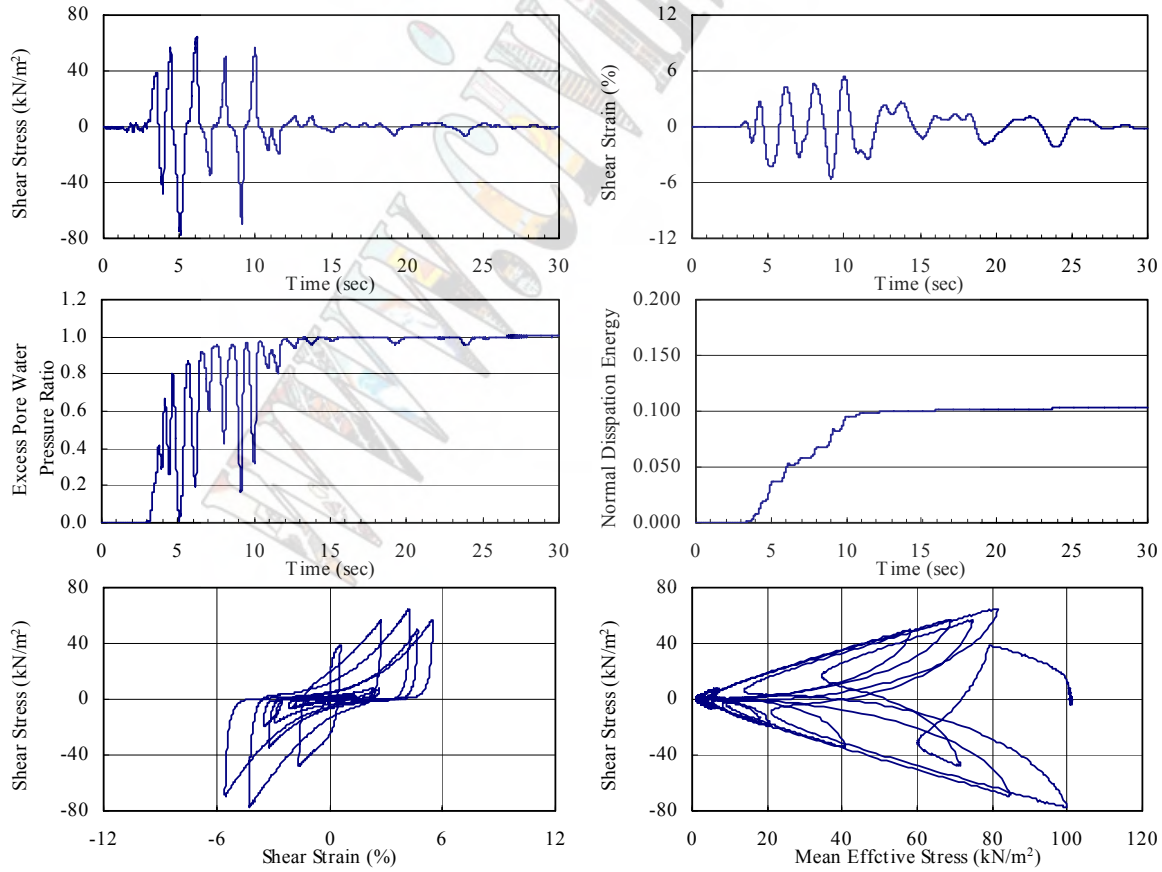

Fig. 15 : Results of Improved Sand (Case-B-2-2)

B. Test Results of Inter-plate Earthquake Motion

Dynamic Characteristic of Improved Sand

Fig. 11 shows the results of Case-B-1-0 of the unimproved sand, and Fig. 12 shows the results of Case-B-1-2 of improved sand with a silica concentration of 2%. In Case-B-1-0 with unimproved sand, the excess pore water pressure ratio rises up to 1.0 at ten seconds after the earthquake occurs, and the mean effective stress becomes zero and liquefaction occurred. On the other hand, in Case-B-1-2 with improved sand, the peak excess pore water pressure ratio is 0.7 or less, and the mean effective stress does not become zero. In the improved sand, the maximum shear strain is about 0.5%. On the other hand, the maximum shear strain of unimproved sand is about 3.0%. Therefore, the effect of improving the sand is remarkabe.

Re-Consolidation Test of Improved Sand

Fig. 13 shows the results of Case-B-1-0 to Case-B-1-6 of unimproved and improved sand. In the case of improved sand, the volumetric strain is almost the same irrespective of silica concentration, but the volumetric strain is suppressed to about 40% or less than that of the unimproved sand.

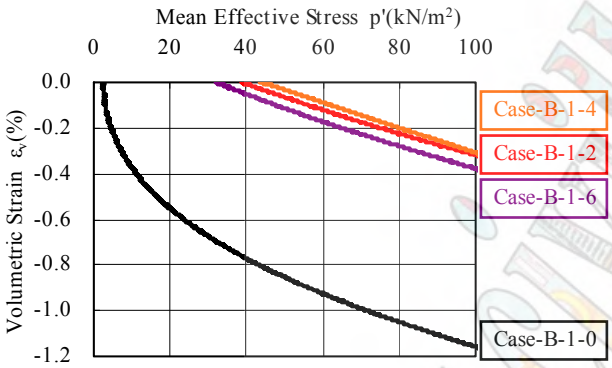

Fig. 13 : Relationship between Volumetric Strain and Mean Effective Stress (Case-B-1-0～6)

C. Test Results of strong shallow crustal Earthquake Motion

Dynamic Characteristic of Improved Sand

Fig. 14 shows the results of Case-B-2-0 with the unimproved sand, and Fig. 15 shows the results of Case-B-2-2 with improved sand with a silica concentration of 2%. In Case-B-2-0 with unimproved sand, the excess pore water pressure ratio rises up to 1.0 a few seconds after the earthquake occurs, and the mean effective stress becomes zero. On the other hand, in Case-B-2-2 with improved sand, the excess pore water pressure ratio rises up to almost 1.0, but the mean effective stress does not completely become zero like the unimproved sand because the mean effective stress recovers with an increase in shear strain. The normalized dissipation energy becomes constant after ten seconds in the case of the unimproved sand. On the other hand, in the case of the improved sand, the normalized dissipation energy does not become constant during earthquake. Additionally, there is an increasing tendency even though the shear modulus decreases. The reason is that the shear modulus almost does not become zero. Consequently, the normalized dissipation energy is about twice that of the unimproved sand. And, as for the residual shear strain after the earthquake, the residual shear strain is hardly generated in case of the improved sand while the residual shear strain of about 9% is generated in the case of the unimproved sand.

Re-Consolidation Test of Improved Sand

Fig. 16 shows the results of Case-B-2-6 from Case-B-2-0 of unimproved and improved sand. In the case of the improved sand, there are few differences of the volumetric strain in Case-B-2-2 and Case-B-2-4 though the volumetric strain is smaller in Case-B-2-6 since the silica concentration is higher. Compared with the improved and the unimproved sand, the volumetric strain is suppressed to about 60% as for the case with considerably low silica concentration.

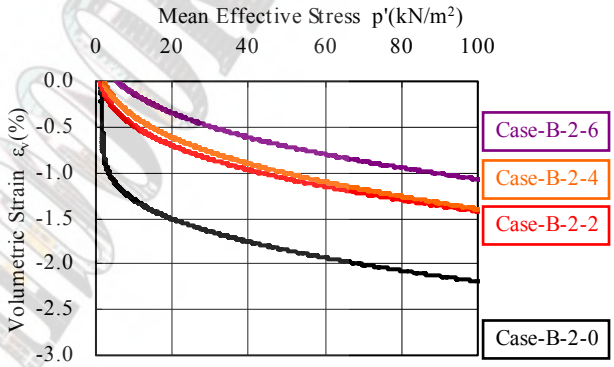

Fig. 16 : Relationship between Volumetric Strain and Mean Effective Stress (Case-B-2-0～6)

CONSIDERATION ABOUT LIQUEFACTION RESISTANCE OF IMPROVED SAND

As for the shear behavior of the improved sand subjected to cyclic shear, regardless of loading conditions (the constant amplitude, the inter-plate and the strong shallow crustal earthquake motion) it was able to be confirmed that liquefaction such as the shear modulus and the effective stress becomes zero was not generated though the shear modulus decreased. In particular, the results of the constant amplitude loading showed that the improved sand had the ductility ofe clay because 30-40% of the initial shear modulus was maintained and the normalized dissipation energy linearly increased gradually though the shear modulus decreased. On the other hand, though making a comparison of the results of the constant amplitude loading and actual earthquake motion is not so easy, it was found that there is a big difference with respect to the residual shear strain after earthquake. Fig. 17 shows the relationship between the silica concentration of the chemical and the residual shear strain. In this figure, it corresponds to the unimproved sand that the silica

concentration of the chemical is 0%. There was hardly any difference based on the silica concentration of the improved sand, but compared with the improved sand with the unimproved sand, especially in the Kobe PI wave, the residual shear strain was 1.0% or less and the residual shear strain was hardly generated in the improved sand though the residual shear strain was about 9% in the unimproved sand. The reason for the abovementioned difference is derived from the ductility of the improved sand. On the other hand, the unimproved sand fails due to shear deformation and the occurrence of liquefaction during the earthquake.

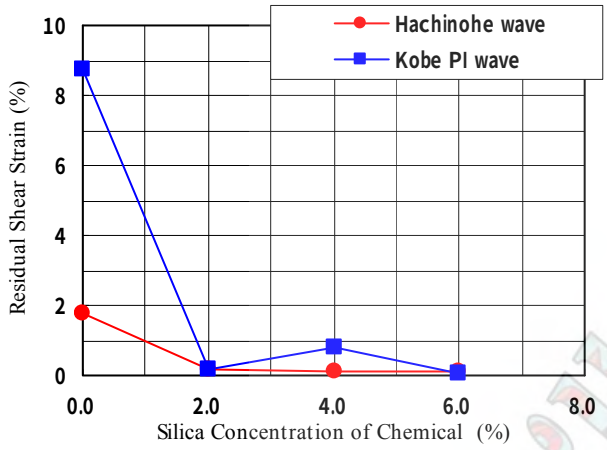

Fig. 17 : Relationship between Residual Shear Strain and Silica Concentration of Chemical

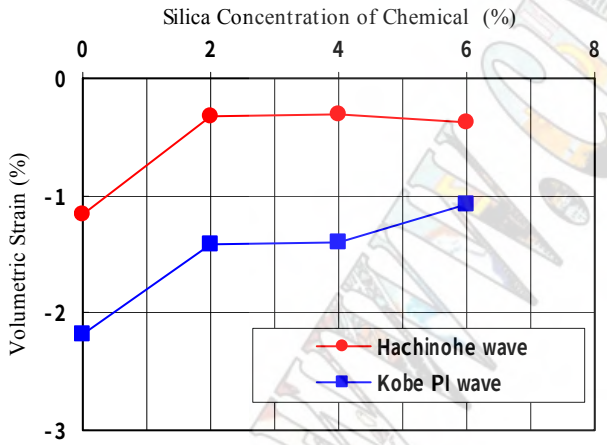

Fig. 18 : Relationship between Volumetric Strain and Silica Concentration of Chemical

As for the re-consolidation behavior according to the excess pore water pressure dissipation, regardless of the cyclic loading condition, the volumetric strain is slowly generated during the recovery of the mean effective stress in the improved sand in the aforementioned figures. On the contrary, the volumetric strain is rapidly generated at the initial stage in the unimproved sand. This is thought to be that the improved sand does not fail completely because the shear modulus does not become zero even though the shear modulus decreases, while the unimproved sand fails completely. Compared with the volumetric strain, as shown in Fig. 18, the volumetric strain in the improved sand is suppressed to about 60% or less of the volumetric strain in the unimproved sand. Therefore, it is expected that some extent of volume change take place in the improved sand after an earthquake while the flow failure due to the rapid redistribution of excess pore water pressure may occur in the unimproved sand.

SUMMARY

In this study, it was confirmed that the improved sand by Permeable Grouting Method had the ductility and the high liquefaction resistance for the cyclic shear loading. Especially, the improved sand with low strength with low silica concentrations had considerably high liquefaction resistance and the improved sand did not fail due to liquefaction subjected to considerably strong earthquake motion. Also, a quantitative evaluation on the re-consolidation deformation characteristics after an earthquake were achieved. In the actual construction, the ground improvement of high strength is executed by the conventional design method, but it is thought that it is possible to contribute to reduction in costs if the result of this study is quantitatively evaluated and a rational design method taking into account the deformation characteristics of the improved sand is established.

REFERENCES

[1] H. Yamazaki, K. Zen, K. Kawamura, Study on applicability of Permeable Grouting Method to countermeasure against liquefaction, Report of Port and Airport Research Institute, Vol.41, No.2, pp.119-151, 2002.

[2] K. Hayashi, K. Zen, H. Yamazaki, A field test on a new chemical grouting method to improve the liquefaction resistance of sandy layers beneath the existing structure, Proceeding of IS-YOKOHAMA, Vol.1, pp.291-297, 2000.

[3] M. Kazama, A. Yamaguchi and E. Yanagisawa, Liquefaction resistance from a ductility view point, Soils and Foundations, Vol.40, No.6, pp.47-60, 2000.

[4] Kon young Choul and Motoki Kazama, Application of Hybrid-Online Testing Method to Geotechnical Engineering Problem, Geoenvironmental Engineering, No.3, pp.80-89, 2003.

[5] N. Sento, M. Kazama, R. Uzuoka, A. Matsuya and M. Ishimaru, Liquefaction-induced volumetric change during re-consolidation of sandy soil subjected to undrained cyclic loading histories, Cyclic behaviour of soil and liquefaction phenomena, Edited by Th. Triantafyllidis, Balkema, pp.199-206, 2004.

Evaluation of Characteristics of Sand Compaction Pile Improved Composite Ground by Online Testing Method

N. H. Priyankara, M. Kazama, R. Uzuoka, N. Sento, K. Sakamoto
Department of Civil Engineering, University of Tohoku, Sendai, Japan

Abstract

Sand Compaction Pile (SCP) method has been widely used as a countermeasure against liquefaction in Japan. Its effectiveness has been confirmed at many sites those have suffered large scale earthquakes in recent past. In the current practice for design, SPT-N value at a mid point of a rectangular area surrounded by four adjacent sand piles, at which the liquefaction resistance to be the smallest, set as a target for the degree of compaction. The main drawback in this method is the rigidity of dense sand pile is not taken into account. As such, in the research reported in this paper an attempt was made to study the characteristics of SCP improved composite ground by parallel elementary test. In order to study the characteristics of the composite ground under undrained cyclic shear loading, multiple series of parallel elementary tests were conducted in the laboratory using two hollow cylindrical tortional shear apparatus. The results of the subsequent tests revealed that most influencing factor on evaluation of composite ground in low area replacement ratio (a_s) is the coefficient of lateral pressure (K).

Keywords— *Composite ground, liquefaction resistance, sand compaction pile*

INTRODUCTION

Compaction methods have been widely used as a countermeasure against liquefaction in Japan. Sand Compaction Pile (SCP) method is considered one of the most reliable of these methods and it has been extensively used to ameliorate liquefaction resistance of loose sandy deposits since 1970's [1], [2]. Its effectiveness has been confirmed at many sites those have suffered large scale earthquakes in recent past [1], [3], [4]. Increase in soil density as well as lateral effective stresses are considered to enhance liquefaction resistance of foundation soils [5], [6].

The installation of sand compaction pile consists of routine work, as illustrated in Fig. 1. A casing pipe with a diameter of 0.4 m is forced into the ground up to the required depth by a casing driving machine under vibration with a frequency of 10 Hz. Then, the casing pipe is retracted stepwise while supplying sand from the ground surface through the casing pipe and compact the sand by its tip under vertical vibration [7]. As this process is repeated, a well compacted, large diameter i.e. 70 cm, sand compaction pile is created that stabilizes the sub soil.

The mechanisms of densification and liquefaction resistance due to SCP installation were discussed by many researchers on the basis of laboratory elementary tests, model tests as well as field evidences [1], [3], [4], [7], [8], [9]. In addition, compaction behaviour of loose sand due to SCP installation was numerically analyzed, as in [5], [6], [10], [11], [12].

In spite of this, current practice for designing SCP as a countermeasure against liquefaction, area replacement ratio (a_s), which is defined as the ratio of the sand pile area over the tributary area of the soil surrounding each sand pile, is often determined using an empirical chart

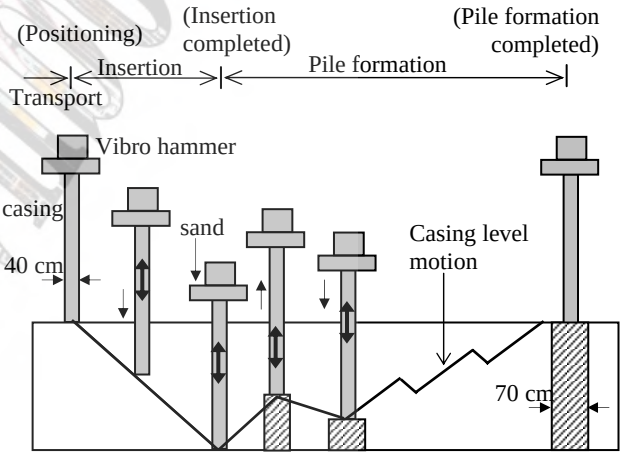

Fig. 1 : SCP installation procedure

which provides a relationship between area replacement ratio and SPT – N values at the mid point of the sand piles, which was established by large number of observed N values in improved grounds [2]. In other words, SPT – N value at a mid point of a rectangular area surrounded by four adjacent sand piles, at which the liquefaction resistance to be the smallest, set as a target for the degree of compaction. The main drawback in this method is the rigidity of dense sand pile is not taken into account. Based on field evidences, it was found that SPT – N value at the mid point of sand piles does not always provide a conservative evaluation of the liquefaction resistance of improved ground [4]. In addition, stability and deformation characteristics of SCP improved composite ground under earthquake induced motion was not elucidated sufficiently by both experimentally and

numerically. Therefore, for a rational design, it is necessary to consider not only the surrounding improved ground, but also the rigidity of dense sand pile.

This paper examines a new evaluation method for liquefaction resistance by considering the characteristics of the composite ground under undrained cyclic shear deformation, using data obtained from parallel elementary test. Cyclic shear triaxial test conducted in this study to understand the stress state and volume change during SCP installation are described first. Coefficient of lateral pressure (K value) has been used as a parameter to indicate the effect of lateral stress on liquefaction resistance. Based on the results of these preliminary tests, parallel elementary tests were conducted by using two hollow cylindrical tortional shear apparatus to study the cyclic shear behaviour of SCP improved composite ground.

THE STRESS STATE AND VOLUME CHANGE DURING SCP INSTALLATION

In order to study stress state and volume change during SCP installation, multiple series of cyclic shear triaxial tests were conducted in the laboratory by simulating the SCP installation process for different soil specimens.

Materials used

Actual ground is often composed of loose sandy soil with certain percentage of silt and clay, and it was anticipated that the way in which compaction occurs might vary depending on the fine content. Therefore, artificial materials having the different fine contents were prepared, and tests were carried out using the different types of such materials.

Toyoura sand mixed with Soma sand, in order to obtain soil specimens having fine content (FC) by weight 0, 10, 20, 30 and 40%. The grain size distribution for Toyoura sand and Soma sand are shown in Fig. 2.

Test procedure

Sand specimens were prepared in the laboratory by air-pluviation method in order to obtain low relative density of 16% to 37%. Samples were isotropically preconsolidated under 20 kPa and were saturated by circulating carbon dioxide, de-aired water and applying back pressure of 100 kPa. When the Skempton's B parameter larger than 0.96 was reached, the specimens were accepted as fully saturated for this research.

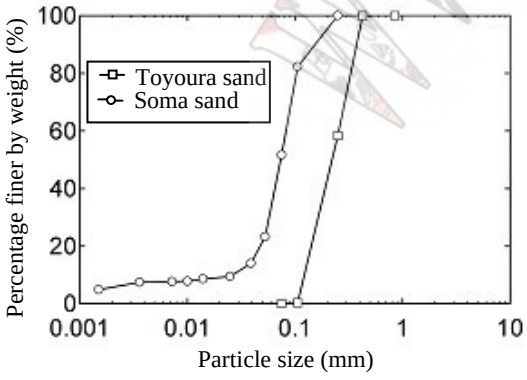

Fig. 2: Grain size distributions for soils tested

Saturated samples were anisotropically consolidated with vertical stress of 100 kPa and cell pressure of 50 kPa, thus the coefficient of lateral pressure K=0.5. Fig. 3 depicts the summary of the experimental procedure. After completion of consolidation, axial strain controlled testing was performed at a frequency of 0.1 Hz using sinusoidal wave form as shown in Fig. 4. The cyclic loading history consists of 6 steps, which gradually increases the axial strain amplitude and each step consists of 10 cycles. The purpose of selection of this type of cyclic loading history was to obtain high area replacement ratio (a_s), in order to simulate the actual SCP installation in the laboratory. In other words, in order to obtain high volumetric strain with reconsolidation, sufficient strain history was applied to test specimens under undrained condition.

The results of the triaxial tests were measured in terms of deviator stress σ_d and converted to shear stress $\tau = 0.5\sigma_d$ using conventional theory of elasticity under undrained condition. Typical test results of stress-strain path and effective stress path are shown in Fig. 5, obtained from triaxial test with FC=20% and initial relative density D_r=25%. In this case, initial shear stress was 25 kPa as initial vertical stress σ_v=25 kPa and K=0.5. As loading proceeds by keeping the horizontal stress constant, the generated pore pressure increases up to the level of confining pressure and reduction of effective stress takes place which is accompanied by the softening of the specimen (σ_h=σ_v=50 kPa).

Fig. 6(a) depicts the relationship between vertical stress σ_v and horizontal stress σ_h where as Fig. 6(b) illustrates the relationship between volumetric strain ε_v and mean effective stress σ_m'. As shown in Fig.6, before open the valve of the drainage system, increased vertical stress up to its initial value (σ_v=100 kPa) from the isotropic state to keep vertical displacement equal to zero by controlling the cell pressure (σ_h). As a result, K value increases due to increases of horizontal stress. Then

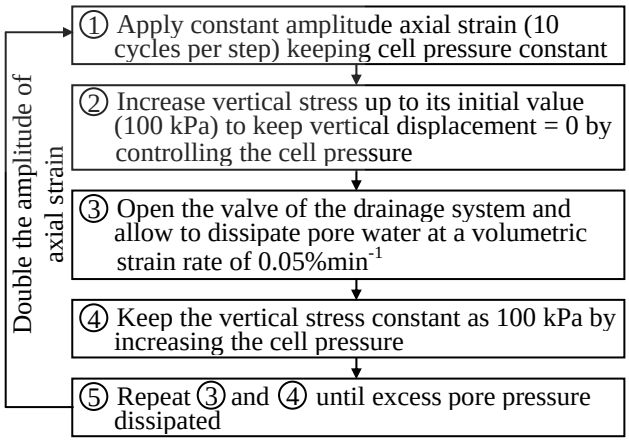

Fig. 3: Flow chart of test procedure

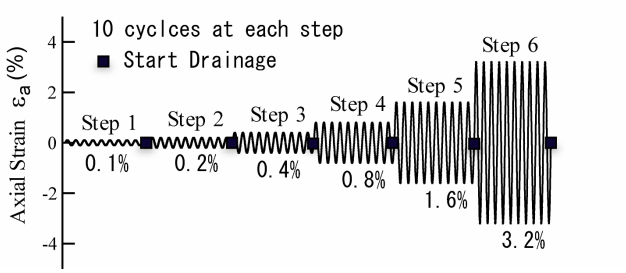

Fig. 4: Axial strain time history

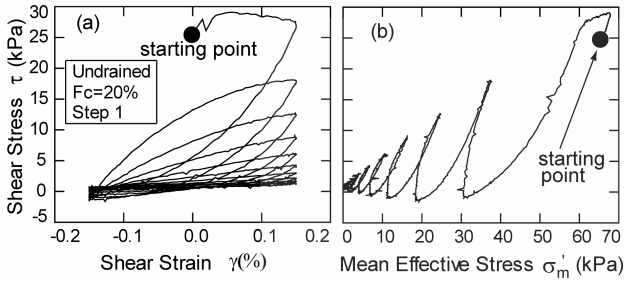

Fig. 5: Axial strain controlled cyclic shear triaxial test under undrained condition ((a) stress-strain path (b) stress path)

opened the valve of the drainage system and allowed to dissipate pore pressure by keeping the vertical stress constant as its initial value by increasing the cell pressure. Reconsolidation occurred during the drainage and significant volumetric strain occurred when mean effective stress gets near to zero (Fig. 6(b)). This process was repeated as shown in Fig. 3 until specimen fails. Reference [13] gives the full details of the test procedure and the results.

Effect of area replacement ratio (a_s) on K value

This effect is illustrated with the help of data obtained from the soil specimens with different fine content and different initial relative densities. The increase of volumetric strain over the loading steps is depicted in Fig. 7. This illustrates the effect of cyclic loading in increasing the densification characteristics. Another notable feature is that volume change in each loading step is almost same irrespective of the fine content and initial relative density, thus it shows a linear upward trend.

The graph of *K* value versus loading step number (Fig. 8) illustrates that the *K* value increased significantly at lower strain level. For example, *K* value increased from 0.5 to 1.3 at the first step. This trend had further increased during the following strain levels. However, graph indicated that the *K* value increased with tapering off as in higher strain level.

It is impossible to obtain large volumetric strain in the laboratory tests due to limitations of the test conditions, when compared with the field situations. It is a well known feature that bulging occurs during SCP installation in the field. That implies volume change occurs in both vertical and radial directions. However, in the laboratory tests, volume changes occur only in radial directions.

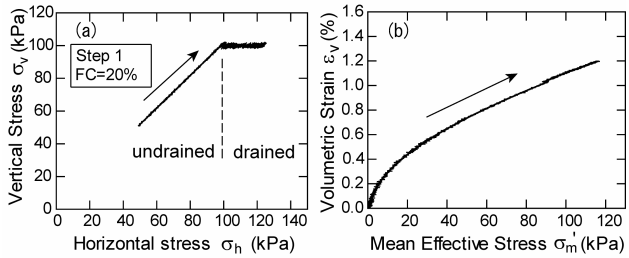

Fig. 6: Stress change and volume change during drainage

Therefore, area replacement ratio (a_s) can be represented by using volumetric strain. Then, *K* values were plotted against a_s with the view of highlighting the effects where the values vary over a reasonable range (Fig. 9).

CYCLIC SHEAR DEFORMATION BEHAVIOUR OF COMPOSITE GROUND

To overcome the shortcomings in the conventional designing of SCP, authors have proposed a new method to evaluate characteristics of composite ground under earthquake induced cyclic shear motion. Parallel elementary tests were conducted in the laboratory, using two soil samples with different relative densities, which represent the sand pile and surrounding improved ground (Fig.10). The concept of this stress control parallel elementary test basically depends on three major hypotheses, namely;

1. Relative density (D_r) and stress state in every where of improved surrounding ground are same. Therefore, use one point of the surrounding improved ground to represent the surrounding whole ground.
2. Shear strain in the sand pile, in the surrounding improved ground and in the composite ground are same.
3. Coefficient of lateral pressure (*K* value) is considered to be the same in both sand pile and surrounding improved ground.

The second hypothesis implies that,

$$\gamma_s = \gamma_b = \gamma_c \qquad (1)$$

where, γ_s, γ_b and γ_c represent the shear strain of sand pile, shear strain of surrounding improved ground and shear strain of composite ground respectively. Then, shear stress of the composite ground can be written as follows.

$$\tau_c = \tau_s a_s + \tau_b (1 - a_s) \qquad (2)$$

where, τ_s, τ_b and τ_c represent the shear stress of sand pile, shear stress of surrounding improved ground and shear stress of composite ground respectively.

Test equipment and specimen preparation

In order to study the characteristics of composite ground, multiple series of parallel elementary tests were conducted in the laboratory, using two hollow cylindrical torsional shear apparatus. The complete experimental setup is shown in Fig. 11. The details of the hollow cylindrical torsional shear apparatus is given in [14].

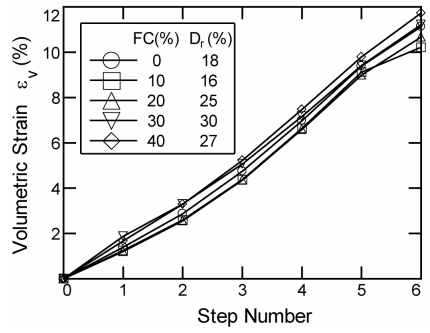

Fig. 7: Relationship between volumetric strain versus number of loading steps

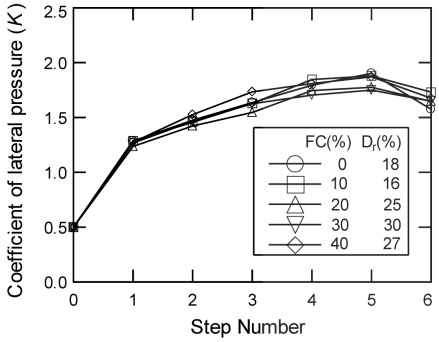

Fig. 8: Relationship between coefficient of lateral pressure versus number of loading steps

All specimens except specimens with a_s=0% were prepared by dry rodding method (lightly in a circular pattern) with a rod of diameter 6 mm. The details of the dry rodding method used for the preparation of the samples are given in [15]. Relative density was chosen as the control parameter. Sand specimens with a_s=0% were prepared by air-pluviation method in order to achieve low relative density. Soil specimens with a_s=3, 6 and 10% were prepared in 5 layers, in order to achieve a more uniform density. The soil for each layer was weighted, placed in 5 separate containers until they were placed in the mold. Reconstituted specimens were compacted in a hollow cylindrical mold 7 cm in outer diameter, 3 cm in inner diameter and 10 cm in height. The each layer was compacted to the required height. In addition, for a proper compaction, vibration was applied by tapping the mold with a wooden mallet in cases of high a_s.

Both soil samples which represent the sand pile and surrounding improved ground were saturated similar to the method mentioned above. Saturated samples were anisotropically consolidated such a way to achieve the required K value by keeping the vertical stress σ_v constant as 100 kPa.

Test procedure

Fig. 12 illustrates the flow chart of the concept of parallel elementary test. Same cyclic shear strain was applied to both specimens, such a way that keeping the vertical stress constant as initial value by controlling the cell pressure. In this method, a computer analysis cyclic

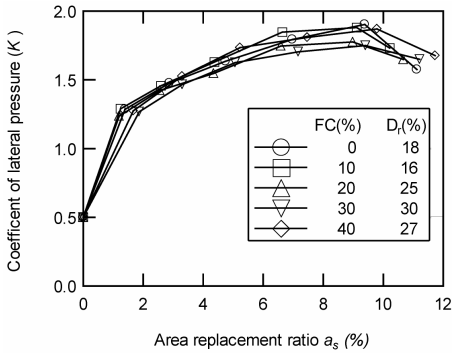

Fig. 9: Relationship between coefficient of lateral pressure versus area replacement ratio

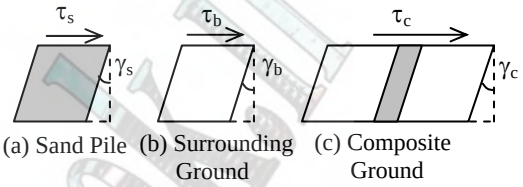

Fig. 10: Shear deformation behaviour of SCP improved composite ground

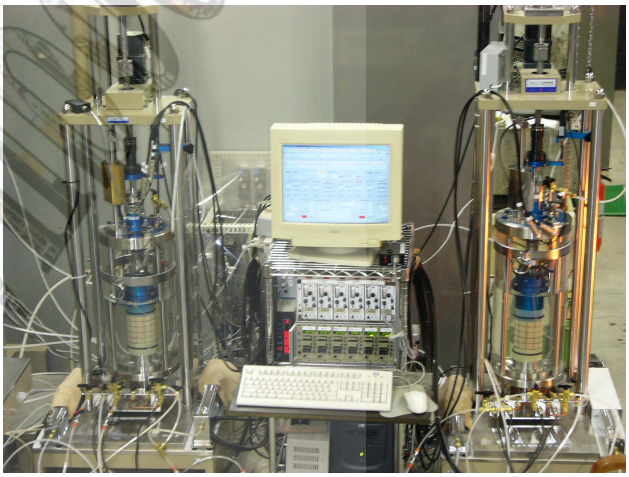

Fig. 11: Complete experimental setup of parallel elementary test

loading which estimates the composite shear stress of elements were combined with the computer online data processing system. It was assumed that the initial liquefaction was occurred when the double amplitude axial strain (DA) reached to 5% [4].

Test Cases

Test cases are shown in Table 1. In the experiment, area replacement ratio (a_s) and composite shear stress amplitude (τ_{amp}) were selected as parameters. Case name displayed in the table implies the combination of area replacement ratio and composite shear stress amplitude. For example case: 3-20 indicates the composite shear stress amplitude of 20 kPa with area replacement ratio of 3%. a_s=0% indicates the unimproved ground where as a_s=3, 6 and 10% indicate the SCP improved ground.

Relative density (D_r) and coefficient of lateral

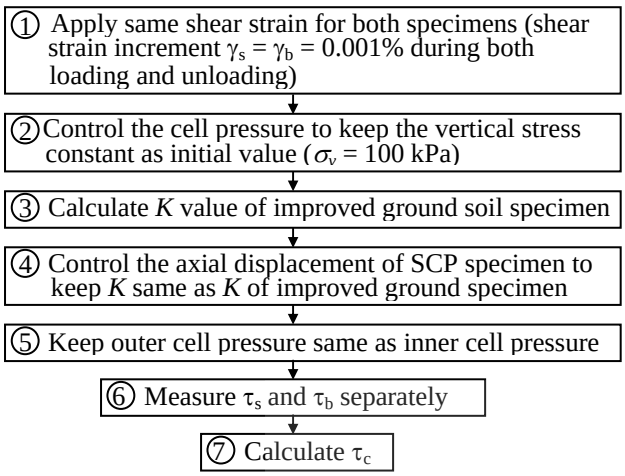

Fig. 12: Parallel elementary test procedure

pressure (*K* value) after SCP installation were given as the initial condition for all test cases except cases with a_s=0%. D_r and *K* value change according to the a_s (based on the previous test results). Relative density of sand pile was kept the same in all test cases as shown in the Table 1. Relative density of the surrounding improved ground (D_{rb}) can be obtained based on the void ratio of the SCP improved ground (e_1).

$$D_{rb} = \frac{e_{\max} - e_1}{e_{\max} - e_{\min}} \quad (3)$$

Where, e_{max} and e_{min} represent the maximum void ratio and minimum void ratio respectively. Similarly, based on the basic principle of soil improvement, area replacement ratio a_s can be represented as,

$$a_s = \frac{e_0 - e_1}{1 + e_0} \quad (4)$$

where e_0 is the initial void ratio *i.e.* void ratio before improvement. By rearranging equation (4),

$$e_1 = e_0(1 - a_s) - a_s \quad (5)$$

By substituting equation (5) in equation (3),

$$D_{rb} = \frac{e_{\max} + a_s - e_0(1 - a_s)}{e_{\max} - e_{\min}} \quad (6)$$

Therefore, relative density of surrounding improved ground (D_{rb}) can be calculated using the void ratio of unimproved ground (e_0) and the area replacement ratio (a_s) as shown in equation (6).

It was assumed that relative density of the unimproved ground is 20% [4]. The *K* value corresponds to the a_s was obtained from the preliminary tests based on the characteristics of the volume change during SCP installation (Fig. 9) [13]. It was revealed that *K* values correspond to a_s=0, 3, 6 and 10% are 0.5, 1.5, 1.7 and 1.9 respectively.

DISCUSSION ON THE RESULTS

Typical test results are shown in Fig. 13 obtained from a test with area replacement ratio (a_s) of 10% and composite shear stress amplitude of 40 kPa (case: 10-40).

Table 1: Test cases

Case Name	a_s(%)	τ_{amp}(kPa)	*K*	D_{rs} (%)	D_{rb} (%)
Case: 0-10		10		-	15
Case: 0-15	0	15	0.5	-	27
Case: 0-20		20		-	15
Case: 3-15		15		85	34
Case: 3-20	3	20	1.5	85	32
Case: 3-25		25		84	32
Case: 6-20		20		82	45
Case: 6-25	6	30	1.7	85	58
Case: 6-30		35		84	49
Case: 10-30		30		86	67
Case: 10-35	10	35	1.9	84	65
Case: 10-40		40		85	65

D_{rs} – Relative density of sand pile
D_{rb} – Relative density of surrounding improved ground

This graph indicates the variation of shear strain, horizontal stress and vertical stress with time. The solid line represents the sand pile where as the broken line represents the surrounding improved ground. It is seen that cyclic shear strain in both samples was the same. Further, it is noticed that horizontal stress and vertical stress of both samples were the same and vertical stress was maintained as a constant value of 100 kPa. As shown in the graph, horizontal stress gradually decreased from 190 kPa (*K*=1.9) under cyclic shear loading and finally reached to the value of vertical stress. *i.e.* isotropic state.

The stress-strain path and effective stress path of sand pile element and surrounding improved ground element are shown in Fig. 14. As shown in the figure, mean effective stress of sand pile element decreases gradually with cyclic loading. However this decrease tendency become tedious when mean effective stress gets near to 70 kPa. Further increases of cyclic shear loading caused dilation of the dense sand. As a result, mean effective stress increased up to 280 kPa where as shear stress increased up to 220 kPa.

In the case of surrounding improved ground element (D_r=65%), mean effective stress reaches to zero with increases of cyclic loading. Further increases of cyclic shear loading caused dilation of the material; however shear stresses were not increased as sand pile element. This is a clear indication of the effect of densification on cyclic shear loading.

Based on the stress-strain path of sand pile element and surrounding improved ground element (Fig. 14(a), (b)), stress-strain path of the composite ground was obtained using equation (2) and plotted in Fig. 15. It is noted that tendency of the stress-strain path is similar to the stress-strain path of the dense sand element subjected to cyclic loading under undrained condition.

Stress ratio of the composite ground

The relationship between stress ratio of composite ground and the number of loading cycles (N_l), which required to cause double amplitude of axial strain (DA) of 5% is shown in Fig. 16. Shear stress of composite ground was obtained by normalizing the composite shear stress amplitude with respect to initial effective vertical stress (σ_{v0}') of 100 kPa. It is clearly seen that the larger the a_s

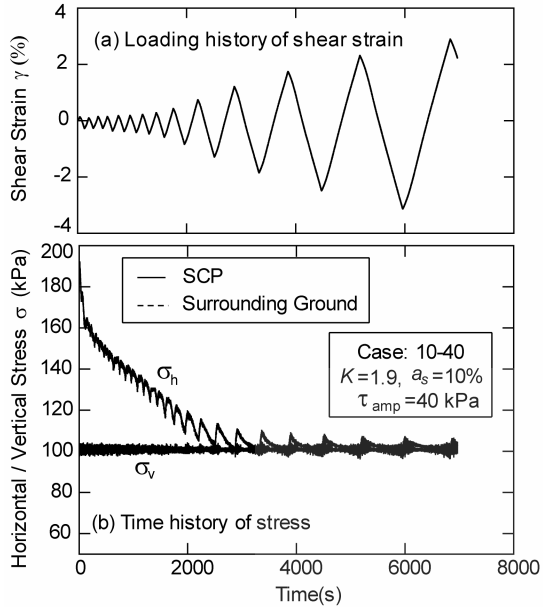

Fig. 13: Strain history and stress variation (Case: 10-40)

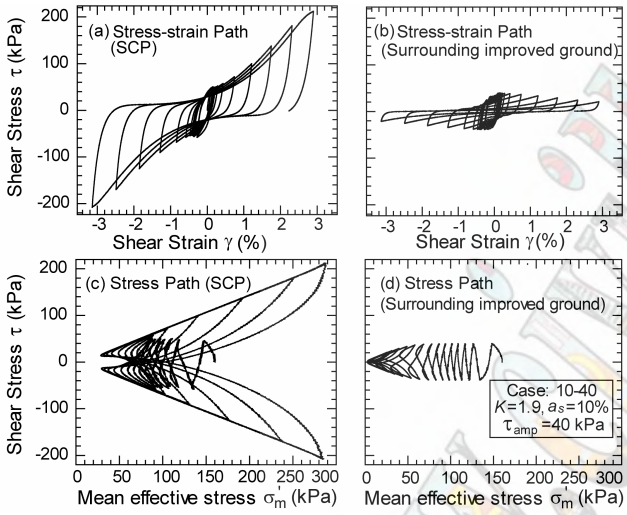

Fig. 14: Typical test results of strain path and mean effective stress path from parallel elementary test

value, the greater the resistance to liquefaction. Therefore, it can be concluded that shear stress ratio of composite ground basically depends on;

1. Relative density of the surrounding improved ground (density effect)
2. Lateral pressure (effect of K)
3. Area replacement ratio a_s (effect of sand pile spacing)

In order to examine the effect of K conditions, the effective vertical stress σ_{v0}' was converted to the mean effective confining stress σ_{m0}' through the relation [16];

$$\sigma_{m0}' = \frac{1+2K}{3}\sigma_{v0}' \qquad (7)$$

If the cyclic stress ratio τ_{amp}/σ_{v0}' in the ordinate of Fig. 16 is changed to the cyclic stress ratio τ_{amp}/σ_{m0}', the test data can be rearranged as shown in Fig. 17, where it may be

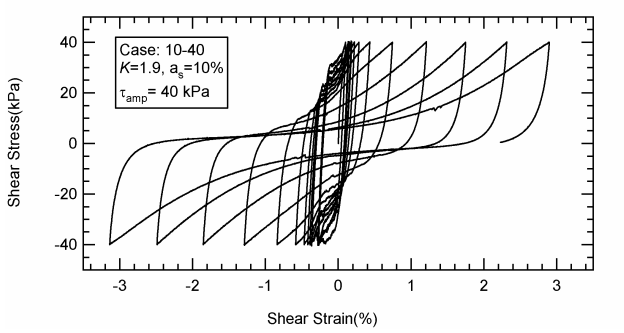

Fig. 15: Stress-strain path of composite ground (Case: 10-40)

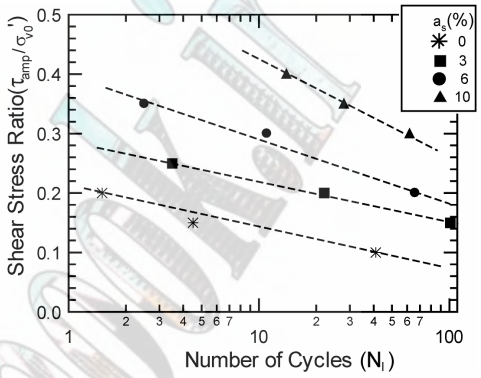

Fig. 16: Shear stress ratio (τ_{amp}/σ_{vo}') versus number of cycles

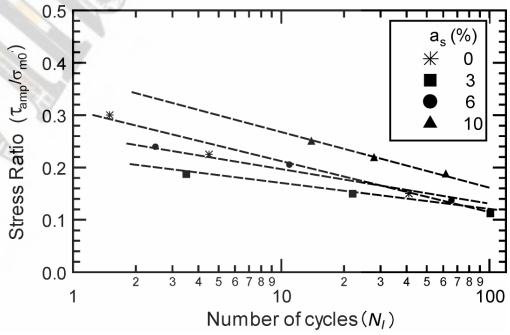

Fig. 17: Shear stress ratio (τ_{amp}/σ_{m0}') versus number of cycles

seen that data of a_s=0, 3 and 6% under different K conditions are correlated uniquely with number of cycles. However, shear stress ratio of a_s=10% deviate from the above uniqueness. Therefore, to get a clear view of the effect of K value, shear stress ratio corresponds to N_l=20 in both figures (Fig. 16 and Fig. 17) were plotted against the area replacement ratio a_s, as shown in Fig. 18. It can be seen that τ_{amp}/σ_{v0}' increases gradually with a_s without illustrating the density effect. However, normalized shear stress ratio with respect to mean effective confining stress (τ_{amp}/σ_{mo}') is almost same in a_s=0, 3 and 6% due to low relative density of the surrounding improved ground. However, a_s=10% shows a higher stress ratio value due to high relative density of surrounding improved ground, thus it implies the density effect as well as the effect of SCP installation.

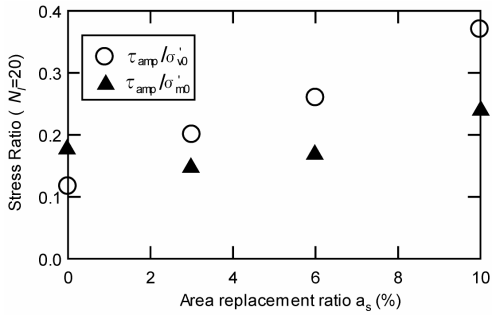

Fig. 18: Shear Stress ratio versus area replacement ratio

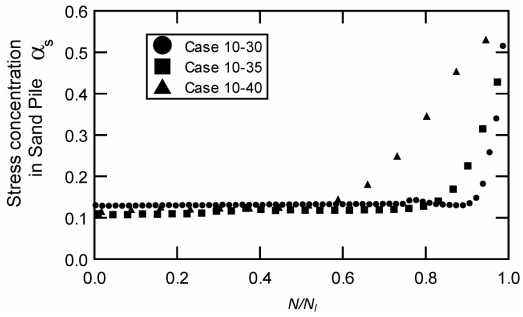

Fig. 19: Stress concentration in Sand Pile

These results are corresponding to the Toyoura sand. As fine content of Toyoura sand is 0%, there is a limitation to achieve higher relative density. Therfore, to get a better view of the effect of densification, it is necessary to conduct further experiments with different fine content and with different materials.

Shear stress distribution in composite ground

Method of analyzing the shear stress distribution in SCP improved ground against the possibility of earthquake induced liquefaction can be represented by normalizing the equation (2) with respect to τ_c.

$$\frac{\tau_s a_s}{\tau_c} + \frac{\tau_b (1-a_s)}{\tau_c} = 1 \qquad (8)$$

The stress concentration ratio in sand pile is represented using α_s and that of surrounding ground is represented using α_b.

$$\alpha_s = \frac{\tau_s a_s}{\tau_c} \quad , \quad \alpha_b = \frac{\tau_b (1-a_s)}{\tau_c} \qquad (9)$$

In order to understand the shear stress distribution in sand pile, α_s was plotted against the ratio of N/N_l, where N is the number of cycles and N_l is the accumulated number of cycles required to cause liquefaction (Fig. 19). It is seen that all such curves were fallen in a fairly narrow band. Note that α_s values are relatively flat for a considerable range of N/N_l, particularly sensitive to the number of cycles, provided that there is some residual margin of safety against liquefaction with use of SCP. This peculiar shape is similar for different a_s, and in fact comparison of α_s values over different a_s is shown in Fig. 20 demonstrates the position of the curve is sensitive to the a_s. For example, the linear portion of case: 3-20, case: 6-30 and case: 10-35 correspond to the α_s=0.03, 0.06 and 0.1 respectively, as shown in Fig. 20. It is seen that increase of α_s mainly depends on a_s. For higher a_s, α_s starts to increase at lower N/N_l ratio. In other words, when a_s is high, the earthquake induced cyclic shear quickly transfer to the sand piles and sand piles function appropriately to mitigate the liquefaction. On the other hand, when the a_s is small, ground between sand piles is more dominant to resist cyclic shear loading and before transfer the cyclic load to the sand piles, ground may occur large deformation. As a result, sand pile can not show its function sufficiently in this situation.

Liquefaction resistance based on the cumulative loss of energy

The concept of loss of energy would be important to evaluate degree of liquefaction, instead of the stress ratio [17]. The dissipation energy (shear work) as a function of time was estimated by integrating the area covered by the stress-strain loops and calculated as follows.

$$\Delta W(t) = \oint \tau(\gamma) d\gamma = \int_0^t \tau(\gamma)\dot{\gamma}(t) dt \qquad (10)$$

where $\Delta W(t)$ = dissipation energy accumulated by time, $\tau(\gamma)$ = shear stress in terms of shear strain, $\dot{\gamma}(t)$ = shear strain rate. In this research study, cumulative dissipation energy was normalized with respect to initial effective vertical stress σ'_{v0}.

It is well known that, high cumulative loss of energy implies the greater resistance to liquefaction. Therefore, in order to evaluate the dissipation of energy in composite ground, equation (11) was obtained using equation (2).

$$E_c = E_s a_s + E_b (1-a_s) \qquad (11)$$

where E_c= normalized cumulative energy loss in composite ground, E_s= normalized cumulative energy loss in sand pile, E_b= normalized cumulative energy loss in surrounding improved ground.

Fig. 21 shows the cumulative energy dissipation in composite ground (E_c) for different area replacement ratios. According to the graph, it is seen that cumulative energy loss in composite ground in cases of a_s =0, 3 and 6% is small. However, in the case of a_s =10%, cumulative energy loss increases rapidly, thus it implies the effect of densification characteristics. Further it was found that, the quantity of energy dissipation is seriously depends on the relative density of the surrounding improved ground.

τ_{amp}/σ'_{v0} versus a_s relationship illustrated in Fig. 18 (indicated as '○') shows a similar tendency as in Fig. 21. It is seen that loss of cumulative energy concept indicates, a_s=10% can improve the liquefaction resistance by an order (10 times) of magnitude when compared with a_s=0%. However, stress ratio concept illustrates that a_s=10% can improve the liquefaction resistance approximately by 3 times of magnitude. This clearly indicates the usefulness of energy dissipation concept over the stress ratio concept for evaluation of liquefaction resistance.

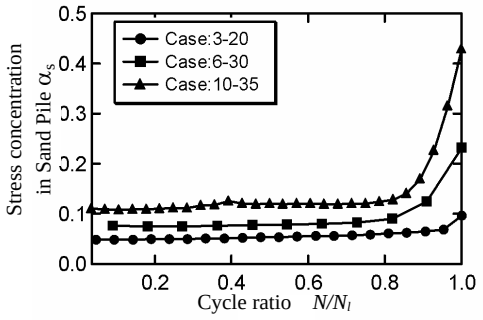

Fig. 20: Effect of area replacement ratio on stress concentration

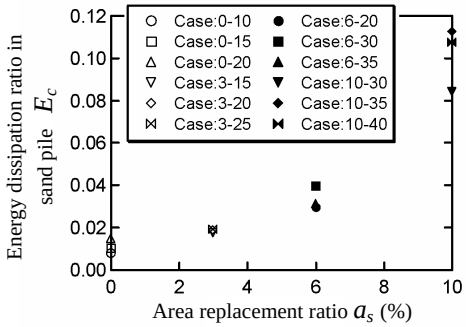

Fig. 21: Effect of area replacement ratio on stress concentration

CONCLUSIONS

Authors have proposed a new method to evaluate SCP improved composite ground using parallel elementary test. Stress state in SCP improved ground was evaluated by simulating SCP installation process. The conclusions obtained from this research study can be summarized as follows.

1. The relationship between K value and a_s, obtained from the cyclic shear triaxial test, simulating SCP installation process, represent the effect of densification on liquefaction resistance.
2. Shear stress-strain relationship of composite ground was obtained using parallel elementary test. Thus, the relationship between stress ratio of composite ground and area replacement ratio provides a new design concept for SCP installation.
3. When area replacement ratio is small, most dominant factor on liquefaction resistance is coefficient of lateral pressure (K value) where as when a_s is large, relative density of surrounding improved ground and stress concentration ratio of sand pile α_s are dominant.
4. The α_s values over the different a_s indicates that, position of the α_s versus N/N_l curve is sensitive to the a_s.
5. Energy dissipation concept shows, a_s=10% can improve the liquefaction resistance by 10 times that of unimproved ground, where as shear stress ratio concept shows, a_s=10% can improve the liquefaction resistance by 3 times that of unimproved ground.

REFERENCES

[1] Ohbayashi, J., Harada, K. and Yamamoto, M., "Resistance against liquefaction of ground improved by sand compaction pile method," *Proc. 2nd Int Conf. on Earthquake Geotechnical Engineering*, Vol. 2, pp. 549–554, 1999.

[2] The Japanese Geotechnical Society (JGS), "Remedial measures against soil liquefaction," *A. A. Balkema*, 1998.

[3] Nakayama, J., Ichimoto, E., Kamada, H. and Taguchi, S., "On stabilization characteristics of Sand Compaction Piles," *Soils and Foundations*, Vol. 13, No. 3, pp. 61–68, 1973.

[4] Okamura, M., Ishihara, M. and Oshita, T., "Liquefaction resistance of sand deposit improved with Sand Compaction Piles," *Soils and Foundations*, Vol. 43, No. 5, pp. 175-187, 2003.

[5] Tsukamoto, Y., Ishihara, K., Yamamoto, M., Harada, K. and Yabe, H., "Soil densification due to Sand Pile installation for liquefaction remediation," *Soils and Foundations*, Vol. 40, No. 2, pp. 123–135, 2000.

[6] Farias, M.M., Nakai, T., Shahin, H.M., Pedroso, D.M., Passos, P.G.O. and Hinokio, M., "Ground densification due to Sand Piles," *Soils and Foundations*, Vol. 45, No. 2, pp. 167–180, 2005.

[7] Nozu, M. and Ohbayashi, J., "Application of the static sand compaction pile method to loose sandy soil," *Proc. Int symposium on Problematic Soils*, IS-TOHOKU, Vol. 2, pp. 751-755, 1998.

[8] Tokimatsu, K., Yoshimi, Y. and Ariizumi, K., "Evaluation of liquefaction resistance of sand improved by deep vibratory compaction," *Soils and Foundations*, Vol. 30, No. 3, pp. 153–158, 1990.

[9] Okamura, M., "Cyclic shear resistance profile of sand deposit improved with Sand Compaction Piles," *12th Asian Region Conf. on Soil Mechanics and Geotechnical Engineering*, pp. 513–517, 2003.

[10] Nakano, M., Asaoka, A., Kaneda, K. and Nakai, K., "Compaction behaviour of Loose Sand due to the decay of soil structure," *12th Asian Region Conf. on Soil Mechanics and Geotechnical Engineering*, pp. 505–508, 2003.

[11] Noda, T., Yamada, E. and Yamada, S., "Compaction of sandy ground by Static Cavity Expansion," *12th Asian Region Conf. on Soil Mechanics and Geotechnical Engineering*, pp. 509–512, 2003.

[12] Asaoka, A., Kodaka, T. and Nozu, M., "Undrained shear strength of clay improved with Sand Compaction Piles," *Soils and Foundations*, Vol. 34, No. 4, pp. 23–32, 1994.

[13] Priyankara N. H., Kazama, M., Uzuoka, R., Sento, N. and Sakamoto, K., "The stress state and volume change of sandy ground established by Sand Compaction Pile installation," *The 15th International Offshore and Polar Engineering Conf. and Exhibition*, ISOPE2005, Vol. 2, pp. 618-624, 2005.

[14] Tatsuoka, F., Sonoda, S., Hara, K., Fukushima, S. and Pradhan, T.B.S., "Failure and deformation of sand in Torsional shear," *Soils and Foundations*, Vol. 26, No. 4, pp. 79–97, 1986.

[15] Mulilis, J. P., Seed, H. B., Chan, C. K., Mitchell, J. B. and Arulanandan, K., "Effect of sample preparation on Sand Liquefaction," *Journal of the Geotechnical Engineering Division*, ASCE, Vol. 103, No. GT2, pp. 91–108, 1977.

[16] Ishihara, K., "Soil behaviour in Earthquake Geotechnics," *Oxford Science Publications*, 1996.

[17] Kazama, M., Yamaguchi, A. and Yanagisawa, E., "Liquefaction resistance from a ductility view point," *Soils and Foundations*, Vol. 40, No. 6, pp. 47–60, 2000.

Shaking Table Tests on the Effectiveness of the Countermeasures by Installing Preventing Piles or a Sheet Pile Against Liquefaction-induced Flow

T. Tanaka[1], S. Yasuda[2] , T. Ishii[3]
[1]*Graduate School of Science and Engineering, Tokyo Denki University, Saitama, Japan*
[2]*Department of Civil and Environmental Engineering, Tokyo Denki University, Saitama, Japan*
[3] *Graduate School of Science and Engineering, Tokyo Denki University, Saitama, Japan*

Abstract

Liquefaction-induced flow occurred in the liquefaction ground behind seawalls and river revetments during several past earthquakes. The authors considered that two kinds of countermeasures, which were sheet pile wall and preventing piles, would prevent the liquefaction-induced flow. The sheet pile wall was continuous plate. On the other hand, the preventing piles studied in this paper, were not continuous so that this method was able to apply in the area, where many structures were buried in the ground. Then, shaking table tests were conducted to demonstrate the possibility to reduce the displacement of pile foundation and seawall. Two kinds of model countermeasures, preventing piles or a sheet pile wall, were placed between seawall and pile foundation. Tests were carried out under several conditions of type and arrangement of countermeasures. Test results showed that the installation of the sheet pile was able to reduce displacement of pile foundation. Effectiveness of the preventing piles, if their moduli of bending rigidity are same, was almost same as the sheet pile wall.

Keywords—*Earthquake, liquefaction, flow, shaking table test*

INTRODUCTION

Liquefaction-induced flow occurred in the liquefaction ground behind seawalls and river revetments during several past earthquakes. For example, liquefied ground behind seawalls at man-made islands in Kobe moved about 2 to 4 m toward to sea during the 1995 Kobe (Hyogoken-Nambu) earthquake. Very large displacement of the ground behind seawalls brought severe damages to buildings, bridges and so on. The authors considered that two kinds of countermeasures, which were sheet pile wall and preventing piles, would prevent the liquefaction-induced flow. The sheet pile wall was continuous plate. On the other hand, the preventing piles were not continuous such as sheet pile wall, so that this method was able to apply in the area, where many structures were buried in the ground such as plants, harbors and so on.

Then, shaking table tests were conducted to demonstrate the possibility to reduce the displacement of pile foundation and seawall. A model seawall and a model pile foundation were placed in the soil container. Two kinds of model countermeasures, preventing piles or a sheet pile wall, were placed between seawall and pile foundation. Tests were carried out under several conditions of type and arrangement of countermeasures. Test results showed that the installation of the sheet pile was able to reduce displacement of pile foundation. Effectiveness of the preventing piles, if their moduli of bending rigidity are same, was almost same as the sheet pile wall.

IDEAS COUNTERMEASURES

After the 1995 Kobe earthquake, appropriate countermeasures against liquefaction-induced flow for the existing bridge foundations of Tokyo Metropolitan Highway was studied. Several centrifuge tests and analyses were carried out to demonstrate the effectiveness of several countermeasures. Then, the method to install sheet pile walls using by steel-pipes were selected as the countermeasure, as shown in Fig. 1.

As similar methods, the authors considered that two kinds of countermeasures, which were preventing piles

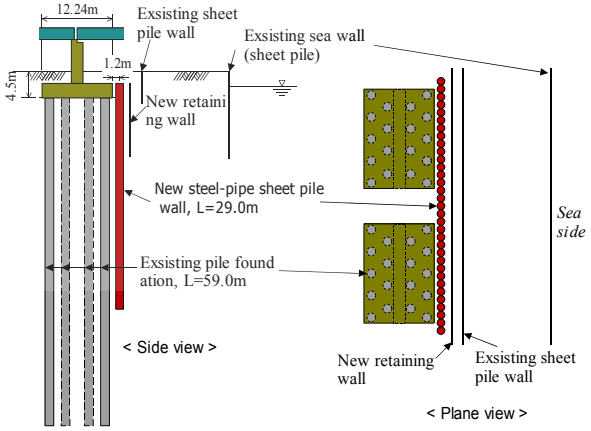

Fig. 1: Countermeasure by steel-pipe sheet pile walls against liquefaction-induced flow in Tokyo Metropolitan Highway (Ogasawara et al., 1999.).

with triangular type and square type arrangement, as shown in Fig. 2, would be also effective. In the case of the sheet pile wall mentioned above, it is easy to apply oil tank yards or electric power plants, because many buried pipes exist in these underground, and it is difficult to install the sheet pile wall with avoiding the pipes. Therefore, installation of not a wall but several piles is desired as a similar countermeasure. Then, the effectiveness of preventing piles was studied by conducting several shaking table tests in gravitational field.

TEST PROCEDURE

The soil container used was 270 cm in length, 100 cm in height and 80 cm in width. Three boxes, which are a measuring caisson and two dummy caissons, were used for the model seawalls. The measuring caisson was 20 cm in length, 50 cm in height and 33 cm in width. Unit weights of the three caissons were adjusted about 20.6 kN/m^3. The measuring caisson was sandwiched by the dummy caissons. Water and sand were not able to leak between the caissons and sidewalls of the container. A model pile foundation, which made of an aluminum plate of 5 mm in thickness, 30 mm in width and 820 mm in height, was fixed on the bottom of the container. Clean silica sand was used to construct the liquefiable layer of the model ground. Relative density of the ground was adjusted about 50 %. A gravel layer was mounted on the sand layer as a surface non-liquefiable layer. Grain size of the gravel was 2 mm to 10 mm. Fig. 3 shows the grain-size distribution curve of the sand and gravel. The model setup used in this study is schematically illustrated in Fig. 4.

As the model for the preventing piles, aluminum plates of 5 mm in thickness, 15 mm in width and 820 mm in height, were used. These piles were placed in two rows

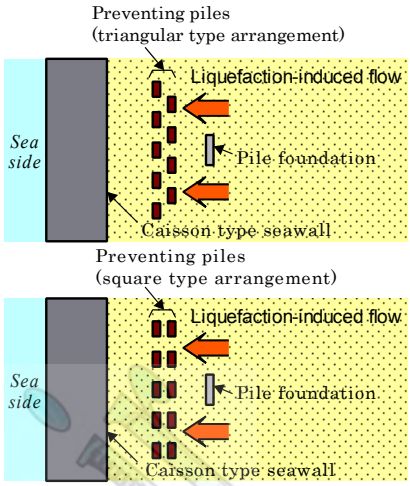

Fig. 2: Ideas of two types of countermeasures against liquefaction-induced flow.

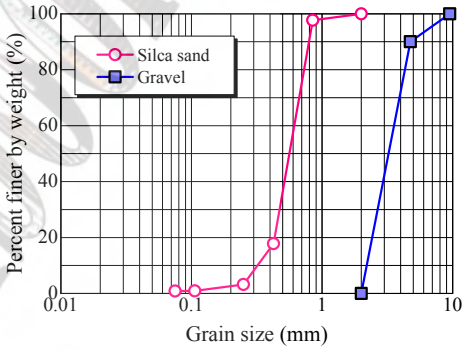

Fig. 3: Grain size distribution curve of silica sand and gravel.

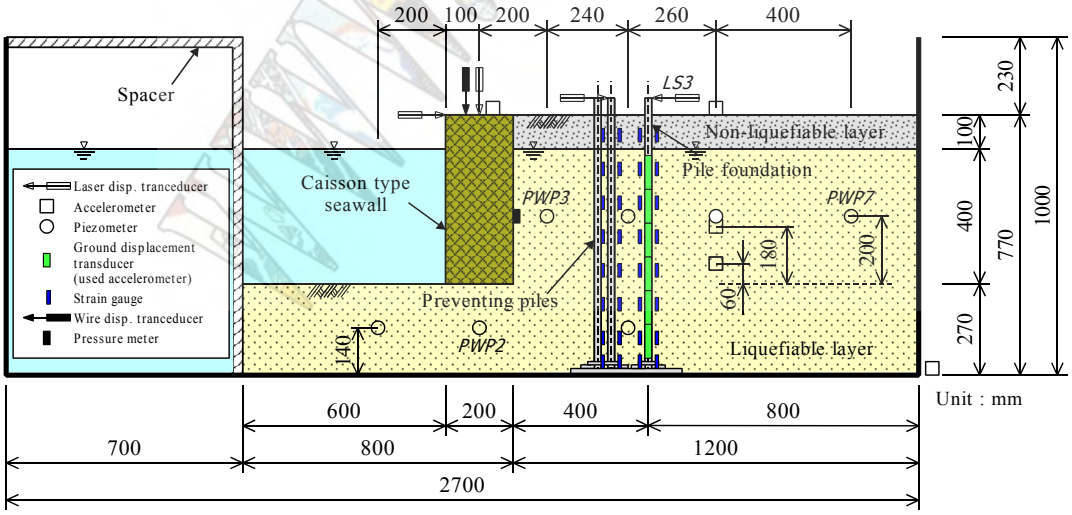

Fig. 4: Schematic diagram of model for shaking table test on countermeasure.

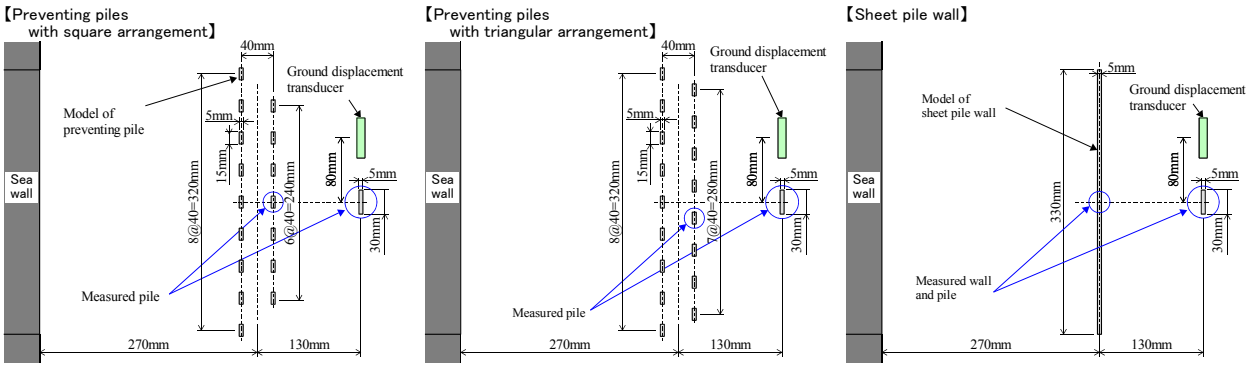

Fig. 5: Schematic diagram of model the preventing piles and sheet pile wall.

between the seawall and the pile foundation, and fixed on the bottom of the container. As show in Fig. 5, two arrangements of preventing piles were used: triangular type and square type arrangement. As the model for the sheet pile wall, an aluminum plate of 5 mm in thickness, 330 mm in width and 820 mm in height, were used. The sheet pile wall were placed between the seawall and the pile foundation, and fixed on the bottom of the container. In addition, sheet pile wall is shown in Fig. 5.

Distributions of pore water pressure and acceleration in the ground were measured by piezometers and accelerographs installed in the ground. Displacement and rotation of the measuring seawall were measured by laser type displacement transducers and an accelerometer. Horizontal displacement of the top of pile foundation and a preventing pile were measured by laser type displacement transducer. Many pairs of strain gages were put on the surface of the pile foundation and a preventing pile. Distribution of the horizontal displacement of the ground in depth were measured by a special transducer, named ground displacement transducer. In the transducer, six accelerometers were put on six wooden plates. These plates were connected by rings. Inclinations of the plates could be measured by the accelerometers and converted to the horizontal displacement. The ground displacement transducer was installed beside the pile foundation as shown in Fig. 5.

All test cases shown in Table 1 were conducted. Tests were conducted with and without countermeasures. Shaking motion with sine wave at 3 Hz was applied for 20 waves.

TEST RESULTS

Behavior of Pore Water Pressure in the Ground

Time histories of excess pore water pressure under the seawall and at a farthest place from the seawall are shown in Fig. 6 and Fig. 7, respectively. When excess pore water pressure increased up to initial effective overburden pressure, it can be judge that liquefaction induced completely. Broken lines in the figures indicate initial effective overburden pressure calculated by the

Table 1: Test cases for shaking table tests.

Test case No.	Type of countermeasure
Case1	No-countermeasure
Case2	Preventing piles with traiangular arrangement
Case3	Preventing piles with square arrangement
Case4	Sheet pile wall

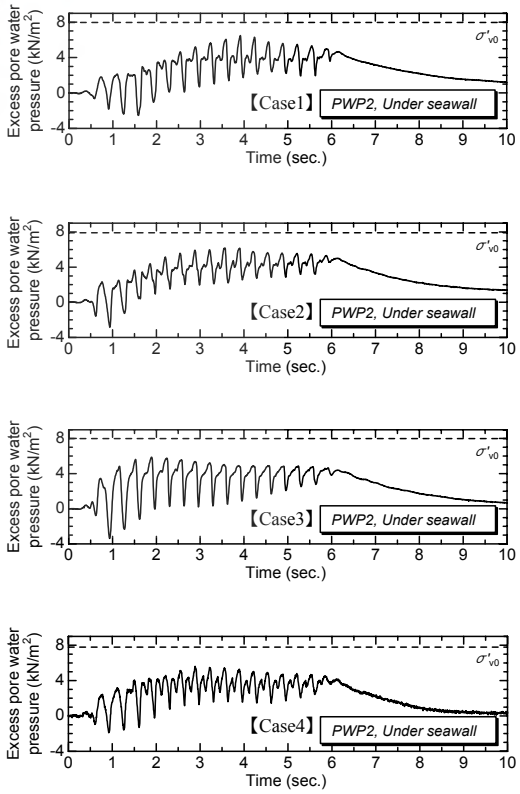

Fig. 6: Time histories of excess pore water pressure under the seawall.

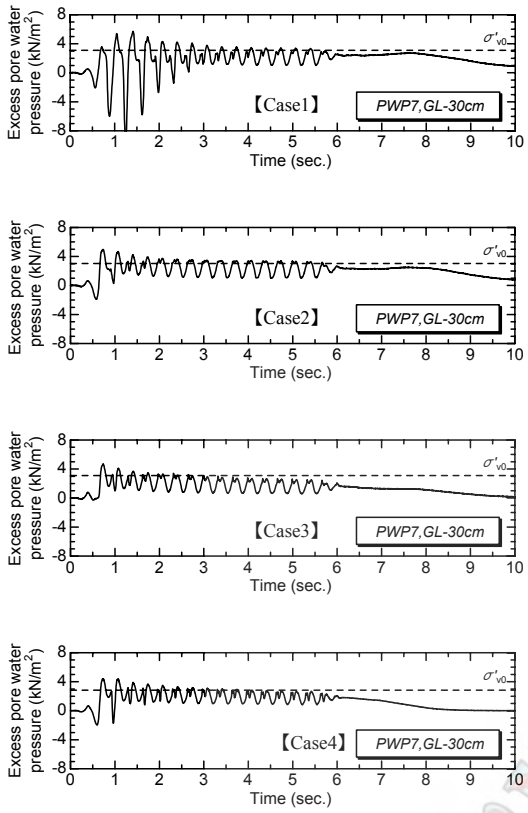

Fig. 7: Time histories of excess pore water pressure at a farthest place from the seawall.

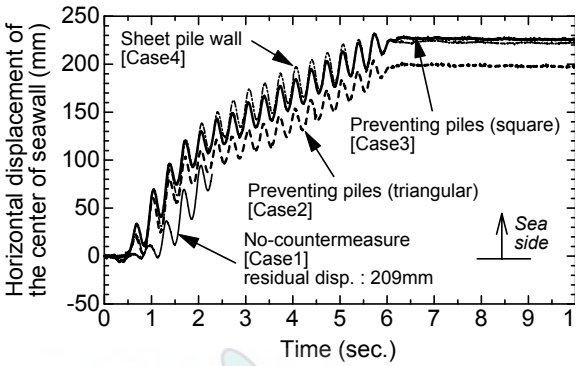

Fig. 8: Time histories of displacement of the center of the seawall.

Photo 1: The seawall and the ground 3 seconds after the start of shaking.

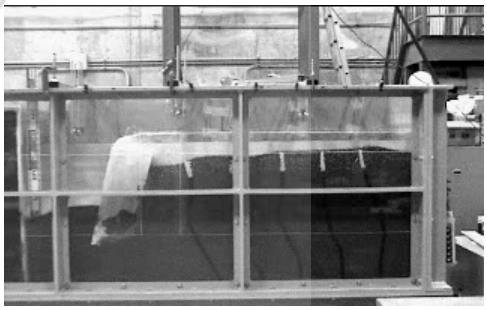

Photo 2: The seawall and the ground after end the shaking.

self-weight analyses.

It can be judged that liquefaction occurred at about one second from the beginning of shaking, because the excess pore water pressure at the farthest place increased up to initial effective overburden pressure. The excess pore water pressure kept liquefaction condition during remaining shaking. About two second after the stop of shaking, the excess pore water pressure started to decrease. On the contrary, the excess pore water pressure ratio under the seawall increased up to 0.7 to 0.8 only and did not reach completely liquefaction condition. This must be because of high initial shear stress and overburden pressure acted in the ground under the seawall due to the weight of the heavy seawall.

Movement of Seawalls

Fig. 8 compares time histories of horizontal displacements of seawall at the center of gravity for all test cases. The seawall was moved and tilted toward the sea soon after the start of shaking. The seawall moved and tilted toward to seaside for 2 to 3 seconds for all test cases. In case with no-countermeasure, it was able to measure the displacement until about 2.5 second only. Photo 1 shows the seawall and the ground 3 seconds after the beginning of shaking. Then, the seawall moved toward to seaside and tilted toward to landside. Photo 2 shows the seawall and the ground after the end of shaking. Displacements for the cases with the countermeasure by preventing piles in square arrangement and by sheet pile wall, were almost same. Fig. 9 shows residual horizontal and vertical displacements, and tilted angle of the seawall after the stop of shaking for all test cases. In case with the countermeasure by preventing piles in triangular arrangement, residual horizontal displacement of the seawall was smallest in all test cases. However, its residual vertical displacement and tilted angle were not smallest. In case with the countermeasure by sheet pile wall, residual tilted angle of the seawall was smallest, but

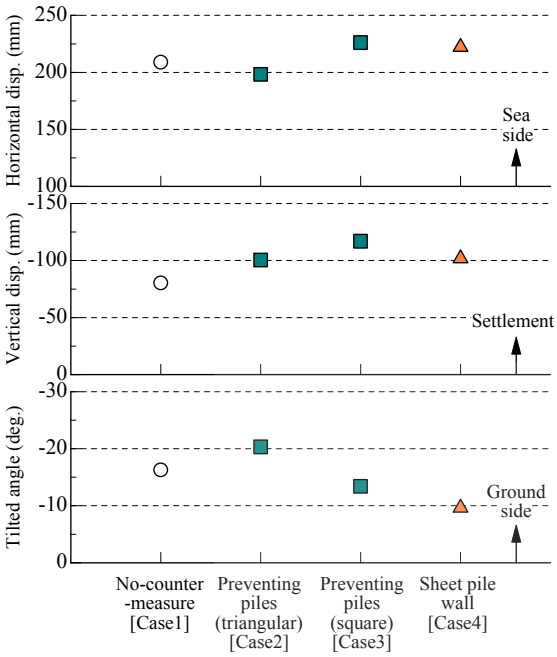

Fig. 9: Residual horizontal and vertical displacements and tilted angle of the seawall.

its horizontal displacement was not smallest. Countermeasure by installing the preventing piles and sheet pile wall were not effective to decrease the displacement and tilted angle of the seawall in these test series. Rigidity of the countermeasures used in this test was not large. This may be the reason why the countermeasures were not effective to decrease the movement of the seawall.

Displacement of the Pile Foundation and Surrounding Ground

Fig. 10 shows that distribution of displacements in depth of the pile foundation and the surrounding ground, at the times of maximum displacement of the pile and end of shaking. In case with the no-countermeasure, liquefied surrounding ground flowed through the pile foundation, because the ground displacement was larger than the displacement of the pile foundation. On the other hand, in case with the countermeasures, displacements of the ground and pile foundation were almost same, although liquefied ground moved toward to seaside. Fig. 11 compares time histories of displacement of the top of pile foundation for all test cases. As shown in this figure, the pile foundation moved toward the seaside due to the movement of the seawall and ground. The maximum and residual displacement of pile foundation decreased with the installation of countermeasures. In case with the countermeasures by preventing piles with triangular arrangement and sheet pile wall, the maximum and residual displacement of pile foundation were smallest in all test cases. In these cases, displacement of the pile

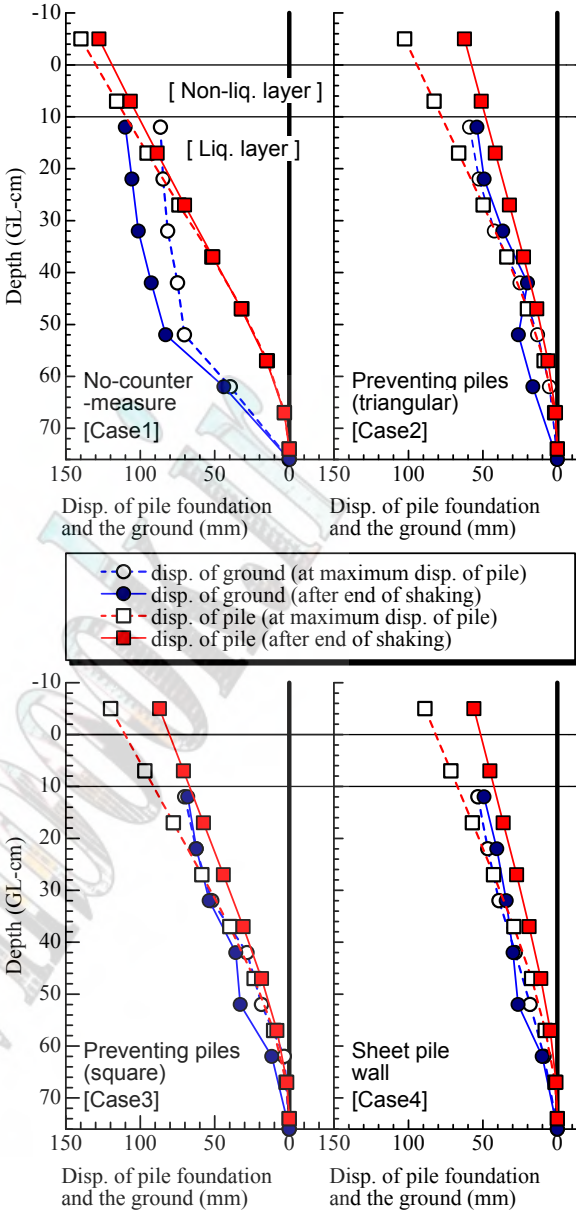

Fig. 10: Distribution of the pile foundation and near the ground.

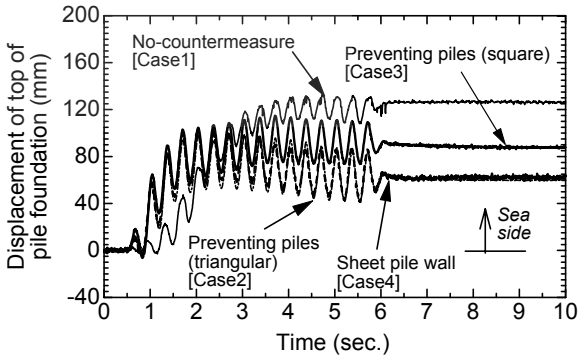

Fig. 11: Time histories of displacement of the top of pile foundation.

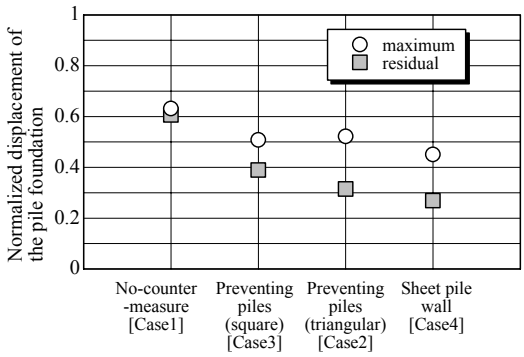

Fig. 12: Normalized maximum and residual displacement of the top of pile foundation.

foundation started to decrease gradually at about 3 second. Fig. 12 shows that maximum and residual displacement of the top of pile foundation in all test cases. In this figure, displacements were normalized dividing by the residual horizontal displacement of seawall in the case of no-countermeasure. Therefore, the value of one in a vertical axis means the same as residual horizontal displacement of seawall. In case with no-countermeasure, maximum and residual displacement of the pile foundation was about 60 % of residual horizontal displacement of seawall. In case with countermeasures, maximum displacement of the pile foundation was smaller than the case with no-countermeasures. Maximum displacement of the pile foundation was almost same in three types of countermeasures. In case with countermeasure by sheet pile wall, residual displacement of the pile foundation was smallest in all test cases.

As shown in Fig. 12, countermeasures by preventing piles were able to decrease the displacement of pile foundation. Especially, installation of preventing piles with triangular arrangement was able to decrease displacement of the pile foundation as much as the countermeasure by sheet pile wall. Thus, countermeasure of installing preventing piles with triangular was effective to decrease of the displacement of pile foundation. In case with countermeasure by preventing piles with square arrangement, residual displacement of pile foundation was larger than the preventing piles with triangular arrangement. The ground between preventing piles with square arrangement must be easier to flow through preventing piles than the case of triangular arrangement.

CONCLUSIONS

Several shaking table tests were carried out to demonstrate the effectiveness of countermeasures by installing preventing piles or a sheet pile wall against liquefaction-induced flow. The following conclusions were derived through the tests:

(1) The countermeasures by installing preventing piles and a sheet pile wall between seawall and pile foundation, is effective to decrease the displacement of existing pile foundation.
(2) Installation of preventing piles, which was not continuous, was able to decrease the displacement of pile foundation as well as a continuous sheet pile wall.
(3) Installation of preventing piles with triangular arrangement was effective to decrease the displacement of the pile foundation rather than square arrangement, because the ground between preventing piles with square arrangement was easier to flow through preventing piles than the ground with triangular arrangement preventing piles.

ACKNOWLEDGMENTS

This study was supported by the special project for earthquake disaster mitigation in urban areas sponsored by Ministry of Education, Culture, Sports, Science and Technology in Japan (MEXT). The shaking table tests were conducted with the assistance of Messrs. Y., Kurimoto and K., Goto, who are undergraduate students at Tokyo Denki University. The authors would like to express sincere thanks to the above organization and them.

REFERENCES

[1] Ogasawara, M., Tani, K., Matsuo, T. and Sakamoto, S. "A study on measures against ground flow using the finite element method," *Proc. of the 2nd International Conference on Earthquake Geotechnical Engineering*, pp. 335–339, 1999 .

[2] Yasuda, S., Tanaka, T. and Ishii, T. "Adaptability of pile installation method as a countermeasure against liquefaction-induced flow," *Proc. of the 15th Southeast Asian Geotechnical Conference*, pp. 917-922, 2004 .

Effect of Ground Motion Scaling in Site Response Analyses

Eser Durukal, Atilla Ansal and Gökçe Tönük
Department of Earthquake Engineering, Kandilli Observatory and Earthquake Research Institute, Boğaziçi University, Istanbul, Turkey

Abstract

The aim of this study is to gain insight into the significance of ground motion scaling in site response analysis. Using 1D site response models at two sites with pre-determined levels of earthquake hazard, the resulting response variability is investigated for the selected series of ground motion records compatible with the site-specific earthquake hazard scaled to different intensity measures such as peak ground acceleration, peak ground velocity and Arias intensity. The uncertainty introduced by scaling and the effectiveness of different scaling methods are evaluated. This preliminary investigation is considered as a step towards understanding how ground motion scaling will affect the non-linear dynamic response of geotechnical structures.

Keywords—*Ground motion scaling, performance based design, site response*

INTRODUCTION

Seismic design practice, that used to be based on a strength based approach, entered a rapidly transforming era in the 1990's [1]. Performance based design philosophy that is taking over, involves designing engineering structures taking into account the expected regional seismic action that may take place during the economic life-time of the structure and is based on design according to limit levels of physical damage due to seismic actions. From the design view point, this requires a detailed understanding of the factors and parameters that describe and quantify damage in a most efficient way for an engineering structure and identification and estimation of earthquake ground motion parameters that correlate with these damage parameters [2].

From the perspective of performance based earthquake engineering, there are three issues that are either being or need to be addressed by the geotechnical earthquake engineering community. The first concerns the setting and estimation of performance and damage criteria for different geotechnical structures. This is often about the estimation of damaging ground deformation levels for a natural site or for a geotechnical structure. The second is related to the estimation and modeling of the uncertainty in the material properties of soils and of ground response. The third is about selection, scaling and modification (i.e. due to soil-structure interaction) of earthquake ground motion to be used as input in the analyses [3].

There are two kinds of scaling used in earthquake engineering: source spectral scaling and ground motion scaling. Source spectral scaling is concerned with the interdependence of parameters related to the earthquake source, such as earthquake magnitude, fault slip, corner frequency, stress drop, fault size (i.e. length and width) etc. How these parameters scale with each other, is ultimately used for the determination of the correct values in ground motion simulation studies in earthquake engineering and in understanding the underlying physics of the rupture processes in geophysics and seismology. Ground motion scaling, on the other hand, is basically emerging as a need following recent developments in the earthquake resistant design philosophy [4], widely called as performance based design, as a need for using the most appropriate set of strong ground motion time series [5] (recorded or simulated) in dynamic analysis of structures.

The uncertainty in ground response is the result of different site conditions, of the variability in soil properties, and of the variability in earthquake ground motion parameters [6, 7]. Studies carried out on the non-linear response of structures analyzed under input ground motion records selected and scaled to certain criteria such as peak ground acceleration, peak ground velocity, Arias intensity, effective peak velocity etc. show that there exists a significant response variability [8], stressing the necessity of a better understanding of the phenomena for a more realistic assessment of structural performance and implying the need for identification of other ground motion parameters in better compliance with non-linear structural response [9]. It can be anticipated that a similar need exists for natural- and man-made geotechnical structures [10].

APPROACH

Using 1D equivalent-linear and non-linear soil models at two sites with pre-determined levels of earthquake hazard, first the resulting response variability is investigated when analyzed under a series of ground motion records selected as compatible with the site-specific earthquake hazard. Then using a family of records scaled to intensity measures, namely to peak ground acceleration (PGA), peak ground velocity (PGV), and Arias intensity (AI), the analysis is repeated and the variability introduced by scaling and the effectiveness of scaling methods are evaluated. The equivalent-linear

method adopted in SHAKE [11] and the 1D non-linear finite element scheme adopted by Cyclic1D [12] are used in site response analyses.

Scaling of input time histories can be carried out in time-domain and in frequency domain. In time-domain scaling involves only the amplitude of the time series (i.e., PGA, PGV, AI, root mean square acceleration, RMSA…), whereas in frequency domain scaling the frequency content is changed within a pre-determined frequency window (i.e. spectral intensity, SI).

This preliminary investigation is considered as a step towards understanding how ground motion scaling will affect the non-linear dynamic response of geotechnical structures. Its extension to other problems such as landslides and lateral spreading etc. will be evaluated based on the results of the current study.

SITE MODELING AND GROUND MOTION DATA

Izmir Case Study

The first case study selected for evaluating the effects of ground motion scaling on site response analyses is a site near the city of Izmir. The site response analyses were conducted using Shake code [11] for the four soil profiles where in-hole shear wave measurements were performed previously. These four soil profiles are shown in Fig.1.

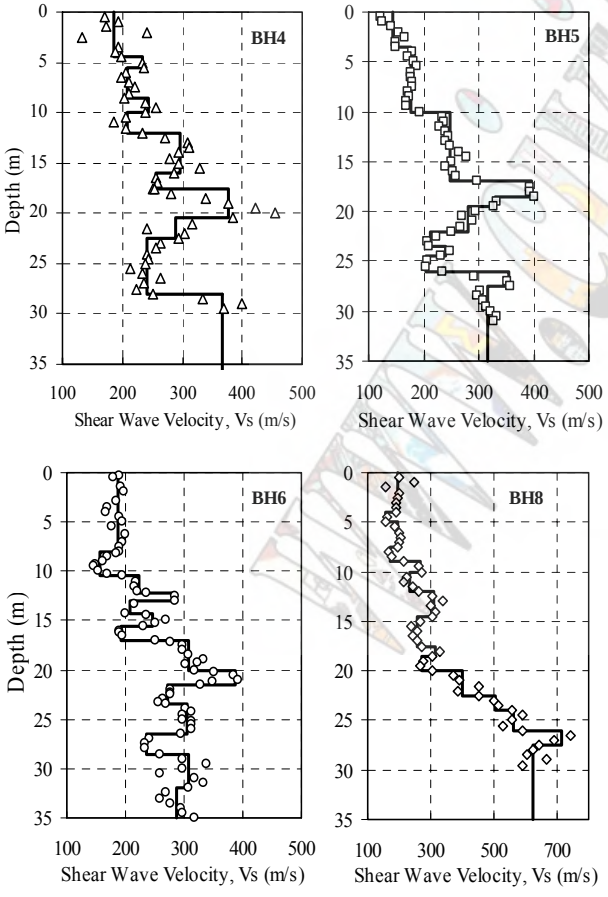

Fig. 1: Four soil profiles used in site response analyses for the first case study

The effects of scaling for each soil profile were evaluated separately and together to observe the effects of site variability in relation with the scaling of input ground motion. The scaled records were applied as outcrop motion where the engineering bedrock (Vs=750m/s) was taken at 45m depth.

The regional earthquake hazard analysis yielded an earthquake magnitude of 6.5-7 with an epicentre distance of 10-20km. The hazard compatible ground motion data, composed of 20 acceleration time histories recorded between 10-20km epicentre distances, downloaded from PEER [13] are shown in Table 1. Site response analyses were conducted using scaling parameters determined from related empirical attenuation relationships [14, 15, 16, 17] as PGA=0.25g, PGV=30cm/s, and AI=0.55m/s.

Table 1: Earthquake records used for first case study

Station	Earthquake	Date	Mw	Re (km)	PGA (g)	PGV (cm/s)
1061-E	Düzce	11/12/99	7.1	15.6	0.134	13.7
1061-N	Düzce	11/12/99	7.1	15.6	0.107	11.5
1062-E	Düzce	11/12/99	7.1	13.3	0.257	16.3
1062-N	Düzce	11/12/99	7.1	13.3	0.114	11.2
531-E	Düzce	11/12/99	7.1	11.4	0.118	14.0
531-N	Düzce	11/12/99	7.1	11.4	0.159	12.9
Arcelik	Kocaeli	08/17/99	7.4	17.0	0.218	17.7
Arcelik	Kocaeli	08/17/99	7.4	17.0	0.149	39.5
Bolu	Düzce	11/12/99	7.1	17.6	0.728	56.4
Bolu	Düzce	11/12/99	7.1	17.6	0.822	62.1
Duzce	Kocaeli	08/17/99	7.4	12.7	0.312	58.8
Duzce	Kocaeli	08/17/99	7.4	12.7	0.358	46.4
Gebze	Kocaeli	08/17/99	7.4	17.0	0.244	50.3
Gebze	Kocaeli	08/17/99	7.4	17.0	0.137	29.7
117ELC	Imperial Valley	05/19/40	7.0	12.0	0.313	29.8
117ELC	Imperial Valley	05/19/40	7.0	12.0	0.215	30.2
Joshua Tree	Landers	06/28/92	7.3	11.3	0.274	27.5
Joshua Tree	Landers	06/28/92	7.3	11.3	0.284	43.2
Morongo	Landers	06/28/92	7.3	17.7	0.188	16.6
Morongo	Landers	06/28/92	7.3	17.7	0.140	20.2

Gölcük Case Study

The second site is located in Gölcük; a town in the epicenter area of the 1999 Mw 7.4 Kocaeli, Turkey earthquake. Detailed site investigations were carried out in the town as a part of the post earthquake studies [18]. The selected soil profile that extends for 30m, shown in Fig. 2, is analyzed by Cyclic 1D [12], using the predefined soil models in the code as composed of 9m thick loose cohesionless soil layer with sand permeability underlain by 6m thick medium-dense cohesionless soil layer having silt permeability. Below these layers there are 6m thick stiff cohesive soil layer and 3m thick medium dense cohesionless soil layer having gravel permeability, underlain by stiff cohesive soil layer that extends for 6m.

The regional earthquake hazard is dominated by strike slip faulting, that generates earthquakes in the magnitude range of 7.0-7.5 that can be characterized by PGA=0.35g, PGV=30cm/sec, SA (0.2s) =0.41g, SA (1.0s) =0.19g [19]. AI is estimated as 2m/s for the magnitude and distance range considered based on the empirical attenuation relationship proposed [15, 16, 17].

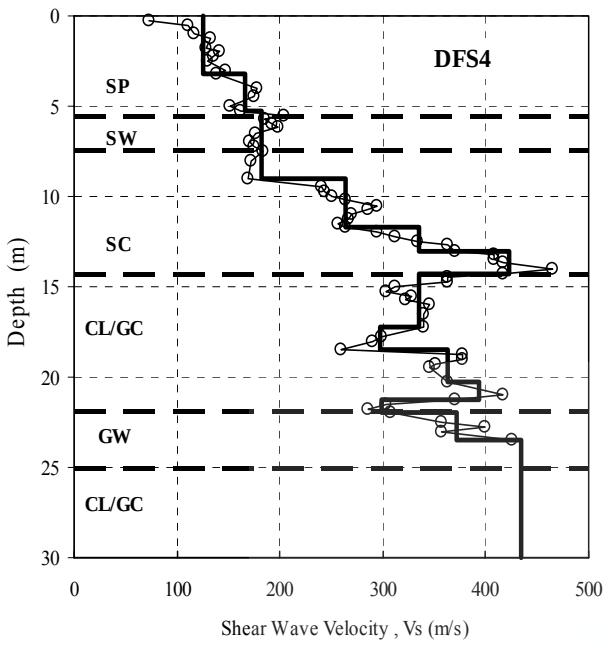

Fig. 2: Soil profile at Golcuk used in site response analyses

The ground motion data are obtained from PEER [13]. The original sources are ERD, Ankara; KOERI, Istanbul and SCE, USA. The criteria used in the selection were: magnitude range 7.0-7.5; distance range 0-20km, earthquake mechanism: strike slip, site conditions B or C according to NEHRP classification. The PGAs are changing between 0.05 g and 0.8 g. The PGVs vary between 11 cm/sec and 98 cm/sec. The data, summarized in Table 2 are scaled to PGA=0.35g, PGV=30cm/s, AI=2m/s for conducting series of site response analysis.

Table 2: Ground motion data set used in analyses Earthquake mechanism: strike-slip, Distance range: 0-20 km, Magnitude range: 7.0-7.5

Earthquake	Station	Site Class NEHRP	Component	PGA (g)	PGV (cm/sec)
Düzce, Turkey 1999	375	B	375-E	0.514	20.2
			375-N	0.97	36.5
	1058	C	1058-E	0.111	14.2
			1058-N	0.073	13.5
	1059	C	1059-E	0.133	13.9
			1059-N	0.147	12.0
	531	B	531-E	0.118	14.0
			531-N	0.159	12.9
	1061	C	1061-E	0.134	13.7
			1061-N	0.107	11.5
	1062	C	1062-E	0.257	16.3
			1062-N	0.114	11.2
Kocaeli, Turkey 1999	Izmit	B	IZT090	0.22	29.8
			IZT180	0.152	22.6
	Sakarya	C	SKR090	0.376	79.5
	Arcelik	C	ARC000	0.218	17.7
			ARC090	0.149	39.5
	Gebze	B	GBZ000	0.244	50.3
			GBZ090	0.137	29.7
Landers, USA, 1992	24 Lucerne	B	LCN000	0.785	31.9
			LCN275	0.721	97.6

RESULTS

Izmir Case Study

The results are presented in terms of histograms of peak accelerations and spectral accelerations at 0.2s obtained by fitting an envelope NEHRP design spectra.

The peak ground acceleration histograms calculated for four soil profiles, shown separately in Fig.3, indicates the importance of the variations in the soil profiles. Thus one option to account for these differences in the soil profile at the site is to consider the site response results obtained for four soil profiles together and determine the variation of peak ground acceleration with respect different scaling procedures adopted.

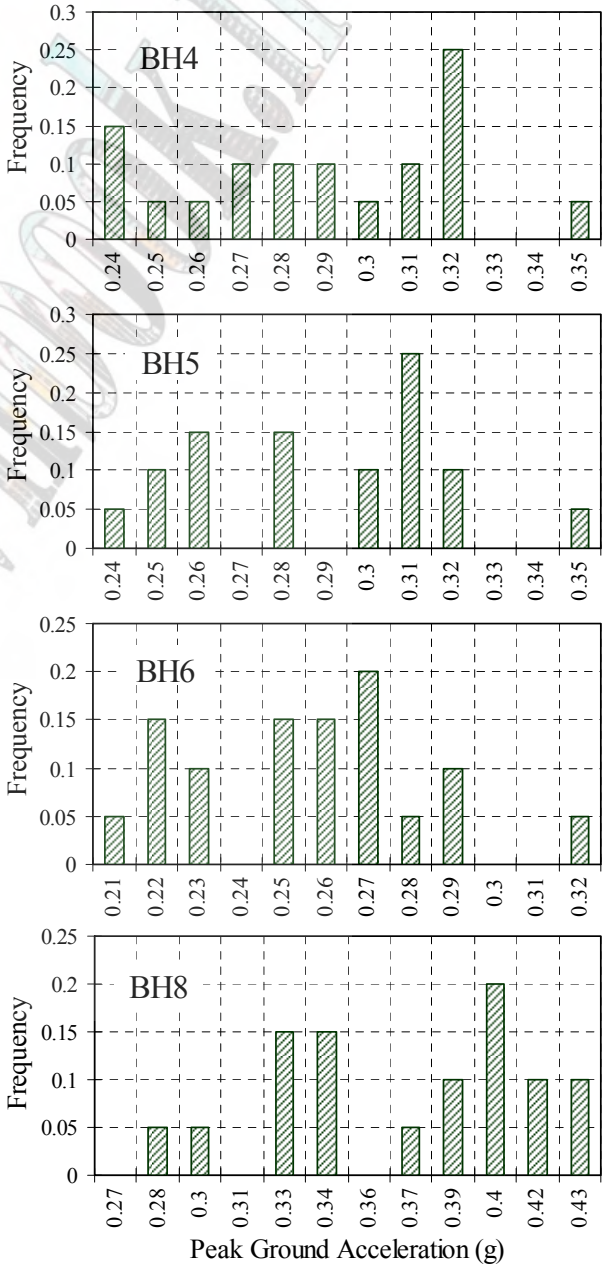

Fig. 3: Histograms of PGA on the ground surface for PGA scaled acceleration records for four soil profiles

The histograms for the calculated PGAs for all four borings for the three scaling option using the considered input motions are shown in Fig.4. Based on these limited results, it seems that among three scaling procedures, taking into consideration all three parameters calculated to determine the variability in each set (kurtosis and normalized standard deviation being minimum, and range being the smallest), the PGA scaling appears to be the most suitable scaling parameter in terms of calculated peak ground accelerations on the ground surface.

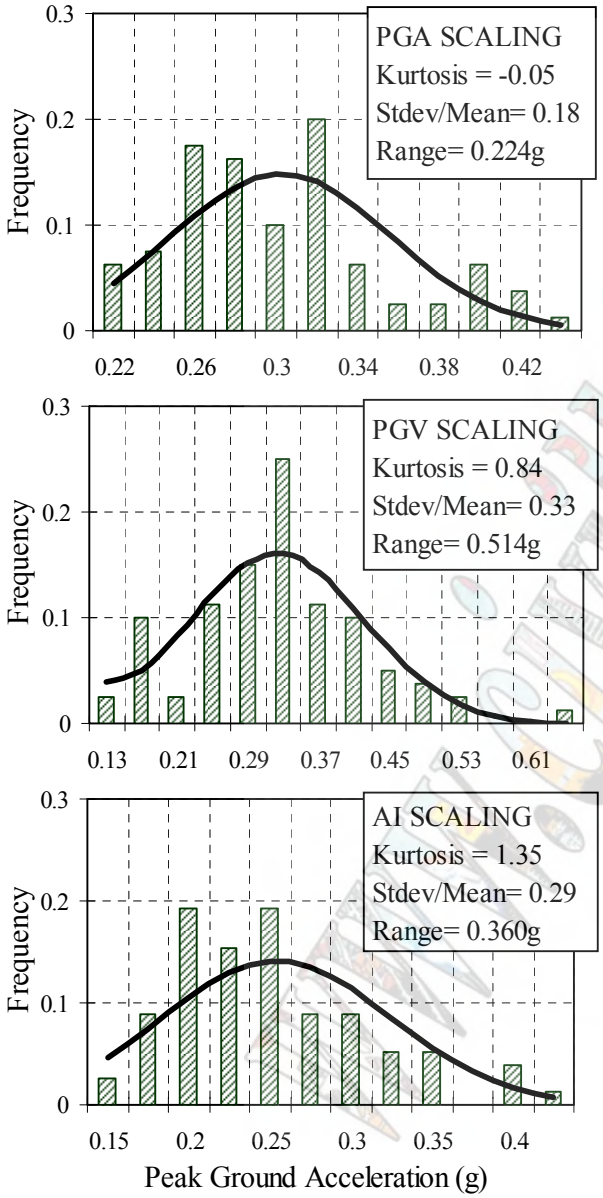

Fig. 4: Histograms of PGA on the ground surface for PGA, PGV, and AI scaled acceleration records

If each PGA distribution is assumed as possible variations concerning the input motion and if each PGA distribution is modeled by probability distribution models, it would be possible to estimate, with certain level of exceedance probability, the peak ground acceleration on the ground surface that can be used for the design of the engineering structures. Thus assuming that the exceedance level can be taken as 10%, the peak ground accelerations were determined based on the best fit by Beta or Weibull statistical distribution models. The calculated PGAs for three scaling method used are shown in Fig.5. It is interesting to note that PGV scaled records gave the largest PGA value while Arias intensity scaled records gave the lowest PGA value.

The second comparison to observe the effects of the scaling schemes was performed with respect to spectral acceleration at 0.2s obtained from the best envelop NEHRP spectra fitted to each of the calculated acceleration response spectra. The results of these calculations are shown in Fig.6 and Fig.7.

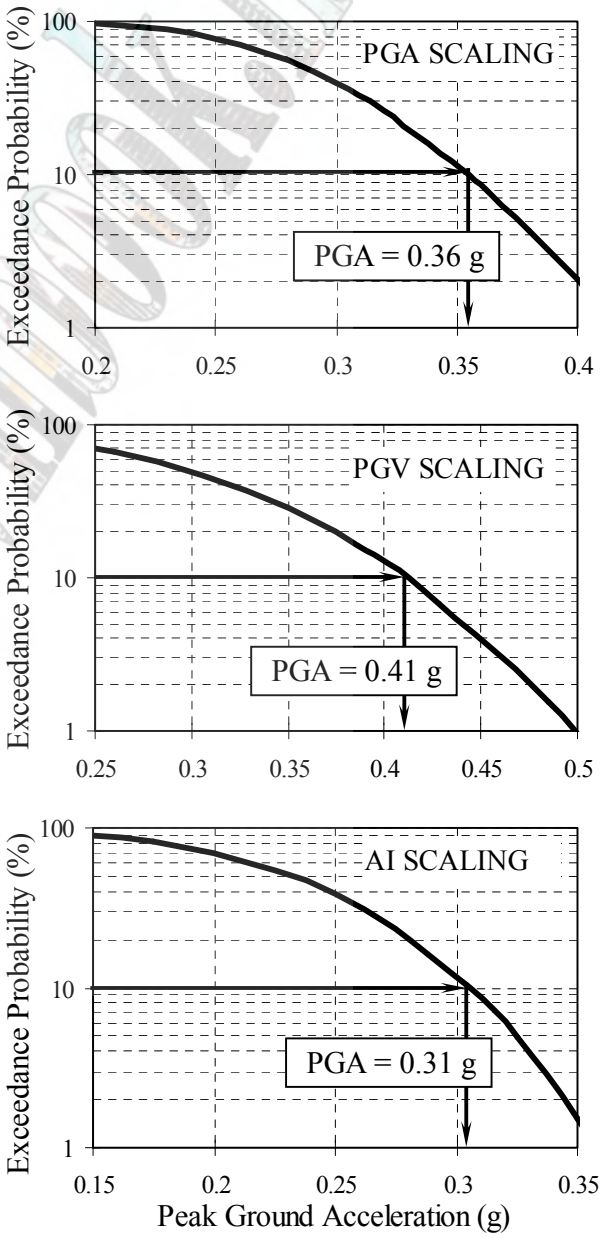

Fig. 5: PGAs on the ground surface for PGA, PGV, and AI scaled records corresponding to 10% exceedance

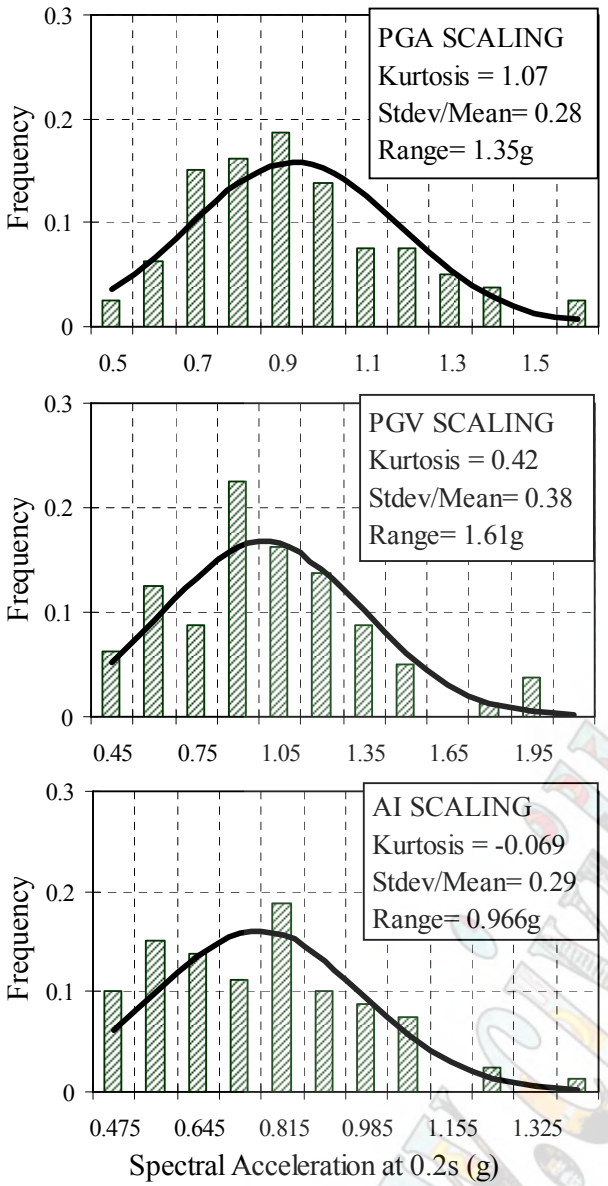

Fig. 6: Histograms of Sa(0.2s) on the ground surface for PGA, PGV, and AI scaled records

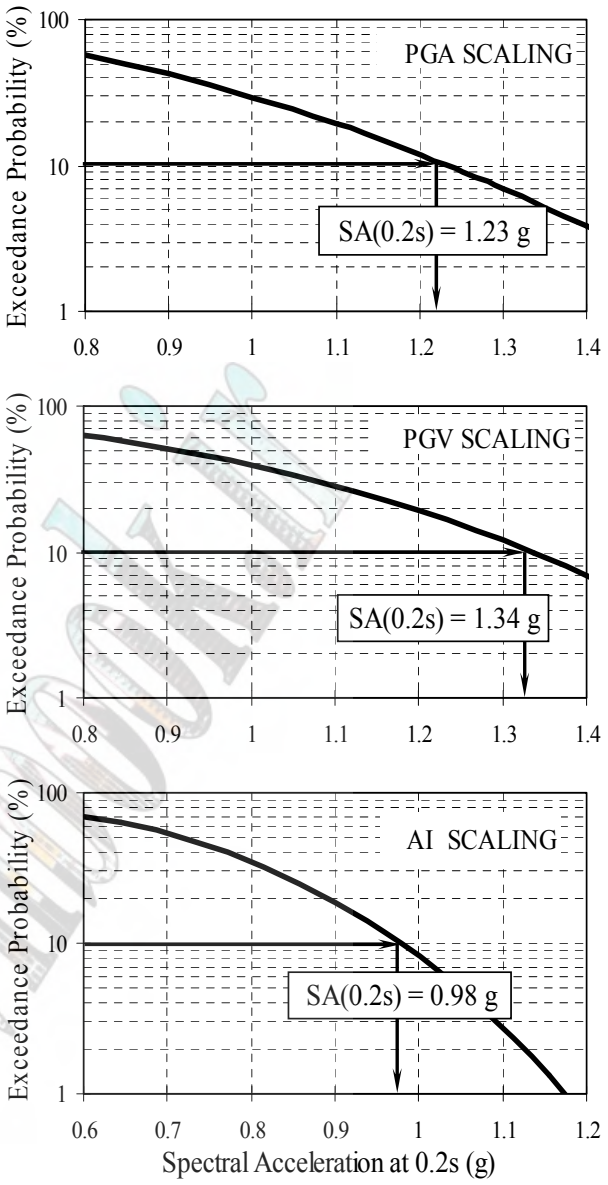

Fig. 7: Sa (0.2s) s on the ground surface for PGA, PGV, and AI scaled records corresponding to 10% exceedance

In the case of spectral accelerations at 0.2s the characteristics of the statistical distributions have changed significantly. Arias intensity (AI) scaling yielded the smallest range and Kurtosis while PGA scaling yielded the largest range and Kurtosis. Thus with respect to spectral accelerations at 0.2s, AI scaling gave the most suitable solution with the smallest variability. In addition the lowest value of the spectral acceleration at 0.2s is also obtained from the AI scaling results. This is also visible in Fig.8 in terms of calculated acceleration response spectra on the ground surface for the scaling methods.

If we consider spectral acceleration at 0.2s as the main damage parameter for the geotechnical engineering structures, than it is possible to suggest the use of AI scaling as the first option when conducting site response at a site to determine the design ground motions for geotechnical engineering structures.

Gölcük Case Study

The results are presented in terms of response spectral accelerations at the top of the soil profile and maximum and minimum accelerations and displacements along the profile. Two cases of site response are considered. In the first case there is no ground water table, in the second case the ground water table is at the ground surface. Ground motions scaled with respect to PGA, PGV and AI are used as input for the two site response cases. It should be noted that the results presented here are limited to the capabilities of the specific software used in the analyses and have to be interpreted accordingly. They are also limited to the distance range 0-20km that basically describes near-fault conditions for the magnitude range 7.0 - 7.5.

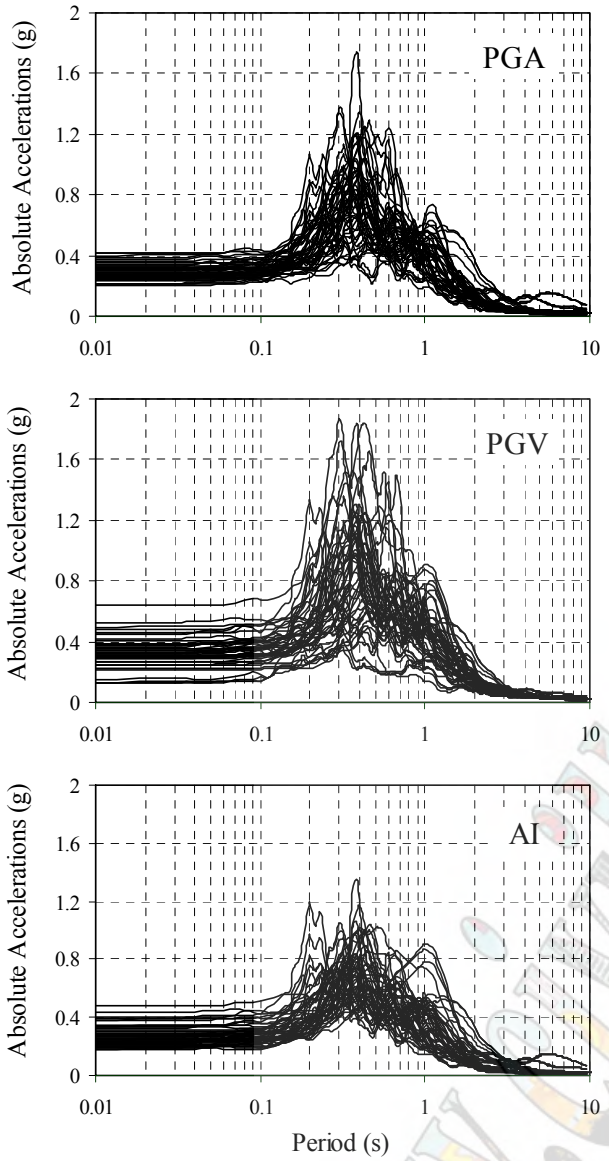

Fig. 8: Calculated acceleration spectra on the ground surface for PGA, PGV, and AI scaled records

Scaling with respect to PGA and AI reduces the variation in the response spectra significantly. The results indicate that AI scaled input ground motions result in response spectral values with variation less than the ones obtained from PGA scaled input motions for the case with no ground water (Fig.9). PGV scaled input motions yield spectral accelerations with significantly reduced scatter for periods larger than after the 0.8-1.0sec range.

In terms of displacements PGV scaled ground motions seem to yield consistent displacements over the profile, while PGA and AI scaling increases the uncertainty in the displacement response over the one where no scaling is applied to the input ground motions (Fig.10). As for the distribution of resulting peak accelerations through the profile, PGA and AI scaled input motion seem to control the resulting peak values with less uncertainty as compared to PGV scaled and unscaled input motion (Fig.11.).

Analyses on the case where the ground water table is near the ground surface indicate that the displacements are strictly controlled by the uppermost layer. Response spectral accelerations, displacements and accelerations do not seem to be sensitive to scaling. This is due to the pore pressure buildup and reduction in the effective stresses modeled by the constitutive model in the Cyclic1D code.

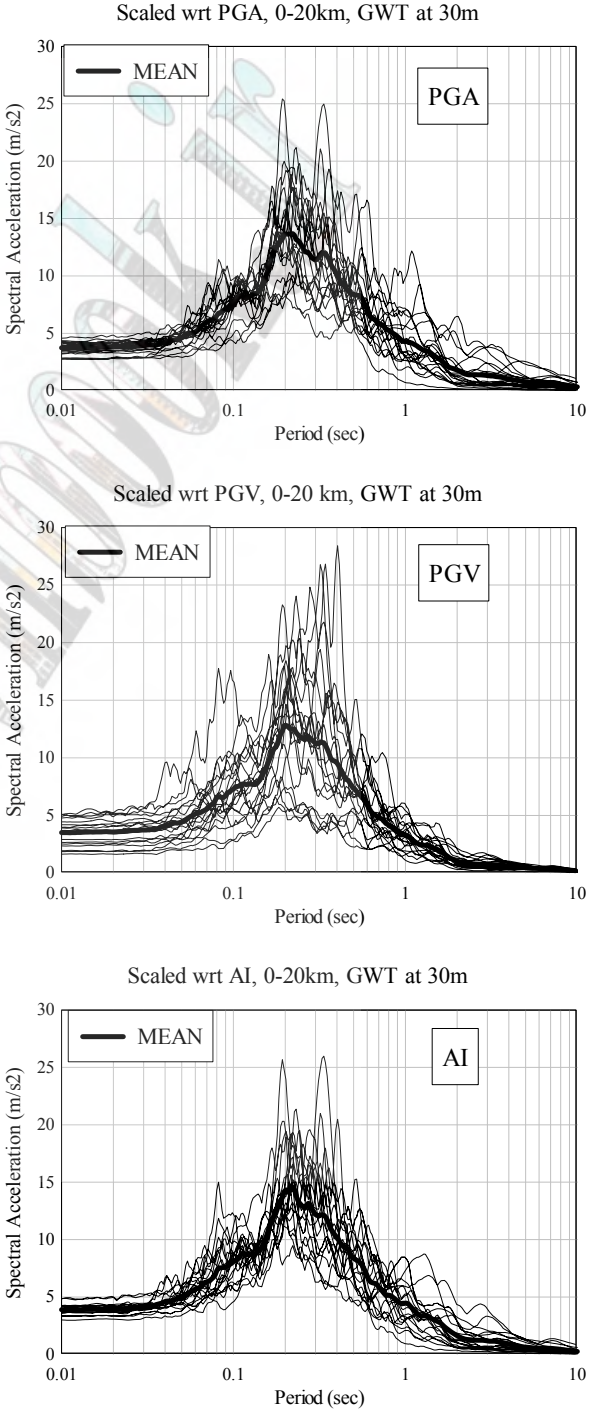

Fig. 9: Acceleration response spectra on the ground surface for the Gölcük case study

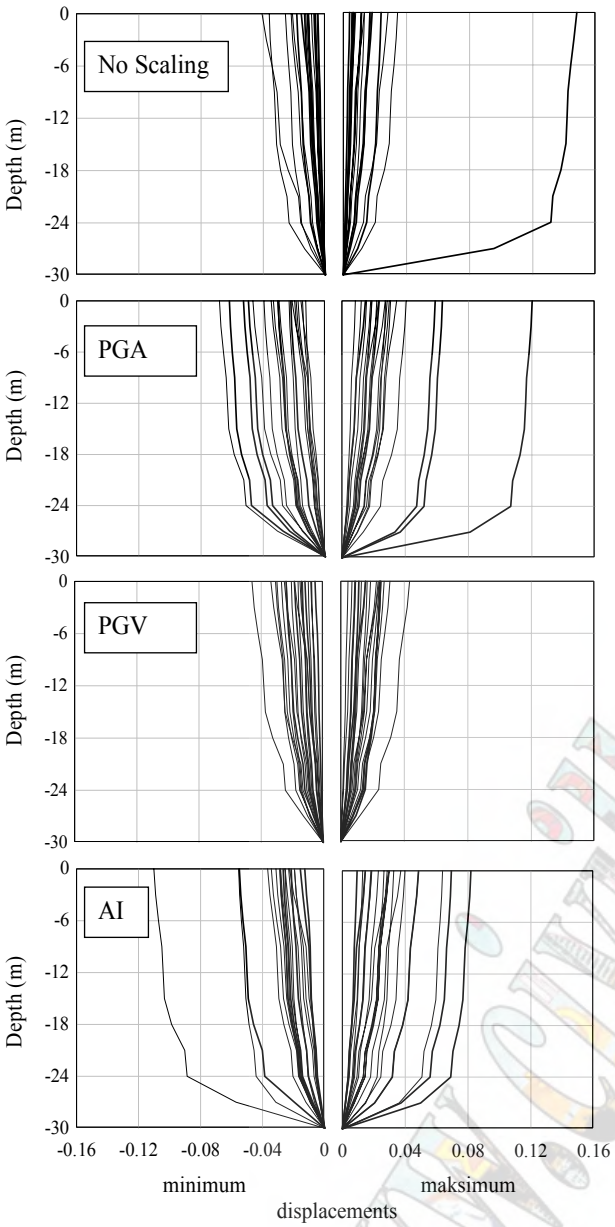

Fig. 10: Variation of maximum displacements with depth for unscaled and PGA, PGV, and AI scaled record

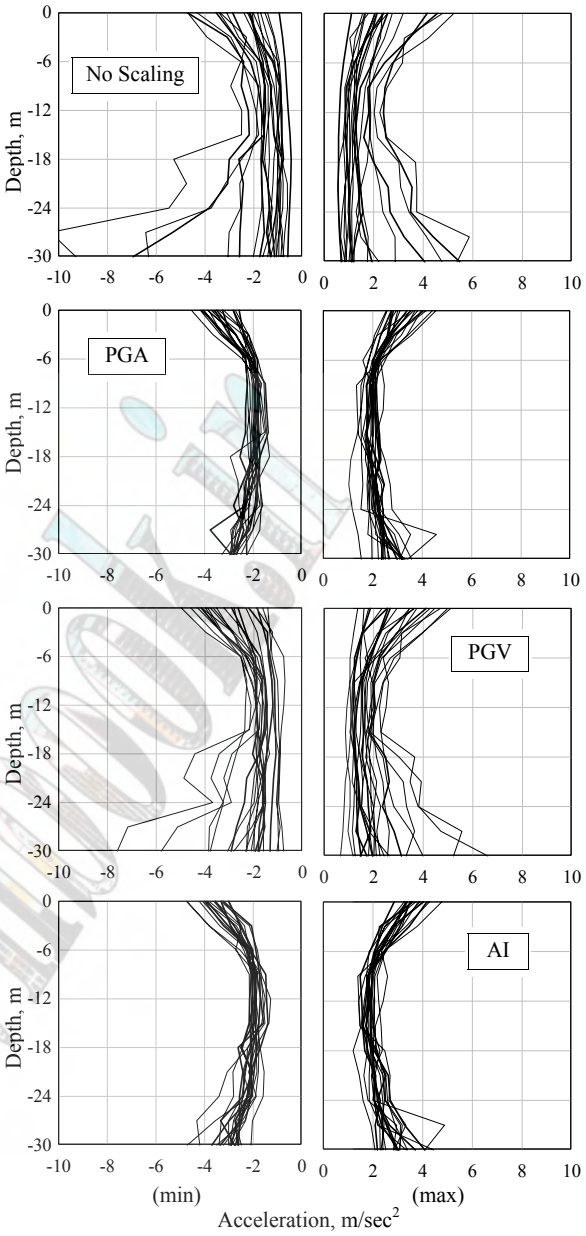

Fig. 11: Variation of maximum accelerations with depth for unscaled and PGA, PGV, and AI scaled record

CONCLUSIONS

Although selected in accordance to the site-specific hazard parameters the ground motions may have different characteristics in time and frequency domain and thus play an important role in model behavior by introducing a significant scatter in non-linear dynamic response. Scaling the records for time-domain analysis to values chosen consistent with site-specific hazard parameters is a way to handle this situation [20]. Scaling the input motion according to the most appropriate parameters so that the scatter of the model response is reduced is also important when design is required for different performance levels such as limit, serviceability etc. and also for displacement and acceleration sensitive structures and components [21.

In the first case study conducted it was observed that scaling with respect to Arias intensity gave lower variability both in terms of peak accelerations and short period spectral accelerations. Especially in the case of spectral accelerations at 0.2s, Arias intensity scaling yielded the most suitable scaling option among the three scaling procedures studied for conducting site response analyses.

In the second case study it was observed that in the short period range acceleration based scaling parameters, in this case PGA and AI, are more effective in reducing the scatter. For the specific case studied in this paper the PGA scaling is found to be effective until about 0.5 sec period, while the efficiency of AI scaling reached about 0.8 sec. In the long period range, i.e. after 0.8-1.0 sec the

PGV was the most effective parameter and the scatter was reduced significantly.

For the displacements over the studied profile, the PGA and AI scaling did not do an overwhelmingly good job over the case with no scaling. The PGV scaling however is seen to be a more efficient parameter in reducing the scatter in displacements through the profile. As for the accelerations PGA and AI scaling both reduced the scatter over the profile significantly compared to the unscaled case.

Presented results are for the 0-20km distance and 7.0-7.5 magnitude range for two case studies. The analyses were carried out using SHAKE and Cyclic 1D computer codes thus the obtained results directly depend on the formulation adopted in these codes.

ACKNOWLEDGMENTS

The authors wish to thank Dr. Farhang Ostadan for bringing up the issue of the effect of ground motion scaling on geotechnical works during a workshop and drawing our attention to it.

REFERENCES

[1] Chandler, A. M. and Lam, N. T. K., "Performance-based design in earthquake engineering: a multidisciplinary review," *Engineering Structures,* Vol.23, pp.1525–1543, 2001.

[2] Priestley, M. J. N., "Performance based seismic design," *Bulletin of the New Zealand National Society for Earthquake Engineering*, Vol.33, No. 3, pp.325-46, 2000.

[3] Stewart, J. P., Chiou, S. J., Bray, J. D., Graves, R. W., Somerville, P. G., and Abrahamson, N. A., "Ground motion evaluation procedures for performance-based design," *Soil Dynamics and Earthquake Engineering*, Vol.22, No.9-12 , pp.765-772, 2002.

[4] Kappos, A. J. and Kyriakakis, P., "A re-evaluation of scaling techniques for natural records," *Soil Dynamics and Earthquake Engineering*, Vol.20, pp.111-123, 2000.

[5] Bommer, J. J. and Acevedo, A. B., "The use real earthquake accelerograms as input to dynamic analysis," *Journal of Earthquake Engineering*, Vol.8, No.1, pp.43-91, 2004.

[6] Boore, D. M., "Can site response be predicted?" *Journal of Earthquake Engineering*, Vol.8, No.1, pp.1-42, 2004.

[7] Finn, W. D. L.., "State-of-the-art of geotechnical earthquake engineering practice," *Soil Dynamics and Earthquake Engineering*, Vol.20, pp.1-15, 2000.

[8] Martínez-Rueda, J. E., "Scaling Procedure for Natural Accelerograms Based on a System of Spectrum Intensity Scales," *Earthquake Spectra*, Vol.14, No.1, pp.135-152, 1998.

[9] Naeim, F., Alimoradi, A., and Pezeshk, S., "Selection and Scaling of Ground Motion Time Histories for Structural Design Using Genetic Algorithms," *Earthquake Spectra*, Vol.20, No.2, pp.413-426, 2004.

[10] Leger, P. and Leclerc, M., "Evaluation of earthquake ground motions to predict cracking response of gravity dams," *Engineering Structures*, Vol.18, No.3, pp.227-239, 1996.

[11] Idriss, I. M. and Sun J. I., "Shake91, A Computer Program for Conducting Equivalent Linear Seismic Response Analysis of Horizontally Layered Soil Deposits Modified based on the original SHAKE program Published in December 1972 by Schnabel, Lysmer and Seed", 1992.

[12] Yang Z., Lu, J., and Elgamal ,A., A Web-based Platform for Live Internet Computation of Seismic Ground Response, Advances in Engineering Software, Vol.35, pp.249-259, 2004.

[13] PEER Strong Motion Data Bank, http:// peer.berkeley.edu.

[14] Ambraseys, N. N., "The prediction of earthquake peak acceleration in Europe," *Earthquake Engineering and Structural Dynamics*, Vol.24, pp.467-490, 1995.

[15] Joyner, W. B. and Boore, D. M., "Measurement, characterization, and prediction of strong ground motion," *Earthquake Engineering and Soil Dynamics II – Recent Advances in Ground Motion Evaluation*, Geotechnical Special Publication 20, ASCE, New York, pp 43-102 , 1988.

[16] Travasarou, T., Bray, J. D., and Abrahamson, N. A., "Empirical attenuation relationship for arias intensity," *Earthquake Engineering and Structural Dynamics*, Vol.32, pp.1133-1155, 2003.

[17] Siyahi, B., Durukal, E., and Altaç, Z., "Evaluation of strong motion data from the Kocaeli and Düzce, Turkey Earthquakes in view of Arias intensity," *Proceedings 15ICSMGE Earthquake Geotechnical Engineering Satellite Conference on Lessons Learned from Recent Strong Earthquakes*, pp. 189-194, Istanbul, Turkey, 2001.

[18] Ansal, A., Togrol, E., Kurtulus, A., Iyisan, R., and Okur, V., "Near fault site effects during 1999 Kocaeli Earthquake", *Proc. 6th Int. Conf. on Seismic Zonation*, Cal., USA, 2000.

[19] Erdik, M., Sesetyan, K., Demircioglu, M., Siyahi, B., and Akman, H., "Assessment of the Seismic Hazards in Adapazarı, Gölcük, Değirmendere and İhsaniye Provinces in Northwestern Turkey," Seismic Microzonation for Municipalities, Pilot Studies. Research Report for Republic of Turkey, Ministry of Public Works and Settlement, General Directorate of Disaster Affairs, World Institute for Disaster Risk Management, Inc. 2003, Ch. 3.

[20] Malhotra, P. K., "Strong-Motion Records for Site-Specific Analysis," *Earthquake Spectra*, Vol.19, No.3, pp.557-578, 2003.

[21] Heuze, F., Archuleta, R., Bonilla, F., Day, S., Doroudian, M., Elgamal, A., Gonzales, S., Hoehler, M., Lai, T., and Lavallee, D., "Estimating site-specific strong earthquake motions," *Soil Dynamics and Earthquake Engineering*, Vol.24, No.3, pp.199-223, 2004.

Using Inverse Random Vibration Theory to Develop Input Fourier Amplitude Spectra for Use in Site Response

E.M. Rathje[1], A.R. Kottke[1], and M.C. Ozbey[1]
Department of Civil, Architectural, and Environmental Engineering, University of Texas, Austin, TX, USA

Abstract

This paper describes an inverse random vibration theory (IRVT) procedure that can be used to develop response-spectrum-compatible Fourier amplitude spectra. The IRVT procedure uses extreme value statistics, the characteristics of single-degree-of-freedom oscillator transfer functions, and a spectral ratio correction to develop the Fourier amplitude spectra. The IRVT procedure is applied to response spectra from a ground motion prediction (attenuation) equation and the resulting Fourier amplitude spectra are compared with predictions from seismological source theory. Finally, the use of this procedure with uniform hazard spectra in RVT site response is discussed.

Keywords—*Random vibration theory, site response, inverse theory*

INTRODUCTION

Traditional site response analysis requires many input motions to produce a statistically stable estimate of the surface response. Random vibration theory (RVT) can be applied to site response analysis to produce a statistically stable estimate of the response with only one analysis. The input used in RVT site response analysis is the square of the Fourier amplitude spectrum (FAS) of the motion at the base rock. The key to accurate RVT site response analysis is the use of an appropriate input Fourier amplitude spectrum. Often, this input spectrum is derived from seismological source theory; however, it is possible to use a rock acceleration response spectrum and an inverse RVT (IRVT) procedure to develop the input spectrum.

Seismological source theory provides a theoretical input FAS that combines the effects of the earthquake source, propagation path, high frequency diminution, and crustal amplification. To produce a FAS using source theory, a large number of parameters must be defined. Many of these parameters are poorly defined and the parameters are foreign to engineers such that choosing appropriate values can be difficult. Additionally, spectra from source models may not always provide a reasonable input motion as compared to rock ground motion prediction (attenuation) equations. An alternative to using source theory to develop the input FAS is inverting a rock acceleration response spectrum into a FAS. Response spectra are commonly used by both structural and geotechnical engineers, making it the preferred input for RVT site response analysis.

This paper provides an introduction to the forward RVT procedure and the concept of extreme value statistics. An inverse RVT procedure, first proposed by Gasparini and Vanmarcke [1], is discussed along with modifications to the procedure that improve the accuracy of the inversion. The IRVT procedure is applied to response spectra from a ground motion prediction equation for a range of earthquake magnitudes and distances, and the resulting FAS are compared to the spectra from seismological source theory.

RANDOM VIBRATION THEORY

Random Vibration Theory (RVT) makes use of Parseval's theorem and extreme value statistics to compute the peak time domain motion from a FAS. The RVT analysis involves three basic steps: (1) calculation of the root-mean-square acceleration (a_{rms}) from the FAS using Parseval's theorem, (2) calculation of the peak factor ($pf = a_{max}/a_{rms}$) using extreme value statistics, and (3) multiplication of the a_{rms} by the peak factor to obtain the peak acceleration (a_{max}). When computing an acceleration response spectrum, the additional step of applying a single degree of freedom (SDOF) oscillator transfer function to the FAS is required. The following is only a brief discussion of RVT; a more thorough discussion can be found in [2] and [3].

Parseval's theorem states that power is conserved in the frequency and time domains, and thus the total power in a signal can be computed in either domain. The a_{rms} is equal to the total power in the time history divided by the ground motion duration (T_d) and can be computed from the square of the FAS ($|A(f)|^2$) using:

$$a_{rms}^2 = \frac{1}{T_d}\int_0^{T_d} a^2(t)\,dt = \frac{2}{T_d}\int_0^{\infty} |A(f)|^2\,df \,, \qquad (1)$$

where $a(t)$ is the acceleration-time history.

The peak factor (pf) is the ratio of the peak acceleration (a_{max}) to the root-mean-square acceleration (a_{rms}), and is a function of the statistical moments of the FAS and the duration of the motion. The statistical moments are used to define the characteristics of the

motion, specifically the frequency bandwidth, the number of extrema in the time series (N_e), and the number of zero crossings in the time series (N_z). The expected value of the peak factor is computed using [4]:

$$pf = \sqrt{2}\int_0^\infty \left\{1 - \left[1 - \frac{N_z}{N_e}\exp(-z^2)\right]^{N_e}\right\} dz \,. \quad (2)$$

To calculate N_e and N_z the statistical moments of the square of the FAS are required. The n-th moment of the square of the FAS is defined as:

$$m_n = 2\int_0^\infty (2\pi f)^n \left|A(f)\right|^2 df \,. \quad (3)$$

The moments are used to describe the frequency at which zero is crossed (f_z) and the frequency of extrema (f_e). Using the duration of the motion (T_d) with f_z and f_e the number of zero-crossings and extrema can be found using [5]:

$$N_z = 2T_d f_z = \frac{T_d}{\pi}\sqrt{\frac{m_2}{m_0}} \text{, and} \quad (4)$$

$$N_e = 2T_d f_e = \frac{T_d}{\pi}\sqrt{\frac{m_4}{m_2}} \,. \quad (5)$$

These values of N_z and N_e are then used in equation (2) to compute the peak factor.

The duration required for equations (1), (4), and (5) is related to the source duration and distance, and can be computed from the earthquake corner frequency using:

$$T_d = 1/f_c + 0.05R \,, \quad (6)$$

where R is distance in km, and f_c is the corner frequency in Hz. For spectral acceleration values, the duration used in equation (1) is corrected for oscillator period as proposed by [6]. If the earthquake is assumed to be a point source, the following relationship can be used to calculate the corner frequency [7, 8]:

$$f_c = 4.9\times10^6 \beta_0 \left(\frac{\Delta\sigma}{M_0}\right)^{1/3} \,, \quad (7)$$

where β_0 is the shear wave velocity of the crust in km/s, $\Delta\sigma$ is the stress drop in bars, and M_0 is the seismic moment in dyne-cm. Typical western US values of β_0 and $\Delta\sigma$ are 3.5 km/s and 100 bars, respectively. The seismic moment is related to the moment magnitude (M_w) of the earthquake using:

$$M_o = 10^{1.5M_w + 16.05} \,. \quad (8)$$

While more complicated source models exist, the single corner frequency model has been shown to produce accurate results for a wide range of seismological and ground motion problems [9].

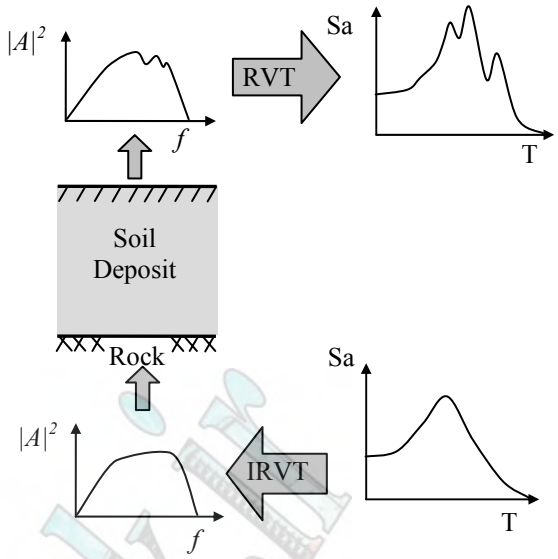

Fig. 1: The application of IRVT in an RVT site response analysis.

The RVT procedure allows one to compute peak time domain motions from a FAS. If the FAS represents the motion on rock, RVT produces the rock response spectrum. Alternatively, the rock FAS can be propagated through a soil column to compute the FAS at the surface of the soil deposit (Fig. 1). This FAS, along with RVT, can be used to compute the soil response spectrum. In an RVT site response procedure, the specification of the input rock FAS is critical. Although seismological source theory has been used for this purpose, source theory may not provide an input motion consistent with a ground motion prediction equation [3] or a uniform hazard spectrum from probabilistic seismic hazard analysis. Thus, a methodology that develops the input rock FAS from a specified input rock response spectrum would be useful in RVT site response analysis.

INVERSE RVT

Inverse RVT (IRVT) takes an acceleration response spectrum and converts it into a frequency domain FAS (Fig. 1). While it is relatively straight forward to produce a response spectrum from a FAS, it is not trivial to perform the inverse. There are two complications for the inversion. First, the spectral acceleration is influenced by a range of frequencies in the FAS, such that a spectral acceleration at a given period cannot be related solely to the Fourier amplitude at the same period. To solve this problem, the IRVT procedure takes advantage of some of the properties of SDOF transfer functions (TF). Specifically, the SDOF transfer function is narrow band for lightly damped systems and it goes to zero at frequencies much larger than the natural frequency (Fig. 2), which limits the frequency range that affects the spectral acceleration at a given period. The second complication is that the peak factor cannot be determined apriori because it is based on the FAS, which is unknown.

However, a peak factor can be assumed to develop an initial estimate of the FAS and then this spectrum can be used in a second iteration to compute peak factors for use in the inversion. The IRVT methodology described below and used in this study is based on the procedure proposed by [1].

Methodology

The acceleration response spectrum represents the peak accelerations of SDOF oscillators of different natural frequencies for a given damping level. Using RVT, the peak spectral acceleration (Sa) is related to the rms spectral acceleration (Sa_{rms}) by the peak factor:

$$(Sa)^2 = pf^2 (Sa_{rms})^2 . \tag{9}$$

To determine the Sa_{rms} for a SDOF system, again Parseval's theorem is used:

$$(Sa_{rms})^2 = \frac{2}{T_d} \int_0^\infty |A(f)|^2 |H_{f_n}(f)|^2 \, df , \tag{10}$$

where $|H_{fn}(f)|$ is the transfer function of a SDOF oscillator with natural frequency f_n and critical damping ratio ξ [e.g. 10]. It is clear from (10) and Fig. 2 that the spectral acceleration is affected by a range of frequencies in the FAS and thus cannot be used directly to solve for a value in the FAS. However, various characteristics of the SDOF transfer function can be used to solve for the FAS.

The characteristics of a lightly damped (e.g. 5% of critical) SDOF oscillator transfer function are illustrated in Fig. 2. The transfer function has three important characteristics: (1) it is equal to unity below the natural frequency, (2) it contains a narrow band of large amplification near the natural frequency, and (3) it approaches zero at frequencies greater than the natural frequency. Using these three properties, an approximation to the integral in equation (10) can be created in terms of the Fourier amplitude at the oscillator natural frequency, $|A(f_n)|$, using [1]:

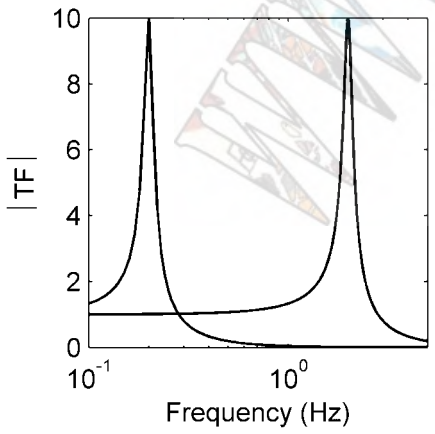

Fig. 2: Single degree of freedom (SDOF) oscillator transfer functions for f_n = 0.2 and 2 Hz.

$$Sa_{rms}^2 \approx \frac{2}{T_d} \begin{bmatrix} \int_0^{f_n} |A(f)|^2 \cdot 1 \cdot df \\ + |A(f_n)|^2 \int_0^\infty |H_{f_n}(f)|^2 \, df \\ - |A(f_n)|^2 f_n \end{bmatrix} . \tag{11}$$

The three terms in equation (11) are illustrated graphically in Fig. 3. The first term represents the integral at frequencies less than the natural frequency, where the SODF transfer function is equal to unity (area (a) in Fig. 3). The second term computes the integral using a constant value of $|A|^2$ equal to its value at the natural frequency (area (b) in Fig. 3). This approximation is valid because the FAS is a relatively smooth function, unlike the SDOF transfer function, and because the SDOF transfer function is large near the natural frequency and then quickly decreases to zero at larger frequencies. The rapid decrease to zero minimizes the error introduced by this approximation. The final term in (11), removes the area below the natural frequency (area (c) in Fig. 3), which has been counted in both terms one and two. Equation (11) is more useful than equation (10) because it is written in terms of the Fourier amplitude at the oscillator natural frequency, $|A(f_n)|$, and can be used to solve for this value.

Equations (9) and (11) can be combined to solve for $|A(f_n)|^2$ in terms of the spectral acceleration (Sa) at f_n, the peak factor (pf), the duration of motion (T_d), the Fourier amplitudes at frequencies less than f_n, and the integral of the SDOF transfer function. The resulting expression is [1]:

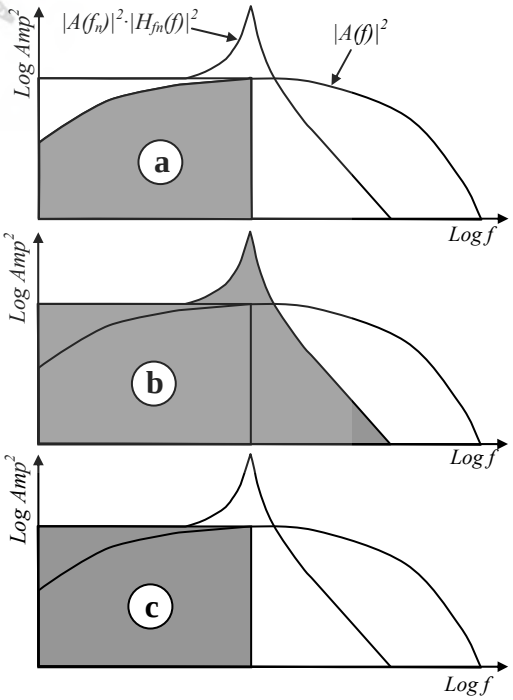

Fig. 3: Integral approximations utilized in equation (11).

$$|A(f_n)|^2 \approx \frac{1}{\int_0^\infty |H_{fn}(f)|^2 df - f_n}\left(\frac{T_d}{2}\frac{Sa^2}{pf^2} - \int_0^{f_n}|A(f)|^2 df\right). \quad (12)$$

The transfer function integral is a constant for a given natural frequency and damping ratio, allowing the equation to be simplified to [1]:

$$|A(f_n)|^2 \approx \frac{1}{f_n\left(\frac{\pi}{4\xi}-1\right)}\left(\frac{T_d}{2}\frac{Sa^2}{pf^2} - \int_0^{f_n}|A(f)|^2 df\right). \quad (13)$$

Equation (13) is applied first at low frequencies, where the integral term in (13) can be assumed equal to zero, and then at successively higher frequencies. In the calculations that were performed in this study the frequency range was composed of 500 points equally spaced in log space. The minimum and maximum frequencies corresponded to the minimum and maximum periods in the input response spectrum. In this study, the Abrahamson and Silva [11] ground motion prediction equation was used with its frequency range of 0.2 to 100 Hz and the spectral accelerations were interpolated to fit the 500 prescribed frequencies.

The inversion of the response spectrum into a FAS relies on the values of peak factor, which vary with spectral period. However, to initiate the inversion and obtain an initial estimate of the FAS, the peak factor is assumed to be 2.5. This initial estimate of the FAS is used to define the peak factors used in a second IRVT computation. On occasion, the ratio $(Sa^2_{rms}/pf^2 \cdot T_d/2)$ in equation (13) is almost identical to the area of the FAS below the natural frequency, which results in a computed zero or negative value for $|A(f_n)|^2$. This problem occurs at high frequencies and is solved by making the FAS match the general shape of a seismological source spectrum in this frequency range.

Fig. 4 illustrates the IRVT procedure. Fig. 4a is the input acceleration response spectrum that is to be matched, and it represents a rock response spectrum from Abrahamson and Silva [11] for a magnitude of 6.5 and a distance of 5 km. Fig. 4b shows the peak factor as a function of the oscillator frequency. Both the initial peak factor estimate of 2.5 and the updated values are shown. Note that the updated peak factors for this scenario vary from 1.6 at low frequencies to 3.6 at high frequencies. Fig. 4c shows the initial estimate of the FAS, assuming a constant peak factor of 2.5, and the final FAS using a variable peak factor (Fig. 4b). Fig 4d compares the response spectrum from the second FAS with the input target response spectrum. The input and predicted spectra were compared quantitatively by the maximum percent error and the sum of the square errors (SSE). SSE is computed by summing the square of the difference between the normalized response spectra (Sa/PGA). The

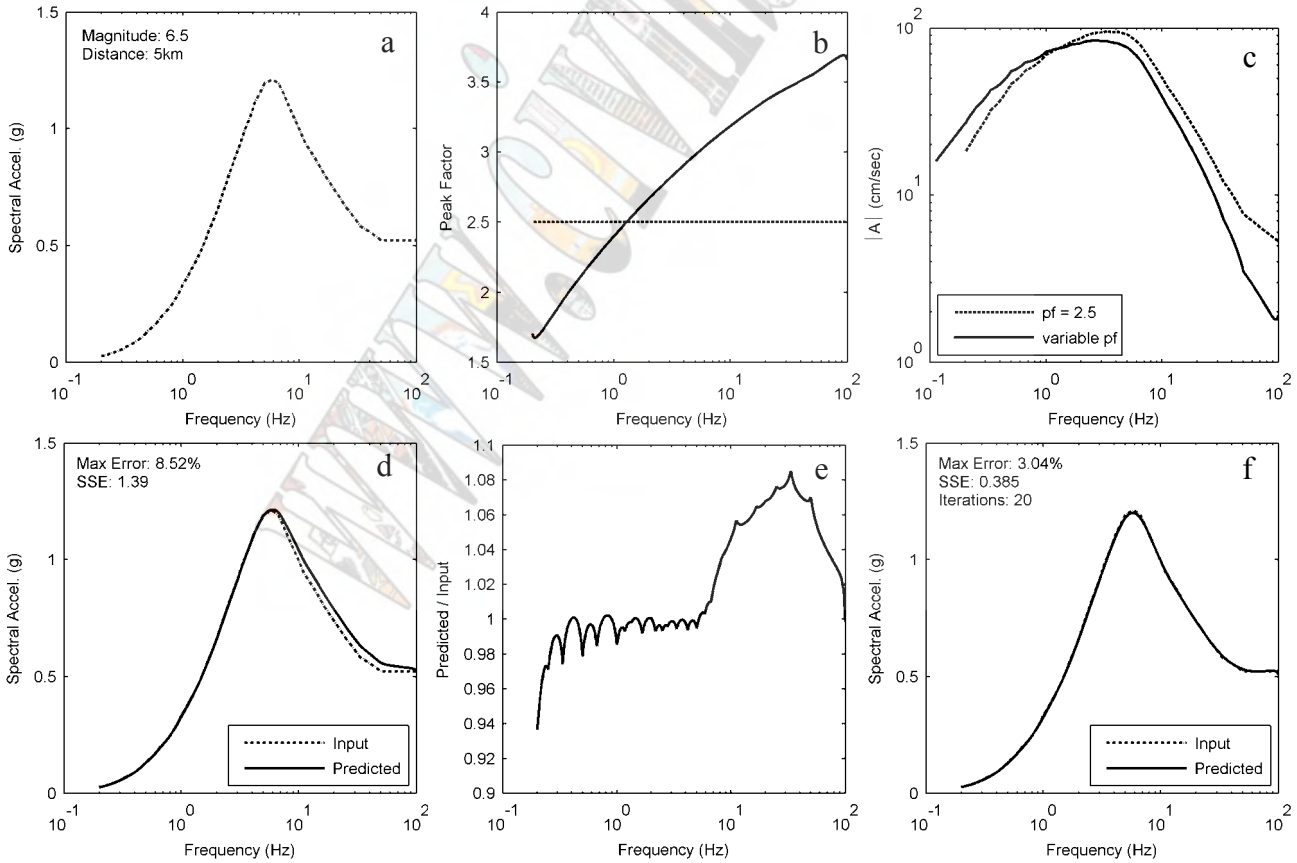

Fig. 4: The process of generating a Fourier Amplitude spectrum from an input response spectrum using IRVT.

match in Fig. 4d is quite good, with a maximum error of 8.5% and an SSE equal to 1.39. Fig. 4e shows the error versus period. Most of the error associated with the predicted response spectrum occurs at frequencies greater than about 5 Hz.

Corrections

The computed FAS from IRVT produces a response spectrum that generally deviates 5 to 10% from the input spectrum (Fig. 4e). To improve the predicted response spectrum, a correction is applied to the FAS based on the error in the response spectrum. Although the spectral acceleration at a given frequency does not directly translate into the FAS at that frequency, the spectral ratio (Sa_{input} /$Sa_{predicted}$) will still be used to modify the FAS. Using this correction, when the predicted response spectrum is smaller than the input response spectrum, the FAS is increased, and when the predicted response spectrum is greater than the input response spectrum, the FAS is reduced. By squaring the ratio, convergence is achieved move quickly [1]. The squared spectral ratio is defined as:

$$r = \left(\frac{Sa_{input}}{Sa_{predicted}} \right)^2 , \quad (14)$$

where Sa_{input} is the input spectral acceleration at a given period and $Sa_{predicted}$ is the calculated spectral acceleration from the IRVT FAS at the same period. The FAS is corrected using:

$$\left| A(f)_{corr.} \right| = r \cdot \left| A(f)_{predicted} \right| . \quad (15)$$

This process is repeated until the desired accuracy is achieved. In this study, the correction is applied until a maximum error of 2% is reached or 20 iterations are performed.

The squared spectral ratio correction introduces complications because the spectral ratio changes erratically with period (Fig. 4e). Using this correction directly results in a FAS that no longer takes on a smooth shape. A smooth FAS is achieved by filtering the corrected FAS by taking a moving average. The filtering window used in the study was 2.5% of the number of data points. This window size balanced the increased accuracy of a narrow window with the smoother FAS of a larger window. One additional correction was required at high frequencies. On occasion, the ratio correction significantly increases the Fourier amplitudes at high frequencies such that the FAS actually curves up at high frequencies. This shape is unreasonable for earthquake motions based on seismological source theory. Thus, to match the expected shape of a FAS for an earthquake motion, the slope of the FAS in log-log space was limited to a maximum value of -0.5 at high frequencies. Fig. 4f shows the final response spectrum after application of the ratio corrections, filtering, and maximum slope criterion. The result is a very good match with a maximum error of 3.04% and an SSE of 0.385.

COMPARISON WITH SOURCE THEORY

The IRVT computation was carried out for several magnitude and distance combinations and compared with Fourier amplitude spectra predicted by the Brune [7, 8] ω^{-2} point source spectrum. This spectrum is defined as:

$$A(f) = \left[0.78 \frac{\pi}{\rho_0 \beta_0^3} M_0 \frac{f^2}{1+\left(f / f_c\right)^2} \right] \cdot \left[\frac{1}{R} \cdot \exp\left(\frac{-\pi f R}{Q(f)\beta_0} \right) \right] \left[\exp\left(-\pi \kappa_o f\right) \right] \; G(f) , \quad (16)$$

where ρ_0 is the mass density of the crust (g/cm^3), $Q(f)$ is the anelastic attenuation, κ_0 is the diminution parameter (s), $G(f)$ is the crustal amplification function, and the remaining parameters have been defined previously. The distance term in (16) is modified by a fictitious depth of 10 km, so that the distance measure is similar to that used in ground motion prediction equations. Typical values of the other parameters in equation (16) are given in Table 1.

The IRVT procedure was applied to input response spectra developed from the Abrahamson and Silva [11] ground motion prediction equation for three magnitude and distance combinations (M_w 6.5 and R 5 km, M_w 6.5 and R 60 km, M_w 7.5 and R 60 km). The IRVT Fourier amplitude spectra and their corresponding acceleration response spectra are shown in Fig. 5. The comparison with the input response spectra from Abrahamson and Silva [11] is excellent, as the spectra are almost indistinguishable.

For the Brune source spectrum with typical western US parameters (Table 1), the resulting response spectrum can deviate from the Abrahamson and Silva [11] response spectrum by upwards of 50% [3]. This deviation can present a problem if one wants to use the Brune source spectrum as input into an RVT site response analysis. To produce a Brune source spectrum consistent with a ground motion prediction equation, some of the source parameters (e.g. $\Delta\sigma$ and κ_0) can be modified within reasonable limits until the resulting response spectrum matches the ground motion prediction equation. However, the resulting spectrum still may deviate from the input spectrum significantly [3].

Table 1: Typical western US source parameters [12]

Parameter	Value
Density, ρ (g/cm^3)	2.8
Shear wave velocity, β (km/s)	3.5
Stress drop, $\Delta\sigma$ (bar)	100
Diminution parameter, κ_0 (s)	0.04
Anelastic attenuation, $Q(f)$	$180 f^{0.45}$

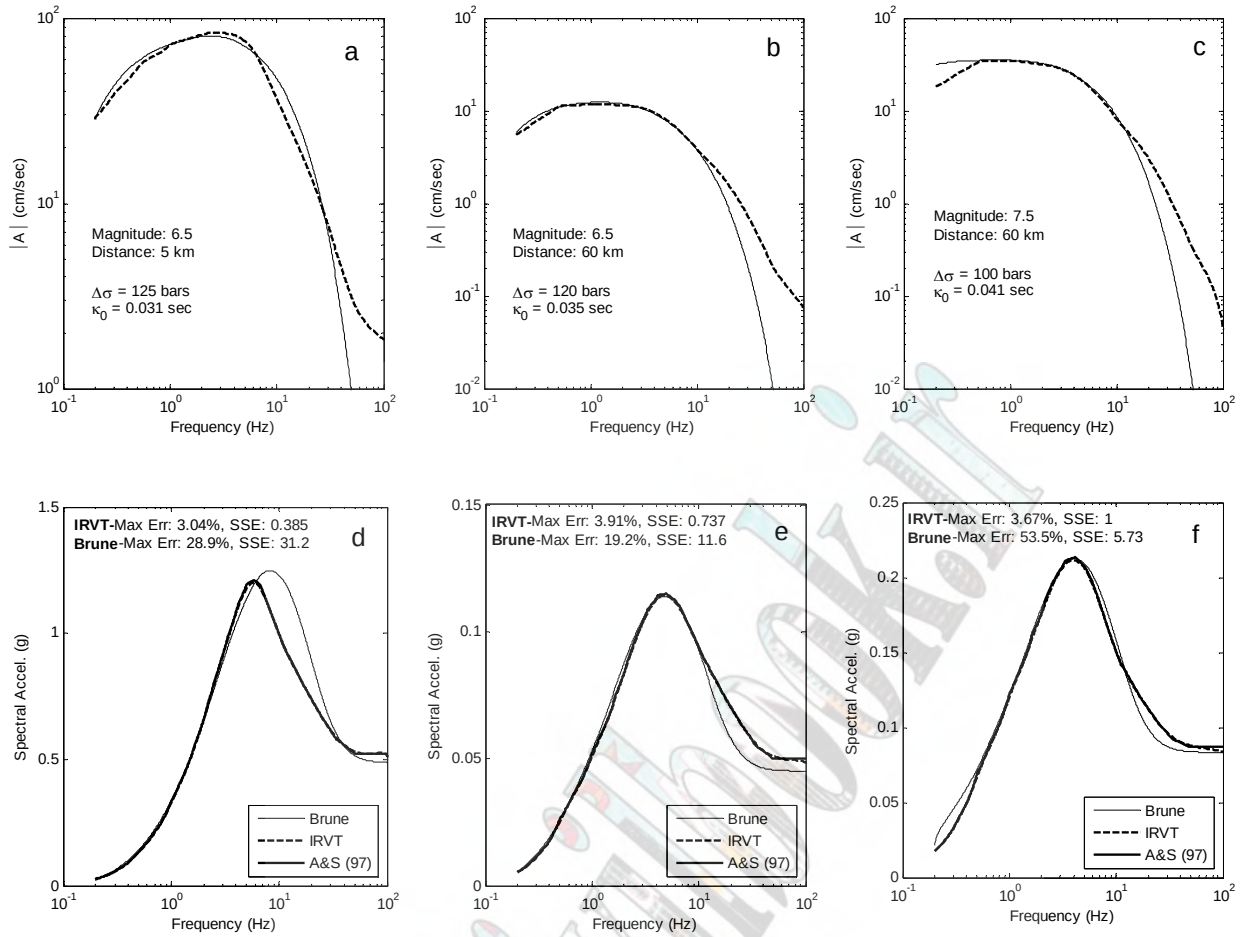

Fig. 5: Comparison of Fourier amplitude spectra and acceleration response spectra from the Brune model and IRVT.

Fig. 5 shows the Brune spectra developed by modifying parameters $\Delta\sigma$ and κ_0 until the corresponding response spectra best fit the ground motion prediction equation. The values of $\Delta\sigma$ and κ_0 that produce the best fit are listed in the Fig. 5, along with the resulting response spectra from Brune and IRVT. Even with the best-fit input parameters, the response spectra from the Brune spectra deviate from the input response spectra. The most noticeable differences occur at low and high frequencies (Fig. 5).

In comparing the FAS from IRVT and the Brune point source model at smaller magnitudes (M_w 6.5, Figs. 5a and b), the spectra match at lower frequencies but start to diverge at larger frequencies. The corner frequency and stress drop control the low frequency part of the spectrum, and thus this favorable comparison indicates the form of the Brune spectrum in terms of these parameters is adequate for this magnitude. The diminution parameter, along with $Q(f)$, control the large frequency part of the spectrum. The deviation of the Brune and IRVT spectra in this frequency range appears to indicate that the $\exp(-\pi\kappa_0 f)$ form of equation (16) is inadequate. As some seismologists consider this term simply a fitting term [13], and other forms of this term have been used in the past [4], perhaps it is not surprising that this term is somewhat inadequate. For the larger magnitude event (M_w 7.5, Fig. 5c), the Brune spectrum is significantly larger than IRVT at lower frequencies, which results in significantly larger spectral accelerations at low frequencies (Fig. 5f). The overprediction of the FAS at low frequencies for larger magnitude earthquakes occurs because of the breakdown of the point source assumption [4]. To address this issue, a two corner frequency model has been proposed [14]. The FAS developed from ground motion prediction equations at large magnitudes are thus in agreement with the two corner frequency model.

DISCUSSION AND CONCLUSION

The IRVT procedure presented in this paper can also be used to develop a Fourier amplitude spectrum that is consistent with a uniform hazard spectrum (UHS) from probabilistic seismic hazard analysis. IRVT is better suited than the Brune model at fitting a UHS because RVT is not constrained to a functional form or a single magnitude and distance combination. Thus, IRVT can directly transform the UHS into a FAS for input into RVT site response analysis [3]. The RVT site response analysis then provides the acceleration response spectrum at the

top of the soil based on the input UHS. Alternatively, RVT site response analysis that uses an IRVT-defined input FAS can be used within the seismic hazard computation to derive soil specific seismic hazard curves.

Random vibration theory (RVT) can be applied to site response analysis to produce a statistically stable estimate of the response with only one analysis. The input into RVT site response analysis is the rock FAS, which can be defined directly using seismological source theory or derived from a rock response spectrum using IRVT. The rock response spectrum can be defined from a ground motion prediction equation or from probabilistic seismic hazard analysis. This study demonstrates that IRVT can produce accurate, response-spectrum-compatible Fourier amplitude spectra. It is more difficult to produce response-spectrum-compatible FAS using source theory, even when the source parameters are modified. Input FAS derived from IRVT will provide for more accurate site response evaluations using RVT.

ACKNOWLEDGMENTS

Financial support was provided by the U.S. Geological Survey under NEHRP grant 04HQGR0071, by the National Science Foundation through the Southern California Earthquake Center (SCEC), and by Pacific Gas and Electric. This support is gratefully acknowledged.

REFERENCES

[1] Gasparini, D. A., and Vanmarcke, E. H., *SIMQKE: Simulated earthquake motions compatible with prescribed response spectra*, Mass. Institute of Tech., Cambridge, Massachusetts, 1976.

[2] Boore, D. M., "Simulation of ground motion using the stochastic method." *Pure Appl. Geophys*., Vol. 160, No. 3-4, pp. 635-676, 2003.

[3] Rathje, E.M. and Ozbey, M.C., "Site Specific Validation of Random Vibration Theory-Based Site Response Analysis," submitted to ASCE *Journal of Geotechnical and Geoenvironmental Engineering*.

[4] Boore, D., "Stochastic simulation of high-frequency ground motions based on seismological models of the radiated spectra." *Bulletin of the Seismological Society of America*, Vol. 73, No. 6, pp. 1865-1894, 1983.

[5] Cartwright, D.E., and Longuet-Higgins, M.S., "The statistical distribution of the maxima of a random function," *Proc. Roy. Soc. London*, Ser. A237, pp. 212-223, 1956.

[6] Boore, D. M., and Joyner, W. B., "A note on the use of random vibration theory to predict peak amplitudes of transient signals," *Bulletin of the Seismological Society of America*, Vol. 74, No. 5, pp. 2035-2039, 1984.

[7] Brune, J., "Tectonic stress and the spectra of seismic shear waves from earthquakes," *Journal of Geophysical Research*, Vol. 75, No. 26, pp. 4997-5009, 1970.

[8] Brune, J., "Correction." *Journal of Geophysical Research*, Vol. 76, No. 20, p. 5002, 1971.

[9] McGuire, R.K., Becker, A.M., and Donovan, N.C., "Spectral estimates of seismic shear waves," *Bulletin of the Seismological Society of America*, Vol. 74, No. 4, pp. 1427-1440, 1984.

[10] Chopra, A.K. *Dynamics of Structures: Theory and Applications to Earthquake Engineering, 2nd ed,* Prentice Hall, New Jersey, 2001.

[11] Abrahamson, N.A., and Silva, W. J., "Empirical response spectral attenuation relationships for shallow crustal earthquakes," *Seismological Research Letters*, Vol. 68, No. 1-2, pp. 94-127, 1997.

[12] Campbell, K.W., "Prediction of strong ground motion using the hybrid empirical method and its use in the development of ground-motion (attenuation) relationships in Eastern North America," *Bulletin of the Seismological Society of America*, Vol. 93, No. 3, pp. 1012-1033, 2003.

[13] Abrahamson, N.A., private communication, 2003.

[14] Atkinson, G. M., and Silva, W., "An empirical study of earthquake source spectra for California earthquakes," *Bulletin of the Seismological Society of America*, Vol. 87, No. 1, pp. 97-113, 1997.

Site Characterisation and Site Response for a Cohesive Soil in the City of Catania

A. Cavallaro[1], S. Grasso[2] , M. Maugeri[2]
[1]*CNR-IBAM, Catania, Italy*
[2]*Department of Civil and Environmental Engineering, University of Catania, Italy*

Abstract

This paper describes and compares the results of in situ and laboratory investigations that were carried out in order to determine the soil dynamic characteristics in the test site of "Via Dottor Consoli" in the city of Catania. Special attention has been paid to the variation of shear modulus and damping ratio with strain level and depth. Moreover normalised laws are proposed to consider shear modulus decay and damping ratio increase with strain level. The deposits under consideration consist of slight overconsolidated cohesive soil. The geotechnical characterization enabled the assessment of site effects and earthquake response spectrum for the restoration and strengthening of a masonry building located on the investigated test site. The excitation at the base of the model were synthetic accelerograms, related to the 1693 scenario earthquake (M = 7.0 – 7.3), considering an extended source model, and the scaled recorded accelerograms of the South Eastern Sicily earthquake of December 13, 1990 (M_L = 5.8). The response of the soil was evaluated with a 1-D non-linear code, considering the upper 30 m of soil profile to compare the result with those suggested by the Eurocode and the Italian new proposed regulation.

Keywords—*Site Characterisation, Cohesive Soil, Site Response*

INTRODUCTION

The city of Catania, located in the South-Eastern Sicily, has been affected in the past by several destroying earthquakes of about magnitude greater than 7.0. The area, belongs to the Ibleo-Maltese escarpment, is placed near the contact between the African and the Euro-Asiatic plates, and it is therefore a seismogenic area. According to the frequency and the importance of the seismic effects suffered in past times, Eastern Sicily must be considered one of the most high seismic risk areas in Italy. The area is densely populated territory; a huge patrimony of historical and monumental buildings is placed in the area.

This paper describes and compares the results of in situ and laboratory investigations that have been carried out in order to determine the soil dynamic characteristics in the test site of "Via Dottor Consoli", located in the centre of the city of Catania. On this site is located a five-stories tall masonry building, built in 1952 and heavy damaged by the South Eastern Sicily earthquake of December 13, 1990 (M_L = 5.8). The masonry building is located at the corner between "Via Dottor Consoli" and "Via Martoglio", with a “L” shape.

In the test site a borehole was made and undisturbed samples were retrieved. In the borehole a Down-Hole geophysical survey were performed. On the undisturbed samples static soil tests and dynamic soil tests were performed. Among the dynamic tests Resonant Column Tests (RCT) and Cyclic Loading Torsional Shear Tests (CLTS) were performed.

BASIC GEOTECHNICAL SOIL PROPERTIES

The eastern coast of Sicily and the city of Catania has been struck by various disastrous earthquakes with a MKS intensity from IX to XI in the last 900 years. For this reason Catania area has been often object of numerous site investigations [1], [2], [3], [4], [5], [6], [7], [8], [9], [10], [11], [12].

The site investigation at the location "Via Dottor Consoli" reached a maximum depth of 30 m. Laboratory tests have been performed on undisturbed samples retrieved by means of a 101 mm tube sampler. This work is part of the study that has regarded the geotechnical characterisation in correspondence of many test sites performed for the Research Project: *Detailed Scenarios and Actions for Seismic Prevention of Damage in the Urban Area of Catania* [13]. The "Via Dottor Consoli" site mainly consists of an alternance of clayey silt, silty sand and grey silty clay soils.

Among static soil tests, classification tests, oedometer test and direct shear tests were performed.

The preconsolidation pressure σ'_p and the overconsolidation ratio OCR = σ'_p/σ'_{vo} were evaluated from the compression curves of incremental loading (IL) oedometer tests. It varies from 3 to 3.5.

The value of the natural moisture content w_n prevalently ranges from between 22 - 24 %. Characteristic values for the Atterberg limits are: w_l = 41 % and w_p = 24 %, with a plasticity index of PI = 16 %, G_s (specific gravity) ranged between 2.54 and 2.67.

SHEAR MODULUS AND DAMPING RATIO

Shear modulus G and damping ratio D of "Via Dottor Consoli" deposits were obtained in the laboratory from Resonant Column Tests (RCT) and Cyclic Loading Torsional Shear Tests (CLTST). A Resonant Column/Torsional shear apparatus [14] was used for this purpose. The Down-Hole test has also been performed for the evaluation of the shear modulus G_0 at small strain.

G_0 is the maximum value or also "plateau" value as observed in the G-log(γ) plot; G is the secant modulus. Generally G is constant until a certain strain limit is exceeded. This limit is called elastic threshold shear strain (γ_t^e) and it is believed that soils behave elastically at strains smaller than γ_t^e. The elastic stiffness at $\gamma < \gamma_t^e$ is thus the already defined G_0.

The damping ratio was evaluated by CLTST using the definition of hysteretic damping ratio (D) by:

$$D = \frac{\Delta W}{4\pi W} \qquad (1)$$

in which ΔW is the area enclosed by the unloading-reloading loop and represents the total energy loss during the cycle and W is the elastic stored energy. For RCTs the damping ratio was determined using the steady-state method during the resonance condition of the sample.

The laboratory undrained test conditions and the obtained small strain shear modulus G_0 are listed in Table 1. The undisturbed specimens were isotropically reconsolidated to the best estimate of the in situ mean effective stress. The same specimen was first subject to RCT, then to CLTST after a rest period of 24 hrs with opened drainage. CLTST were performed under stress control condition by applying a torque, with triangular time history, at a frequency of 0.1 Hz. The size of solid cylindrical specimens are Radius = 25 mm and Height = 100 mm.

The $G_0(1)$ and $G_0(4)$ values, reported in Table 1, indicate moderate influence of strain rate even at very small strain where the soil behaviour is supposed to be elastic. In order to appreciate the rate effect on G_0, it is worthwhile to remember that the equivalent shear strain rate ($\dot{\gamma} = 240 \cdot f \cdot \gamma$ [%/s]) experienced by the specimens during RCT can be three orders of magnitude greater than those adopted during CLTST. The initial shear modulus value, reported in Table 1, for repeated RCT [$G_0(2)$] are always lower than that obtained by first performing of RCT [$G_0(1)$].

This modulus reduction was probably caused by these factors:

- pore pressure build up with a reduction of effective stress;
- soil degradation caused by the maximum shear strain level investigated during the test.

Moreover, the shear modulus value at small strain obtained by repeated RCT after 24 hrs [$G_0(3)$] is comparable to that obtained by RCT [$G_0(1)$]. The difference ranged between 2 % and 9 %. It is possible to assume the reduction of shear modulus as the consequence of effective stress reduction for the pore pressure build up. So it is possible to consider that the elastic energy loosed was recovered in a period of 24 hrs with the dissipation of pore pressure.

Figure 1 reports the G-γ curves from RCT and CLTST. As can be inferred from data shown in Figure 1 the rate effects on the shear modulus are the same until the strain reaches the elastic threshold $\gamma_t^e = 0.004$ %. The ratio $G_0(RCT)/G_0(CLTST) \cong 1.24$.

Finally higher values of the initial shear modulus [$G_0(5)$] have been obtained from Down- Hole tests.

In Figure 2 the pore pressure build-up is reported when volumetric strain occurs.

Higher values of pore pressure was obtained during CLTST rather than during RCT (Figure 2).

For strain level of about 0.02 % it is possible observed a rapid pore pressure build-up during RCT.

Table 1: Test Condition for Augusta Hangar area Specimens.

Test No.	σ'_{vc} [kPa]	$G_0(1)$ [MPa]	$G_0(2)$ [MPa]	$G_0(3)$ [MPa]	$G_0(4)$ [MPa]	$G_0(5)$ [MPa]	Δu [kPa]	γ_{max} [%]
1	101	49	40	54	44	128	17.97	0.64
2	201	61	54	62	49	50	9.48	0.22
3	557	136	123	139	112	282	18.32	0.18

where: Test No. 1: Depth 5.00 m; Test No. 2: Depth 10.00 m; Test No. 3: Depth 28.00 m; G_0 (1) RCT, G_0 (2) repeated RCT, G_0 (3) repeated RCT after 24 hrs, G_0 (4) from CLTST, G_0 (5) from Down-Hole.

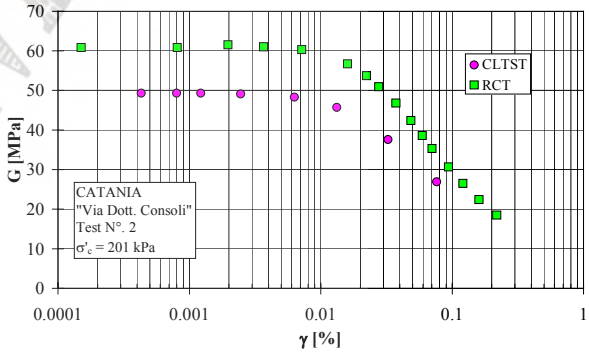

Figure 1: G-γ curves from CLTST and RCT tests.

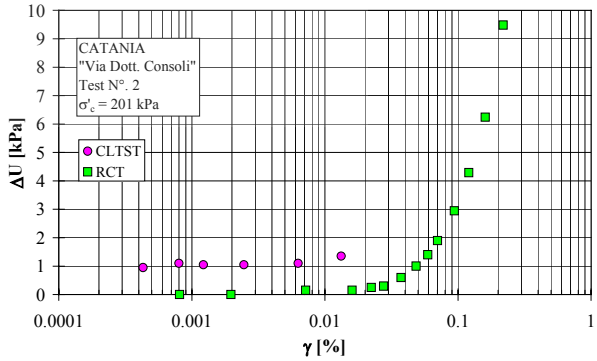

Figure 2: Pore pressure build-up from CLTST and RCT tests.

Figure 3 shows the results of RCTs normalised by dividing the shear modulus G(γ) for the initial value G_0 at very low strain.

The experimental results were used to determine the empirical parameters of the eq. proposed by Yokota et al. [15] to describe the shear modulus decay with shear strain level:

$$\frac{G(\gamma)}{G_0} = \frac{1}{1+\alpha\gamma(\%)^{\beta}} \qquad (2)$$

in which: G(γ) = strain dependent shear modulus; γ = shear strain; α, β = soil constants.

The expression (2) allows the complete shear modulus degradation to be considered with strain level. The values of α = 16 and β = 1.2 were obtained for "Via Dottor Consoli" clay soil.

A comparison between the damping ratio values obtained from RCT and those obtained from CLTST is shown in Figure 4.

The damping ratio values obtained from RCT by steady-state method are quasi constant until strain level of about 0.02 %, higher values of D have been obtained from strain level higher than 0.02 %. It is possible to see that the damping ratio from CLTST, at very small strains, is equal to about 1 %. Greater values of D are obtained from RCT for the whole investigated strain interval.

Considering that the influence of number of cycles N on D has been found to be negligible, in the case of clayey soils for strain levels less than 0.1 % [16], [17], [18], [19], [20], it is supposed that RCT provide larger values of D than CLTST because of the rate (frequency) effect, in agreement with data shown by Shibuya et al. [21] and Tatsuoka et al. [22]. According to these researchers the experimental results show that the soil damping can be linked to the following phenomena:

- Non-linearity which governs the so called hysteretic damping controlled by the current shear strain level. This kind of material damping is absent or negligible at very small strains;
- Viscosity of the soil skeleton (creep) which is relevant at very small strain rates;
- Viscosity of the pore fluid which is relevant at very high frequencies.

Soil damping, at very small strains, is mainly due to the viscosity of the soil skeleton or of the pore fluid, depending on the strain rates or frequencies. Moreover, according to Shibuya et al. [21] a partial drainage condition can provide very high values of the damping ratio.

As suggested by Yokota et al. [15], the inverse variation of damping ratio with respect to the normalised shear modulus has an exponential form as that reported in Figure 5 for the "Via Dottor Consoli" soil:

$$D(\gamma)(\%) = \eta \cdot exp\left[-\lambda \cdot \frac{G(\gamma)}{G_0}\right] \qquad (3)$$

in which: D(γ) = strain dependent damping ratio; γ = shear strain; η, λ = soil constants.

The values of η = 33 and λ = 2.4 were obtained for "Via Dottor Consoli" area.

As comparison, the values of empirical parameters of eqs, (2) and (3) obtained by the authors for eight different areas of Catania are reported in Table 2.

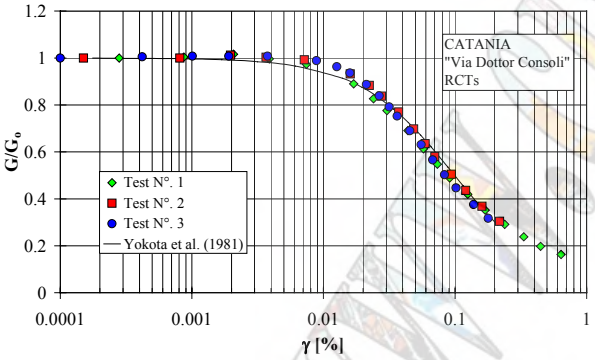

Figure 3: G/G_0-γ curves from RCT tests.

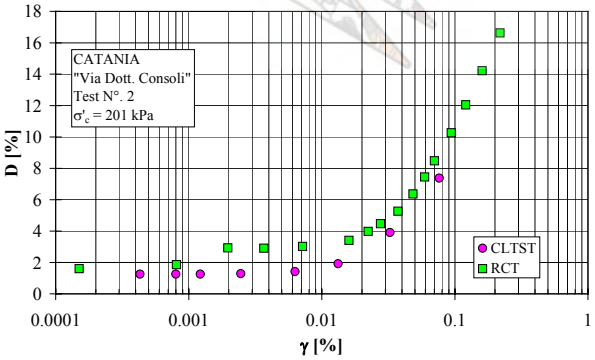

Figure 4: Damping ratio from CLTST and RCT tests.

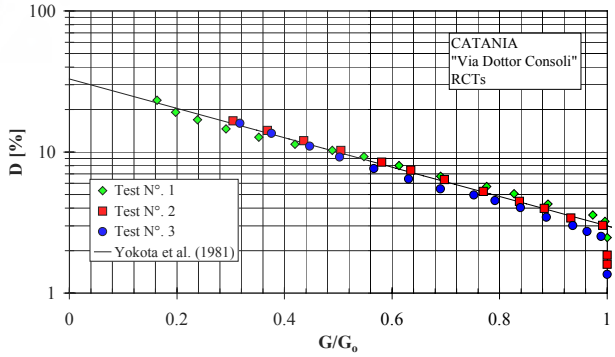

Figure 5: D-G/G_0 curves from RCT tests.

Table 2: Soil constants for the municipal area of Catania.

Site	α	β	η	λ
1. Piana di Catania	7.15	1.223	19.87	2.16
2. ENEL box	-	-	-	-
3. Plaja beach	9	0.815	80	4
4. Tavoliere	-	-	-	-
5. Via Stellata	11	1.119	31	1.921
6. Piazza Palestro	6.9	1	23	2.21
7. San Nicola alla Rena Church	7.5	0.897	90	4.5
8. Via Dottor Consoli	16	1.2	33	2.4

1-D NON-LINEAR ANALYSIS OF THE GROUND MOTION AT THE SURFACE

The site response was made by 1-D code, which is commonly used in the engineering practice. The code implements a one-dimensional simplified, hysteretic model for the non-linear soil response [23].

The S-wave propagation occurs on a 1-D column having shear behaviour. The column is subdivided in several, horizontal, homogeneous and isotropic layers characterized by a non-liner spring stiffness G(γ), a dashpot damping D(γ) and a soil mass density ρ. Moreover, to take into account the soil non-linearity, laws of shear modulus, given by Equation (2), and damping ratio against strain, given by Equation (3) have been inserted in the code.

The 1-D column has a height of 30 m and is excited at the base by the scenario earthquake.

The scenario earthquake

It is reasonable to assume in Catania the maximum expected earthquake as a repetition of the event of 1693, with intensity X-XI MCS and estimated magnitude between 7.0 and 7.3 [24]. The scenario earthquake has been evaluated by synthetic accelerograms.

The approach adopted is based on the modelling of the source mechanism in a 2-D section, by the 2-D full-wave seismic equation through the Chebyshev Spectral Element Method (SPEM) [25].

An investigation of SPEM and its application to the solution of both acoustic and elastic wave equations has been described elsewhere [26], [27] and [28]. All the information available on the structure of the upper 20 km of the Earth's crust of the study region, in terms of propagation velocities, density, and attenuation has been used to construct the model.

The destructive event of 1693 is commonly associated to ruptures with a normal mechanism along the Ibleo-Maltese escarpment, a system of sub-vertical normal faults, NNW-SSE oriented, which runs for about 70-100 km offshore along the Ionian coast of Sicily. The reference earthquake of this study is associated to the northern part of the system, which is simplified in a segment about 25 km long. On average, the size of the computational models is 45 km x 25 km and the meshes contain 170,000 - 200,000 nodes.

Synthetic seismograms have been drawn for the "Via Dottor Consoli" test site long a set of six receivers placed at different depths, starting from the surface up to almost 170 m. Synthetic seismograms are computed up to a maximum frequency of 8 Hz and for a total propagation time of 20 s (Figure 6). To evaluate the seismic response at the surface, the synthetic accelerograms evaluated at 31 m depth, was used as input motion at the base of the 1-D column of 30 m height.

Seismic response at the soil surface

The soil response, in the free field and also considering the surcharge at the top of the soil profile, is determined just next to the borehole location using the 1-D code into non-linear conditions.

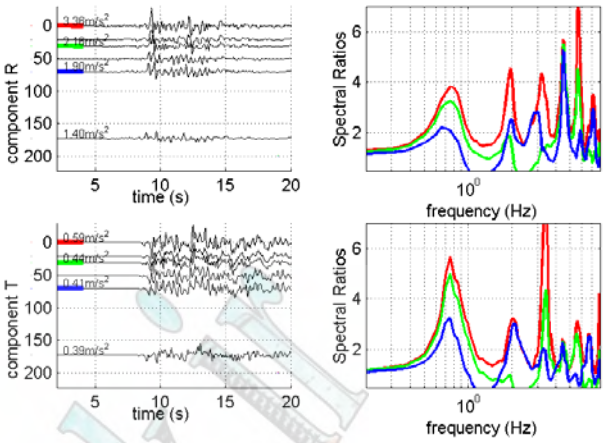

Figure 6: Input motion at the bedrock. Synthetic accelerograms obtained by 2-D SPEM simulation for via Dottor Consoli site at various depths.

The analysis provides the time-history response in terms of displacements (a), velocity (b) and acceleration (c) at the surface (Figure 7). Using the time history, response spectra concerning the sites are deduced.

Figure 7 shows, as an example, the time-history response (free field) in terms of acceleration at the surface into non-linear analysis for the soil profile related to borehole. Also scaled recorded accelerograms of the South Eastern Sicily earthquake of December 13, 1990 (d) have been used.

The structure surcharge was fixed in 104 kN/m^2, depending on the loading analysis performed for the masonry building. Globally 10 elastic response spectra and 10 inelastic design spectra are plotted. The elastic response spectra are initially subdivided in different groups to investigate the effects of the structural surcharge presence.

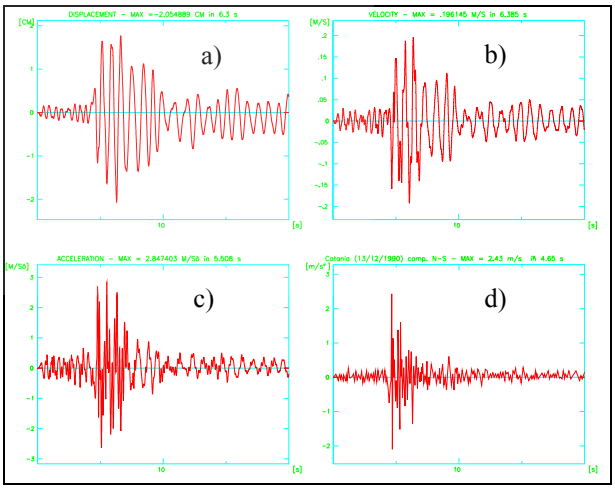

Figure 7: Time-history response just next to borehole (free field) in terms of displacement, velocity and acceleration at the surface.

Then, the inelastic spectra are derived from the elastic response spectra including the structure ductility. These last spectra are compared with those suggested by the European Code No. 8 [29] and by the new Italian O.P.C.M. 3274/2003 [30], in order to propose a site-dependent inelastic spectrum for "Via Dottor Consoli" masonry building.

Computed elastic response spectra

Ten elastic response spectra have been evaluated for the test site. Four of these response spectra are summarized in Figure 8; so, in each graphic it is possible to observe a different spectrum in relation to the presence or absence of the structural surcharge and in relation to the input accelerogram. So, for example the first graphic on the top-left (a) refers to the spectrum computed neglecting the structural surcharge and for the scaled Catania N-S component (a_{max} = 2.43 m/s^2) of the input recorded accelerogram of the South Eastern Sicily earthquake of December 13, 1990; while the graphic on the top-right (b) refers to the spectrum computed considering the structural surcharge and for the same input accelerogram.

The graphic on the bottom-left (c) refers to the spectrum computed neglecting the structural surcharge and for the input synthetic accelerogram related to the 1693 scenario earthquake considering an extended source model; while the graphic on the bottom-right (d) refers to the spectrum computed considering the structural surcharge and for the same input synthetic accelerogram.

Moreover, all the computed spectra refer also to a structural damping ratio of about D = 10 %, considering that the structure is a masonry structure.

Analysing Figure 8 it is possible to observe that to consider the structural surcharge leads to a decrease of the entity of the spectral acceleration peak, that is also generally reached for periods greater than those at which the spectral acceleration peak is reached neglecting the structural surcharge. In any case the period at which the spectral acceleration peak is reached does not exceed 0.6 sec.

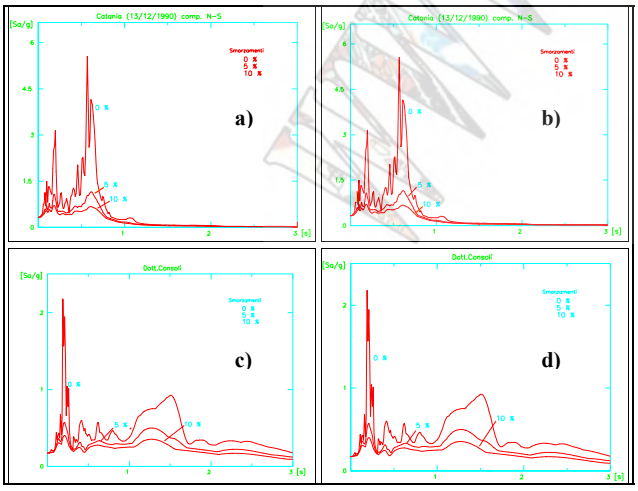

Figure 8: Elastic spectra at the soil surface.

Computed inelastic spectra

The inelastic design spectra can be evaluated on the basis of the elastic response spectra utilizing the following expression:

$$\frac{S_d}{g} = \frac{\left(\frac{S_a}{g}\right)}{b} \tag{4}$$

where S_a/g is the ordinate of the generic elastic response spectrum and S_d/g is the ordinate of the corresponding inelastic spectrum and b is the normalized yield strength of the structure if we consider that it behaves as an elasto-plastic structure, and so it is related to the structure ductility.

In the present case the quantity b is evaluated according to Giuffrè and Giannini [31] by means of the following expressions:

$$\text{for } T \le T_0 \qquad b = 1 + 2(q_0 - 1)\frac{T}{T_0}\left(1 - 0.5\frac{T}{T_0}\right) \tag{5}$$

$$q_0 = 1 + (\mu - 1)^{0.87 - 0.05T_0}$$

$$\text{for } T \ge T_0 \qquad b = 1 + (\mu - 1)^{0.87 - 0.05T_0} \tag{6}$$

being T_0 = 0.5 sec and μ the structure ductility, which is assumed equal to 1.5 for the "Via Dottor Consoli" masonry building.

Applying expressions (4), (5) and (6) first of all the 10 elastic response spectra discussed in the previous sub-section have been transformed in 10 inelastic spectra.

Figure 9 shows some of the inelastic spectra computed considering the presence or the absence of the structural surcharge.

The first graphic on the left (a) refers to the spectra computed for the scaled Catania N-S component (a_{max} = 2.43 m/s^2) of the input recorded accelerogram of the South Eastern Sicily earthquake of December 13, 1990, considering and neglecting the structural surcharge; while the graphic on the right (b) refers to the spectra computed for the input synthetic accelerogram related to the 1693 scenario earthquake considering an extended source model, considering and neglecting the structural surcharge.

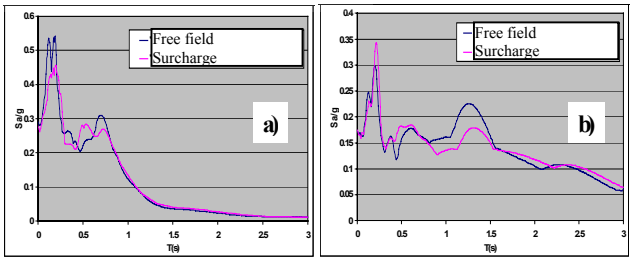

Figure 9: Inelastic spectra at the soil surface.

Design spectra proposed by the European Code and by the Italian O.P.C.M: comparison with the computed inelastic spectra

The computed inelastic spectra have been compared with those proposed by the European code No. 8 [29], named EC8, and by the new Italian O.P.C.M. [30].

For the horizontal component of the seismic action EC8 proposes to compute the inelastic spectrum by the following expressions:

$$\text{for } 0 \le T \le T_B \qquad S_d(T) = a_g \cdot S \cdot \left[\frac{2}{3} + \frac{T}{T_B} \cdot \left(\frac{2.5}{q} - \frac{2}{3}\right)\right] \qquad (7)$$

$$\text{for } T_B \le T \le T_C \qquad S_d(T) = a_g \cdot S \cdot \frac{2.5}{q} \qquad (8)$$

$$\text{for } T_C \le T \le T_D \qquad S_d(T) = a_g \cdot S \cdot \frac{2.5}{q} \cdot \left[\frac{T_C}{T}\right] \qquad (9)$$

$$\&$$

$$S_d(T) \ge \beta \cdot a_g \qquad (10)$$

$$\text{for } T \ge T_D \qquad S_d(T) = a_g \cdot S \cdot \frac{2.5}{q} \cdot \left[\frac{T_C \cdot T_D}{T^2}\right] \qquad (11)$$

$$\&$$

$$S_d(T) \ge \beta \cdot a_g \qquad (12)$$

where:

- a_g is the design ground acceleration on type A ground, that should be chosen by the National Authorities in relation to the local seismic hazard. For the Catania site the Italian Authority has recently chosen a_g = 0.25g [30];
- S is the soil amplification factor;
- q is the structure behaviour factor. For the "Via Dottor Consoli" masonry building this factor is fixed equal to 1.5, according to EC8 [29]. It has substantially the same meaning of the quantity b given by expression (5) and (6). The different values given to “b” and “q” are mainly due to the different structural damping ratios which the spectra computed by the Authors (D = 10%) and the spectra given by EC8 (D = 5 %) refer to [23];
- b is the lower bound factor for the horizontal design spectrum. The value to be ascribed to b should be found in the National Codes, however, the value suggested by EC8 is 0.2. The new Italian O.P.C.M. [30] fixes once more b = 0.2;
- T_B, T_C and T_D are respectively the lower limit of the period of the constant spectral acceleration branch, the upper limit of the period of the constant spectral acceleration branch and the value defining the beginning of the constant displacement response range of the spectrum.

The values of S, T_B, T_C and T_D are suggested by EC8 in relation to the site seismic hazard and to the ground dynamic geotechnical properties.

The new Italian O.P.C.M. [30] is substantially the application for Italy of the EC8, in the respect of the aim of the European Technical Codes. However, at the present it is possible to observe some divergences between the European and Italian O.P.C.M. In particular, the Authors in the following will focus their attention in the design spectra proposed by the two codes for the via Dottor Consoli site.

For the horizontal component of the seismic action the new Italian O.P.C.M. proposes to compute the design spectrum by means of the same expressions given by EC8, apart for $0 \le T \le T_B$; in this last case the new Italian O.P.C.M. proposes the following expression:

$$S_d(T) = a_g \cdot S \cdot \left[1 + \frac{T}{T_B} \cdot \left(\frac{2.5}{q} - 1\right)\right] \qquad (13)$$

Furthermore, the new Italian O.P.C.M. distinguishes the design spectra only in relation to the ground type, only for M > 5.5.

Comparisons between obtained inelastic spectra with those proposed by the European code No. 8 [29] and by the new Italian O.P.C.M. [30] are reported in Figure 10. The first graphic on the left (a) refers to the inelastic spectra at the soil surface computed for the scaled Catania N-S component (a_{max} = 2.43 m/s^2) of the input recorded accelerogram of the South Eastern Sicily earthquake of December 13, 1990, considering the structural surcharge; while the graphic on the right (b) refers to the inelastic spectra at the soil surface computed for the input synthetic accelerogram related to the 1693 scenario earthquake considering an extended source model, considering the structural surcharge.

CONCLUSIONS

In this paper a site characterisation of "Via Dottor Consoli" area for seismic response analysis has been presented.

On the basis of the data shown it is possible to draw the following conclusions:

- the small strain shear modulus obtained from RCT, after a rest period of 24 hrs with opened drainage, is comparable to that obtained by first performing of RCT;
- the small strain shear modulus obtained from RCT is about 24 % greater than that inferred from CLTST;
- damping ratio values determined from RCT are greater than those obtained from CLTST;
- higher values of G_o was obtained by Down-Hole tests.

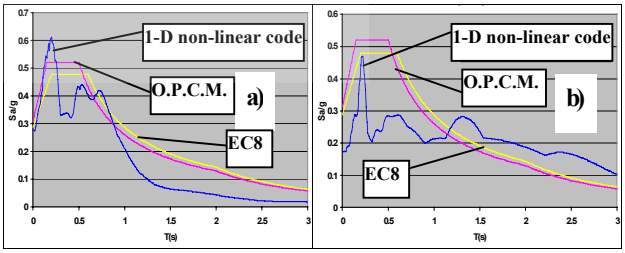

Figure 10: Comparisons between the inelastic spectra at the soil surface with the design spectra suggested by EC8 [29] and by the new Italian O.P.C.M. [30].

The investigated site has been severely damaged by the South Eastern Sicily earthquake of December 13, 1990 (M_L=5.8). The damage caused by the seismic event leaded to plan a wide and accurate investigation of the subsoil and of the masonry building under restoration. As far as the geotechnical investigation is concerned, boreholes and Down-Hole (D-H) tests have been carried out. Moreover, RC Tests and CLTS Tests, have been carried out on undisturbed samples for detecting soil non-linearity and damping.

It was then possible to evaluate the seismic response of the soil in the upper 30 m with a 1-D non-linear code. The excitation at the base of the model are synthetic accelerograms, which refer to the 1693 scenario earthquake (M= 7.0 – 7.3), considering an extended source model, or scaled recorded accelerograms of the South Eastern Sicily earthquake of December 13, 1990 (M_L=5.8) . Analysing the elastic response spectra obtained for the soil profile and considering different input accelerograms, the presence or the absence of the structure surcharge due to the masonry building weight, it is possible to observe that to consider the structural surcharge leads to a decrease of the entity of the spectral acceleration peak, that is also generally reached for periods greater than those at which the spectral acceleration peak is reached neglecting the structural surcharge. In any case the period at which the spectral acceleration peak is reached does not exceed 0.6 sec.

Finally, comparing the inelastic computed spectra with the design spectra suggested by EC8 and by the new Italian O.P.C.M., it is possible to observe that both the design spectra suggested by EC8 and by the new Italian O.P.C.M. sometimes do not cover the medium inelastic spectra concerning soil profile given by the borehole, in the range of T equal to 0.15 – 0.4 sec;

ACKNOWLEDGMENTS

The authors wish to thank the geotechnical engineer Cristian Turco, for his contribution to the work.

REFERENCES

[1] Carrubba, P. and Maugeri, M., "Determinazione delle Proprietà Dinamiche di un'Argilla Mediante Prove di Colonna Risonante," Rivista Italiana di Geotecnica, Vol. 22, No. 2, pp.101 - 113, 1988.

[2] Carrubba, P. and Maugeri, M., "Sulle Correlazioni tra il Modulo Dinamico Trasversale e le Caratteristiche dei Terreni in Campo Statico," Atti Convegno C.N.R., Deformazione dei Terreni ed Interazione Terreno – Struttura in Condizioni di Esercizio, Monselice (PD), 5 - 6 Ottobre 1988, pp. 305 - 325, 1988.

[3] Cascone, E., "Analisi Sperimentale e Modellazione del Comportamento Dinamico dei Muri di Sostegno," Ph. D. Thesis, University of Catania, 1996.

[4] Castelli, F., Cavallaro, A., Grasso, S. and Maugeri, M., "Seismic Geotechnical Hazard of the City of Catania (Italy)," Proceedings of the 3rd Japan-Turkey Workshop on Earthquake Engineering, Istanbul, 21 - 25 February 2000, pp. 167 - 178, 2000.

[5] Cavallaro, A., Maugeri, M., Lo Presti, D. C. F. and Pallara, O., "Characterising Shear Modulus and Damping from in Situ and Laboratory Tests for the Seismic Area of Catania," Proceedings of the 2nd International Symposium on Pre-failure Deformation Characteristics of Geomaterials, Torino, 28 - 30 September 1999, pp. 51 - 58, 1999.

[6] Cavallaro, A., Grasso, S. and Maugeri, M., "A Dynamic Geotechnical Characterization of Soil at Saint Nicola alla Rena Church Damaged by the South Eastern Sicily Earthquake of 13 December 1990," Proceedings of the 15th International Conference on Soil Mechanics and Geotechnical Engineering, Satellite Conference "Lessons Learned from Recent Strong Earthquakes", Istanbul, 25 August 2001, pp. 243 - 248, 2001.

[7] Cavallaro, A., Grasso, S. e Maugeri, M., "Parametri Geotecnici Significativi per lo Studio di Pericolosità Geotecnica Sismica di un'Area Storica della Città di Catania," ANIDIS, 10° Convegno Nazionale, L'Ingegneria Sismica in Italia, Potenza, 9 - 12 Settembre 2001.

[8] Cavallaro, A., Grasso, S. and Maugeri, M., "Seismic Geotechnical Hazard and Soil Response Analysis for the Historical Ecclesiastical Buildings of the City of Catania (Italy)," Proceedings of the 7th U.S. National Conference on Earthquake Engineering, Boston, 21 - 25 July 2002.

[9] Frenna, S. M.. and Maugeri, M., "Analisi della Risposta del Terreno nella Piana di Catania," ANIDIS, 7° Convegno Nazionale, L'Ingegneria Sismica in Italia, Siena, 25 - 28 Settembre 1995, pp. 205 - 214, 1995.

[10] Maugeri, M., Carrubba, A. and Carrubba, P., "Caratterizzazione Dinamica e Risposta del Terreno nella Zona Industriale di Catania," Ingegneria Sismica, No. 2, pp. 9 - 18, 1988.

[11] Maugeri, M., Carrubba, P. e Frenna, M., "Frequenza e Modi di Vibrazione di Terreni Eterogenei," Rivista Italiana di Geotecnica, Vol. XXII, No. 3, Luglio - Settembre 1988.

[12] Maugeri, M. and Cavallaro, A., "Non Linear Soil Behaviour of Catania Clays," The Catania Project; Earthquake Damage Scenarios for High Risk Area in the Mediterranian. Ed. E. Faccioli & V. Pessina. CNR-Gruppo Nazionale per la Difesa dai Terremoti, Roma, pp. 38 - 41, 2000.

[13] Maugeri, M., "Seismic Prevention of Damage for Mediterranean Cities: A Case History: the City of Catania (Italy)," M. Maugeri Editor. WIT Press, Southampton (UK), 2005.

[14] Lo Presti, D. C. F., Pallara, O, Lancellotta, R., Armandi, M., Maniscalco, R., "Monotonic and Cyclic Loading Behaviour of Two Sands at Small Strains," Geotechnical Testing Journal, Vol. 16, No. 4, pp. 409 - 424, 1993.

[15] Yokota, K., Imai, T. and Konno, M., "Dynamic Deformation Characteristics of Soils Determined by Laboratory Tests," OYO Tec. Rep. 3, pp. 13 - 37, 1981.

[16] Lo Presti, D. C. F., Jamiolkowski, M., Pallara, O. and Cavallaro, A., "Rate and Creep Effect on the Stiffness of Soils," ASCE Convention, Washington, 10-14 Nov. 1996, Geotechnical Special Publication No. 61, pp. 166 - 180, 1996.

[17] Cavallaro, A. M. F., "Influenza della Velocità di Deformazione sul Modulo di Taglio e sullo Smorzamento delle Argille," Ph. D. Thesis, University of Catania, 1997.

[18] Lo Presti, D. C. F., Jamiolkowski, M., Pallara, O., Cavallaro, A. and Pedroni, S., "Shear Modulus and Damping of Soils," Proceedings of the International Symposium on the Pre-failure Deformation Behaviour of

Geomaterials, 50th Geotechnique, London, 4 September 1997, Geotechnique 47, N°. 3, pp. 603 - 617, 1997.

[19] Lo Presti, D. C. F., Pallara, O. and Cavallaro, A. M. F., "Damping Ratio of Soils from Laboratory and in Situ Tests," Proceedings of the 14th International Conference on Soil Mechanics and Foundations Engineering, Hamburg, 6 - 12 September 1997, Special Volume TC4, pp.391 - 400, 1997.

[20] Lo Presti, D. C. F., Maugeri, M., Cavallaro, A. and Pallara, O., "Shear Modulus and Damping of a Stiff Clay from in Situ and Laboratory Tests," Proceedings of the 1st International Conference on Site Characterization, Atlanta, 19 - 22 April 1998, pp. 1293 - 1300, 1998.

[21] Shibuya, S., Mitachi, T., Fukuda, F. and Degoshi, T., "Strain Rate Effect on Shear Modulus and Damping of Normally Consolidated Clay," Geotechnical Testing Journal 18:3, pp. 365 - 375, 1995.

[22] Tatsuoka, F., Lo Presti, D. C. F. and Kohata, Y., "Deformation Characteristics of Soils and Soft Rocks Under Monotonic and Cyclic Loads and Their Relations," Proceedings of the 3rd International Conference on Recent Advances in Geotechnical Earthquake Engineering and Soil Dynamic, State of the Art 1, 2, pp. 851 - 879, 1995.

[23] Frenna, S. M. and Maugeri, M., "GEODIN: a Computer Code for Seismic Soil Response," Proceeding of the. 9th Italian Conference of Computational Mechanics, Catania, Italy, 20-22 June 1995, (in Italian): pp. 145 - 148.

[24] Azzaro R. and Barbano M. S., "Seismogenic Features of SE Sicily and Scenario Earthquakes for Catania," In The Catania Project: Earthquake Damage Scenarios for a High Risk Area in the Mediterranean. Editors: Faccioli and Pessina. CNR-Gruppo Nazionale per la difesa dai terremoti-Roma 2000: pp. 9 - 13.

[25] Priolo, E., "2-D Spectral Element Simulations for a Catastrophic Earthquake," In Faccioli and Pessina (eds), The Catania Project: Earthquake Damage Scenarios for a High Risk Area in the Mediterranean, 2000: pp. 67 - 83, Roma: CNR-Gruppo Nazionale per la difesa dai terremoti.

[26] Priolo, E. and Seriani, G., "A Numerical Investigation of Chebyshev Spectral Element Method for Acoustic Wave Propagation," In: Vichnevetsky, R. (ed.), Proceedings of 13th IMACS Conf. on Comp. Appl. Math., Criterion Press, 1991: pp. 551 - 556.

[27] Padovani, E., Priolo, E. and Seriani, G., "Low-and High-Order Finite Element Method: Experience in Seismic Modelling," J. Comp.Acoust., 2, 1994: pp. 371 - 422.

[28] Seriani, G. and Priolo, E. "Spectral Element Method for Acoustic Wave Simulation in Heterogeneous Media" Finite Elements in Analysis and Design, 16, 1994: 337–348.

[29] CEN. "Design of Structures for Earthquake Resistance. Part 1: General Rules, Seismic Actions and Rules for Buildings," Final Draft. Brussels: European Committee for Standardization (CEN), December 2003, 215 pp.

[30] O.P.C.M. No. 3274/2003, "Primi Elementi in Materia di Criteri Generali per la Classificazione Sismica del Territorio Nazionale e di Normative Tecniche per le Costruzioni in Zona Sismica," Ordinanza del Presidente del Consiglio dei Ministri, Rome, Italy, 2003 (in Italian).

[31] Giuffrè, A. and Giannini, R., "La Risposta non Lineare delle Strutture in Cemento Armato," Progettazione e Particolari Costruttivi in Zone Sismiche. ANCE-AIDIS, 1982.

Experimental and theoretical studies of topographic effects

K. Pitilakis[1], O.-J. Ktenidou[1], P. Apostolidis[1], D. Raptakis[1], M. Manakou[1], Makropoulos[2], D. Diagourtas[2]

[1] *Laboratory of Soil Mechanics, Foundation Engineering and Geotechnical Earthquake Engineering, Aristotle University of Thessaloniki, Greece*

[2] *Seismological Laboratory, National Kapodistrian University of Athens, Greece*

Abstract

The effect of topography is studied along a typical cross-section through the city of Aegion, Greece, which presents a characteristic landscape and combines good knowledge of morphology, geology and soil properties with a permanent array of accelerometers. Knowledge of the site has been enhanced after extensive geotechnical and geophysical investigations, including dynamic soil tests. The site is modeled and analyzed with a finite difference code, using as input motion both synthetic wavelets and an actual recording at the basement rock. Results are studied both in the time and frequency domain so as to reveal the effects of surface topography near the crest and toe of the topographic feature. A strong diffracted wave field is generated near the feature, probably due to P-SV interaction and surface wave generation, causing modification of ground motion in the vicinity. These effects are among the complex effects caused by the surface topography as well as the subsurface lateral discontinuities. Recordings are available at stations uphill and downhill are used to validate the numerical results and study the complex physics of ground motion.

Keywords — *Aegion, CORSSA experimental site, down-hole array, topographic amplification effects, 2D modeling*

THE STUDY OF TOPOGRAPHIC EFFECTS

Introduction

Local site conditions are among the factors that can influence the characteristics of strong ground motion in various ways which are collectively referred to as site effects. The local geology at a site can modify the amplitude, frequency content and duration of seismic motion as it travels from bedrock to the ground surface. Site effects are related to the thickness and impedance contrast between soil layers, the surface topography as exhibited by the relief, as well as the subsurface topography in terms of lateral discontinuities, faults, valley and basin edges, inclined soil layers or soil-bedrock interfaces.

Whilst soil layer effects have been investigated fairly extensively, surface and subsurface topography effects present more complications, since they are tied to two-dimensional phenomena such as focusing and defocusing of seismic energy, diffraction and refraction of body waves, generation of surface waves and interference patterns leading to complex wave fields. Evidence of such effects can be grouped into the following main approaches [1]: observations, instrumental studies, theoretical approaches and numerical modeling.

Observations

In areas which exhibit some kind of topographic relief, following strong earthquakes, observation of the damage pattern and distribution often shows that most damage tends to concentrate around hilltops and slope crests rather than near the toe. Examples of such cases have been reported for the Friuli, 1976 earthquake [2], in Irpinia, 1980 [3, 4], in Chile 1985 [5] and in Whittier-Narrows 1987 [6]. More recently there has also been some discussion regarding the Aegion 1995 earthquake [7] and the Athens 1999 event [8, 9, 10].

Instrumental approaches

In areas presenting some topographic irregularity where instrumental studies were carried out, there exist indications of the relief affecting the strong motion characteristics. Such instances have been noted for a ridge in the Matsuzaki area, Japan [11], for a very steep site in the Southern Alps [12, 13], and also on two separate occasions at the Tarzana station near Pacoima Dam, during the 1971 San Fernando as well as the 1994 Northridge earthquakes [14 and 5, 15 respectively]. Some other reported cases are those of Kitherion, Greece [16] and in Epire, Greece [17, 18]. Some more such reports are given by [19, 20, 21]. The amplification ratio has on occasions reached very high values: around 5 in cases [16, 17, 18] and several tens in case [12] around a narrow band of frequencies (about 5Hz). In general, however, there have only been a limited number of such studies; thus, the results cannot be generalized.

Theoretical studies

Theoretical approaches have focused more on 2D configurations than 3D geometries. It has been shown that amplification generally takes place over convex surfaces and deamplification happens over concave ones, leading to strong differential motions between the two, e.g. the crest of a hill with respect to its toe.

A simple wedge was used by [22] to demonstrate that the amplification at the vertex of a triangular configuration compared to its base, when impinged by SH waves, is equal to 2/v, where vp is the angle of the vertex. Such a geometry was also implemented by [20] to simulate amplification and deamplification effects on ridges and canyons respectively.

According to [1], the basic physical phenomena responsible for such effects are the following: 1) Surface motion is sensitive to the angle of incidence, particularly for SV waves around the critical angle – thus the angle of a slope affects the motion at its surface [6]. 2) Seismic waves focus or defocus under a topographic feature, depending on the multiple reflections inflicted on the initial wave field [23]. 3) Body waves are diffracted upon the surface irregularity creating surface waves, which propagate downwards and outwards and interfere with the incident wave field.

Numerical modeling and analysis

Numerical analysis has been implemented in order to investigate the parameters affecting topographic effects, such as the geometry of the topographic feature, the dynamic soil parameters and the type and incidence angle of the incoming wave field [24, 9, 25]. It has been reported [1] that horizontal components of motion are generally amplified more than the vertical component and that amplification is stronger for steeper topographies. Furthermore, topographic effects are found to be more pronounced around certain frequencies, particularly for wavelengths that are of the same order of magnitude as the dimensions of the topographic irregularity [19]. It should be pointed out that results of numerical analyses differ from experimental results in that they often predict lower values of amplification factors than those observed [1].

Though the study of topographic effects is rendered more difficult due to the complexities already mentioned, it is well worth the effort since many inhabited areas are located on hilltops and also due to the fact that stronger ground motion near crests results in larger triggering forces in terms of seismically-induced landslides.

THE CORSSA EXPERIMENTAL SITE

Location and aim

The Corinth Soft Soil Array (CORSSA) was developed in the region of the Gulf of Corinth, Greece, one of the most highly seismic areas in Europe, as seen in Fig. 1. The Gulf of Corinth comprises many WNW-trending, north-dipping active normal faults.

The city of Aegion, near which the array is located, is traversed by one of those normal faults, the Aegion fault. This consists of three segments, the central one having an escarpment of around 40m-100m, thus dividing the city into two levels (Fig. 2). The CORSSA array lies at the lower part of the city, on the hanging wall, near the coast.

The city has been struck by significant earthquakes in the past, the strongest recent one being that of June 15, 1995. The main event had a surface magnitude of Ms=6.2 and caused severe damage to buildings and loss of lives. Nearly all damage was concentrated in the upper part of town, on the hanging wall, even though the buildings there were generally more recent than those on the footwall [7]. The peak ground acceleration recorded at a station (OTE) on the terrace during this event was PGA=0.45g. No recordings of that event are available from the coastal area, since the array has only been in full operation since March 2002 and there are no other stations downhill.

The installation of the CORSSA surface and vertical array was undertaken within the scope of European research project CORSEIS (CORinth SEISmicity), which in turn is part of a multidisciplinary project called the Corinth Rift Laboratory (CRL – www.corinthrift.org). The purpose was to provide a well-instrumented site of known geometry, surface and subsurface geology and soil properties, so as to allow for confrontation and validation of numerical analysis results with experimental data.

The site was chosen so that it lies in a highly seismic region, in order to provide good quality recordings for weak-to-moderate ground motion datasets; these can be used in conjunction with recordings from the uphill stations, such as OTE. The vertical array downhill consists of soft loose materials at the surface (top 20m) so as to aid the study of soft soil effects, non-linearity and liquefaction phenomena; these soft soils overlie stiffer soil formations. Beneath these, at 170m depth, a hard conglomerate is encountered which is considered as seismic bedrock. Thus, the soil motion can be studied with respect to that as a reference site. The chosen region is marked by a characteristic surface and subsurface topography defined respectively by the relief and the strong lateral discontinuity, both due to the presence of the fault; thus the site is suitable for the study of topographic and complex site effects.

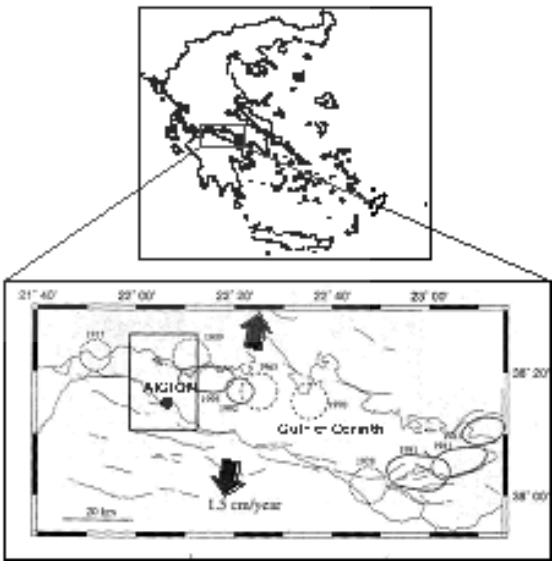

Fig. 1: Location of the area under study in Greece.

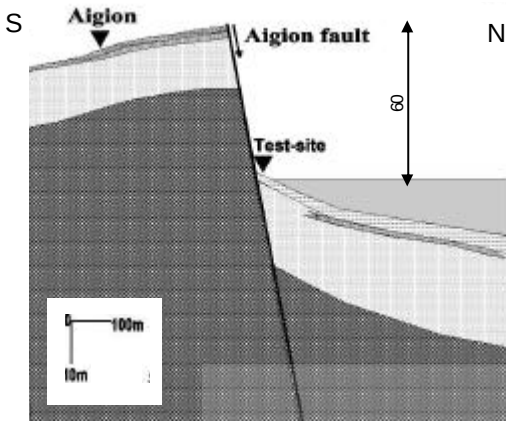

Fig. 2: Sketch of a N-S cross-section passing through Aegion, indicating the difference in elevation for the two parts of the town.

Configuration

As shown in Fig. 3, CORSSA vertical array consists of a down-hole array of four broad-band 3D accelerometers lying at depths: -14m, -31m, -57m and -178m as well as a surface accelerometer. The deepest accelerometer lies within a layer of stiff conglomerate, so as to be used as a kind of reference station. All the instruments above it lie within softer soil layers consisting mainly of CL, ML and SC, so as to be used for the study of site effects and soil non-linearity. All five stations are connected to a 15-channel main recorder.

Two pore-pressure transducers have also been installed at depths of -6m and -14m, within saturated loose soil layers, mainly SM and ML marine deposits that were deemed as susceptible to liquefaction. Both pore pressure probes are connected to a 2-channel data logger which is synchronized with the main recorder of the accelerometers.

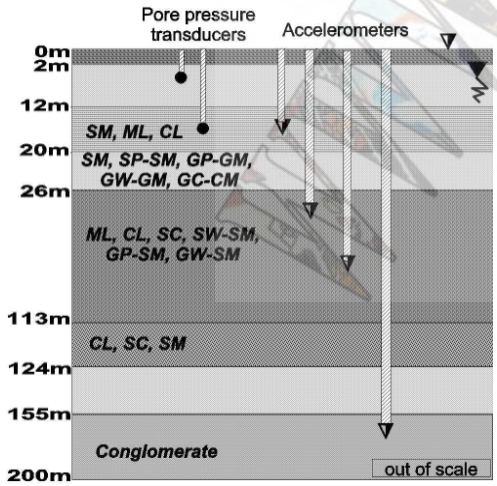

Fig. 3: Description of downhill soil profile and vertical layout of the CORSSA array.

GEOLOGICAL-GEOTECHNICAL-GEOPHYSICAL DATA

Investigations and surveys performed

After a series of field and laboratory tests and investigations, the complex geology of the site has finally been modeled in sufficient detail and the geotechnical and dynamic soil properties have been estimated to a satisfactory degree. This knowledge is essential in order to perform accurate theoretical predictions of the ground motion as well as reliable interpretations of experimental observations.

Originally, within the scope of CORSEIS [26, 27], detailed geological mapping was performed for the greater region under study. This was complemented by the drilling of six geotechnical boreholes (one for each of the CORSSA down-hole accelerometers and pore-pressure transducers described above). In-situ tests were performed on the soils encountered within these boreholes, including standard penetration tests (SPT) and water-table measurements. Laboratory tests were performed both on intact and disturbed samples from the aforementioned boreholes, in order to classify the formations and estimate their static and dynamic properties – the latter were investigated through resonant column and cyclic triaxial tests. The field surveys also involved cross-hole (CH) and down-hole (DH) borehole geophysics, as well as spectral analysis of surface waves (SASW) and surface wave inversion (SWI) techniques. These investigations helped define primary and shear wave velocities (Vp and Vs) as well as the shear modulus and damping ratio for a range of strains (G-γ-D curves).

In addition to this data, which pertains to relatively shallow depths (down to 180m), data from a deep borehole penetrating the Aegion fault was also used in order to establish the geology at depths down to 1000m, including the actual shear zone.

All of the above provide data at a distance from the hanging wall region. Two additional sampling boreholes were performed in order to gain knowledge of the geological and geotechnical conditions near the toe of the escarpment and on the footwall.

Moreover, new field measurements were performed both on the hanging wall (downhill) and on the footwall (uphill), for the purpose of determining the shear wave velocity profile with depth along a typical cross-section normal to the fault. This was achieved through array measurements of microtremors using the SPAC method [28]. Finally, single-station ambient noise recordings were performed at several locations along the cross-section in order to complement the existing dataset of recorded earthquakes at the CORSSA array in terms of site response estimation by means of empirical spectral ratios.

Most recently proposed cross-section

A characteristic feature of the site, as seen in Fig. 2, is that the depth of the soil layers uphill is very shallow, the conglomerate laying only a few tens of meters below the ground surface. On the other hand, the soft deposits have

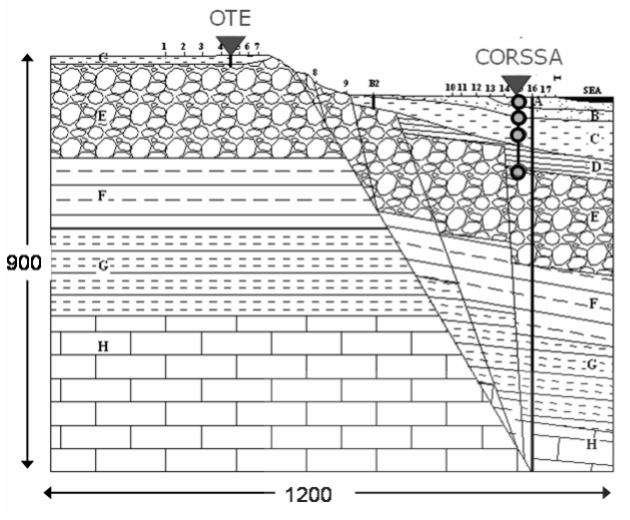

Fig. 4: Proposed 2D geological model based on field surveys, showing the location of the uphill (OTE) and downhill (CORSSA) recording stations [28].

a significant thickness downhill, which at CORSSA is about 170m.

By combining and comparing all the data available [28] from the boreholes and geophysical surveys, conclusions were drawn as to the depth and thickness of each soil layer at different locations along the typical cross-section. One of the most important factors was the depth of the stiff conglomerate, which is the formation underlying all the soft surface materials.

It was deduced that the soil layers as well as the conglomerate at the hanging wall are not horizontal, as had been the original assumption [7, 29, 30, 31], but are actually inclined in the direction of the sea. The Aegion fault was found to be part of a complex geological structure which demonstrates a step-like morphology, the actual shear zone consisting of several incidental transitional faults. This contradicts the original assumption of a single normal fault dipping at a constant angle, constituting a single lateral discontinuity between the soft deposits downhill and the conglomerate uphill.

The final model proposed can be seen in Fig. 4. The materials have been classified according to geological and geotechnical criteria, by comparing and contrasting all available data regarding soil classifications and properties. There are roughly two main soil formations, the upper one consisting of Holocene alluvial fan and marine deposits of low Vs (<600m/s), while the lower one comprises Pleistocene deltaic and alluvial fan deposits of higher Vs (>800m/s). These formations overlie the alpine substratum, which in turn is made of an upper unit of Jurassic limestone and a lower unit of Cretaceous limestone, both of them having Vs values higher than the soil formations.

SITE RESPONSE ANALYSIS

Results of microtremor data processing

Single-station noise measurements lead to the estimation of the dominant frequency and the amplification factor through the HVSR method. As seen in Fig. 5, the predominant frequencies along the hanging wall (downhill) are about 0.7-1.0Hz, exhibiting amplifications between 3 and 7, whereas the dominant frequencies along the footwall (uphill) are higher, around 5 to 7Hz, corresponding to amplification factors of 2 to 4. These results are compared in the same figure with 1D theoretical predictions, which appear unable to describe the amplification factors beneath the fault. This is a good indication that complex site effects take place downhill, possibly due to the effects of lateral discontinuities as dictated by the fault zone and the different formations on either of its sides. These factors could lead to multiple diffractions of the incident waves and generation of surface waves which in turn may interfere with the direct waves, leading to a complex wave field.

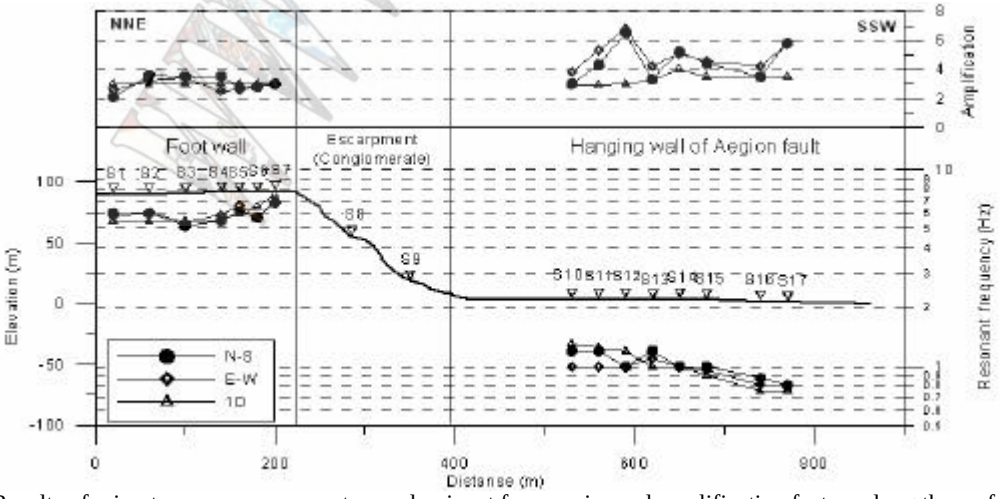

Fig. 5: Results of microtremor measurements: predominant frequencies and amplification factors along the surface [28].

Results of preliminary 2D finite-difference analysis

The preliminary numerical analyses presented herein were performed with the finite difference code *FLAC 2D* [32]. A simplified geotechnical model was implemented, which did not account for the complex, segmented nature of the shear zone, nor the dipping upper layers at the hanging wall. The geometry and soil parameters attributed to the model are shown in Fig. 6. The grid zones have dimensions of 4 to 15m for regions where the shear wave velocity ranges between 200 to 1250m/s respectively. This discretization allows for a maximum frequency of 6.5Hz to propagate through the grid without any distortion. Rayleigh damping is used, centered around a certain frequency which ensures a quasi-equal mass and stiffness contribution. The lateral boundaries simulate free-field conditions, while the base through which the input motion is inserted is elastic (since the conglomerate is not the actual seismic bedrock – the underlying limestone is). The input motion consists of SV waves, vertically propagating from the base. Several analyses are performed using linear elastic and equivalent-linear models.

The input motions used in the parametric analyses comprise of: • Ricker wavelets of various central frequencies (0.88Hz, 1.43Hz and 3Hz, the first two expressing the eigen-frequencies of the 1D downhill and uphill soil columns respectively) for a global damping of the model around 2% • Gabor wavelets for two different assumptions as to the damping of the model (2% global and varying with stratigraphy) which excite a broad band of frequencies up to 7Hz • A small earthquake recorded at all five stations of the CORSSA array, as well as at an uphill station (OTE), which has the following characteristics: 18/11/2003, 18:32:11.000, 38.410°N, 22.000°E, h=13km, M_L=4.1, R_e=19km.

The linear elastic analysis performed using the recorded small event at CORSSA is used in order to provide a means of validation for the numerical model used. Analytical transfer functions are estimated at the surface of CORSSA and OTE sites based on the results of the analysis. These are compared to experimental spectral ratios (standard spectral ratios, SSR) derived from the recordings at the surface stations with respect to the CORSSA recording at -178m (within the stiff conglomerate). As seen in Fig. 7, the analytical and experimental ratios are in good agreement. The predominant peaks are around 0.9Hz for the soft CORSSA deposits and around 4.5Hz for the stiff OTE profile. The experimental amplification is however higher in both sites, as is often the case; this however may also be due to simplifications and damping.

Fig. 8 shows the recorded time-histories at all five depths of CORSSA array and at the surface of OTE station, in comparison with those calculated through 2D modeling. It can be seen that the predicted amplitude is systematically lower than that observed, especially for the depth of 14m at CORSSA. This may be due to the simplifications introduced by the modeling or by the damping effect. Besides, the input motion was filtered and thus the estimated time-histories present fewer zero crossings. However, the results for OTE appear relatively satisfactory. Further elaborations are still in process.

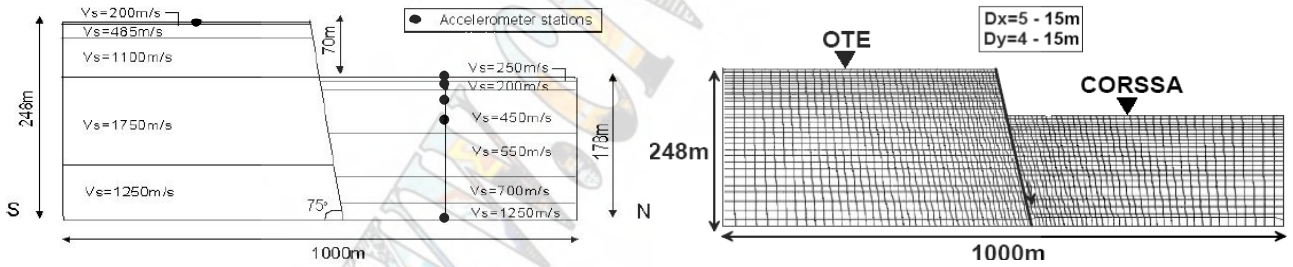

Fig. 6: Numerical model, finite difference grid and dynamic soil properties used for analysis [31].

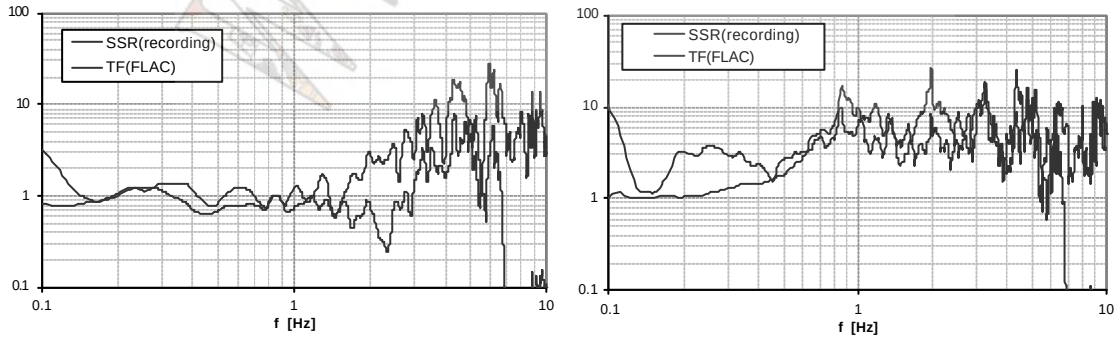

Fig. 7: Comparison of SSR ratios from recordings at OTE station (left) and CORSSA surface station (right) with the analytical transfer functions.

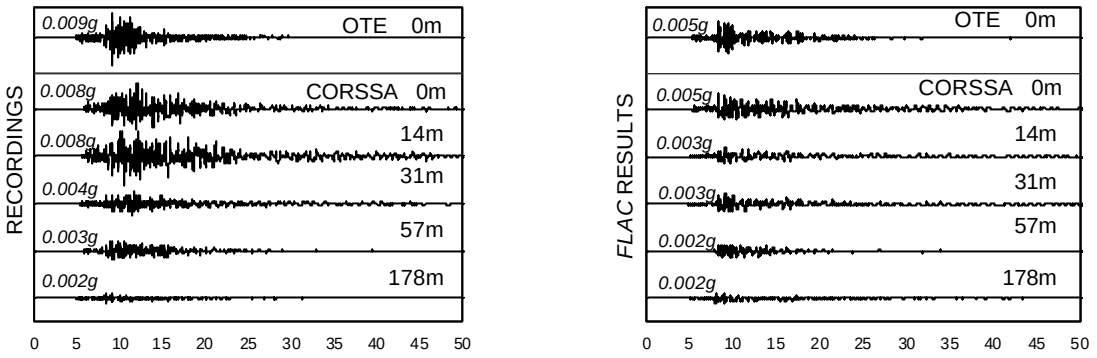

Fig. 8: Comparison of recordings at all CORSSA stations and at OTE station with the analytical time-histories (on the same scale).

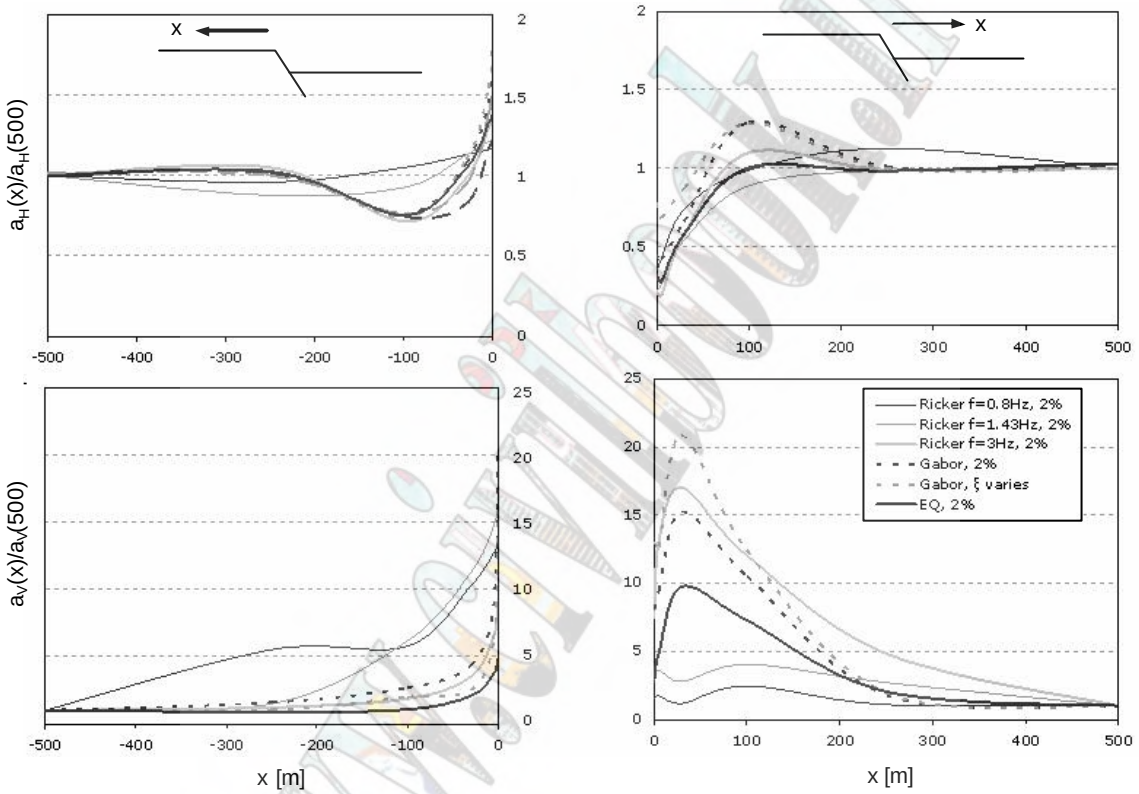

Fig. 9: Surface distribution of maximum values of horizontal (top) and vertical (bottom) acceleration, normalized to x= 500m.

After the validation of the model, a set of analyses is undertaken, using the different input motions cited above. Fig. 9 shows the maximum horizontal and vertical acceleration along the surface of the model. The maximum values at several distances from the crest and toe of the fault have been normalized with respect to the response of the "free field", which is taken at a distance of 500m from the fault. It can be seen that amplification of horizontal motion takes place over a narrow zone near the crest of the slope, with a maximum value of around 50%. Correspondingly, deamplification of the horizontal component is observed over a narrow zone from the toe by approximately 50%.

The vertical component, which was not originally inserted into the model but is generated through the P - SV interaction and surface wave generation at the subsurface and surface irregularities, appears strong on both sides of the fault, but mostly near the toe.

Fig. 10 shows the response along the surface of the model in the form of time-histories, for a different analysis. This was performed on a homogeneous model, under a synthetic Gabor wave input motion, thus not accounting for lateral discontinuities and heterogeneities. It was performed in an attempt to isolate the purely "surface" topography effects from the subsurface effects. It shows the horizontal components of motion as well as the "parasitic" vertical components generated at the slope. In both cases it can be seen that the uphill region near the crest is affected by stronger waves with respect to the far-field.

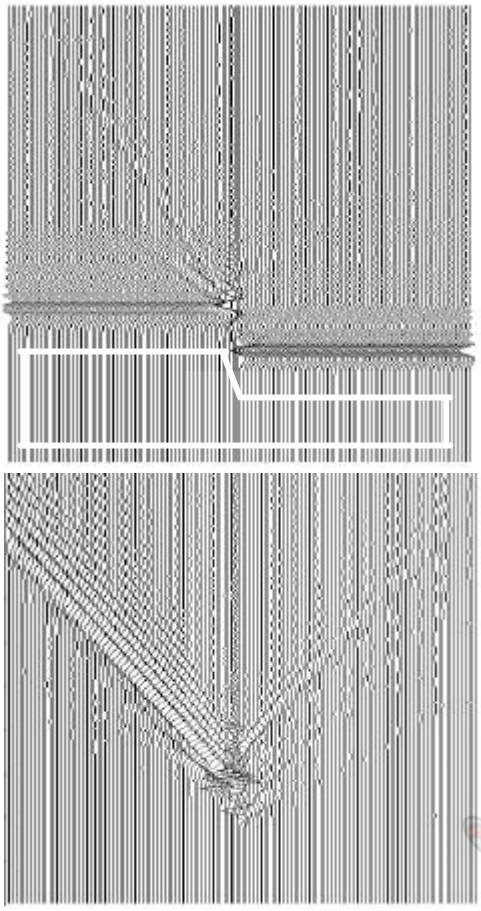

Fig. 10: Time-histories along surface, showing horizontal-SV (top) and vertical-P (bottom) components of motion.

In the frequency domain, the factor usually calculated in such studies is the Topographic Amplification Factor (TAF). This is defined as the ratio of the Fourier spectrum of the motion at the crest (say, at a distance of x=0m) with respect to the spectrum of the motion at a great distance from it (in this case, x=500m is far enough). This factor is calculated here and presented in Fig. 11 for all analyses performed. The results agree in that the TAF increases at higher frequencies and within a frequency band of engineering interest (around 1 to 5Hz) has a value of about 1.2 to 1.5. Indeed, the few existing code recommendations that take into account topographic effects, namely EC8 and the French AFPS [33, 34], suggest a value of 1.4 for this particular geometry of slope. Thus, the numerical results indicate that the design provisions constitute a step towards the right direction.

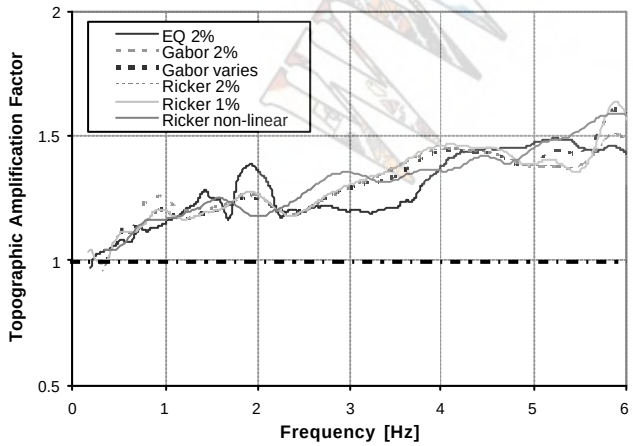

Fig. 11: Topographic aggravation factor for all analysis sets

CONCLUSIONS

The experimental site CORSSA offers several advantages for the study of site effects, as it combines good knowledge of ground conditions with a permanent surface and downhole accelerometer array. In this paper, focus was placed on surface topography effects; however, as this is a very complex site, there are bound to be effects from lateral discontinuities and soil heterogeneity.

The analytical results are compared to experimental data at stations both uphill and downhill, in the form of spectral ratios, so as to validate the numerical model and assumptions made.

In the time domain, results of the numerical simulation and dynamic analysis of the site reveal amplification of horizontal motion near the crest and deamplification near the toe, as well as generation of significant vertical motion near either side of the fault, which is due to P and surface wave generation. In the frequency domain, TAF values estimated are in agreement with those proposed in code provisions.

ACKNOWLEDGMENTS

The installation of CORSSA was funded by European research project “CORSEIS” (EVG1-1999-00002). The field survey was partially financed by the General Secretariat of Research and Technology, Greece, through project “XSOILS” (contract DP 23) and by European research project “NEMISREF” (G1RD-CT-2002-00702). The financial support of European research project “LESSLOSS” (GOCE-CT-2003-505448) is also gratefully acknowledged.

REFERENCES

[1] Bard P.-Y. "Local effects on strong ground motion: Physical basis and estimation methods in view of microzoning studies" *Proc. of Advanced Study Course in 'Seismotectonic and Microzonation techniques in Earthquake engineering, Kefalonia, Greece* (1999).

[2] Brambati A., Faccioli E., Carulli E.B., Culchi F., Onofri R., Stefanini S., and Ulcigrai F. "Studio de microzonizzazione sismica dell'area di Tarcento (Friuli), Edito da Regiona Autonoma Friuli-Venezia-Giulia" (in Italian) (1980).

[3] Siro L. "Southern Italy November 23, 1980 earthquake" *Proceedings of the 7th European Conference on Earthquake Engineering, September 20-25, Athens, Greece* (1982): 419-429.

[4] Castellani A., Chesi C., Peano A., Sardella L. "Seismic response of topographic irregularities" *Proceedings of Soil*

Dynamics and Earthquake Engineering Conference, Southampton, (1982): 251-268.

[5] Celebi M. "Northridge (California) earthquake: Unique ground motions and resulting spectral and site effects" *Proceedings of 5th International Conference on Seismic Zonation, October 17-19, Nice, France* (1995): 988-995

[6] Kawase H., and Aki K. "Topography effect at the critical SV wave incidence: possible explanation of damage pattern by the Whittier-Narrows, California, earthquake of 1 October 1987" *Bull. Seism. Soc. Am*. 80 (1990): 1-22.

[7] Athanasopoulos G.A., Pelekis P.C., and Leonidou E.A. "Effects of surface topography on seismic ground response in the Egion (Greece) 15 June 1995 earthquake" *Soil Dyn. Earth. Eng*. 18 (1999): 135-149.

[8] Gazetas G., Psarropoulos P., Assimaki D., and Kallou P.V. "Soil and topographic amplification of the seismic motion in Parnitha earthquake (7-9-99)" *Proc. of the 4th Panhellenic Conference in Geotechncial and Geoenvironmental Engineering, Athens* (in Greek) 2 (2001): 139-146

[9] Gazetas G., Kallou P.V., and Psarropoulos P.N. "Topography and soil effects in the Ms 5.9 Parnitha (Athens) earthquake: The case of Adames" *Natural Hazards* 27 (2002): 133-169.

[10] Bouckovalas G.D., and Kourtetzis G. "Review of soil and topographic effects in the September 7, 1999 Athens (Greece) esrthquake" *Proc. of 4th Int. Conf. on Recent Advances in Geotechnical Engineering and Soil Dynamics, San Diego, California* (2001).

[11] Jibson R. "Summary of research on the effects of topographic amplification of earthquake shaking on slope stability" USGS Open-file report 87-268, Menlo Park, California (1987).

[12] Bard P.-Y., and Meneroud J.-P. "Modification du sugnal sismique par la topographie - Cas de la vallee de la Roya (Alpes-Maritimes)" *Bull. Liaison Laboratoires des Ponts-et-Chaussees*, Numero special 'Risques Naturels' (1987): 140-151.

[13] Nechtschein S., Bard P.Y., Gariel J.C., Menourd J.P., Dervin P., Cushing M., Gaubert C., Vidal S., and Duval A.M. "A topographic effect study in the Nice region" *5th Int. Conf. Seismic Zonation, Nice* (1995): 1067-1074.

[14] Boore D.M. "A note on the effect of topography on ground motion" *Bull. Seism. Soc. Am*. 60 (1972): 29-61

[15] Bouchon M., and Barker J.S. "Seismic response of a hill: The example of Tarzana" *Bull. Seism. Soc. Am*. 86 (1996): 66-72.

[16] LeBrun B., Hatzfeld D., Bard P.Y., and Bouchon M. "Experimental study of the ground motion on a large scale topographic hill at Kitherion (Greece)" *J. Seismology* 3 (1999): 1-15.

[17] Chavez-Garcia F.J., Sanchez L.R., and Hatzfeld D. "Topographic site effects and HVSR. A comparison between observations and theory" *Bull. Seism. Soc. Am*. 86.5 (1996): 1559-1573.

[18] Chavez-Garcia F.J., Rodriguez M., Field E.H., and Hatzfeld D. "Topographic site effects - A comparison of two nonreference methods" *Bull. Seism. Soc. Am*. 87.6 (1997): 1667-1673.

[19] Geli L., Bard P.Y., and Jullien B. "The effect of topography on earthquake ground motion: a review and new results" *Bull. Seism. Soc. Am*. 78 (1988): 42-63.

[20] Faccioli E. "Seismic amplification in the presence of geological and topographic irregularities" *Proceedings of the 2nd Int. Conf. on Recent Advances in Geotechnical Earthquake Engineering and Soil Dynamics, March 11-15, St Louis, Missouri,* S. Prakash (ed.), Univ. of Missouri-Rolle (1991): 1779-1797.

[21] Finn W., and Liam D. "Geotechnical Engineering aspects of seismic microzonation" *Proceedings of 4th International Conference on Seismic Zonation, August 25-29, Stanford, California*, EERI (editor) Oakland, CA (1991): 199-250.

[22] Aki K. "Local site effects on strong ground motion" Earthq. Eng. Soil Dyn. - Recent advances in ground motion evaluation (ASCE Geotechnical Special Publication 20 (1988): 103-155.

[23] Sanchez-Sesma F.J. "Elementary solutions for response of a wedge-shaped medium to incident SH and SV waves" *Bull. Seism. Soc. Am*. 80.3 (1990): 737-742.

[24] Pedersen H., Sanchez-Sesma F.J., Campillo M. "Three-dimensional scattering by 2-dimensional topographies" *Bull. Seism. Soc. Am*. 84 (1994): 1169-1183.

[25] Assimaki D., and Gazetas G. "Soil and topographic amplification on canyon banks and the 1999 Athens earthquake" *J. Earthq. Eng*. 8.1 (2004): 1-43.

[26] CORSEIS 2nd Year Scientific Report, An integrated study of seismic hazard assessment in the area of Aigion, Gulf of Corinth, Greece – EVG1-1999-00002. Laboratory of Soil Mechanics and Foundation, Civil Engineering Department, Aristotle University of Thessaloniki, Greece (2001).

[27] CORSEIS Final Scientific Report, An integrated study of seismic hazard assessment in the area of Aigion, Gulf of Corinth, Greece – EVG1-1999-00002. Laboratory of Soil Mechanics and Foundation, Civil Engineering Department, Aristotle University of Thessaloniki (2002).

[28] Apostolidis P.I., Raptakis D.G., Pandi K.K., Manakou M.V, and Pitilakis K. "Definition of subsoil structure in Aigion city (Greece) and preliminary estimate of its site response" *Soil Dyn. Earthq. Eng*. (in press).

[29] Pitilakis K., Makropoulos K., Bernard P., Lemeille F., Berge-Thierry C., Tika Th., Manakou M., Diagourtas D., Kallioglou P., Makra K., Pitilakis D., and Bonilla L.F. "The Corinth Gulf Soft Soil Array (CORSSA) to study site effects" *Comptes Rendus Geoscience* 336.4-5 (2004): 353-365.

[30] Pitilakis K., Raptakis D., Makra K., Ktenidou O.-J., Pandi K., Manakou M., Pitilakis D., and Diagourtas D. "Effects of surface and subsurface topography on strong ground motion at the city of Aegion-Greece" *13th World Conf. Earth. Eng. Vancouver, BC, Canada* (2004b).

[31] Ktenidou O.-J. "2-D dynamic ground response analysis and study of topographic and site effects of strong ground motion for the city of Aegion, Greece" Diploma thesis, Aristotle University of Thessaloniki, Greece (in Greek) (2003).

[32] FLAC v. 3.4, User's Guide, Itasca Consulting Group Inc., Minneapolis MN, USA (1999)

[33] EUROCODE 8 Design provisions for earthquake resistance of structures. European Committee for Standardisation. Brussels, Belgium (2000).

[34] AFPS, Guidelines for seismic microzonation studies, AFPS/DRM (1995).

Study of the Soil-Structure Interaction using an equivalent linear and an elastoplastic soil model: Comparative results

D.Pitilakis[1], F. Lopez-Caballero[1], A. Modaressi[1], D. Clouteau[1]
[1] Lab.MSS-Mat CNRS UMR 8579, Ecole Centrale Paris, France

Abstract

In this paper, an equivalent linear and an elastoplastic soil model are incorporated in the soil-structure interaction analysis of a simplified soil-structure system. It is known, in the literature and the engineering practice, that in the case of strong earthquake shaking, the soil exhibits large deformations which cannot be adequately captured with a linear elastic constitutive model. Using a linear elastic approach for the modeling of the soil behavior may lead to overestimation of the response, and thus cause a conservative design of the structure. In this study, the soil-structure interaction response obtained from the two nonlinear soil models is compared with the linear response.

Keywords— *dynamic soil-structure interaction, equivalent linear, elastoplastic, performance based design*

INTRODUCTION

In the engineering practice, soil-structure interaction analyses are performed mainly in the linear elastic domain for the soil. This is due to the simplicity of the constitutive models used to simulate the soil behavior, the plethora of the existing analytical solutions, as well as the minimal computation effort needed for the analysis.

Vucetic showed that a linear soil model is restricted to small shear strain amplitudes, up to 10^{-5} (γ_{tl}), which suggests that the linear elastic approximation can provide reasonable estimates of the soil response only for small to moderate ground motions [1]. However, it is well established in the engineering practice that the soil, when subjected to a strong ground motion, exhibits large deformations. This nonlinear behavior cannot be captured by a linear elastic or viscoelastic model, emerging thus the need for more elaborated constitutive soil models.

In the present study, a nonlinear soil model is introduced in the soil–structure interaction analysis with two different approximations. The first approximation is through an equivalent linear soil model behavior. FLUSH and PILE3D are well–known software that can perform nonlinear soil-foundation-structure interaction analyses [2],[3]. In this study the software MISS3D (*Modélisation de l'Interaction Sol-Structures en 3D*), developed in Ecole Centrale Paris, was used [4]. Designed initially to perform 3D soil-structure interaction analyses in the linear elastic or viscoelastic domain, it was properly modified to take into account the nonlinear (equivalent linear) soil behavior [5], [6]. The shear strain compatible soil shear modulus is able to capture adequately the large soil deformations, the stiffness degradation and the higher energy dissipation, characteristics of a nonlinear response [7].

The only drawback in the abovementioned numerical code is that it remains, in its essence, a linear analysis. To this end, GEFDYN was used to introduce an elastoplastic model for the soil [8]. A two–dimensional plane-strain finite element model was used, having a realistic constitutive model which takes into account complex aspects of the non-linear elastoplastic soil behavior, such as the densification and the dilatancy or strength degradation.

The soil-structure interaction response obtained using the equivalent linear soil model is compared with the response of the elastoplastic model case and with the linear elastic case. The effects of the nonlinear soil behavior on the structural response are highlighted.

Moreover, the influence of the soil's stiffness degradation and energy dissipation, through material and radiation damping, on the seismic response of the soil-foundation-structure system is studied. Important conclusions are extracted for the structural seismic demand, in terms of displacements, in order to accommodate for the performance based design.

NUMERICAL METHODS

The first approach to the nonlinear soil-structure interaction problem, as mentioned before, adopts an equivalent linear soil behavior. The assumption of the linearity allows the use of the superposition method which, in turn, allows the solution in the frequency domain, the dynamic sub-structuring technique and the use of the boundary element method [9], [10]. Using the virtue of superposition, the structure can be modeled with any external finite element code; a modal analysis is then performed and the structural modes are projected on the interface between the structure and the soil, imposed as the interface modes. Then, the response of the soil to a unitary incident wave field propagating from the half-space is calculated, as the superposition of the incident wave field and the diffracted wave field from the soil-structure interface.

This numerical solution of the problem was modified in order to accommodate for the equivalent linear

behavior of the soil profile [5]. That is, the iterative procedure described in [7] was applied, in order to take into consideration the shear strain dependence of the shear modulus G of the soil. A maximum variation of 5% in G, for every soil layer, between two consecutive iterations is considered to be adequate for the convergence. One important difference, though, is that in every next iteration, when calculating the updated soil properties to be introduced in the analysis, the shear strain γ_{eff} (based on which the soil shear modulus G and consecutively the shear wave velocity Vs, are going to be modified) contains the effects of the structural oscillation on the soil (calculated through the diffracted wave). This means that the updated soil property values contain the effects of the structural vibration, allowing a more realistic approach to the soil-foundation-structure interaction phenomenon.

The equivalent linear MISS3D numerical code was validated through comparisons with other well known software that perform equivalent linear analyses for the soil, such as SHAKE and CyberQuake [7], [12]. In [5] and [6] it was shown that the three software gave the same results for the soil response and it was proven theoretically that it is valid to use this approach in a soil-structure interaction analysis.

The incremental elastoplastic constitutive model, implemented in the GEFDYN FE code, and used in this analysis can take into account the soil behavior in a large range of deformations. The model is written in terms of effective stress and is based on the following assumptions: Mohr-Coulomb type failure criterion; critical state concept; progressive mobilisation of the friction by shear strain based hardening; Roscoe's dilatancy/contractancy type flow rule; decomposition of the behavior into pseudo-elastic, hysteretic and fully mobilized domains and kinematical hardening to take into account cyclic behavior. Time domain computations are performed in order to capture the nonlinear phenomena.

DESCRIPTION OF THE MODEL

A simple soil-structure model was used in this study to elucidate the effects of the nonlinear soil behavior on the structural response. A single-degree-of-freedom structure, founded on a shallow foundation, was chosen to reveal, with great simplicity, the effects of the soil-structure interaction phenomenon in the case of an equivalent linear and an elastoplastic soil behavior.

The structure is a lumped-mass of 100t at a height of 3.8m over the rigid surface square foundation of dimensions 4m x 4m. The fixed base natural frequency of the linear structure is 3.19Hz and the structural damping 5%. The structural stiffness of the SDOF was calculated afterwards by the values of the mass and the fundamental frequency. The soil profile consists of 30m of clayey soil, separated into four layers with different properties, overlaying deformable bedrock with significant interface impedance with the soil. The properties for the soil and the structure are shown in Fig. 1.

The $G-\gamma$ and $D-\gamma$ curves describing the soil profile are given in Fig. 2. These curves were obtained by simulation of cyclic shear tests on each type of the soil material, using an elastoplastic model. These curves were then used in the equivalent linear analysis, in order to have coherent results with the elastoplastic model.

In the nonlinear domain, the input motion and its characteristics play a significant role in the soil response, which needs to be identified. Thus, the soil-structure system was analyzed using both approaches under three different excitations. These excitations were chosen judiciously, in order to reveal the effects of the different amplitude, frequency content and duration of the motion on the complete soil-foundation-structure system.

First a 2nd order Ricker wavelet was used, having a PGA amplitude of 0.5m/s^2 and period 0.2s, centered at 0.43s, as shown in Fig. 3.

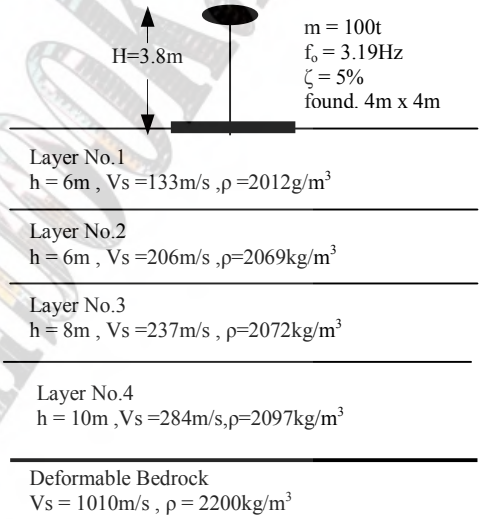

Fig. 1: Simplified soil-structure model used for the analyses

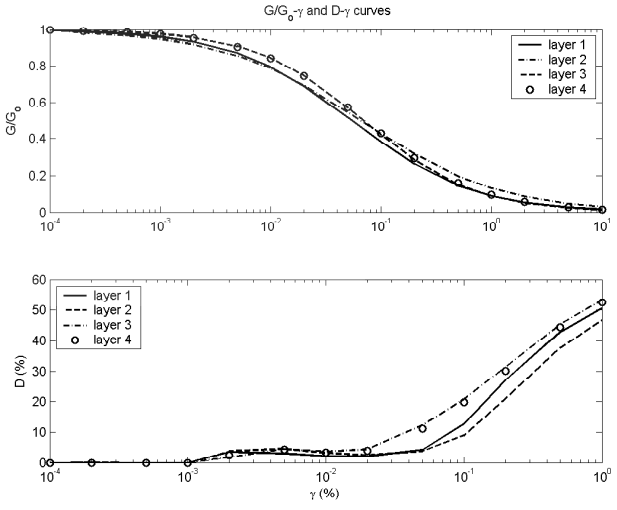

Fig. 2: Shear modulus G/Go and damping D against shear strain γ curves for the soil profile

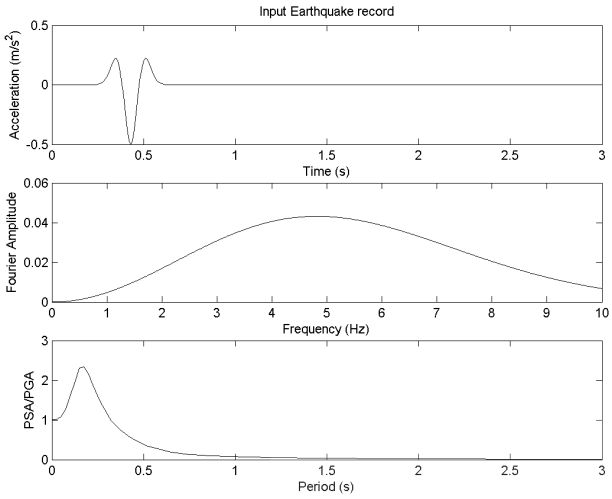

Fig. 3: Ricker wavelet of PGA=0.5m/s^2 and period 0.2s.

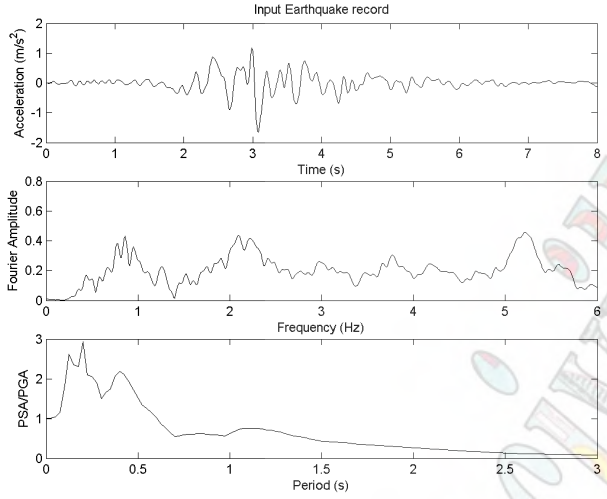

Fig. 4: San Rocco, 1976 Friuli, Italy earthquake (PGA=2.3m/s^2)

The same Ricker wavelet was introduced afterwards with the double PGA amplitude (1m/s^2). Finally, a real accelerogramme recorded during the San Rocco, 1976 Friuli, Italy earthquake, with PGA of 2.32m/s^2, was applied to the soil-structure system. The San Rocco earthquake record and its response spectrum are shown in Fig. 4.

COMPARATIVE RESULTS

First the soil-structure system was subjected to the Ricker wavelet shown in Fig. 3. The small amplitude of the input motion, as well as the characteristics of the soil, force the soil-structure system to behave almost linearly and no significant soil-structure interaction effects take place. Minor soil stiffness degradation is noticed and the only important modification from the elastic reference case is the increase in the damping of the soil, mainly due to the given properties of the soil represented here with the G–γ and D–γ curves. These are shown in Fig. 5 in the form of transfer functions for the soil and the structure.

In Fig. 6 is shown the comparison between the results obtained for the soil response using the two different approaches for the soil behavior, expressed in terms of the transfer function of the motion between the bedrock and a point in the center of the foundation, under the SDOF structure. It can be seen that the equivalent linear soil approximation is capable of capturing adequately the first natural vibration mode of the soil.

The first natural frequency of the soil profile is found to be, for the linear elastic case, at 2.1Hz, but a small peak arises in the transfer function of the equivalent linear soil around 2.5÷2.6Hz, which is the natural frequency of the structure founded on a flexible base, as shown in Fig. 7. This discontinuity is a proof that minor soil-structure interaction effects take place, but do not alter the general trend of the response. It is worthy to note, however, that there is a shifting in the fundamental frequency of the structure to lower values, pronouncing the effects of the translation and rotation of the foundation.

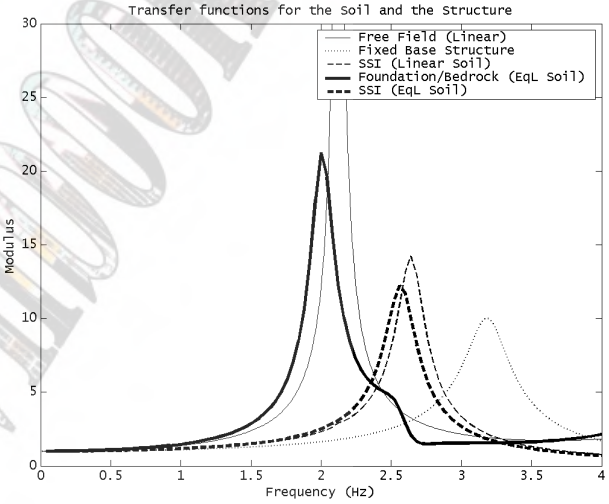

Fig. 5: Transfer functions for the soil and the structure using linear and equivalent linear soil behavior

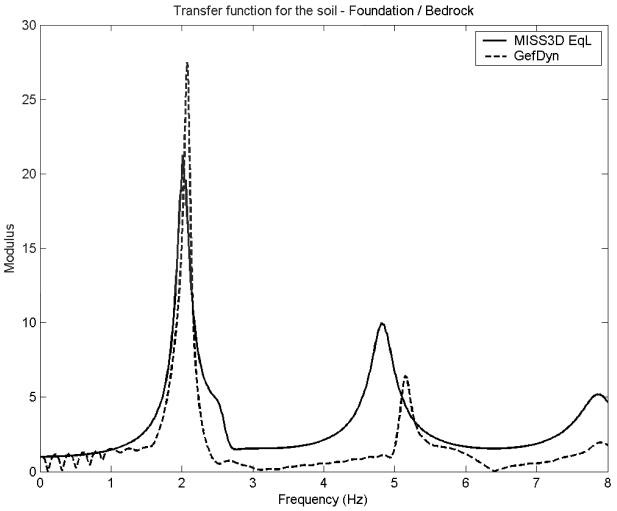

Fig. 6: Transfer functions between the center of the foundation and the bedrock, obtained with MISS3D-EqL and GEFDYN. (Ricker PGA=0.5m/s^2)

Dividing the Fourier amplitude of the response on the top of the structure by the response at the free field, we obtain the transfer function of the complete soil–foundation–structure system, shown in Fig. 8. A good matching is accomplished between the two models. The difference in the amplitude of the amplification factor in the vicinity of the resonance frequency of the structure is due to the different damping configuration used in the two models. It can be seen that the resonance frequency of the structure has decayed from 3.19Hz at fixed–base conditions (single-degree-of-freedom structure) to 2.6Hz, when the foundation is free to follow the ground movement, as well as to rotate, becoming a multi-degree-of-freedom structure.

It is interesting to notice that at the resonance frequency of the complete soil–foundation-structure system, at 2.6Hz as shown in Fig. 8, the amplification of the response in the structure only is larger when using the equivalent linear model, than the one of the elastoplastic, as shown in Fig. 7. Thus, even though in the overall frequency range of interest one may observe larger amplifications for the elastoplastic model, Fig. 9 shows that on top of the structure the equivalent linear approximation causes larger acceleration amplitude.

It is clear that the two different nonlinear approaches for the soil behavior are able to simulate adequately the response of the system, when subjected to a small ground motion. However, the main difference in the response of the two approximations can be found in the configuration of the energy dissipation in the system. For weak ground motions, the elastoplastic soil model introduces less damping in the system through the soil material deformation in the vicinity of the foundation. This is obvious by the different amplification amplitudes obtained for the response of the system shown in Fig. 6 to 8.

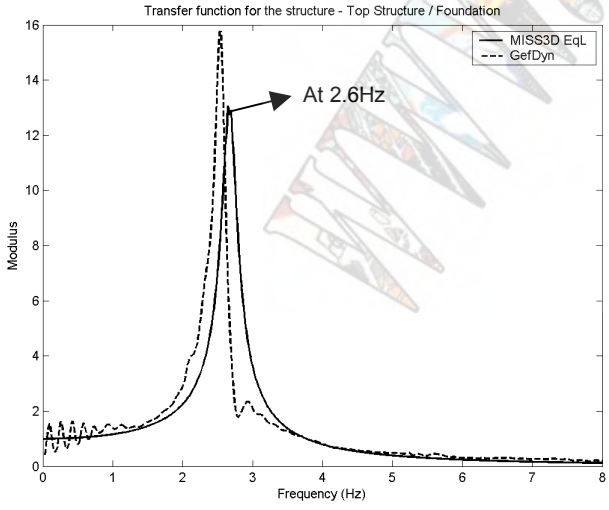

Fig. 7: Transfer functions between the top of the structure and the center of the foundation (Ricker PGA=0.5m/s^2)

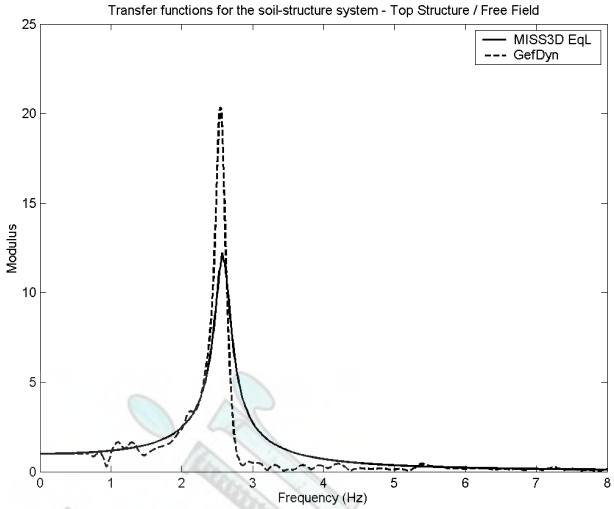

Fig. 8: Soil–structure interaction transfer function (top structure/free field) (Ricker PGA=0.5m/s^2)

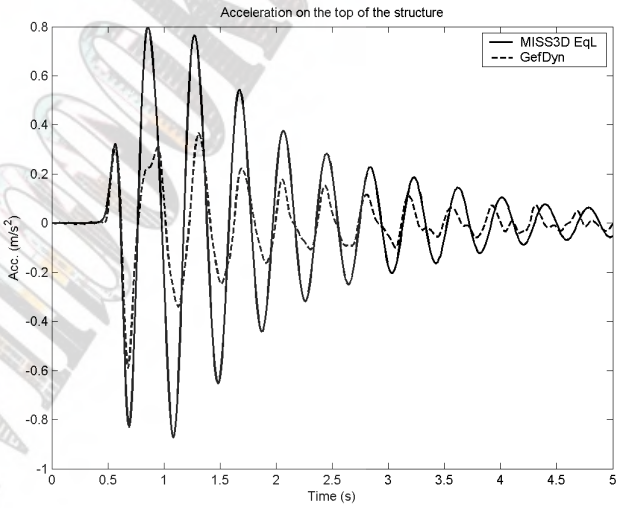

Fig. 9: Acceleration time history on top of the structure (Ricker PGA=0.5m/s^2)

When the same system is subjected to a moderate amplitude Ricker wavelet (PGA=1m/s^2, Tp=0.2s) input motion, much more damping is introduced in the elastoplastic soil model. Fig. 10 shows the transfer functions for the soil, from the bedrock to the center of the foundation.

There is good agreement between the two models in the structural response, in terms of amplitude and shape in the transfer function (Fig. 11), meaning that both models can capture the stiffness degradation of the structure due to the induced flexibility of the foundation and the soil softening. However, the combined response of the soil and the structure, expressing the complete system, produces a more complex transfer function for the elastoplastic soil behavior, with two main peaks close to each other representing the soil and the structure and smaller amplitude than in the equivalent linear case (Fig. 12). This difference in amplitude is reflected in the acceleration response on top of the structure, in time and in frequency domain, shown in Fig. 13 and 14.

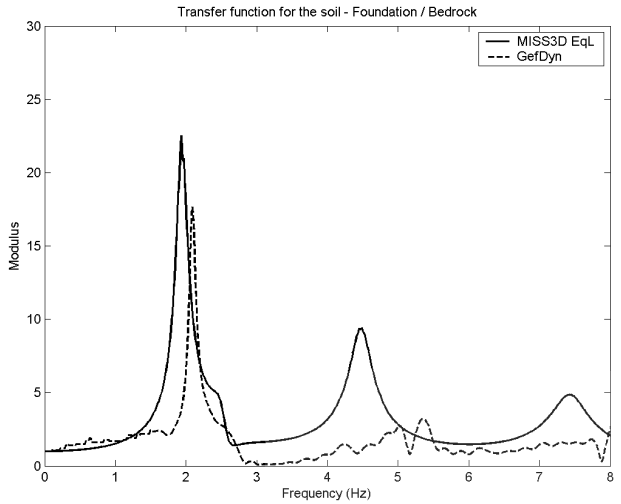

Fig. 10: Transfer functions for the soil, for a Ricker input motion with PGA=1m/s^2, Tp=0.2s

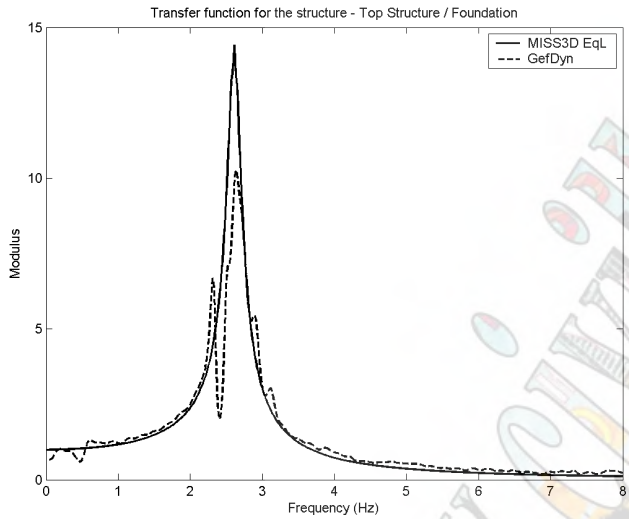

Fig. 11: Transfer functions between the top of the structure and the center of the foundation (Ricker PGA=1m/s^2)

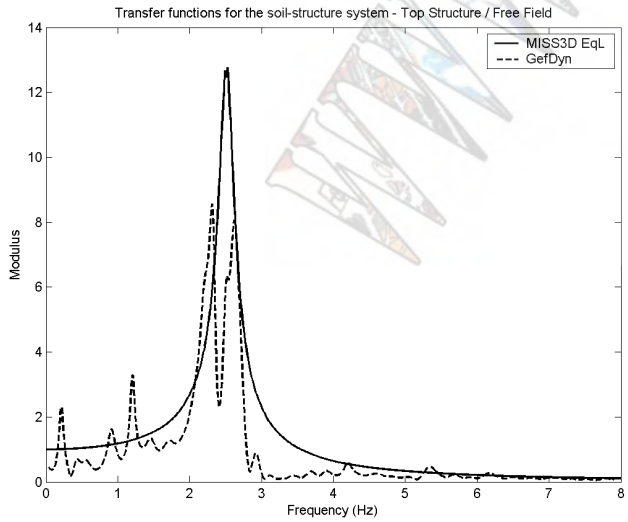

Fig.12: Soil–structure interaction transfer function (top structure/free field) (Ricker PGA=1m/s^2)

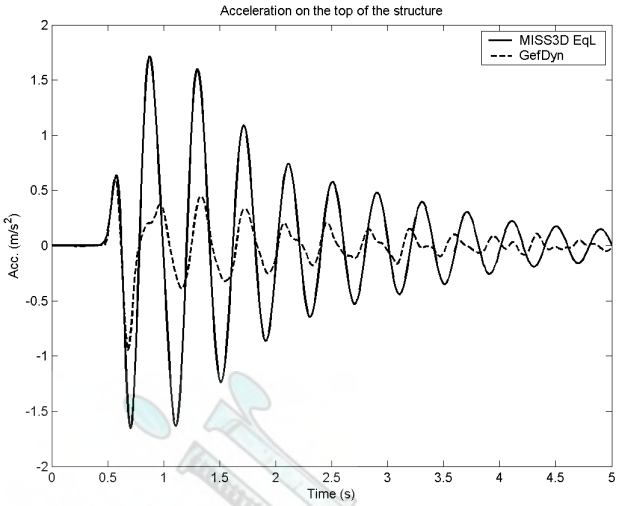

Fig. 13: Acceleration time history on top of the structure (Ricker PGA=1m/s^2)

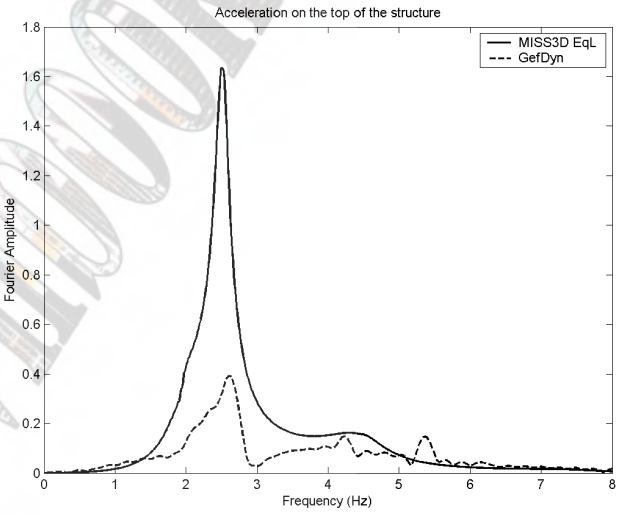

Fig. 14: Fourier spectrum of the acceleration on top of the structure (Ricker PGA=1m/s^2)

The main difference in the two models can be seen in Fig. 15. The horizontal displacement response time history at the center of the foundation is plotted for the two Ricker input ground motions. It is immediately apparent that for the weak Ricker (0.05g) the response remains linear. The two models give similar results (thin lines) and the displacement at the end of the ground shaking is almost null. However, when applying a stronger ground motion (Ricker 0.1g), the nonlinear response is promoted and can be easily identified only by the elastoplastic mode (thick dashed line). One may observe that the elastoplastic model produces permanent displacements at the base of the structure. The equivalent linear model remains, essentially, in the linear domain, and thus is not capable of capturing effects like the permanent displacements.

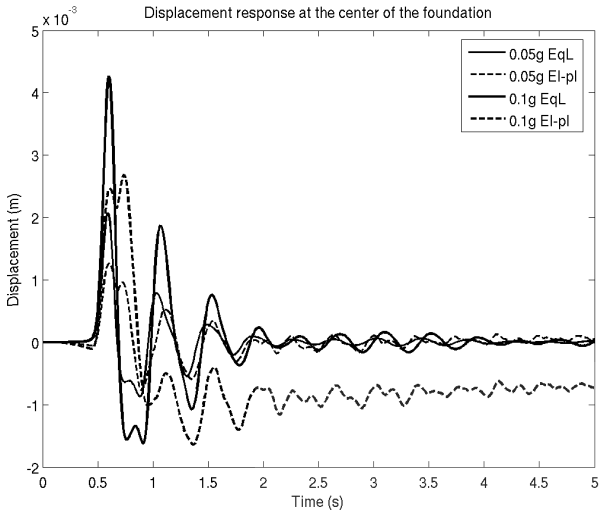

Fig.15: Displacement time history at the foundation for the two models and the two Ricker excitations

Next the simplified soil-foundation-structure system is subjected to a real earthquake, recorded at San Rocco during the 1976 Friuli, Italy earthquake. The characteristics of this earthquake are shown in Fig. 4.

Since the comparison between the two nonlinear approximations gave similar results for the simple cases of the Ricker wavelet input motion, in order to elucidate the effects of the soil nonlinearity on the soil-structure interaction, only the results from the equivalent linear model will be shown. The obtained response is always compared to the case of a linear elastic soil under the foundation. The response of the soil profile when subjected to the earthquake record is plotted in Fig. 16, in terms of transfer functions.

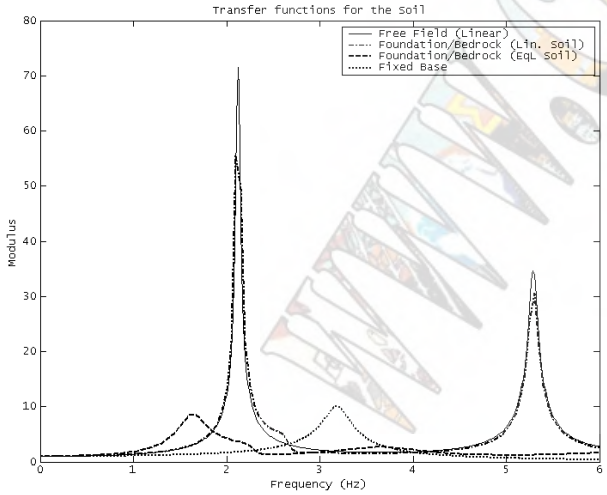

Fig. 16: Transfer functions for the soil (foundation to bedrock response), and the fixed base structure, for San Rocco, 1976 Friuli, Italy earthquake (PGA=2.3m/s^2)

As it can be seen in Fig. 16, the first natural mode of the soil decreases from 2.1Hz to 1.6Hz. This shifting is due to the soil softening in the vicinity of the foundation. As measure of the higher energy dissipation, one may notice that the peak amplification of the soil response decreases from a factor of 70 to 8. This energy is dissipated by the nonlinear deformations of the soil around the foundation.

Furthermore, the abovementioned effects of the soil's nonlinear response are apparent in the transfer functions of the complete soil-foundation-structure system shown in Fig. 17. From the fixed-base fundamental frequency of the structure, at 3.19Hz, with a linear soil-structure analysis there is a shifting to 2.66Hz. However, when introducing an equivalent linear model for the soil behavior, the natural frequency of the complete system is found at 2.25Hz. The magnitude of the amplification factor decreases as well, from 10 for fixed-base conditions to 7 when the equivalent linear model is incorporated.

The stiffness degradation of the system and the higher energy dissipation appear at the response on top of the structure. It can be seen in Fig. 18 that the amplitude of the acceleration has decreased by 30% and the vibration cycles are of longer period.

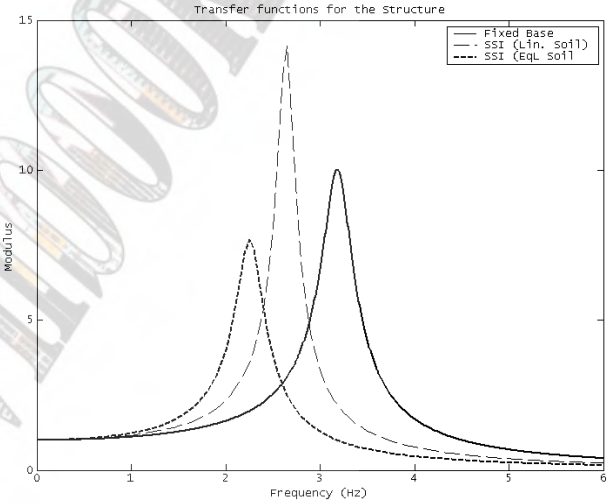

Fig. 17: Transfer functions between the top of the structure and the free field, for linear and equivalent linear soil (San Rocco earthquake record)

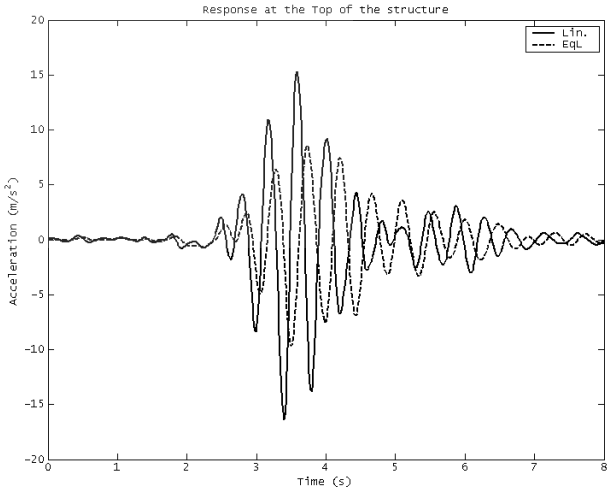

Fig. 18: Acceleration time history on top of the SDOF structure (San Rocco earthquake record)

EFFECTS ON THE PERFORMANCE BASED DESIGN

Needless to say is that the nonlinear response of the soil, combined with soil–structure interaction effects, may modify significantly the response of the structure and, consequently, its design. In Fig. 19 and 20 are shown the demand spectra for the complete system, using an equivalent linear approximation for the soil behavior, when subjected to the two different earthquake ground motions shown in Fig. 3 and 4. It can be seen that, depending on the ground motion, for the same soil conditions, in the first case (Fig. 19) the structural demand is generally decreased when taking into account the interaction between the soil and the structure, while it mostly increases in the second (Fig. 20). Thus, not taking into account the soil–foundation–structure interaction may lead into conservative performance based design in the first case (Fig. 19) or underestimation of the design performance (Fig. 20), depending on the structure.

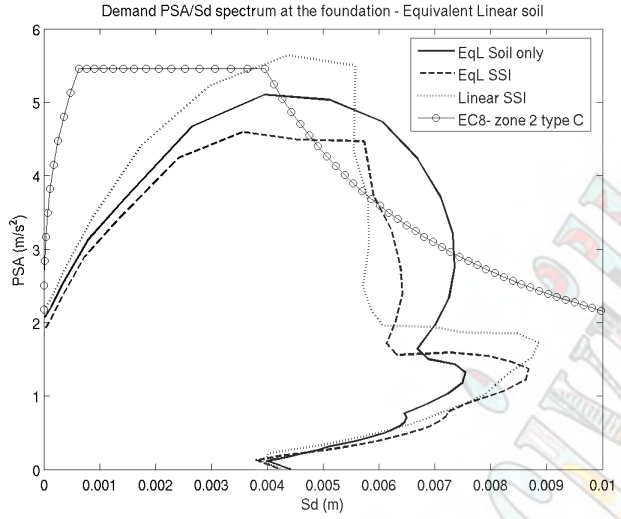

Fig. 18: Demand spectrum at the center of the foundation, using an equivalent linear soil model, for a ground shaking with the Ricker of PGA=0.1g.

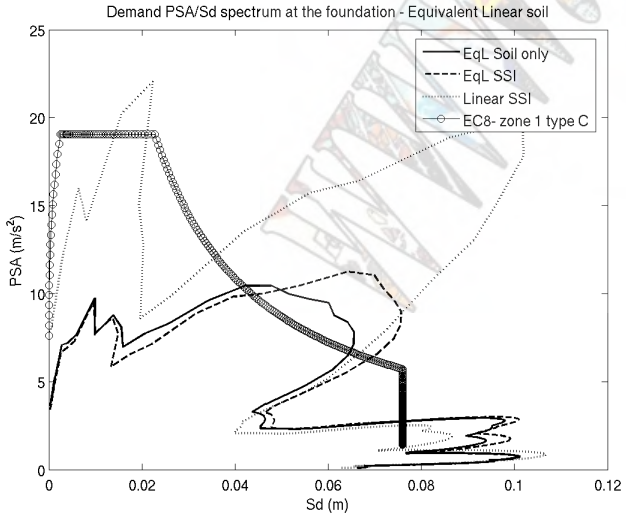

Fig. 19: Demand spectrum at the center of the foundation, using an equivalent linear soil model, for a ground shaking with the San Rocco earthquake shown in Fig. 4

However, it is obvious that not including the nonlinear behavior of the soil in the computations, in general leads to conservative design of the structure. Moreover, from Fig. 19 and 20 can be seen that in general it is at the side of safety to design according to the Eurocode 8.

CONCLUSIONS

A soil–foundation–structure interaction analysis was performed for a simplified single–degree–of–freedom structure founded on the surface of a soil stratum. The solution of the problem incorporated the use of two nonlinear models for the soil: an equivalent linear and an elastoplastic one. The equivalent linear soil model uses given $G–\gamma$ and $D–\gamma$ curves, produced by the simulation of cyclic shear tests for each soil layer in order to verify the elastoplastic model's parameters. The equivalent linear solution of the problem is an iterative linear approach of the soil behavior in the frequency domain, while the elastoplastic model is a direct soil–structure finite element approximation in time domain.

Results are presented for three different input motions, as for the nonlinear response of a system, the ground shaking characteristics play an important role. The two nonlinear approaches were found to give quite similar results for the response of the system, in terms of the resonance frequencies, while there is a difference in the estimation of the amplitude of the vibration.

It is very important to note, however, that it is very difficult to obtain exactly the same response, as the two approximations follow completely different solution schemes. In the equivalent linear soil behavior, the soil damping is taken into account by the given $D–\gamma$ curves, and thus, for a certain level of excitation and soil deformation (shear strain γ_{eff}) it is rather easy to be determined. On the other hand, in an elastoplastic model, the identification and incorporation of the soil damping in the direct soil–structure time domain analysis is not straight-forward. It is implicitly induced by the incremental response of the complete model under the applied cyclic internal loads. For the abovementioned reasons, the complete calibration of the two models is a very complicated task. A difference in the amplitude of the response is expected, due to the different damping introduced in the soil and transferred to the structure.

Nevertheless, the equivalent linear approach is considered to be a good – even though simplistic – approximation of the soil's nonlinear behavior; it can capture all the principal effects of the large deformations exhibited by the soil during a strong earthquake shaking and produce a preliminary assessment of the nonlinear soil–structure interaction phenomenon. The primer advantage of this solution is the rather easy concept of the linear elastic theory, laying beneath, as well as the

reduced computational effort needed, compared to a direct nonlinear soil–structure finite element analysis.

On the other hand, the equivalent linear solution remains approximate and can never reproduce the entire phenomenon, as it is done with a complex analysis using an elastoplastic constitutive soil model. Some basic features of the final response, such as the permanent displacement at the end of the shaking and the plastic deformations of the soil, cannot be captured.

Finally, taking into account the soil nonlinearity and the soil-foundation-structure interaction effects, may alter significantly the conception and design of the structure; more parameters are now induced in the problem. The stiffness degradation of the complete soil-foundation-structure system has to be taken into account, as well as the higher energy dissipation by the soil in the vicinity of the foundation, due to the large deformations.

REFERENCES

[1] Vucetic, M.,. "Cyclic threshold shear strains in soils", *J. of Geotechnical Engineering – ASCE*, Vol. 120, No.12, pp.2208-2228, 1994.

[2] Lysmer, J., Udaka, T., Tsai, C.F., Seed, H.B., "FLUSH: A computer program for approximate 3-D analysis of soil-structure interaction problems", Earthquake Engineering Research Center, U.C.Berkeley, Rep. EERC 75-30, 1975

[3] Travaraj, T.,Finn, W.D. Liam, "PILE-3D-EFF: A program for nonlinear dynamic effective stress analysis of pile foundations", Anabuki Chair of Foundation Geodynamics, Kagawa University, Japan, 1999.

[4] Aubry D., Clouteau D., *Computational soil-structure interaction*, Kluwer, 2003, ch. 2, pp. 61–125.

[5] Pitilakis, D., Lopez-Caballero, F., Modaressi, A., Clouteau, D., "Effects of the soil non-linearity on the soil-foundation-structure interaction", *Proc. 11th International Conference of IACMAG, Turin, Italy, 2005*, pp. 691-698

[6] Pitilakis, D., Lopez-Caballero, F., Clouteau, D., Modaressi, A., "Soil-Structure Interaction analysis using an equivalent linear model for the soil – real case application", *International Geotechnical Conf. on Soil-Structure Interaction: Calculation methods and engineering practice, St. Petersbourg, Russia, 2005,* in press

[7] Schnabel, P.B., Lysmer, J., Seed, H.B., "SHAKE: a computer program for earthquake response analysis of horizontally layered sites" Earthquake Engineering Research Center, U.C.Berkeley, Rep. EERC 72-12, 1972

[8] Aubry, D., Chouvet, D, Modaressi, A., Modaressi, H., "GEFDYN: Logiciel d'analyse de comportement mécanique des sols par éléments finis avec prise en compte du couplage sol-eau-air", Manuel Scientifique, Ecole Centrale Paris, LMSS-Mat, 1986

[9] Aubry D., Clouteau D., "A subdomain approach to dynamic soil-structure interaction", Ouest Editions/AFPS, Nantes, 1992, pp. 251-272

[10] Brebbia, C.A., Wrobek, L., Telles, J., *Boundary element techniques.* Theory and Application in Engineering. Springer-Verlag, 1984

[11] Modaressi H., Foerster E., "*CyberQuake"*, User's manual, BRGM, 2000

A Simplified Method to Avoid Buckling of Piles in Seismically Liquefiable Soils

S. Bhattacharya[1], S.P.G.Madabhushi[2], T. R.Aldridge[1]
[1]*Fugro Limited, Wallingford (U.K)*
[2]*Department of Engineering, University of Cambridge, UK*

Abstract

Collapse and/or severe damage of pile-supported structures is still observed after strong earthquakes, despite the fact that a large factor of safety against axial capacity and bending due to lateral loads is employed in their design. Recent research has identified a fundamental omission in seismic pile design. Currently, piles in liquefiable soils are designed as beams to avoid bending failure arising from lateral loads due to inertia and/or slope movement (lateral spreading). New research findings suggest that the part of the pile in liquefiable soil needs to be treated as an unsupported structural column, to avoid buckling failure. Essentially, P-delta effects should be taken into account for fully-embedded piled foundations passing through liquefiable soils. The current design codes such as Eurocode 8 and the Japanese, Indian and NEHRP codes, however, provide very little guidance in this regard. This paper describes a simplified method to avoid buckling of piles in areas of seismic liquefaction. Although many sophisticated numerical models and computer programs are available (SPASM, BMCOL) or can be written to incorporate the P-delta effect, it is considered useful to have a simple back-of-the envelope type of design chart based on classical understanding of buckling. This can be particularly helpful for preliminary design, and for verifying and interpreting results obtained from sophisticated analyses.

Keywords—*buckling, piles, liquefaction*

INTRODUCTION

Failure of pile-supported structures during seismic liquefaction

Collapse and/or severe damage of pile-supported structures is still observed in liquefiable soils after most major earthquakes such as the 1995 Kobe earthquake (JAPAN), the 1999 Kocheli earthquake (TURKEY), and the 2001 Bhuj earthquake (INDIA). The failures not only occurred in laterally spreading ground but were also observed in level ground where no lateral spreading would be anticipated; see for example [1]. The failures were often accompanied by settlement and tilting of the superstructure, rendering it either useless or very expensive to rehabilitate after the earthquake. Following the 1995 Kobe earthquake, an investigation was carried out to find the failure pattern of the piles [2, 3]. Piles were excavated or extracted from the subsoil, borehole cameras were used to take photographs, and pile integrity tests were carried out. These studies hinted at the location of the cracks and damage patterns for the piles. Of particular interest is the formation of plastic hinges in the piles. This indicates that the stresses in the pile during and after liquefaction exceeded the yield stress of the material of the pile, despite the large factors of safety employed in the design. As a result, the design of pile foundations in seismically liquefiable areas still remains a continuing area of concern for the earthquake geotechnical engineering community. The next section describes the different phases of loading of a piled foundation that need consideration during the foundation design process.

Different phases of loading in a pile during earthquake liquefaction

During earthquakes, the soil layers overlying bedrock are subjected to seismic excitation consisting of numerous incident waves, namely shear (S_h) waves, dilatational or pressure (P) waves, and surface (Rayleigh and Love) waves, all of which result in ground motion. The ground motion at a site will depend on the stiffness characteristics of the layers of soil overlying the bedrock. This motion will also affect a piled structure. As the seismic waves arrive in the soil surrounding the pile, the soil layers will tend to deform. This seismically deforming soil will try to move the piles and the embedded pile-cap with it. Subsequently, depending upon the rigidity of the superstructure and the pile-cap, the superstructure may also move with the foundation. The pile may thus experience two distinct phases of initial soil-structure interaction:

1. Before the superstructure starts oscillating, the piles may be forced to follow the soil motion, depending on the flexural rigidity (EI) of the pile. Here the soil and pile may take part in kinematic interplay and the motion of the pile may differ substantially from the free field motion. This may induce bending moments in the pile.
2. As the superstructure starts to oscillate, inertial forces are generated. These inertial forces are transferred as lateral forces and overturning moments to the pile via the pile-cap. The pile-cap transfers the moments as varying axial loads and bending moments in the piles. Thus the piles may experience additional axial and lateral loads, which would cause additional bending moments in the pile.

These two effects occur with only a small time lag. If the section of the pile is inadequate, bending failure may occur in the pile. The behaviour of the pile at this stage may be approximately described as a beam on an elastic foundation, where the soil provides sufficient lateral restraint. The available confining pressure around the pile is not expected to decrease substantially in these initial

phases. The response to changes in axial load in the pile would not be severe either, as shaft resistance continues to act. This is shown in Figure 1 (Stage II).

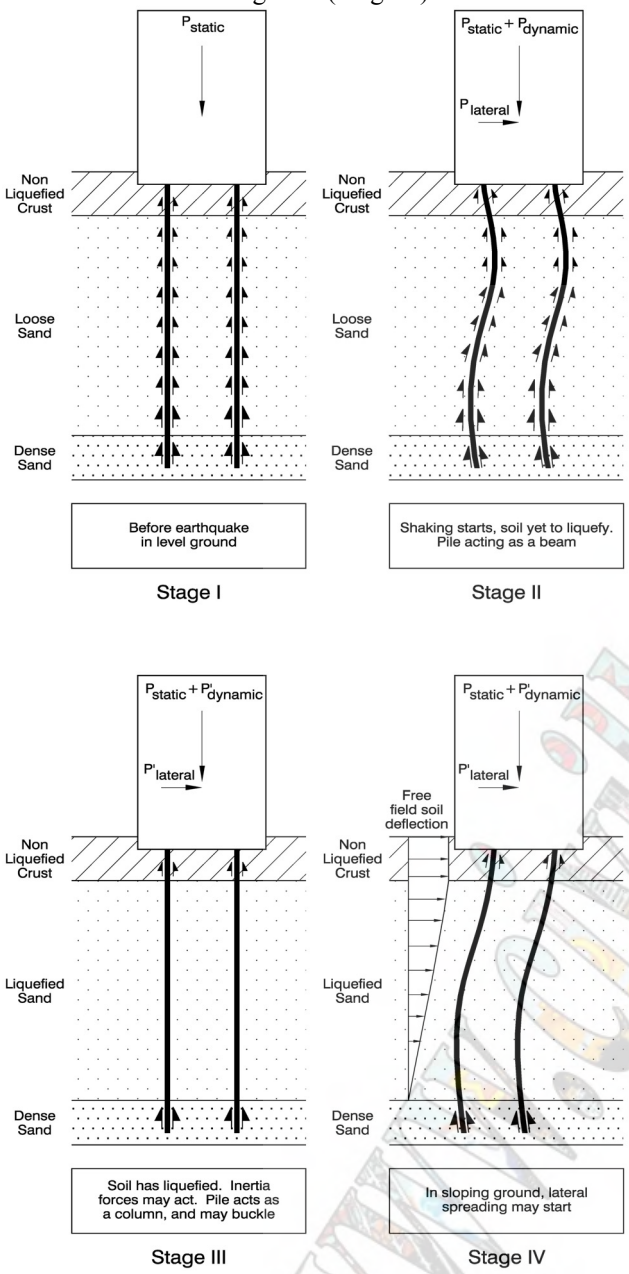

Fig 1: Different stages of the loading

In loose saturated sandy soil, as the shaking continues, pore pressure will build up and the soil will start to liquefy. With the onset of liquefaction, an end-bearing pile passing through liquefiable soil will experience distinct changes in its stress state.

The pile will start to lose its shaft resistance in the liquefied layer and shed axial loads downwards to mobilise additional base resistance. If the base capacity is exceeded, settlement failure will occur.

The liquefied soil will begin to lose its stiffness, so that the pile acts as an unsupported column as shown in Figure 1 (Stage III). Piles that have a high slenderness ratio will then be prone to axial instability, and buckling failure will occur in the pile, enhanced by the action of lateral disturbing forces and also by the deterioration of bending stiffness due to the onset of plastic yielding. Dynamic centrifuge tests [4, 5, 6, 7], studies of case histories [4, 5], numerical work [8] and analytical work [4, 9] have conclusively shown the above failure mechanism. Figure 2 shows photographs of buckling failures of piles. This particular mechanism is not explicitly mentioned in most codes of practice but has been observed in the dynamic centrifuge tests referenced above.

In sloping ground, even if the pile survives the above load conditions, it may experience additional drag load due to the lateral spreading of soil. Under these conditions, the pile may behave as a beam-column (column with lateral loads); see Figure 1 (Stage IV). This bending mechanism is currently considered most critical for pile design and is incorporated in JRA (1996).

Fig 2: Buckling of single pile [4] and pile group [6] in a centrifuge test.

An interesting hypothesis of pile-soil interaction during buckling is proposed in [4], based on the observations and measurements in the centrifuge tests. As the pile buckles sideways, it shears the initially liquefied soil in front of it. The liquefied soil in front of the pile offers temporary resistance to the buckling pile as it is subjected to monotonic shearing, due to its dilatant response, and may induce a reduction in pore pressure relative to the liquefied far field (some distance away from the pile). The temporary resistance of the liquefied soil to the buckling pile diminishes as the pore pressure difference between the liquefied far field and the near field creates a transient flow that overcomes the drop in excess pore pressures, resulting in pore pressure equalization, which restores the liquefied state. The resistance from the liquefied soil is therefore unsustainable, and cannot be relied upon to prevent buckling of a susceptible pile. The main issue relevant to the formulation of a design procedure against buckling is that liquefied soil cannot prevent the initiation of buckling, despite the fact that some secondary resistance become available. This secondary resistance would dictate the location of the hinge. A discussion on the shape of the pile after buckling and its comparison with the classical buckled shape can be found in [4, 10].

Structural design of piles

Most piles are structurally designed against bending

failure due to lateral loads. The semi-empirical p-y concept is normally used to predict the maximum bending moment in the piles. However, this approach is essentially a "Lower Bound Theorem of Plasticity" and cannot be applied if buckling under axial loading is a possibility for the member under consideration. These considerations would lead to the conclusion that, if part of the pile loses lateral support during the design event, the pile should then be treated as an unsupported column. The structural design of the pile in the unsupported zone may be performed by modeling the pile as a column carrying lateral loads, i.e. a beam-column.

Codes of practice

It is of interest to review the standard practice for pile design in seismic areas. The current methods of pile design given in Eurocode 8, JRA (1996) and the Indian Code (IS 2911, IS 1893) are based on a bending mechanism where lateral loads due to inertia or slope movement cause bending failure of the pile. These codes omit considerations of the bending stiffness required to avoid buckling in the event of soil liquefaction. As a result, these codes are inadequate to address this failure mechanism. Table 1 and Figure 3 collate 40 published records where the length of pile in liquefiable soil and the pile diameter are used to indicate the long column nature of piles.

Table 1: Pile diameter and its length in liquefiable soils [Fig 3]

Length of pile in liquefiable soil (m)	Pile diameter (m)	Reference
14 data points from Table 1 in [4]		
12	0.35, 0.5,	Building site A,C, D [1]
12.8	0.6	Building site B [1]
13	0.4,0.5	Building site E,F [1]
11.5	0.406	Building site G [1]
13.35	1.5	Building site H [1]
13	1.2, 1.7	Osaka bay [11]
5	1.3,1.5, 1.6	11, 12 and 13 storey buildings with basements [12]
11.75	0.4,0.5	111 piles in the structure
15	0.51, 0.75, 1	Kandla port [13]
14	0.4	Piled silo [14]
13.6	0.45	Oil storage tank [15]
5.9	0.3,0.35, 0.4	[16]
6.15	0.43	[16]

Figure 3 shows that the ratio of unsupported length i.e. the length of the pile in the liquefiable soils to the pile diameter, ranges between 3 and 50 with the major portion exceeding 12. It is interesting to note that most of the piles with L_0/D values between 3 and 12 performed well. These are classified as short columns in structural engineering terms, and only fail by crushing of the material, not requiring lateral support for stability, see [4,5]. The high slenderness ratios for most piles hints at the fact that buckling might have been a consideration, but would not have been considered in most of the cases.

The purpose of this paper is to develop a simplified procedure to incorporate buckling into design. Incorporation of buckling in pile design involves not only estimating the critical load based on Euler's formula but also understanding the role of imperfections and lateral loads in the initiation of buckling. It will be shown that the true failure load may be at factor of 3 or more less than that predicted by Euler's formula.

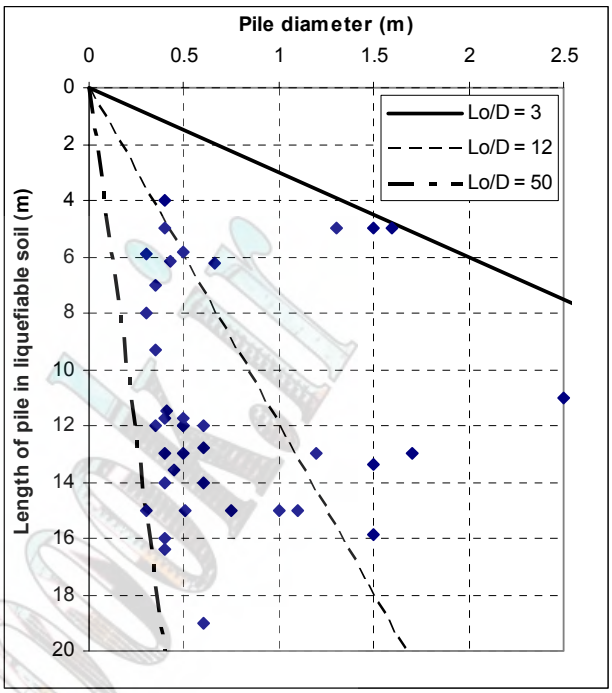

Fig 3: Plot of the length of pile in liquefiable soils (L_0) against pile diameter (D).

CRITERIA FOR DESIGN

A safe design procedure should ensure that the pile has adequate strength and stiffness to meet the following criteria:

(1) The pile should have adequate strength and stiffness to carry the axial load acting on it during full liquefaction without buckling and becoming unstable. It has to sustain the axial load and horizontal oscillations of the superstructure, i.e. must be in stable equilibrium while the surrounding soil has very little stiffness, as a result of liquefaction.

(2) A collapse mechanism should not form under the combined action of lateral loads imposed by the earthquake and axial load. At any section of the pile, the bending moment should not exceed the allowable moment for the pile section. The shear stress at any section of the pile should not exceed the allowable shear capacity.

(3) A pile should have sufficient embedment in the non-liquefiable soil strata below the liquefiable layer to achieve fixity to carry moments. If proper fixity is not achieved, the piled structure may slide due to the kinematic loads. In addition, lack of full fixity may also adversely affect the critical load that would initiate pile buckling.

(4) The settlement of the foundation due to the loss of soil support should be within acceptable limits. This settlement should also not induce end-bearing failure of the pile.

ISSUES IN DESIGN

Buckling of a slender pile may occur owing to the loss of lateral support, as a result of liquefaction. Buckling is sensitive to imperfections and lateral loads. The loss of lateral support may also lead to other considerations, as will be explained in this section. Critical design issues include:

1. Construction-induced imperfections of pile,
2. Lateral loads on the pile,
3. Depth of fixity at the non-liquefiable bearing layer below the liquefiable layer,
4. Amplification of lateral deflections (generated by lateral loads) resulting from P-delta effects, and
5. Changes in the period of the structure, due to loss of support in the liquefied soil. During or after liquefaction, part of the pile in liquefied zone acts as an additional storey (Stage III in Figure 1) which alters the vibrational characteristics of the structure when compared with Stage II in Figure 1. Typically, the time period of vibration of the structure increases during partial or full liquefaction. If there is a stiffness discontinuity across the pile cap i.e. between the pile groups and the columns above, failure may occur at this interface, as it is here that the structure can deform most, i.e. has higher flexibility. This is explained in detail using a typical example. This is similar to the "soft-storey" consideration termed by structural engineers.

Imperfections in the pile

Piles can never be assumed to be straight or free from residual stresses resulting from the construction process. Piles are likely to have greater out-of-line straightness than ordinary structural columns in buildings and, more significantly, may suffer yielding during installation. Also, piles are relatively more slender than building columns.

Table 2: Summary of reported pile bending measurements

Deviation of base x (m)	Pile length L (m)	x/L (%)	Pile and soil details
1.37	18.0	7.6	End bearing pile passing through silt and resting on schist bedrock.
3.04	27.4	11.1	Friction pile in sand.
3.19	25.9	12.3	End bearing pile passing through silt and resting on dense sand.
11	60	18.3	End bearing pre-cast concrete pile passing through soft clay and resting on bedrock.
1.85	24.6	7.5	Friction steel H pile passing through stiff clay and dense sand
2.16	42.6	5.1	End bearing steel H pile through soft to stiff clay, to shale bedrock.
2.65	40	6.7	End bearing pre-cast concrete pile, through soft clay to mudstone bedrock
1.06	12	8.9	Endbearing steel H pile through soft to firm clay, to limestone bedrock.

Table 2 collates some of the reported pile bending measurements following [17]. Figure 4 explains the terminology used in the table. It is clear that pile bending or deviation during driving is not restricted to a particular soil type, pile system, or pile length. Buckling being sensitive to imperfections, this becomes a major consideration in design. Apart from out-of-line straightness, a pile may be thin walled and therefore vulnerable to local buckling. This has been observed in a number of cases where offshore piles have collapsed during driving due to progressive closure of the internal dimensions – the initiating mechanism being local buckling. Thus the design method has also to consider the interaction between local and global buckling.

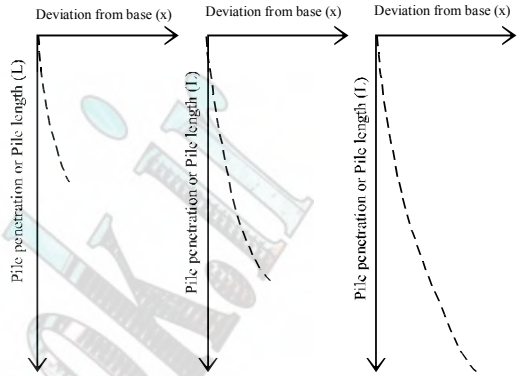

Figure 4: Imperfections in driven pile.

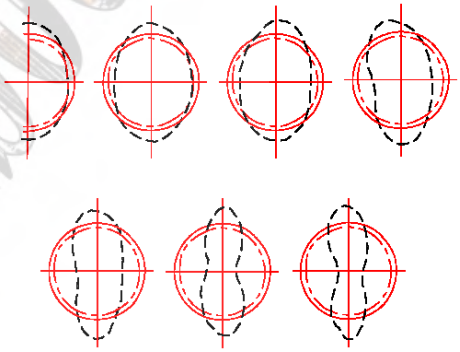

Figure 5: Cross-sections showing progressive pile collapse during driving following an initial deformation of the pile tip.

Lateral loads on pile

During earthquakes, the predominant lateral loads acting on a pile are:

1. Inertial loads due to the superstructure that are oscillatory in nature, and
2. Loads due to ground movement commonly known as kinematic effects. This load may be of two types, transient (during shaking due to the dynamic effects) and residual (after the shaking ceased due to lateral spreading).

JRA (1996) is the only code that provides design guidelines to estimate the residual lateral forces in the pile due to lateral spreading. Kinematic loads and inertial loads may act in two different planes, as shown in Figure 6. Thus the pile not only has axial stress but also may have bending stresses in two axes. The pile thus represents a most general form of beam-column element (Columns carrying lateral loads) with bi-axial bending. The analysis of such a problem demands an understanding

of the way in which various structural actions interact with each other, i.e. how the axial load influences the amplification of lateral deflection produced due to lateral loads.

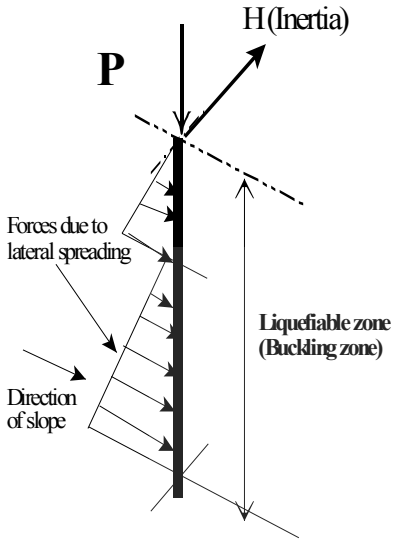

Figure 6: Generalized loading in a single pile

In the simplest cases, i.e. when the section is a short column, (i.e. unsupported length to diameter less than 12), the superposition principle can be applied, allowing direct summation of the load effects. For long columns, careful consideration of the complicated interaction needs to be accounted for. Designing such members needs a three-dimensional interaction diagram where the axes are: Axial (P), Major-axis moment (M_X) and minor-axis moment (M_Y). The shape of the interaction curve of M_X and M_Y, depends on the ratio of actual load P to the ultimate axial load capacity in the absence of moments (P_{UZ}). Equation 1 shows the equation of the curve for a general value of (P/P_{UZ}).

$$\left[\frac{M_X}{M_{UX}}\right]^{\alpha_N} + \left[\frac{M_Y}{M_{UY}}\right]^{\alpha_N} = 1 \qquad (1)$$

where

M_X = Moment about the major axis due to ultimate loads.
M_Y = Moment about the minor axis due to ultimate loads
M_{UX} = The maximum moment capacity assuming ultimate axial load P and bending about the major axis only.
M_{UY}= The maximum moment capacity assuming axial load P and bending about the minor axis only.
α_N = A numeric coefficient the value of which depends on the ratio (P/P_{UZ}) where P_{UZ} is the ultimate axial load capacity in the absence of moments. Typical values of α_N are presented in Table 3.

Table 3: Relationship between (P/P_{UZ}) and α_N

P/P_{UZ}	≤ 0.2	0.4	0.6	≥ 0.8
α_N	1.0	1.33	1.67	2.0

While this bi-axial bending is a possibility, the worst loading remains when the inertial loads and kinematic loads act in the same direction. Some experimental results exist on the phase relationships between kinematic and inertial load, University of California (Davis).

Fixity at the non-liquefiable dense layer below the liquefiable layer

Ideally, fixity of a pile at its tip can be achieved by grouting into a rock-socket. Fixity at the junction between liquefiable and non-liquefiable soils below the liquefiable soils is, however, impossible. It must be recalled that the base of a liquefied soil layer is at zero effective stress, and therefore acts temporarily as a free surface for any underlying soil. Fixity therefore requires pile penetration of several diameters into the dense soil.

Reference [18] developed an approximate procedure for analyzing partially embedded piles. In the procedure, the partially embedded pile is assumed to be fixed at some point in the ground, the depth of which depends on the relative stiffness between the soil and the pile. This method, widely used in practice, involves the computation of stiffness factor T for a particular combination of pile and soil defined by equation 2.

$$T = \sqrt[5]{\frac{EI}{\eta_h}} \qquad (2)$$

where
EI = Stiffness of the pile
η_h= Modulus of subgrade reaction having units of Force/Length^3.

The depth to pile diameter ratio to the point of fixity is taken as 1.8T for granular soils whose modulus increases linearly with depth as recommended by [18]. Figure 7 summarizes the results from a simple calculation assuming that the non-liquefiable dense soil beneath the liquefiable layer is sand of 80% relative density. The Modulus of subgrade reaction is taken as 40MN/m^3, following the API code. The graph shows that fixity can be achieved by embedding the pile to a depth of 3 to 5 times the pile diameter.

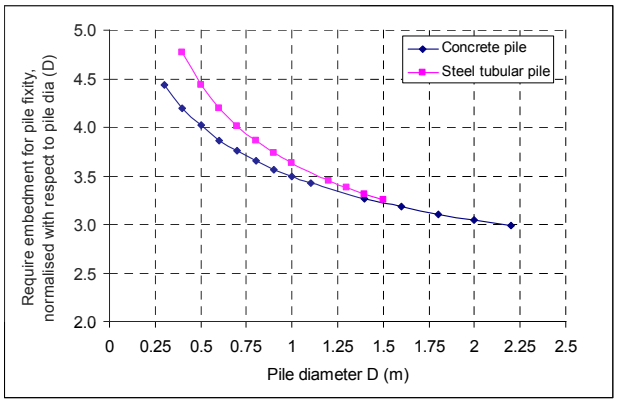

Figure 7: Depth required for fixity.

The unsupported length to be considered for buckling calculations should be the liquefiable soil thickness plus the depth of fixity.

Amplification of lateral deflections in the presence of axial load

As mentioned earlier, a pile can be best described as a

beam-column i.e. a column section carrying lateral loads. A general equation can be described as follows.

$$EI\frac{d^4y}{dx^4}+\left[P-\int_0^x f(x)dx\right]\frac{d^2y}{dx^2}-f(x)\frac{dy}{dx}+k(x).y=0 \quad (3)$$

where

P = External axial compressive force applied at the top of the pile i.e. $x = 0$

f (x) is the friction per unit length

k (x) is the modulus of subgrade reaction.

The above equation suggests that if part of the soil surrounding the pile loses its effective stress, then f(x) = 0 and k(x) will be near zero, and the equation reduces to Euler's buckling equation. The theoretical buckling load can be estimated by equation 4.

$$P_{cr}=\frac{\pi^2 EI}{L_{eff}^2} \quad (4)$$ where

L_{eff} = Effective length of the pile in the unsupported zone. This depends on the boundary condition of the pile below and above the support loss zone, see Bhattacharya et al (2004). Figure 8 shows 4 theoretically possible cases.

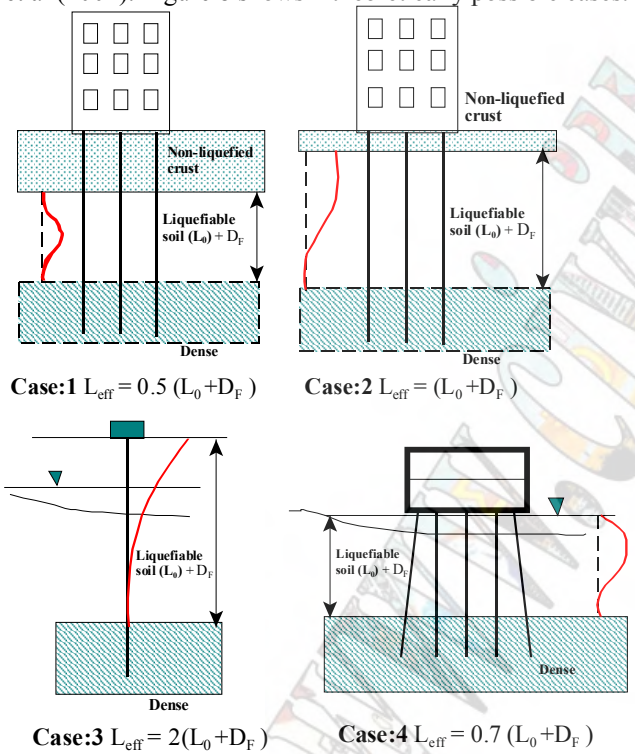

Case:1 $L_{eff} = 0.5\ (L_0 + D_F)$ **Case:2** $L_{eff} = (L_0 + D_F)$

Case:3 $L_{eff} = 2(L_0 + D_F)$ **Case:4** $L_{eff} = 0.7\ (L_0 + D_F)$

Figure 8: Effective length of piles

Rankine (1866) recognized that the failure load of structural columns predicted by equation 4 is more than the actual failure load (P_F) i.e. equation 4 is unconservative. This is because buckling is very sensitive to imperfections in the pile and to lateral loads. The collapse also involves an interaction between elastic and plastic modes of failure.

Lateral loads and geometrical imperfections both lead to the creation of bending moments in addition to axial loads. Bending moments have to be accompanied by stress resultants that diminish the cross-sectional area available for carrying the axial load, so the failure load P_F is less than the plastic squash load (P_P) given by A. σ_y (A=area of the pile section, σ_y is the yield stress of the material). Equally, the growth of zones of plastic bending reduces the effective elastic modulus of the section, thereby reducing the critical load for buckling, so that $P_F < P_{cr}$. Furthermore these processes feed on each other, as explained in Horne and Merchant (1965). As the elastic critical load is approached, all bending effects are magnified. If lateral loads in the absence of axial load would create a maximum lateral displacement δ_o in the critical mode-shape of buckling, then the displacement δ under the same lateral loads but with a co-existing axial load P is given by equation 5 following Timoshenko and Young (1961).

$$\left(\frac{\delta}{\delta_0}\right)=\frac{1}{1-\left(\frac{P}{P_{cr}}\right)} \quad (5)$$

The same magnification factor applies to any initial out-of-line straightness of the pile in the mode shape of potential buckling. Correspondingly, all curvatures are similarly magnified and so are the bending strains induced in the column by its lateral loads or eccentricities. The progression towards plastic bending failure is accelerated as axial loads approach the elastic critical load (P_{cr}). Not only do axial loads induce extra bending moments (P-Δ effects), but the full plastic bending resistance cannot be mobilized due to the fact that part of the pile section is required to carry the axial loads. Equation 5 indicates that for a column carrying an axial load of half its Euler load, the lateral displacements and therefore bending moments would be 1/(1-0.5) times, i.e. 100% bigger, than those calculated ignoring axial load effects. This is important if significant lateral loads must also be carried. Equation 5 is sketched in Figure 9. In the figure exact equations derived by [19] for different boundary conditions of piles are sketched. The figure shows as the (P/P_{cr}) ratio approaches 1, the amplification of lateral deflections tends to infinity.

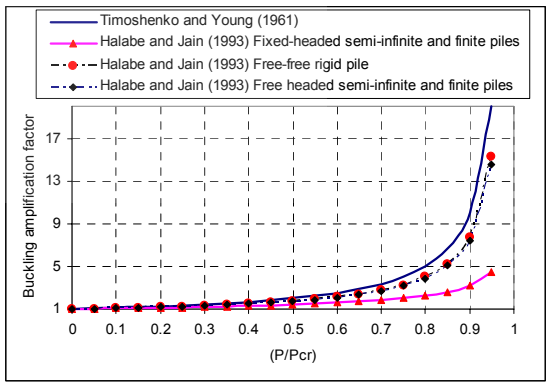

Figure 9: Amplification factors of piles for lateral loads

Soft storey consideration due to stiffness discontinuity at the pile cap due to liquefaction

Figure 10 shows a typical piled structure. Before

liquefaction, the stiffness of the piles beneath the soil is high due to the soil stiffness surrounding it. During and after liquefaction, the stiffness of the pile-soil system in the zone of liquefaction reduces and as a result, the period of the structure increases. The pile cap then acts as continuity between the relatively stiff column above the pile cap and the reduced stiffness of the pile group. Structural engineers generally prefer to keep the stiffness of the storey within 70% of the previous level, see IS 1893, whereas the foundation here effectively acts as a weak or "soft" storey. It is therefore necessary to check against such failure.

The lateral stiffness of a column fixed at one end and free to translate but restrained against rotation at other end as shown in Figure 11 is given by equation 6.

$$\frac{12EI}{L^3} \qquad (6)$$

The force that would result in unit deflection at the top of the column may also be derived from equation 6. The ratio of the stiffness of the pile group to that of a column, for the structure shown in Figure 10, is given by equation 7. Figure 12 shows a typical pile cap supporting the column. The ratio of the second moment of area of a pile group with 4 piles of diameter D spaced at 3×D to that of a column of diameter b is given by equation 8. For simplicity, the contribution of the pile cap itself and the soil between the piles is ignored in this equation.

$$\frac{S_{PG}}{S_C} = \frac{12E_P.I_{PG}.L_C^3}{12E_C.I_C L_P^3} = \left(\frac{I_{PG}}{I_C}\right).\left(\frac{L_C}{L_P}\right)^3 \qquad (7)$$

where

S_{PG} = Stiffness of the pile group

S_C = Stiffness of the column

I_{PG} = Second moment of area of the pile group forming the pile cap for the column.

I_C = Second moment of area of the column section.

L_P = Storey height of the pile = $L_0 + D_F$ (depth of fixity)

L_C= Storey height of the column.

E_C and E_P are the Young's modulus for the materials for the column and pile respectively.

$$\frac{I_{PG}}{I_C} = \frac{4.\frac{\pi}{64}D^4 + 4.\left(\frac{\pi}{4}D^2\right)(1.5D)^2}{\frac{\pi}{64}b^4} = 148\left(\frac{D}{b}\right)^4 \qquad (8)$$

A TYPICAL EXAMPLE

This section will take a particular example to illustrate the importance of this calculation. A group of 4 500mm diameter piles spaced at 1500mm c/c (3 pile diameters) supports a 600mm diameter column. The storey height is 3 metres for the building, i.e. L_C in Figure 10. The ratio of pile group stiffness (S_{PG}) and column stiffness (S_C) when the unsupported length (depth of liquefied soil layer) is 14 metres (L_0 = 12m, D_F=2.0m and thus L_P = 14) is given by equation 9 following equations 7 and 8.

$$\frac{S_{PG}}{S_C} = 148.\left(\frac{0.6}{0.5}\right)^4\left(\frac{3}{14}\right)^3 = 0.7 \qquad (9)$$

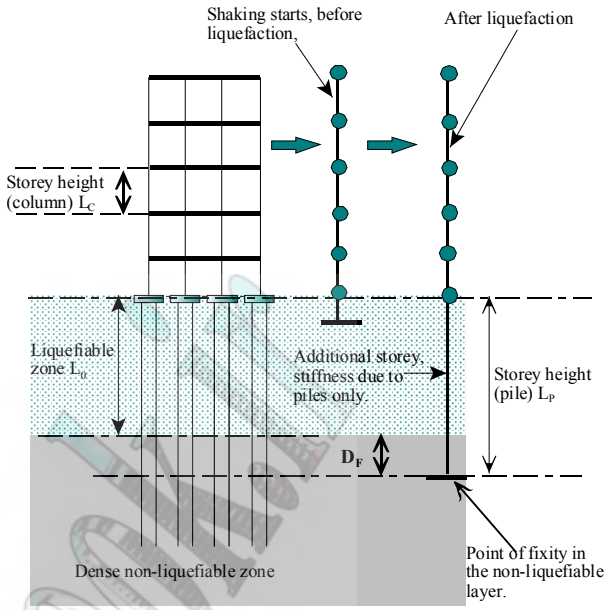

Figure 10: A piled building

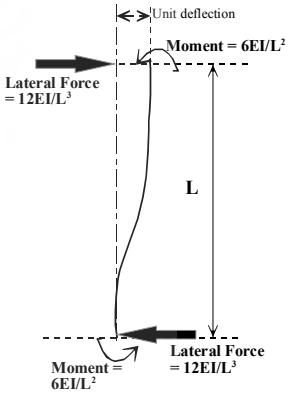

Figure 11: Lateral stiffness of a column fixed.

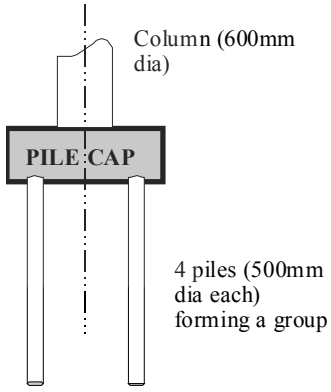

Figure 12: Typical pile-pile cap connection in a building.

This example shows that the physical dimensions used are only just adequate to avoid the "soft" storey type of collapse. This indicates that it is important to carry out such a design check, to avoid a stiffness mismatch between the first floor and the softer pile group below.

CONCLUSIONS

The failure of piled foundations can be classified into two groups:

(a) Structural failure of the pile whereby the load carrying capacity of the foundation drops. The fundamental failure mechanisms that can cause plastic hinge formation in a pile are shear failure, bending failure and buckling failure. The above three forms of failure are often known as LIMIT STATE OF COLLAPSE. It must be mentioned that each of these types of failure can cause a complete collapse of the piled structure.

(b) Failure by excessive settlement, rendering it useless. Often the settlement of piled foundations exceeds the acceptable limits of the structure, which is essentially SERVICEABILITY LIMIT STATE. In this type of failure, the piles may not fail structurally.

Consequently the design steps should include:

1) Finding the point of fixity at the non-liquefiable bearing layer.
2) Estimating the depth of potentially liquefiable soils.
3) Predicting the unsupported length.
4) Estimating the Euler buckling load – and using a Factor of Safety (FOS) of at least 3 (to remain in the linear part of Figure 9). This is the allowable axial load in the pile.
5) Checking the axial load acting on the pile.

The allowable axial load of a pile increases with the length of the pile mainly due to skin friction but also due to the enhanced base capacity at deeper depths. Thus, it is considered important to limit the axial load based on buckling considerations. Reference [4,5] studied 14 case histories of pile foundation performance during earthquakes and showed that a slenderness ratio L_{eff}/r_{min} of 50 could differentiate between the good and poor performance. (r_{min}= minimum radius of gyration, given by $\sqrt{I/A}$, I being the second moment of area of the pile and A the area. This implies that for a solid concrete pile, the unsupported length to the pile diameter should not exceed about 12.

Although many sophisticated numerical models and computer programs are available or can be written to incorporate the P-Δ effect, it is considered useful to have a simple back-of-the envelope type design chart based on basic or classical understanding. This can be particularly helpful for preliminary design and checking and interpreting results obtained from other sophisticated analyses.

REFERENCES

[1] K. Tokimatsu and Asaka, Y (1998): "Effects of liquefaction-induced ground displacements on pile performance in the 1995 Hyogoken-Nambu earthquake", Soils and Foundations, pp 163-177, Sep 1998.

[2] Yoshida, N and Hamada, M (1990) Damage to foundation piles and deformation pattern of ground due to liquefaction-induced permanent ground deformation, Proc 3rd Japan-US Workshop on Earthquake Resistant design of Lifeline Facilities and Countermeasures for Soil Liquefaction, San Francisco, pp 147-161.

[3] BTL Committee (2000) Study on liquefaction and lateral spreading in the 1995 Hyogoken-Nambu earthquake, Building Research Report No 138, Building Research Institute, Ministry of Construction, Japan (in Japanese).

[4] Bhattacharya, S., "Pile instability during earthquake liquefaction," PhD thesis, University of Cambridge, 2003.

[5] Bhattacharya, S., Madabhushi, S.P.G. and Bolton, M.D. (2004): An alternative mechanism of pile failure in liquefiable deposits during earthquakes, Geotechnique 54, No 3, 203-213.

[6] Knappett, J.A and Madabhushi, S.P.G (2005): "Instability of slender pile groups during earthquake-induced liquefaction", Proceedings SECED Young Engineers Conference, University of Bath (U.K), 21-22 March, 2005.

[7] Knappett, J.A and Madabhushi, S.P.G (2005): "Modelling of liquefaction-induced instability in pile groups", Workshop on piled foundations, University of California (Davis), ASCE Special Publications.

[8] Lin, S.S., Tseng, Y.J., Chiang, C.C. and Hung, C.L. (2005): Damage of piles caused by lateral spreading – Back study of three cases. Workshop on piled foundations. University of California (Davis), ASCE Special Publication.

[9] Kimura, Y and Tokimatsu, K (2004): Buckling load of slender piles in liquefied soil; Proc 39th Japan National Conference on Geotechnical Engineering, Niigata, pp 1579-1580.

[10] Bhattacharya, S Madabhushi, S.P.G and Bolton, M.D (2003): Pile instability during earthquake liquefaction, 16th Engineering Mechanics Conference of ASCE, Seattle, 16th to 18th July, Paper no 404.

[11] Kuwabara, F. and Yoneda, K (1998): An investigation on the pile foundations damaged by liquefaction at the Hyogoken-Nambu earthquake, Journal of Structural Construction Engineering., AIJ, No 507 (in Japanese).

[12] Hausler, E and Sitar, N (2003), Performance of Soil Improvement Techniques in Earthquakes, Pacific Earthquake Engineering Research Centre, Report.

[13] 2001 Bhuj (India) Earthquake Reconnaissance Report, EERI (USA)

[14] Mori, S. Numata, A and Guan, A.B. (2000): Damage to a piled foundation due to liquefied ground motion, 12th WCEE.

[15] Cubrinovski, M. and Ishihara, K. and Kijima, T (2001): Effects of liquefaction on seismic response of a storage tank on pile foundations, Proc 4th Int. Conf of Recent advances in geotechnical earthquake engineering, San Diego, California, paper no 6.15.

[16] Takada, S. (1968): "Steel reinforced concrete structures", General report on the Niigata earthquake of 1964, Tokyo Electrical Engineering College Press; editor: H.Kawasumi.

[17] Burgress, I.W and Hanna, T.H (1977): "Do piles bend during driving and, if so, does it matter?", British Geotechnical Association, Informal discussion, 7th Dec 1977, ICE, One Great George Street.

[18] Davisson, M.T and Robinson, K.E (1965): Bending and buckling of partially embedded piles, Proceedings of the 6th ICDMFE, Vol 2, pp 243-246.

[19] Halabe, U.B. and Jain, S.K (1993): Amplification factors for piles, Journal of Engineering Structures (Butterworth-Heinemann Ltd), Volume 15, No 2, pp 97 to 101.

3-D Numerical simulation of shake-table tests on piles subjected to lateral spreading

M. Cubrinovski[1], H. Sugita[2], K. Tokimatsu[3], M. Sato[4], K. Ishihara[5], Y. Tsukamoto[5], T. Kamata[5]
[1]*Department of Civil Engineering, University of Canterbury, Christchurch, New Zealand*
[2]*Public Works Research Institute, Tsukuba, Japan*
[3]*Department of Architecture and Building Engineering, Tokyo Institute of Technology, Tokyo, Japan*
[4]*Hyogo Earthquake Engineering Research Center, NIED, Miki, Japan*
[5]*Department of Civil Engineering, Tokyo University of Science, Noda, Japan*

Abstract

A fully-coupled effective stress method of analysis incorporating an elastic-plastic constitutive model specifically designed for modelling sand behaviour was used to numerically simulate shake table experiments on piles in laterally spreading soils. Details of numerical procedures including modelling of stress-strain behaviour of sand, identification of the initial stress state and 3-D dynamic analysis of the soil-pile system are presented in this paper. Primary objective of the simulation was to assess the accuracy of the 3-D analysis in predicting the response of the pile foundation and to identify parameters that are critically important for successful numerical simulation of lateral spreading experiments. The computed response is compared to that measured in the test and key features of the behaviour of the ground, foundation piles and sheet pile wall are discussed.

Keywords—*3-D effective stress analysis, lateral spreading, liquefaction, piles, shake-table test*

INTRODUCTION

The dynamic analysis based on the effective stress principle has been established as one of the principal tools for analysis of liquefaction problems. Over the past two decades, the application of the effective stress analysis has been gradually extended from the 1-D site response analysis to more complex 2-D analyses involving earth structures and soil-structure interaction systems. Recently, attempts have been made to apply this method to a three-dimensional analysis of large-deformation problems. When applying this analysis to large-deformation problems such as those associated with lateral spreading of liquefied soils, questions arise about the accuracy of the prediction as well as about key numerical parameters influencing the analysis. This paper examines some of these aspects by using 3-D numerical simulations of medium-scale shake table experiments on piles subjected to spreading of liquefied soils.

This study was conducted within a benchmark research project [1] in relation to the future experiments planned for execution with the recently built large-scale shake table, in Miki city, Japan (E-Defense). One of the research objectives in this project was to investigate the behaviour of piles in liquefied soils undergoing lateral spreading, from both experimental and numerical viewpoints. A series of shake-table experiments on piles embedded in liquefiable soils was conducted for this purpose and 3-D numerical simulations were carried out to predict the behaviour of the piles. The principal objective of the numerical simulations was to assess the accuracy and capability of an advanced 3-D effective stress analysis in predicting the response of piles to lateral spreading. In this paper, results of the 3-D analysis are compared with the behaviour observed in the shake table tests, and key features of the behaviour of the ground and foundation piles are discussed.

DESCRIPTIPON OF THE EXPERIMENT

A series of shake-table experiments on piles subjected to lateral spreading was conducted at the Public Works Research Institute (PWRI), Tsukuba, Japan [1]. Various factors were varied in these experiments such as the amplitude and direction of shaking, mass of pile cap and number and arrangement of piles. In this paper, the numerical simulation of one of these tests is presented and discussed in detail.

The physical model of the experiment in question is schematically shown in Fig. 1. It consists of a pile foundation embedded in liquefiable sand deposit, located in the vicinity of a sheet pile wall (waterfront). The pile foundation consists of 9 stainless steel piles arranged in a 3x3 group with a spacing of 2.5 diameters. Each pile has a length of 1.45 m, diameter of 50.8 mm, thickness of 1.5 mm and flexural rigidity of EI = 12.8 kN-m^2. The piles are fixed at the base (GL-165cm) and rigidly connected to a pile cap at the top (GL-20cm). The mass of the pile cap is 21.6kg.

The pile foundation is embedded in 1.8 m thick sand deposit consisting of three-layers: a crust layer of coarse sand above the water table overlying a loose saturated layer of Toyoura sand (Dr=35%) and a dense layer of Toyoura sand (Dr=90%), at the base. The layers have thicknesses of 40 cm, 90 cm and 50 cm respectively.

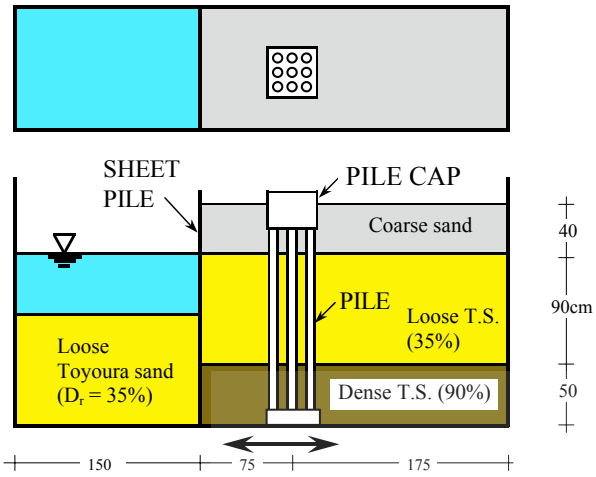

Figure 1: Schematic plot of plan view and side view of the soil-pile model used in the experiment

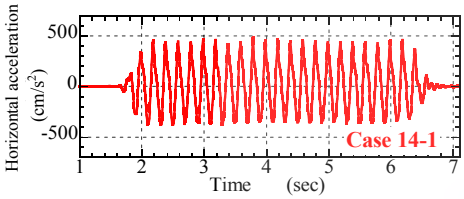

Figure 2: Horizontal accelerations recorded at the shake table

The submerged sand in front of the sheet pile wall is also loose Toyoura sand with a relative density of about 35 %. A relatively rigid steel plate with a thickness of 6 mm was used for the sheet pile, which was set free to move horizontally and rotate at its base.

The model was built in a rigid container bottom-fixed at the shake table, and was subjected to a horizontal base excitation in the longitudinal direction (perpendicular to the sheet pile wall). The shake table motion consisted of 20 uniform cycles with a frequency of 5 Hz and peak amplitude of about 470 cm/sec^2, as shown in Fig. 2. A large number of accelerometers, pore pressure transducers, displacement and pressure gauges were used to measure the response of the piles and ground in the test. Pairs of strain gauges were installed at 12 elevations along the length of the piles for measuring bending strains. Details of the experimental setup, layout of the instrumentation and results of the tests are given in [1].

METHOD OF ANALYSIS AND NUMERICAL PROCEDURES

The shake table experiment was numerically simulated using a 3-D dynamic analysis based on the effective stress principle [2] incorporating an elastic-plastic constitutive model specifically designed for modelling sand behaviour [3, 4]. Key features of the analysis including material modelling and employed numerical procedures are described in this section.

Material Modelling

The employed elastic-plastic model for sand (Stress-Density Model) is based on the state concept, and therefore it incorporates the combined effects of density and confining stress on sand behaviour. Consequently, the model has a capacity to simulate deformational behaviour of sand at all densities and stress states by using a single set of material parameters. The particular parameters of the constitutive model for Toyoura sand have been established in a previous comprehensive study [3, 4] using results of a series of torsional tests including monotonic drained p'-constant tests, monotonic undrained tests and cyclic undrained (liquefaction) tests. These model parameters are summarized in Table 1.

Table 1: Model parameters for Toyoura sand

Type	Parameter		Value
Elastic	Shear constant	A	250
	Poisson's ratio	ν	0.15
	Exponent	n	0.60
State	Quasi steady state line:		(e, p')-values
Stress-strain curve	Peak stress ratio coef.	a_1 , b_1	0.592,
	Max. shear modulus coef.	a_2 , b_2	291 , 55
	Min. shear modulus coef.	a_3 , b_3	98 , 13
	Degradation constant	f	4
Dilatancy	Dilatancy coef. (small strains)	μ_o	0.15
	Critical state stress ratio	M	0.607
	Dilatancy strain	S_c	0.0055

Scaled-down 1-g shake table models are characterized by relatively low stresses in the ground model. Thus, for the model shown in Fig. 1, the effective overburden stress in the loose sand was mostly in the range between 6 kPa and 14 kPa. Since low confining stresses are known to affect both the stress-strain behaviour and liquefaction resistance of sands, in the element test simulations and determination of model parameters particular attention was given to the modelling of sand behaviour at low confining stresses. Thus, using the model parameters listed in Table 1 and different values for the initial void ratio of e = 0.839, 0.802 and 0.653 which correspond to a relative density of D_r = 40 %, 50 % and 90 % respectively, element test simulations were conducted for these three relative densities at low initial confining stresses of 10-20 kPa. Figure 3 shows the liquefaction resistance curves simulated with the model. The experimental data that served as a target in the element test simulations included both results from tests on samples under confining stress of 98 kPa [5] and data from tests with very low confining stress of 9.8 kPa [6]. The latter test data were considered representative of the liquefaction resistance of the ground model prepared in the shake table test and were therefore the principal target in the simulations.

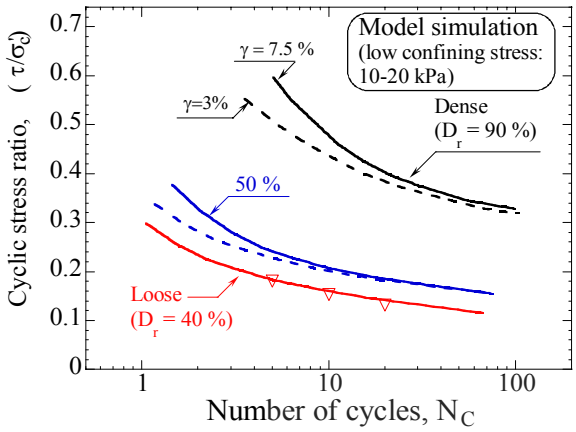

Figure 3: Model simulations of liquefaction resistance of Toyoura sand at different relative densities and low confining stress

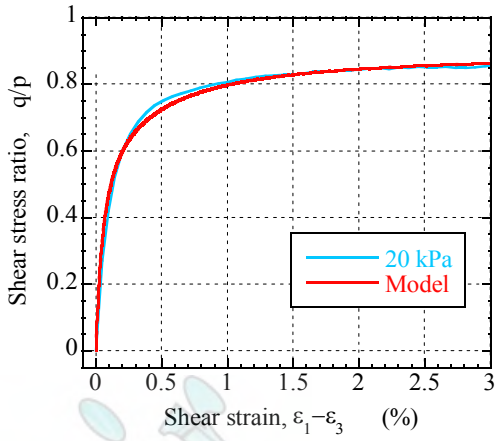

Figure 4: Model simulation of stress-strain curve of coarse sand observed in drained triaxial test at confining stress of 20 kPa

Stress-strain parameters of the coarse sand (surface layer in the ground model) were evaluated using results from a series of drained triaxial compression tests at confining stresses of 20, 40, 60 and 80 kPa [1]. The stress-strain curve observed in the test with the smallest confining stress of 20 kPa was adopted as a target curve in the evaluation of model parameters. As shown in Fig. 4, the adopted model parameters for the coarse sand provide reasonably good simulation of the stress-strain curve observed in the laboratory test.

It was anticipated that the behaviour of the foundation piles and the sheet pile wall will remain in the range of elastic deformations, and therefore, the piles, pile-cap and sheet-pile wall were modelled as linear elastic materials.

Initial Stress Analysis

Considering the preparation of the ground model and employed experimental procedures prior to the application of shaking, two phases in the development of the initial stress state in the soil can be distinguished. In the first phase during the soil deposition and preparation of the ground model, the sheet pile wall was supported with horizontal struts, as shown schematically in Fig. 5a. Hence, the soil deposit underwent consolidation under constrained lateral deformation imposed by the rigid container and the sheet pile wall. Before the application of shaking, the horizontal supports were removed (Fig. 5b) thus subjecting the sheet pile wall to an unbalanced earth pressure from the backfill soil and submerged sand causing lateral movement towards the water and significant change of the stresses in the soil mass. An initial stress analysis was conducted to simulate the lateral loads as above and evaluate the resulting stresses in the soil.

Details about the horizontal support as above were not available to the predictors at the time of execution of the initial stress analysis. Instead, it was assumed in the analysis that the sheet pile was fixed in the horizontal direction during the model preparation and that the sand deposit practically underwent K_o-consolidation. Based on this reasoning, it was assumed that the vertical and horizontal stresses in the soil attained after consolidation might be approximated as $\sigma'_v = \gamma h$ and $\sigma'_h = K_o \sigma'_v$ where $K_o = 0.5$ for the loose sand and $K_o = 0.4$ for the crust soil and dense base layer were adopted, as illustrated schematically in Fig. 6a. In the initial stress analysis, the post-consolidation stress estimated as above was used as an initial stress state, and then, a distributed lateral load simulating the resultant earth pressure induced upon the removal of the horizontal supports was applied to the sheet pile wall, as depicted in Fig. 6b. Here, the lateral load was defined by the difference between the lateral soil

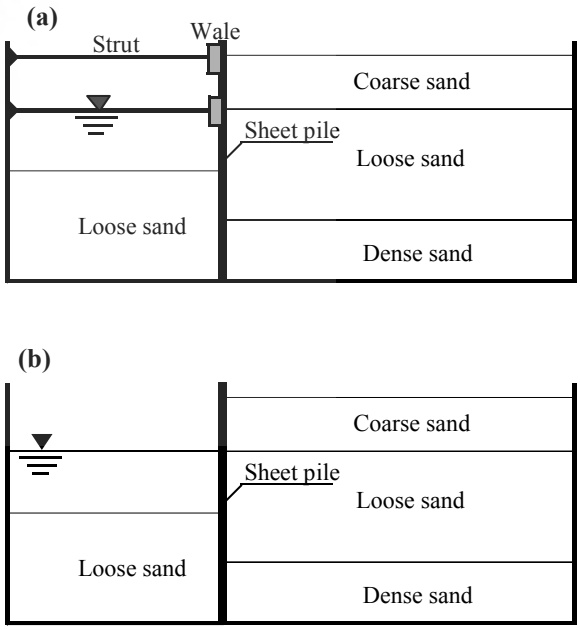

Figure 5: Schematic illustration of the experimental procedures: (a) horizontally constrained sheet pile wall during soil deposition; (b) unconstrained sheet pile wall prior to shaking

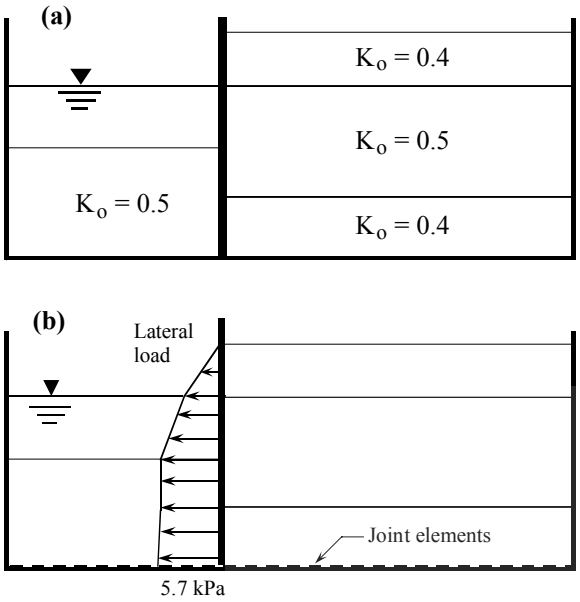

Figure 6: Schematic illustration of initial stress analysis: (a) assumed K_o values for the post-consolidation stress; (b) applied lateral load simulating the resultant soil pressure induced upon the removal of struts

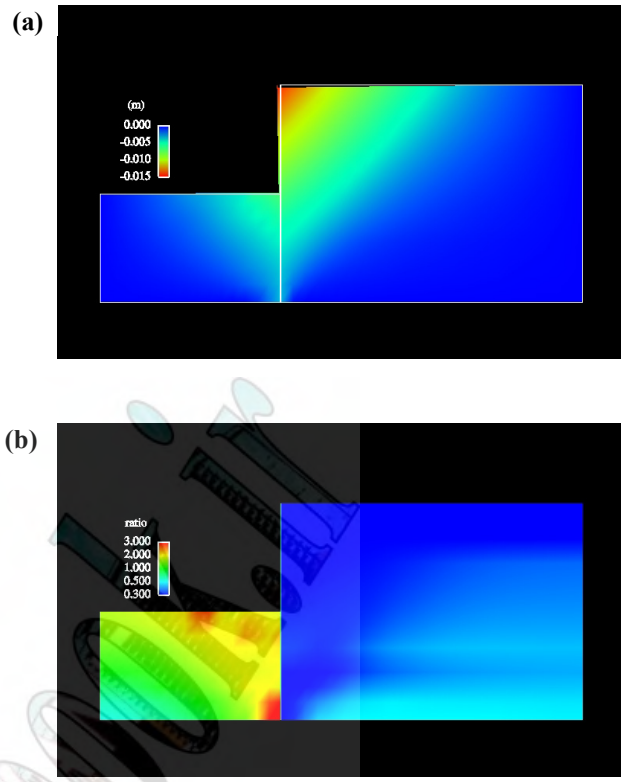

Figure 7: Results of initial stress analysis: (a) computed horizontal displacements; (b) computed normal stress ratios (σ'_h / σ'_v)

pressures in the backfill soil and submerged sand throughout the depth of the deposit. In order to simplify the initial stress analysis and avoid problems associated with stress concentration and boundary effects, the presence of the pile foundation was ignored and the calculation was made using 2-D plane strain analysis.

Results of the initial stress analysis are summarized in Fig. 7a and Fig. 7b where computed horizontal displacements and normal stress ratios are depicted respectively. The displacement pattern computed in the analysis was found to be very similar to that observed in the test in which the sheet pile moved laterally and slightly tilted towards the water as a result of the induced lateral soil pressure. In accordance with the deformation mode involving horizontal expansion of the backfills and contraction of the submerged sand, settlement occurred in the backfill soil whereas heaving occurred in the submerged sand in front of the wall. In the analysis, a permanent horizontal displacement of 1.42 cm was computed at the top of the sheet pile (Fig. 7a) whereas the corresponding displacement observed in the experiment was about 3 cm. The maximum settlement computed in the analysis was approximately 1.1 cm.

The lateral movement of the sheet pile wall and surrounding soil resulted in relaxation of the lateral stresses in the backfill soil towards the active state with values of $K = \sigma'_h / \sigma'_v$ mostly around 0.3 in the vicinity of the sheet pile wall and their gradual increase to about 0.5 with the lateral distance from the sheet pile wall. On the other hand, the stress ratio values in the submerged sand approached the passive state in the soil adjacent to the wall showing gradual decrease in K from about 3 to 1 with the distance from the sheet pile wall. The horizontal shear stress ratios were mostly in the range of τ_{hv} / σ'_v = 0.02–0.20. By and large, significant shear stresses were generated in the soil deposit upon removing the horizontal supports of the sheet pile wall. The stresses computed in the analysis as above were employed as initial stresses in the subsequent dynamic analysis.

3-D Dynamic Analysis

A fully coupled 3-D finite-element analysis based on the effective stress principle was carried out to simulate the response of the soil-pile model during the shaking. The employed numerical model consisted of eight-node solid elements and beam elements representing the soil and the piles respectively. Solid elements were also used for modelling the pile cap and sheet pile wall. As shown in Fig. 8, half of the model was adopted in the analysis by cutting the physical model along its axis of symmetry in the longitudinal direction. Therefore, only 6 piles were included in the numerical model.

The lateral boundaries of the model were fixed in the horizontal directions thus representing the constraints imposed by the rigid container in the test. Horizontal displacements in the y-direction were also constrained along the symmetry boundary of the model. Along all soil-sheet pile and soil-pile interfaces, a condition was specified that yields the soil and the pile to share identical displacements in the horizontal direction, but that allows different vertical displacements between the soil and the

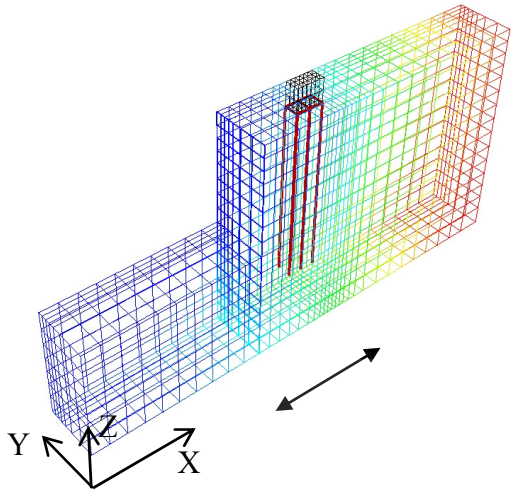

Figure 8: Numerical model used in the dynamic analysis

pile and hence unconstrained settlement of the ground.

The analysis was conducted assuming drained conditions with permeability of k = 3x10^{-5} and 6x10^{-5} m/sec for the dense and loose Toyoura sand respectively. The total computational time was 6 sec with a time step of Δt = 0.0004 sec. Thus, only the response during the shaking was computed, and therefore, effects of pore pressure dissipation and post-shaking deformation are beyond the scope of this paper. Rayleigh damping with parameters α=0 and β=0.003 was employed for numerical damping in the analysis.

COMPARISON OF COMPUTED AND MEASURED RESPONSE

The experiment was characterized by a sudden pore pressure build-up and liquefaction of the loose sand layers within the first two cycles of shaking. In the course of the subsequent shaking after the liquefaction, a large lateral movement of the sheet pile wall occurred towards the water accompanied with spreading of the liquefied backfills. The lateral displacement of the sheet pile wall at the end of the shaking was about 38 cm. In spite of the large lateral ground movement associated with the spreading of liquefied soils, the peak lateral displacement of the foundation piles was only 12 mm thus exhibiting typical behaviour for relatively stiff piles. By and large, the ground and pile response features as above were very well predicted in the analysis including the development of excess pore pressures and extent of liquefaction, ground deformation pattern (Fig. 9), and displacements and bending stresses of the piles. The only notable exception from this trend of accurate predictions was the displacement of the sheet pile wall which was underestimated in the analysis. In what follows, characteristic features of the behaviour of the ground, foundation piles and sheet pile wall are discussed through comparisons between the computed and measured data.

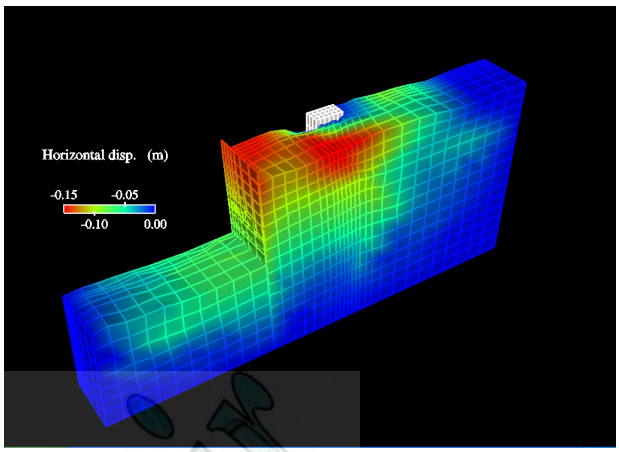

Figure 9: Computed ground displacements at the end of shaking

Sheet Pile Wall

The computed lateral displacement of the sheet pile wall at the end of shaking was about 12 cm or approximately 1/3 of the one measured in the test, as depicted in Fig. 10. When evaluating the numerical response it is worth noticing that, in the experiment, the sheet pile wall moved laterally nearly 40 cm while the peak displacement of the foundation piles was only slightly above 1 cm. Since the closest row of piles was located about 60 cm from the sheet pile wall, the equivalent lateral strain in the crust layer and shear strain in the loose sand layer exceeded 60 % and 40 % respectively. It is considered that the above configuration in conjunction with the coarse mesh and high-order integration rule (eight Gauss points) created severe numerical conditions that limited the lateral movement of the sheet pile wall. This reasoning was supported by results of 2-D analysis in which a low order integration rule (one Gauss point) was used and restraining effects from the foundation piles were eliminated. As shown in Fig. 10, a large displacement of the sheet pile wall similar to that observed in the test was computed in the 2-D analysis. It is to be mentioned however that correctly predicting the movement of the sheet pile wall was found to be the most difficult task in the 3-D numerical simulations of the lateral spreading experiments.

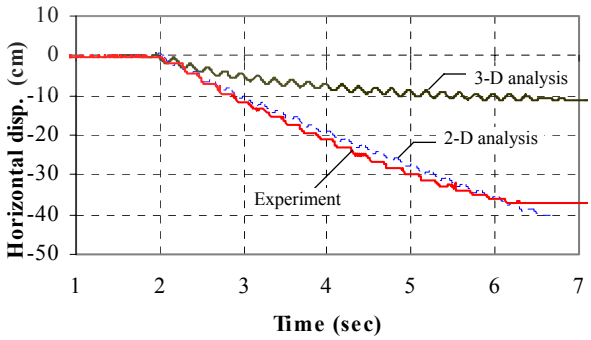

Figure 10: Comparison of computed and recorded horizontal displacement at the top of the sheet pile wall

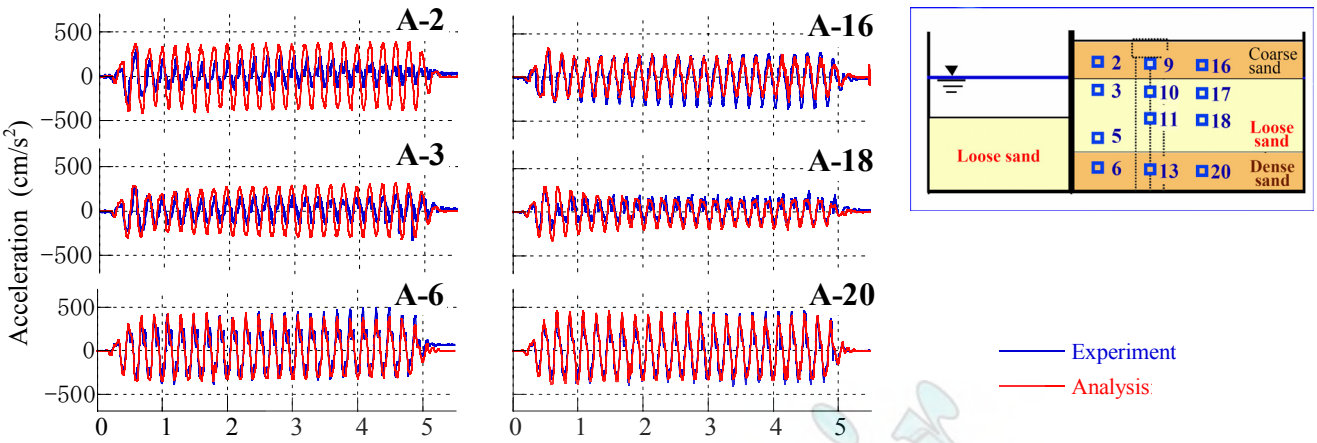

Figure 11: Comparison of computed and recorded horizontal accelerations of the ground

Ground Response

The computed ground response was found to be in good agreement with that observed in the experiment including the deformation pattern, development of excess pore pressures and ground accelerations. To illustrate the accuracy of the numerical prediction, comparisons of computed and measured horizontal accelerations at 6 different locations in the backfill soils are presented in Fig. 11 for two arrays of accelerometers located between the pile foundation and the sheet pile wall (A2-A6) and behind the pile foundation (A16-A20) respectively. In the dense sand layer near the base of the model (A6 and A20), the accelerations preserved the amplitudes of the input motion whereas clear signs of liquefaction are evident in the large reduction of the accelerations in the loose Toyoura sand, at A3 and A18. Slight amplification of the motion is seen in the accelerations of the surface layer. The largest disagreement between the computed and recorded accelerations is seen for the accelerometer A2 where the computed accelerations are larger than the measured ones. As discussed previously, the conditions in the analysis are the most severe for this portion of the ground model where large relative displacements and constraining effects of boundary conditions at the sheet pile and foundation piles concurrently occur.

Horizontal Displacement of Piles

Comparison of computed and measured horizontal displacements of the pile cap (top of the foundation piles) is shown in Fig. 12. Both the computed and recorded displacements sharply increased towards the water (negative amplitude on the ordinate) in the first two cycles and reached the peak displacement at the third cycle of shaking. The measured and computed peak horizontal displacements are 12.3 mm and 11.4 mm respectively. Very good agreement is seen between the computed and measured displacements for the first 10-12 cycles or up to about 4 seconds on the time scale. Over the last two seconds of shaking the displacement recorded in the test tends to gradually decrease both in amplitude and in its residual component. It is conceivable that this reduction in the displacement was caused by the settlement of the ground and consequent reduction in the lateral loads from the surface layer on the foundation. Namely, the settlement of the ground resulted in a gradual reduction in the contact area between the crust layer and the pile cap until eventually the contact was completely lost as the ground surface subsided below the bottom of the pile cap. The reduction in the lateral displacements as above could not be captured in the analysis since the initial configuration of the model was preserved throughout the entire calculation.

As previously described, very large relative displacement between the pile cap and the adjacent soil was observed in the test, and therefore, attention was given to the modelling of the soil-pile cap interface. In order to investigate the effects of the modelling of this interface on the response of the piles, preliminary analyses were conducted considering two different conditions at the interface: one that allows the soil on the front side and along the side of the pile cap to move independently from the pile cap, and the other in which the surrounding soil was set to move together with the pile cap. It was found that, in general, the former condition provided better simulation of the behaviour observed in the experiment yet the effects on the peak displacements and bending moments of the piles were negligible. Needless to say, the interface modelling allowing large relative displacements between the elements of the pile cap and adjacent soil increased the potential for numerical instability in the analysis.

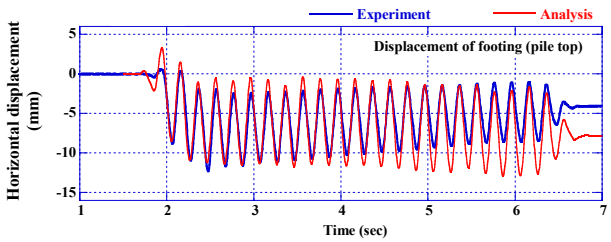

Figure 12: Comparison of computed and recorded horizontal displacement at the pile cap

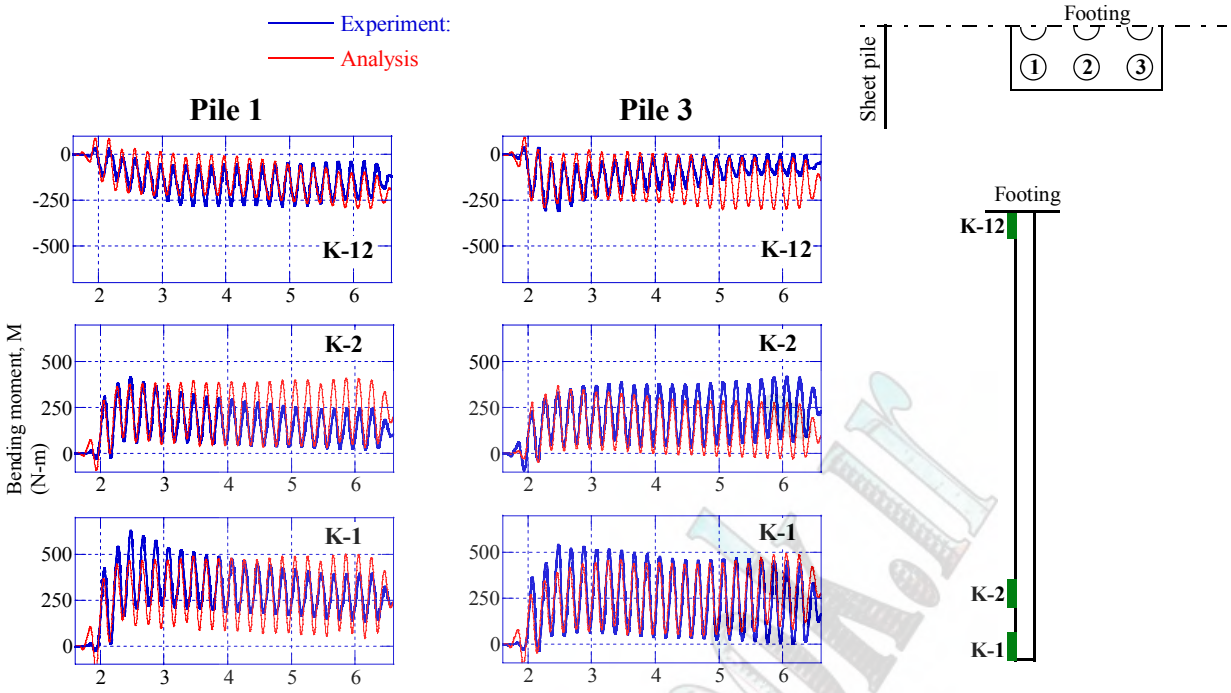

Figure 13: Computed and recorded bending moment time histories at three elevations of Pile1 and Pile 3

Bending Moments

Time histories of computed and recorded bending moments are compared in Fig. 13, for two piles of the foundation. As shown in the inset of this figure, Pile 1 and Pile 3 are corner piles in the nearest row to the sheet pile and on the backfill side respectively. The uppermost plots in Fig. 13 are for strain gauges near the pile top (K-12) while the two lower sets of time histories are for strain gauges near the base of the pile (K-1 and K-2). By and large, good agreement is seen between the computed and recorded bending moments with features of agreement or disagreement similar to those discussed for the lateral displacements.

The computed and measured bending moments along the length of Pile 1 are shown in Fig. 14. These are bending moments at the time of the peak response observed in the third cycle of shaking, as described previously. In general, similar accuracy as that shown in Fig. 14 was obtained for all piles irrespective of their particular position within the group. Some differences were evident between the bending moments of the front row piles and those on the backfill side, particularly near the top of the piles. However, these differences were not pronounced, and for all piles the maximum bending response was obtained near the base of the pile.

It is important to recognize that good accuracy has been achieved in predicting the response of the foundation piles in spite of the underestimated displacement of the sheet pile wall thus indicating that the displacements at the waterfront are not critically important for correctly predicting the response of relatively stiff piles.

CONCLUSIONS

A fully-coupled effective stress method of analysis incorporating an elastic-plastic model for sand was used to numerically simulate a shake table experiment on piles subjected to lateral spreading. The objective of this study was to investigate the accuracy of the 3-D effective stress analysis in predicting the behaviour of piles and to identify key modelling features and numerical parameters

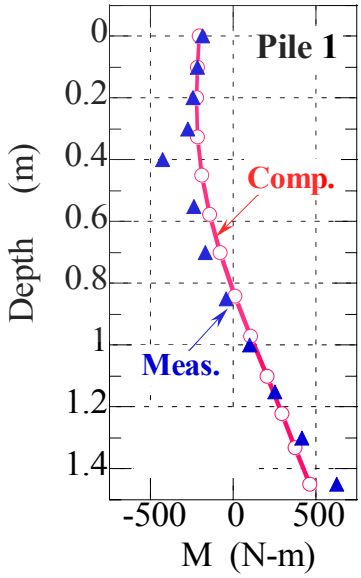

Figure 14: Computed and recorded bending moments along the length of Pile 1 at the time of peak lateral displacement

influencing the analytical response. The key findings of this study can be summarized as follows:

1) The computed ground response was found to be in good agreement with that observed in the experiment including the deformation pattern, development of excess pore pressures, extent of liquefaction and ground accelerations. In the experiment, the loose sand layer liquefied within the first two cycles of shaking causing large lateral movement of the sheet pile wall. This lateral movement was associated with spreading of the backfill soils and settlement of the ground in a typical fashion for lateral spreading of liquefied soils. This pattern in the ground movement including 3D effects and flow-like movement of the soil around the foundation was captured in the analysis. The computed ground accelerations were also in very good agreement with those measured in the tests. In the shallow part of the deposit between the sheet pile wall and the foundation, some discrepancies between the computed and recorded responses were seen apparently due to severe numerical conditions imposed by the large lateral displacements and boundary constraints.

2) The computed response of the foundation piles including both lateral displacements and bending moments was in very good agreement with the response measured in the experiment. Particularly good agreement was obtained for the peak response of the piles.

3) The displacement of the sheet pile wall was underestimated in the analysis and was about 1/3 of the measured one. The results of this study indicate however that the displacements at the waterfront are not critically important for correctly predicting the response of relatively stiff piles.

4) The 3-D effective stress analysis involves a number of complex procedures associated with the constitutive and numerical modelling that require due attention. First of all, it is essential that the constitutive model provides reasonably good accuracy in predicting the excess pore pressures and ground deformation, thus allowing proper evaluation of the soil-pile interaction effects. The particular stress conditions and anticipated deformation pattern are equally important for correctly predicting the behaviour of the piles. In this study, for example, particular attention was given to the initial stress state and relatively low stresses associated with the ground model in the shake table test. In addition, boundary conditions and soil-pile interfaces were specified so that large deformation and typical displacement pattern associated with lateral spreading can be simulated. It is to be mentioned that reasonably good accuracy in simulating the behaviour of piles was achieved in the 3-D analysis despite using conventional beam elements for modelling of the piles.

ACKNOWLEDGMENTS

This study was conducted within the "Special project for earthquake disaster mitigation in urban areas: (II) Significant improvement of seismic performance of structures, (3) Test and analysis of soil-pile-structure systems," in preparation of the large-scale shake table experiments of E-Defense, in Miki city, Japan. This collaborative project was sponsored by the Ministry of Education, Culture, Sports, Science and Technology of Japan (MEXT) and was conducted under the guidance of the National research Institute for Earth Science and Disaster Prevention (NIED), Japan.

REFERENCES

[1] "Special project for earthquake disaster mitigation in urban areas: (II) Significant improvement of seismic performance of structures, (3) Test and analysis of soil-pile-structure systems," Technical Report of NIED, ch. 3.3, 2004.

[2] Diana-J3: Finite-element program for effective stress analysis of two-phase soil medium.

[3] Cubrinovski, M. and Ishihara, K., "Modelling of sand behaviour based on state concept," *Soils and Foundations*, 38 (3), pp. 115-127, 1998.

[4] Cubrinovski, M. and Ishihara, K., "State concept and modified elastoplasticity for sand modelling", *Soils and Foundations*, 38 (4), pp. 213-225, 1998.

[5] Tatsuoka, F., Ochi, K., Fujii, S. and Okamoto, M., "Cyclic triaxial and torsional strength of sands for different preparation methods," *Soils and Foundations*, 26(3), pp. 23-41, 1986.

[6] Kawakami, S., Itakura, D., Sato, T. and Koseki, J., "Liquefaction characteristics of sand from cyclic torsional shear test at low confining pressure," *Proc. 33rd Annual Conf. of Japanese Geotech. Soc.*, D-7, pp. 725-726, 1998.

Piles under seismic excitation and lateral spreading in liquefiable soils

W.D Liam Finn[1], N. Fujita[2]
[1]*Department of Civil Engineering, University of British Columbia, Vancouver, Canada*
[2]*Anabuki Komuten, Takamatsu, Japan*

Abstract

This paper presents an assessment of engineering practice for estimating the bending moments and shearing forces in pile foundations in liquefiable soils during earthquake shaking, considering both kinematic and inertial interactions, The pile cap deflections and stiffness components are also studied. Special attention is devoted to the case where a non-liquefiable surface layer of soil covers the liquefiable zone. This is considered the worst case scenario, when there are significant post-liquefaction ground displacements.

Keywords— *inertial interaction, kinematic interaction, liquefaction, piles, pile cap stiffness*

INTRODUCTION

Large post liquefaction displacements can occur in liquefiable soils and these can be very damaging to pile foundations. These potential deformations can control design but they are very difficult to predict reliably. In engineering practice, the displacements at the top of the liquefied layer are often estimated by empirical formulas based on field data from past earthquakes. The first predictor equation was developed in Japan by Hamada et al., [1]. Comprehensive predictor equations have been developed by Youd et al., [2] in the USA which are used in practice in North America. An updated version of the Hamada equation was adopted in1997 by the Japan Water Works Association [3] which is based only on ground slope and thickness of the liquefied layer. Bardet et al., [4] developed a method for modeling post–liquefaction displacements on a regional basis. In practice, the free field displacements are assumed usually to vary linearly from top to bottom of the liquefied layer. The deformed shape of a pile foundation caused by these displacements is shown in Fig. 1. In this case there is a non-liquefiable surface layer. This is considered to the most critical case and is considered to control design.

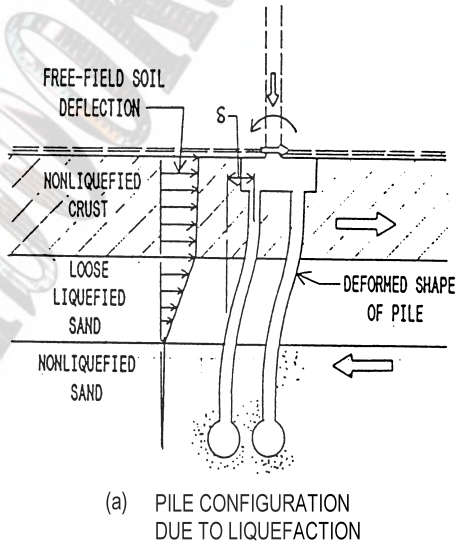

Fig. 1: Distortion of pile foundation by lateral soil displacements [6].

METHODS OF ANALYSIS

Force Analysis

A force based analysis is recommended in a number of Japanese design codes, JWWA [3] and JRA [5], for analysis of piles foundations in liquefied soils, undergoing lateral flow. The underlying concepts are rational and simple. On the basis of back analysis of case histories, a non-liquefied surface layer, which is transported on the moving liquefied soil, is assumed to apply passive pressure on the foundation and a liquefied layer is assumed to apply a pressure of about 30% of the overburden pressure. The design pressure distributions against the foundation are shown in Fig. 2. These pressure distributions are associated with potentially large ground displacements, similar to those that foundations close to sea-walls experienced during the 1995 Kobe earthquake. The pressures can be reduced by 50% for distances between 50m and 100m from the wall. The codes should be consulted before use. Only the essential outline is given here to indicate what is available for solving this difficult problem. An attempt to convert the distance criteria to displacement criteria to broaden the area of application of the method was abandoned because the two databases available [7, 8] give significantly different displacement /distance relationships.

Brandenburg et al., [9] studied load transfer from the non-liquefied layer to piles in centrifuge tests.. Their results show that the load transfer is a function of displacement. Large relative displacements are required to develop peak load against the piles. Their study confirms in a qualitative way the guideline in JRA [5].

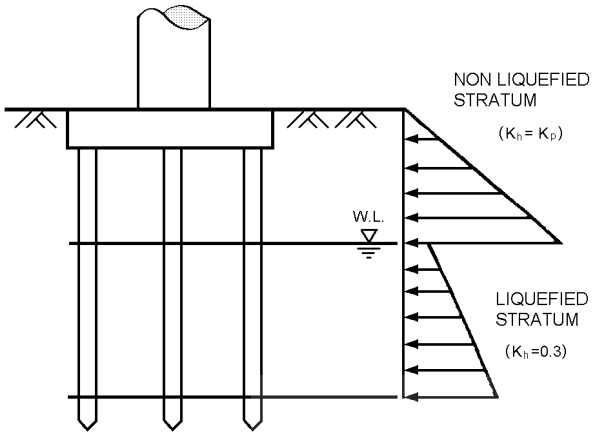

Fig. 2: Design pressures against piles in laterally flowing liquefied soils [5].

DISPLACEMENT ANALYSIS

The first step in the analysis is to estimate the post-liquefaction free field displacements using one of the empirical formulas or by an appropriate method of analysis. These displacements are usually assumed to vary linearly from the top to the bottom of the upper liquefied layer. These displacements are then applied to the free field ends of the near field springs in the very general Winkler model shown in Fig. 3 and a static analysis is performed. Degraded p-y curves have usually been used for this kind of analysis.

The effects of lateral spreading on 1.5m diameter CDIH piles supporting the structure shown in Fig. 11 later were analyzed as described above. The free field displacements at the surface were estimated to be between 15 cm and 25cm. The computed pile displacements, assuming that the pile head is fixed against rotation, are shown in Fig 4.

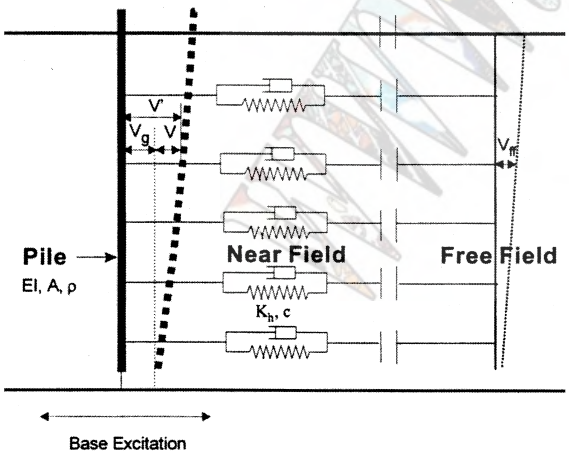

Fig. 3: Winkler spring model for pile foundation analysis [10].

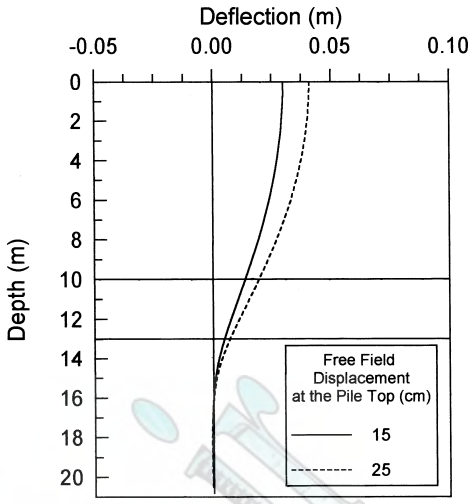

Fig. 4: Calculated pile displacements for specified ground displacements [6].

The resulting bending moments are shown in Fig. 5. Note that the maximum bending moment is near the interface between the liquefied and non-liquefied layers.

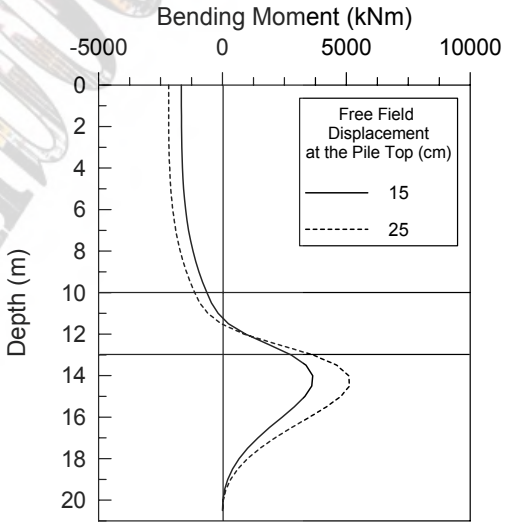

Fig. 5: Pile moments induced by field displacement [6].

SOIL PROPERTIES FOR DISPLACEMENT ANALYSIS

Japanese Practice

In Japanese practice, the springs in the Winkler model are linearly elastic-plastic. The elastic soil stiffness is determined by semi-empirical code formulas related to the elastic modulus of the soil. This modulus is deduced from plate loading tests or correlations with the SPT- N measurements and therefore includes some non-linear effects. In some design offices, the spring constant is taken as zero in liquefied soil.

The JRA code [5] for highway bridges recommends reductions in the spring stiffness for use in liquefiable soils that depend on the factor of safety, F_L, against liquefaction. The cyclic resistance ratio against

liquefaction, R_L, is determined by cyclic triaxial tests on undisturbed samples obtained by in-situ freezing techniques. The resistance ratio is modified depending on whether Type 1 or Type 2 motions are used in design, by a factor c_w giving the modified resistance $R = c_w R_L$. The code should be consulted for details of the 2 types of motions. Generally Type 1 motions are the design motions before the Kobe earthquake. Type 2 motions were introduced to provide protection against another earthquake like Kobe. The factor c_w has a value of 1 for Type 1 motions. For Type 2 motions, $c_w = 1.0$ for $R_L \leq 0.1$, $c_w = 3.3\ R_L + 0.67$ for $0.1 < R_L \leq 0.4$ and $c_w = 2.0$ for $0.4 < R_L$. The code should be consulted for details.

North American Practice

There is no general consensus in North American practice on the appropriate modeling of the Winkler springs for post-liquefaction analysis. The basis of most analyses is a degraded form of the API p-y curves [11] or curves due to Reese et al. [12]. The practice is to multiply the p-y curves, by a uniform degradation factor called the p-multiplier, which ranges in value from 0.3 to 0.1. This follows from the original work of Liu and Dobry [13]. Wilson et al. [14] confirmed these results but showed that the p-multiplier for fully liquefied soil depended also on relative density, ranging in value from 0.1-0.2 for sand at about 35% relative density and 0.25-0.35 for a relative density of about 55%.

Wilson et al. [14] also found that the resistance of the loose sand did not pick up even at substantial strains but that the denser sand, after an initial strain range in which it showed little strength, picked up strength with increasing strain. This finding suggests that the good performance of the degraded p-y curves which did not include an initial range of low or zero strength, must be test specific and the p-multiplier may be expected to vary from one design situation to another.

The very low initial strength range in the laboratory p-y curves followed by a range of increasing strength is related to the dilatancy characteristics of sand at low effective stresses. Similar behavior is observed in tests in which undrained monotonic loading is conducted on sand specimens after cyclic loading to liquefaction. Typical examples of this phenomenon from undrained torsional tests by Yasuda et al. [15] are shown in Fig. 6. The strain range of very low undrained resistance after liquefaction depends also on the number of cycles of stress reversal the sand experiences after liquefaction before the undrained monotonic loading is applied.

LATERAL SPREADING IN CENTRIFUGE TESTS

Brandenburg et al [16] conducted a very comprehensive series of tests to determine the effects of various parameters on pile performance in laterally spreading ground. Centrifuge tests on single piles and 2-pile groups were conducted on the centrifuge at UC Davis. Pipe piles were used. The single piles had prototype diameters of 0.36m, 0.73m, and 1.45m. The piles in the

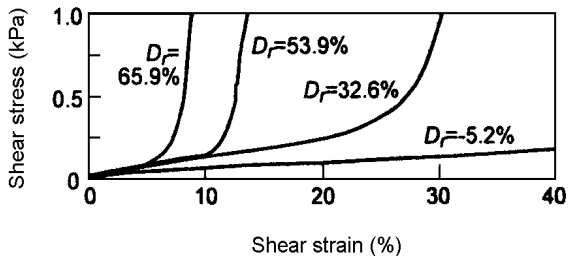

Fig.6: Post-liquefaction undrained stress-strain behaviour of sand [15].

pile group were 0.73m in diameter. The foundation soil profile sloped gently towards a channel at one end of the shear box as shown in Fig. 7. It consisted of a non-liquefiable layer of clay, with a thin sand cover, underlain by a liquefiable layer of sand with a relative density of 35% and a base layer of dense sand at a relative density of 85%.

The responses of the piles to lateral spreading were analyzed using a non-linear Winkler model. The Matlock [17] static p-y relation for soft clay and the Reese et al., (1974) static p-y relation for sand were used to represent the non-linear interaction springs. A p-multiplier = 0.1 was used for fully liquefied sand.

Three cases were considered: (1) original p-y curves for loose sand with p-multiplier = 0.1 and only the properties in the loose liquefied sand were degraded for pore pressure effects : (2) original p-y curves for loose sand with p-multiplier = 0.1and reductions in p-y stiffness and capacity of the dense sand due to pore water pressures in that layer; (3) the same as case (2) except that the standard p-y adjustment factors to the static p-y curves for cyclic loading were made also. As Brandenburg et al. [16] point out these latter adjustments were developed for the large number of water wave generated stress cycles associated with a major offshore storm and are probably not applicable to the far fewer significant stress cycles associated with earthquake shaking. Comparison of measured and computed responses led to a number of important conclusions. The three most important ones are quoted verbatim below.

- the recorded responses of the three single piles and the one group of two piles could be modeled

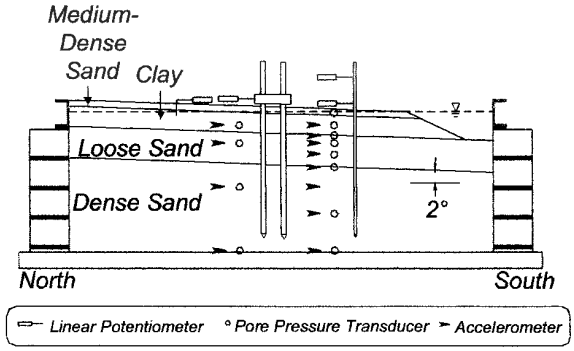

Fig.7: Centrifuge model test [16].

within the range of parameter variations that were studied, but all the responses could not be accurately modeled with the same set of input parameters.

- the parameter studies also showed that the standard adjustments to p-y relations for cyclic loading would have resulted in substantial under-prediction of lateral loads from the clay layer
- the calculated bending moments were more sensitive to the strength and p-y parameters for the upper clay and sand cover layers, and less sensitive to the p-multiplier assigned to the liquefied layer.

These findings pose clear warnings for anyone contemplating analyses of piles in laterally spreading soils using the standard North American p-y curves. The crucial factors seem to be; the dominating role of the non-liquefiable layer, the inappropriateness of using the standard cyclic loading reduction factors for earthquake shaking and the large uncertainty associated with the results of any analysis.

Some of the problems of arriving at a generally acceptable set of Winkler non-linear p-y curves for analysis of post liquefaction deformations in liquefiable soils arise from the assumed form of the curves. If the form is incompatible with the actual stress-strain behaviour of the soil, problems in simulating the responses of different pile foundations with one set of p-y curves is not surprising. The North American p-y curves are concave downwards and this is not compatible with the post-liquefaction stress-strain behavior of liquefiable sand under monotonic loading which is concave upwards [Fig. 6].

MCEER/ATC (2003): LATERAL SPREADING AND BRIDGE FOUNDATIONS

In 2003 MCEER/ATC [contains recommended guidelines for evaluation and design of pile foundations for bridges in laterally spreading soil. .

The guidelines cover the same two ground conditions as the Japanese codes; liquefiable soils with and without a non-liquefiable surface layer. Liquefied soils are assigned a residual strength and treated as cohesive soils. The friction angle of cohesionless soils is taken as 10^0 when the factor of safety against liquefaction is FS = 1.0 and is interpolated between for $1.0 \leq FS \leq 1.5$. The modulus of subgrade reaction is reduced in a similar way, with a value equal to that of a soft clay at FS = 1.0. The recommendations for analysis are presented in the context of single pile response. If there is no non-liquefiable layer at the surface, the likely result is that the soil will flow around the pile and exert passive pressure on it. In this case, the ground deformations are likely to be much greater then the pile deformations as shown in Fig. 8. If there is a non-liquefiable layer at the surface, this layer will either grip the foundation, forcing it to follow the ground deformation, (Fig.9), or the soil will flow around the foundation. In the first case, if the pile cannot withstand structurally the imposed ground displacements, then remedial action is necessary. One option is to retrofit the pile foundation by adding either active or passive piles.

The analysis to determine the number of piles is treated as an uncoupled problem. The Newmark rigid block analysis [19] is suggested for estimating ground displacements. The pinning action of the piles is represented in the sliding block model by their shearing resistance. The displacements can be plotted against the pinning forces as shown in Fig. 10 [20]. The pile displacements needed to mobilize different amounts of shearing resistance are shown also in Fig.10. The intersection of the two curves gives the equilibrium state for the pile foundation. If the displacement meets the performance objective, the retrofitted foundation is satisfactory. The guidelines allow the designer to use more sophisticated methods of analysis, if the benefits justify the additional costs, but it is difficult to see how this judgment can be made without actually doing the analysis.

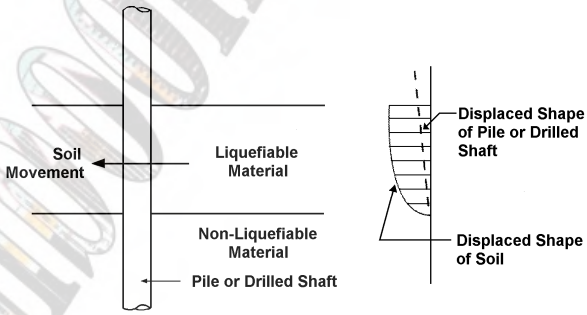

Fig. 8: Pile-soil relative displacements in fully liquefiable soil [18].

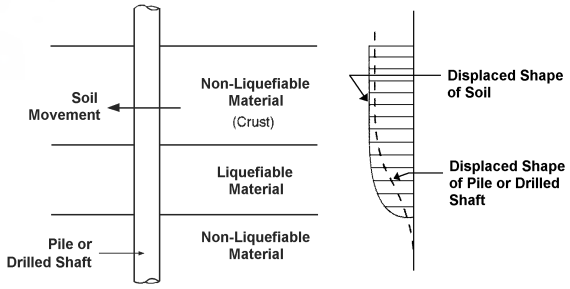

Fig. 9: Pile-soil displacements with non-liquefiable surface layer {18}.

SEISMIC ANALYES

In this section some important problems related to the dynamic response of pile foundations are investigated using nonlinear dynamic effective stress analysis. The computer program Pile-3DEFF [21] was used to perform the analyses. This program is an effective stress version of the total stress program PILE-3D [22.23]. Analyses were conducted to determine the pile cap stiffness components in potentially liquefiable soil, the relative

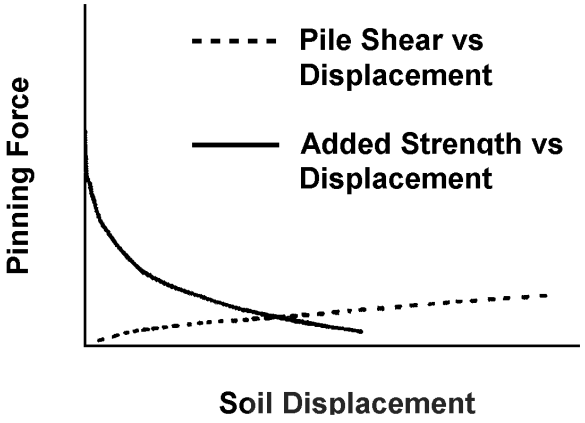

Fig: 10: Determining compatible pile pinning forces [20].

contributions of inertial and kinematic interactions to pile moments and the effects of a nonliquefiable surface layer on pile moments and displacements. As noted earlier, this latter case is considered the critical case for design in laterally spreading ground.

Seismic analyses were conducted on a 1.5 m diameter cast-in-place reinforced concrete pile supporting a column of a 14 storey building. The soil conditions and pile are shown in Fig. 11. The soils in the upper 10m are expected to liquefy or develop high pore water pressures (pwp) during the design earthquake.

The mass mounted on the pile in Fig. 84 represents the mass equivalent of the static reaction force carried by the pile. The purpose in placing the mass on the pile is to model approximately the inertial interaction between the super-structure and the pile foundation. It is mounted on the pile head by a massless support with a stiffness that ensures a period of vibration of 1.4s corresponding to the estimated fundamental period of the prototype structure.

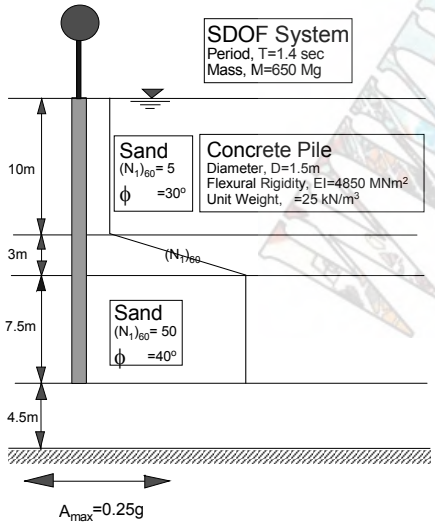

Fig. 11: Model of soil-structure-interaction.

Dynamic effective stress analyses of this system include both inertial and kinematic interactions and the effects of high pore water pressures and liquefaction. Analyses were also conducted without including the mass of the superstructure. These latter analyses give the kinematic deflections and moments. In all these analyses, the non-linearity of the soil and the effects of seismic pore water pressures are taken into account by adjusting the soil properties continuously for current pore water pressures and shear strains.

The peak acceleration of the input acceleration record is 0.25g. and is amplified to 0.4g at the surface.

Pile head stiffnesses in liquefiable soils.

The time histories of pile stiffnesses for the 1.5m foundation pile are shown in Fig. 12 for 3 different conditions; liquefaction, no seismic pore water pressures and high intermediate pressures. Clearly it is not enough to consider liquefaction but to take into account any reasonably high pore water pressures, when evaluating pile head stiffnesses. In this case the major impact on stiffness occurs after the peak ground motions have passed. Then pore water pressures prevent the foundation soils from recovering their stiffnesses as the seismic strains become smaller. The non-liquefiable soils recover fully by the end of shaking.

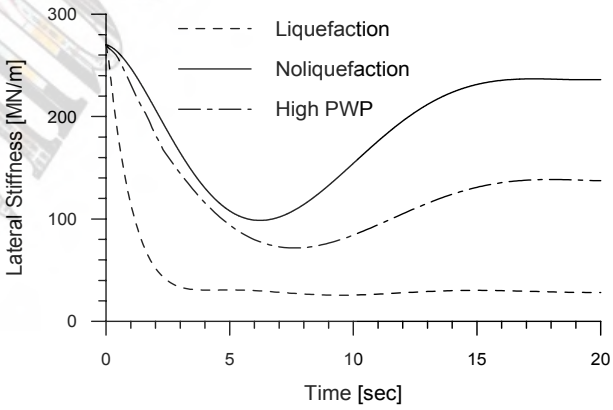

Fig. 12: Time histories of lateral stiffness for various pore water pressures [24].

PILE MOMENTS WITH UPPER CRUST

Inertial and kinematic interactions considered.

The dry crust is assumed to be stiff, corresponding to an overconsolidated clay layer or a layer densified to prevent damages to infrastructure or lighter structures not on piles. Deflections at the instant of maximum pile head displacement are shown in Fig.13.

The displacements are shown for two pile head conditions; no rotation and free to rotate. The pile head displacements are about the same whether the pile head is fixed against rotation or not. This is due to the restraint of the pile by the upper layer and the rigid body relative displacements after liquefaction between the upper and

lower stiff layers.

The bending moments in the pile at the instant of maximum pile head displacement are shown in Fig. 14.

The stiff upper layer greatly increases the moment demand on the pile during earthquake shaking, when the pile cap is fixed against rotation. This pile cap condition is often assumed in design. The moments at the pile head are 30% larger compared to the case without the upper layer (Fig 15) and are almost 100% larger at the interface between the soft and stiff soils. When the pile is fixed against rotation the moments at the pile head and the interface are about the same.

The behaviour of the upper layer is clarified further in the next section which presents results from kinematic analyses.

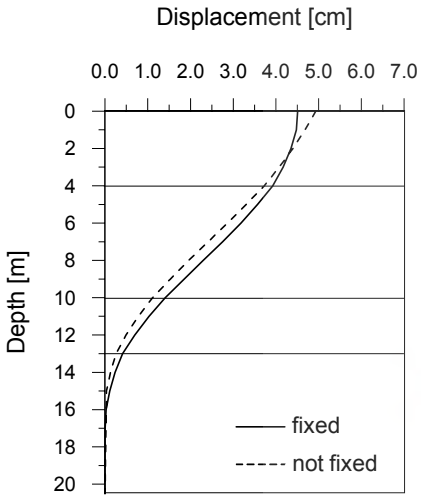

Fig. 13: Pile displacements in layered soils [24].

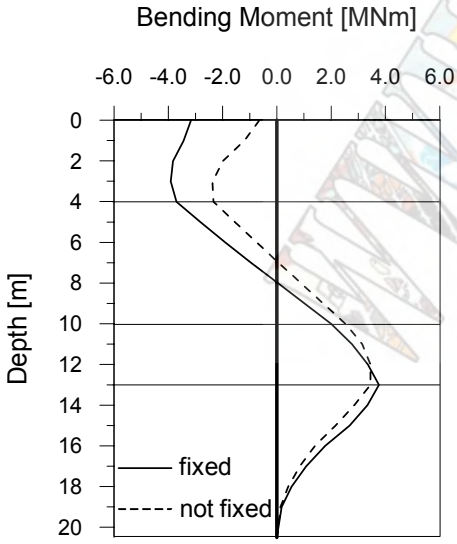

Fig. 14: Pile moments in layered soils [24].

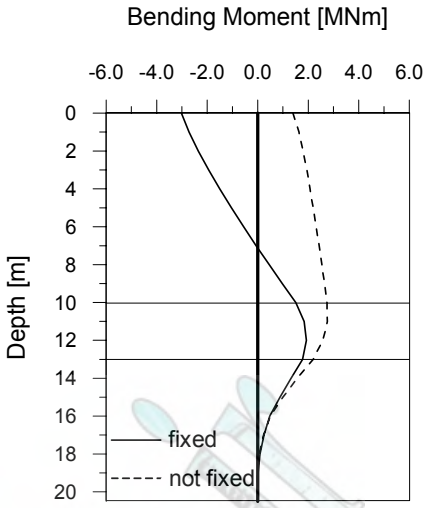

Fig. 15: Moments along the pile [24].

Kinematic interaction only considered

Kinematic analyses were conducted on the 1.5 m diameter pile with and without the stiff surface layer to assess the importance of kinematic interaction. In each case, the pile head was considered either fixed against rotation or not. The kinematic analyses were conducted by removing the super-structural mass in Fig.11 above.

The free field displacements of the foundation soils and the pile displacements, both at the instants of maximum pile head displacement, are shown in Fig.16. It is evident from Fig.16 that the stiff upper layer is moving at this time as a rigid body.

The displacement patterns of the soil in the free field and pile are different. The compatibility of displacements must be preserved along the interfaces, wherever the soil and pile maintain contact during earthquake shaking.

Significant moments and shears may develop in the pile in order to maintain this compatibility requirement as shown in Fig.17 and Fig. 18. In the case of the stiff upper layer, the moments are about twice as large as for the case with no such layer. In both cases, the moments are of the same order as when the inertial mass is incorporated. This indicates that, for these conditions, the kinematic

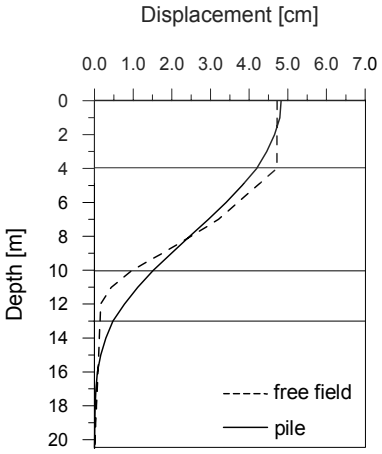

Fig. 16: Displacements of pile and free field [24].

moments dominate the moment response of the foundation.

These analyses were repeated with a much softer surface layer. The 4m surface layer was assigned stiffness compatible with the gravitational effective stresses in the layer. Moments from kinematic analyses only are shown in Fig.19 for the cases where the pile head is fixed against rotation. The results, when there is no non-liquefiable surface layer are also shown for comparison.

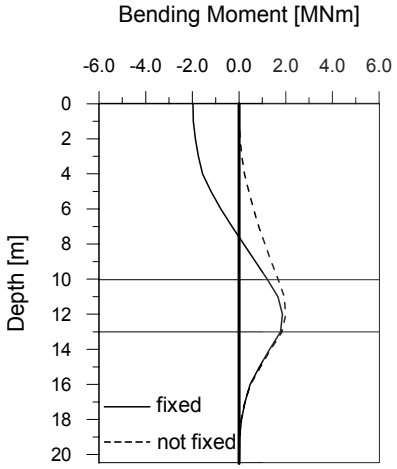

Fig. 17: Kinematic moments along pile with no stiff upper layer [24].

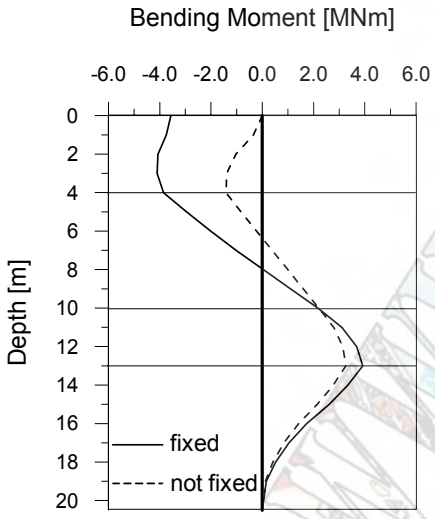

Fig. 18: Bending Moments in pile: stiff upper layer [24].

When the pile head is fixed against rotation, the pile head moment is increased by 75% and the moment at the boundary between soft and stiff soils is increased by 50%. Clearly a non-liquefiable surface layer can have a major effect on the dynamic moments and shears in piles. The pile needs to be analyzed by a method that can pick up these effects. The analyses also make clear that kinematic interaction should not be routinely neglected as in the basic pseudo-static analysis procedure used in practice.

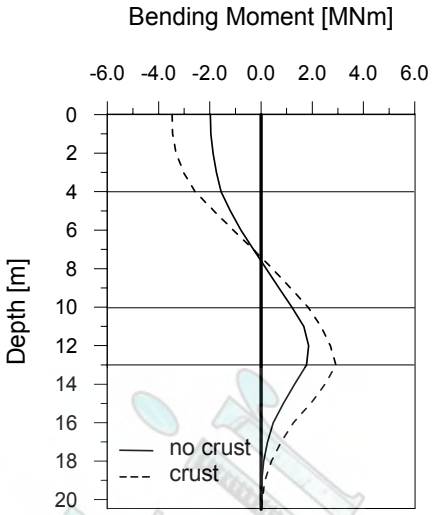

Fig. 19: Kinematic moments: pile head fixed against rotation and no stiff upper layer [24].

Eurocode 8, Part 5, [25] recognizes the importance of kinematic interaction. It directs that the bending moments due to kinematic interaction be computed for important structures in regions of moderate to high seismicity, when the ground profile contains consecutive layers of sharply differing stiffness. These ground conditions are met in liquefiable soils. Some very important cases are, if a non-liquefiable layer overlies the liquefiable layer or if there is a layer of soft clay between two much stiffer layers.

ACKNOWLEDGMENTS

This paper is based on research conducted at Kagawa University in Takamatsu, Japan, when the first and second authors were Anabuki Professor of Foundation Geodynamics and Research Assistant there respectively. The financial assistance of Anabuki Komuten is gratefully acknowledged,

REFERENCES

[1] Hamada, M., Yasuda, S., Isoyama, R. and Emoto, K., *Study on liquefaction induced permanent ground displacements,* Association for Development of Earthquake Prediction, Tokyo, 1986.

[2] Youd, T.L., Hansen, C.M. and Bartlett, S.F., Revised MLR equations for predicting lateral spread displacement, *Proc., 7th U.S.-Japan Workshop on Earthquake Resistant Design of Lifeline Facilities and Countermeasures against Liquefaction,* Technical Report MCEER-99-0019, MCEER, University of buffalo, Buffalo, NY., 2003.

[3] JWWA, *Seismic design and construction guidelines for water supply facilities,* Japan Water Works Association, Tokyo, 1997.

[4] Bardet. J, Tobita, T., Mace, N. and Hu, J., Regional modeling of liquefaction induced ground deformation, *Earthquake Spectra,* Vol. 18, No.1, 19-46, 2002.

[5] JRA, *Specifications for Highway Bridges, Part V, Seismic Design,* Japan Road Association, 1996.

[6] Finn, W.D. Liam, Lessons from recent earthquakes on Foundation Performance, Design and Analysis, Proc., *Inaugural Anabuki Chair Symposium, Faculty of Engineering, Kagawa University, FEKU TN009,* 13-38, 1999.

[7] Ishihara, K., Yasuda, S. and Nagase, H. Soil characteristics and Ground damage, Soils and Foundations, , *Special Issue of Soils and Foundations,* Japanese Geotechnical Society, January, 109-118, 1996

[8] Hamada, M. and Wakamatsu, K. Liquefaction inducedground displacement triggered by quay wall movement, S*pecial Issue of Soils and Foundations,* Japanese Geotechnical Society, Sept, 85-92, 1998.

[9] Brandenburg, S. J., Boulanger, R.W., Chang, D. and Kutter, B.L., Mechanisms of load transfer between pile groups and laterally spreading non-liquefied crust layers, *Proceedings, International Symposium on Earthquake Engineering Commemorating 10th Anniversary of the 1995 Kobe Earthquake (1SEE Kobe 2005)*, Abstract Volume, p 59, 2005.

[10] Thavaraj, T. *Seismic analysis of pile foundations for bridges*, PhD. Thesis, University of British Columbia, Vancouver, Canada, 2001.

[11] API, *Recommended practice for planning, deigning, and constructing fixed offshore platforms,* American Petroleum Institute, 1993.

[12] Reese, L. C., Cox, W. R. and Koop, F. D. Analysis of laterally loaded piles in sand, *Proc., 6th. Annual Offshore Technology Conf,* Houston, Tex., Paper No. 80, 1974

[13] Liu, L. and Dobry, R. "Effect of liquefaction on lateral response of piles by centrifuge tests," *Nat. Ctr for Earthq. Engrg. Res. (NCEER) Bull.,* 9 (1), 7-11. 1995.

[14] Wilson D.W., Boulanger, R.W. and Kutter, B.L., Observed lateral resistance of liquefying sand. *J. of Geotech. and Geoenvir, Engrg.,* ASCE, 126 (10), pp. 898-906, 2000.

[15] Yasuda, S., Yoshida, N., Adachi, K., et al. Simplified practical method for evaluating liquefaction induced flow, Journal of Geotechnical Engineering, Proceedings, JSCE, No. 638/III-49, pp71-89, (in Japanese), 1999.

[16] Brandenburg S.J., Singh, P, Boulanger, R.W, Kutter. B.L., Behavior of piles in laterally spreading ground during earthquakes. *CDROM Proc. 6th CALTRANS Seismic Research Workshop,* Sacramento, CA., 2001.

[17] Matlock, H., Foo, S. H. C. and Bryant, L. M., Simulation of lateral pile behaviour under earthquake loading, *Proc., Earthquake Engineering and Soil Dynamics, ASCE Specialty Conference,* Pasadena, California. 601-619, 1970.

[18] MCEER/ATC, *Recommended LFRD guidelines for the seismic design of highway bridges, Part I: Specifications,* Part I: Commentary and Appendices, MCEER/ ATC49, MCEER Report No. MCEER-03SP03, University of Buffalo, Buffalo, N.Y., 2003.

[19] Newmark, N. M., Effects of earthquakes on dams and embankments, *Geotechnique*, Vol. 15, No. 2, 139-160, 1965

[20] Martin, Geoffrey R., The seismic design of bridges- - geotechnical and foundation design issues, Proc., *ASCE Specialty Conference on Geotechnical Engineering for Transportation projects, Los Angeles, July, ASCE Geotechnical Special Publication, No. 126,* Vol. 1, 137-166, 2004.

[21] Finn, W. D. Liam and Thavaraj, T. Deep foundations in liquefiable soils: Case histories, centrifuge tests and methods of analysis, CD-ROM *Proceedings, 4th Int. Conf. on Recent Advances in Geotechnical Earthquake Engineering and Soil Dynamics,* San Diego, CA, March 26-31, 2001.

[22] Wu, G. and Finn, W. D. Liam, Dynamic elastic analysis of pile foundations using the finite element method in the frequency domain, *Canadian Geotechnical Journal,* 34, No. 1, 34-43, 1997.

[23] Wu, G. and Finn, W. D. Liam, 1997b, Dynamic nonlinear analysis of pile foundations using the finite element method in the time domain, *Canadian Geotechnical Journal, Vol. 34, No.1, 44-52, 1997.*

[24] Finn, W. D. Liam, A Study of piles during earthquakes: issues of design and analysis. The tenth Mallet-Milne Lecture, Bulletin of Earthquake Engineering, Vol. 3, No.2, pp 141-234, 2005

[25] ECN (2003), prEN 1998-5:2003, *Eurocode 8: Design of structures for earthquake resistance, Part 5: Foundations, retaining structures and geotechnical aspects,* European

Design of pile foundation in liquefiable soil using seismic deformation method

K. Hayashi[1], A. Takahashi[2], H. Sugita[2], S. Tanimoto[2]
[1]*Eight Consultants Co., Ltd., Okayama, Japan (Formerly, Public Works Research Institute, Tsukuba, Japan)*
[2]*Public Works Research Institute, Tsukuba, Japan*

Abstract

This paper reports preliminary consideration on application of seismic deformation method (beams on nonlinear Winkler foundation approach) to economical design of pile foundation in liquefiable soil. Some pilot analyses are made to demonstrate pile foundation design procedure concept based on the seismic deformation method considering allowable displacement and pile reserve capacity.

Keywords—*Pile foundation, liquefaction, seismic deformation method*

INTRODUCTION

One of the major sources of earthquake-induced damage to pile foundations is liquefaction of saturated sandy soils. In many cases pile damage occurrs not only at pile heads, but also near interfaces between liquefied and non-liquefied soils due to large liquefied soil deformations [1]. This is a major cause of damage and is consequently a major concern both in research and design practice.

In practice seismic deformation method (beams on nonlinear Winkler foundation approach) is believed to be a promising candidate for pile performance assessment in large soil deformation for conventional design procedure. This method is a pseudo-static analysis on piles subjected to a superstructure inertia force and soil movement through Winkler springs that model soil-pile interaction (kinematic interaction). Although it has already introduced in some of practical design codes in Japan [2], this approach has been mainly used for (1) simulations of damaged piles in an earthquake to identify (or confirm) causes of damage, and (2) final screening in design procedure (e.g., the seismic design for railway structures in Japan). These suggest that the seismic deformation method is not effectively used in practical design even though the method has capability to assess pile performance rationally.

This paper reports preliminary consideration on application of seismic deformation method to economical design of pile in liquefiable soil and demostrates pile foundation design procedure concept considering allowable bridge pier displacement and pile reserve capacity

TARGET BRIDGE PILE FOUNDATION

The target piles form a foundation of one of concrete single column piers supporting a five-span continuous steel plate girder bridge (L=200m (40m×5 spans) and W=12m) through rubber bearings (Fig. 1). The pier height is 10m. The foundation consists of nine 1.2m-cast-in-place concrete piles (32-D32 reinforcement with hoops of D25@150mm) whose length=27.5m. The piles are arranged in 3x3 grids having 3.05m spacing. This foundation is placed in liquefiable ground as shown in Fig. 2.

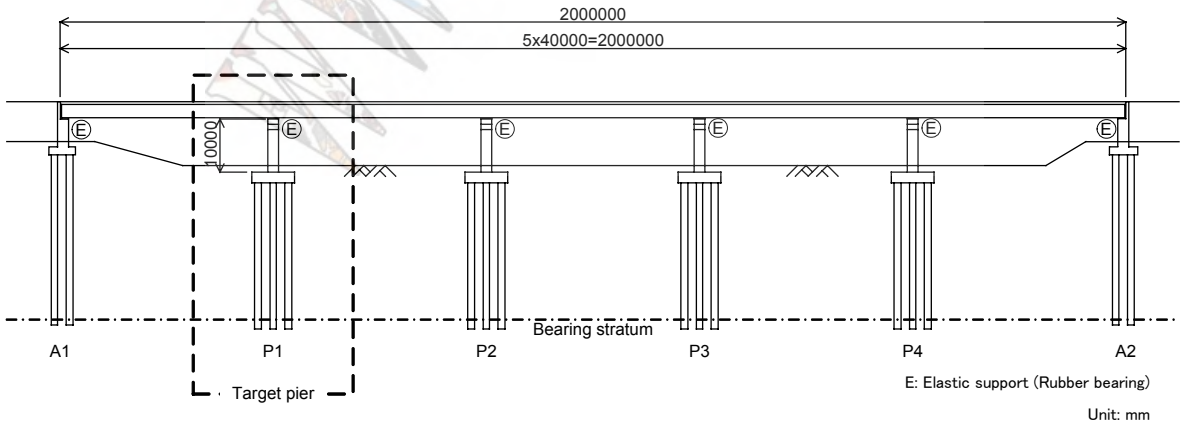

Fig. 1. Target bridge pier

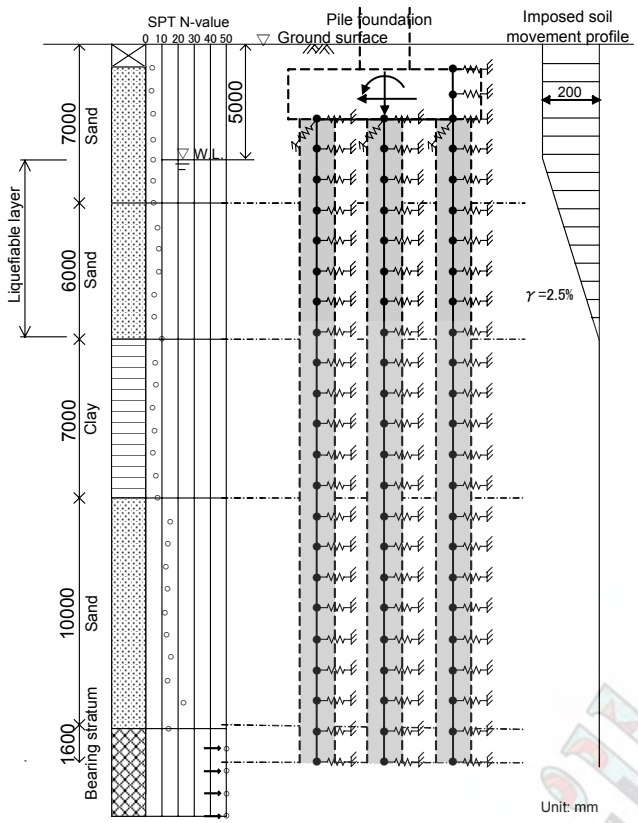

Fig. 2. Soil profile, analytical model and imposed soil movement profile used in analyses

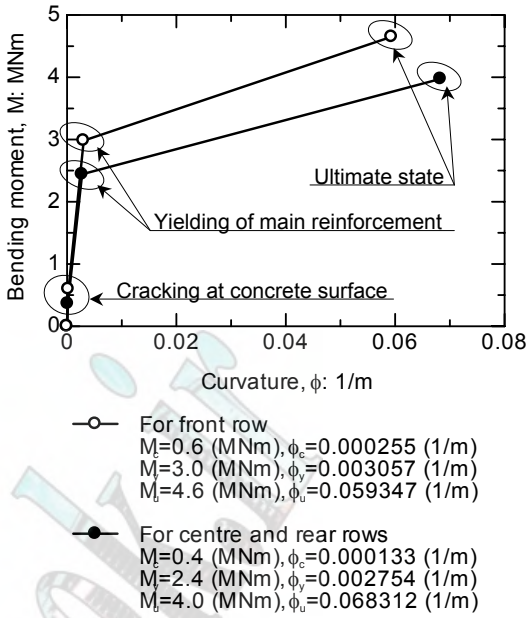

Fig. 3. Tri-linear M-ϕ relationship of piles

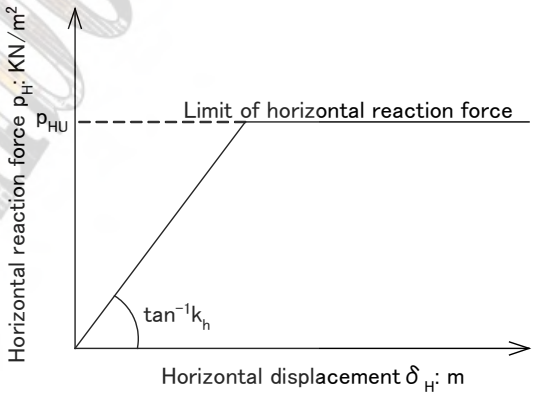

Fig. 4. Force-displacement model for soil-structure interactions

CALCULATION PROCEDURE AND CONDITIONS

Performance of the target foundation is analysed by the seismic deformation method. Analytical model and initial and boundary conditions used are based on the specifications for highway bridges in Japan [3], except (1) stiffness and strength of the surface non-liquefiable layer, and (2) imposition of the soil movement of liquefiable ground to the piles through the Winkler springs.

Tri-linear M-ϕ relations used in the pile modelling are shown in Fig. 3. For soil-structure interaction modelling, bilinear force-displacement relationship is used (Fig. 4).

In the current road bridge design code, only the soil resistance below the footing is taken into account. However, many researchers have pointted out the significance of the surface non-liquefiable layer resistance on pile foundation responses [4][5][6]. In the analysis, existance of the surface layer is taken into account.

At the moment, there is no established method, except dynamic ground response analysis, to determine the soil displacement profile of liqefiable ground, even though some empirical correlations between in-situ logging data and estimated soil shear strain in liquefiable soil are proposed [1]. In the analyses, maximum shear strain at liquefiable layer calculated from the accerelation records at the Port Island in Kobe Earthquake (2.5%) is used for the liquefied soil displacement profile determination. The soil displacement profile used is illustated in Fig. 2.

Having these boundary conditions, performance of the target foundation is analysed by the seismic deformation method. The inertia force application and soil movement imposition are made simultaneously. By changing (1) the magnitude of the inertia force acting on a pile head, (2) the stiffness and strength of surface non-liquefiable layer, and (3) the stiffness and strength of piles, feasibility of pile foundation design using the seismic deformation method is examined with reference to allowable displacement and pile reserve capacity.

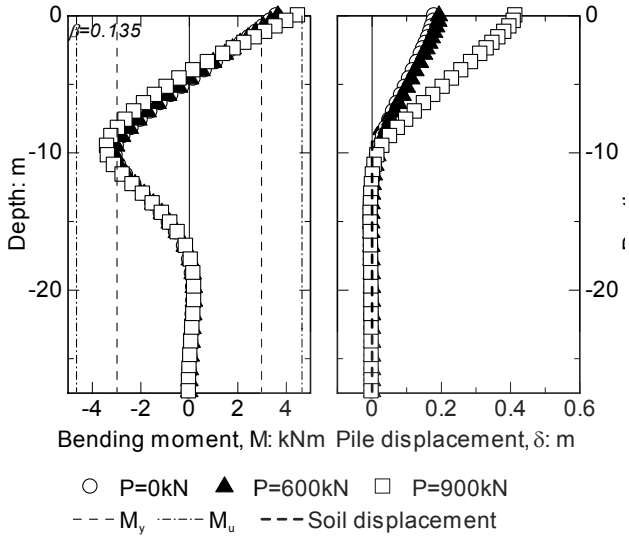

Fig. 5. Profiles of pile bending moment and horizontal displacement with different magnitude of the inertia force acting on a pile head (β=0.135)

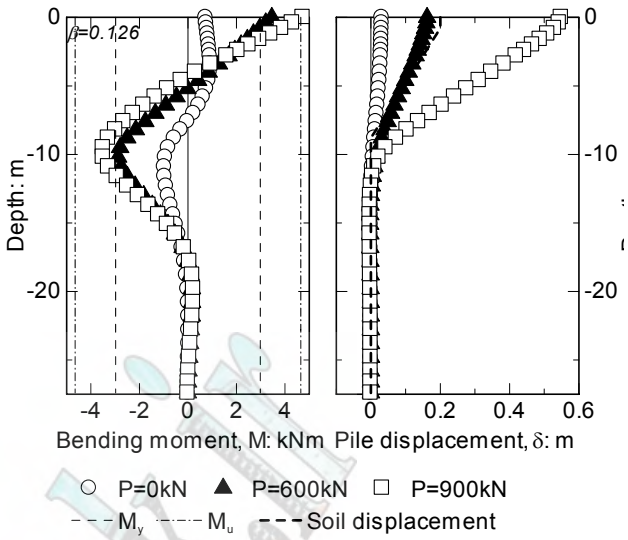

Fig. 6. Profiles of pile bending moment and horizontal displacement with different magnitude of the inertia force acting on a pile head (β=0.126; no horizontal resistance in surface layer)

DIFFICULTIES IN SEISMIC DESIGN METHOD

Figure 5 shows profiles of the bending moment and horizontal displacement of the front row pile at the end of loading for the foundation subjected to different inertia force acting on a pile head (P=0, 600, 900kN). In this case, the stiffness and strength of the surface layer are one-third of those in the pre-earthquake state (β=0.135). The pile responses are more or less the same irrespective to the inertia force magnitude (except pile displacement for P=900kN), which implies that the surface non-liquefiable layer is strong and thick enough to resist against the inertia force of the supporting structure. However, when the soil resistance of the surface layer (above the pile head) is not considered (β=0.126), which is the case for the current road bridge design code, it makes all the difference. Similar plots for the cases without surface soil layer resistance are shown in Fig. 6. Without surface layer resistance, the inertia force dominates the pile responses. In these cases, kinematic loading on piles due to large ground deformation during earthquake is not large as the soil springs connecting the pile and surrounding soils are soft and weak, and the surface layer cannot be a strong register against the inertia force of the supporting structure. Comparison of these figures reveals that the horizontal soil displacement imposition dominates the pile responses when the surface layer resistance is considered, while the pile responses are sensitive to the inertia force magnitude without the surface layer resistance.

With the conventional design procedure specified in the current road bridge design code, it is relatively easy to determine foundation design details, as kinematic loading is not considered, i.e., stiffer and stronger piles always improve the foundation performance since ground simply behaves as a resister against loads acting on a pile cap. However, once the kinematic loading is considered in design procedure, such stiffer and stronger piles do not necessarily perform well, e.g., at times pile responses are insensitive to the inertia force magnitude as demonstrated above.

For determination of foundation design details that satisfy required reserve capacity with the seismic deformation method, it would be helpful if a simple procedure that navigates designers toward economical (or optimal) foundation design details is provided. Aim of this study is to demonstrate a conceptual design procedure to obtain such foundation design details.

CHARTS FOR ECONOMICAL PILE DESIGN

Figures 7 & 8 plot variation of (1) horizontal displacement of bridge pier at the top (δ) and (2) normalised pile curvature where maximum bending moment is observed (R_ϕ) in P-β space, where P=inertia force acting on a pile head and $\beta=(k_H D/4EI)^{0.25}$ (stiffness ratio of the soil near the surface to the pile in elastic state, k_H=average horizontal subgrade reaction, D=pile diameter & EI=flexural rigidity of pile). These plots are obtained from 24 analyse with different combinations of the magnitude of the inertia force acting on a pile head (six values) and the stiffness and strength of surface non-liquefiable layer (four values). Used values for the inertia force and soil stiffness ratio (β) are listed in Table. 1.

The smaller β represents the relatively softer and weaker surface non-liquefiable layer (the relatively stiffer pile) and the smaller P corresponds to the smaller

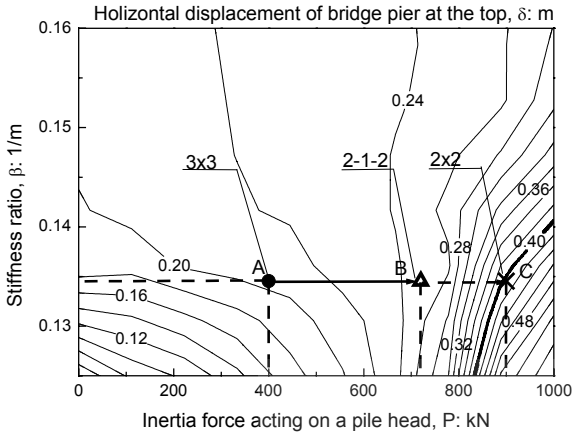

Fig. 7. Variation of normalized pile curvature at the pile head in *P-β* space

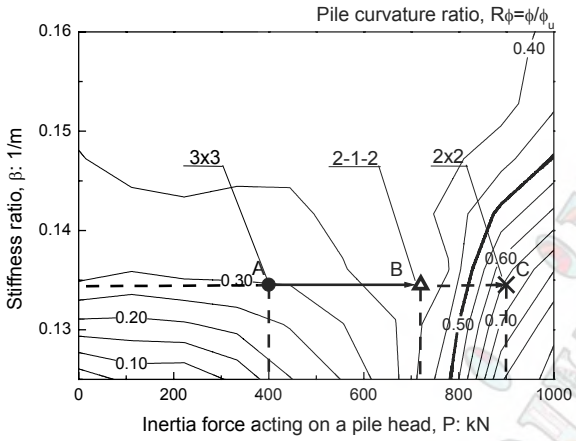

Fig. 8. Variation of horizontal displacement of bridge pier at the top in *P-β* space

Table. 1. Inertia force and β used in analyses

Inertia force on a pile head (kN)	Scale factor for the surface layer stiffness and strength (Corresponding β in 1/m)	
0		
267	0	(0.171)
567	1/3	(0.151)
700	1	(0.135)
832	2	(0.126)
917		

superstructure inertia force or the larger number of piles in foundation. R_ϕ is defined as the maximum pile curvature normalised by that at the ultimate state. This R_ϕ is an index for the pile reserve capacity: the pile is about to fail when R_ϕ is closer to one and the pile has enough reserve capacity when R_ϕ is closer to zero. As seen in the figures, δ and R_ϕ get larger when P gets larger and β gets smaller (lower right region in the figures). This is due to

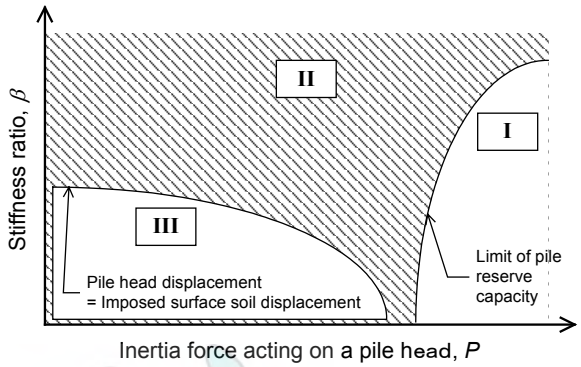

Fig. 9. Schematic diagram of the pile performance in *P-β* space

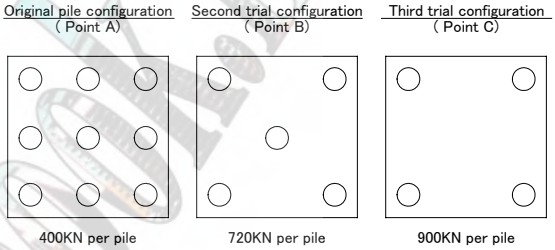

Fig. 10. Pile configuration in example usage of chart

the relatively smaller surface soil resistance against the inertia force acting on a pile head, resulting in failure of the foundation. In this region, contour lines tend to be vertical and their interval is relatively small, which indicates that small change in the inertia force results in large change in foundation responses when β kept constant.

On the other hand, at the lower left of the graphs (the foundation is subjected to the smaller inertia force with the smaller surface soil resistance), the foundation stands still as it is stiff and strong enough against the horizontal soil movement and the inertia force, resulting in the smaller δ and R_ϕ. In this region, contour lines tend to be horizontal, which indicates that change in the inertia force less affects on foundation responses when β kept constant.

Figure 9 illustrates schematic diagram of the pile performance in *P-β* space by analogy with Figs. 7 & 8. When the state of a trial pile foundation locates in Zone I, it's beyond the limit of pile reserve capacity and revise in pile configuration and strength is required. Above this limit line (Zone II), the trial satisfies the requirement for δ and the reserve capacity and is acceptable. However, if the state of a trial pile is in Zone III where δ is smaller than the imposed soil movement at the surface, the pile configuration and strength is too conservative and more economical pile foundation design can be made. Thus, using the charts like Figs. 7 & 8, a designer can visually confirm the state of a trial pile foundation and can see

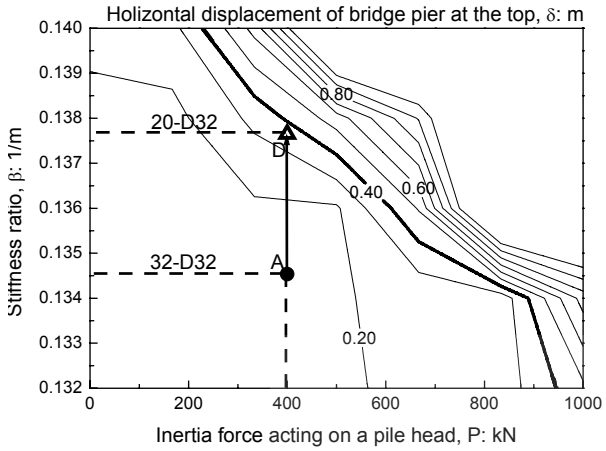

Fig. 11. Variation of horizontal displacement of bridge pier at the top by changing P and stiffness and strength of piles in P-β space

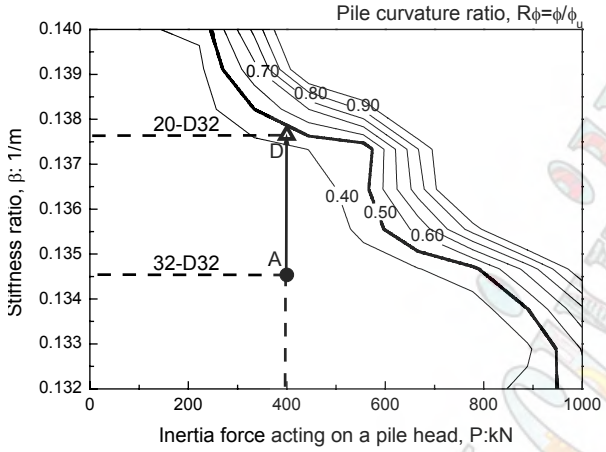

Fig. 12. Variation of normalized pile curvature at the pile head by changing P and stiffness and strength of piles in P-β space

where it should go for economical design.

Let us illustrate example usage of the charts. Here assume that requirement for the bridge pier is δ<0.4m and that for the pile is R_ϕ<0.5, and P=400kN and β=0.135 for the first trial pile foundation (Point A in Figs. 7 & 8). In the first trial, since it's on the edge of Zone III (δ=0.2 and R_ϕ=0.3), more economical pile configuration or strength can be made:

Example 1: Reduction of pile number[1]

If number of piles is reduced from original nine (3x3) to five (2-1-2), the second trial state moves to Point B (P≅720kN with the same β). At Point B, δ and R_ϕ still satisfy their requirement (δ=0.26 <0.4m and R_ϕ=0.38<0.5) and this pile configuration change can be accepted.

[1] Pile group effects change due to pile spacing change is not considered in this example.

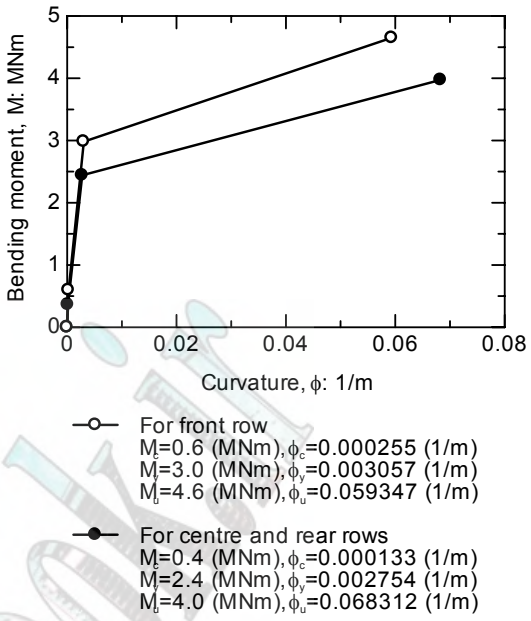

Fig. 13. Tri-linear M-ϕ relationship of piles (32-D32 reinforcement with hoops of D25@150mm) for second trial in Example 2

Assume that further reductions of number of piles are made (Point C, four piles, P≅720kN with the same β). At Point C, δ and R_ϕ beyond the required limit of pile reserve capacity (δ=0.41 >0.4m and R_ϕ=0.65 >0.5) and modification in pile configuration is required. Accordingly, Point B (5piles) is acceptable in the example.

Example 2: Reduction of pile reinforcement

Figures 11 & 12 are the similar plots to Figs. 7 & 8, but they are drawn by changing the magnitude of the inertia force acting on a pile head and the stiffness and strength of piles.

At Point A, the first trial piles have 32-D32 reinforcements. When number of main reinforcements is reduced from original 32 to 20, the second trial state moves to Point D (β=0.138 with the same P). M-relationships for the piles in the second trial are plotted in Fig. 13. At Point D, δ and R_ϕ still satisfy their requirement (δ=0.35<0.4m and R_ϕ=0.45<0.5) and this pile reinforcement change can be accepted.

CONCLUSIONS

Preliminary consideration on application of seismic deformation method to road bridge pile foundation in liquefiable soil is made and pile foundation design procedure concept considering allowable bridge pier displacement and pile reserve capacity is demonstrated. Although the charts illustrated here may change in accordance with the soil profile, soil movement input and

so on, by following the design procedure concept described here, a designer can visually confirm the state of a trial pile foundation and would see where it should go for economical design.

REFERENCES

[1] Tokimatsu, K. & Asaka, Y. 1998. Effects of liquefaction-induced ground displacements on pile performance in the 1995 Hyogoken-Nambu Earthquake, *Soils and Foundations, Special Issue on Geotechnical Aspects of the Jan. 17 1995 Hyogoken-Nambu Earthquake*, No. 2, 163--177.

[2] Japan Society of Civil Engineers. 2000. Earthquake Resistant Design Codes in Japan.

[3] Japan Road Association. 2002. Part V Seismic design, *Specifications for highway bridges*.

[4] Tokimatsu, K. 2004. Behavior and design of pile foundation subjected to earthquakes, *Proceedings of 12th Asian Regional Conference on Soil Mechanics and Geotechnical Engineering*, Vol.2.

[5] Miura, F., Stewart, H. E. & Rourke, T. D. O., 1991. The effects of liquefaction-induced lateral spreading on pile foundation, *Soil Dynamics and Earthquake Engineering*, Vol.10, pp.271-279.

[6] Cubrinovski, M. & Ishihara, K, 2002. Prediction of pile response to lateral spreading of liquefied soil, *The 12th Japan Earthquake Engineering Symposium Proceedings*, pp.841-846.

Experimental Study on Large Pile Group Response Subjected to Lateral Flow of Liquefied Ground

Vlatko Sesov[1], Ikuo Towhata[1], Marcelo Gonzalez[1] , Rory Ball[2] , Shinya Ishimatsu[1]
1. The University of Tokyo, Department of Civil Engineering, Japan
2. University of Illinois, USA

Abstract

This paper presents results of shaking table tests on large pile group behavior under the liquefaction induced ground flow. The present study consists of several series of 1G shaking table tests on pile foundation embedded in gently sloped liquefiable soil layer. Two models of group piles were investigated: i.e. 6 x 6 and 11 x 11 group pile models. The kinematic effects of liquefaction induced horizontal displacements and influence of pile spacing on pile response were the primary goals which were observed during the tests. Results from the experiments show that the piles responses upon liquefaction induced flow greatly depend on the location of the pile in the pile group. Distribution of liquefaction-induced soil horizontal displacements was affected by presence of the pile group. Maximum soil displacements were observed far from the pile group while the magnitude of soil movement between piles was decreasing, from front row toward inner row of piles. This was more significant with 2.5D than 5D pile spacing. With these findings it is suggested that piles in pile group were subjected to different lateral loading due to liquefaction-induced ground flow. This idea could be used also as mitigation measures to design protective row(s) of pile around the pile foundation against lateral spreading of liquefied soil.

Keywords—*Liquefaction , soil flow, pile group, shaking table*

INTRODUCTION

Permanent displacements of ground induced by seismic liquefaction often caused severe damages to structures. Many case reports have shown damages and collapses of pile foundations during past earthquakes. Investigations carried out after the Niigata 1964 Earthquake showed that damages observed on pile foundations were strongly related to large permanent ground displacement which was induced by intensive liquefaction[1]. A large number of pile foundations were deformed and damaged during the Kobe Earthquake 1995 due to movement of quay walls and revetments toward the sea which brought extensive flow of the ground behind them [2,3,4,5]. These and also other case histories clearly [6] demonstrate that pile foundations are susceptible to seismic damages. Pile foundation which is mainly designed to carry the vertical loads, during the earthquakes looses the lateral support of surrounding liquefied ground and at the same time is exposed to large lateral ground deformation induced by flow of liquefied soil.

Extensive studies were done after the 1995 Kobe Earthquake to investigate the mechanism of pile damages. Tamura et al. [7] performed back analysis of damaged bridge foundations and shaking table tests. Based on their results they concluded that the ground flow force acting on pile foundation can be estimated as the sum of the passive earth pressure of the surface non-liquefiable layer and 30% of the overburden pressure of the liquefiable layer which had been incorporated into the Specifications for Highway Bridges in Japan, PartV , Seismic design [8]. Imamura et al. [9] conducted several centrifuge model tests investigating the pile group behavior subjected to lateral flow of liquefied ground. Their study demonstrated that when the pile spacing is more than 3 to 4 times of pile diameter there are no interactions between piles , so the pile responses can be treated as single pile response.

Most of the present information about seismic behavior of pile foundation in liquefied soils is still based on results of studies which represent the pile foundation as single pile or small group pile (2x2 or 3x3). Knowledge of the group pile response on lateral spreading of liquefied soil is very limited.

This study investigates the behavior of large group of piles on lateral flow of liquefied soil by performing a series of shaking table tests.

SHAKING TABLE TESTS

Table 1 summarizes main characteristics of eight experiments which were conducted on shaking table facility at the University of Tokyo, Civil Engineering Department, Japan. Tested models were prepared in a rigid square container with dimensions of 2 m side and 0.60 m high which was mounted on a shaking table.

Two different setups of group piles were investigated i.e. 6 x 6 and 11 x 11 group pile models. Fig.1 presents pile models with 6x6 pile group (Model1, Model2 & Model3) and Fig. 2 presents pile models with 11x11 pile

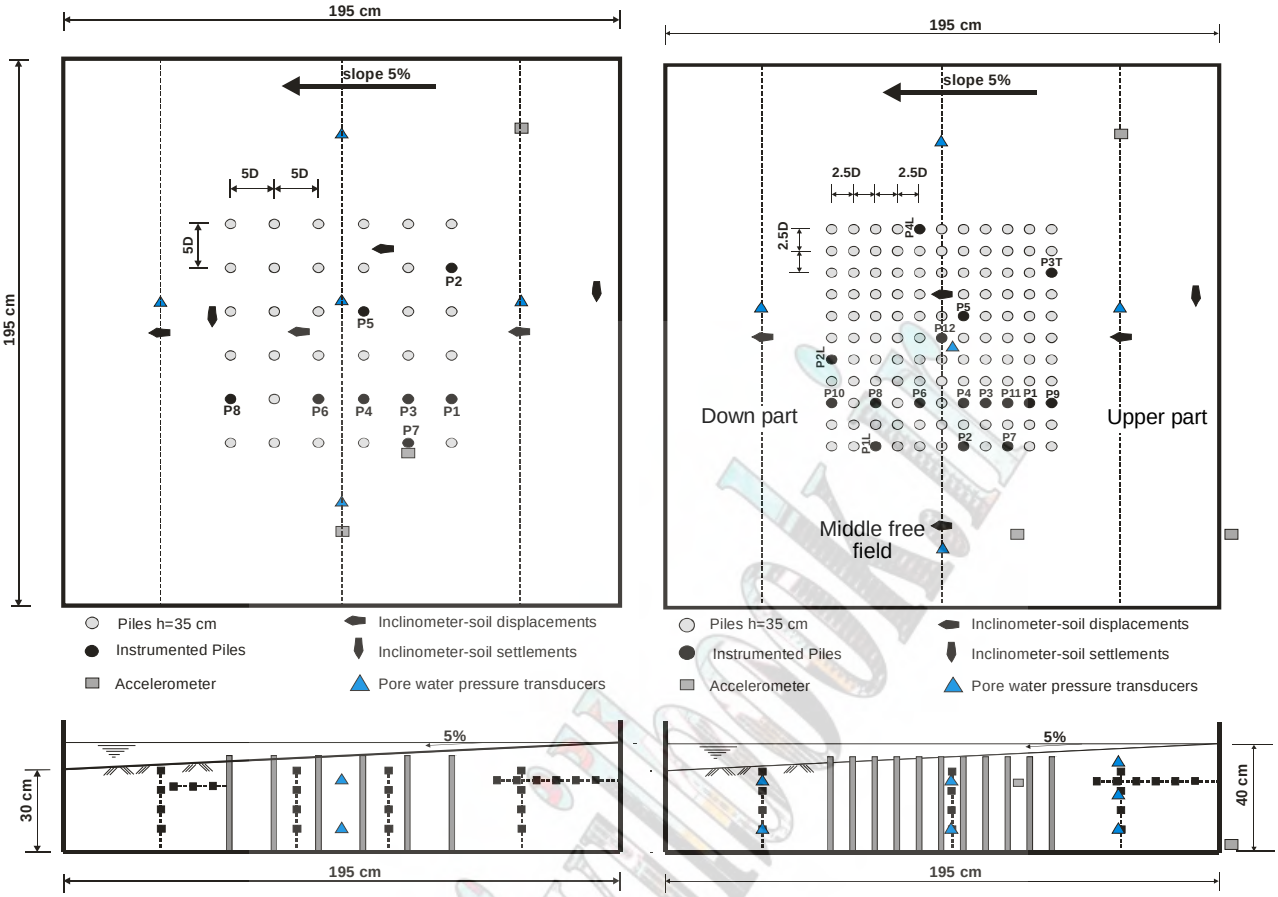

a) 6 x 6 pile group (5D spacing) b) 11 x 11 pile group (2.5D spacing)

Figure 1 Layout of the soil profiles, pile models and used instrumentation.

group (Model4 - Model8). The pile group models consider two type of pile spacing: 5 times of pile diameter in case of 6x6 group piles and 2.5 pile diameter in case of 11 x 11 piles group.

Table 1 Tested models

Test	Sand	Piles	Spacing	Shaking
Model1	Toyoura (Dr=35%)	- 6 x 6	- 5 D	- Td=30 sec - in slope dir.
Model2	Toyoura (Dr=60%)	- 6 x 6	- 5 D	- Td=30 sec - in slope dir.
Model3	Toyoura (Dr=40%)	- 6 x 6	- 5 D	- Td=30 sec - perpendicular
Model4	Toyoura (Dr=35%)	- 11 x 11	- 2.5 D	- Td=30 sec - in slope dir.
Model5	Toyoura (Dr=35%)	- 11 x 11	- 2.5 D	- Td=30 sec - perpendicular
Model6	Toyoura (Dr=40%)	- 11 x 11	- 2.5 D	- Td=5 sec - perpendicular
Model7	Toyoura (Dr=45%)	- 11 x 11	- 2.5 D	- Td=5 sec - in slope dir.
Model8	Toyoura (Dr=65%)	- 11 x 11	- 2.5 D	- Td=30 sec - in slope dir.

Piles whose characteristics are shown in Table2 were fixed at the bottom and free at the top. Such a simple pile model can eliminate the inertial effects of super structure on pile response and more clearly observe the kinematic effects of liquefaction induced horizontal displacements which were the primary goal of this study. Toyoura sand was used to prepare the ground model, Table 3. Model1 and Model4 were prepared by water sedimentation method.

Table 2. Properties of pile

Material	Plastic
Height , (cm)	35
Outer / Inner diameter , (cm)	3.2 / 2.5
E, (N/cm^2)	400000
EI, (Ncm^2)	1200000

Table 3. Material properties of Toyoura sand

Property	Toyoura
Specific weight Gs, kg/m3	2.653
Maximum void ratio, e_{max}	0.93
Minimum void ratio, e_{min}	0.62
Mean particle diameter, D_{50}, mm	0.16
Fines content,%	2.95

First, piles were mounted at the bottom of container and then the container was filled with water to a certain level. Predetermined mass of sand was rained through system of sieves into the container to form 5 cm layer. The procedure was repeated until final height of soil model was reached and initial slope of 5% was formed. With this procedure relative density of 30-40% of soil was obtained. Model2, Model3, and Model5 to 8 were prepared by jetting of pressurized water into the ground to create loose deposit. Once the sand was in container the hose, through which the pressurized water was supplied, was constantly moved though-out whole area in order to produce a uniform deposit. To prepare denser soil models shaking of low amplitude and high frequency with long duration was applied until desired density was achieved. Soil settlements and pore water pressure were monitored during this pre-shaking. In all tests level of water inside the container was made equal to maximum elevation of slope. Piles were instrumented with strain gauges which were attached on different location along the pile height, Fig2.

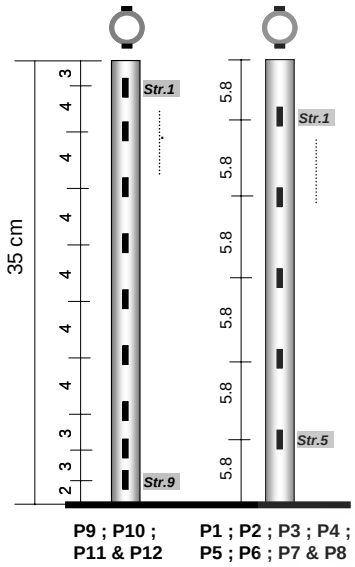

Fig.2 Locations of strain gauges along the pile height

Accelerations, excess pore water pressures, soil displacements and pile bending strains were recorded during the tests. Also colored sand lines were used to observe the soil deformations during the shaking through a transparent side window of the container. All models were subjected to same amplitude of 250 gal and frequency f=10 Hz of shaking only direction and duration of shaking were varied.

TEST RESULTS

Permanent ground displacements

In order to investigate mechanism of ground flow induced by liquefaction and its effects on pile group response, several parameters were varied during the shaking table tests. Initial slope inclination of 5% was kept unchanged constant in all the experiments while direction of shaking was changing and duration of shaking, too. Permanent ground displacements were measured with inclinometers canceling the cyclic components by filtering the time histories with low pass filter. These recorded displacements were in good agreement with the displacements observed by colored markers on the transparent side of wall and on the surface of the soil model. Effects of shaking on permanent displacements of liquefied soil during the experiments can be observed in Fig.3a, Fig.3b and Fig.3c.

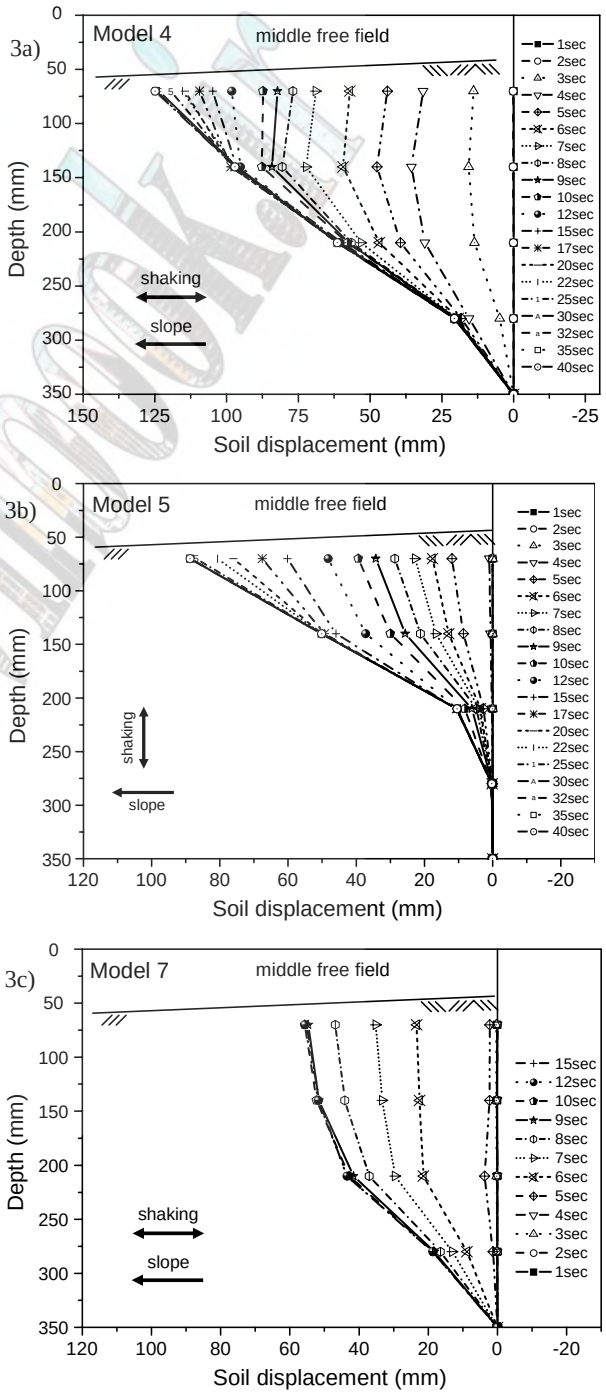

Fig.3 Effects of shaking on permanent ground displacements

Time histories of permanent ground displacement presented in Fig.3 were measured by inclinometer located at the middle free field of the models. Fig. 3a presents results of permanent ground displacements in Model4 where shaking was applied in the same direction as slope inclination. Fig. 3b presents results of permanent ground displacements in Model5 where shaking was applied in the perpendicular direction as slope inclination and Fig. 3c presents results of permanent ground displacements in Model7 where shaking was applied in the same direction as slope inclination but the duration of shaking was only 5 sec. Soil displacements presented in Fig.3a-3c were recorded by inclinometers located in middle section between the pile group and the side wall of the container (see Fig.1). Shapes of presented soil displacements Fig.3a to Fig.3c were no different so much, showing smaller values at the bottom and increasing to maximum values at top of the soil profile, but the magnitude of permanent ground displacements shows different values in each of the presented models. Maximum ground displacements were observed in Model4 (Fig.3a) while in Model5 (Fig.3b) and in Model7 (Fig.3c) permanent ground displacements were smaller.

Fig.4 and Fig.5 presents the time histories of excess pore water pressure ratio and permanent ground displacements recorded at middle section of slope between piles in Model1 and Model4.

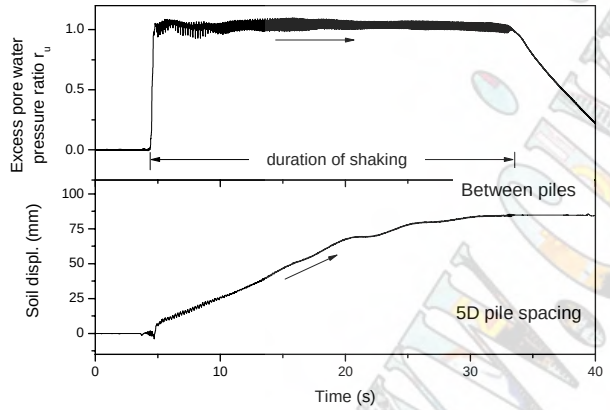

Fig.4 Time history of excess pore water pressure ratio and permanent ground displacement in Model1

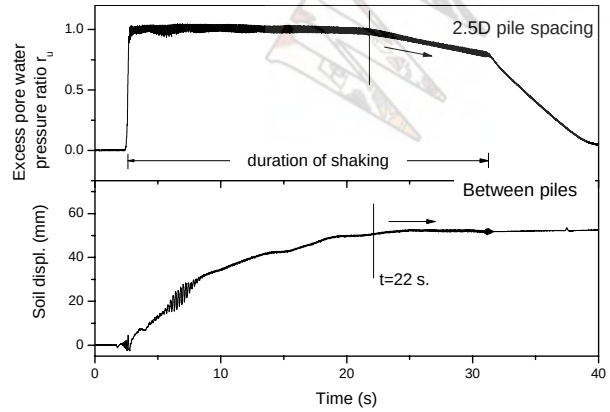

Fig.5 Time history of excess pore water pressure ratio and permanent ground displacement in Model5

Fig.4 shows that excess pore water pressure ratio history in Model1 was maintained at constant high value r_u=1.0 ($r_u=\Delta u / \sigma_v'$, Δu-excess pore water pressure during the shaking, σ_v'-initial effective stress) during the entire time of shaking, while in Model4 (Fig.5) it can be observed that after some period of constant high value, excess pore water pressure decreased to some extent at the end of shaking. Time history of permanent ground displacement in Fig.4 shows tendency of continuously increasing and accumulation of ground displacement reaching the maximum almost at the end of shaking. The history of permanent ground displacement in Model4 Fig5, has tendency of increasing and accumulation until t=22 sec. at the same time where decreasing in excess pore water pressure ratio was started. After this no increasing was observed and permanent ground displacement shows constant value till the end of shaking.

Figure 6 shows maximum ground displacements in soil profile obtained between the piles in the pile group on two locations and maximum ground displacements observed in the middle free field at Model 1. Figure 7 presents results of maximum ground displacements in soil profile obtained between the piles in the pile group and in the middle free field at Model4.

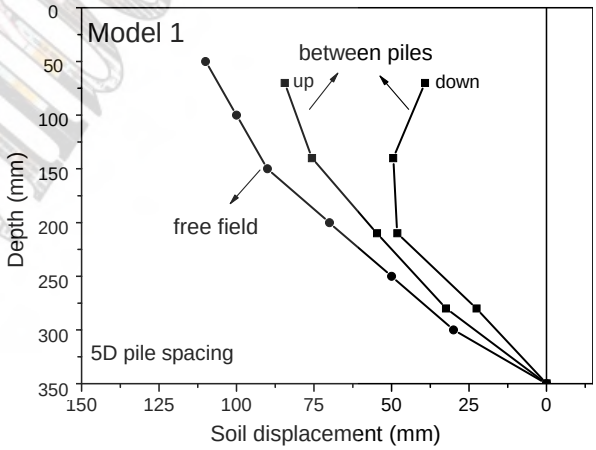

Fig.6 Permanent ground displacement in Model1

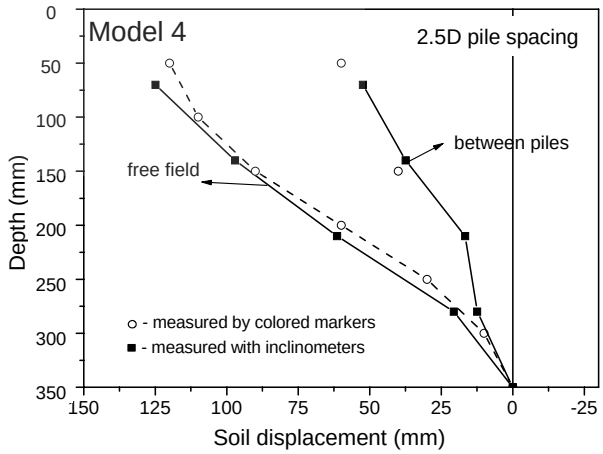

Fig.7 Permanent ground displacement in Model4

Ratio between maximum ground displacement measured at the middle free field and maximum ground displacement measured between piles is presented in Table4.

Table 4 Maximum ground displacements

Soil Displacement (cm)	Model1	Model2	Model3	Model4
max δ_y free field / max δ_y between piles	11 / 6	8.5 / 7	9.5 / 6	12.5 / 5
Soil Displacement (cm)	Model5	Model6	Model7	Model8
max δ_y free field / max δ_y between piles	9 / 3.5	5 / 1	5.8 / 2	9.5 / 5

Results presented in Table 4 shows that in the case of 5D pile spacing soil flow between piles was restrained to 54-82 % of maximum measured ground displacement at the middle free field. In the case of 2.5D pile spacing soil flow between piles was restrained to 20-50 % of maximum measured ground displacement at the middle free field. Restrain of the soil flow between piles was observed to be larger in the cases when the shaking was applied perpendicular to the direction of the slope. Here it should be pointed out that the measurement of permanent ground displacement between piles especially when the pile spacing is smaller is a quite difficult task. Although inclinometers can give us information about soil displacements their reliable measurement can be affected when the surrounding free space (soil) is limited. In this study soil displacement obtained by inclinometers were compared with the maximum soil displacements measured by the colored lines and markers, Fig.7. Agreement between these two measurements was satisfactory in most of the performed tests.

Pile Group Response

Piles were instrumented with strain gauges attached on different locations along the pile height, Fig.2. Strain gauges were attached on the outer wall of the pile and were covered by tape to protect them and secure reliable functioning in wet environment. Results which were directly measured by strain gauges were the pile bending strains. Pile bending moments are linearly dependent on bending strains in elastic domain, so the pile bending moments were directly estimated by the recordings of strain gauges during the tests. Interpolating polynomials were fit to the recorded moment data. Shear forces and lateral loading acting on pile were obtained by differentiation, while rotation and pile displacement were obtained by integration of the bending moment polynomial curve at each time step. Fig.8 and Fig.9 present time histories of bending moments obtained at the bottom on two piles during the shaking table test on Model1 and Model4. In case of Model1 (Fig.8) Pile1 which is located in front pile row shows larger bending moment as compared with Pile3 located in inner pile rows. Bending moments measured in front pile row Pile9 are significantly large than bending moments measured at inner pile row Pile4 in Model4 (Fig.9). Locations of piles in the pile group presented in Fig.8 and Fig.9 are illustrated in Fig.1.

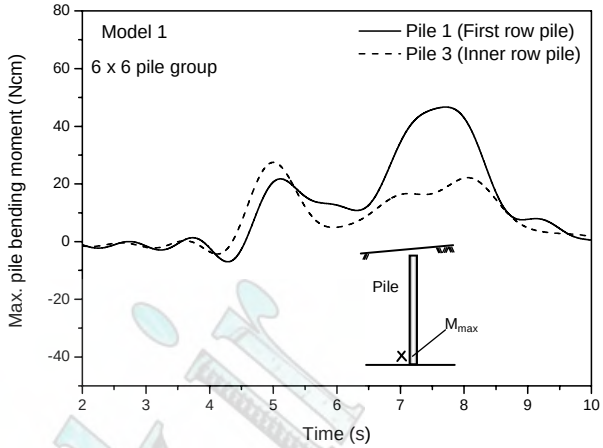

Fig.8 Time histories of pile bending moment in front and inner pile row in Model1

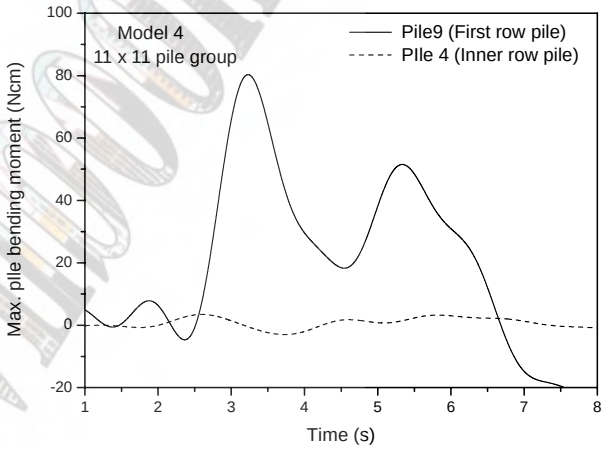

Fig.9 Time histories of pile bending moment in front and inner pile row in Model4

Mechanism of soil-pile interaction during the performed tests can be clarified in Fig.10 and Fig.11. Figure 10 shows test results of permanent ground displacement along the soil profile and pile deformation in three different time steps. As it can be seen from the Fig.10 soil displacements are much larger then pile displacements throughout the shaking. The permanent soil displacements are the cause and lateral loads along the piles are the consequences. This is characteristic behavior of so called “passive piles” [10]. Pile bending moment measured at the bottom of the pile and histories of soil displacement and soil flow velocity measured at the top portion of soil profile are presented in Fig.11. Results of soil flow velocities were calculated by differentiation of permanent soil displacements time histories. The pile response has a similar shape with that of the soil flow velocity. This suggests that lateral force which is acting on the pile during the soil flow has a liquid-like nature. Similar observations had been presented in reference [11].

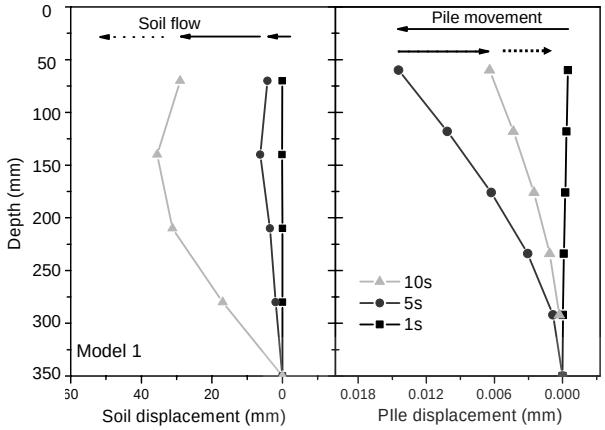

Fig.10 Soil flow vs. pile displacements

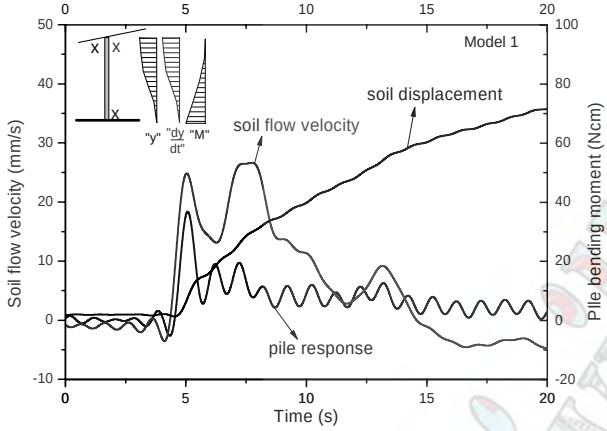

Fig.11 Pile bending moment vs. ground surface displacement and flow velocity

Fig 12 and Fig 13 present distribution of normalized maximum bending moments recorded in each pile of the pile group in case of 5D and 2.5 D pile spacing. Maximum pile bending moments were normalized by maximum bending moment measured in front row pile. Distribution of maximum bending moments in pile group presented in Fig.12 and Fig.13 shows that pile bending moments is decreasing toward the inner pile rows and slightly increasing at the last pile row. Decreasing of bending moments measured in inner pile rows compare to those in front pile row was more significant in the case of 2.5D pile spacing (Fig.13) than in 5D pile spacing (Fig.12).

Fig.14 presents the participation of each pile row of the total lateral force that is acting on the pile group due to ground flow of liquefied soil in the case of 5D pile spacing and Fig 15 presents the results for the case of 2.5D pile spacing. Two series presented in Fig15 refer to results obtained when shaking was applied in the same direction as slope and direction of shaking perpendicular to slope inclination. Total lateral force acting on each pile row was calculated as a sum of maximum lateral forces acting on each pile in the row. In case when there was only one instrumented pile in the row, lateral force per pile row was estimated by multiplying this force with the number of piles in the row.

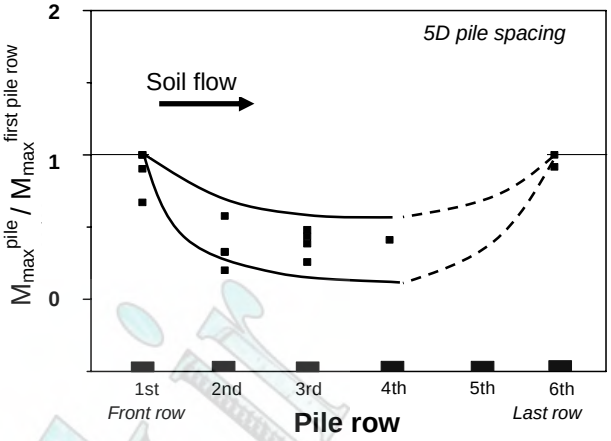

Fig.12 Distribution of maximum bending moments in the pile group with 5D pile spacing

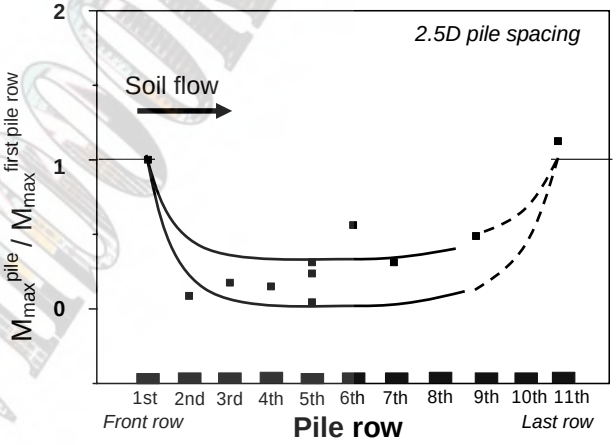

Fig.13 Distribution of maximum bending moments in the pile group with 2.5D pile spacing

Fig.14 and Fig.15 show that piles in the pile group were subjected to different lateral loading due to soil flow of liquefied soil. First pile row received the biggest portion of the total lateral force while inner pile rows were subjected to much smaller lateral forces. Total lateral force acting on pile group in case of 5D pile spacing was estimated to be 110 N , while in the case of 2.5D spacing 350 N (shaking in the direction of slope and 200 N (shaking in perpendicular direction). Total lateral force due to lateral spreading of liquefied soil was also calculated using the formula given by the Specifications for highway bridges PartV Seismic design (Japan Road Association). According to this design code total lateral force was 260 N. It is important to be pointed that this design codes calculates liquefaction-induced lateral spreading force per unit area for pile foundation shall be multiplied by the outermost width between the piles at the both ends of the surface resisting the lateral spreading force [8]. It also assumes that this force is acting on the first row of piles and it is equally shared by all piles.

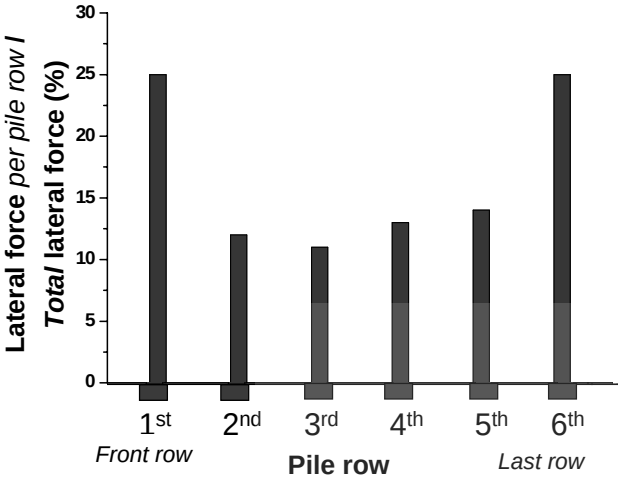

Fig.14 Participation of each pile row in the total lateral force acting on the pile group – 5D pile spacing

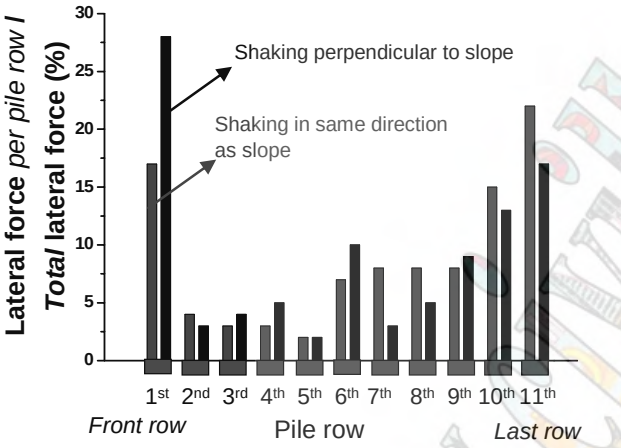

Fig.15 Participation of each pile row in the total lateral force acting on the pile group – 2.5D pile spacing

CONCLUDING REMARKS

Shaking table tests were conducted to investigate the pile group behavior in a sloping liquefied ground. The main findings can be summarized as follows:

1) Magnitude of permanent displacements induced by soil liquefaction in the pile group mainly depends on the pile spacing. Smaller pile spacing produced larger effects on soil displacements between piles.

2) Pile response correlates much better with the soil flow velocity than soil displacement, indicating the viscose nature of lateral pressure.

3) Piles in the pile group were subjected to different lateral force due to ground flow of liquefied soil. Pile spacing play a significant role in distribution of lateral force.

4) First row piles received largest portion of total lateral force while the inner row of piles received much smaller portion. This finding gives an idea to use the row of piles as a mitigation measures against liquefaction induced lateral spreading.

5) Shadowing effect was more significant in case of 2.5D than 5D pile spacing.

ACKNOWLEDGMENT

Investigation presented in this paper was supported by JSPS (Japanese Society for the Promotion of Science) program. Authors are gratefully acknowledged this support.

REFERENCES

[1] Hamada, M., Yasuda,S., Isoyama, R., & Emoto, K., Study on liquefaction induced permanent ground displacements (1986), *Report of Association for The Development of Earthquake Prediction*

[2] Kamon, M., Wako, T., Isemura,K., Sawa,K., Mimura, M., Tateyama,K., & Kobayashi, S., Geotechnical Disasters on the Waterfront, *Special issue on Geotechnical Aspects of the January 17 1995 Hyogoken-Nambu Earthquake, Soils&Foundations* Jan., 1996, 137-147

[3] Hamada, M., Isoyama, R., & Wakamatsu, K., Liquefaction-Induced ground displacement and related damage to lifeline facilities. *Special issue on Geotechnical Aspects of the January 17 1995 Hyogoken-Nambu Earthquake, Soils and Foundations* January, 1996, 81-97

[4] Matsui, T., & Oda, K., Foundation damage of structures. *Special issue on Geotechnical Aspects of the January 17 1995 Hyogoken-Nambu Earthquake, Soils and Foundations* January, 1996, 189-200

[5] Tokimatsu, K., Mizuno, H., & Kakurai, M., (1996) Building damage associated with geotechnical problems. *Special issue on Geotechnical Aspects of the January 17 1995 Hyogoken-Nambu Earthquake, Soils and Foundations* January, 1996, 219-234

[6] Yasuda, S., and Berrill J.B. Observations of the earthquake response of foundations in soil profiles containing saturated sands. Invited Paper, *An International Conference on Geotechnical and Geological Engineering, GEOENG2000* , Melbourne, Australia

[7] Tamura, K., Azuma, T., and Hamada T., Seismic Design of Bridge foundation against liquefaction-induced ground flow. Paper No.1231, *12 World Conference on Earthquake Engineering* , Auckland, New Zealand

[8] Specifications for Highway Bridges in Japan, Part V , Seismic design, Japan Road Association

[9] Imamura,S., Hagiwara, T., Tsukamoto, Y., Ishihara, K., Response of pile groups against seismically induced lateral flow in centrifuge model tests , *Soils and Foundations* June, 2004, Vol. 44, No.3 , 39-55

[10] De Beer, E., Piles subjected to static lateral loads, *The effect of horizontal loads on piles, due to surcharge or seismic effects*,. Ninth International Conference on Soil Mechanics and Foundation Engineering , Tokyo, 1997

[11] Hamada, M., Performances of foundations against liquefaction-induced permanent ground displacements, Paper No.1754, *12 World Conference on Earthquake Engineering* , Auckland, New Zealand

Lateral Resistance of Piles in Ground Improved by Compaction Method Using Iron and Steel Slag -An Experimental Study-

Y.Homma[1], K.Tominaga[2], O.Nagai[3]
[1] *Engineering Division, JAPANPILE CORPORATION, Tokyo, Japan*
[2] *IDEC, Hiroshima University, Hiroshima, Japan*
[3] *HIROKOU-GIKEN, Hyogo, Japan*

Abstract

In Japan, efficient use and recycling of materials from production, distribution, consumption, through to disposal are actively promoted. Thus, iron and steel slag is recycled in cement, road subbasecourse, and so on. Slag has hydraulic and expansive properties, which might be useful in some of its applications. The authors have been researching these applications in pile foundations, and have carried out a series of load tests on full-scale nodular piles in ground improved by compacted slag. This paper presents test results that showed that compacted slag around piles increased their lateral resistance.

Keywords— *Iron and steel slag, soil improvement, Lateral load test, Lateral resistance*

INTRODUCTION

In Japan, efficient use and recycling of materials from production, distribution, consumption, through to disposal are actively promoted. Thus, iron and steel slag is used for raw materials of cement and for road subbasecourse. Furthermore, the development of applications that best utilize slag's characteristics, particularly its hydraulic property and expandability, is required. In recent years, a method has been developed for compacting highly expandable slag around nodular-piles to increase the vertical bearing capacity of the pile-soil system [1].

However, in many cases, lateral resistance is a more important factor than vertical bearing capacity in determining the number of piles, pile diameter, and so on. The importance of an earthquake-proof pile foundation began to be recognized after the 1995 Hyogoken-Nanbu Earthquake. Pile foundations are required that have sufficient bearing capacity and deformation performance against large earthquakes. This has focused attention on developing a method for improving the lateral resistance of pile foundations.

One method of increasing the lateral resistance of pile foundations is to improve the ground around them. The most commonly used ground improvement method is the Deep Mixing Method [2], [3].

The authors are also carrying out research for the efficient use of slag. For example, they have been developing a method for increasing the lateral resistance of pile foundations by improving the ground over the whole pile length and the partial surface of the ground with slag [4]. This paper presents results of experiments showing that slag around piles has increased their lateral resistance.

KINDS AND BASIC CHARACTERISTICS OF IRON AND STEEL SLAG

2.1 Kinds of iron and steel slag

Iron and steel slag is generated in iron and steel production. This includes blast-furnace slag produced in the iron smelting process and steelmaking slag generated in the steel manufacturing process in a converter or an electric furnace. Blast-furnace slag ejected during melting and cooled down rapidly is called granulated slag. Granulated slag has a hydraulic property, and it is used as a raw material for cement and for fine aggregate.

However, steelmaking slag has an expandability property. An aging process is carried out to restrain expandability, and this material is used for the raw materials of road subbasecourse and so on. It also has a slight hydraulic property.

The chief ingredients of both are SiO_2 and CaO, as shown in Table 1, which shows the chemical composition of blast-furnace slag and steelmaking slag.

Table 1: Chemical composition

Type	SiO_2	CaO	Al_2O_3	MgO	T-Fe	S	MnO	TiO_2	Others
Steelmaking slag	11.3	37.3	3.9	15.7	20.4	0.04	6.1	1.5	3.8
Blast-furnace slag	33.8	42.0	14.4	6.7	0.3	0.84	0.3	1.0	0.7

2.2 Characteristics of slag used in experiment

Two kinds of slag were used for ground improvement in these experiments: mixed slag (weight ratio 80% steelmaking slag before aging process + 20% granulated slag) and steelmaking slag (100% steelmaking slag after aging process). Fundamental examinations comprising expansion test, permeability test and tri-axial compression test (CD) were carried out to examine mechanical characteristics.

A test piece (dimension: ϕ100× 200mm) was cured by leaving it at normal temperature in a closed plastic bag. The particle size distribution used for the examination was the same as that of the iron and steel slag used in the field tests, as shown in Fig.1. Curing periods were 1, 3, 6, and 12 months. The results of expansion tests and permeability tests were obtained up to 6 months in the incumbent stage, and the results of tri-axial compression tests were obtained up to 3 months. The results of these tests on mixed slag and steelmaking slag are shown in Fig. 2-3. The following can be understood from these figures.

(a) The coefficient of permeability decreased with time. In particular, the coefficient of permeability of mixed slag was small from the early stage, because it contains granulated slag with the hydraulic property.

(b) The expansion ratio increased with time. This tendency was more pronounced in mixed slag than in steelmaking slag.

The material constant obtained from the tri-axial compression test is shown in Table 2. The following can be understood from Table 2.

(a) Mixed slag had greater cohesion than steelmaking slag, and it increases with the curing period. This is a result of the hydraulic property.

(b) There was no difference between the internal friction angles.

(c) The elastic modulus of mixed slag is greater than that of steelmaking slag, and it changes little with lateral pressure. However, steelmaking slag increases under lateral pressure. This shows the influence of the hydraulic property of granulated slag.

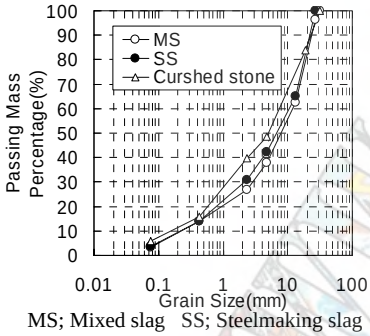

MS; Mixed slag SS; Steelmaking slag

Fig. 1: Particle size distribution

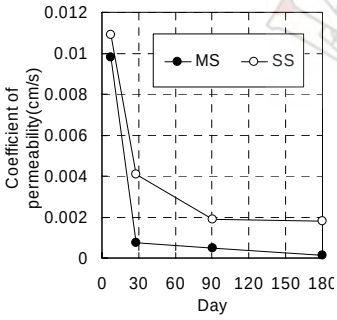

Fig. 2: Result of permeability

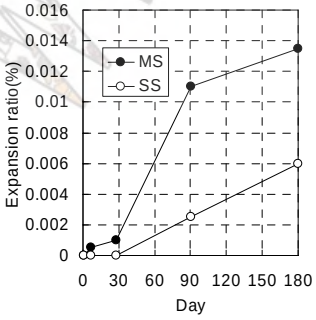

Fig. 3: Result of expansion test

MS; Mixed slag SS; Steelmaking slag

Table 2: Material constant obtained from tri-axial compression test

Slag	Curing month	Cohesion (kN/m^2)	Internal friction angle (°)	Elastic modulus E_{50} (kN/m^2) Lateral pressure (kN/m^2) 20	50	100
MS	1M	144.9	53.7	77228	109423	115225
	3M	259.5	48.4	129568	150050	121750
	3M/1M	1.79	0.90	1.68	1.37	1.06
SS	1M	45.0	49.6	16645	33567	51037
	3M	55.8	50.0	23232	44944	62006
	3M/1M	1.24	1.01	1.40	1.34	1.21

OVERVIEW OF TESTS

3.1 Test Ground

In the test ground, there was a layer containing slag and iron scraps around the surface. At 1.0m to 12.0m below the ground, there were loose silt layers with N-values of 0 to 7 and silty sand layers with N-values of 8. The surface ground to a depth 0.75m below ground level was replaced with sand, because the condition of the ground near the surface greatly influences lateral resistance. The underground water level was about 1.6m below the surface, and the substituted sand was in a humid condition. The soil boring log of the neighboring ground is shown in Fig. 4.

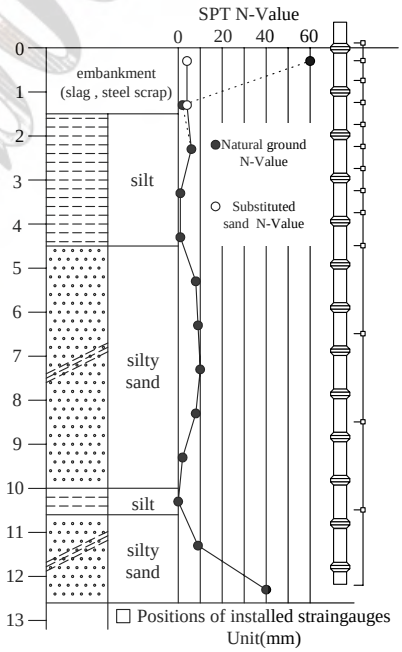

Fig. 4: Soil boring log

Table 3: Concrete nodular pile

Max diameter Do (mm)	Minimum diameter D (mm)	Equivalent cross section Ae (mm^2)	Prestress (N/mm^2)	Bending stiffness EI ($N \cdot mm^2$)
500	400	7.03×10^4	8.0	4.20×10^{13}

3.2 Outline of test pile

The test piles were pretentioned high strength concrete nodular piles of max diameter D_0=500mm to minimum

Table 4: Test cases

Case	Pile			Curing month (M)	Improvement of ground around pile		Improvement of subsurface ground			
	Diameter(mm)		Type		Improvement material	diameter Ds(mm)	Improvement material	Breadth		Depth
	Max	Min						B1(mm)	B2(mm)	F(mm)
Case1	500	400	Single pile	1	Crushed stone	750	-	-	-	-
Case2				1	MS	750	-	-	-	-
Case3				1,3,6,12			-	-	-	-
Case4				1,3,6,12			SS	2000	2000	750
Case5			Two piles in series	1,3,6,12	MS	750	SS	2000	3000	750
Case6				1,3,6,12			SS			1500

MS:Mixture of two kinds of slag (80% Steel slag before the aging process + 20% Blast furnace slag)
SS:100% Steel slag after the aging process

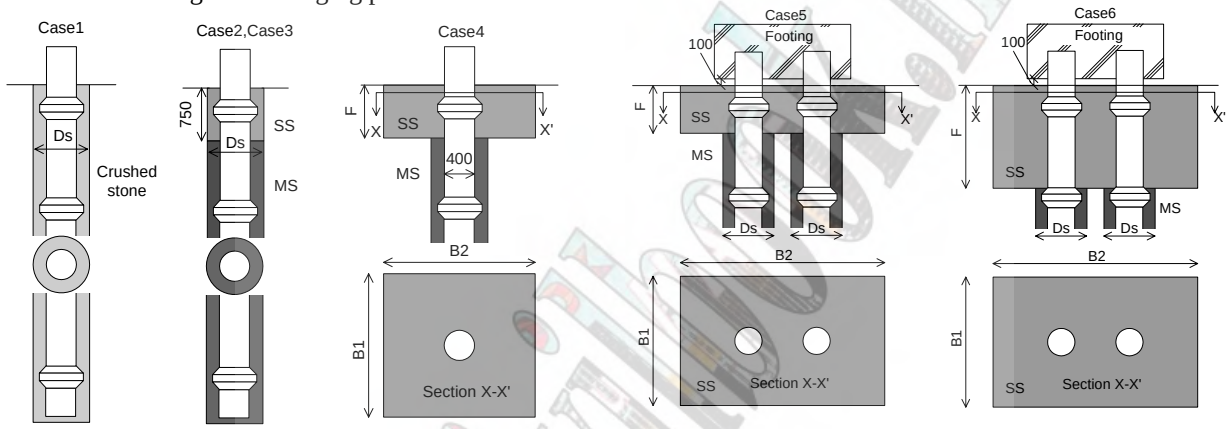

Fig. 5: Details of cases

diameter D=400mm, and length 13m, as described in Table 3. Strain gauges were installed at 12 locations.

3.3 Test case

The main specifications of each test case are shown in Table 4, and outline figures are shown in Fig.5. The ground improvement comprised improvement of ground around the pile near the surface (called improvement of ground around pile) and the improvement of subsurface ground around pile over its whole length (called subsurface ground improvement). The improvement of ground around the pile was provided in all cases. However, subsurface ground improvement was provided only in Cases 4-6.

The materials used for ground improvement around the piles were iron and steel slag and crushed stone (Case 1) for comparison with iron and steel slag. The crushed stone had about the same particle size distribution as the iron and steel slag (see Fig.1). Each improvement diameter Ds was 1.5 times the max pile diameter D_0 over the whole pile length. There was a concern that expansion of slag would adversely influence the footing slab and so on when slag with expansibility was used near the surface. Thus, in application to the actual pile foundations, the improvement of ground around the pile (Case 2 and Case 3) with steelmaking slag whose expansion was restrained from the surface to a depth of 0.75m below ground level, and mixed slag with expandability and hydraulic property below 0.75m below ground level.

To meet the specifications of improvement width, improvement depth of subsurface ground around pile, subsurface ground improvement was provided to Case 4 in the range of 2.0m (four times the max diameter D_0) ×2.0m× depth 0.75m. Moreover, for Case 5, which comprised two piles in series, subsurface ground improvement was provided in the range of width ($B1$) 2.0m× depth ($B2$) 3.0m× depth (F) 0.75m. For Case 6, the depth of subsurface improvement was twice that of Case 5. The subsurface ground improvement was achieved with steelmaking slag whose expansion was restrained.

Incidentally, the pile-center distance for two piles in series was 1.0m (four times the max diameter D_0). A rigid footing (1.0m×2.0m×0.8m) was provided to fix the pile heads, and a clearance of 100mm was provided between the footing bottom and the earth surface.

3.4 Test pile construction method

1) Construction of test pile and improvement of ground around pile

Test piles were constructed by the pre-boring method using a specific auger for compaction. The construction

flow is shown in Fig.6 and the construction processes are shown in Fig. 7. A test pile is inserted in a hole excavated using the auger, and then the casing is inserted. Fixed material for improvement of ground around the pile is packed into the clearance between the excavation and casing from the surface and compacted.

2) Substitution of surface ground and construction of subsurface ground improvement

To provide for a layer of gravel with slag and iron scraps around the surface of the test ground, the ground was dug to a depth of 1.5m. Then, to achieve the required ground improvement around the pile and the subsurface, the test pile was enclosed with a wooden pattern frame. Sand was packed outside the frame and the fixed improvement material inside the frame, and these were compacted while pulling up a wooden pattern frame (see Photo.1). Using vibration to achieve an N value of about 4, the improved part and sandy ground were compacted.

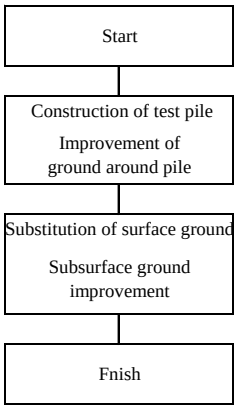

Fig. 6: construction flow

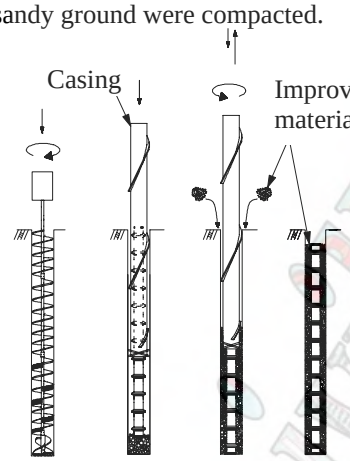

Fig. 7: Construction method and improvement of ground around pile

Photo. 1: Construction of subsurface ground improvement

TEST METHOD

Lateral load tests were carried out on Case 1 and Case 2 up to almost the ultimate condition after one-month curing. To examine the influence of change with time of the physical and mechanical characteristics of the slag, as well as to examine the effect of the subsurface ground improvement on the lateral pile resistance, lateral load tests were carried out for Cases 3-6 after curing periods of 1 month, 3 months, 6 months, and 12 months.

The lateral load tests within the curing period of 6 months were finished when a load that did not cause damage to the subsurface improved ground, and the lateral load tests for the 12-month curing period were carried out up to almost the ultimate condition.

4.1 Loading method

The test pile arrangements are shown in Fig.8. Case 5 and Case 6 were used as reaction piles. Cases 1 and 4 were arranged around Case 6, and Cases 2-3 around Case 5. Cases 5 and 6 were carried out together by pushing one another.

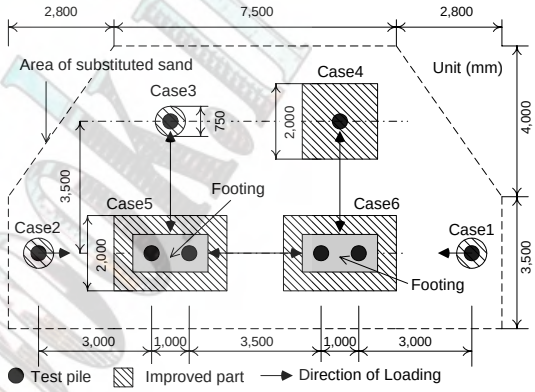

Fig. 8: Test pile arrangement

4.2 Data to be recorded

The lateral load tests were carried out in accordance with the standards of the Japanese Geotechnical Society [5]. The loading method consisted of one-direction multi-cycle loading.

Table 5 shows the standard load step sequence. Data to be recorded were lateral load, test pile displacements (loading point: G.L.+250mm, G.L.+100mm) and bending strains of test pile. However, displacements for Case 5 and Case 6 were measured at the top and bottom of the footing.

Table 5: Standard load step sequence

		Loading		Unloading
Loading method	Loading rate	(planned maximum load / number of step) / number of step		twice the rate used loading rate
	Period of loading	180sec		180sec
		900sec(No load)		
Items to be measured	Load	New load, Reload	0, 120sec	0sec
		No load	0,120,240,480,840sec	
	Displacement	New load, Reload	0, 120sec	0sec
		No load	0,120,240,480,840sec	

RESULT OF LATERAL LOAD TESTS

5.1 Effect of ground improvement by slag

The relations between lateral load H and lateral displacement y obtained from the lateral test carried out up to ultimate load are shown in Fig.9. The displacements for Cases 5 and 6 appear at the bottom edge of the footing, and the lateral loads are defined by those values divided

by the pile number. The lateral load tests for Case 5 and Case 6 were finished when Case 5 reached the ultimate condition. The following points can be understood from Fig.9.

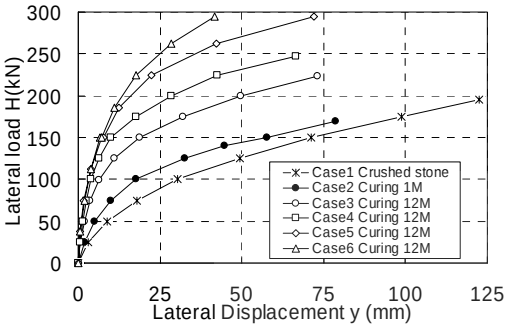

Fig. 9: Relationship between lateral load *H* and lateral displacement *y*

(a) By comparing Case 1 and Case 2, it can be seen that the initial lateral stiffness (lateral load / lateral displacement) of Case 2 shows greater improvement than Case 1 of ground around the pile. However, Case 2 is inferior by about 15% to Case 1 in lateral bearing capacity.

(b) By comparing Case 2 (Curing period 1 month) and Case 3 (curing period 12 months), it can be seen that the initial lateral stiffness of Case 3 is about three times that of Case 2, and the lateral bearing capacity is about 1.3 times with change of time of the physical and mechanical characteristics of slag.

(c) Comparison of the existence of the subsurface ground improvement showed that the initial lateral stiffness of Case 4 (curing period 12 months) is about 1.5 times that of Case 3 (curing period 12 months) due to the subsurface ground improvement.

(d) Comparison of the different depths (subsurface ground improvement) showed that the initial lateral stiffnesses of Case 5 and Case 6 were the same, although Case 6 was twice the depth of Case 5. Therefore, improvement in the depth direction didn't influence the improvement of initial lateral stiffness of the pile.

(e) Cases 4-6, provided with subsurface ground improvement, showed large lateral resistance to loads of 100-150kN. After this load, displacement increased nonlinearly, and the lateral stiffness decreased.

The crack development states in the subsurface ground improvement part observed visually during lateral load tests carried out at the curing period of 12 months are shown in Fig.10. The loads when cracks appeared are also shown. Micro-cracks began to form in each case at between 112-125kN. The subsurface ground improvement part thus became plastic, and it can be considered that (e) above occurred. However, it can be seen from Fig.9 that the load didn't decrease rapidly even when the subsurface ground improvement part became plastic.

As discussed above, piles provided with subsurface ground improvement can achieve large lateral resistance due to the stiffness of slag in the elastic range. It is also confirmed that lateral resistance didn't decrease rapidly after the subsurface ground improvement part became plastic.

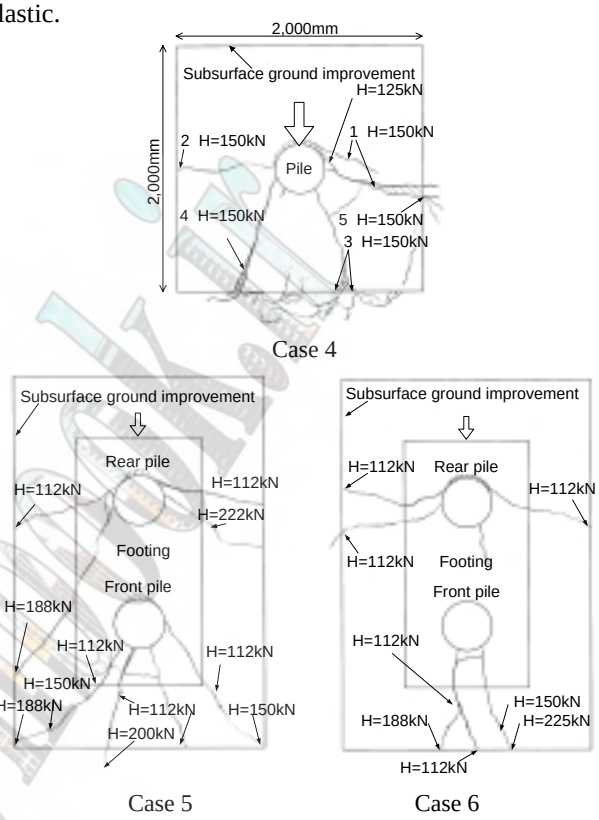

Fig. 10: Crack development state in subsurface ground improvement part

5.2 Effect of change with time of physical and mechanical characteristics of slag

The relations between lateral load *H* and lateral displacement *y* of Cases 3-6 for each curing period are shown in Fig.11. It can be seen from these figures that the lateral resistance increased with curing period. However, Case 5 and Case 6 with curing periods of 12 months showed a smaller tendency than those with curing periods of 6 months, because Case 5 and Case 6 were carried out after they were used as the reaction piles of Case 3 and Case 4.

To examine the increase in coefficient of lateral sub-grade reaction for each curing period due to the subsurface ground improvement, the coefficients of lateral sub-grade reaction k_h of Case 3 and Case 4 were computed. Assuming that the coefficient of lateral sub-grade reaction k_h is distributed uniformly in the depth direction, it was calculated in reverse using the elastic beam method proposed by Chang from the relations between lateral load and lateral displacement obtained from the lateral load test.

The coefficients of lateral sub-grade reaction for Case 3 and Case 4 are shown in Figs.12 and 13. The coefficient of lateral sub-grade reaction k_{h4} for lateral displacement 4.0mm (0.1D) calculated by the approximate curves shown in these figures are shown in Table 6. The ratio for the value of 1 month is shown in parenthesis in Table 6.

It was understood that the coefficient of lateral sub-grade reaction k_{h4} increased with increase in curing period. The increase rate of 12 months with that of 1 month was 1.70 for Case 3, 2.57 for Case 4, and the rate of Case 3 with Case 4 was 1.10 for 1 month and 1.67 for 12 months. A clear difference in effect appeared with change with time of the physical and mechanical characteristics of slag, although the effect of the subsurface ground improvement was the same as the effect of ground improvement around the pile after curing for 1 month.

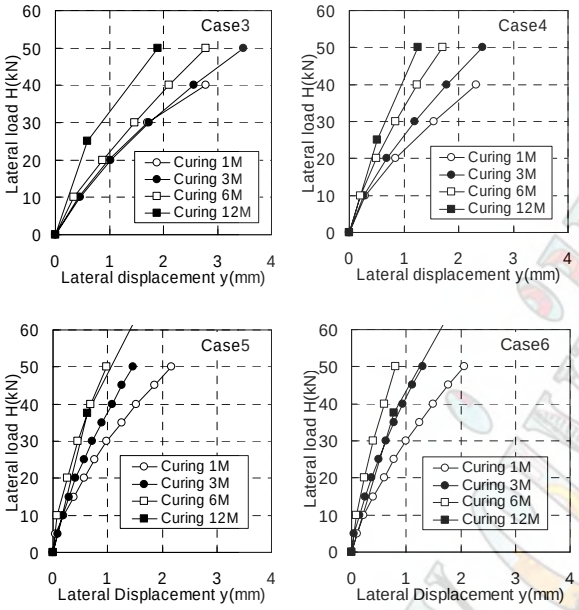

Fig. 11: Relationship between lateral load H and lateral displacement y of Case3-Case6

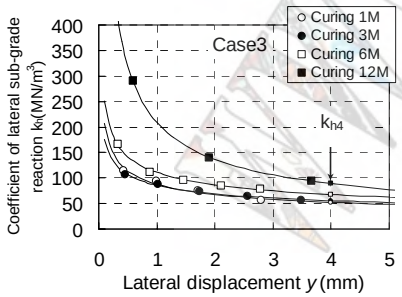

Fig.12: Relationship between k_{h4} and y (Case3)

Table 7: Comparison between k_{h4} and ${}_sk_{h4}$

Curing month	Cofficient of lateral subgrade reaction (MN/m^3)		
	k_{h4} obtained by the reverse calculation	${}_sk_{h4}$ obtained by the equation (1)	${}_sk_{h4}$ / k_{h4}
1M	57.8 (1.00)	132.7(1.00)	2.3
3M	82.5 (1.43)	184.6(1.39)	2.24

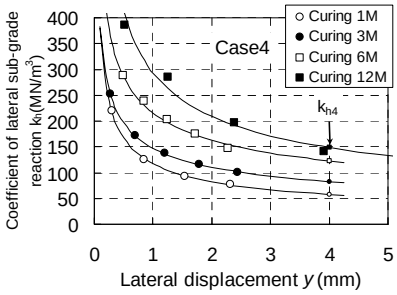

Fig.13: Relationship between k_{h4} and y (Case4)

Incidentally, the coefficient of lateral sub-grade reaction k_{h4} for Case 1 (crushed stone) for the curing period of 1 month calculated by the same method was 26.3MN/m^3. Compared to Case 1 with the curing period of 1 month, Case 3 with the curing period of 12 month was 3.4 times, and Case 4 with the curing period of 12 months was about 5.6 times.

Furthermore, using the elastic modulus obtained in the tri-axial compression test, we tried to evaluate the coefficient of lateral sub-grade reaction ${}_sk_{h4}$ for the subsurface ground improvement for Case 4. The subsurface ground improvement part was slag ground spread out in the horizontal direction to infinity over its whole depth, and the coefficient of lateral sub-grade reaction ${}_sk_{h4}$ was calculated from equation (1), as recommended by the Architectural Institute of Japan.

$$ {}_sk_{h4} = k_{h0} \times y^{-0.5} \quad (1) $$

where, $k_{h0} = \alpha \cdot E_{50} \cdot (B/0.01)^{-(3/4)}$ (2)

in which k_{h0} is the coefficient of lateral sub-grade reaction (kN/m^3); y (=0.4) is lateral displacement (cm); α is 60 for clay and 80 for sand; E_{50} is elastic modulus (kN/m^2), and B is pile diameter (m).

The elastic modulus E_{50} (lateral pressure 20kN/m^2) adopted the value obtained from the tri-axial compression test. The coefficient of lateral sub-grade reaction ${}_sk_{h4}$ was calculated for the curing period of 3 months, in which the elastic modulus E_{50} was obtained in the incumbent stage. The coefficient of lateral sub-grade reaction k_{h4} obtained by the reverse calculation and ${}_sk_{h4}$ calculated by equation (1) are shown in Table 7. Although the rates of increase with the curing period are equal, the rates for the coefficient of sub-grade reaction ${}_sk_{h4}$ with coefficient of sub-grade reaction k_{h4} are about 2.3 times.

Table 6: Coefficient of lateral sub-grade reaction

Curing month	Cofficient of lateral sub-grade reaction k_{h4}(MN/m^3) k_{h4} obtained by the reverse calculation		
	Case3	Case4	Case4/Case3
1M	52.4 (1.00)	57.8 (1.00)	1.10 (1.00)
3M	55.5 (1.06)	82.5 (1.43)	1.49 (1.35)
6M	67.7 (1.29)	123.1 (2.13)	1.82 (1.65)
12M	89.0 (1.70)	148.3 (2.57)	1.67 (1.52)

5.3 Digging test

To investigate the form of the improvement part after the lateral load test for the curing period of 12 months, the ground was dug up to a depth of 1.5m. The crack position

of the pile body for this test is shown in Table 8. The knowledge obtained from the test is stated in the following.

(a) The subsurface ground improvement part improved by steelmaking slag with a slight hydraulic property solidified for a thickness of 100-50mm on the surface of the earth, and a thickness of about 10-5mm on the surrounding of improvement part. However, the inside slag didn't solidify very much (see Photo. 2). The surface on the earth side is where the supply of water is most abundant due to rain and so on, and it could be thought that solidification advanced. Furthermore, because the ground in the neighborhood was sandy and water permeability was large, water from rain and so on permeated inside. As a result, solidification was promoted in the surrounding improvement part. It is considered that the solidification of steelmaking slag with a slight hydraulic property didn't progress because permeability to the inside of the improvement part was obstructed by solidified parts. It is understood that a moderate water supply is necessary for the solidification of steelmaking slag.

(b)For the improvement of ground around the pile improved by steelmaking slag from surface to a depth of 0.75m, solidification on the earth surface and the surrounding improvement part was similarly advanced, but its inside didn't solidify very much.

(c) For the improvement of ground around the pile at depths below 0.75m, the solidification progressed to the inside of the improvement part due to the potential hydraulic property of the granulated slag contained in the mixed slag, and a column body was formed. Moreover, the sandy ground around the circumference was left under the compacted condition, to a thickness of about 100mm around the improvement part, without collapsing against digging (see Photo. 3). It can be considered that the sandy ground around the improvement part was compacted due to the expandability of steelmaking slag in the mixed slag before the aging process. Incidentally, for Case 1 in which crushed stone was used for the improvement of ground around the pile, this tendency wasn't observed.

(d) In Cases 1-4, carried out under free conditions at the pile head, a crack in the pile body appeared in the neighborhood of the boundary (depth of 0.75m) of the two kinds of slag. This is considered to be caused by stress concentration at the boundary, where the stiffness of ground improvement was greatly different, because lateral load tests were carried out under the condition where maximum bending strain occurred in the ground part. However, in Cases 5-6, which were carried out under fixed conditions at the pile head, no crack appeared in the pile body below the ground. However, a crack appeared around the projected pile head. This phenomenon shows that stress didn't concentrate at the boundary.

With regard to the subsurface ground improvement, solidification around the extreme surface of the earth only influenced the improvement of the lateral resistance of the pile, because the inside slag didn't solidify very much. Therefore, even though the depth of the surface improvement was two times, no great difference was seen in the initial lateral stiffness of the pile (mentioned in 5.1(d)). However, for the pile foundation structure, water isn't supplied to the extreme surface of the earth of the subsurface ground improvement part directly. The way of curing on this test is thought to be greatly different from that in the actual environment. Thus, if mixed slag with a larger hydraulic property than steelmaking slag is used as the ground improvement material, lateral pile resistance can be expected to increase, as the solidification is promoted to the inside of the subsurface ground improvement part. Therefore, the expansion pressure of slag is grasped quantitatively, and its influence on the footing slab needs to be evaluated. This is a future subject.

As discussed, the following factors showing that the lateral pile resistance increases with increase in curing period can be understood from this digging test.

(1) Solidification of the subsurface ground improvement and the improvement of ground around the pile at the extreme surface of the earth

(2) Solidification of the improvement of ground around pile which was improved by mixed slag and the effect of compaction by the expandability of mixed slag

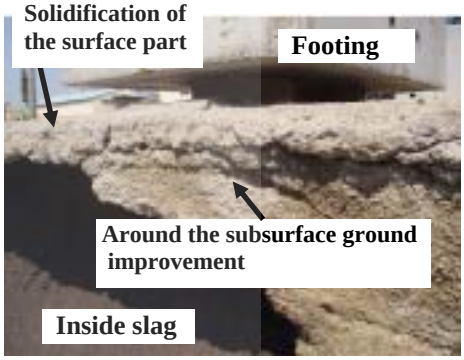

Photo. 2: Form of subsurface ground improvement part

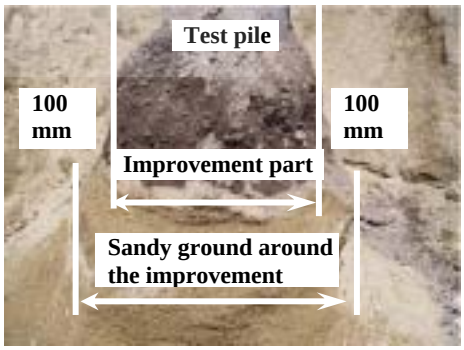

Photo. 3: Form of the improvement part (mixed slag)

Table 8 :Crack position of piles

Case		Crack number	Crack occurrence depth(mm)		
Case1		3	660	980	1260
Case2		3	620	920	1190
Case3		3	760	990	1340
Case4		3	540	730	940
Case5	Front pile	1	-50		
	Rear pile	1	-100		
Case6	Front pile	0	It can't be confirmed.		
	Rear pile	1	-50		

CONCLUSION

We examined methods of increasing lateral pile resistance by improving the ground around pile foundations by using iron and steel slag. The following were confirmed from the results of lateral load tests.

(1) Iron and steel slag as an improvement material around piles is effective in increasing lateral resistance.

(2) Lateral pile resistance in ground improved by iron and steel slag increases with time as the physical and mechanical characteristics improve. The coefficient of sub-grade reaction increase by about 1.7 times for improvement of ground around a pile, about 2.6 times at subsurface ground improvement by curing for twelve months. Accordingly, the use of slag as an improvement material enables reduction in cost if such a lateral pile resistance at the completion of building structures can be used during design.

(3) A pile provided with subsurface ground improvement can achieve large lateral resistance due to the stiffness of slag in the elastic range, and it doesn't decrease rapidly after the subsurface ground improvement part becomes plastic.

(4) In this test, the ground improvement around the surface of the earth was improved by steelmaking slag in which expansion is restrained in consideration of the application to the actual pile foundation. When using mixed slag with larger potential hydraulic property than steel making slag, greater lateral pile resistance can be expected.

ACKNOWLEDGMENT

The authors are grateful to HIROHATA WORKS NIPPON STEEL CORPORATION's, Mr. Michishita for providing us with the test site, and other project participants. They also express their gratitude to the members of a committee of JAPAN ASSOCIATION FOR BUILDING RESEARCH PROMOTION "A practical use to pile foundations of iron and steel slag" (Chairman of a committee: a professor emeritus of Tokyo Institute of Technology. Hideaki. Kishida).

REFERENCES

[1] S.Yabuuchi, A.Nishiwaki, K.Kobayashi, K.Hirao and N.Yoshikawa, "Bearing capacity of bored pile packed with iron and steel slag using precast concrete pile," Deep Foundations on Bored and Auger Piles, W.F.Van Impe – Editor, 2003, 275-284

[2] Kouno Masami, Suzuki Noriyuki, Wada Norifumi, Sakate Michiake, "Acomposite Pile Foundation with Improved Soil and Loading Test," Brige and Foundation Engineering, 2000-1, pp.21-27.

[3] Shogo MIYAJIMA, Masaki KITAZUME, Kiyoshi IIDA, "Dynamic resistance of a pile in cay ground improved by Deep Mixing Method,"(in Japan), TECHNICAL NOTE OF THE PROT AND AIRPORT RESERCH INSTITUTE, N0.1048, 2003.

[4] Yusuke Homma, Koji Tominaga, Hitoshi Ogura, Oyobu Nagai , "Lateral resistance of piles in ground improved by compaction method with iron and steel slag," (in Japan), the 49th Geotechnical Engineering Symposium, 2004, pp. 165-172.

[5] The Japanese Geotechnical Society, "JSSMFE STANDARD METHOD FOR LATERAL LADING TEST FOR A PILE," 1983.

[6] The Architectural Institute of Japan, "Recommendations for Design of Building Foundations" (in Japan), pp. 277–278, 2001.

Procedure of Seismic Risk Assessment for Underground Transportation Tunnel

C.H. Chen[1], C.H. Wang[2], Wei F. Lee[2], Hsing-Tai Mei[2], Chia-Fang Chang[2]
[1]*Department of Civil Engineering, National Taiwan University, Taiwan*
[2]*Taiwan Construction Research Institute, Taiwan*

Abstract

After 1999 Chi-Chi earthquake, two major concerns were raised by the authority of transportation facilities in Taiwan: adequacy of present seismic design codes, and seismic resistant capacity of existing structures. As a result of extensive studies and investigations, not only seismic design codes of transportation infrastructures were upgraded, yet major amount of structures were found to suffer damages at different levels. An extensive seismic risk assessment program was therefore initiated by the authorities in an effort to collect performance data of existing structures, to re-examine seismic design of existing projects, and finally to develop an feasible nation-wide retrofit program. In this paper, the authors will present procedures conducted as well as preliminary results of seismic risk assessment of an underground tunnel project: the Kaoshiung cross-harbor Tunnel. The Kaoshiung cross harbor Tunnel was a submerged pre-cast pre-stressed concrete tunnel constructed in 1983. Structure damage inspections was first conducted to access the damage or current performance level. Analytical models were then developed to both re-examine the seismic design under the new code as well as simulate possible damage under specified earthquake magnitude. Purpose of this study is to obtain adequate procedures of seismic risk assessment for an important existing underground tunnel.

Keywords—*Seismic Risk Assessment, Underground Tunnel, Existing Structure*

INTRODUCTION

With high seismic event occurrence, the seismic design has been an important issue for the Taiwan civil engineering practice. When the Chi-chi earthquake struck central part of Taiwan island at 1999, not only the central island suffered great losses on property and casualty, but also the Taipei city, which is about 200km away from the epicenter, experienced several building collapsed due to the basin effect. This catastrophic event reveals that the seismic design specification needs to be reevaluated with involving proper design procedure. In the past 6 years, combining efforts from research and practice, the seismic design specification in Taiwan has been revised several times based on the conclusions of analyzing seismology data and structure performance. Those efforts lead government and private consultants for more reliably design, particularly the design on the public transportation system.

In the past several decades, most of the engineers and researchers concentrated on improving the design specifications of new structures. However, as the increasing of the public needs, the usage of the existing transportation system usually exceeds it original design capacity during the service life. This may seriously affect the performance of structures in their future service life span. Combined with some other factors, such as construction defects and material property decay, the performance may drop to a dangerous level. It produces an important issue: will this structure fulfill its designed purpose when the next big earthquake strikes?

In order to insure an existing structure behaves in an adequate safety level during the seismic event, it is necessary to establish a detailed procedure for a appropriate seismic risk assessment. From the standpoint of designing new structure, the purpose is to satisfy the performance criteria. For an existing structure, however, the assessment need to review the past history, to examine the current safety statues, to assess the seismic performance, and finally to evaluate the maintenance requirement for remaining this performance. This article presents a four-stage procedure to provide a proper seismic assessment procedure, which includes: initial condition assessment; seismic risk assessment; impact and retrofitting assessment; and total solution plan.

The Kaoshiung cross-harbor tunnel, which is an underground tunnel, connects the transportation between the Kaoshiung city and the Port of Kaoshiung. In its past 20 years of service, this underground tunnel provides the only route for fully loaded vehicles to access to harbor. In order to ensure another 30 years of future service life, the authority of the Port of Kaoshiung issued a project to investigate the current safety status, including the seismic performance. Currently this project is being executing on the retrofitting design, this article presents the early finding of this project as an example to illustrate the four-stage seismic risk assessment procedure.

The purpose for this article is to propose a proper procedure for the seismic risk assessment, especially for the underground structure. This procedure will give researchers and engineers a guideline to evaluate the performance of the existing structures. Furthermore, this procedure can also provide a suitable long-term

maintenance strategy to remain the structure in an adequate service condition.

PROCEDURE OF SEISMIC RISK ASSESSMENT

When the human development marches into the 21st century, as the population and economy growing rapidly, the transportation system plays an important role to transport people and produced for further achievements. When the new construction is design with the up-to-date specification, the existing structures that were designed with the previous standards could be challenged for their safety sufficiency. Especially, when this challenge is threatened by the potential of hazard occurrence, it will be an important step to undergo the risk assessment procedure. In the history of Taiwan, the earthquake events happened frequently. One of the most serious events was the 1999 Chi-chi earthquake, which killed more than two thousand people and produced great society loss. In order for the existing public transportation system to encounter any possible seismic event, a properly defined approach for seismic risk analysis is an important thing to be completed. In this article, a proposed procedure for the seismic risk assessment is presents. This procedure emphasized on several important components (shown in Fig. 1).

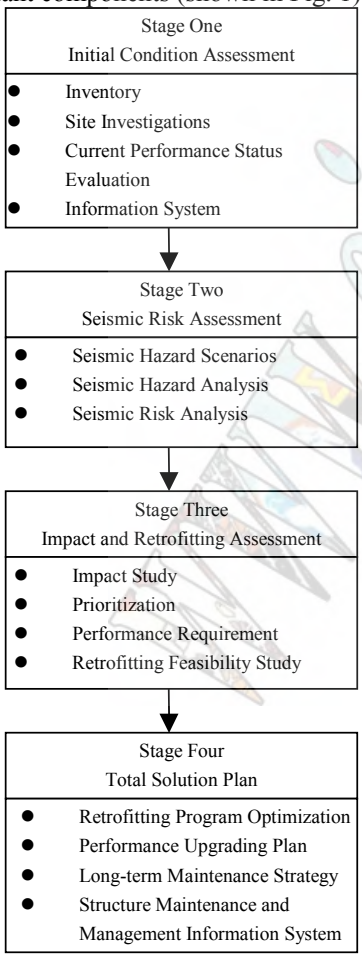

Fig. 1: Proposed Seismic Risk Assessment Procedure

For the region with high seismic event occurrence, usually an important existing transportation structure, such as bridges and tunnel, should be considered to have a seismic upgraded regularly. It is because not only the technology has been progressed to gain more understanding on the earth tectonics, but also the structure that decays over time requires a proper maintenance with the acceptable performance level. This proposes procedure is designed to have a complete performance evaluation over the seismic risk assessment. The following sections explore the details of each stage with further dissensions.

Stage one: initial condition assessment

Inventory

The performance of the structure was decided from the initial design stage. In order to define the starting point of the performance, this assessment procedure starts from collecting the original design of the structure and the original construction records. During the information collecting, it shows that the current performance of the existing structure depends on the factors that may decrease the performance level in the past service life. These factors include the maintenance records, hazard and recovery history. Furthermore, some environmental, such as temperature, may produce damages for structure and material property degrading.

Site Investigations

Other than the inventory process, the site investigations provide evidence of the current condition for the structure. In these investigations, the targets may include the reinforced concrete, pavement, soil exploration, drainage system, electrical system, etc. The results of those investigations should be able to show the extent of damages with various severity levels. The conclusions contribute to the analysis of possible hazard contributions; hence, the similar hazard may be expected in the future service live.

Current Performance Status Evaluation

One of the most important things for the risk assessment is to evaluate the current stability, or the performance status. The evaluation should first re-evaluate the feasibility of the original design. Combined with the information that obtained from the site investigation results, another analysis should involve the current reality, such as the material property degradation, to estimate the current performance level.

The outcome may show the comparison between the current performance level and the required performance level. Combined with the hazard analysis, it will provide the needs for retrofitting program and the long-term maintenance strategy.

Information System

While information collecting and performance analysis are carried out in this stage, an information system is required for storing these knowledge. In current advance of technology, the type of information can be document, still pictures, motion pictures, sound, etc.

With proper organization, the history and current condition of all facilities and structures can be systematical stored in this system. Most importantly, this system should be expanded into the structure maintenance and management information system, which will be further discussed in the Stage Four.

Stage two: seismic risk assessment

Hazard Scenarios

In the conventional approach, the seismic hazard is only to estimate the possible seismic hazard produced by the earthquake. However, this type of hazard analysis neglects the current condition the existing structure. The various types of seismic hazard scenarios should consider all possible factors that may decrease the performance level. Those factors and their effects can be concluded from the works done in the first stage: history data, site investigation, and current performance status evaluation. For example, in a possible seismic hazard scenario, the structure performance should be evaluated according to a possible seismic magnitude and a deduction of material strength due to deterioration.

Seismic Hazard Analysis

The approaches for seismic hazard analysis have been standardized in several ways, for example, deterministic seismic hazard analysis, probabilistic seismic hazard analysis, earthquake scenario analysis, etc. Because the tectonic activities in each faulting system have their unique features, the seismic hazard analysis requires frequently updated from new earthquake events. However, the most conveniently method is to obtain the seismic hazard map, for example the maps provided by the U.S. Geological Survey.

Seismic Risk Analysis

In the hazard scenario analysis, the hazard can be produced by the combination of the earthquake force and other factors. Based on the characteristics of various scenarios and their uncertainties, the seismic risk analysis should emphasize on the risk produced from various extent and severity of hazard. For example, a possible hazard scenario for the seismic risk analysis of a 20-year-old freeway bridge should consider several factors, including surrounding environmental effect (e.g. slope stability and river flooding), material stiffness decay, possible foundation problem, etc. A combination of effect produced from the uncertainties of all factors will produce a complete seismic risk analysis.

Stage three: impact and retrofitting assessment

Impact Study

In addition to the hazard occurred to the facilities or structure itself, another important subject is the subsequent impacts. These impacts include the human life loss, property loss, society impact, and so on. Additionally, the loss of function for a specific facility or structure may shift the load to others, which may bring the secondary impacts when the other facilities or structures fail. At last, in order to recover from those impacts, the cost from the recovering action will bring another impact. For example, when an important bridge fails in a seismic event, it may produce a great impact to the transportation system. Besides, the rescuing action and the rebuilding process will also cost countless society assets.

From the impact study, the outcomes may be traced back to the causes of damage, which will give a great guideline to define the performance requirement. This will lead the choice of retrofitting program to reestablish the performance to a desired level.

Prioritization

An earthquake event may only strike some facility or structure among an infrastructure system. The damages occurred on the facility and structure may also concentrate some specific components. For a massive retrofitting plan, for example the ongoing projects of retrofitting plan for the bridges of Taiwan freeway system, the government annual budget only allows a limited amount of bridge to be retrofitted in every year. A prioritization process is required In order to upgrade freeway bridges to the desired performance level in every year.

From the point view of damage level, the prioritization process should depend on the risk assessment and the impact study. On the other hand, the sequence to retrofit bridges in an infrastructure system should depend on their importance to the system. In the further analysis of the retrofitting on a single structure, the cost and type of construction on every component should be judged by the importance of the component, also the improvement on the component performance that contributes to the overall performance of the structure. To sum up all considerations above, it provides the guideline for the prioritization process.

Performance Requirement

The performance requirement should be illustrated in three different levels: the entire infrastructure system, the individual facility or structure, and the individual component. According to Vision 2000 (SEAOC, 1995) [1], the definition of performance level is based on three factors. First factor is the earthquake performance level, which describes the required condition (e.g. fully operational, operational, life safe, and collapse) after the structure suffered from the earthquake damage. Second factor is the earthquake design level, which involves the magnitude of design earthquake (e.g. reoccurrence period of 970, 475, 72, or 43 years). Third factor is the importance of the structure, which is defined in terms of basic objective, essential/hazardous objective, and safety critical objective.

Retrofitting Feasibility Study

Before draw the conclusion for the final retrofitting plan, many techniques can be chosen for individual component. However, due to the limitations from the budget, time, human factors, environmental restrictions, etc., some of the techniques may not be suitable. Besides, in the feasibility study, the decision-making process should also depend on the importance/priority and the

required performance level.

Stage four: total solution plan

Retrofitting Program Optimization

The retrofitting program optimization provides the final solution to upgrade the performance to the desired level. In this optimization process, retrofitting program not only includes the retrofitting construction, but also includes the possibility of rebuilding. When the structure service life approaches to its end, or the cost of upgrading plan is too high, the process of demolition and rebuilding may bring a better chance to upgrade the entire infrastructure system.

In some occasions, the retrofitting program should also consider the regular inspection procedure and the real-time monitoring system. Especially for the important structure, it will ensure the performance can be closely observed. The re-time monitoring system can provide pre-warning action that allows people to react before and after any disaster occurred.

Performance-Upgrading Plan

After the retrofitting program optimization, the performance-upgrading plan provides the action plan to carry the construction. This plan should prioritize the individual construction among the entire infrastructure system. It should also give a proper schedule for the construction.

Long-term Maintenance Strategy

The lowering of performance level for the existing structure is usually caused by the lack of maintenance or the poor maintenance procedure. In order to keep the desired performance, a proper maintenance approach should be planned. The plan may include regular inspection, repairmen, and future retrofitting plan.

The strategy should also include the real-time monitoring and response system. For the important structure, once the damages occurred, the monitoring system provides a pre-warning response to alarm people to act before disaster happened. When the worse scenario strikes, the re-time response system may provide the solution for rescuing and minimize the loss.

Structure Maintenance and Management Information System

In the first stage of this proposed procedure, the initial study involves woks to collecting information about the target facility or structure. In order to preserve those data in an organized system, an information system is recommended. At the stage four, when the performance upgrading for the facility or structure is completed, the efforts on maintaining the performance become an essential duty.

The arrangement of the structure maintenance and management information system includes several important purposes. First, the information (stage one) and the conclusions (stage two to four) from this procedure should be properly preserved. Second, in order to closely monitor and inspect the quality of the regular maintenance, the system should be able to identify the elements among the entire facility or structure and properly accumulate the maintenance records. These records can provide people to predict the possible maintenance needs and the approximate budget. Third, once a hazard occurred, this system that connects to the real-time monitoring and response system can be triggered. The information that related to the occurrence of this hazard, as well as the impact with its recover results, should also be preserved in the system. Fourth, this system is able to control and monitor the electrical elements, for example the drainage, venting, and lighting systems.

CASE STUDY: KAOSHIUNG CROSS-HARBOR TUNNEL

Located at the south of Taiwan, the major function of the Kaoshiung cross-harbor tunnel is to link the transportation between the Kaoshiung city and the Port of Kaoshiung (Fig. 2). The construction began from May 1981 and end at May 1984. The entire tunnel can be divided into three parts: the Chiang-chen Entrance section, the Chung-chin Entrance section, and the 6 submerged segments. In this study, the main concern focuses on the submerged segments.

The 6 submerged segments were manufactured separately in factory with pre-stressed and pre-cased reinforced concrete in length of 120m. After the manufacture was finished, the segments were shipped by boat to the pre-dug trench. The construction was finished by backfilled sand and gravel on the top of the 6 submerged tunnel segments. In Fig. 3, the top of the 6 submerged tunnel segments (labeled as U1 to U6) are located 14m below the seawater. Fig. 4 shows the cross section with the formation of backfilled layers. In order to prevent the possible differential settlement to causes any structural damage, only J5 was designed as a fixed joint, J1 to J4 were designed to be flexible and able to against certain level of differential settlement. Fig. 5 shows the typical cross section of the submerged tunnel.

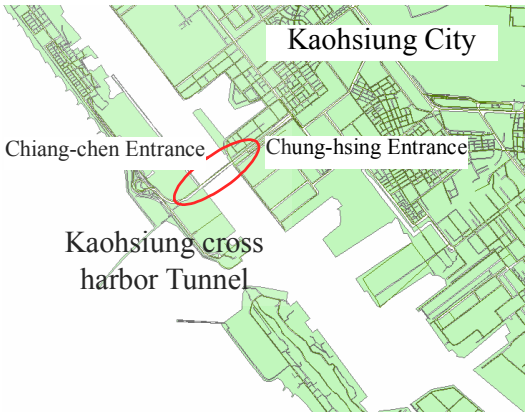

Fig. 2: Location of Kaoshiung cross-harbor tunnel

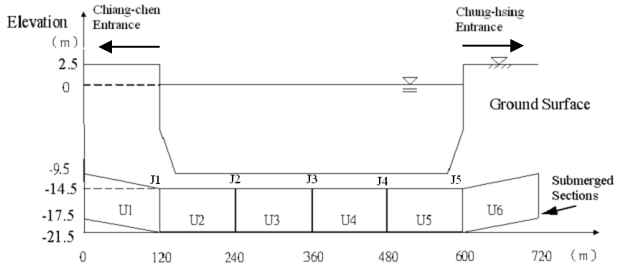

Fig. 3: Side view of the submerged tunnel sections

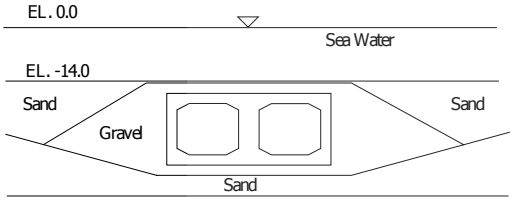

Fig. 4: View of backfilled soil and the submerged tunnel section

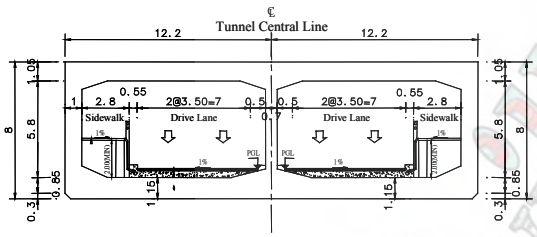

Fig. 5: Typical cross section view of the submerged tunnel

In the past 20 years of the service life, in addition to the regular maintenance requirement, there is no serious damage has occurred. The only one emergence event was caused by the heavy rainfall in 2001. The pumping system was not able to pump out the inflow water immediately, which caused water to accumulate insides the tunnel. However, as an important transportation structure, any minor malfunction can cause serious impact to the surrounding environment. In order to ensure that the Haoshiung cross-harbor tunnel can provide sufficient service in the next 30 years, the authority of the Port of Kaoshiung issued a site investigation and safety evaluation program. This article presents a brief summary of part of this program. For the current working progress in this program, the results provide a good example for the first and second stages in the proposed procedure of the seismic risk analysis.

Review of stage one

Besides the structure of the tunnel itself, the Kaoshiung cross-harbor tunnel includes several important facilities: drainage system, anti-corrosion system, joint-controlling system, pavement system, venting system, lighting system, and monitoring system. In the first stage of this procedure, documents that have been reviewed include the original design, the construction records, and the construction summary report. However, the same as many other facilities in Taiwan, due to the lack of a systematic collection, the maintenance records are very difficult to locate. In this case, the possible factors that may affect the performance can only be concluded by collecting the environmental condition data and the site investigations.

The environmental condition data include the weather records, geology data, earthquake records, the traffic condition, and the ocean sedimentation records. This review indicates a soft sandy soil layer exists among the harbor region. The same concern as the initial design, the soil liquefaction is a factor that will affect the performance. A further investigation will be present in the review of stage two.

A comprehensive sit investigation program has performed for this program. Some major investigation items include:

- Structural defects on cracks, joint leaking, material strength, and corrosion.
- Structure vibration test.
- Assessment on pavement condition.
- Assessment on electrical facilities.
- Settlement assessment.

Based on the findings from the site investigations, this article will concentrate on the structure dynamic stability and the settlement-related problem. There are several findings that may provide information in future safety evaluations. First, by using visual inspection and impact echo testing, there are 10 major cracks have been found with the average depth of 7.3cm. Second, the settlement was observed among the entire tunnel. Particularly, the amount of settlement becomes larger near the connections between the submerged tunnel and the entrances. Third, the vibration mode were measured in three different methods, including the background noise measurement, the impact measurement, the measurement of single truck, and the measurement of normal traffic.

Review of stage two

In order to simulate the possible hazard scenarios in the analytical models, the factors that may affect the performance level must be identified. First, one of the major tasks for the safety evaluation is the dynamic force. Twenty years ago, the initial design only used 0.15g for the seismic evaluation. Currently, the seismic force in the Koashiung area has been upgraded to 0.23g. The models need to evaluate the effect that caused by this difference. Second, in order to simulate the effect caused by the real earthquake motion, a synthesized time history was used to assess the structural response. Third, structural defects, such cracks and material strength decay, were involved to evaluate the performance level. Fourth, due to this region contents a loose sandy deposit, the soil liquefaction potential was evaluated with further settlement analysis.

In the structural analysis, the purpose is to locate the possible stress concentration that may causes structural

damages. A three-dimensional analytical model was established by using the SAP2000 program, as seen in Fig. 6. Because the current attention is on the submerged tunnel, this model only simulates the submerged segments. In this model, the hazard scenarios include using the actual material properties combined with the seismic evaluation. For purpose of the seismic evaluation, the time history of the 1999 Chi-chi earthquake at the nearby strong-motion station was chosen. Furthermore, this earthquake time history was scaled to have the peak acceleration of 0.23g. Fig. 7 shows the plot of input earthquake time history. The results of this analysis show the stress concentration occurs near the joint J5 (shown in Fig. 8), which is a fixed joint connecting U5 and U6 segments. A further assessment is required to estimate any possible retrofitting plan for upgrading the current performance.

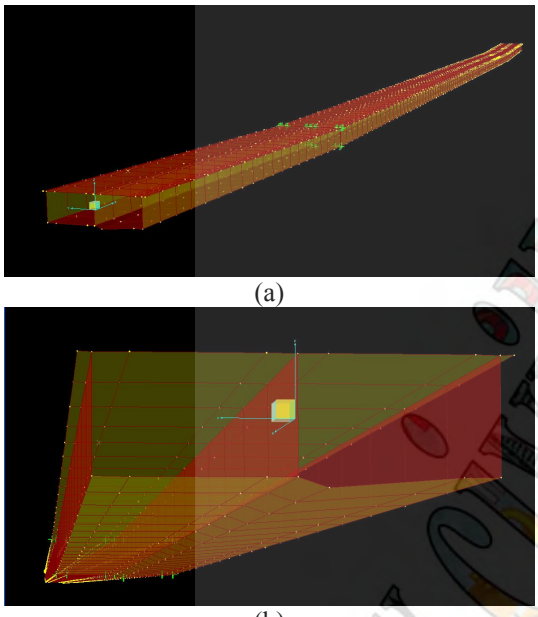

(a)

(b)

Fig. 6: Three-dimensional SAP2000 model (a) side view and (b) front view

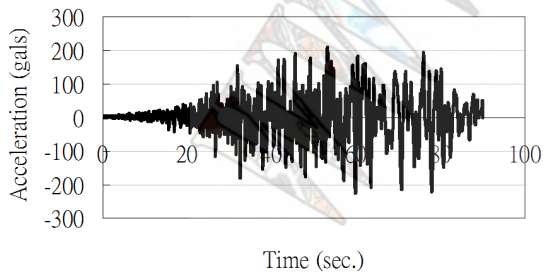

Fig. 7: Input earthquake time history for the three-dimensional SAP2000 model.

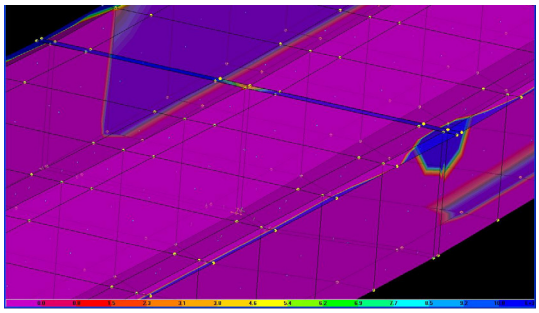

Fig. 8: Stress concentration plot.

The damage assessment caused by the soil liquefaction started from the evaluation of soil liquefaction potential. Soil boring data were collected for the nearby region. First, the safety against the soil liquefaction was calculated by using the modified Seed approach (NCEER, 1997) [2]. Second, the Iwasaki method (Iwasaki et al., 1982) [3] was then used to estimate the liquefaction potential. The Iwasaki method used P_L to define the liquefaction potential, in which $P_L<5$ for none to low potential, $5<P_L<15$ for the moderate potential, and $15<P_L$ for high potential. In this analysis, the input maximum earthquake acceleration (a_{max}) was chosen as 0.15g and 0.23g. As shown in Fig. 9, by using the original design a_{max} of 0.15g, the region surrounding the tunnel shows none to low soil liquefaction potential. When a_{max} increases to 0.23g, Fig. 10 shows that the soil liquefaction potential among this region shifts to the high potential. The difference can also be examined from the safety against liquefaction within various depths. Table 1 shows the boring data at Site A (location shown in Fig. 9). The safety factor (FS) of soil liquefaction demonstrates great difference when a_{max} changes from 0.15g to 0.23g.

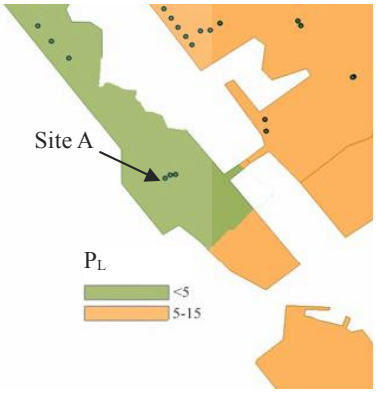

Fig. 9: Soil liquefaction potential map for the harbor area, a_{max}=0.15g

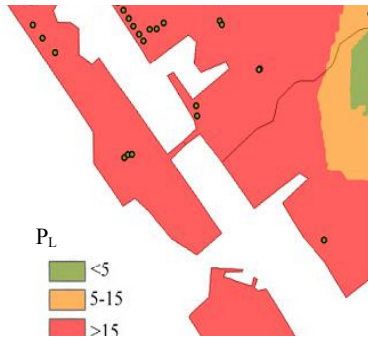

Fig. 10: Soil liquefaction potential map for the harbor area, a_{max}=0.23g

Table 1: Soil liquefaction potential evaluation of Site A

Depth (m)	SPT-N	USCS	FS (a_{max}=0.23g)	FS (a_{max}=0.15g)
1.75	6	SM	0.99	1.52
3.75	5	CL		
5.75	4	CL		
7.75	6	CL		
7.75	11	SM	0.92	1.41
9.25	8	SM	0.71	1.08
10.75	11	SM	0.88	1.35
12.25	9	SM	0.77	1.19
13.75	14	SM	1.09	1.67
15.25	13	SM	1.04	1.60
16.75	14	SM	1.14	1.74
18.25	15	SM	1.24	1.91
19.75	16	SM	1.36	2.09

The soil data show that the liquefaction susceptible soil layer extend with various depth underneath the submerged tunnel. When soil liquefaction was triggered by the seismic event, the submerged segments may be damaged by the differential settlement. For this reason, the analytical models were setup to simulate the settlement after the liquefaction occurred at U3 and U5 cross sections. Fig. 11 and Fig. 12 show the results of settlement calculation from PLAXIS simulations. The post-liquefaction settlements are estimated as 2.6cm and 14.3cm for U3 and U5 cross sections, respectively. The future retrofitting program will need to identify the possible impacts caused by these amounts of settlement.

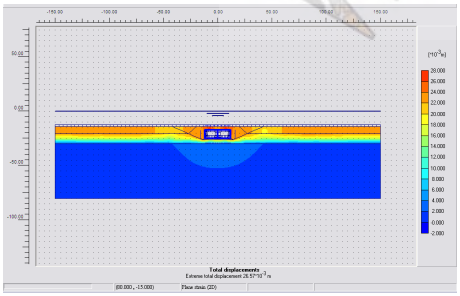

Fig. 11: Soil liquefaction induced settlement of section U3

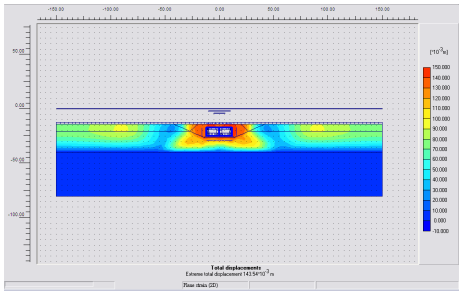

Fig. 12: Soil liquefaction induced settlement of section U5

CONCLUSIONS

The region of Taiwan has high occurrence of seismic actives. After the 1999 Chi-chi earthquake, the society starts to aware the importance of evaluating the possible hazards and their impact caused by the seismic events. While the existing structure is evaluated for its seismic vulnerability, it requires an appropriate seismic performance standard and a proper procedure to assess the seismic risk. Furthermore, in order to maintain a suitable performance level for the remaining structural service life, the subsequent long-term plan should be scheduled in advance.

This article presents a proposed four-stage procedure for the seismic risk assessment. The first stage, the initial condition assessment, aims to collect the background information of the examined structure and evaluate the current performance level. In the second stage, the seismic risk assessment, the factors that may affect the structural seismic vulnerability should be first identified. These factors can be the environmental consideration, material property decay, structure usage, etc. Combined with the seismic event, the seismic hazard scenarios can then be chosen for the further risk analysis. In the third stage, the impact and retrofitting assessment, the decision of planning the possible retrofitting approaches is made by the possible impacts study, prioritization the importance of structure, and the performance requirement. Finally, in the stage four, a total solution plan not only defines the retrofitting program and its action plan, but also provides the long-term maintenance strategy to provide a better future service quility.

In the past 20-year service of the Kaoshiung cross-harbor tunnel, it provides an essential transportation access between the Kaoshiung city and the Port of Kaoshiung. In order to ensure a good service quality, the authority of the Port of Kaosiung issued the site investigation and safety evaluation program for this tunnel. According to the proposed procedure of seismic risk assessment, this program gives a good example for the first and second stages of this procedure.

ACKNOWLEDGMENTS

The site investigation and safety evaluation program of the Kaoshiung cross-harbor tunnel was issued by the

authority of the Port of Kaoshiung.

REFERENCES

[1] SEAOC, VISION 2000 – Performance based seismic engineering of buildings. Structural Engineering Association of California, Sacramento, California, USA, 1995.

[2] National Center for Earthquake Engineering Research, Proceeding of the NCEER Workshop on Evaluation of Liquefaction Resistance of Soils, 1997.

[3] Iwasaki, T., Arakawa, T. and Tokida, K., "Simplified Procedures for Assessing Soil Liquefaction During Earthquakes", Soil Dynamics and Earthquake Engineering Conference, Southampton, 1982, pp. 925-939.

A Case Study on the Response of Shield Tunnel Near a Thrust Fault Offset

Chun-Fu Chung[1], Ming-Lang Lin[1], Fu-Shu Jeng[1] , Li-Sheng Tsai[1]

Chung-Tien Chin[2], Sung-Ju Chan[2]

[1] *Department of Civil Engineering, National Taiwan University, Taipei, Taiwan.*
[2] *Moh and Associates. Inc., Taipei, Taiwan.*

Abstract

As observed from the earthquake disasters occurred over the decades in Taiwan, the deformation of near surface soil was one of the major causes leading to damages of underground structures or pipe lines. For instance, the damage of the diversion tunnel of the Shih-Kang Dam by the Chichi earthquake is a typical case.

The scope of the study mainly focuses on the soil deformation near a thrust fault through which the MRT tunnel passes. The results, obtained from numerical analyses by using a finite element method, were analyzed to further explore the deformational behavior of soil and structure during the faulting process as well as the degree of damage of a shield tunnel when it is close to the faulting zone during the earthquake.

Comparing to the field observation, the results of the numerical analysis reveal that the degree of damage of a shield tunnel is severer when it is closer to the faulting zone. This research can enable the development of proper remedial measures to promote the safety of the tunnel near a faulting zone. In the future, when conducting a risk evaluation for an earthquake-induced damage on underground structure, the numerical stimulation seems to be capable of serving as a handy tool for the earthquake resistance design.

Keywords—*thrust fault, numerical analysis, shield tunnel. MRT*

INTRODUCTION

Observations on several major earthquakes indicate that, in addition to the damages induced by the inertial force, the damage of near fault structures is mainly caused by the co-seismic fault movement triggered by the major earthquakes. For instance, the Landers Earthquake in California (1992; Mw=7.3), the Chichi Earthquake in Taiwan (1999; Mw=7.6), and the Duzce Earthquake in Turkey (1999; Mw=7.1) activated the co-seismic fault movement on ground surface and accounted for the severe damages of structures (houses, bridges and roadways) along the fault traces with only a few exceptions. For example, the structures, on the top of fault trace, were not damaged but subjected to significant amount of rigid body motion [1]. The future prevention of such damage highlights the need for understanding the behavior of the fault movement, including the knowledge of how the top soil deforms according to the fault movement, what the range of deformation is, and how this deformation affects or interacts with the structure.

The existing studies on the fault movement are based on either the numerical approach or the experimental method. For the numerical approach, a analysis was conducted to evaluate the deformation of the top soil associated with the fault movement, e.g., Bray (1994), Nino (1998), Erickson (2001), [1-3]. For the experimental method, the model sandbox simulation was conducted to observe the process of the fault movement and to explore the underlain mechanism. To further interpret the results of the experimental simulation, they are than compared with the results of the numerical analysis or field observations such as, Cole and Lade (1984), Larzarte and Bray (1996) [4,5,6]. The underground structure damage induced by the fault movement is evaluated by a numerical approach. Duncan and Lefebvre (1973) [7] used a regular external force exerted on the structure to simulate the fault influence on the structure. Yeh and Liaw (1985) and Matsubara and Urano (1992) [8, 9] applied a sine wave to the structure to simulate the fault movement. There are few studies discussing the stress and the strain behavior of an underground structure induced by the deformed layers during the faulting.

Accordingly, understanding of where and how the top soil will deform, develop or fracture has been continuously accumulated. However, the knowledge of how the shear zone within the top soil develops and migrates when subjected to the large strain (or deformation) condition and the interaction with the structures, still waits for further studies.

METHODOLOGY

This research aims at studying the deformation of top soil subjected to a large deformation and its interaction with a submerged tunnel by comparing the experimental and the numerical studies. Based on the calibrated small-scale numerical model, a full-scale numerical model was then established and used to simulate the deformation behavior of the full-scaled thrust fault deformation. The results, analyzed to further explore the deformational behavior of soil and structure during the faulting process as well as the degree of damage of the shield tunnel when

it is close to the faulting zone during earthquake have been revealed.

Setup for experimental study

Sandbox containing quartz sand is adopted to simulate the fault movement and the associated top soil deformation. The quartz sand was tested under dry condition with a relative density of 55%. The sand was dyed layer by layer with varied colors and put in the sandbox in order to differentiate each layer. The deformation could be observed from the boundary of colored layers. The thickness of the top soil was 20 cm, and the maximum uplift of the hanging wall was 6 cm. The dip angle of the simulated thrust fault was 60°. Furthermore, to test the influence of the fault movement and the corresponding interactions, a model tunnel was installed at the depth of 9 cm with different distances to the fault line.

The sandbox has a size of 100 cm (length) × 20 cm (width) × 60 cm (height), and it bottom is divided into a footwall and a hanging wall. The hanging wall, driven by a motor, can be uplifted with designated dip angles ranging from 30 to 90 degrees. Both sides of the sandbox are bounded by transparent plastic plates with a thickness of 2 cm, allowing direct observation of the deformational process. Since a model tunnel will be installed when it is needed, holes on the plastic plate were made to allow future installation of the model channel, as shown in Fig. 1.

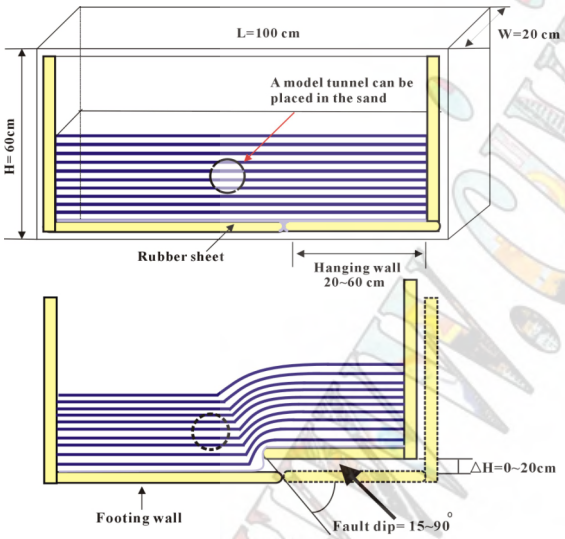

Figure 1 Configuration of the model sandbox

The model soil, quartz sand, was from Vietnam and it was characterized with: (1) having uniform sizes between sieve sizes from 40 to 140; (2) comprising 99% of quartz with a very minor portion of feldspar and mica; (3) having a specific weight, maximum and minimum dry density of 2.65, 1.67 g/cm^3 and 1.47 g/cm^3, respectively. The quartz sand has a frictional angle of 35 degrees, obtained from direct shear tests, and a secant shear modulus G of 0.5 MPa, obtained at a relative density of 55%.

The model tunnel was made up of paper, which is weak enough to allow deformation of itself when subjected to the fault movement. The paper has a Young's modulus of 400 MPa, which is about 330 times of the stiffness of the sand. The properties of the model material are summarized in Table 1.

To record the deformation process, photos were stranded during the entire experiment at same location and angles and, later on, the images were further processed to correct their distortion. As a result, all the images can be overlapped and compared based on the same orthogonal scale. Consequently, the deformation of the fault tip, the shear zone and the submerged structured can be precisely identified.

To facilitate observation on the deformation, a thin layer (1 mm) of dyed sand was paved within the un-dyed sand every 2 cm. The deformation of the sand can easily be obtained.

Table 1 Summary of the properties of the material

Parameter	Experimental simulation	Full- scale simulation	Unit
Model Tunnel (paper)			
E	400	31.8	MPa
ν	0.3	0.2	
Model soil (sand)			
E	1.29	19	MPa
ν	0.3	0.3	
c	1	1	kPa
ϕ (frictional angle)	35	34	degree
ψ (dilation angle)	6	34	degree
γ (dry unit weight of soil)	15.7	20	kN/m^3
k_o (stress ratio at rest)	0.43	0.73	
Frictional property of interfaces			
μ (soil – rock)	0.43	0.43	
μ' (soil – tunnel)	0.43	0.43	

Setup for the sandbox numerical study

The numerical analysis with finite element methods was adapted to model the experiments. As shown in Fig. 2, the model for numerical analysis has a size of 100 cm in width and 20 cm in height with a mesh size of 1 cm by 1cm. The side and bottom boundaries were set to be movable. A rigid boundary is capable of simulating the fault uplifting with various dip angles. The interface frictions μ and μ' were tan (2ϕ/3).

Setup for the case numerical study

The scope of the study mainly focuses on the soil deformation near the thrust faults, where the MRT tunnel passes. The fault dip angle has 60 degrees. The maximum surface displacement of the fault was 2.5m thrusting along the fault surface. This study concerns the process of the fault propagation, the associated soil, and the structure deformation during a fault offset event. The diameter of tunnel is 6m, and the center of tunnel is 14 m below the ground surface. The top layer is sand, with a thickness of 20m. The sand has a density of 20 kN/m^3. The sand frictional angle is 34 degrees. The properties of the model material were summarized in Table 1.

The numerical analysis using finite element methods was adopted with a model identical to the model experiments. As shown in Fig. 2, the model for the numerical analysis has a size of 120 m in width and 20 m in height with a mesh size of 1 m by 1m. The side and bottom boundaries were set to be movable. A rigid boundary was capable of simulating the fault uplifting

with various dip angles. The interface frictions μ and μ' were set to be tan (2ϕ/3).

Dimension	Model type		Unit
	Sandbox Model	Full-Scales	
L	1	120	m
H	0.20	20	m
ΔH	0.06	2	m
T1	0.11	14	m
D	0.06	6	m
FW	1D~2D	1D~7D	
HW	-	1D~3D	

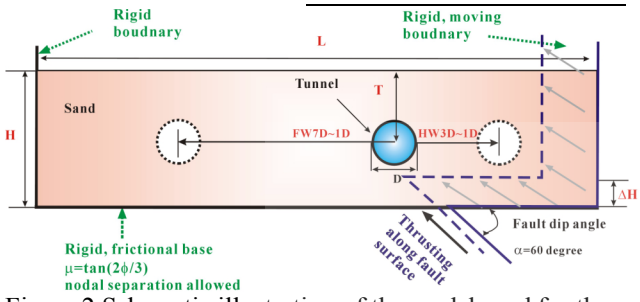

Figure 2 Schematic illustration of the model used for the numerical analysis

A typical shield tunnel inner diameter is 5.6m, outer diameter is 6.1m, the shield lining section is 0.25m, and thickness is 1.0m. The shield tunnel consists of 6 segments, 3 units of type A, 2 units of type B, and a unit of type K. The shield tunnel section shear strength and the moment were lower than those in the concrete section because the segment has a flexible joint. The numerical analysis, using the model and reducing a half-length of the shield segment, was shown in Fig. 3.

The numerical analysis using a beam element to model the shield tunnel has 74 elements. The beam element has a size of 25cm in length. The model reduced a half of shield segments because the shield tunnel had 6 segments, and 12 no-continue points for strength and stiffness.

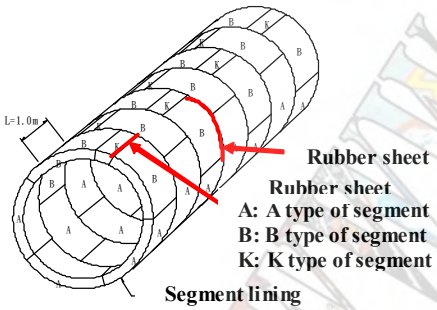

(a) Configuration of the shield segment of the tunnel

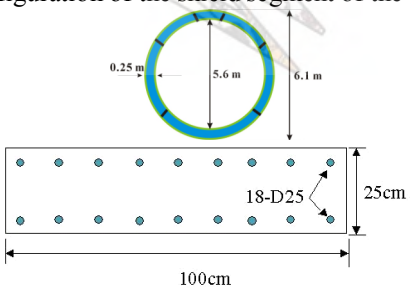

(b) The shield section used in the numerical analysis

Figure 3 Schematic illustration of the shield segment of the tunnel used in the numerical analysis

RESULTS

A. Deformation observed from the experimental simulation and numerical analysis

There is no tunnel presented, the shear zone by uplift with dipping angle 60° shown in Fig. 4a. A major fracture zone was developed within the shear zone, extending from the ground surface to the underlain fault tip, and followed by a minor fracture zone near the fault tip.

In both cases of deforming with a submerged tunnel and deforming without the tunnel, the fracture zones were initiated from the fault tip. When the tunnel is closer to the fault tip, comparing Fig. 4b and Fig. 4c, the fracture zones bypassed the tunnel, as shown in Fig. 4c. As a result, in terms of the spreading of the fracture zones, the tunnel closer to the fault tip leads to a division of the shear or the fracture zones. On the other hand, the closer the tunnel to the fault tip, the severer distortion into an ellipse as well as the more significant displacement of the tunnel itself, indicated by the two circles, representing the original state and the after-deformation of the tunnel.

The numerical simulation yields the deformation similar to that yielded by experiments. As shown in Fig. 4a, a shaper dip angle of uplifting also results in a narrower shear fracture zone, and the fracture zone extends from the ground surface to the fault tip, as the development observed by the experiments.

While the tunnel was far from the fault tip, as shown in Fig. 4b, a minor shear zone firstly developed near the ground surface, followed by the development of a major shear and a major fracture zone initiated from the uplifting fault tip and eventually extended to the ground surface. While the tunnel was closer to the fault tip, it suffered from the severe distortion and displacement, as shown in Fig. 4c. It is similar to the phenomena observed from experiments.

Amazingly the similarities between the deformations yielded by the experiments and those yielded by the numerical analysis are shown in Fig. 5. The location and the range of the shear zone yielded by these two approaches match well. Meanwhile, the similarity in the patterns of tunnel deformation was also observed.

B. Deformation observed in the field case from numerical analysis

Figure 6 plots the plastic shear zone of the shield tunnels in different locations, from the hinge wall FW7D to the foot wall HW3D after the fault movement.

In the tunnel, which is the nearest one and located at 1D, the plastic shear zone becomes more obvious because of the interaction between the tunnel and the fault tip. The influence region is from the foot wall 3D to the hinge wall 1D. While the tunnel is located at 1D on the foot wall, the plastic shear zone separates into two branches. One propagates firstly below the tunnel, and then the other propagates above the tunnel.

Figure 7 shows the maximum moments on the shield segments of the tunnel. In this figure, different cases are located in various distances from FW7D to HW3D. The moment before the fault movement is about 5.0 (t-m), and

the moment is larger after the fault movement. In addition, while the receiver is closer to the fault, the value of moment is rapidly increasing. The maximum value of moment below the fault, about 1D, is 178.5 (t-m). The slop of the curve in Fig. 7 shows that the value between FW3D and FW1D is increasing, and the value between HW1D and FW1D is steeply decreasing and equivalent to the value in FW7D. These phenomena indicate that the influence of the hinge wall is smaller and narrower than that of the foot wall.

Comparing the design moment of the shield segment of the tunnel, the moments of the elements in different tunnels are obtained numerically, as shown in Fig. 8. The figure shows that the larger design moment is, the closer the tunnel is located. The values exceed the design moment where the tunnel is located between FW7D and HW3D. It presents that the tunnel is destroyed and the degree of damage of a shield tunnel gets higher while the tunnel is closer to the fault.

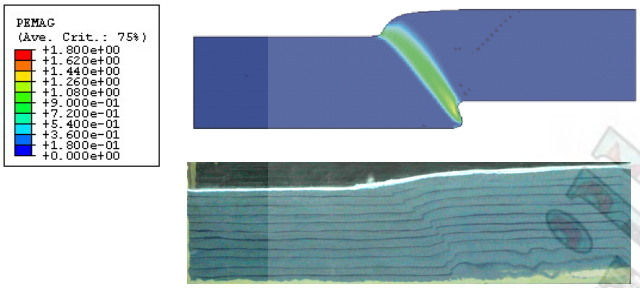

(a) Without a submerged tunnel

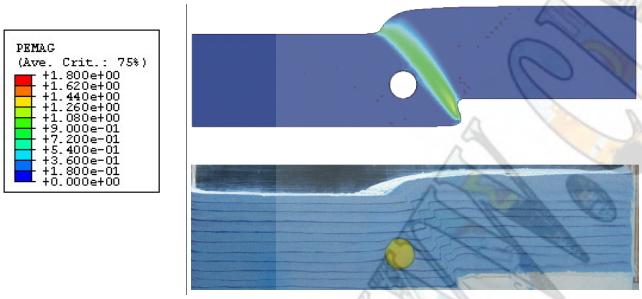

(b) 2 D from the fault tip submerged tunnel

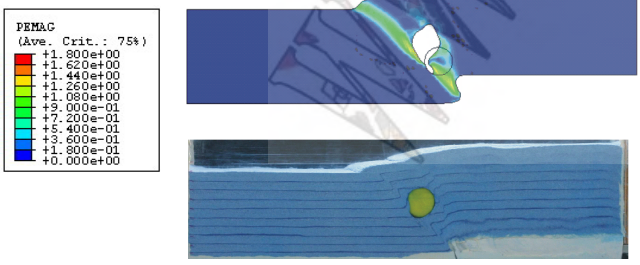

(c) 1 D from the fault tip submerged tunnel

Figure 4 Comparison of the deformation with the numerical simulation and the experiment results.

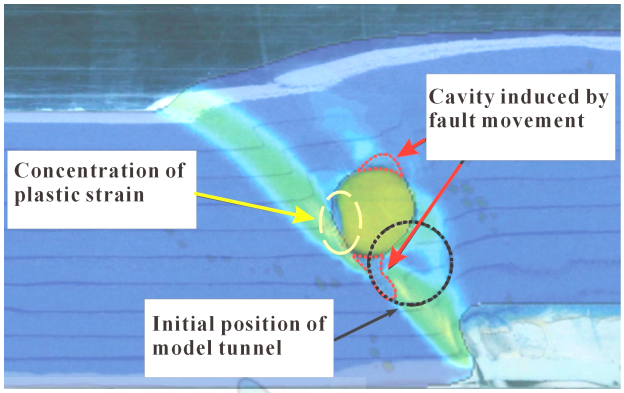

Figure 5 Comparison of the deformations obtained from the numerical simulation and the experiment results near the tunnel.

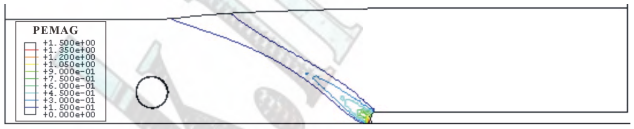

(a) 7D from the fault tip on the foot wall

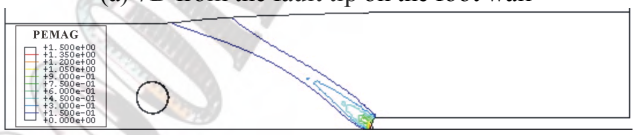

(b) 5D from the fault tip on the foot wall

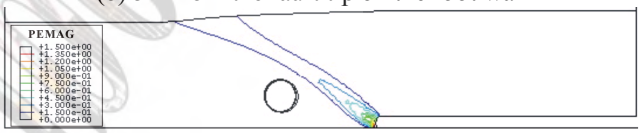

(c) 3D from the fault tip on the foot wall

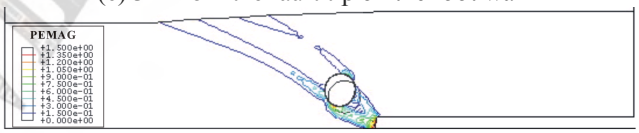

(d) 1D from the fault tip on the foot wall

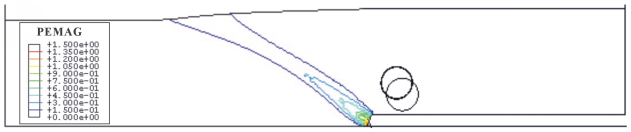

(e) 1D from the fault tip on the hinge wall

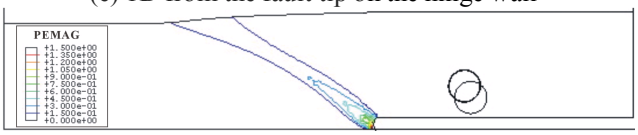

(f) 3D from the fault tip on the hinge wall

Figure 6 Influence of tunnel locations on plastic strain activated by the fault movement.

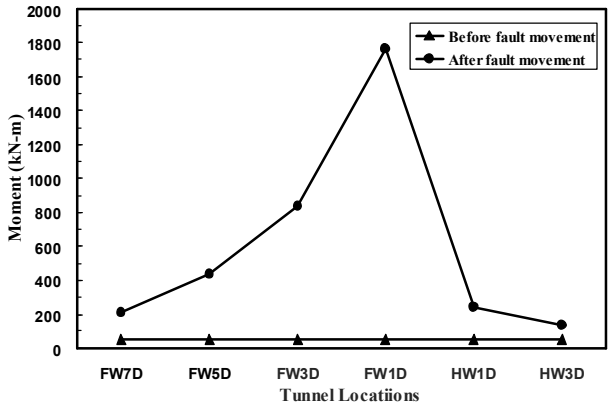

Figure 7 The maximum moments on the shield segments of the tunnel in different cases located from FW7D

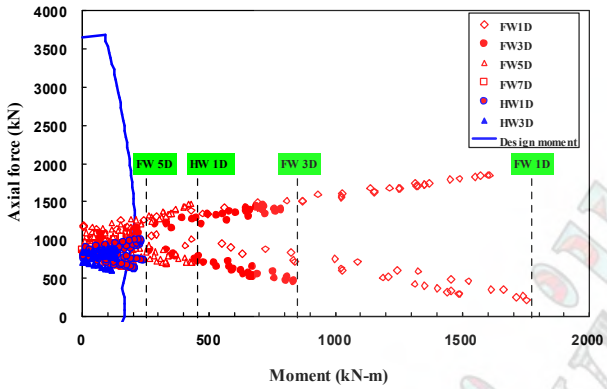

Figure 8 Comparison of the design moments and the shield segment moments for different tunnel locations.

CONCLUSIVE REMARK

The similarity of these results indicates that these two methods can serve as supplemental methods to one another, since the experimental one is characterized with the large deformation but has limitations in compensating a size effect and in obtaining quantitative measurements in stress or in strain. On the other hand, the numerical approach is limited by the small displacement and the undetermined representative parameters. The numerical analysis presented that using the small model-scale, which had been proven by the physical experiment, to pursue and to predict the full-scale deformational behaviors is a foundation method.

From the small model-scale of the physical experiment, a closer distance of the tunnel to the fault tip leads to a serious damage of the tunnel. It is not beyond our expectation. Based on this study and the corresponding configuration, 2 times distance of diameter of the tunnel seems to be the least requirement to ensure the safety of the tunnel.

To compare with the field observation, the numerical results reveal that the induced moment of the lining segments exceeds the design capacity in the faulting zone which is ranged from 7 D on footwall to 3 D on hanging wall. For the locations outside the abovementioned zone, the moment applied on the lining segments shall be lower than value of the design capacity. Therefore, the degree of damage of a shield tunnel is severer when the tunnel is closer to the faulting zone.

ACKNOWLEDGMENT

The authors gratefully acknowledge the financial support granted by Moh and Associates. Inc., Taipei, Taiwan. The authors wish to thank Prof. C. N. Yang of National Taiwan University for his continuing encouragement. The authors thank the research assistants, Messrs. Y. S. Shin, W. C. Tsai, C. C. Huang, and F. M. Chang in preparation of this manuscript.

REFERENCES

[1] Bray, J. D. (2001), "Developing mitigation measures for the hazards associated with earthquake surface fault rupture", *Proceeding of Workshop on Seismic Fault-Induced Failures, Tokyo*, pp.55-80.

[2] Fernando Nino, Herve Philip and Jean Chery (1998), " The role of bed-parallel slip in the formation of blind thrust faults", Journal of Structural Geology, Volume 20, pp. 503-516.

[3] Erickson, S. G., Strayer, L. M., Suppe, J. (2001), "Initiation and reactivation of faults during movement over a thrust-fault ramp numerical mechanical models", Journal of Structural Geology, Volume 23, pp.11-23.

[4] Cole D. A. and P. V. Lade (1984), " Influence Zones in Alluvium Over Dip-Slip Faults", Journal of Geotechnical Engineering, ASCE, Vol. 110, No.5, pp.599-615.

[5] Lade P. V., Cole D. A. and D. Cummings. (1984), " Multiple Failure Surfaces Over Dip-Slip Faults", Journal of Geotechnical Engineering, ASCE, Volume 110, No. 5, pp.616-627.

[6] Lazarte, C. A. and J. D. Bray. (1996), " A Study of Strike–Slip Faulting Using Small-Scale Models", Geotechnical Testing Journal, GTJ0DJ, Volume 19, No.2, pp. 118-129.

[7] Duncan, J. M. and Lefebvre, G. (1973), "Earth Pressures on Structures Due to Fault Movement", J. Soil Mechanics and Foundation Division, ASCE, Vo1.99, SM12, pp. 1153-1163.

[8] Yieh, Y. H. and Liaw, T. C. (1985),"Design Consideration for Pipelines Buried Through Fault Zone", *Proceeding of the Trilateral Seminar-Workshop on Lifeline Earthquake Engineering, Taipei, Taiwan*, pp.309-316.

[9] Matsubara, K. and Urano, K. (1992),"Seismic Design Method of Tunnels with Axial Prestressing By Means of Rubber and PC Bar", *Proceeding of the 4th U.S.-Japan Workshop on Earthquake Disaster Prevention for Lifeline Systems, CA, USA*, pp.229-243.

A Study on Computing Method of Negative Skin Friction on Pile in Subsiding Loess Ground

Wang Lanmin[1,2,3] Sun Junjie[1,2,3]
[1]*Lanzhou Base of Institute of Earthquake Prediction, CEA, Lanzhou, China*
[2] *Lanzhou Institute of Seismology, CEA, Lanzhou, China*
[3] *Open Laboratory of Loess Earthquake Engineering, CEA, Lanzhou, China*

Abstract

This paper deals with the investigation on computing method of negative skin friction (NSF) on pile in collapsing, liquefying and seismic subsiding loess ground. Through analyzing and discussing micro-mechanism and macro-phenomena of collapse, liquefaction and seismic subsidence of loess mass in detail, we discover that as results of the specific microstructure of soil mass influenced by different external conditions, collapse, liquefaction and seismic subsidence of loess are related each other. In theory, it is revealed that NSF could be simply regarded as a force on pile due to lost gravitational potential energy (GPE) of subsiding soil mass and limited by shear strength of soil mass; lost GPE of subsiding soil mass and shear strength of soil mass are the dominating factors to generate NSF on pile, whereas the detail deformation mechanism of soil mass, e.g. why and how settlement taking place, is not a key influencing factor. Finally, the computing method of NSF on pile in subsiding loess ground, in which collapse, liquefaction or seismic subsidence occurs, is proposed by authors; and a case, to estimate NSF on pile in collapsing loess ground in north of Shaanxi, China, provides the main computation procedures of above-mentioned computing method.

Keywords—C*ollapse, computing method, liquefaction, loess ground, negative skin friction, seismic subsidence*

INTRODUCTION

In China, there is the largest area of loess in the world [1]; the acreage of the loess reaches 640,000 km^2, in which collapsible loess acreage is about 500,000 km^2 [2].

As a result of a special microstructure [3], the compressibility of loess mass is low at natural moisture content. While the water immerges, however, the strength of loess mass will be reduced obviously, and this could make loess collapse [4-7]. Furthermore, the most loess area in China also is the seismic region, in which there has been much strong shock occurring. Acting on moderate or strong earthquake, liquefaction or seismic subsidence of loess takes place easily. Above-mentioned three kinds of settlement due to collapse, liquefaction and seismic subsidence of loess, which relate to immerging water, additional load or ground shock, could come into being negative skin friction (NSF) on pile, which badly endangers pile foundation and its top out.

NSF is a complicated problem and it connects with some other theoretical problems in soil mechanics area. Because to take in-situ test needs much money and a long-time period, existing test data does not satisfy the study on NSF. Consequently, concerned investigation on NSF on pile is not perfect still. Heretofore, there is no research data to be found yet on the NSF on pile in loess ground, in which especially liquefaction and seismic subsidence is occurring.

RELATION BETWEEN COLLAPSE, LIQUEFACTION AND SEISMIC SUBSIDENCE OF LOESS

There are three kinds of settlement respectively caused by collapse, liquefaction and seismic subsidence of loess. Although the actual process and behavior of above disasters are different, they relate to a same special microstructure of loess.

Origin of Collapse, Liquefaction and Seismic Subsidence of Loess

Because of specific geologic condition, the deposition of loess is very secular. In this process, the accretion rate of burden pressure is less than the corresponding accretion rate of strength of solidifying connection bond and thus structural strength between loess grains exceeds the cover load all the time. Contrasted to consolidating compaction, therefore, the structure of loess appears as a characteristic of high porosity.

It has been accepted that collapse, liquefaction and seismic subsidence of loess mainly depends on its specific microstructure [8-12]. This specific microstructure of loess is a structure that consists of moderate pore built by loosening deposition of framework grains [7, 13].

The characteristic of the loess microstructure could be summarized as follow [14]: pore is large; structure system is loose; cementation point of identity structure is lack; and total strength of unit volume soil is low. While external force load the soil mass, stress will concentrate at contact point; framework grains of loess tend to slip and dislocation appears. Consequently, collapse, liquefaction or seismic subsidence takes place because of instability of the typical internal structure of loess due to immerging water, cover load or ground shock.

Relation Between Three Kinds of Settlement of Loess

Porosity is the critical reason to generate collapse of loess. To all sorts of pore in loess mass, whose type and size are different, middle-sized pore plays a significant role in settlement by soaking [13]. Acting on immerging water and burden pressure, the specific structure of loess will be destroyed and settlement of soil mass occurs. Under compaction, high porosity of loess structure provides a possible space for this settlement [15].

Liquefaction of loess depends on its physical property, microstructure characteristics and hydroelectricity chemical property [16]. It is revealed by experiment that middle-sized and large-sized pore content reduces and micro-sized pore content increases as liquefaction of loess occurs; hereinto, decrease of middle-sized pore content and increase of micro-sized pore content are visible (Fig. 1). Relative decrease quantity of middle-sized pore, moreover, closely relates to relative increase quantity of micro-sized pore [Fig. 2, Fig. 3]. This fact shows that in liquefaction process, micro-sized pore content increases due to decrease of middle-sized pore content.

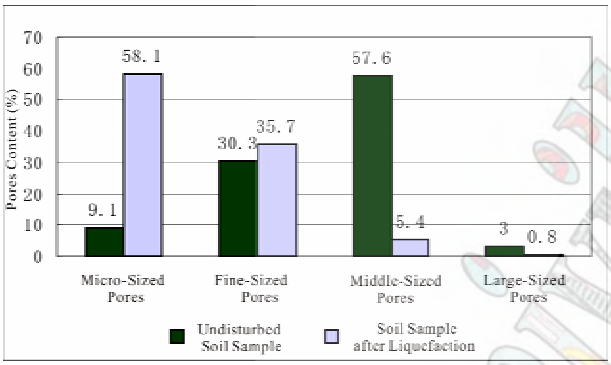

Fig. 1: Pores content before and after liquefaction

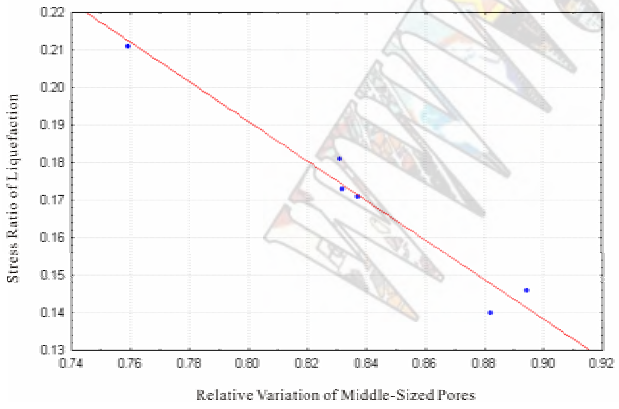

Fig. 2: Influence of relative variation of middle-sized pores on stress ratio of liquefaction

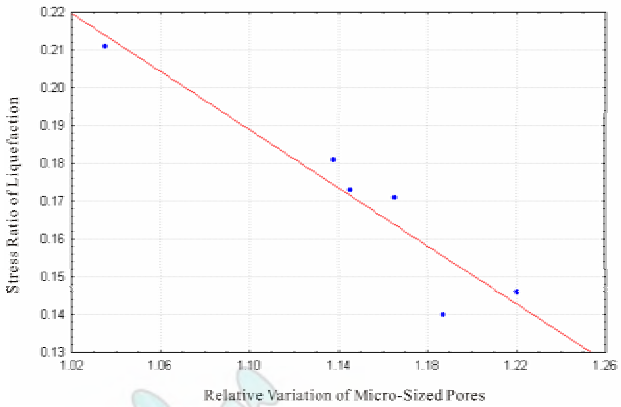

Fig. 3: Influence of relative variation of micro-sized pores on stress ratio of liquefaction

Liquefaction of loess and sand soil are uniform by the concept of liquefaction, whereas they are distinguishing by the settlement of soil mass. Because of the typical water sensitivity of soil, settlement of loess mass in liquefaction process consists of three portions, i.e. settlement by soaking, seismic settlement and consolidation settlement; settlement of sand soil in liquefaction process only refers to consolidation settlement due to dissipation of pore water pressure. In liquefaction process to distinguish above three kinds of settlement in detail is very difficult, also not practically. On the basis of essential origin of NSF on pile, it could be believed that NSF on pile in liquefying loess ground is able to be estimated by determining the settlement of loess mass in liquefaction process. Seismic settlement and settlement by soaking are related: seismic settlement will be difficult to occur as settlement by soaking progresses completely and vice versa. Taking into account water sensitivity and immerging process of loess mass, the dominating one of above mentioned three kinds of settlement could be determined and its possible settlement volume of soil mass could be estimated, too. In liquefaction process, contrasted to settlement of collapsible loess, settlement of non-collapsible loess and settlement of sand soil are similar; settlement of loess non-collapsible under overburden pressure mostly consists of seismic settlement and consolidation settlement; settlement of loess collapsible under overburden pressure mainly includes settlement by soaking and consolidation settlement. In this paper, authors select three computing methods to estimate above three kinds of settlement, respectively [17-19].

Seismic subsidence of loess is an abrupt settlement of loess ground due to seismic loading in the non-saturated and low degree of moisture condition. The specific microstructure of soil mass dominates the dynamic characteristic of loess. There has been experiment results show that coefficient of seismic subsidence increases by accretion of void ratio; at the same seismic standard, the more middle-sized and large-sized pore content (especially middle-sized pore content) of loess mass increases, the more seismic subsidence loess ground

occurs [8].

The typical microstructure of loess provides a possible space for corresponding settlement and settlement of soil mass is the macroscopic characteristic of collapse, liquefaction and seismic subsidence. Settling volume due to instability of loess mass chiefly relates to the destructiveness of middle-sized pore content. The macro-phenomena and micro-mechanism of collapse, liquefaction and seismic subsidence, therefore, are all similar. Although external conditions of above three kinds of settlement are different, the process to generate settlement, in which these conditions destroy the specific structure of loess mass, is uniform.

RELATION BETWEEN NSF ON PILE IN COLLAPSING, LIQUEFYING AND SEISMIC SUBSIDING LOESS GROUND

The definition of NSF implies that the generation of NSF on pile relates to the effective settlement of soil mass around pile, which is one of the dominating factors to influence NSF [20]. At a certain condition, NSF on pile is relatively determinate and it could be estimated.

Lost gravitational potential energy (GPE) of subsiding soil mass is the energy source to generate NSF. GPE is a dot product between gravitation and displacement. The lost GPE of subsiding soil mass, thus, could be also described as a dot product between effective weight of soil mass above certain depth and settlement of soil mass around the pile at that depth.

NSF acts on the interface between pile and near soil; according to law of action and reaction, we introduce symbol f and f^{-}, which express NSF and its reacting force, respectively. f depends on lost GPE of subsiding soil mass and shear strength of soil mass, whereas f^{-} relates to residual positive skin friction on pile and carrying capacity of pile tip. Relation between lost GPE of subsiding soil mass, shear strength of soil mass, f and f^{-} could be written as

$$-\langle f^{-} \bullet S_f \rangle = \langle f \bullet S_f \rangle \propto [\![\langle G_{sm} \bullet S_{sm} \rangle : \tau_f]\!] \tag{1}$$

where $\langle b \bullet c \rangle$ is a dot product between b and c; $[\![x : y]\!]$ expresses that x is limited by y; S_f is operating displacement of f and f^{-}; G_{sm} is effective weight of soil mass above a certain depth; S_{sm} is settlement of soil mass around the pile at above certain depth; and τ_f is shear strength of soil mass.

Equation (1) describes that f could be simply regarded as a force on pile due to the lost GPE of subsiding soil mass and limited by shear strength of soil mass, and f^{-} is a reacting force due to above lost GPE, too. There is energy dissipation in this process because soil mass is not perfect elastic body.

Because the direction of settlement of soil mass and gravitation are consistent, dot product in eq. (1) can be replaced by product. Thus, we obtain

$$-\left(f^{-} \times S_f \right) = \left(f \times S_f \right) \propto [\![\left(G_{sm} \times S_{sm} \right) : \tau_f]\!] \tag{2}$$

(i) Ignoring the difference between S_f and S_{sm}, Eq. (2) becomes

$$-f^{-} = f \propto [\![G_{sm} : \tau_f]\!] \tag{3}$$

Equation (3) gives us a force conversion from gravitation to f, i.e. a conversion from body force to surface force; this means that f is a surface force on pile due to corresponding gravitation and limited by shear strength of soil mass.

(ii) Considering the difference between S_f and S_{sm}, define diversity factor

$$\eta = S_{sm} / S_f \tag{4}$$

Substituting Eq. (4) in (2) gives

$$-\left(f^{-} \times S_f \right) = \left(f \times S_f \right) \propto [\![\left[G_{sm} \times \left(\eta \times S_f \right) \right] : \tau_f]\!] \tag{5}$$

which is identical with

$$-\left(f^{-} \times S_f \right) = \left(f \times S_f \right) \propto [\![\left[\eta \times \left(G_{sm} \times S_f \right) \right] : \tau_f]\!] \tag{6}$$

that is

$$-\left(f^{-} \times S_f \right) = \left(f \times S_f \right) \propto \eta \times [\![\left(G_{sm} \times S_f \right) : \tau_f]\!] \tag{7}$$

which simplifies to

$$-f^{-} = f \propto \eta \times [\![G_{sm} : \tau_f]\!] \tag{8}$$

Equation (8) differs from Eq. (3) only on a constant coefficient η (η ≥ 1, which in a degree expresses the consolidation of pile to near soil mass, usually allowing η = 1). Whether we take into account the difference between S_f and S_{sm} or not, NSF always could be regarded as a force on pile due to lost GPE of subsiding soil mass and limited by shear strength of soil mass.

Effective stress method (ESM) to estimate NSF on pile is given

$$f_{Q\max} = \sigma * k * tg\phi, \sigma = p + \gamma * z - u \tag{9}$$

where σ is vertical effective stress of soil mass around pile; k is a ratio of horizontal effective stress to vertical effective stress; φ is effective angle of internal friction; p is a cover load; γ is effective unit weight of soil mass around pile; z is a depth from the ground; and u is pore water pressure. Equation (9) shows that ESM just is a case of eq. (8) or (3).

Lost GPE of subsiding soil mass and shear strength of soil mass are the dominating factors to generate NSF on pile. It is not the key factors that why and how settlement of soil mass takes place. Consequently, there are not essential difference between three kinds of NSF due to collapse, liquefaction and seismic subsidence. A computing method of NSF, which depends on the radical origin of NSF on pile, could be applied to estimate above three kinds of NSF in loess ground [20].

COMPUTING METHOD OF NSF ON PILE IN SUBSIDING LOESS GROUND

For the time being in-situ test data of NSF on pile is lack still, especially real data of NSF on pile in liquefying and seismic subsiding loess ground. Based on the uniform essential origin of NSF on pile in collapsing, liquefying and seismic subsiding of loess ground and the ESM, we

establish a computing method to estimate the NSF due to above three kinds of settlement of soil mass. It has been proved that to apply this computing method to estimate NSF on pile in collapsing loess ground is practical (see Ref. [20]).

Computing Method of NSF on Pile in Collapsing Loess Ground

Detail approach to estimate NSF on pile in collapsing loess ground please see the following text (section 4: prediction of the NSF on pile in a hypothetical loess ground). The estimation of maximum value of NSF on pile in collapsing loess ground is given by

$$f_{Q\max} = \sigma * k_0 * tg\phi, \sigma = p + \gamma_J * z - u_0 \quad (10)$$

where k_0 is a static lateral pressure coefficient (simply, $k_0 = 1 - \sin\varphi$, see Ref. [19]); γ_J is a weighted mean of effective unit weight of each soil layer around pile; φ is an angle of internal friction of saturate with water; and u_0 is a static pore water pressure, which approximatively equals the product of γ_w and z (γ_w is unit weight of water).

Computing Method of NSF on Pile in Liquefaction Loess Ground

Replacing settlement of collapse by seismic settlement, the maximum value of NSF on pile in seismic subsiding loess ground is given by

$$f_{Q\max} = \sigma_d * k_d * tg\phi_d, \sigma_d = p + \gamma_J * z - u_d \quad (10)$$

where k_d is a dynamic lateral pressure coefficient (simply, $k_0 = 1 - \sin\varphi_d$, see Ref. [19]); φ_d is an effective angle of internal friction on dynamic stress; and u_d is pore water pressure on dynamic stress and is about zero because the low water content of loess does not come into being high pore water pressure.

Computing Method of NSF on Pile in Seismic Subsiding Loess Ground

In liquefaction process, settlement of noncollapsible loess just is consolidation settlement; settlement of loess noncollapsible under overburden pressure mostly consists of seismic settlement and consolidation settlement; settlement of collapsible mainly includes settlement by soaking and consolidation settlement (to estimate the three kinds of settlement see Ref. [17]-[19]). The maximum value of NSF on pile in liquefaction loess ground is given by

$$f_{Q\max} = \sigma_d * k_d * tg\phi_d, \sigma_d = p + \gamma_J * z - u_d \quad (11)$$

where φ_d is an effective angle of internal friction on dynamic stress and equals zero in liquefaction process; and u_d is pore water pressure on dynamic stress and the estimation of u_d see Rif. [8].

PREDICTION OF NSF ON PILE IN A HYPOTHETICAL LOESS GROUND

Applying the computing method of NSF established by authors, the approach to estimate the NSF on pile in collapsing loess ground in north of Shaanxi, China is given as follow (Table 1 presents the detail parameter of loess ground and pile).

Table 1: Parameters of engineering condition of a loess ground in north of Shaanxi, China (see Ref. [21])

Property (unit)		Soil layer	
		1	2
Water content (%)		13	9.7
Unit weight (10^3 kg/m^3)	Natural	1.48	1.51
	Dry	1.31	1.38
Coefficient of collapsibility δ_s		0.056	0.026
Coefficient of collapsibility under overburden pressure δ_{zs}		0.025	0.025
Angle of internal friction φ (°)	Natural	27	30.4
	Saturated	20	21
Length of pile (m)		25	
Radius of pile (m)		0.4	
Thickness of soil layer (m)		7.5	10.5

A) Settlement of Soil Mass around Pile

Method to estimate the settlement of self-weight collapsibility, Δ_{zs}, is not provided here (see Ref. [17]). Allowing coefficient of correction, $\beta_0 = 1.2$, which changes with different area, we obtain the final result $\Delta_{zs} = 0.54$ m.

B) Total NSF on Pile Ignoring the Settlement of Pile

Firstly, detail equations to calculate NSF on pile in loess ground is not provided here (see Ref. [20]). Coefficients of collapsibility under overburden pressure of top soil layer and of bottom soil layer are similar. Accepting $\lambda = 0.938$, we obtain the variation of settlement of soil mass versus depth, which is

$$f(x) = 0.063*x^2 + 1.866*x - 54$$

where f (x) is settlement volume of soil mass; and x is depth.

Secondly, by accepting angel of internal friction, φ, to be a value of water saturated soil mass and lateral pressure coefficient, k (simply, $k = 1 - \sin\varphi$, see Ref. [19]), the variation of NSF versus depth could be given by

$$f_Q(x) = 0.0076*x^3 + 0.2256*x^2 - 6.5274*x$$

where $f_Q(x)$ is NSF; and x is depth.

Finally, applying the equation to calculate total NSF, f_z, we obtain the total NSF value, $f_z = 1054$ kN.

C) Total NSF on Pile Considering the Settlement of Pile

The depth of neutral point could be estimated by settlement of pile and the variation of settlement of soil mass around pile versus depth [20]. If settlement of pile is 0.046 m, based on the definition of neutral point, settlement of soil mass around pile at the depth of neutral point is also 0.046 m; thus, the final result of depth of neutral point is 16.868 m.

Substituting the new depth of neutral point in above approach B) and repeating the computing procedure again, we could gain the result of total NSF, $f_z = 923$ kN, which consider the settlement of pile.

Compared above two kinds of total NSF on pile, it is revealed that settlement of pile does reduce NSF obviously.

CONCLUSION

This paper deals with the investigation on computing method of NSF on pile in collapsing, liquefying and seismic subsiding loess ground.

The characteristics of the loess microstructure could be summarized as follow [14]: pore is large; structure system is loose; cementation point of identity structure is lack; and total strength of unit volume soil is low. While external force load the soil mass, stress will concentrate at contact point; framework grains of loess tend to slip and dislocation appears. Consequently, collapse, liquefaction or seismic subsidence takes place because of instability of the typical internal structure of loess due to immerging water, cover load or ground shock.

The typical microstructure of loess provides a possible space for corresponding settlement and settlement of soil mass is the macroscopic characteristic of collapse, liquefaction and seismic subsidence. Settling volume due to instability of loess mass chiefly relates to the destructiveness of middle-sized pore content. The macro-phenomena and micro-mechanism of collapse, liquefaction and seismic subsidence, therefore, are all similar. Although external conditions of above three kinds of settlement are different, the process to generate settlement, in which these conditions destroy the specific structure of loess mass, is uniform.

Lost GPE of subsiding soil mass and shear strength of soil mass are the dominating factors to generate NSF on pile. NSF could be regarded as a force on pile due to lost GPE of subsiding soil mass and limited by shear strength of soil mass. It is not the key factors that why and how settlement of soil mass takes place. There are not essential difference between three kinds of NSF due to collapse, liquefaction and seismic subsidence. A computing method of NSF, which depends on the radical origin of NSF on pile, could be applied to estimate above three kinds of NSF in loess ground [20].

It has been proved that to apply this computing method established by authors to estimate NSF on pile in collapsing loess ground is practical (see Ref. [20]). Because corresponding in-situ test data is lack, the computing method of NSF on pile in liquefying and seismic subsiding loess ground proposed by authors is not proved by real data. But it is practicable to think of collapse, liquefaction and seismic subsidence of loess together because of their macro-phenomenon relating to one same typical microstructure of loess mass. As results of the specific microstructure of soil mass influenced by different external conditions, collapse, liquefaction and seismic subsidence of loess are related each other. To take into account these results completely could help to advance our understanding on essential relation between microstructure and macro-phenomenon of loess mass.

Collapse, liquefaction and seismic subsidence of loess are able to come into being settlement, a macro-phenomenon due to destroyed microstructure of soil mass. Without essential difference between above three kinds of settlement, there is a little distinction in these settling processes of soil mass. This should make the detail process of NSF on pile in collapsing, liquefying and seismic subsiding loess ground different.

ACKNOWLEDGMENTS

This work was supported by National Natural Science Foundation of China with grant No.50379049.

REFERENCES

[1] Zhang Zhenzhong, *Prediction on Seismic Hazard of Loess*. Beijing: Earthquake Press, 1999, pp. 13.

[2] Wang Guolie, Ming Wenshan, "Water immerging, deformation and engineering technique of collapsible loess," Engineering and Research on Collapsible Loess, Luo Yusheng and Wang Guolie, Ed. Beijing: China Architecture Industry Press, 2001, pp. 21–32.

[3] Miao Tiande, "Present status of collapse deformation mechanism of loess," Engineering and Research on Collapsible Loess, Luo Yusheng and Wang Guolie, Ed. Beijing: China Architecture Press, 2001, pp. 73–82.

[4] Rogers, C. D. F., Dijkstra, T. A., and Smalley, I. J., "Hydroconsolidation and subsidence of loess: studies from China, Russia, North America and Europe", Engineering Geology, Vol. 37, No. 2, pp. 83–113, 1994.

[5] Feda, J., "Structural stability of subsident loess soils from Praha-Dejvice", Engineering Geology, Vol. 1, No. 3, pp. 201–219, 1996.

[6] Yang Yunlai, "Study on collapse mechanism of loess" (in Chinese), *Science in China Series (B)*, No. 7, pp. 754–766, 1988.

[7] Gao Guorui, "Classification of loess microstructure and its collapsibility" (in Chinese), *Science in China Series*, No. 12, pp. 1203-1208, 1980.

[8] Wang Lanmin, *Loess Dynamics*. Beijing: Earthquake Press, 2002, pp. 41, 94–101.

[9] Gao Guorui, "Study of the microstructures and the collapse mechanism in loess from Lanzhou" (in Chinese), *Journal of Lanzhou University*, No. 2, pp. 123–134, 1979.

[10] Gao Guorui, "Microstructure of loss in China" (in Chinese), *Chinese Science Bulletin*, Vol. 25, No. 20, pp. 945–948, 1980.

[11] Zhang Zhenzhong and Duan Ruwen, "Study on seismic subsidence and seismic hazard of loess" (in Chinese), *Northwest Seismological Journal*, Vol. 9, Supp., pp. 63–69, 1987.

[12] Xie Dingyi, Qi Jilin and Zhang Zhenzhong, "A constitutive laws considering soil structure properties" (in Chinese), *China Civil Engineering Journal*, Vol. 33, No. 4, 35–41, 2000.

[13] Lei Xiangyi, "Pore type and collapsibility of loess in China" (in Chinese), *Science in China Series (B)*, No. 12, pp. 1309–1316, 1987.

[14] Gao Guorui, “Microstructure of loess soil in China relative to geographic and geologic environment” (in Chinese), *Acta Geologica Sinica*, Vol. 58, No. 3, pp. 266–272, 1984.
[15] Liao Shengxiu, “Relation between variation of microstructure of loess and collapsibility,” *Proceeding Conference on Classification, Denominate and Application of Loess in China*, Xi’an: Shannxi People Education Press, 1990, pp. 144–154.
[16] Wang Lanmin, Liu Hongmei, Li Lan and Sun Chaoshao, “Laboratory study on mechanism and behaviors of saturated loess liquefaction” (in Chinese), *Chinese Journal of Geotechnical Engineering*, Vol. 22, No. 1, pp. 89–94, 2000.
[17] Ministry of Construction and General Administration of Quality Supervision, Inspection and Quarantine of the People's Republic of China, *Code for building construction in collapsible loess regions (GB50025-2004)*, Beijing: China Architecture Industry Press, 2004, pp. 17–19.
[18] Wang Lanmin and Zhang Zhenzhong, “Estimating method of seismic subsidence on earthquake” (in Chinese), *Journal of Natural Disasters*, Vol. 2, No. 3, 85–94, 1993.
[19] Qian Jiahuan and Yin Zongze, *Theory and Calculation of Soil Engineering*. Second Edition, Beijing: Chinese Water Conservancy and Hydroelectricity Press, 1996, pp. 171, 213.
[20] Sun Junjie, “A study on computing method of negative skin friction on pile in subsiding loess ground,” Master’s Degree Thesis, Lanzhou Institute of Seismology, CEA, Lanzhou, China, 2004.
[21] Editing Committee on Handbook of Engineering Geology, *Handbook of Engineering Geology*, Beijing: China Architecture Industry Press, 1992, pp. 449–451, 455.

Energy Approach to Slope Failures and a Case Study during 2004 Niigata-ken Chuetsu Earthquake

T. Kokusho[1] and T. Ishizawa[2]
[1] *Professor, Faculty of Science and Engineering, Chuo University, Tokyo, Japan.*
[2] *PhD student, ditto.*

Abstract.
So far, earthquake-induced slope stability has been evaluated by the force-equilibrium of soil mass in normal engineering practice, which cannot evaluate failure deformation once large failure occurs. The energy approach is proposed, in which the amount of earthquake energy is evaluated in conjunction with the gravitational potential energy to be dissipated in slope displacement including large flow deformations. An energy balance in a model of a rigid block resting on an inclined plane is examined. Then, shake table tests of dry sand slope are carried out in which the earthquake energy used for the slope failure can be successfully quantified. It is shown that the energy balance holds in the sand slope and its displacement can be evaluated from the rigid block model by modifying the friction coefficient of the slope. The energy approach is then applied to one of the slope failures occurred during the 2004 Niigata-ken Chuetsu earthquake to discuss its applicability in the field.

Keywords—*slope displacement, flow failure, seismic wave energy, friction coefficient, rigid block model*

ENERGY APPROACH

Seismically induced slope failures have normally been evaluated based on the equilibrium of forces acting on a potentially sliding soil mass. This force approach can evaluate the initiation of slide or the safety factor against the slope failure, but it cannot predict slide deformations, once failure occurs. From the viewpoint of the performance based design or the risk evaluation of slope failures, it is very important to evaluate not only the safety factor but also how large the deformation will develop and how far the effect reaches down-slope. The Newmark method [1] can evaluate slope displacement along a fixed slip surface based on a double integration of acceleration of a potentially sliding soil block. In actual slope failures, sliding soil may not always behave as a rigid body but deforms continuously without distinct slip surfaces. It sometimes tends to become destructive due to a shift from slow slide to fast flow because the soil strength decreases drastically after the initiation of failure.

In this research, an energy approach is proposed to evaluate slope failures including flow failures from their initiation to termination. The basic idea, first proposed in [2], is shown in Fig.1. In case of earthquake- induced slope failures, four energies; potential energy by the gravity E_p, kinetic energy E_k of sliding soil mass, earthquake energy contributing to the slope failure E_{EQ} and energy dissipated in soil due to the slope deformation E_{DP}, can be correlated by the following equation;

$$E_{DP} + E_k = E_{EQ} - \delta E_p \tag{1}$$

or in an incremental form as;

$$\triangle E_{DP} + \triangle E_k = \triangle E_{EQ} - \triangle \delta E_p \tag{1'}$$

Note that the potential energy change before and after failure δE_p in Eq.(1) or $\triangle \delta E_p$ in Eq.(1') is normally negative. If failures occur after the end of earthquake shaking as often observed in case histories, the energy balance becomes identical with that in slope failures due to rainfall or other non-seismic causes without the earthquake energy;

$$\triangle E_{DP} + \triangle E_k = -\triangle \delta E_p \tag{2}$$

In non-seismic cases, if $-\triangle \delta E_p$ is larger than $\triangle E_{DP}$ in Eq.(2), then $\triangle E_k > 0$ and failure starts. Namely the condition for initiation of failure is;

$$\triangle E_k = -\triangle \delta E_p - \triangle E_{DP} > 0 \quad \text{or} \quad -\triangle \delta E_p > \triangle E_{DP} \tag{3}$$

Once failure starts, the amount of the dissipated energy is critical to decide if it develops as a flow-type failure and how far it flows. If $\triangle E_{DP}$ is smaller than

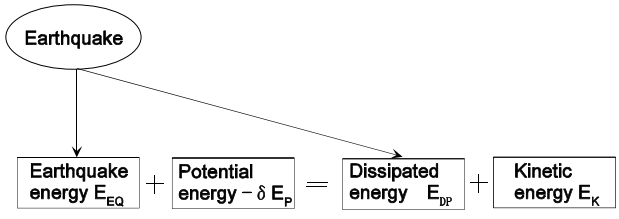

Fig.1 Energy balance during seismically induced slope failure

$-\triangle\delta E_p$ in some time increments, then $\triangle E_k$ is increased and the soil movement is accelerated. A shift from slow slide to fast flow may occur not only due to increase in $-\triangle\delta E_p$ but also due to drastic decrease of $\triangle E_{DP}$ caused by pore-pressure buildup in liquefiable soil, strength loss in high-sensitivity clay, etc. In fast flow failures, soil mass can keep flowing unless the kinetic energy at a time (E_k) plus the subsequent potential energy change ($-\delta E_p$) is all dissipated.

If $-\triangle\delta E_p$ is smaller than $\triangle E_{DP}$, then $\triangle E_k$ is negative, hence the soil mass decreases the speed and comes to a halt if reserved kinetic energy E_k is all consumed. If the failure mode and the energy dissipation mechanism in flowing soil mass are known, it is possible to evaluate how far the flow will reach in the down-slope direction.

ENERGY BALANCE IN RIGID BLOCK MODEL

The Newmark Method based on a rigid block model, a commonly accepted practice in geotechnical earthquake engineering to estimate seismically induced displacement of earth-structures, has recently been examined from the viewpoint of energy by Kokusho et al.[3]. The application of the energy approach to the rigid block model gives the potential energy change δE_p and the dissipated energy due to the block slippage E_{DP} to be correlated with horizontal residual displacement δ_r as;

$$-\delta E_p = Mg\beta\delta_r \tag{4}$$

$$E_{DP} = \frac{\mu\left(1+\beta^2\right)}{1+\mu\beta} Mg\delta_r \tag{5}$$

Then, based on Eq.(1) and using $E_k = 0$ if compared before and after slope failure, the earthquake energy is correlated with δ_r as;

$$E_{EQ} = \frac{\mu-\beta}{1+\mu\beta} Mg\delta_r \tag{6}$$

The ratios of E_{EQ} to $-\delta E_p$ and E_{EQ} to E_{DP} are after Kokusho et al.[3];

$$\frac{E_{EQ}}{-\delta E_p} = \frac{(\mu-\beta)}{\beta(1+\mu\beta)} \tag{7a}$$

$$\frac{E_{EQ}}{E_{DP}} = \frac{(\mu-\beta)}{\mu\left(1+\beta^2\right)} \tag{7b}$$

The contribution of the earthquake energy in comparison to the dissipated energy or the potential energy depends only on slope inclination β and the friction coefficient μ. Also note that the contribution of E_{DP} becomes smaller with larger slope inclination β and smaller friction coefficient μ. Also note that, in these relationships, dynamic changes of seismic inertia force affect not only the driving force of the sliding block but also the shear resistance along the slip surface. If the soil mass is saturated, however, seismic inertia force is all carried by temporary pore-water pressure and does not change the effective stress normal to the slip plane and hence the shear resistance. Consequently, for saturated soil, Eqs.(5) and (6) is replaced by the next equation in which σ_{n0} and σ'_{n0} are total and effective stresses normal to the slip plane, respectively and E_{EQ}/A is the energy per unit area.

$$\delta_r = \frac{\left(E_{EQ}/A\right)}{\left(1+\beta^2\right)\left(\mu\sigma'_{n0}-\beta\sigma_{n0}\right)} \tag{6'}$$

$$E_{EQ}/-\delta E_p = \frac{\left(\mu\sigma'_{n0}-\beta\sigma_{n0}\right)}{\beta\sigma_{n0}} \tag{7a'},$$

$$E_{EQ}/E_{DP} = \frac{\left(\mu\sigma'_{n0}-\beta\sigma_{n0}\right)}{\mu\sigma'_{n0}} \tag{7b'}$$

It is needless to say that the rigid block model on the slip plane, although it captures basic physics of slope failure mechanism, cannot directly reproduce the failure of sloping soil mass. One of the most significant differences is that, in actual slope failures, soil mass may not slide as a rigid body along a fixed slip plane but deforms continuously with or without movable slip planes. Furthermore, if the friction coefficient μ reduces due to pore pressure buildup or other mechanisms after the initiation of failure, it cannot predict the displacement of the failed soil mass anymore. Consequently, a shake table test of sand slope was carried out (Kokusho et al. [3]) to quantify energies involved in slope failures more realistic than the rigid block model.

SHAKE TABLE MODEL TESTS

A spring-supported shaking table shown in Fig.2 was utilized to apply vibrations to a model slope made from sand, called Model-A here, in a rectangular lucite box. The model slope (base length; L = 60 cm, height; H = 33 cm, width; B = 40 cm) was made by air-pluviating dry clean Toyoura sand to a prescribed relative density of $Dr \approx 40\%$. The slope angle was about 29 degrees. In order to evaluate the friction coefficient μ of the model slope, the slope was gradually inclined statically until the onset of slope failure. The static tests carried out three times with the same initial slope angle of 29 degrees and $Dr \approx 40\%$ gave the angle of repose 34.8 to 36.0 (average 35.3) degrees.

The table was initially pulled to a prescribed horizontal displacement and then released to generate damped free vibration. Dissipated energy, which can be calculated from the decay in displacement amplitude in

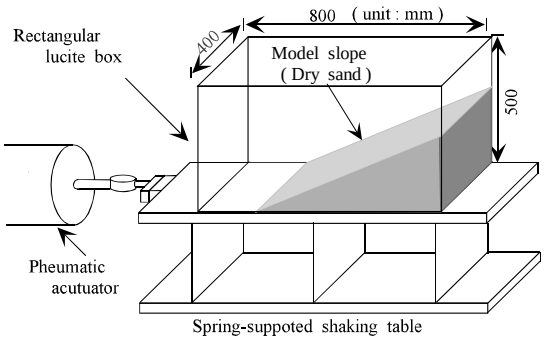

Fig.2 Shake table test apparatus for model slopes.

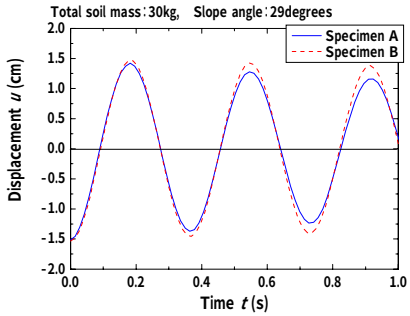

Fig.3 Decay vibrations measured by a LVDT displacement gauge in the Model-A and B.

each cycle depends not only on the energy dissipation due to slope deformation but also on other energy loss mechanisms such as radiation damping in the shake table foundation. In order to extract the dissipated energy due to slope deformation, a dummy model, called Model-B consisting of a pile of rigid concrete blocks, was made in the same lucite box and vibrated in the same way. The total weight and the center of gravity were adjusted to be almost identical in the two models.

The decay in amplitudes, measured by a LVDT displacement gauge in both Model-A and B are shown in Fig.3. Notes that, though the initial table displacement, 2.0 cm, and the vibration period of the table, are almost the same, the difference in amplitudes grows larger with increasing number of cycles. It may be reasonable to assume that this difference reflects the greater energy dissipated in Model-A (the model slope) due to its internal deformations, since almost negligible energy is dissipated in the rigid concrete blocks in Model-B.

The loss energy per cycle $\triangle W$ can be calculated as

$$\triangle W = 4\pi WD \qquad (8)$$

in which W, representing the strain energy in the same cycle, can be evaluated from the spring constant κ and the displacement amplitudes of the shaking table. The earthquake energy increment in the model slope $\triangle E_{EQ}$ can then be evaluated from the loss energies per cycle in Model-A and Model-B, $\triangle W_A$ and $\triangle W_B$, respectively as;

$$\triangle E_{EQ} = \triangle W_A - \triangle W_B \qquad (9)$$

The total earthquake energy E_{EQ} calculated as a sum of $\triangle E_{EQ}$ in each cycle represents the amount of earthquake energy involved in producing the final displacement in the model slope. To be more precise, E_{EQ} also includes the energy dissipated by soil damping in the model during vibration, which is neglected in the interpretation of the model test results. The total input energy applied to the shaking table E_{IP} can be calculated from the initial pull displacement u_o of the table as;

$$E_{IP} = \frac{1}{2}\kappa u_o^{\,2} \qquad (9)$$

It is found that the relationship between E_{EQ} and E_{IP} is almost constant despite increasing input energy. It indicates that the ratio of the earthquake energy actually used for slope failure to the total input energy may be assumed almost constant no matter how large the input seismic energy is or how much slope failure occurs. Such decay vibration tests were carried out under different frequencies by changing the mass of the table in four steps in order to know the effect of the input frequency on the slope displacement.

The deformation of the model slope was observed by two video cameras, one from the side and the other from above. Column-shaped markers made from colored sand were installed at the side of the model. On the slope face, dry noodle sticks of 5 cm length were set up in line. The interval of these markers was 10 cm in the slope direction. The slope surface indicated almost uniform deformation in the direction normal to the cross-section. The slope deformation was also measured before and after the end of tests by a laser beam displacement sensor and compared with the video data to check their reliability. In order to correlate the energies with the residual displacement of the slope, the horizontal residual displacement of the slope surface was evaluated here as an average of the displacements of the sticks. This calculation was implemented in each cycle of the input vibration to obtain the incremental residual displacement $\triangle \delta_{rs}$.

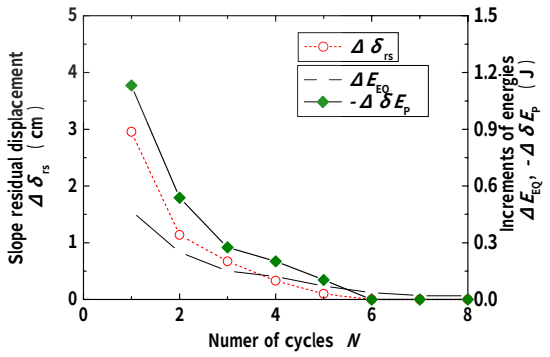

Fig.4 Displacement $\triangle \delta_r$, incremental energies, and $-\triangle \delta E_p$ plotted versus the number of cycles N.

In Fig.4, $\triangle\delta_{rs}$ is plotted versus the number of cycles, N. The incremental earthquake energy $\triangle E_{EQ}$ and the potential energy change $-\triangle\delta E_p$ are also plotted against N in the same chart. From the change in the slope surface geometry $-\triangle\delta E_p$ is calculated cycle by cycle as;

$$\triangle\delta E_p = \triangle\left(\rho_d g B \int z dx dz\right) \tag{10}$$

where z is the vertical coordinate and ρ_d is the dry soil density (assumed constant). The integration is carried out over the cross-sectional area of the slope. It is confirmed that measurable slope deformation occurs only until about 5th cycle, which is almost consistent with the variation in the energies $\triangle E_{EQ}$ and $-\triangle\delta E_p$.

SLOPE DISPLACEMENT VERSUS ENERGY

The incremental energies, $\triangle E_{EQ}$ and $-\triangle\delta E_p$ calculated in each cycle are summed up to evaluate the corresponding total energies, E_{EQ} and $-\delta E_p$. The dissipated energy E_{DP} can be readily evaluated from Eq.(1) because E_k =0 if the energy balance before and after slope failure is compared. The total residual displacement δ_{rs} is also calculated by summing up all incremental displacements $\triangle\delta_{rs}$. In Fig.5 the residual displacements are plotted versus the vibration energy E_{EQ} used for slope deformations. Here, the results obtained under 4 different input frequencies for the same 29 degrees slope are plotted. It is remarkable that all plots can be approximated as a single curve despite the difference in the input frequency, indicating that the energy can serve as a determinant for slope displacement even under different earthquake inputs. Also noted in Fig.5 is that there exists a threshold energy below which no residual displacement occurs.

In Fig.6, the values of $-\delta E_p$ and E_{DP} are plotted versus the earthquake energy E_{EQ} for numerous test data with different initial table displacements under different input frequencies. In the light of the energy considerations on the rigid block model discussed before, the ratios $-\delta E_p / E_{EQ}$ and E_{DP}/E_{EQ} can be calculated theoretically based on the rigid block model by Eqs.(7a) and (7b). The angle of the slope is 29 degrees ($\beta = 0.55$) and the angle of repose of the sand is about 35 degrees (μ =0.70). This value was measured by a different series of tests, in which the same sand slope was statically inclined until failure to measure the angle of repose. Using these values in Eqs.(7a) and (7b), $-\delta E_p / E_{EQ}$ =5.1 and E_{DP}/E_{EQ} =6.1, which are drawn in Fig.6 by two dotted lines. Obviously there is a wide gap between the theory on the rigid body model and the sand slope. However, it is noted that the experimental results can also be roughly approximated by straight lines, indicating that $-\delta E_p$ and E_{DP} tend to increase almost in proportion with E_{EQ} irrespective of the intensity of shaking and the input frequency. Actually, if μ =0.86 is used instead of μ =0.70, the theoretical line can predict the test results almost perfectly as shown with the solid line in Fig.6. The gap between μ =0.70 and μ =0.86 may be explained by the difference in the failure mode of the sand slope. The depth of slipped sand was limited near the surface in the static test, while in the dynamic test it extended to a depth with larger volume of sheared zone.

From Eq.(6) for the rigid block model, the residual slope displacement can be formulated as;

$$\delta_r = \frac{1+\mu\beta}{\mu-\beta}\frac{E_{EQ}}{Mg} \tag{11}$$

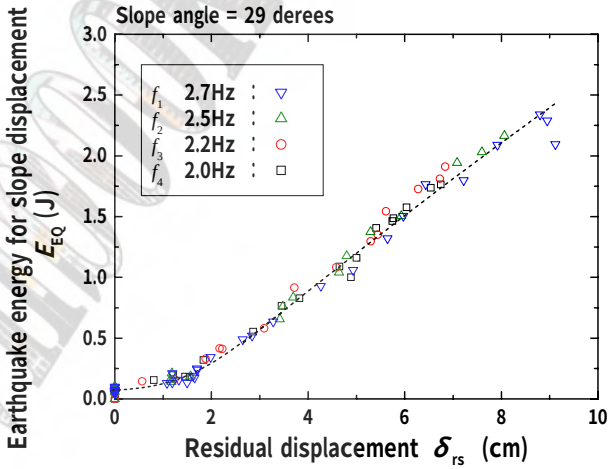

Fig.5 Earthquake energy E_{EQ} plotted versus resisual slope displacement for several test cases with different initial table displacement.

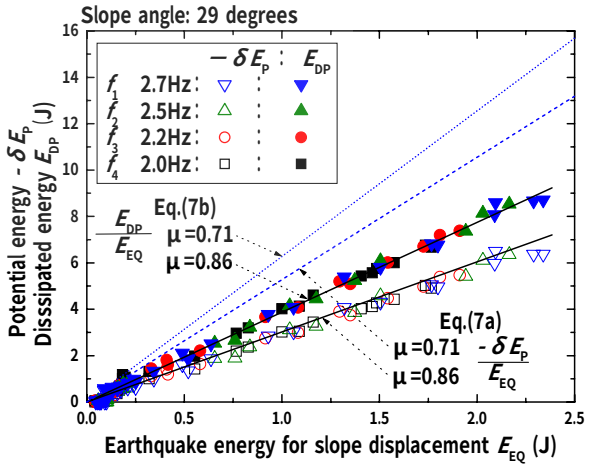

Fig.6 Earthquake energy E_{EQ} plotted versus potential e nergy or dissipated energy for several test cases with different initial table displacement.

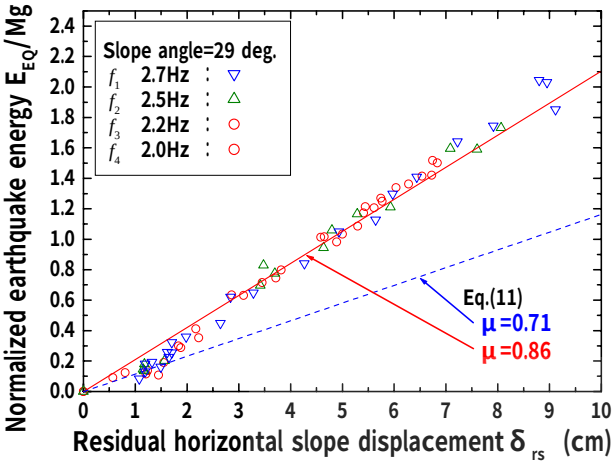

Fig.7 Relationships between residual displacement δ_r and earthquake energy E_{EQ}/Mg for different initial table displacements compared with the rigid block theory.

In Fig.7, the residual displacement δ_{rs}, which is considered to be equivalent to δ_r in the rigid block model, obtained by numerous tests are plotted versus the normalized earthquake energy E_{EQ}/Mg. The weight of the displaced soil mass Mg was evaluated from Eq.(4) using the displacement δ_{rs} and the measured potential energy change $-\delta E_p$. The dotted line corresponding to the theoretical relationship of Eq.(11) by the rigid block model for μ =0.70 and $\beta = 0.55$ overestimates the observed residual displacement for the same normalized energy. However, another theoretical relationship by solid line for μ =0.86 and $\beta = 0.55$ can predict the residual slope displacement almost perfectly. This indicates that if an appropriate friction coefficient is chosen, the simple rigid block model, which apparently possesses different failure mechanism, can successfully simulate sand slope.

ENERGY BASED SLOPE FAILURE EVALUATION

Based on the theoretical considerations on the simplified block model and the model test explained above, a energy-based design method in which post earthquake residual slope displacements can be evaluated may be proposed as shown in Fig.8.

First, the input earthquake energy E_{IP} defined at the base of slopes or embankments is designated site by site. The energy E_{IP} can be evaluated [3] as;

$$E_{IP} = \rho_2 Vs_2 \int \left(du/dt\right)^2 dt \qquad (12)$$

where du/dt is the particle velocity of the design motions in terms of time t and $\rho_2 Vs_2$ is the impedance of the base layer as shown in Fig.9. By assuming the energy radiating downward through the base, E_d, the earthquake energy, E_{EQ}, which can be consumed inside the slopes or embankments can be obtained as;

$$E_{EQ} = E_{IP} - E_d \qquad (13)$$

In the present model test, E_{EQ}/E_{IP} = 0.25 could be assumed despite the difference of slope displacement.

Theoretically, the energy ratio is controlled by the impedance ratio $\alpha = \rho_1 Vs_1/\rho_2 Vs_2$ between the sloping ground and a base layer as illustrated in Fig. 9. Here a sloping ground is approximated by a horizontal 2-layers system with the average height H in the upper layer. Under stationary vibration by sinusoidal input motion, the ratio between the energy flux of downward radiation wave $\bar{E}_d$ and that of upward input wave $\bar{E}_{IP}$ can be formulated as Eq.(14) based on the one-dimensional SH wave propagation [3]. Here, the energy flux means the amount of harmonic wave energy transmitted in a unit time.

$$\bar{E}_d/\bar{E}_{IP} = \left| \frac{\left(1-\alpha^*\right)+\left(1+\alpha^*\right)e^{-2ik_1^* H}}{\left(1+\alpha^*\right)+\left(1-\alpha^*\right)e^{-2ik_1^* H}} \right|^2 \qquad (14)$$

Here, $k_1^* = \omega/Vs_1^*$ (ω is the angular frequency) and complex impedance ratio α^* can be written as;

$$\alpha^* = \rho_1 Vs_1^*/\rho_2 Vs_2^* = \alpha\left\{(1+2iD_1)/(1+2iD_2)\right\}^{1/2} \qquad (15)$$

in which Vs_1^*, Vs_2^* = complex S-wave velocity and D_1, D_2 = damping ratios of the upper and lower layer,

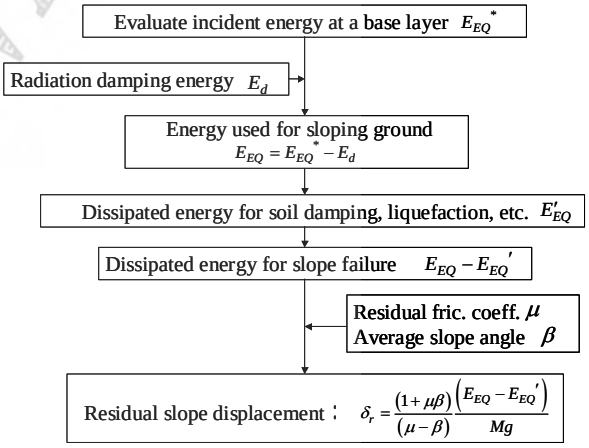

Fig.8 Flow chart for evaluation of slope displacement by energy approach

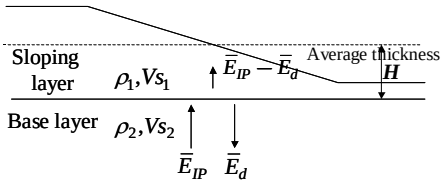

Fig.9 Definition of seismic wave energy at the base of a sloping layer

respectively. If the energy flow is stationary by harmonic wave propagation, the energy stored in the sloping layer is $W = \bar{E}_{IP} - \bar{E}_d$ and the energy dissipating downward by radiation is $\triangle W = \bar{E}_d$. From an analogous expression for a lumped mass linear viscous system which is in resonance with a harmonic input motion, the damping ratio due to wave radiation D_R may be defined as;

$$D_R = \triangle W / 4\pi W = \bar{E}_d / 4\pi \left(\bar{E}_{IP} - \bar{E}_d \right) \quad (16)$$

Consequently the energy flux ratio $\bar{E}_d / \bar{E}_{IP}$ can be correlated with the damping ratio by radiation D_R as;

$$\bar{E}_d / \bar{E}_{IP} = 4\pi D_R / (1 + 4\pi D_R) \quad (17)$$

If Eq.(17) can also be assumed for transient earthquake waves then;

$$E_d / E_{IP} = 4\pi D_R / (1 + 4\pi D_R) \quad (17')$$

The rest of the energy $E_{EQ} = E_{IP} - E_d$ is the maximum energy which can potentially be used for deformation and failure of the sloping ground. If, for instance D_R =15% as sometimes used in embankment dams in Japan, then, E_d / E_{IP} =0.65 and E_{EQ} / E_{IP} =0.35.

More practically, the energy ratio E_{EQ} / E_{IP} may be quantified by FEM analyses in which the design input motions are given at the base layers and the motions at the levels of the estimated slip plane are computed. Of course, E_{EQ} varies along the layer boundary in two dimensional problems and some averaging process may be needed.

The energy E_{EQ} is dissipated by residual slope deformation as well as by internal soil damping in the sloping layer. The present model tests indicate that the energy by internal damping E'_{EQ} seems small compared to E_{EQ} . If necessary, it is possible to evaluate the energy E'_{EQ} associated with internal soil damping based on FEM analyses and thus the earthquake energy to be used for the residual slope deformation $\left(E_{EQ} - E'_{EQ} \right)$ can be differentiated.

Fig.10 Aerial view of slope failure (top) and slip plane behind soil block (bottom) at Higashi-Takezawa.

Based on the rigid-block simple model, the residual horizontal displacement is expressed based on Eq.(6) as;

$$\delta_r = \frac{(1 + \mu\beta)}{(\mu - \beta)} \frac{\left(E_{EQ} - E_{EQ}{}' \right)}{Mg} \quad (18)$$

This equation is applicable to unsaturated slope where seismic inertia affects not only driving force but also shear resistance along the slip plane. If a slip plane is saturated, then the following equation should be used based on Eq.(6').

$$\delta_r = \frac{\left(E_{EQ} - E'_{EQ} \right) / A}{\left(1 + \beta^2 \right) \left(\mu \sigma'_{n0} - \beta \sigma_{n0} \right)} \quad (18')$$

The thickness or the mass of sliding soil may be determined by conventional slip surface analyses. As previously mentioned, the test results may be approximated by a dashed line 70% steeper than the theoretical line, indicating the rigid block model may be applicable by modifying the friction constant μ . In order to know how μ should be determined in actual design, the friction coefficient μ in Eq.(18) is back-calculated from recent case history during the 2004 Niigata Chuetsu earthquake.

CASE HISTORY DURING 2004 CHUETSU EQ.

Niigata-ken Chuetsu earthquake in October 2004 caused more than 1600 slope failures in the middle part of the main island of Japan. Among them, the failure in Higashi-Takezawa was the one of the largest which filled a valley and stopped a river flow, making a large natural reservoir. Fig.10 shows an aerial photograph of the slope failure stopping the river at the top and a close-up of the slip plane which appeared behind the slipped soil mass at the bottom. As indicated in Figs.11(a) and (b), the failure occurred along a sedimentation plane between mudstone and sandstone of Neogene. The inclinations of slope and slip plane were about 20 degrees. A sandstone soil block of 20 m in maximum depth and 300 m x 250 m in maximum horizontal dimensions slid along the sedimentation plane and plugged the valley. The total volume of displaced soil calculated three-dimensionally was 0.9 x 10^6 m^3 and 1.2 x 10^6 m^3 before and after the failure, respectively.

The failure was idealized here by simplifying the soil mass by a flat block of 6.9 x 10^4 m^2 (in horizontal area) by 15.2 m (in thickness) slipping down along the slip plane with the total mass unchanged. The center of gravity moved by 94 m laterally and 21 m vertically.

(a)

(b)

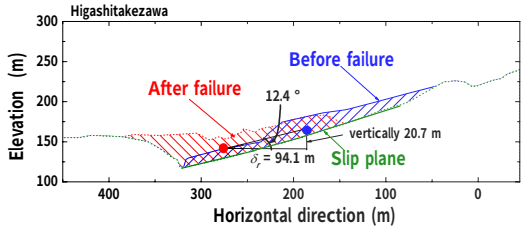

Fig.11 Plan (a) and cross-section (b) along blue chain-dotted line of Higashi-Takezawa slope failure along gentle slip plane of about 20 deg.

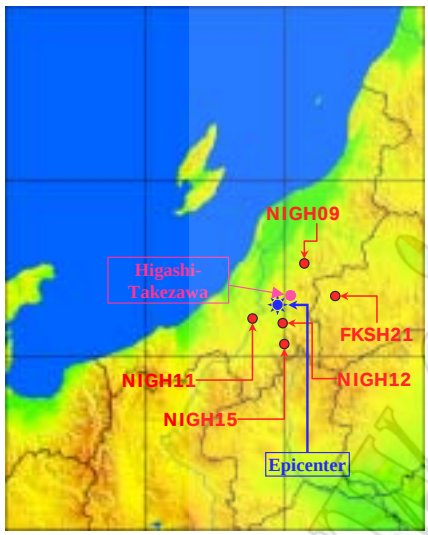

Fig.12 Locations of Higashi-Takezawa slope failure together with the epicenter and KIK-net sites.

The equivalent slip inclination connecting the center of gravity before and after the failure is 12.4°, which is considerably lower than 20° because the front portion of the failed soil mass crashed against and piled up on the opposite side of the valley.

The input earthquake energy E_{IP} defined at a base layer of the slope was extrapolated from several KIK-net vertical array records around the area. Fig.12 shows the locations of KIK-net sites around Higashi-Takezawa together with the epicenter of the main shock. Table 1 shows the calculated input energies per unit area E_{IP}/A at the base layers and related values at the 5 vertical array sites. The S-wave velocities of the base layers in those sites span from 780 to 1600 m/s. In Fig.13, the values of

Table-1 Evaluated energies and related values in nearby vertical array sites.

Ranking	Site No.	A_{CCmax} (gal)	Epc. Dist.(km)	Base layer Depth (m)	Vs at base layer (m/s)	Upward energy at base layer (kJ/m^2)
2	NIGH11	587.9	17.0	205.0	850.0	122
3	NIGH12	410.0	13.0	110.0	780.0	149
5	NIGH09	390.1	36.0	100.0	1380.0	33
6	FKSH21	361.7	40.0	200.0	1600.0	74
7	NIGH15	242.8	29.0	100.0	1540.0	5

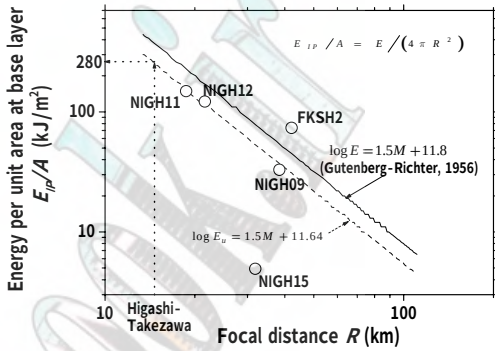

Fig.13 SH wave energy versus focal distance compared with Gutenberg-Richter relationship.

E_{IP}/A are plotted versus focal distances (focal depth=13.4 km) on a log-log chart. The solid line in the chart indicates the wave energy per unit area theoretically calculated from the total wave energy E released at a point source using an empirical equation by Gutenberg and Richter [4]

$$\log E = 1.5M + 11.8 \tag{19}$$

and from the focal distance R based on the spherical energy radiation of body waves, in which $E_{IP}/A = E/\left(4\pi R^2\right)$. It is noted that the input energies calculated from earthquake records tend to change in a similar manner to the theory. The plots for the calculated energy may be approximated by the dashed line parallel to the solid line, indicating that the SH-wave energy is slightly smaller than the theoretical energy assuming the point source. The input energy at the base layer of Higashi-Takezawa which is assumed to have the comparable S-wave velocity to the nearby KIK-net sites can be extrapolated by this dashed line in Fig.13 as E_{IP}/A =280 kJ/m^2. If the radiation damping D_R =15% is assumed in this site, then E_{EQ}/E_{IP} =0.35 as previously mentioned, and hence the maximum energy potentially used for the slope failure in Higashi-Takezawa was E_{EQ}/A=98 kJ/m^2.

Estimating that the slip plane was saturated at the time of earthquake (water was actually running on the impervious mudstone plane when we visited after the earthquake), Eq.(18') is expressed here to back calculate

equivalent friction coefficient μ or equivalent friction angle ϕ_{eq} as;

$$\mu = \tan\phi_{eq} = \left(E_{EQ} - E'_{EQ}\right) \Big/ \left(AD_{av}\rho_t g\,\delta_r\right) + \beta \qquad (20)$$

where A = horizontal area, D_{av} = thickness, $\rho_t g$ =unit weight of failed slope. The internal dissipating energy E'_{EQ} by liquefaction or soil damping is assumed negligibly small compared to other energies and ρ_t =1.8 t/m^3, assuming that the major portion of the slid soil block was unsaturated except along the slip plane. Then, substituting equivalent slip inclination $\beta = \tan 12.4^\circ$ into Eq.(20), the friction coefficient μ is or the friction angle ϕ_{eq} is 12.6°. This value corresponds to equivalent friction coefficient representing failure modes such as the rigid block slide along the smooth slip plane, the crash and pile-up in the front, etc. This equivalent friction angle is much lower than the inclination of the slip plane 20°, indicating that the slope starts to glide very easily. It seems that the large difference between 12.6° and 20° allowed the failed soil mass to accelerate and pile up on the opposite side of the valley.

The exact mechanism why this low friction angle could be realized is not yet known. The sandstone overlying the slip plane of cemented mudstone was highly weathered and almost equivalent to decomposed dense sand. It may somehow be explained by seismically induced high water pressure acting on the slip plane, although the dense sand deposit is unlikely to have liquefied.

CONCLUSIONS

The energy approach for slope failure evaluation has been developed by first examining the energy balance in the Newmark-type block model, comparing it to innovative shake table tests of a model slope of dry sand and then applying it to an actual slope failure during the Niigata-ken Chuetsu earthquake, yielding the following major findings.

1) The energy balance in the rigid block model indicates that the ratio of the earthquake energy E_{EQ} used for slope failure to the potential energy change of the slope depends only on slope inclination β and friction coefficient μ. The slope displacement can be formulated to be proportional to E_{EQ}.
2) In shake table tests of dry sand slope to quantify energies involved in slope failures more realistically than the rigid block model, E_{EQ} can be successfully measured, quantifying the energy balance involved in the failure of the model slope. Comparison of the energy theory with the test results indicates that the simple rigid block model, which apparently possesses different failure mechanism, can satisfactorily simulate a continuously deforming sand slope if an appropriate friction coefficient μ is chosen.
3) Based on the theoretical considerations and the model tests, an energy-based design method in which post earthquake residual slope displacements can be evaluated is proposed.
4) In order to back-calculate the friction coefficient μ, the energy-based method was applied to a recent case history during the 2004 Niigata Chuetsu earthquake. The input earthquake energy E_{IP} defined at a base layer of the slope was extrapolated from several KIK-net records in the area. If, the radiation damping D_R =15% is assumed based on dam engineering practice in Japan, the maximum energy potentially used for the slope failure in Higashi-Takezawa is E_{EQ}/A=98 kJ/m^2. The equivalent friction angle ϕ_{eq} = 12.6° was obtained, which represents a combination of different failure modes of the failed slope including the slide along the smooth slip plane and the crash and pile-up in the front. This friction angle is much lower than the inclination of the slip plane 20° of the sedimentation rock, indicating that the failed soil mass accelerated and piled up on the opposite side of the valley.

Finally, NIED (National Research Institute for Earth Science and Disaster Prevention) in Tsukuba, Japan, who generously provided KIK-net data through internet, is gratefully acknowledged.

REFERENCES

[1] Newmark, N. M. “Effects of earthquakes on dams and embankments,” Fifth Rankine Lecture, Geotechnique Vol.15, pp.139-159, 1965.

[2] Kokusho, T. and Kabasawa, K.: “Energy approach to flow failure and its application to flow due to water film in liquefied deposits,” Proc. of International Conference on Fast Slope Movement, Naples, May 2003.

[3] Kokusho, T., Ishizawa, T. and Harada, T. Energy approach for earthquake induced slope failure evaluation, Proc. 11th International Conference on Soil Dynamics & Earthquake Engineering and 3rd International Conference on Earthquake Geotechnical Engineering, Berkeley, California, Vol.2, 260-267, 2004.

[4] Kokusho, T., Motoyama, R. and Mantani, S.: H. Motoyama, “Seismic wave energy evaluation in surface layer for performance based design”. 13th World Conference on Earthquake Engineering, Vancouver, Paper No.3480, 2004.

[5] Gutenberg, B. and Richter, C. F.: “Earthquake magnitude, intensity, energy and acceleration (Second paper)” Bulletin of Seismological Society of America, Vol.46, pp.105-145, 1956.

Effect of cyclic behavior of soils on seismic response of clay slopes

G. Biondi, M. Maugeri
Department of Civil and Environmental Engineering, University of Catania, Catania, Italy

Abstract
A model for the assessment of seismic stability condition of cohesive slopes including the effects of cyclic strength degradation is presented. The model was developed starting from a modified Newmark-type analysis in which the degradation effect was accounted for introducing the degradation parameter. Two threshold values of the degradation index were used to predict the seismic slope behavior and the influence of the inertial and weakening effects. The proposed procedure allows to detect the occurrence of different type of instabilities and the proper approach for the assessment of the earthquake-induced permanent displacements in presence of cyclic soil shear strength reduction.

Keywords—*Clayey slopes, cyclic strength degradation, Newmark analysis, permanent displacements*

INTRODUCTION

The occurrence of earthquake-induced landslides is documented in many post-earthquake damage reports and field observations and the experience of last decades has shown that these phenomena represent one of the most damaging hazards associated with large earthquakes.

During strong earthquakes soils develop significant deformations that may affect the stability condition of slopes and earth structures possibly causing failures and damages on the environment, structures and lifelines. The analysis of the earthquake-induced damage reveals that frequently damages induced by earthquake-triggered landslides exceed damages directly related to the ground shaking; then damage due to landslides is remarkable as that due to all other seismic hazards combined [1,2,3].

Starting from these statements, the study of earthquake-induced landslides is nowadays considered a crucial point in the procedure for mitigation of geotechnical seismic hazard [4,5,6]. The main goal of this kind of analyses is the evaluation of the stability condition during the earthquake shaking and the assessment of the post-seismic slope serviceability. The experiences of recent strong earthquakes reveal that the seismic response of slope and the stability conditions is greatly influenced by the soil cyclic behavior. In particular, failure and large deformation may occur even for moderate earthquakes if the cyclic soil behavior is characterized by significant strength and stiffness degradation. In this case a stability analysis that does not take into account these aspect could lead to an unsafe estimation of the slope response.

The paper presents a procedure for the assessment of the influence of cyclic behavior of cohesive soils on the seismic stability condition of slopes. The proposed approach was developed starting from a critical review of procedures available in the literature and represents an extension of the traditional Newmark sliding block approach to the case of weakening instabilities and of instabilities caused by both inertial and weakening effects.

STABILITY ANALYSIS INCLUDING STRENGTH REDUCTION

The assessment of the slope stability condition under earthquake loading is usually performed using the pseudo-static method [7] based on the limit equilibrium or the limit analysis approach. This method provides a factor of safety against the failure condition that is generally defined as the ratio between the *strength capacity* of the slope and the *strength demand* imposed by the earthquake loading.

Generally, the pseudo-static approach disregards a number of aspects that significantly affect the dynamic slope response in terms of cyclic soil behavior, slope stability condition and permanent deformation response. First, the adoption of a single constant pseudo-static force to represent the complex transient, dynamic effects of seismic loading does not allow to reliable model the slope response; then for the selected design earthquake the soil *strength demand* could not be well estimated. Furthermore, under seismic loading condition, soils could experience strength and stiffness degradation. Since these aspects are not taken into account in the traditional pseudo-static approach, an accurate estimation of the *strength capacity* could not be generally achieved. For these reasons the pseudo-static method should be adopted with caution as it gives only an idea of the slope stability condition under earthquake loading.

It is well known that under seismic loading conditions, the assessment of earthquake-induced permanent displacements represents a more suitable criterion for the evaluation of seismic slope response and post-seismic serviceability.

Considerable efforts have been done in the last decades to propose advanced and accurate methods and procedure for analyzing the dynamic response of slopes and earth structures. These methods range from the sliding block analysis proposed by Newmark [8] to three-dimensional non-linear dynamic FEM analyses including large strain soils behavior. As far as the sliding block procedure is concerned a number of studies have shown that, due to the uncertainties in the input ground motion

and slope characteristics, this approach represent a good compromise between the pseudo-static ones and more sophisticated analyses and provide a good balance between the computational effort and the results accuracy. At the same time the importance of the cyclic soil behavior on seismic slope response has been recognized and attempts to take into account this aspect in a displacement-based approach were made.

Based on these assumptions a displacement-based approach was considered in this paper in order to develop a predictive model that allows to take into account the effect of cyclic soil shear strength degradation on seismic response of cohesive slopes.

INERTIAL AND WEAKENING INSTABILITIES OF SLOPES

The knowledge of the causes of earthquake-induced landslides is the basis for modeling the slope seismic behavior with predictive purposes. Concerning the consequence of an earthquake, two different kinds of effects should be considered. The shaking related to the earthquake motion generates a change in soil stress state, commonly identified as the *inertial effect*; this effect generally produce an increase of the driving force that may affect the slope stability condition leading to a failure. Moreover, during strong shaking soils show stiffness and strength degradation due to pore water pressure change and cyclic degradation. These aspects, commonly referred as *weakening effect*, depend on the earthquake-imposed loading path and on the dynamic soil behavior. This categorization of the earthquake effects could be suitably adopted to state the effect of soil shear strength reduction on the stability condition of slopes and on their displacement response.

Seismic slope instabilities are related to both the inertial and the weakening effects and the characteristics of the potential failure mechanism depend on which of these effects prevails. If the weakening effect is negligible compared to the inertial one, instability may occur when the earthquake-induced shear stresses are large enough to overcome the soil shear strength available along a potential failure surface. In this condition the slope response is generally classified as an *inertial instability*: the instability may be mainly ascribed to the inertial effect and is triggered by the temporarily unbalanced driving forces. This slope behavior is characterized by a stepwise accumulation of permanent deformations and generally ceases at the end of earthquake shaking.

Conversely, if the reduction in soil shear strength prevails on the inertial effect, a *weakening instability* may occur as a consequence of the reduction in soil shear strength. Usually, in clay slopes this behavior is the consequence of the pore pressure build-up and of soil cyclic degradation due to the cyclic loading imposed by the earthquake. Depending on the magnitude of the strength reduction and on the initial stability condition, different slope response can develop. If soil shear strength undergoes a remarkable reduction and drops below the static shear stress required for the equilibrium, a *failure* of the slope occurs involving very large deformations. Otherwise, if the reduced shear strength temporarily drops below the earthquake-induced shear stress but remains higher than the static shear stress required for the equilibrium, permanent deformations develop in the slopes but a failure condition is not achieved. For cohesionless slopes this behavior is traditionally described as a *deformation failure* [9] and is generally related to the reduction in soil shear strength due to the earthquake induced pore pressure build-up. Since in this case the slope does not experience a failure condition and response must be analyzed in term of admissibility of permanent displacements, the term *deformation failure* will be adopted in this paper also for slopes in cohesive soils. In this case, depending on the initial slope stability condition, the earthquake induced permanent displacements must be ascribed only to the weakening effect or to a combined inertial and weakening effect. At last if the available shear strength keeps it larger than the earthquake-induced shear stress during the whole earthquake shaking, the slope does not experience permanent displacements regardless the occurrence of shear strength degradation.

Referring to this different seismic slope behavior, the procedures available in the literature for the analysis of seismic slope stability can be grouped in two main categories. The first concerns with the so-called *inertia slope stability analysis* consisting in the traditional pseudo-static approach and in the Newmark sliding block procedure with its different applications proposed for several slope schemes and geometry of failure mechanism [10,11,12]. This kind of approaches are generally adopted in the analysis which involves soils that retain their shear strength during the earthquake shaking without showing any degradation of mechanical properties. The second category includes different methods and procedures developed for the analysis of those phenomena that may occur in soils that exhibit significant strength degradation during cyclic loading. These kinds of approaches are traditionally denoted as *weakening slope stability analyses*, and, in order to overcome the implicit limit of the pseudo-static method, have been generally developed referring to a displacement-based analysis. They have been traditionally developed for the analysis of the instabilities of saturated cohesionless soils that are significantly affected by the cyclic pore pressure build-up and may undergo liquefaction [9,13,14,15,16].

Concerning the seismic response of cohesive slopes a number of studies was developed to account for the effect of soil strength degradation in the evaluation of slope response [17,18,19,20,21,22]. These approaches were developed using the effective stress analysis or the total stress analysis. In the first case the *strength capacity* was estimated as a function of the pore pressure build-up due to the cyclic loading; in this way only the effect the cyclic reduction of effective stress was taken into account. In the latter case the effect of soil strength degradation is accounted for using the cyclic reduction of undrained shear resistance and the concept of degradation parameter

[23]; in this case an accurate evaluation of the degradation parameter [24] allows to take into account the effect of both cyclic degradation and pore pressure build-up.

A MODIFIED NEWMARK-TYPE ANALYSIS

The analysis presented in the paper concern with slopes of cohesive soils and is performed using the total stress approach. The considered scheme is the infinite slope whose characteristics are described by the slope angle β, the soil unit weight γ and the thickness D of the potential failure surface.

In the stability analysis of an infinite slope the potential failure plane is taken parallel to the slope profile and a plane strain condition is considered together with a rigid-plastic stress-strain behavior of soil. With this assumption, denoting with C_{uo} the static value of the undrained shear strength available at the depth of the failure surface, the slope static factor of safety can be expressed as:

$$F_s = \frac{C_{uo}}{\gamma \cdot D} \cdot \frac{1}{\sin\beta} \tag{1}$$

During the earthquake shaking the slope equilibrium condition is affected by two different factors: the inertial effect arising in the soil mass and the reduction of available undrained shear strength. If k(t) represents the time-dependent amplitude of the earthquake-induced acceleration and C_{uc}(t) denotes a time-dependent value of the undrained shear strength available in the dynamic stage, the slope seismic safety factor can be computed as:

$$F_d(t) = \frac{C_{uc}(t)}{\gamma \cdot D} \cdot \frac{1}{\sin\beta + k(t) \cdot \cos\beta^*} \tag{2}$$

where β*=β+ω, being ω the inclination of k with respect to the horizontal. In equation (2) the influence of inertial and weakening effects on the slope stability condition is clearly pointed out through k(t) and C_{uc}(t) respectively.

In the current stability analyses the possible reduction in soil shear strength is generally neglected and the slope seismic safety factor is evaluated referring to the static value C_{uo} considering the maximum value k_{max} of the earthquake-induced acceleration:

$$F_{do} = \frac{C_{uo}}{\gamma \cdot D} \cdot \frac{1}{\sin\beta + k_{max} \cdot \cos\beta^*} \tag{3}$$

However, a number of experimental researches have shown that during cyclic loading, cohesive soils could experience a strength reduction that is related to both cyclic degradation and pore pressure build-up. Generally, cyclic strain-controlled tests were performed to analyze these phenomena and to quantify the influence of the characteristics of the applied load, of the nature of soil and of its stress history. Usually, the characteristic of the applied load is described in terms of shear strain amplitude γ_c and number of imposed loading cycles N; the influence of soil nature is generally described referring to some intrinsic characteristics accounted for through the plasticity index and the overconsolidation ratio [23,25,26]. In these approaches, the reduction of shear strength is quantified introducing the degradation parameter t and is generally expressed in the form:

$$C_u^* = \frac{C_{uc}}{C_{uo}} = N^{-t} \tag{4}$$

were C_u^* represent the degradation index that is the ratio between the undrained shear strength available under cyclic loading condition and its initial static value. The degradation parameter t is related to γ_c and to the volumetric threshold shear strain of the soil and, generally, is expressed as a function of γ_c, plasticity index and overconsolidation ratio [27]. In this way in the evaluation of cyclic soil shear strength both the pore water pressure generation and the cyclic degradation that simultaneously occurs in cohesive soils are accounted for.

A number of studies [28,29] have been proposed in order to analyze the validity of this kind of approach to the case of irregular cyclic loading such as those imposed in the field by earthquakes. Using the results of staged cyclic loading tests performed on different clays Vucetic [27] showed that the cumulative results of the staged tests reflect reasonably well the effect of true irregular cyclic loading. Using a large number of experimental results obtained in uniform cyclic strain-controlled test, Matasovic & Vucetic [29] developed a generalized degradation-pore water pressure generation model; the model reasonably fits also results of staged tests performed on different soils revealing the applicability of models developed for strain-controlled conditions to the case of true irregular cyclic loading.

Based on these results the degradation model described by equation (4) will be adopted in this study in order to estimate the reduction of the undrained shear strength of cohesive soils. In this way equation (2) can be rewritten in the form:

$$F_d(t) = \frac{C_{uo}}{\gamma \cdot D} \cdot \frac{C_u^*}{\sin\beta + k(t) \cdot \cos\beta^*} \tag{5}$$

In order to estimate the influence of the shear strength reduction on the displacement response of the slope, the same procedure described by Newmark can be followed. According to this approach the potential unstable soil mass is assumed to behave as a rigid body and a threshold value of the seismic acceleration (the slope critical acceleration k_c) was estimated imposing that the driving forces equal the resisting ones along the sliding surface; this means that the seismic slope safety factor is unity and an incipient failure condition has been reached.

In the traditional displacement analysis the weakening effect is neglected and the resisting forces are estimated referring to C_{uo} instead of C_{uc}; then a traditional constant value k_{co} of the slope critical acceleration can be estimated from equation (3) imposing F_{do}=1:

$$k_{co} = \frac{C_{uo}/(\gamma \cdot D) - \sin\beta}{\cos\beta^*} \tag{6}$$

In this case, according to the Newmark procedure, permanent displacements start when the ground acceleration exceeds k_{co} and take place whenever the relative velocity of the unstable soil mass remains greater

than zero. The slope seismic behavior can then be predicted comparing k_{max} with k_{co} and the ratio k_{co}/k_{max} can be assumed as an index of the seismic slope stability condition allowing to distinguish seismically stable slopes ($k_{co}/k_{max}\geq 1$) and seismically unstable ($k_{co}/k_{max}<1$) ones.

During cyclic loading the strength may drop below its static value and the evaluation of the resisting forces should take into account this weakening effect. In this case the slope critical acceleration should not be considered as a constant value and a possible reduction should be evaluated for a reliable displacement analysis. A procedure with this intent was recently proposed for cohesionless slopes [9,16]. As an example Fig.1 shows the reduction of k_c computed for two different slopes (*A* and *B*) characterized by the same initial value k_{co} and different hydraulic conditions that lead to different soil cyclic response in terms of pore pressure build-up. The consequent reduction of k_c clearly points out the inadequacy of the traditional Newmark-type analysis (*TNA*) in comparison with a modified Newmark-type analysis (*MNA*) when significant strength reduction takes place in the soil during the earthquake. Concerning the slopes in cohesive soils, the strength degradation model described by equation (4) can be adopted; then, the current value k_c of slope critical acceleration can be evaluated through equation (2) imposing F_d=1:

$$k_c(t) = \frac{C_{uc}(t)/(\gamma \cdot D) - \sin\beta}{\cos\beta *} \qquad (7)$$

This time-dependent definition of k_c points out the possible influence of soil shear strength reduction in the displacement response of a cohesive slope. Using this approach the possible degradation of the soil shear strength can be accounted for in a Newmark-type analysis allowing to estimate both the inertial and weakening effects. According to equation (4), equation (7) shows that the reduction in slope critical acceleration can or can not affect the displacement response depending on the value of the degradation index and on the characteristics of the earthquake-imposed loading path expressed in terms of the number of loading cycles *N*. Finally, from equations (4),(6) and (7) it is evident that during the earthquake shaking, k_c decays from its initial value k_{co} following a degradation path that depends on the occurrence of soil cyclic strength degradation.

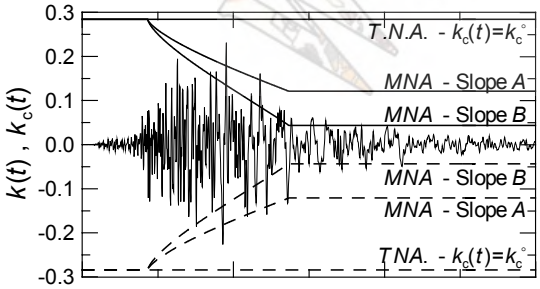

Fig. 1: Reduction of slope critical acceleration due to the earthquake-induced pore pressure build-up in cohesionelss slopes (modified from ref. [9,16]).

In this way a *modified Newmark sliding block analysis* can be performed taking into account the cyclic response of cohesive soils.

REDUCTION OF SLOPE CRITICAL ACCELERATION

The ratio k_{co}/k_{max} can be assumed as an index of the slope seismic stability condition only for soils that do not show significant strength reduction. In the general case, the ratio k_{co}/k_{max} can be adopted only to classify the initial slope conditions allowing to detect the slope initially stable under seismic condition ($k_{co}/k_{max}\geq 1$) and those initially unstable under seismic condition ($k_{co}/k_{max}<1$).

A suitable parameter for estimating the slope response without *a priori* neglecting the weakening effect is the ratio between the current value of the slope critical acceleration and its initial value:

$$\frac{k_c}{k_{co}} = \frac{C_{uc}/(\gamma \cdot D) - \sin\beta}{C_{uo}/(\gamma \cdot D) - \sin\beta} = \frac{N^{-t} \cdot F_s - 1}{F_s - 1} \qquad (8)$$

For several slope conditions and for different values of *t* and *N*, Fig. 2 shows the effect of the strength reduction on the ratio k_c/k_{co}. In particular, Fig. 2a shows the influence of the degradation index C_u^* for different values of slope angle and for $C_{uo}/(\gamma D)$=1; Fig. 2b shows the influence of *N* for $C_{uo}/(\gamma D)$=1, β=30° and *t* varying in the range 0-0.5. The influence of ω was not considered because equation (8) shows that the reduction of k_c does not depend on the inclination of the seismic force.

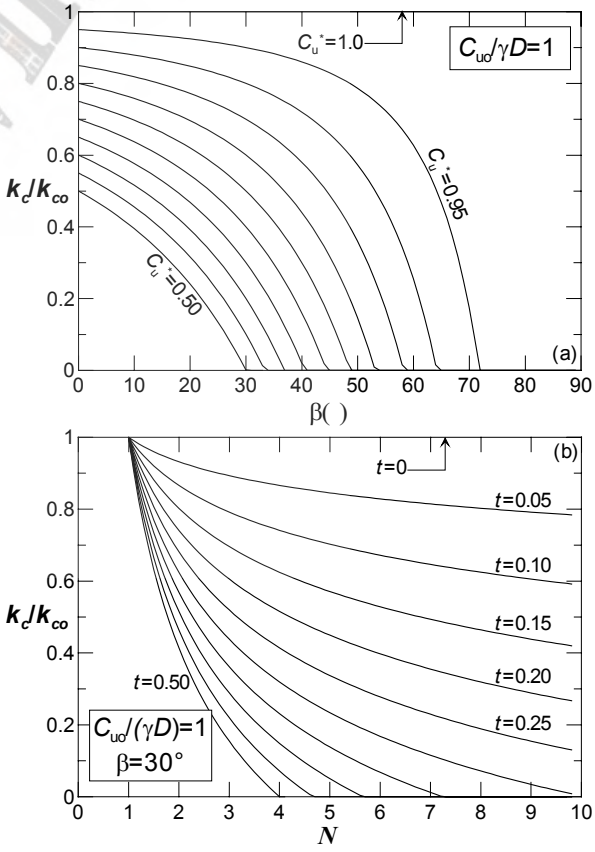

Fig. 2: Effect of the cyclic shear strength degradation on the reduction of slope critical acceleration.

From Fig. 2 it is evident that only if the shear strength reduction is negligible, the traditional value k_{co} can be utilized to perform a reliable displacement analysis. In the same time the influence of the degradation parameter t is clearly pointed out. As an example for a slope with $C_{uo}/(\gamma D)$=1 a value of C_u^*=0.90 reduces k_c to 80% of k_{co} for the case β=30° (F_s=2) and to 65% of k_{co} for the case β=45° (F_s=1.41); for C_u^*= 0.80 k_c drops to 60% of k_{co} and 30% of k_{co} respectively for β=30° and β=45°.

The reduction of k_c is then related to the initial slope stability conditions (for both static and seismic conditions), to the characteristics of the applied cyclic loading and to the dynamic soil response. It is apparent that for a given slope, depending on the magnitude of the strength degradation, k_c can drop to zero (Fig. 2).

In a Newmark-type analysis this condition can be assumed as a failure of the slope [9,16]; if this condition is reached during an earthquake, the slope response becomes prevalently governed by gravity forces and is characterized by very large displacements. If a failure condition is not reached the slope response must be evaluated taking into account the possible reduction of k_c and its value in comparison with k_{max}.

For the same slopes considered in Fig. 2a, Fig. 3a compares the ratios k_c/k_{co} and k_{max}/k_{co}. Each couple of the plotted line detects different areas corresponding to the different slope behaviors summarized in Fig. 3b.

If k_c/k_c° remains greater than zero, the slope response could be affected by both inertial and weakening effects but no failure condition is achieved. In this case, depending on the initial slope stability condition (k_{co}), on the magnitude of strength reduction (C_u^*) and on the amplitude of the earthquake-induced acceleration (k_{max}) the slope can remain stable (k_{max}/k_c<1) or could experience permanent displacements (k_{max}/k_c>1). In this latter case the response of the slope consist in a *deformation failure* whose causes must be detected considering the initial seismic slope stability condition. For slopes initially stable under seismic condition (k_{max}/k_{co}<1), the occurrence of permanent displacements (k_{max}/k_c>1) must be ascribed only to the cyclic strength degradation and the consequent slope response represents a *weakening instability*; in this case the slope behavior can not be evaluated using the traditional Newmark-type analysis and a measure of the slope seismic stability condition can be related to the ratio k_{max}/k_c in spite of k_{max}/k_{co}. For slopes initially unstable under seismic condition (k_{max}/k_{co}>1), permanent displacements would have occurred anyway due to the inertial effect and despite the cyclic strength degradation; in this case if the soil does not show strength reduction (C_u^*=1; k_c/k_{co}=1) the slope response represent an *inertial instability* and permanent displacements could be evaluated using the traditional Newmark approach; if, otherwise, the cyclic response is characterized by strength reduction (C_u^*<1; k_c/k_{co}<1), the displacements must be ascribed to both inertial and weakening effects and the slope response represents an *inertial-weakening instability*.

On the other hand if k_c/k_c° drops to zero, the slope

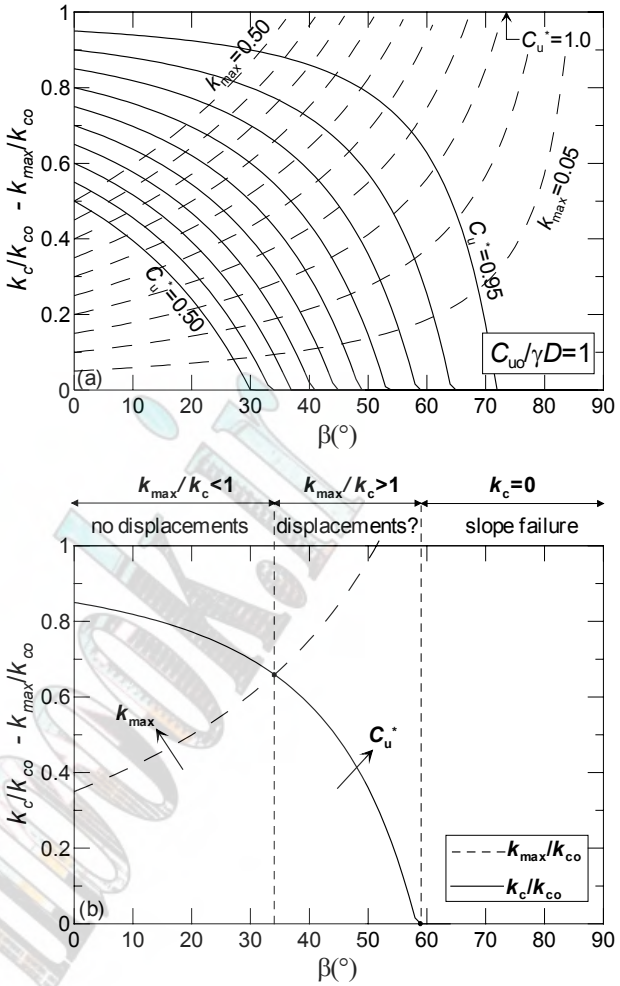

Fig. 3: Comparison between the slope critical acceleration k_c and the maximum earthquake-induced acceleration k_{max}: a) parametric analysis; b) scheme of the chart.

reach the failure. The occurrence of this case depends on the initial slope stability condition (k_{co}), on the magnitude of strength reduction (C_u^*) and can not be detected without taking into account the effect of cyclic strength reduction. Again, depending on the initial seismic stability condition (k_{max}/k_{co}) the failure of the slope could be ascribed only to the weakening effect (k_{max}/k_{co} <1) or to both inertial and weakening effects (k_{max}/k_{co}>1).

THRESHOLD VALUES OF DEGRADATION INDEX

Based on this assumption it is useful to develop some parameters that allow to identify the causes of the potential slope instability and the proper approach for the displacement analysis. In particular it is useful to detect threshold values of the degradation index to be used for predicting the slope behavior through a comparison with the degradation index C_u^* related to the earthquake-imposed cyclic loading.

A first threshold value of the degradation index can be evaluated estimating the value of C_u^* which produces the failure condition previously described; this is the value of the degradation index that makes the slope

critical acceleration to vanish. Using equations (7) and (4) the condition $k_c(t)=0$ lead to:

$$C_{uf}^{*} = \frac{\sin\beta \cdot \gamma \cdot D}{C_{uo}} = \frac{1}{F_s} \quad (9)$$

If this value of the degradation index is reached during the earthquake, k_c drops to zero and then, regardless the inertial effect, the slope reaches a *failure* condition characterized by very large permanent displacements mainly driven by gravity. If the degradation index imposed by the earthquake-induced cyclic loading do not reduce to C_{uf}^{*} no failure occurs; in this case, a *deformation failure* may or not occur depending on the value of the ratio k_{max}/k_c. For these reason, C_{uf}^{*} separates two different seismic behaviors of the slope: *failure and deformation failure*. Since C_{uf}^{*} depends only on the static slope stability condition, it represents an intrinsic parameter of the slope. Fig. 4a shows the value of C_{uf}^{*} for different slope conditions. Each of the plotted curves separates the diagram into different zones whose meaning is shown in Fig. 4b. A first zone (*zone 1*) represents points characterized by values of C_{uf}^{*} greater than unity and then related to slope unstable under static condition (F_s<1) for which the seismic stability analysis is insignificant.

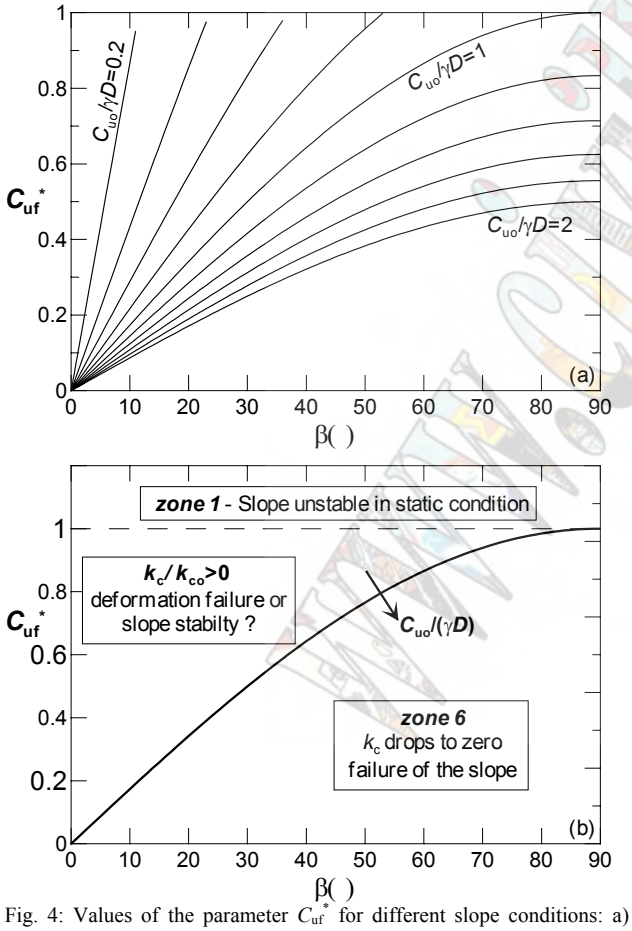

Fig. 4: Values of the parameter C_{uf}^{*} for different slope conditions: a) parametric analysis; b) scheme of the chart.

With the exclusion of these cases, points located above each curve correspond to values of the degradation index greater than C_{uf}^{*} then, the point represents slopes for which no failure occurs despite the strength degradation which worsen the slope stability condition; in this case permanent displacements may or not take place and the possible occurrence of a *deformation failure* should be evaluated. Points located below each curve (*zone 6*) represent conditions for which the earthquake-imposed degradation index is lesser than C_{uf}^{*}. In this case the slopes reaches a *failure* condition caused by the weakening or by a combined inertial-weakening effect.

Using the parameter C_{uf}^{*} is then possible to predict if during or after the seismic event the failure conditions is attained or not. However several aspects of the slope behavior are not entirely described by C_{uf}^{*}: i) if no failure occurs, does the slope remain stable or a deformation failure will occur? ii) in both cases what is the specific contribute of the inertial and of the weakening effect to the slope response? iii) if the slope response is characterized by the occurrence of permanent displacements does the traditional Newmark-type analysis describe the phenomenon? In order to answer to these questions another threshold value of the degradation index must be introduced.

Considering a design earthquake (i.e. a selected value of k_{max}) and a slope initially stable under seismic condition (k_{max}/k_{co}<1) it is useful to estimate the value of the earthquake-induced degradation index that produces a reduction of the slope critical acceleration k_c from its initial value k_{co} to k_{max}. This value of C_u^{*} is that required to convert a seismically stable slope in a unstable one (k_{max}/k_c>1) and can be evaluated from equations (7) and (4) imposing the condition $k_c(t)=k_{max}$:

$$C_{ud}^{*} = \frac{(\sin\beta + k_{max}\cos\beta^{*}) \cdot \gamma \cdot D}{C_{uo}} = \frac{1}{F_{do}} \quad (10)$$

The previous equation shows that C_{ud}^{*} is affected by the earthquake-induced state of stress; then, unlike C_{uf}^{*}, C_{ud}^{*} does not represent an intrinsic characteristic of the slope. Moreover, due to its relation with F_{do}, C_{ud}^{*} separates two different conditions: slope initially stable (F_{do}>1; C_{ud}^{*}<1) or unstable (F_{do}<1; C_{ud}^{*}>1) under seismic condition. Finally, since F_s>F_{do}, C_{ud}^{*} is always greater that C_{uf}^{*}.

Fig. 5a shows the value of C_{ud}^{*} for different slope conditions, values of k_{max} and ω=0. Each of the curves separates the diagram into zones with different meaning schematized in Fig. 5b. If the cyclic strength reduction imposed by the earthquake leads C_u^{*} to values lower than C_{ud}^{*} also an initially stable slope could experience permanent displacements due to the reduction of the critical acceleration. In the diagram, points located below each curve represent this condition. In this case, if no failure condition is reached (C_u^{*}>C_{uf}^{*}) a *deformation failure* may occur in two different ways. If the slope is initially stable (C_{ud}^{*}<1), the deformation failure must be ascribed only to the weakening effect (*weakening instability*) and could not occur in absence of the cyclic strength reduction; a modified Newmark-type analysis is required in this case in order to estimate the displacement response. Otherwise if the slope is initially unstable under

seismic condition (C_{ud}^*>1), permanent displacements will be driven by both the inertial effect and the cyclic strength reduction denoting an *inertial-weakening instability*; again a modified Newmark-type analysis is necessary in order to reliably estimate permanent displacements.

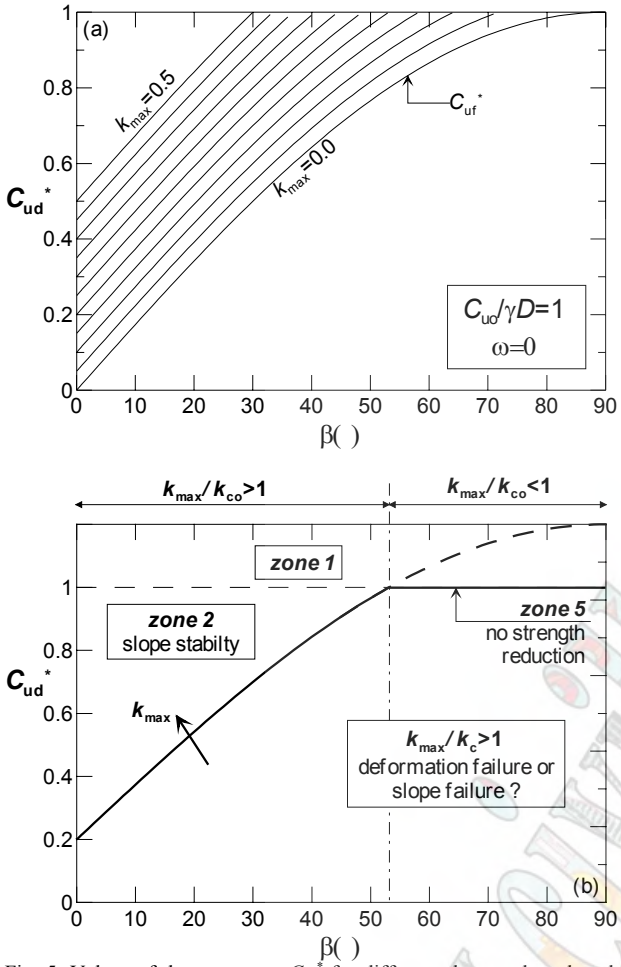

Fig. 5: Values of the parameter C_{ud}^* for different slope and earthquake conditions: a) parametric analysis; b) scheme of the chart

If no strength reduction occurs (C_u^*=1) the slope behavior is affected only by the inertial effect. In this case, if the slope is initially stable (C_{ud}^*<1) no permanent displacements occur and the slope remains stable; if the slope is initially unstable (C_{ud}^*>1) the slope response is characterized by the occurrence of a *deformation failure* consisting in an *inertial instability*. This latter case requires a traditional Newmark-type analysis for the displacement analysis and is represented in the diagram by points located in the segment denoted as *zone 5*.

Finally, if the earthquake-induced degradation index is greater than C_{ud}^*, the slope critical acceleration remains greater than k_{max}; then the slope does not experience permanent displacements despite the cyclic strength reduction. In Fig. 5, points located above each of the plotted curves (*zone 2*) represent this stability condition.

The combined use of C_{uf}^* and C_{ud}^* and the comparison with the earthquake-induced value of C_u^* allows to detect the possible slope behavior and, if required, the proper approach for the displacement analysis. Then, a procedure for the seismic stability analysis of cohesive slopes can be developed using the threshold values of the degradation index introduced herein.

Knowing the slope characteristics (β, γ, C_{uo}, D) and assuming a value for ω, the evaluation of C_{uf}^* and C_{ud}^* can be performed using equations (9) and (10). For a design earthquake, one or more acceleration time-histories must be selected and C_u^* can be evaluated starting from the degradation parameter t and counting the earthquake-imposed cycles assuming that they are similar in shape to the acceleration time-histories [9]; alternatively experimental results can be adopted in order to estimate a reliable value of C_u^*.

Starting from the knowledge of these parameters, the slope behavior can be detected comparing C_{uf}^*, C_{ud}^* and C_u^*. To this purposes equations (9) and (10) can be plotted together for different slope and earthquake conditions. As an example C_{uf}^* and C_{ud}^* were superimposed in Fig. 5a for different values of slope angle and for the case $C_{uo}/(\gamma D)$=1 and ω=0. The obtained diagram can be assumed as a seismic stability chart whose meaning is described in the scheme of Fig. 6. For a given slope and earthquake, excluding slopes of the *zone 1*, one of the following conditions may occur.

For slope initially stable under seismic condition (C_{ud}^*<1) if C_{ud}^*<C_u^* (*zone 2*) the slope remains stable during the earthquake shaking; as shown in Fig. 4a the extension of this unconditioned stability zone decreases with increasing k_{max}. If C_{ud}^*>C_u^*>C_{uf}^* (*zone 3*) a *weakening instability* may occur and a modified Newmark-type analysis must be performed in order to evaluate the occurrence of permanent displacements.

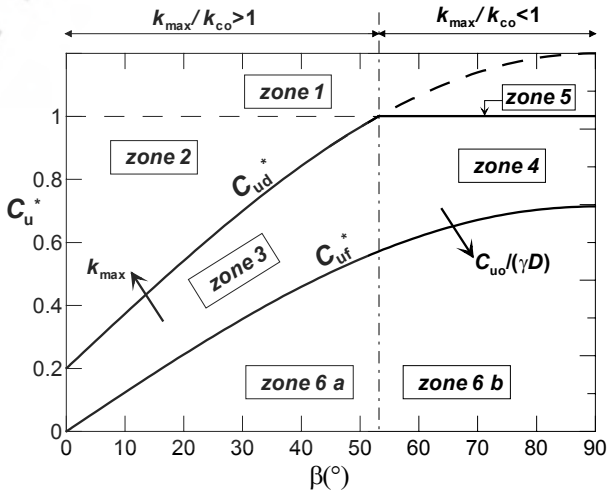

Fig. 6: Scheme of the proposed charts for seismic stability analysis of cohesive slopes.

For slope initially unstable under seismic condition (C_{ud}^*>1) if C_{ud}^*>C_u^*>C_{uf}^* (*zone 4*) an *inertial-weakening instability* may occur and again a modified Newmark-type analysis must be applied; if no strength reduction takes place in the soil (C_u^*=1) no weakening effect occurs and permanent displacements are triggered by the inertial

effect (*inertial instability*) and can be evaluated using the traditional Newmark-type analysis (*zone 5*).

Finally, for slopes either stable or unstable under seismic condition, if $C_u^* < C_{uf}^*$ a *failure* occurs (*zone 6*) with consequences that can not be predicted with a traditional approach that neglects the cyclic strength reduction; as shown in Fig. 5a, *zone 6* enlarges with decreasing of $C_{uo}/(\gamma \cdot D)$. In the case $C_{ud}^* < 1$ the failure must be ascribed only to the weakening effect (*zone 6a*); if $C_{ud}^* > 1$ the failure is a consequence of both inertial and weakening effect (*zone 6b*).

CONCLUDING REMARKS

The analysis presented in the paper describes a method for the assessment of seismic stability condition of cohesive slopes based on a modified Newmark-type analysis. The procedure was developed to introduce the effects of the cyclic strength degradation due to the dynamic behavior of cohesive soils. The strength degradation was accounted for by means of a simple relationship based on experimental evidence and using a degradation parameter. Two threshold values of the degradation index were introduced in order to describe the potential slope behavior in relation to the slope geometry, the soil characteristics and the earthquake-induced loading. The proposed model provides a useful and practical tool to evaluate the seismic and post-seismic stability condition of the slope and the proper approach for the assessment of earthquake-induced permanent displacements taking into account the shear strength degradation. Finally, the proposed approach defines the field of validity of the traditional Newmark-type analysis and provides an extension for the general case of both inertial and weakening instabilities.

REFERENCES

[1] Kobayashi Y., "Causes of fatalities in recent earthquake in Japan", *J. of Disaster Science*, 1981, Vol. 3, pp. 15-22.

[2] Ishihara K., "Geotechnical aspects of the 1995 Kobe earthquake", *Proc. 14th Int. Conf. SMFE*, Hamburg, 1997.

[3] Ishihara K., Erken A., Hiroyoshi K., "Geotechnical aspects of the ground damage induced by the fault", *Proc. of 3rd Japan-Turkey Workshop on Earthquake Engineering*, vol.1.

[4] Jibson R.W., "Predicting earthquake-induced landslide displacement using Newmark's sliding block analysis. *Transportation Research Record*, 1993, No. 1411, TRB, Washington, D.C., pp. 9-17.

[5] Mankelow J.M., Murphy W., "Using GIS in the probabilistic assessment of Earthquake triggered landslide hazards", *Journal of Earthquake Engineering*, 1998, Vol. 2.

[6] Biondi G., Condorelli A., Mussumeci G., Maugeri M., "Earthquake-triggered landslides hazard in the Catania area", *Proc. 4th Int. Conf. on Computer Simulation in Risk analysis and Hazard Mitigation*, Rhodes, Greece, 2004.

[7] Terzaghi K., "Mechanism of landslides", The geological survey of America", *Engineering Geology*, Berkeley, 1950.

[8] Newmark, N.M., "Effects of earthquakes on dams and embankments", *Geotechnique*, 1965, vol. 15, pp. 139-160.

[9] Biondi G., Cascone E., Maugeri M., "Flow and deformation failure of sandy slopes". *Soil Dynamics and Earthquake Engineering*, 22 (2002), pp. 1014-10.

[10] Prater, G., "Yield acceleration for seismic slopes", *Journal of Geotechnical Engineering*, ASCE, 1979, 105(5).

[11] Sarma S.K., "Seismic displacement analysis of earth dams", *Journal of Geotechnical Engineering*, ASCE, 1981,107 (GT12).

[12] Chang, C.J., Chen, W.F., Yao, J.T.P., "Seismic displacements in slopes", *Journal of Geotechnical Engineering*, ASCE, 1984, vol. 110 (7), pp. 860-874.

[13] Hadj-Hamou T. & Kavazanjian E. Jr., "Seismic stability of gentle infinite slopes", *Journal of Geotechnical Engineering*, ASCE, 1985, Vol. 111 (6), pp. 681-697.

[14] Conte E., Dente G., "Deformazioni permanenti indotte da carichi sismici nei pendii sabbiosi in falda", *A.G.I., XVI Convegno Nazionale di Geotecnica*, 1986 (in Italian).

[15] Dobry R., Baziar M.H., "Modelling of lateral spreads in silty sands by sliding soil blocks". Stability and performance of slopes and embankments", *ASCE, Geotechnical Special Publication*, 1992, (31), pp. 625-652.

[16] Biondi G., Cascone E., Maugeri M., Motta E., "Seismic response of saturated cohesionless slopes". *Soil Dynamics and Earthquake Engineering*, 20 (2000), pp. 209-215.

[17] Sarma K.S., "Seismic stability of earth dams and embankments", *Geotechnique*, 1975, 25(4), pp.743-761.

[18] Tika-Vassilikos T.E., Sarma S.K., Ambraseys N. "Seismic displacements on shear surfaces in cohesive soils", *Earthquake Engineering and Structural Dynamics*, 1993, vol. 22, pp. 709-721.

[19] Lemos L.J.L., Gama A.M.P., Coelho P.A.L.F., "Displacements of cohesive slopes induced by earthquake loading". *Proc. 13th Int. Conf. on Soil Mechanics and Foundation Engineering*, New Delhi, 1994, pp.1041-1045.

[20] Crespellani T., Ghinelli A., Madiai C., Vannucchi G. "Analisi di stabilità dei pendii naturali in condizioni sismiche", *Rivista Italiana di Geotecnica*, 1990, XXIV (2).

[21] Crespellani T., Madiai C., Vannucchi G. "A Procedure for the seismic and post-seismic analysis of natural slopes". *Proc. 13th Int. Conf. on Soil Mechanics and Foundation Engineering*, New Delhi, 1994.

[22] Cascone E., Maugeri M., Motta E., "Seismic response of clay slopes. *Proc. 11th European Conf. on Earthquake Engineering*, Paris, 1998.

[23] Idriss I.M., Dobry R., Singh A.M. "Nonlinear behavior of soft clays during cyclic loading", *Journal of Geotechnical Engineering, ASCE*, 1978, 104(12), pp. 1427-1447.

[24] Vucetic M., "Soil properties and seismic response", *Proc. 10th World Conf. on Earthquake Engineering.*, 1992, 3.

[25] Vucetic M., "Cyclic threshold shear strain in soils", *Journal of Geotechnical Engineering, ASCE,* 1994, vol. 120 (12), pp. 2208-2228.

[26] Lo Presti D.C.F., Pallara O., Cavallaro A., Maugeri M., "Non linear stress-strain modelling of geomaterials under stable and unstable cyclci loading", *Proc. 2nd Int. Conf. on Earthquake Engineering*, 1999, Lisboa, Vol.1, pp. 29-34.

[27] Vucetic M., "Normalized behavior of clay under irregular cyclic loading", *Canadian Geotech. Journal*, 1990, 27(1).

[28] Matasovic N., "Seismic response of composite soil deposits", Ph.D. Dissertation, University of California, Los Angeles, California, 1993.

[29] Matasovic N., Vucetic M., "Generalized cyclic-degradation-pore pressure generation model for clays", *Journal of Geotechnical Engineering, ASCE,* 1995, 121, No.1, pp. 33-42.

An Approach to Compute the Permanent Seismic Displacement of Embankments considering Vertical Seismic Motion and Heterogeneity of the Ground Strength

Yoshiya HATA[1], Norihiko YAMASHITA[2]
[1]*R&D Center, Nippon Koei Co., Ltd., Tsukuba, Ibaraki, Japan*
[2]*Kobe City College of Technology, Kobe, Hyogo, Japan*

Abstract

Since the UD component of the Hyogoken-nanbu (1995) and Niigataken-chuetsu (2004) earthquakes in Japan was very powerful, it could be important in estimating the influence of structural damage on the investigated system by vertical seismic motion. However, the effects aren't taken sufficiently into account in the aseismic standard code of embankments. Moreover for the very reason that soils are heterogeneous in nature, we must take into consideration the heterogeneity of the ground in the seismic design of embankments; nevertheless this is not done for the current seismic design of earth structures. So, in this study, the destruction of embankments was evaluated by computing the permanent seismic displacement of embankments, and we proposed the modified Newmark method with consideration of vertical seismic motion and the heterogeneity of the ground strength.

Keywords—*Embankment, Modified Newmark method, Vertical seismic motion, Heterogeneity of ground strength*

INTRODUCTION

The damage to civil structures by caused the *Hyogoken-nanbu* earthquake (1995) in Japan triggered major change to current Japanese earthquake resistant design systems. However, it is realistically difficult to design earth structures, such as embankments, capable of sustaining no damage when subject to Level 2 seismic motion, this also proved to be uneconomical. Therefore, as for creating a design which takes into consideration the occurrence of damage within a permissible range, it is reasonable to acknowledge the need for quantitative evaluation of the damage. The amount of deformation in the slope collapse represents the index of quantitative evaluation, and the Newmark method [1] is one of the recognized evaluation methods applied for the embankment. There is no seismic response acceleration of the embankment but the ground acceleration that shows seismic force on the slide clod with the usual Newmark method. However, the embankment itself seismic response properties weren't taken into consideration by this perspective, so the modified Newmark method, with the seismic response character added by modeling the embankment with the SDOF model is proposed by *Kramer et al* [2] [3].

Significant vertical seismic motion has been shown to be one of the characteristics of the *Hyogoken-nanbu* (1995) and *Niigataken-chuetsu* (2004) earthquakes [4]. The UD component exceeding 1G was particularly observed in the *Takezawa*, *Yamakoshi* villages (JMA) by the *Niigataken-chuetsu* earthquake, while an enormous ground disaster hit the *Yamakoshi* village. So, it could be important to estimate the influence of the structural damage on systems by vertical seismic motion. However, the effect doesn't take sufficient account of the data of the aseismic standard code of embankments. And as for the study on the effects caused by a vertical seismic wave on the system, leading to the destruction of embankments, this is currently an area requiring further study.

Moreover, soils are heterogeneous in nature. However, at present, the design of the embankment has been implemented assuming the ground strength to be homogeneous. When an embankment is constructed, it is almost unacceptable to make the ground strength homogeneous, and this supposition is only allowed in an effort to facilitate calculations. So far, studies on the effect which the heterogeneity of ground strength has on the destruction of the embankments have been done common [5]. However, there are too few studies showing that the effect was adopted in the modified Newmark method [6].

Relying on the above background, for this study, the destruction of embankments was evaluated by the permanent seismic displacement of embankments, and we proposed the modified Newmark method in consideration of the vertical seismic motion and the heterogeneity of the ground strength.

PROPOSED ANALYTIC METHOD

Modeling the embankment

Fig. 1 shows the proposed analytic flow and Fig. 2 the computational concept of seismic sliding displacements used in this study. To begin with, the data that composed the embankment, such as the height of embankment H, breadth of crest B, gradient of embankment, unit of weight γ, cohesion c, angle of internal friction ϕ and shear wave velocity V_s were input.

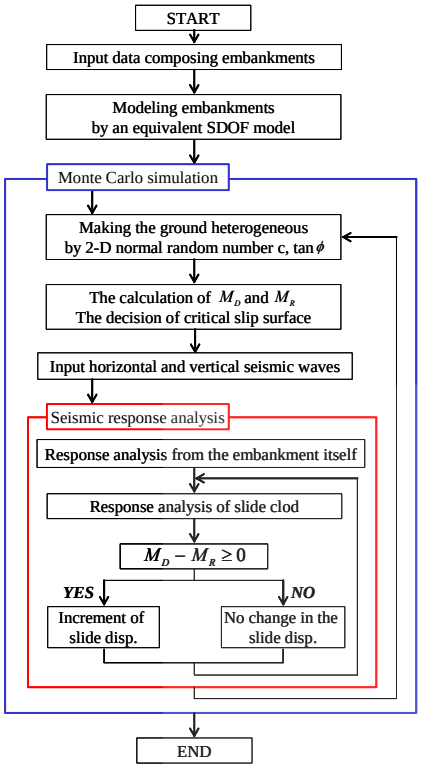

Figure 1: Analytic flow adopting this study

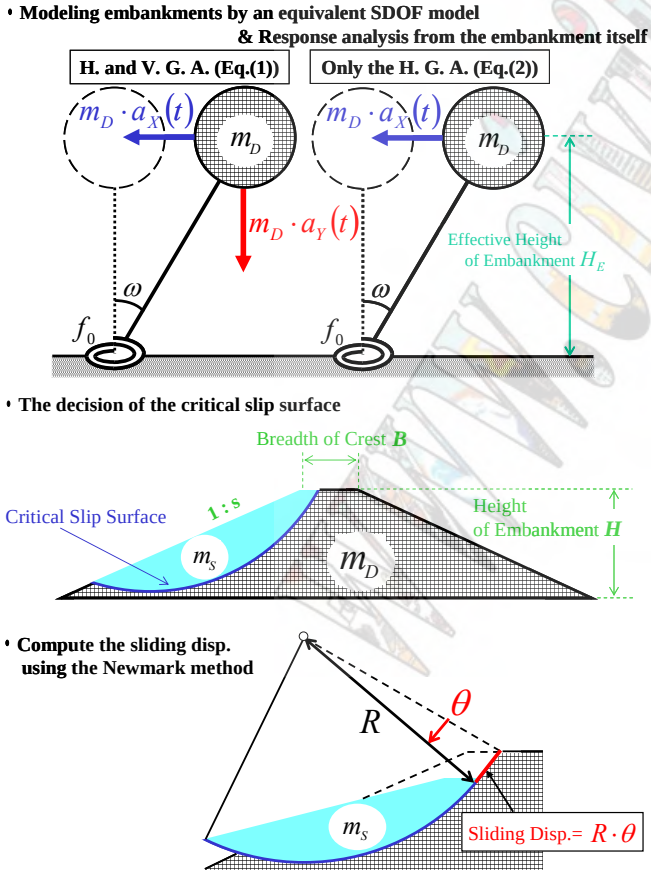

Figure 2: Concept of seismic sliding displacement

Next, an embankment was modeled with an equivalent SDOF model so that not only the horizontal but also the vertical seismic wave could be taken into consideration (Fig. 2) [7]. From the moment of equilibrium of the rocking axis in Fig. 2, an equation of motion of the equivalent SDOF model that takes account of the vertical seismic motion can be expressed with the following equation (1). Minute deformation was presumed in this study, and geometrical approximation ($\cos\omega$=1, $\sin\omega$= ω) was carried out in equation (1).

$$\ddot{\omega} + 4\pi\xi f_0\dot{\omega} + 4\pi^2 f_0{}^2\omega = -\frac{\ddot{X}}{H_E} + \frac{\ddot{Y}}{H_E}\omega \qquad (1)$$

Where, ω is the angle of seismic response rotation, $\ddot{X}$ is the horizontal ground acceleration, $\ddot{Y}$ is the vertical ground acceleration, g is the gravity acceleration (=980gal), ξ is the damping coefficient (=5%), f_o is the natural frequency of the embankment and H_E is the effective height of the embankment. In the case without consideration of vertical seismic wave, the motion equation of the equivalent SDOF model derives from equation (1) as follows.

$$\ddot{\omega} + 4\pi\xi f_0\dot{\omega} + 4\pi^2 f_0{}^2\omega = -\frac{\ddot{X}}{H_E} \qquad (2)$$

In addition, an equation (3) of horizontal motion of the usual shearing SDOF model can be substituted for the equation (2). In other words, there was the equivalent relation between equations (2) and (3).

$$\ddot{x} + 4\pi\xi f_0\dot{x} + 4\pi^2 f_0{}^2 x = -\ddot{X} \qquad (3)$$

Where, x is the horizontal displacement of the embankment. The absolute response acceleration of the horizontal and vertical directions of the equivalent SDOF model of the embankment $a_X(t)$, $a_Y(t)$ were expressed as follows.

$$a_X(t) = \ddot{X} + H_E\ddot{\omega} \qquad (4)$$

$$a_Y(t) = \ddot{Y} - H_E(\dot{\omega})^2 \qquad (5)$$

The natural frequency of embankment f_o was estimated by using the following formula that was proposed by *Nakamura et al* [8].

$$f_0 = 0.28\cdot(B/H)^{0.84}\cdot B^{-0.97}\cdot V_S \qquad (6)$$

Fig. 3 shows the computational concept of the effective height of the embankment. In this study, as it investigated an embankment modeled with the equivalent SDOF model, the effective height of the embankment was calculated using the inertia moment of the embankment I as follows.

$$H_E = \frac{I}{\sum_{j=1}^{n}(m_{Dj}\cdot H_j)} \qquad (7)$$

Hence, the relation of $H_E < H$ is concluded in the equation (7) geometrically.

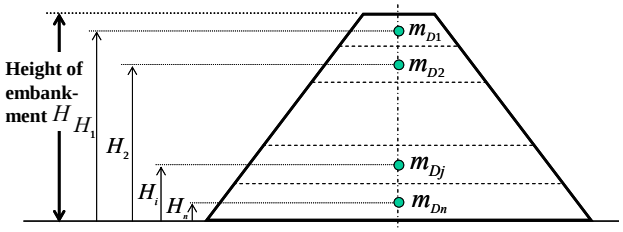

Figure 3: Computation of the effective height of embankments

Reliability analysis of embankments

In this study, a method involving the Monte Carlo simulation [9] was adopted concerning the effect which the heterogeneity of the ground strength had on the embankment during an earthquake. Then, the constant of ground strength (c and $\tan\phi$) which has the most significant influence on the slope stability of the embankment wasn't made uniform, and the analysis was carried out. According to some studies, it is known that the dispersion of c and $\tan\phi$ can be approximated in normal distribution. The random number which followed the 2-dimensional probability density of the ground strength (c and $\tan\phi$) was made to intervene by using the variation and correlation coefficient of the ground strength, and the heterogeneous embankment ground model (Fig. 4) was made by assigning this to all slices in the slope embankment.

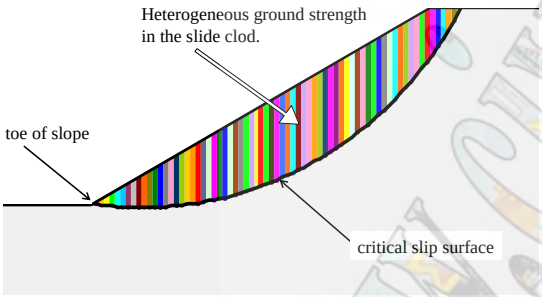

Figure 4: Image of heterogeneous ground embankment model

Here, because the relationship between c and $\tan\phi$ has a negative correlation in the equation calculating the safety factor using the slope stability of the embankment, the relation of ground strength was expressed by using a 2-dimensional normal random number of c and $\tan\phi$ [10]. The 2-dimensional normal random number which has c and $\tan\phi$ to probability variable follows the simultaneous normal probability density expressed with an equation (8).

$$f_{c|\tan\phi} = \frac{1}{\sqrt{2\pi}\sigma_c\sqrt{1-\gamma^2}} \exp\left[-\frac{1}{2}\left\{\frac{c-\mu_c-\gamma(\sigma_c/\sigma_{\tan\phi})(\tan\phi-\mu_{\tan\phi})}{\sigma_c\sqrt{1-\gamma^2}}\right\}^2\right] \quad (8)$$

Where, σ_c, $\sigma_{\tan\phi}$ are the standard deviation of c and $\tan\phi$, μ_c, $\mu_{\tan\phi}$ are the mean values of c and $\tan\phi$ and γ is the correlation coefficient. In this analysis, the degree of heterogeneity of the embankment ground is expressed not by using the standard deviation but the variation coefficient, and those relations became as follows [11]:

$$V_i = \frac{\sigma_i}{\mu_i} \quad (i = c, \tan\phi) \quad (9)$$

Decision of the critical slip surface

In this study, the decision of the critical slip surface was carried out using the method proposed by *Tateyama et al* [12]. This method improved the presently designed equation so that it could take the effect of the vertical seismic wave into consideration. The computational equation of the sliding safety factor during an earthquake was shown in equation (10).

$$F_s = \left[\frac{\sum c\cdot l + W(1-k_V(t)\cos\beta - k_H(t)\sin\beta)\tan\phi}{\sum W\{(1-k_V(t))\sin\beta + k_H(t)\cdot(h/R)\}}\right]_{MIN} \quad (10)$$

Where, as Fig. 5 shows, R is the radius of the sliding circle, l the width of each slice, W the weight of each slice, β the angle with the straight line from the center of the sliding circle to the center of gravity of the each slice and the vertical line and h the vertical distance from the center of gravity of each slice to the center of the sliding circle. c, ϕ are the ground strengths of each slice of the heterogeneous embankment ground model, mentioned in the preceding section. In addition, the horizontal and vertical seismic intensity $k_H(t)$, $k_V(t)$ can be shown respectively like the equation (11)-(13).

$$k_H(t) = K(t)\cdot\sin\delta(t) \quad (t = 0 \to T) \quad (11)$$

$$k_V(t) = K(t)\cdot\cos\delta(t) \quad (t = 0 \to T) \quad (12)$$

$$K(t) = \frac{1}{g}\sqrt{a_X(t)^2 + a_Y(t)^2} \quad (13)$$

Where, $K(t)$ is the composition seismic intensity, $\delta(t)$ is the affection direction of $K(t)$and T is the length of time of the seismic response of the embankment. In addition, $a_X(t)$, $a_Y(t)$ are response accelerations that can be computed from equations (4), (5).

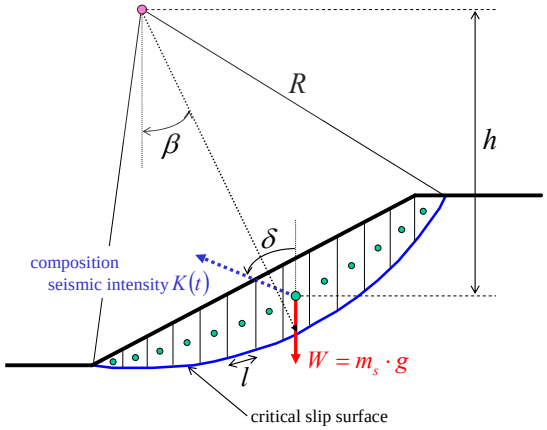

Figure 5: Concept of the decision of the critical slip surface

Computation of the sliding disp.

The reasoning leads to the following equation (14) from the equilibrium of the driving and resisting moment M_D, M_R shown in Fig. 6 [13] [14].

$$R_{cg}{}^2 m_s \ddot{\theta} = M_D - M_R \tag{14}$$

Where, R_{cg} is the distance from the center of the sliding circle to the center of gravity of the slide clod, m_s the mass in the part of the slide clod, and $\ddot{\theta}$ the angle acceleration of the slide clod. The Sliding displacement of embankment occurs when the absolute driving moment $|M_D|$ is beyond the absolute resisting moment $|M_R|$.

$$|M_D| \le |M_R| \Rightarrow \ddot{\theta} = 0 \tag{15}$$

In this study, the process was divided into the portions of the slide clod and the embankment itself which doesn't slide, and not only the horizontal seismic wave but also the vertical seismic motion modeled in the embankment itself for the SDOF analysis model could be taken into consideration. In other words, the interaction has no effect between the embankment itself and the slide clod. At the very start, the absolute response acceleration in horizontal and vertical directions against the input seismic ground motion of the SDOF model, which has the natural frequency of the embankment, were calculated (Eq. (4), (5)); next, these accelerations were input in to the equation (14) based on which the part of the slide clod was modeled; finally, the sliding angle acceleration of the embankment $\ddot{\theta}$ was calculated. Then, the sliding angle θ of the embankment was calculated by carrying out the numerical integral calculus by the Newmark- β method [15].

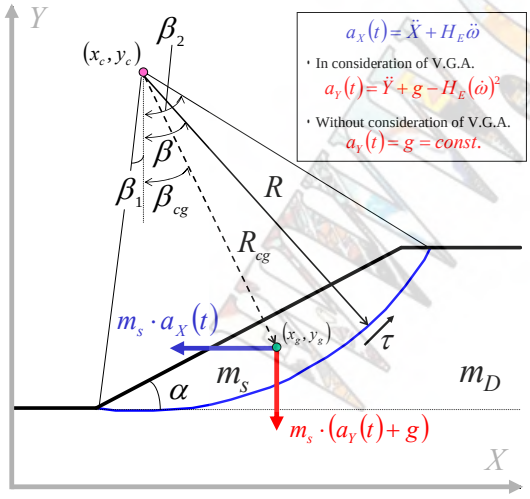

Figure 6: Concept of the equilibrium of the moment

EXAMPLE OF NUMERICAL ANALYSIS

Numerical analysis model

Table 1 shows the parameter of numerical analysis model adopted by this study. *Okamoto* [16] reported that the natural frequency of the embankment in a cross direction constituted a range from 2.0Hz to 4.3Hz. Therefore, first of all 3.15Hz was adopted as the natural frequency of the analytic embankment model by this study. The height of the embankment was calculated conversely using the equation (6) as Vs=100m/sec and B=8m; the effective height of the embankment was computed using the equation (7). The gradient of the slope, the unit of weight γ and the mean of cohesion c and the angle of internal friction ϕ were adopted as constants. As for the damping constant ξ in the equation (2), (3), it was set at 5%, referring to the study of *Razaghi* [17]. Because a stable distribution of the permanent seismic displacement of the embankment was obtainable, the repetition number of the Monte Carlo simulation was set at 1000 times. In this study, the coefficient of variation, assuming the ground strength was homogeneous, dealt with the case of 0.0 as a basic case. The coefficient of variation that expressed the degree of heterogeneity of the ground was $V_c = 0.3$, $V_\phi = 0.1$ considering the nugget effect [18] [19]. A coefficient of correlation was made $\gamma = -0.5$ [10].

Table 1: Parameter of the analytic model

Breadth of crest B (m)	8
Height of embankment H (m)	15.829
Ratio of B/H (-)	0.505
Gradient of embankment (-)	1∶1.8
Unit of weight γ_t (kN/m^3)	18
The mean value of cohesion c (kPa)	30
The mean value of angle of internal friction ϕ (deg)	30
Shear wave velosity V_s (m/sec)	150
Effective height of embankment H_E (m)	5.855
Damping Coefficient ξ (%)	5.0
Natural frequency of embankment f_0 (Hz)	3.15

Input ground motion

Figure 7 shows the time history acceleration of the input ground motion adopted in this study. According to this figure, vertical seismic wave in Bam and *Yamakoshi-village* provided a very strong motion close to 1G. As for the input horizontal wave, all the results are the absolute maximum acceleration of about 800 gal. When it pays attention for the duration of time of the seismic wave, *Hiroo* has the longest time in the both horizontal and vertical waves. Figure 8(a) shows the response spectrum of the input horizontal ground motion indicated on the left side of Fig. 7. According to this figure, the absolute horizontal response accelerations in *Kobe JMA* and *Hiroo* were about 2000 gal in the neighborhood of the natural period of the embankment model adopting in this study. Figure 8(b) shows the response spectrum of vertical acceleration indicated on the right side of Fig. 7. From this figure, the absolute vertical response acceleration in *Yamakoshi-village* was about 2000 gal and was extremely strong in comparison with others within the natural frequency of the embankment model.

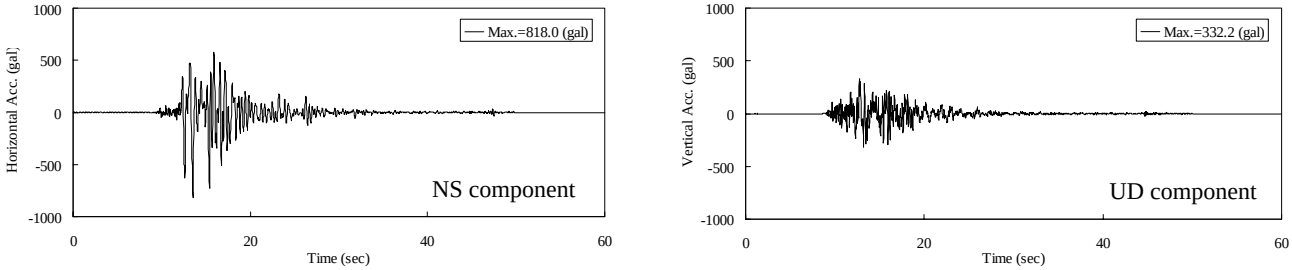

(a) Kobe JMA（Hyogoken-nanbu earthquake (1995)）

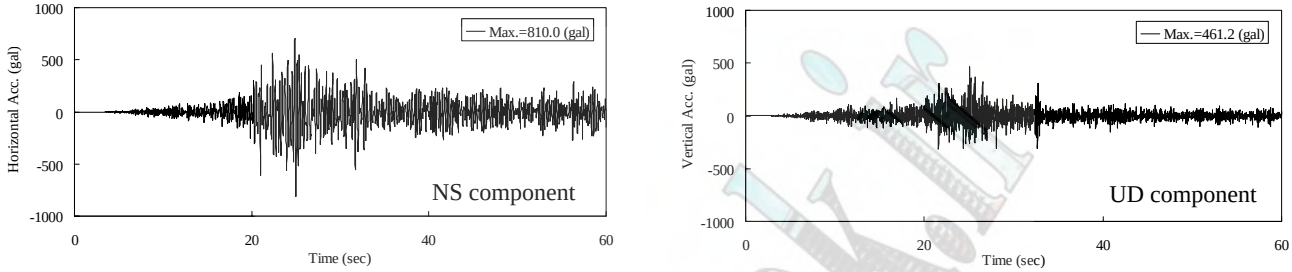

(b) Hiroo（Tokachi-oki earthquake (2003)）

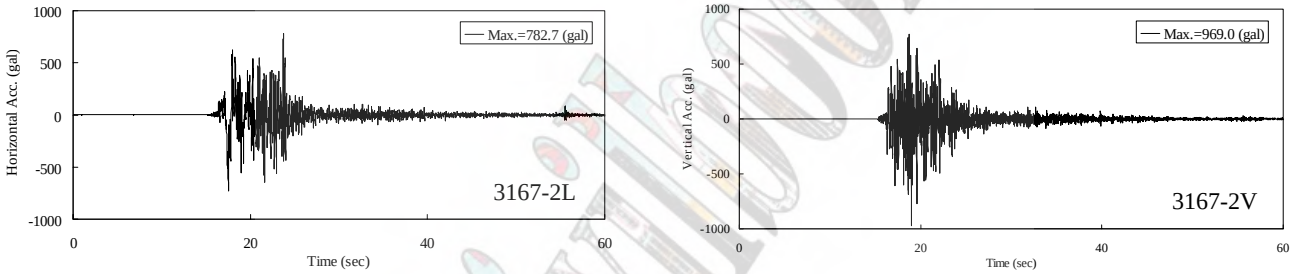

(c) Bam（Bam earthquake(IRAN) (2003)）

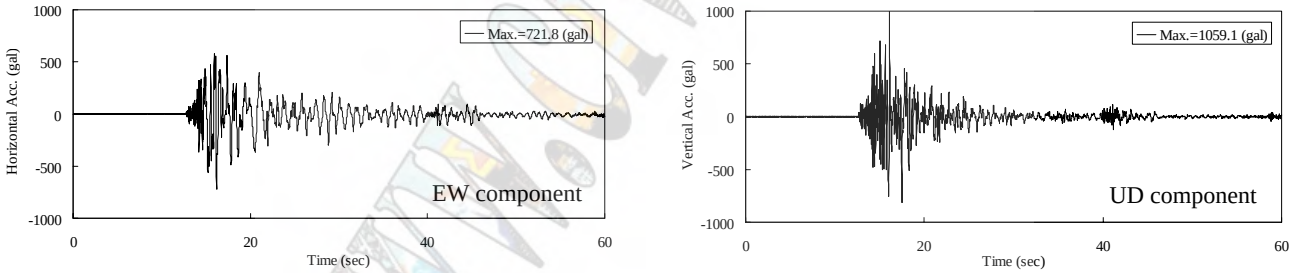

(d) Yamakoshi（Niigataken-chuetsu earthquake (2004)）

Figure 7: Time history of the input ground motion

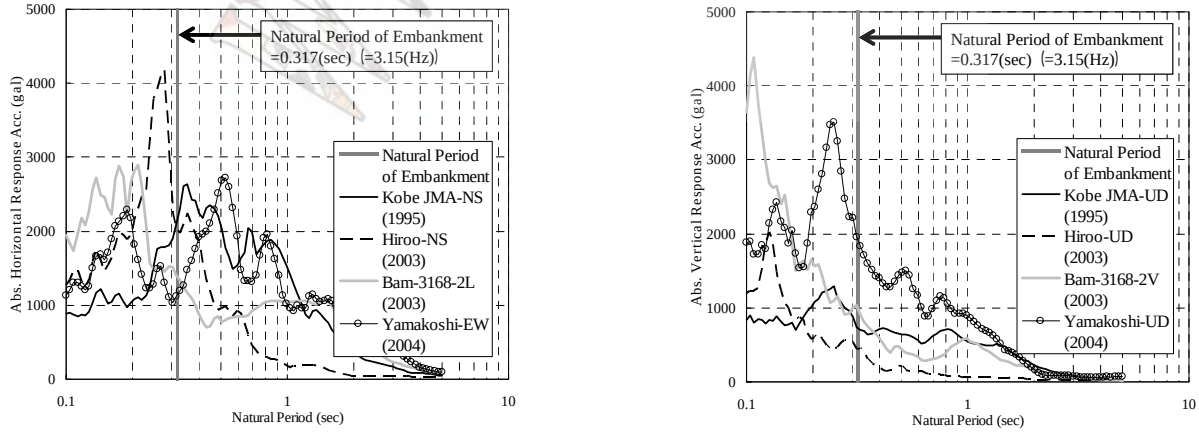

(a) Horizontal response

(b) Vertical response

Figure 8: Response spectrum against the input ground motion

Time history of the sliding displacement

Fig. 9 shows the time history of the sliding displacement of the embankment model adopted in this study. According to Fig. 9(a), the sliding displacement increases by taking the vertical seismic wave into consideration. It can be seen from Fig. 9(c) that the difference in the seismic permanent displacement of embankments peaks within the case in consideration of vertical seismic motion and the heterogeneity of the ground strength. In this study, the ratio of permanent displacement of the standard deviation to mean displacement is defined as the "*extra coefficient*", and discussed in the following.

DISCUSSION

Okimura et al. proposed the seismic intensity of the acceleration response *SI'* as the easy index of the evaluated permanent seismic displacement of the embankments [20] [21]. The equation for computing the *SI'* was shown as an equation (16) using the acceleration response spectrum S_A of the damping coefficient ξ=5%.

$$SI' = \frac{f_0}{\beta - \alpha} \int_{T_U}^{T_D} S_A(T, \xi = 0.05) dT \qquad (16)$$

Where, f_0 is the natural frequency of the embankment model, which can be computed using the equation (6). And, T_U and T_D are the upper and lower periods in the integral calculus section as follows.

$$T_U = \beta / f_0 \qquad (17)$$

$$T_D = \alpha / f_0 \qquad (18)$$

Where, α =0.4 and β =1.5 are provided from equation (16) to equation (18) [21].

In this study, we are discussing the effects of vertical seismic motion and the heterogeneity of ground strength on the permanent seismic displacement of embankments using the *SI'* as follows. Fig. 10(a) shows the relationship between the *SI'V/SI'H* and the *extra coefficient* of the permanent displacement of the embankments which depends on whether the vertical ground acceleration is taken into consideration or not. Where, *SI'V* and *SI'H* are the *SI'* against input horizontal or vertical motion. From this figure, the extra ratio of the permanent displacement increases as the *SI'V/SI'H* becomes higher. And, the *extra coefficient* correlates closely with *SI'V/SI'H*. In other words, this result indicated that *SI'V/SI'H* is useful as an index of extra sliding displacement of the embankment, from which the vertical seismic wave originates. Fig. 10(b) shows the relationship between the *SI'H* and the extra ratio of the permanent displacement of the embankments, which depends on whether the heterogeneity of ground strength is taken into consideration. According to this figure, the *extra coefficient* of the permanent displacement becomes smaller as the *SI'H* becomes higher. Moreover, the *extra coefficient* correlates closely with *SI'H*. Therefore, this result suggested that *SI'H* is very useful as an index of the extra displacement, from which the heterogeneity of the ground strength originates. Fig. 10(c) shows the relationship between the *SI'V+SI'H* and the extended ratio of the permanent displacement of the embankments which depends on whether not only the vertical ground acceleration but also the heterogeneity of ground strength is taken into consideration. From this figure, the *extra coefficient* becomes higher as the *SI'V+SI'H* becomes higher. In addition, the *extra coefficient* correlates closely with *SI'V+SI'H*. In other words, it is necessary to take the extra of the sliding displacement of the embankments from which the vertical seismic wave and the heterogeneity of ground strength originate into account for the seismic design of the embankments in the case where the predominant frequency of the horizontal and vertical seismic waves is near that of the natural frequency of the embankments.

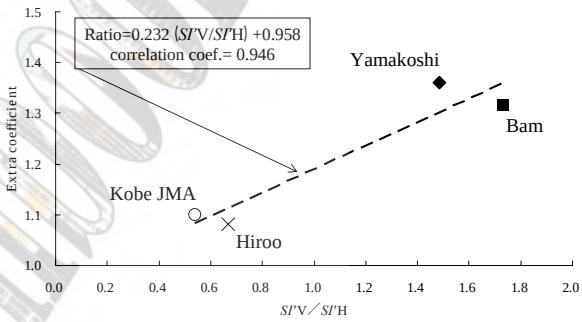

(a) In consideration of vertical seismic motion

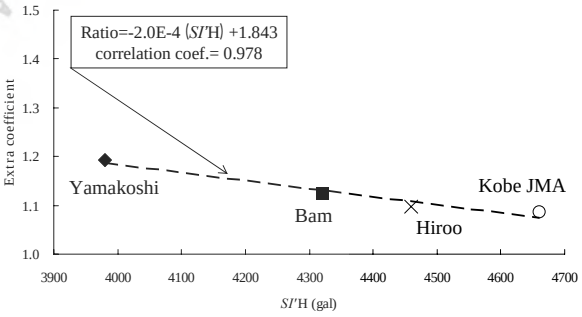

(b) In consideration of the heterogeneity of ground strength

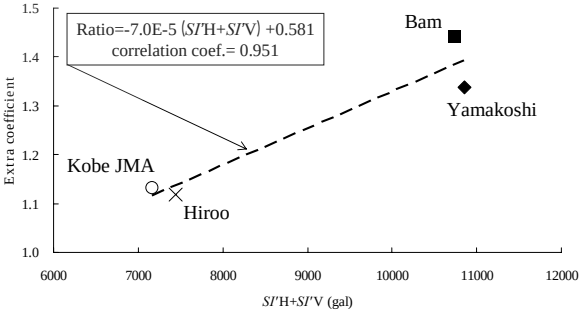

(c) In consideration of vertical seismic motion and the heterogeneity of ground strength

Figure 10: Relationship between *extra coefficient* and *SI'*

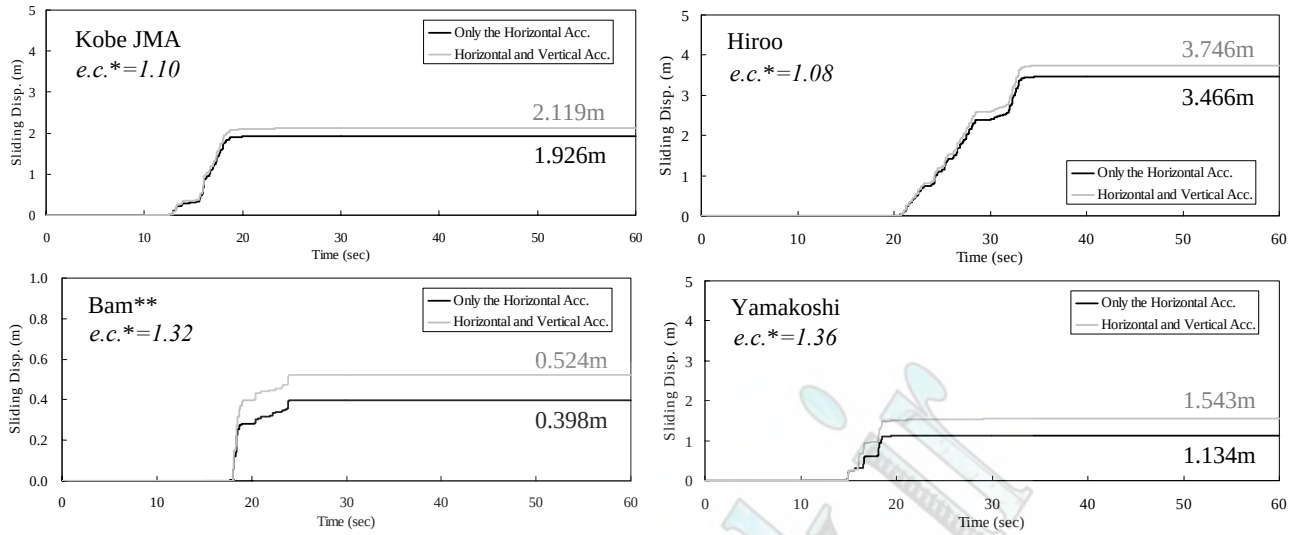

(a) In consideration of vertical seismic motion

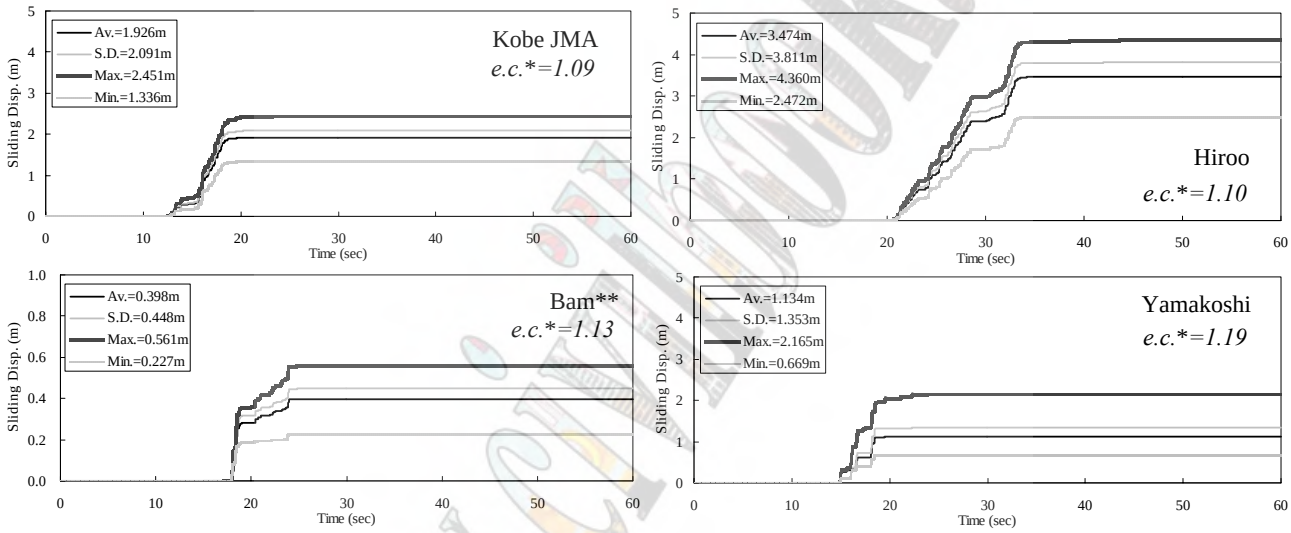

(b) In consideration of the heterogeneity of ground strength

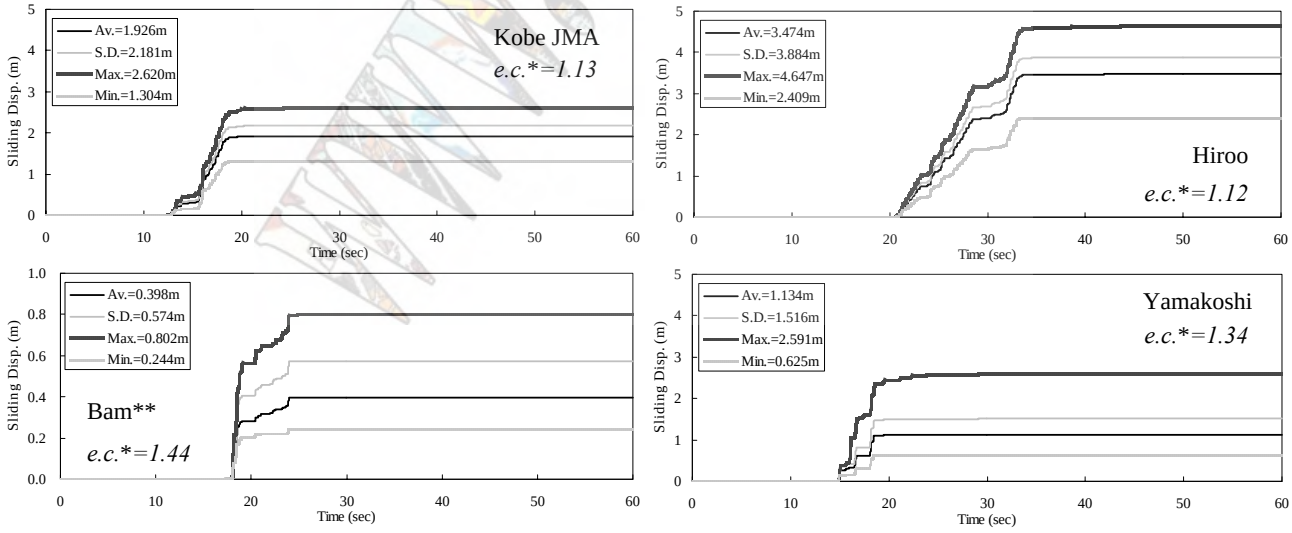

(c) In consideration of vertical seismic motion and the heterogeneity of ground strength

Figure 9: Time history of the sliding displacement

* *e.c. = extra coefficient* (Defined in *Time history of the sliding displacement* section which been ex-page)

** Note the scale of the displacement (lengthwise) axis in the case of the Bam earthquake.

CONCLUSIONS

The vertical seismic motion and the heterogeneity of ground strength have not been taken into consideration in the current seismic design of earth structures. So, in this study, the destruction of embankments was evaluated by the permanent seismic displacement of embankments, and we proposed the use of the modified Newmark method in relation to vertical seismic motion; supposing the heterogeneity of the ground strength. This paper shows the permanent seismic displacement of embankments taking into consideration the vertical seismic motion and the heterogeneity of the ground strength which correlate closely with the seismic intensity of the acceleration response *SI'*; proposed by *Okimura et al*. In addition, in this case, *SI'* is useful as an index of the extra sliding displacement of the embankment from which the vertical seismic wave and the heterogeneity of ground strength are generated. Therefore it is necessary to take the extension of the sliding displacement of the embankments in the aim, to originate the analysis in the vertical seismic wave and the heterogeneity of ground strength into account for seismic design where the predominant frequency of horizontal and vertical seismic wave is near the natural frequency of the embankments. From now on, we consider carrying out a more detailed examination of this kind of problems during our future realization of parametric studies.

ACKNOWLEDGMENTS

For allowing me to use earthquake wave data, the Japan Meteorological Agency (JMA), *Kyoshin* net (K-net) of the National research Institute for Earth science and Disaster prevention (NIED in JAPAN) and Building and Housing Research Center (BHRC in IRAN). I would like to extend my appreciation to all those concerned.

REFERENCES

[1] N. M. Newmark, "Effects of Earthquakes on Dams and Embankments," Fifth Rankin Lecture, *Geotechnique*, Vol.15, No.2, pp. 139–160, 1965.

[2] S. L. Kramer, M. W. Smith, "Modified Newmark Model for Seismic Displacements of Compliant Slopes," Jour. of *ASCE*, Vol.123, No.7, pp. 635–644, 1997.

[3] S. L. Kramer, N. W. Lindwall, "Dimensionality and Directionality Effects in Newmark Sliding Block Analyses," Jour. of *ASCE*, Vol.130, No.3, pp. 303–315, 2004.

[4] E. Zhai, M. Miyajima and M. Kitaura, "Nonlinear Amplifications of Vertical Ground Motions in the 1995 Hyogoken Nanbu Earthquake," Jour. of *JSCE*, No. 582/ Ⅲ-41, pp. 1–10, 1997.

[5] P. Dakoulas, G. Gazetas, "A Class of Inhomogeneous Shear Models for Seismic response of Dams and Embankments," *Soil Dynamics and Earthquake Engineering*, Vol.4, No.4, pp. 166–182, 1985.

[6] N. Yamashita, K. Takeuchi and Y. Hata, "The Effect of the Heterogeneity of the Ground Strength on Seismic Permanent of Embankments" (in Japanese with English abstract), Jour. Geotechnical Symposium, *JGS*, Vol.49, No.58, pp. 415–422, 2004.

[7] Y. Hata, N. Yamashita, "A Study on the Effect of Vertical Seismic Motion of Permanent Displacement of Embankments" (in Japanese with English abstract), Jour. *JSCE Earthquake Engineering*, Vol.28, 2005.

[8] Y. Nakamura, S. Nakano, "How to Estimate that Material Value at the Analysis of the Change in the Natural Frequency along with the Form of the Embankments" (in Japanese), Proc. of the 43rd *JSCE* annual meeting, Ⅰ-561, pp. 1172–1173, 1988.

[9] R. Y. Rubinstein, "Simulation and the Monte Carlo Method," *John Wiley & Sons, Inc.*, *New York*, 1981.

[10] N. Yamashita, H. Tanaka, "A Study of the Failure Behavior during the Earthquake of the Embankment with a Banquette in Consideration of the Heterogeneity of the Ground" (in Japanese with English abstract), Jour. *JSCE Earthquake Engineering*, Vol.27, No.115, 2003.

[11] J. M. Duncan, "Factors of Safety and Reliability in Geotechnical Engineering," Jour. of *ASCE*, Vol.125, No.4, pp.307–316, 2000.

[12] M. Tateyama, K. Horii, F. Tatsuoka and J. Koseki, "A Method of Seismic Stability Analysis of Earth Structure considering Vertical Ground Motion" (in Japanese), Proc. of the 56th *JSCE* annual meeting, Ⅲ-494, pp.988–989, 1995.

[13] H. R. Razaghi, E. Yanagisawa and M. Kazama, "An Approach to Seismic Permanent Displacement of Slopes," Jour. of *JSCE*, No.659/Ⅲ-52, pp. 1–16, 2000.

[14] H. R. Razaghi, E. Yanagisawa and M. Kazama, "Permanent Displacement Analysis of Circular Sliding Block during Shaking," Proc. of *IS-Shikoku*, Slope Stability, Vol.1, pp. 641–646, 1999.

[15] N. M. Newmark, "A Method of Computation for Structural Dynamics," Jour. of *ASCE*, Vol.85, No.EM3, pp. 67–94, 1959.

[16] S. Okamoto, "Introduction to Earthquake Engineering," University of Tokyo Press, pp.427-490, 1973.

[17] H. R. Razaghi, "Permanent Displacement Analysis of Slopes during Earthquake," Thesis submitted in partial fulfillment for the degree of Ph.D. in Engineering, Tohoku University, 2000.

[18] E. H. Vanmarcke, "Probabilistic Modeling of Soil Profiles," Jour. of *ASCE*, Vol.103, No.GT11, pp.1227–1246, 1977.

[19] R. M. Barcker, J. M. Duncan, K. B. Rojiani, P. S. Ooi, C. K. Tan and S. G. Kim, "Load Factor Design Criteria for Highway Structure Foundations," *NCHRP*, final report, No.24-4, 1991.

[20] T. Okimura, N. Torii and K. Tamada, "A Study on the Factors Affecting permanent Displacement of Fill Slope due to Earthquake" (in Japanese), Jour. of *Construction Engineering Research Institute Foundation*, No.45, pp. 147–152, 2003.

[21] T. Okimura, N. Torii, K. Tamada and R. Toyofuku, "Applicability of Acceleration Response Spectrum Intensity on Estimation for Seismic Permanent Displacement of Embankment" (in Japanese), Proc. of the 39th *JGS* annual meeting, No.1001, pp.1999–2000, 2004.

Seismic Risk Reduction in Venezuela: Recent Developments

Juan Murria[1]
[1]*Venezuelan Foundation for Seismological Research, FUNVISIS,,Caracas, Venezuela*
Centro de Investigación de Riesgos ,CIR, Universidad de Falcón, UDEFA, Punto Fijo, Venezuela

Abstract

Venezuela is seismic country. It is located in northern South America and its north central region contains the boundary of the Caribbean and South American plates. In this region live more than 80% of the population.
The Caracas July 1967 prompted the creation of the Venezuelan Foundation for Seismological Research (FUNVISIS) which has played a leading role in seismic risk reduction in Venezuela

The Venezuelan oil industry (PDVSA) has been instrumental in seismic risk reduction in the country, in particular in its own facilities

The hazards mapping project (PROYECTO AVILA), carried out by the Instituto Cartográfico Nacional Simón Bolívar" with financing of the World Bank was the first such effort in Venezuela and will serve as a pilot project for the rest of the country.

Seismic microzonation efforts have continued intermittently with projects in Caracas A FUNVISIS project has been already approved for the seismic microzonation of both Caracas and the city of Barquisimeto in western Venezuela.

The establishment in FUNVISIS in 1999 of the "Aula Sísmica (Seismic Classroom) Madeileinis Guzman so named after a teacher that lost her life while attempting to rescue her pupils during the 1997 Cariaco earthquake has given additional impetus to the educational aspects seismic risk reduction

It is hoped that seismic risk reduction activities will be continued - both by the public and private sectors - so as to continue to mitigate the negative effects that earthquakes have on the population, on sustainable development plans and on the built environment.

Keywords—*Hazards, mapping, microzonation, risk, seismic,, Venezuela*

INTRODUCTION

Venezuela is seismic country:. Located in northern South America, its north central region contains the boundary of the Caribbean and South American plates. In this region live more than 80% of its population.

The boundary of the South American and the Caribbean plates consists of a system of mainly right lateral strike-slip faults in the northern part of Venezuela composed by the (from west to east) the Bocono, Oca-Ancon, San Sebastian, La Victoria and El Pilar faults The relative movement of this fault system is in the order of 1 cm/year (Figure 1)-

Despite the only moderate seismicity of the country, compared to other Latin America and Caribbean countries, there is a high vulnerability due to the mountainous topography and local, soil conditions. (Schmitz and Gonzalez, 1992; Murria, 1992) Disastrous earthquakes have occurred in Venezuela in 1530, 1641, 1812, 1894, 1900, 1929 The Caracas 1967 earthquake emphasized the importance of soil structure interaction [1,2,3].

Fig 1: Caribbean and South American Plate Boundaries

BRIEF HISTORICAL REVIEW OF SEISMIC RISKS REDUCTION IN VENEZUELA

On the 27th of July 1967 the capital city of Caracas suffered a Ms 6.3 earthquake with its epicenter some 40 km north-northwest of Caracas in the Caribbean Sea,. The earthquake destroyed several buildings in the eastern neighborhoods of Caracas, particularly Altamira and Los Palos Grandes and in the coastal area of Caraballeda with more than 300 fatal victims, 2.000 wounded and material damages in excess of 120 million US dollars [4]

The Caracas 1967 attracted the attention of internationally known experts in seismology and seismic geology, earthquake engineering and earthquake geotechnics [4,5,6]

The very evening of July 27th the Minister of Public Works (MOP) appointed a Commission (COMISION PRESIDENCIAL PARA EL ESTUDIO DEL SISMO) charged with the task of studying the direct and indirect effects of the earthquake. A second commission was appointed late in 1967 to continue with these studies.

In July 27, 1972 - the fifth anniversary of the Caracas

earthquake, the Venezuelan Foundation for Seismological Research FUNVISIS was created to continue and extend the work of the activities of the aforementioned Commissions. [4]

THE VENEZUELAN FOUNDATION FOR SEISMOLOGICAL RESEARCH (FUNVISIS)

As stated above FUNVISIS was founded on July 27, 1972

The fifth anniversary of the Caracas July, 1967 earthquake

FUNVISIS is the governmental foundation charged with the promotion and execution of specialized research, and studies in the fields of seismology, earth science sand earthquake engineering with the aim of reducing seismic risk, as well as the dissemination of new knowledge and techniques for disaster risk reduction through its "Aula Sísmica" (Seismic Classroom).

FUNVISIS is also responsible for the installation, operation, maintenance and upgrading of both the seismological and strong motion nationwide networks.

FUNVISIS was created to continue and extend the work of the activities of the aforementioned Commissions. In July 27, 1972 - the fifth anniversary of the Caracas earthquake.

FUNVISIS, has from its beginning played - and is still very much playing - a leading role in seismic risk reduction efforts in Venezuela, including the first national inventory of geological risks [1] and the projects presently being carried out both in Caracas and in cities in the interior of the country.

The scientific and technical activities of FUNVISIS are carried out by five Departments Seismology, Earthquake engineering, Earth sciences, Instrumentation and the Center for Documentation and Information, CEDI. The heads of these departments report to a Directorate composed of the President, and the Technical and Administrative Directors

A Board of Directors (Consejo Directivo) oversees the activities of FUNVISIS. At the present time the Board of Directors of FUNVISIS is composed of representatives of the Ministries of Science and Technology and Education, Culture and Sports; Civil Protection and Disaster Management of the Ministry of the Interior and Justice; and FONACIT, the National Fund for Science, Technology and Innovation of the Ministry of Science and Technology. [4]

The main activities carried out by FUNVISIS can be summarized as follows [2]:

a.. The installation, operation, maintenance and upgrading of both the seismological and strong motion networks.

b.. Seismic hazard evaluation

c.. Applied geophysics:

+ Geodynamics
+ Seismic microzonation

· Instrumentation

· Seismic geology

+ Neotechtonics
+ Paleoseismology
+ Historical seismology
+ Geological risks

· Seismic risk prevention an mitigation

In order to carry out its seismic risk reduction activities, FUNVISIS has organized in the last several years workshops and seminars with the participation, among others, of Professor E.L. Quarantelli, Co-Founder of the Disaster Research Center; University of Delaware; Professor I. M. Idriss, then at the University of California, Davis; Dr. Michel Feuillard from the Seismological and Vulcanological Observatory La Soufriere in Guadeloupe; Drs. S. Herath and D. Dutta, Researchers,, INCEDE (now ICUS/INCEDE), Institute of Industrial Science, University of Tokyo; Mr. Yukio Aoshima, then Head of the Hydraulics Section of the Osaka Prefecture Engineering Department, and, Dr. Diego Ferrer, geotechnical consulting engineer, Caracas, among others. [7]

In addition of the activities carried out by CEDI, FUNVISIS has been carrying out in last several years a series of activities which, directly or indirectly are related to them pact on seismic risk reduction

The following is a partial listing of the most relevant of those of those activities:

Revision and updating of building codes

The first building codes were prepared by the Ministry of Public Works (MOP) in the early 1940, while the first seismic resistant building code was prepared by FUNVISIS and published by COVENIN/FUNVISIS as 1756-82 Norma Venezolanas antisísmicas,

This building code was revised in 1998 and issued as "Norma COVENIN 1756-98. Edificaciones sismorresistentes", which was, in turn, revised in 2001 and issued under the same name [8, 9, 10, 11] and which included Venezuela's latest seismic zonation map (Figure 2)

Historical seismology

In recent years FUNVISIS has given considerable impetus to historical seismicity activities as described below:

Personnel from FUNVISIS participated in organization of The International Course on the Protection of the Built Environment in Seismic Areas which was held at the Universidad Central de Venezuela (UCV) in Caracas in July 1999. [12

FUNVISIS also played a relevant role in the organization of and participation in the three INTERNATIONAL MEETINGS OF HISTORICAL SEISMOLOGY and in Caracas, July 2002. and is now in the process of organizing the fourth meeting to be held Venezuela at the. Universidad Centro Occidental Lisandro Alvarado in the city of Barquisimeto in western November 2005, in conjunction with the Fourth

International Symposium on Seismic Microzonation (See below)

These events attest to the increased interest that the study of both historical seismology and the preservation of the our built historical heritage has experienced not only in Venezuela but in Latin America, as indicated the variety of countries represented in both events [12,13]

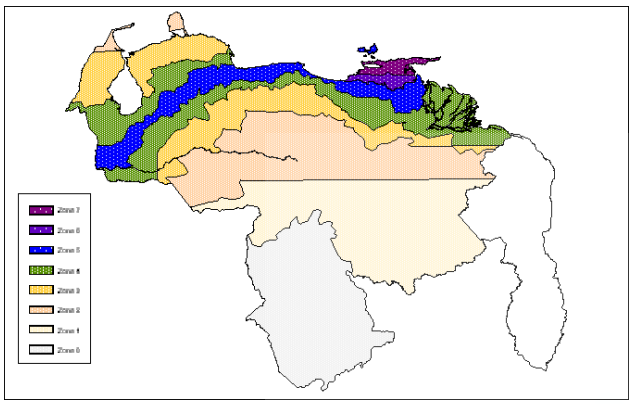

Fig 2 Seismic Zonification Map (1999)

The Aula Sísmica (Seismic Classroom) "Madeileinis Guzman"

The late Professor Flor Ferrer de Singer, wife of Professor Andre Singer, internationally known Venezuelan geomorphologist and university professor and at that time President of FUNVISIS were instrumental in the founding on 16 February 1998 of the "AULA SISMICA (SEISMIC CLASSROOM) "MADELEILIS GUZMAN", so named after a high school teacher who lost her life trying to save her pupils in the aftermath of he 1967 Cariaco, Eastern Venezuela earthquake.

The author of this paper had the honor of working with both Professors Singer in the early stages of the Aula Sísmica and is still involved in its activities and can attests to their dedication to the task of making FUNVISIS an efficient tool in seismic risk reduction in Venezuela

Since its foundation in February 1998 the Aula Sísmica has been in the forefront of educational and awareness activities in the Caracas metropolitan area as well as in some other cities in Venezuela., reaching not only school communities (students, parents and teachers), but also other communal organizations.

These activities are coordinated by two full time professors trained in seismic risk reduction education. They are assisted, as needed, by FUNVISIS scientists and engineers in the areas of expertise, as well as highly recognized experts from Venezuela and abroad.

In the period January 2000 to April 2004 a total of 51,713 persons have participated in the Aula Sísmica's activities both in FUNVISIS and on the road, including 11.495 teachers and school administrative personnel; 20.115 grammar and high school students, as well as 20103 members of community organizations [7]

THE CONTRIBUTION OF THE VENEZUELAN OIL INDUSTRY

Even though what follows in this section cannot be considered seismic microzonation in its most strict sense, it is nevertheless directed toward the seismic risk reduction, which is in fact the final purpose of seismic microzonation. [14, 15, 16]

The Venezuelan Oil Industry and Seismic Risk Reduction

The facilities of Venezuela's oil industry are located throughout Venezuela, and being Venezuela a seismic country, many of its facilities are located in areas of high to medium seismicity. As a consequence the Venezuelan oil industry has had special interest in seismic risk associated activities.

In 1991 Petróleos de Venezuela S.A. (PDVSA) the national oil company, initiated a project directed at the assessment and mitigation of the seismic risk in their critical facilities. This project was carried out by INTEVEP, PDVSA's R & D subsidiary with the cooperation of PDVSA's operating subsidiaries. The Venezuelan Foundation for Seismological Research, (FUNVISIS), as well as universities, consulting firms, and experts, both from Venezuela and abroad, actively participated in this project.. [17, 18]

Unfortunately, this project had to be terminated years later due to the economic situation of the country. Nevertheless, and spite of the above considerations, PDVSA has established as a company policy the concept of disaster risk reduction, particularly seismic risk reduction the for the design and construction of new critical facilities as well as for the operation and maintenance of their existing facilities.

The political and economic woes which have plagued PDVSA in the last several years have reduced its participation in seismic risk reduction activities.

Study of the 1989 Boca del Tocuyo Earthquakes

On April 30 and May 1, 1989 two earthquakes, Mb = 6.1 and Mb = 6.7 were felt in the Boca del Tocuyo area in western Venezuela (Figure 1). PDVSA decided to thoroughly investigate these earthquakes because of the resulting extensive liquefaction in spite of the relatively low magnitude and to the fact that these area is less than 25 Km from the Amuay and Cardón refineries. The liquefied soils in the Boca del Tocuyo area, moreover, have characteristics similar to those in the COLM The studies were coordinated by MARAVEN and INTEVEP with the cooperation of FUNVISIS. [19]

Study of the 1997 Cariaco Earthquake

On 9 July 1997 a Mw 6.9 earthquake struck the city of Cariaco in Easter Venezuela (Figure 1) and its surrounding area. The epicenter was located on the El Pilar fault in the easternmost section of the boundary between the Caribbean and the South American plate. [20, 21]

THE COSTA ORIENTAL OF LAKE MARACAIBO (COLM) PROTECTION SYSTEM

Brief historical summary

Oil production from comparatively shallow (300 to 1000 m), unconsolidated reservoirs has caused significant ground subsidence in the eastern coast of Lake Maracaibo in western Venezuela. This area is generally known as the Costa Oriental del Lago de Maracaibo (COLM) and it contains some of the oldest and most prolific oil fields in the world. (Figure 1)

Oil production began in 1926 and has continued uninterruptedly to date [23]. Ground subsidence was first detected in 1929 and has been monitored since then by means of biennial precision leveling surveys. Maximum cumulative subsidence has reached 6.2 m. as of April 2004 with rates that range between 5 cm/yr and 20 cm/yr.

As the original terrain consisted mostly of swamps and lagoons barely above lake level, both earthen coastal and inner (diversion) dikes as well as an elaborate drainage system had to be built in each of the three oilfields of Lagunillas, Tia Juana and Bachaquero to protect the lives of more than 60.000 inhabitants, the industrial facilities required to produce and/or handle - even as we write - more than 500.000 barrels of oil per day, the equivalent of ca. 40% of the country's total oil production in Venezuela

The gradual character of the ground subsidence has allowed for the staged construction of the coastal dikes and for the periodic upgrading of the drainage system and inner dikes. (Figure 3)

The COLM oilfields are located in an area of moderate seismicity but, initially, the coastal dikes were designed with no consideration for seismic forces. In 1966, however, Compañia Shell de Venezuela, the operator of the coastal protection system, decided to investigate the seismic behavior of the coastal dikes [24]

Seismic geology and seismicity studies carried out from 1968 onwards indicated the probability of dike failure due to the liquefaction in the foundation soils. In 1976 additional studies confirmed this probability and, as a result, mitigation measures were implemented, consisting of revision to the geometry of the dikes (downstream berm construction), and foundation soil improvement (stone piles) bringing the safety factor against dike failure to internationally accepted levels.

Seismic microzonation" in the COLM

Perhaps the only seismic microzonation project integrally developed in Venezuela has been the one related to the seismic integrity of The Costa Oriental of Lake Maracaibo Protection System [25,26,27] In this project: a problem was detected: The behavior of the earthen coastal protection dikes under the effects of an earthquake in this area of low to medium seismicity (Figure 2).Appropriate studies and investigations were carried out that resulted in the fact that the dikes foundation soils could liquefy under the appropriate seismic loading

As a consequence, mitigative measures were implemented that consisted, basically of:

- Modifications to the dike geometry (generally the construction of an inner berm
- Soil improvement by means of the implantation of stone compaction columns
- Modification to the outer (lakeside) riprap

The implementation of measures resulted in the reduction of the risk of a dyke failure - and consequent flooding - to acceptable levels.

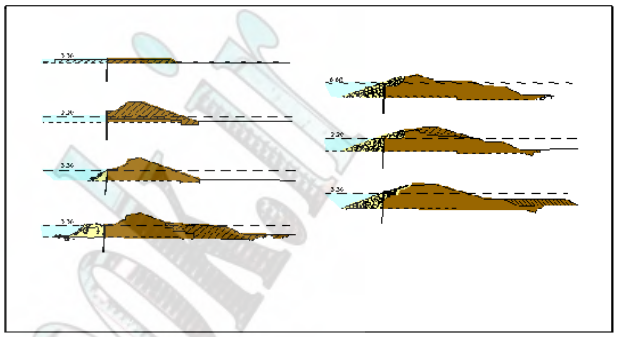

Fig 3 Progressive Rising of the Dikes Scale: 1:2000

The 2002 Technical Audit (TAG COLM)

In 2001, PDVSA PETROLEO, Lagunillas, undertook a project directed at a reevaluation of protection function of the COLM protection dikes. This author was retained by PDVSA to coordinate the audit activities consultant. A team of three well know Venezuelan and international experts were retained. to conform a Technical Audit Group. Politécnica de Valencia, 28-29 Febrero, 1992. [16] Their final report stated that, in general, the coastal dykes would appropriately fulfill their function of protecting human life and facilities in case of an earthquake. The Technical Audit Group (TAG) additionally recommended a series of studies and research activities directed at confirming their findings. These recommendations, however, have only been partially carried out due to the political problems that affected the oil industry in December 2002, immediately after the TAG COLM submitted their report [16]

SEISMIC MICROZONATION PROJECTS IN VENEZUELA

The first seismic microzonation efforts in Venezuela go back to the early 70's, as a consequence of the 1967 Caracas earthquake, in the cities of Caracas and Mérida with varying degrees of success [28,29,30].

The late 80's saw a resurgence in the interest in seismic microzonation projects as evidenced by projects initiated, among others, by PDVSA through INTEVEP, its research and development subsidiary together with its operating companies, with the participation of FUNVISIS and several Venezuelan universities. [31,32,33,34,35].

At the present time efforts are being made by FUNVISIS (the Venezuelan Foundation for Seismological

Research) and other private and public entities to implement seismic microzonation projects both in Caracas and other cities located in seismic regions with the cooperation of Japan, France and international organizations. [36]

Ongoing projects

FUNVISIS has received government funding to carry out the seismic microzonation of Caracas and Barquisimeto

The project will include from the description of the subsoil conditions to the delimitation of areas with different soil responses, as well as the expected behavior therein so as to be able to prepare recommendations on building typology for the different micro zones.

In addition FUNVISIS is a member of the "Comisión Nacional de Gestión de Riesgos" (National Commission for Risk Management) charged with the task of implementing the " Sistema Nacional de Prevención de Riesgos y Protección Civil" (National System for Risk Prevention and Civil Protection) and is striving for the inclusion of distaste risk reduction in Venezuela - seismic risk for the principal cities located in high to moderate seismic risk. [36]

International Colloquia on Seismic Microzonation

FUNVISIS has been instrumental in the organization of the INTERNATIONAL COLLOQUIA ON SEISMIC MICROZONATION. The first Colloquium was held in Cardón in western Venezuela in November 1993. The second took place in Cumaná in eastern Venezuela in June 1995, while the third was held in Caracas in July 2002.

The fourth Colloquium is programmed to take place in Barquisimeto (western Venezuela) in November 2005, together with the 4th INTERNATIONAL MEETING ON HISTORICAL SEISMOLOGY... [36]

FUNVISIS in recent years has been working the Greater Caracas area in local seismic risk reduction projects that include in specific instances seismic microzonation. [37].

The Contribution of the Universidad de Los Andes

The Universidad de Los Andes (ULA) has its main campus in the city of Mérida, which is located literally on top of the Bocono Fault one of the most seismically active faults in Venezuela (Figures 1 and 2)

The Laboratorio de Geofisica of ULA has been very active in seismic research activities.

The Contribution of the Univarsidad de Oriente(UDO)

The main campus of the Universidad de Oriente (UDO) is located in the city of Cumana, capital of the State of Sucre in eastern Venezuela, in the most active seismic region of Venezuela due to the presence of the El Pilar part, the easternmost section of the boundary between the South American and Caribbean plates (Figures 1 and 2)

The Laboratorio de Sismología was (Seismological Center) was founded in 1976 and has its headquarters in UDO's Cumana campus.

Activities of the Laboratorio include the operation and maintenance of the local seismological network.

The Laboratorio was also an important factor of FUNPRIS, the Foundation for the Prevention of Seismic risk in the Sucre State

At the present time the Laboratorio is which involved in a seismic microzonation project of the city of Cumana was initiated but was not completed in 1995-FUNVISIS is actively cooperating in this project.

The Hazards Mapping Project (PROYECYO AVILA)

In the aftermaths of the hydro meteorological disasters that affected a large portion of the Venezuelan Caribbean coast in December 1999, it was decided by the Venezuelan government via the Ministry of Environment and Natural Resources (MARN) to implement a protect directed at the evaluation and mapping of the various hazards geological, seismic, hydro meteorological technical) that affect the metropolitan area of Caracas and part of the coastal area of State of Vargas. This project was partially financed by the World Bank and was carried out by the Instituto Geográfico Venezolano Simón Bolivar (IGVSB), the Venezuelan geographic Institute in charge of geographic, geodetic and cartography activities in Venezuela

The Avila Project was limited to hazard assessment but it can be considered an s a very important first step toward risk microzonation projects, including seismic microzonation. Which were coordinated by FUNVISIS [38]

SOCIAL, POLITICAL, ECONOMIC AND CULTURAL ASPECTS OF SEISMIC RISK REDUCTION IN VENEZUELA

The lack of success of many of the seismic risk reduction projects initiated in the last several years in Venezuela cannot and should not be attributed to the lack of technical and scientific expertise as there exists in Venezuela sufficient knowledge and information about the techniques and procedures that have been successfully used elsewhere in the world in the implementation of seismic risk reduction projects.

In this writer's opinion the main drawback to the successful implementation of seismic risk reduction projects in Venezuela - and elsewhere in the world for that matter - are of a social, political, cultural and economic nature rather than the purely scientific and engineering aspects.

There exist in Venezuela engineers and scientists well prepared to undertake these types of projects for which, in addition, there are financial and financial resources available internationally which have not been properly utilized.

Another very important factor contributing to the above mentioned lack of success has been the apparent failure of the scientific and technical community to "sell" these types of projects to the decision makers at the

different levels of government (national, regional, state, municipality and city) and to the leaders of private enterprise,

Efforts should continue to be made by the scientific and engineering community to convince decision makers - both public and private - that sound the implementation of risk reduction projects s are a valid instrument to mitigate the negative effects that earthquakes have both on the population and on the built environment. [30, 39]

CONCLUSIONS

Seismic risk reduction activities have experiences a new impetus sin Venezuela in the last few years as indicated above FUNVISIS have been in the forefront of these activities The Venezuelan oil industry has played an important role in seismic risk reduction activities but, unfortunately, recent problems both in the country and in the industry have considerably reduced their efforts in this respect.

ACKNOWLEDGEMENTS

I would like to acknowledge the following FUNVISIS staff assistance given to this writer in the preparation of this paper Dr. Michael Schmitz and Mr.. Daniel Moreno

In addition I would like to thank the staff of the United Nations International Strategy fro Disaster Reduction in Geneva, Switzerland and San Jose de Costa Rica for the partial funding for my participation in this Satellite Conference..

REFERENCES

[1] Singer, A., C. Rojas and M. Lugo. Inventario Nacional de Riesgos Geológicos, Estado Preliminar. Fundación Venezolana de Investigaciones Sismológicas (FUNVISIS), Caracas, 122 p, 1982..

[2] FUNVISIS (2005) www.funvisis. gob. ve

[3] FUNVISIS, ¿Qué es FUNVISIS? Booklet prepared by FUNVISIS, Caracas. (No date given)

[4] FUNVISIS.(1978) Segunda fase del Estudio del Sismo ocurrido en Caracas el 19 de julio de 1967, Ministerio de Obras Publicas, Comisión Presidencial para el Estudio del Sismo, FUNVISIS, Caracas, Venezuela, Volumen A, pp. 517 1978

[5] Seed, H.B., I.M. Idriss, and H. Dezfulian. "Relationship between soil conditions and building damage in the Caracas earthquake of July, 19, 1967. EERC Report 70-2, Berkeley, California, pp.40, 1970

[6] Weston Geotechnical Engineering International WGEI (1969) l"Investigaciones sísmicas en el valle de Caracas y en el Litoral Central bajo la Planificación y supervisión de la Comisión Presidencial para el Estudio del Sismo, pp. 1-32 1969

[7] Moreno, D. Personal communication, March, 2005

[8] COVENIN/FUNVISIS. 2001. Norma COVENIN 1756-98 (Revisión. 2001). Edificaciones sismorresistentes, Caracas.

[9] COVENIN/FUNVISIS. 1999. Norma COVENIN 1756-98. Edificaciones sismorresistentes, Caracas.

[10] COVENIN/FUNVISIS 1982. Norma Venezolana para edificaciones antisísmicas, 1756-82, Caracas.

[11] COVENIN.1981. Normas para edificaciones antisísmicas. (Norma COVENIN 1754-81) Caracas, 64 p. III Congreso Venezolano de Sismología e Ingeniería Sísmica, Caracas.

[12] Guevara, L..T. (1999) "Introducción" in Memorias, Ponencias presentadas en el Curso Internacional protección del patrimonio construido en zonas sísmicas, Comisión de Estudios de Postgrado de la Facultad de Arquitectura. y Urbanismo de la Universidad. Central de Venezuela, Caracas, 26-30 July 1999, L. Guevara, Compiler

[13] FUNVISIS 2002 "Introducción" III Coloquio sobre Microzonificación Sísmica y III Jornadas de Sismología Histórica, Caracas, 18-20 July, 2002, Serie Técnica No. 1-2002, Fundación Venezolana de Investigaciones Sismológicas, 2002.

[14] Murria,, J. 1995. "La evaluación y mitigación de riesgo sísmico en las instalaciones de la industria petrolera venezolana" in: Taller Latinoamericano Reducción de los Efectos de los Desastres Naturales en la Infraestructura Energética, San José, Costa Rica.

[15] Murria, J. (1992).. Desarrollos Recientes en la Evaluación del Riesgo Sísmico en el Occidente de Venezuela. Conferencia en el Seminario "El Riesgo Sísmico: Experiencia Nacional e Internacional'como parte del Programa de Master "Técnicas de Prevención y Gestión de Emergencias en Entornos Urbanos," Universidad Politécnica de Valencia, 28-29 Febrero, 1992.

[16] TAG. COLM 2002 Technical Audit Group (2002). Report " INTEGRITY OF THE LAKE MARACAIBO COSTA ORIENTAL PROTECTION SYSTEM", November 2002. Submitted to PDVSA OCCIDENTE, Lagunillas, Venezuela.

[17] PDVSA "Planificación de Evaluación de Riesgos Mayores para la IPPCN", Internal Report of the "Coordinación de Protección Integral", September 1987, 61 p.

[18] PDVSA Conservation and protection of the environment and industrial safety are two keystones of the petroleum industry's activities. Published by Petróleos de Venezuela's Public Affairs Department, Caracas, Venezuela, 40 p., (1995)..

[19] Murria, J.; Echezuria, H.; Malavé, G.; de Santis, F. & Audemard, F. 1994. The 1989 Boca del Tocuyo Venezuela, Earthquake. Performance of Ground and Soil Structures during earthquakes. In: 13th Int. Conf. of Soil Mechanics and Foundation Eng., New Delhi, 1994

[20] FUNVISIS 1997. Evaluación preliminar del sismo de Cariaco del 09 de Julio de 1997., Estado Sucre, Venezuela (versión revisada). FUNVISIS. 123 pp + 5 anexos.

[21] Gonzalez, J. and M. Schmitz, M. Masali, F.; De S antis, F(1999). Characterization of the soils in Cariaco using seismic refraction, microtremor measurements & geotechnical information. In: AGU Spring Meeting, May 31-June 4, 1999, Boston, S228.

[22] Murria, J. and A. Hernandez (1999) Seismological, geological geotechnical and engineering of the July 9, 1997 Cariaco, Venezuela earthquake in Proc. of the Second Int.l Conf. On Earthquake Geotech. Rng., Lisboa, Portugal 21-25 June 1999, pp 765-769..

[23] Martínez, A, 1986. Cronología del Petróleo Venezolano, Ediciones de CEPET, 1986, Caracas, 767 p.

[24] Murria, J.(1991) Earthquake countermeasures for the Costa Oriental of Lake Maracaibo, Venezuela. Proc. of the United States-Latin American Partnership to Enhance Cooperation in Earthquake Hazard Reduction, a conference conducted by the Central United States

Earthquake Consortium (CUSEC), December 4-6, 1991, Indianapolis,

[25] Sully, J. P and J. Murria (1992) Microzonificación Sísmica en la Costa Oriental del Lago de Maracaibo. Comunicaciones del 1er. Simposio Iberoamericano sobre Técnicas Aplicadas a la Gestión de Emergencias para la Reducción de Desastres Naturales. Valencia, España, 1-4 de Diciembre de 1992.

[26] Sully, J.P., O. Morales, E. Gajardo, J. Murria and J. Abi Saab (1992) Microzonation studies for Lake Maracaibo coastal protection system. Proc. of the Conf. on Recent Advances in Geotech. Eng., St. Louis, MI, U.S.A., 1995.

[27] .Sully, J.P. y E. Gajardo, J. Murria, J. Abi Saab, Seismic Zonation for COLM Dykes. Proc. Caribbean Conf. on Natural Hazards: Volcanoes, Earthquakes, Windstorms, and Floods. St. Augustine, Trinidad.. Oct. 11- 1993

[28] Alonso, J. L (1976) "Microzonificación sísmica de Mérida. Espectros sísmicos, coeficientes de corte basal diseño y recomendaciones finales". Ministerio de Obras Publicas, Oficina Especial del Sismo, Caracas, Nov. 1976.6.

[29] Alonso, J.L. and Urbina, (1978) L. « A new microzonation technique for design purposes". Proc. of the 2nd Int. Conf. on Microzonation, Vol. 1, San Francisco, CA, USA, 1978

[30] Murria, J. "Seismic geotechnical hazards zonation in Venezuela. Recent developments ". Proc. of IS/Tokyo '95. The First Int. Conf. on Earthquake. Geotech. Eng., Tokyo, pp. 647-653 14-16 November 1995.

[31] Schmitz, M. and J. Gonzalez (1992) "A review on seismic microzonation studies in Venezuela and changes in the new seismic building code" Contribution to Workshop "Joint study on Seismic Microzonation in Earthquake Countries", Yohokama, December 5, 1998.

[32] ENOMOTO, T.; SCHMITZ, M.; MATSUDA, I.; ABEKI, N.; MASAKI, K.; NAVARRO, M.; ROCABADO, V. & SÁNCHEZ, A. 2000. Seismic risk assessment using soil dynamic characteristics in Caracas, Venezuela. In: 6th International Conference on Seismic Zonation, Palm Springs, Nov. 12-15, 2000,

[33] Murria, J. (1992).. Desarrollos Recientes en la Evaluación del Riesgo Sísmico en el Occidente de Venezuela. Conferencia en el Seminario "El Riesgo Sísmico: Experiencia Nacional e Internacional'como parte del Programa de Master "Técnicas de Prevención y Gestión de Emergencias en Entornos Urbanos," Universidad Politécnica de Valencia, 28-29 Febrero, 1992.

[34] Murria, J. "Seismic geotechnical hazards zonation in Venezuela". Proc. of 15-Tokyo '95/The First Int. Conf. on Earthquake. Geotech. Eng., Tokyo, pp. 647-653 14-16 November 1995

[35] Schmitz, M. and J. Gonzalez (1992) "A review on seismic microzonation studies in Venezuela and changes in the new seismic building code" Contribution to Workshop "Joint study on Seismic Microzonation in Earthquake Countries", Yohokama, December 5, 1998.

[36] Schmitz, M. (2005) personal communication

[37] Gonzalez, J. and T. Enomoto, T.; Navarro, M.; Abeki. And M. Schmitz M (2001). Study on natural period of buildings estimated by microtremor measurements for seismic disaster risk evaluation in Caracas, Venezuela. In: 5th European conference on Structural Dynamics, 2-5 September 2002, Muenchen.

[38] IGVSB, 2003 PROYECTO AVILA, CD ROM prepared by the National Program for Environmental Management, Instituto Geográfico Venezolano Simón Bolívar, Caracas, Venezuela, 2003

[39] Murria, J.(2002) Aspectos sociales, culturales, económicos y políticos de la microzonificación sísmica en Venezuela in Foro de discusión, Memorias III COLOQUIO SOBRE MICROZONIFICACION SÍSMICA, Camino hacia una menor vulnerabilidad, Caracas, 13 -l 18 June 2002

A Hidden Active Fault in Osaka-Sakuwagawa Flexure Fault-

Y. Iwasaki
Geo Research Institute, Japan

Abstract

This paper presents a hidden fault in Osaka area. Based upon the estimated fault by boring log section, we have carried out seismic study and confirmed the active fault underneath the horizontal formation of alluvial layer. Seismic profile does not give enough resolutions near the top surface. Boring log section based upon computerized data system had provided to supply the necessary surface structure of the geology. Analysis showed that the fault movement in the recent 0.5 my became faster and is 200m/1my at present in average. 4-5m fault movement is the restored amount that should be released when the next movement takes place.

Keywords— *Active Fault, Hidden Fault, Fault Displacement, Osaka*

INTRODUCTION

Osaka area locates at the eastern side of Osaka Basin that has been created by the neotectonic movement in the past Quaternary period.

Study based upon geomorphology has suggested that the straight line of the west side of the Uemachi Terrace was caused by a fault as shown in Fig.1.

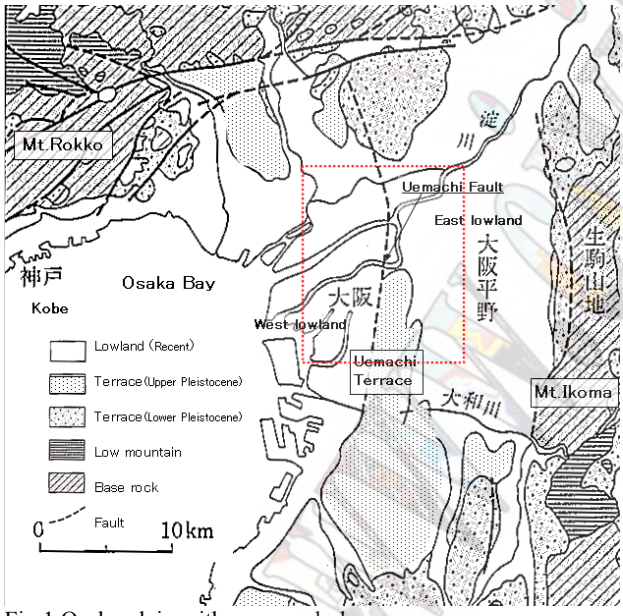

Fig.1 Osaka plain with geomorphology

In the 1960', several deep boring were performed to study settlement problems in Osaka region. A systematic geological study started to clarify geological and geotechnical characteristics.

It was found that the geological condition of Osaka plain consists alternation of sandy and clayey layers of more than 500m in thickness. Uemachi terrace was

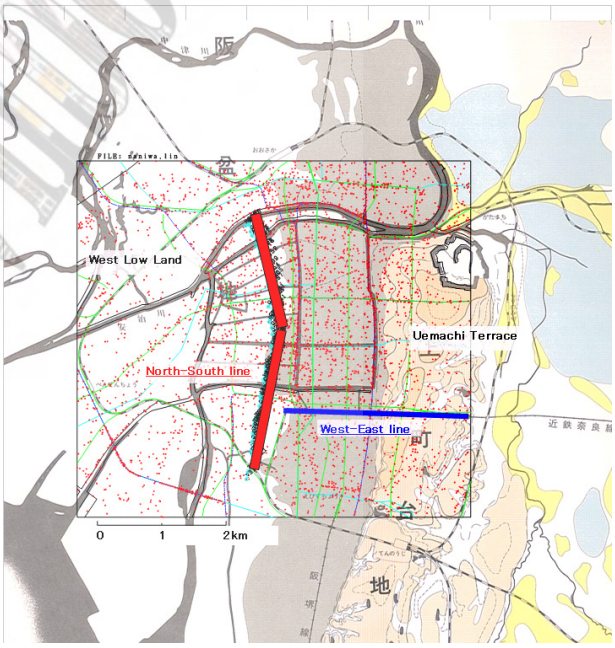

Fig.3

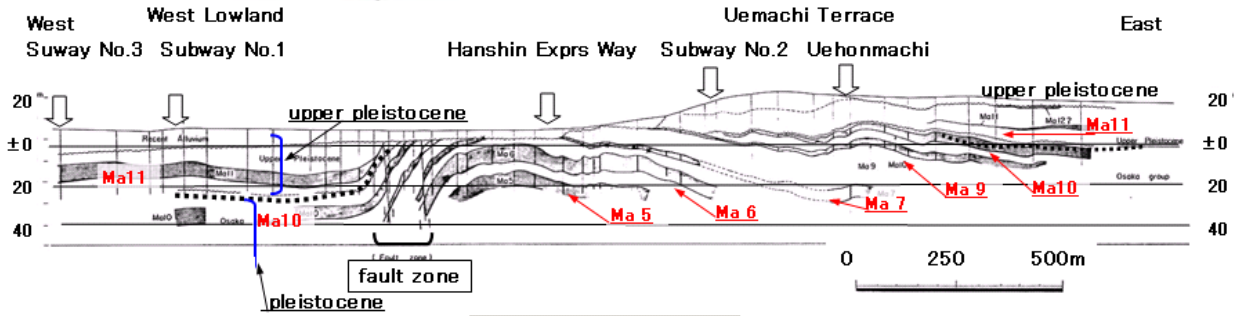

Fig.2 West-East section (from Takenaka and Huzita [1])

confirmed as rifted as about 500m by comparing the geological samples between west lowland and Uemachi Terrace.

GEOTECHNICAL BORING NEAR THE FAULT

In 1970, subway construction at Uemachi Terrace had provided a continuous trench to see the west-east section near the Uemachi fault. The boring log sections were collected and geological structures were carefully discussed.

The diagrammatic section as shown in Fig.2 revealed the west edge of the Uemachi Terrace located several hundreds meters away from the location of the fault identified by the boring logs.

GEOTECHNICAL BORING SECTION IN WEST LOW- LAND OSAKA IN NORTH-SOUTH LINE

Based upon boring log data, we become rather easy to obtain boring section in Osaka area. Fig. 3 shows the central part of Osaka with two lines for boring sections. West east line is shown in Fig.2. North south section is

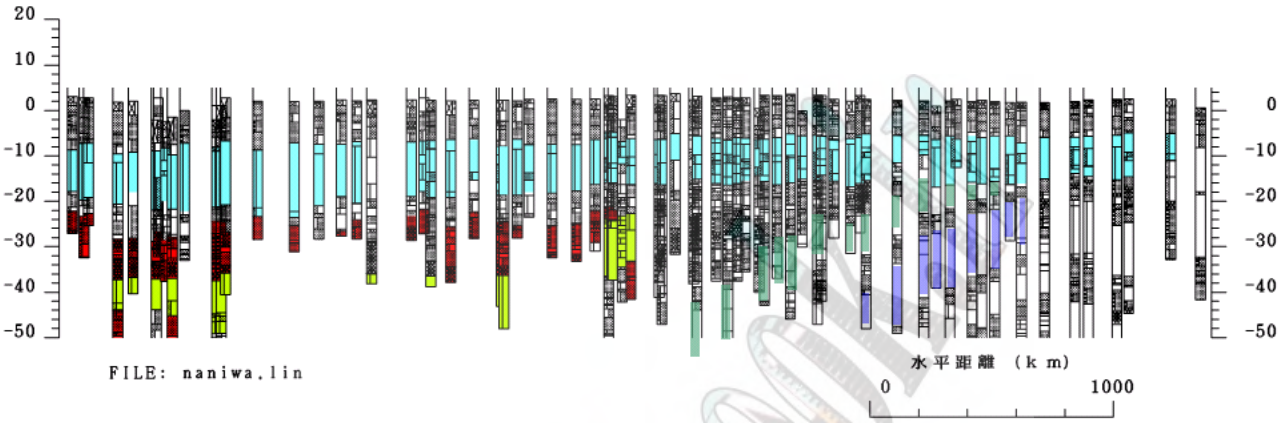

Fig.4 Boring log section along North-South line in Osaka

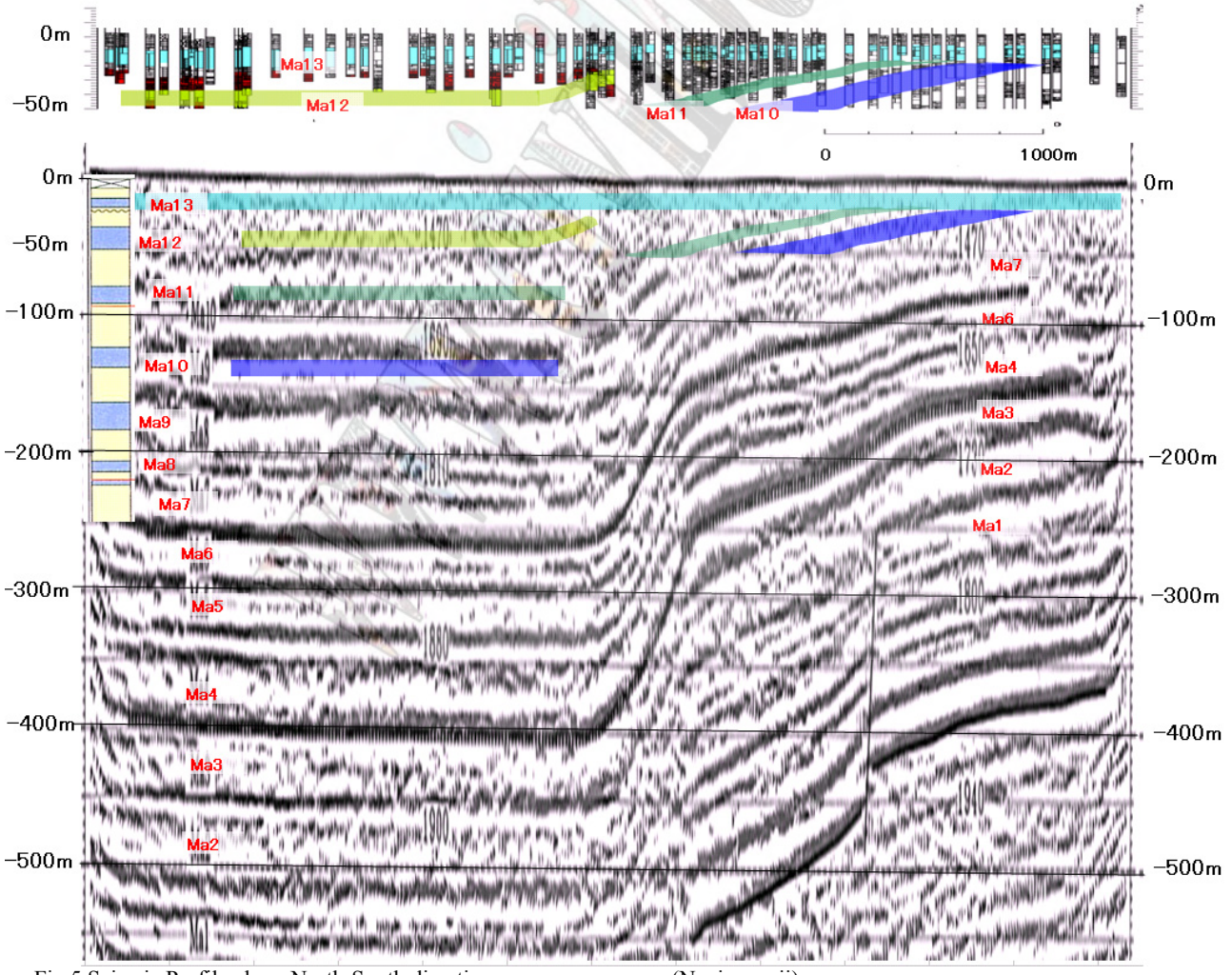

Fig.5 Seismic Profile along North-South direction (Naniwa-suji)

shown in Fig.4. The geological section in Fig.4 is very similar to Fig.2.

SEISMIC SECTION IN OSAKA CITY IN NORTH-SOUTH DIRECTION

The boring section as shown in Fig.4 strongly suggests the existence of a fault. After the Kobe earthquake, we had a chance to carry out the seismic survey along the boring log section. The seismic section is shown in Fig.5.

We found the inclined structure in the left side of Fig.4 is due to the flexure that was formed by fault movement after these formations deposited. The fault is named "Sakuragawa flexure."We also noticed that the top deposits in Holocene does little effect by the faault movement.

The upper portion of seismic profile becomes unclear to identify the formations. Here, we can supply the geotechnical boring log sections to supply the seismic profile with formation structures of Ma 12 and Ma11.

FAULT MOVEMENT BASED UPON LAYER STRUCTURE

The marine deposit in Osaka was named as Ma and number like Ma13, Ma12, ----- Ma1,and Ma0. These marine deposits corresponds with the period of warm climate when the depth of the bay becomes deep, say more than 5m, and the depositional environment for clay was satisfied.

Based upon the global trend of paleo climate determined in the Atlantic sea as shown in Fig.6, we may estimate the depositional period for each marine clay formation.

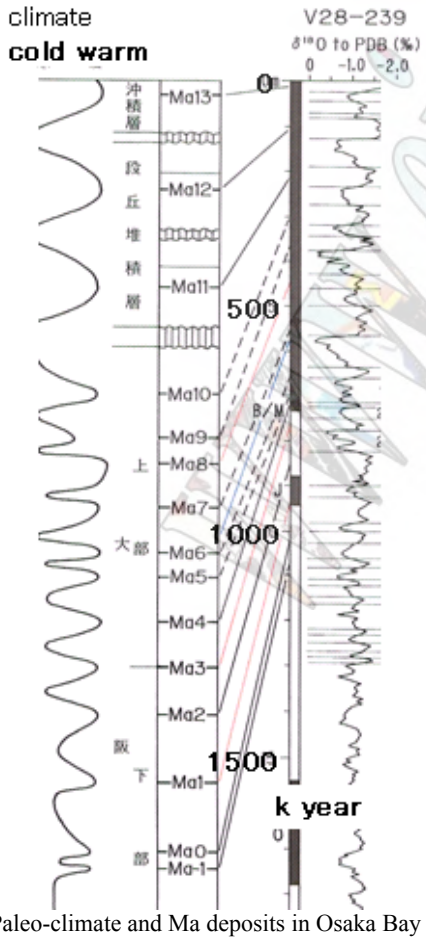

Fig.6 Paleo-climate and Ma deposits in Osaka Bay (by Ichihara [2])

Table-1 Deposited age and present depth for each Ma layer

	Deposited Age	Depth (OP−m)	
	(k year BP)	north side	south side
Ma13		15	15
Ma12	97.8	46	
Ma11	217.4	82	44
Ma10	326.1	126	68
Ma 9	413.0	168	88
Ma 8	489.1	202	108
Ma 7	597.8	228	128
Ma 6	684.8	260	152
Ma 5	782.6	296	176
Ma 4	847.8	356	220
Ma 3	945.7	408	268
Ma 2	1,076.1	468	308

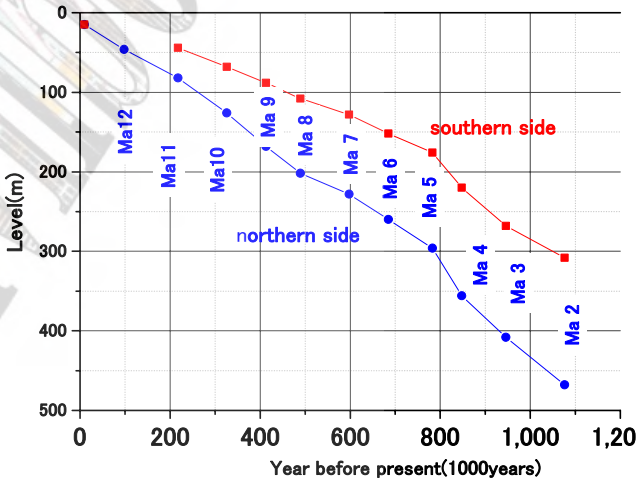

Fig.7 Present Depth of each Ma formation and Deposited Age

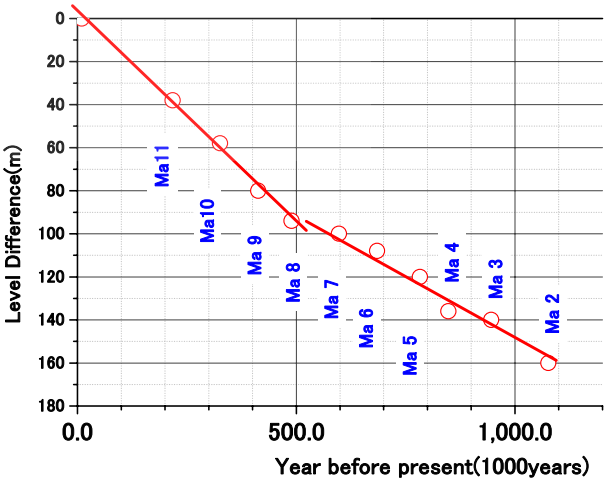

Fig. 8 level difference between North and South sides

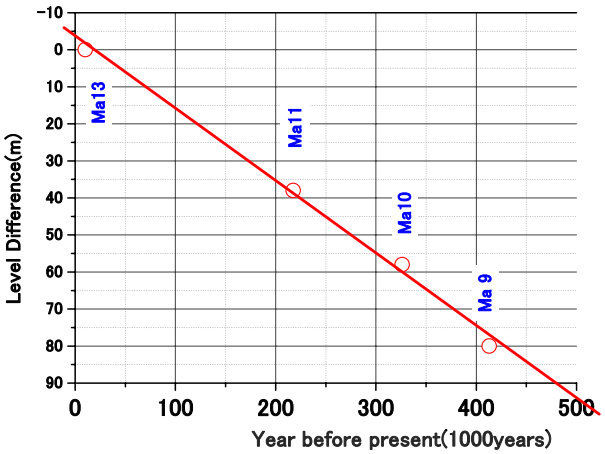

Fig.9 Level difference vs. Deposited age(enlarged)

If we take the warmest time as the representative period for each formation, the estimated deposited time before present is shown in Table-1.

Fig.7 shows relation between the deposited age and the present depth for both sides of the fault. When each Ma formation deposited, the level of the formation is almost the same as Ma13 of the present alluvial clay deposit.

The depth of the same Ma layer in the north side is deeper than those in the south side. The difference of the north and south side is the result of the fault movement. If the difference between both sides is constant, the fault movement took place after the concerned formations had deposited. In Fig.7, the difference of the both sides is not constant but increasing with the deposited age.

In Fig.8, the difference of level between two sides is shown.

The figure shows the accumulated fault movement of the Sakuragawa flexure.

It is interesting to notice that the rate of the fault movement becomes rather fast in the past 500kyears of 100m/500k years.

Fig.9 shows the same as Fig.8 enlarged to see the present trend of the fault movement.

If we assume the same trend of the fault movement in the past 500,000 years, we could see the present fault movement is -4-5m, which means that the fault movement is being sustained somehow at the moment. However, this fault movement is ready to release at any time.

CONCLUSIONS

Conbination between seismic profile provided by geophysics and boring log profiles by geotechnical science together with quaternary geology in Osaka is useful to evaluate the nature of the fault in the urbanized Osaka.

We do not know the precise return peiod of the Sakuragawa flexure at the moment. We know the present situation of the fault is 4-5m to move awainting for the big one.

REFERENCES

[1] Takenaka,"geologic structure of Osaka Basin,"Report on land Subsidence in Osaka, Editorial Committee for technical report on Osaka Land Subsidense, 1969, p83

[2] Ichihara, Boudary problem of Pliocene and Pleistocene, Urban KUBOTA, March, 2001, p39